Exploring the Dynamic Radio Sky: The Search for Slow Transients with the VLA

Thesis by

Kunal P. Mooley

In Partial Fulfillment of the Requirements

for the Degree of

Doctor of Philosophy

California Institute of Technology

Pasadena, California

2015

(Defended 25 Feb 2015)

Dedicated to my advisors:

Shrinivas “India’s new SRK” Kulkarni
who showed me astronomy in the form of a business model.

Dale “Morning person” Frail
who showed me the big picture, encouraged me, and took me as an
apprentice when I was a fledgling in radio astronomy.

Gregg “Three G” Hallinan
who, as a mentor and friend, worked tirelessly and patiently with me,
and trained me on large and ambitious projects.

Steven “Stevil” Myers
who made me think about the nitty gritty
of radio interferometry.

Acknowledgments

Although this thesis is certified as being my own work, I confess that it is no less than a massive team effort. I seem to have contributed the least and yet, somehow, the Ph.D. degree has been conferred upon me. If it weren't for Krishna, the cause of all causes[1], there wouldn't have been the myriad of wonders in our Universe to keep all the astronomers occupied!

The ideas that flow through my mind right now are shaped by the past. Hence, this section would be incomplete without acknowledging the events from the days gone by. It is the relentless support, encouragement, and guidance of my parents and my brother that awakened the astronomer within me during my childhood. Through them, I learned that the sky is not the limit for human achievement; there is much more beyond it. The countless memories of my childhood that I wish to reproduce here will be much of a thesis by itself. With apologies, therefore, I simply pause and remember the joyous moments spent with my dear relatives and childhood friends; memories that I carry around with me all the time.

I would like to fast forward and mention about the two special years of my life at IIT Bombay. These were two very eventful years when I also worked towards my Masters degree in physics. From a person who liked to always be within himself, IIT Bombay quite rapidly transformed me into a multi-faceted, sociable personality. This institution gave me some of the closest friends that I now have. IIT Bombay is also the place where I met Yamini, who has really been the woman behind my success, and has, time and again, proved herself to be my better half.

My time at Caltech has similarly been very special. I still quite vividly remember my first visit to Caltech almost six years ago — my informal meetings with Mark Kamionkowski, Andrew Blain, Lynne Hillenbrand, Shri Kulkarni, and Mansi Kasliwal — which ultimately got me admitted to Caltech! Throughout my Ph.D., I have admired the enthusiasm and hard work of the other Caltech astronomy graduate students. I am indebted to them for making Cahill such a lively and cheerful work environment. My batchmates, Matthew Schenker and Ke Zhang, with whom I have spent some of my most wonderful moments, receive a special mention. Gwen Rudie and Laura Perez have been like Ph.D. role models to me. Shriharsh Tendulkar and Varun Bhalerao have been my mentors and friends. Ryan Trainor continues to be my best student of Bollywood dance. One day, his enthusiasm and diligence will help him reach great heights, I'm sure. I feel kinship with Sebastian, Jackie, and Allison, who have been my office mates for the past three years. The time that I have

[1] *sarva karana karanam* (Brahma Samhita Ch. 5)

spent with my buddies playing soccer will be missed. Lastly, I cannot thank Gregg Hallinan and my fellow graduate students enough for organizing for me the best farewell party ever! I express my gratitude to Jackie, Marin, and Sebastian, for getting together the dance troupe (photograph shown below) at the farewell.

During my time at Caltech, I have certainly grown intellectually, thanks to the Astronomy professors who have been a source of unlimited inspiration and advice. I am grateful to Gregg Hallinan, Shri Kulkarni, Dale Frail, and Steven Myers, for giving me a wonderful Ph.D. thesis to work on. Thanks to Sterl Phinney, Lynne Hillenbrand, and Tom Prince for serving on the committees for my candidacy examination and the thesis defense. I have learned a great deal about research from Stephen Bourke, Dom Walton, Talvikki Hovatta, and Andrea Isella. The optical observing that I did during my Ph.D. has been fun, thanks to the staff at Caltech Optical Observatories, and the Palomar and Keck observing sites. I extend sincere thanks to Gita Patel, Gina Armas, Judith Mack, Althea Keith, and Sandy Lester, for their tireless assistance with administrative matters, and to Patrick Shopbell and Anu Mahabal for extensive help with computing facilities.

I fondly remember the time that I spent at NRAO in Socorro as a Grote Reber fellow. The staff at NRAO have been responsible for making me an expert user of the Jansky VLA. Drew and Heidi Medlin's stargazing sessions and breathtaking photography have both inspired and fascinated me.

I would like to end with a few useful quotes which I came across during my Ph.D.

SRK: "*In nature, there are innumerable factors contributing to any physical process. The real skill of a scientist is in identifying and studying the most dominant factor(s).*"

Chris Carilli: "*In every research paper you submit, there will be some amount of incorrect information. You just have to accept it. This is part of the growth of human knowledge.*"

Milan Bogosavljevic: "*Make sure that you choose an advisor who is too busy. That way you will be able to take a break whenever you wish, without the advisor knowing it*"

SRK: "*Major breakthroughs in astronomy are driven not only by curiosity and the ability of human beings in understanding the cosmos, but equally so by the advances technology and computing.*"

Abstract

While synoptic surveys in the optical and at high energies have revealed a rich discovery phase space of slow transients, a similar yield is still awaited in the radio. Majority of the past blind surveys, carried out with radio interferometers, have suffered from a low yield of slow transients, ambiguous transient classifications, and contamination by false positives. The newly-refurbished Karl G. Jansky Array (Jansky VLA) offers wider bandwidths for accurate RFI excision as well as substantially-improved sensitivity and survey speed compared with the old VLA. The Jansky VLA thus eliminates the pitfalls of interferometric transient search by facilitating sensitive, wide-field, and near-real-time radio surveys and enabling a systematic exploration of the dynamic radio sky. This thesis aims at carrying out blind Jansky VLA surveys for characterizing the radio variable and transient sources at frequencies of a few GHz and on timescales between days and years. Through joint radio and optical surveys, the thesis addresses outstanding questions pertaining to the rates of slow radio transients (e.g. radio supernovae, tidal disruption events, binary neutron star mergers, stellar flares, etc.), the false-positive foreground relevant for the radio and optical counterpart searches of gravitational wave sources, and the beaming factor of gamma-ray bursts. The need for rapid processing of the Jansky VLA data and near-real-time radio transient search has enabled the development of state-of-the-art software infrastructure. This thesis has successfully demonstrated the Jansky VLA as a powerful transient search instrument, and it serves as a pathfinder for the transient surveys planned for the SKA-mid pathfinder facilities, viz. ASKAP, MeerKAT, and WSRT/Apertif.

Contents

Acknowledgments **iv**

Abstract **vi**

1 Introduction **1**

1.1 Slow Radio Transient Phenomena And Physical Mechanisms for Transient Emission 2

1.1.1 Extragalactic Phenomena 3

1.1.1.1 Active Galactic Nuclei 3

1.1.1.2 Supernovae 4

1.1.1.3 Beamed Afterglows from Long and Short γ-ray Bursts and their Orphan Counterparts 8

1.1.1.4 Non-thermal Tidal Disruption Events 11

1.1.2 Galactic Phenomena 14

1.1.2.1 Active Stars 14

1.1.2.2 Active Binaries 14

1.1.2.3 X-ray Binaries 14

1.1.2.4 Cataclysmic Variables 17

1.1.2.5 Pulsars 17

1.1.2.6 Magnetars 19

1.1.2.7 Brown Dwarfs 19

1.1.2.8 Novae 22

1.2 Exploration of the Dynamic Radio Sky In Literature 24

1.3 An Improved Interferometer: the Karl G. Jansky Array 26

1.4 Goals of this Thesis 28

2 The Birth of a Relativistic Outflow in the Unusual γ-ray Transient, Swift J164449.3+573451 **37**

Abstract **38**

2.1 Introduction 39

2.2 Archival Data and Followup Radio Observations 39
2.3 15 GHz Followup Observations With the OVRO 40-m Telescope 39
2.4 Discussion 40
2.5 Conclusions 41

3 Sensitive Search For Radio Variables And Transients In The Extended Chandra Deep-Field South 48

Abstract 49

3.1 Introduction 50
3.2 Observations and Data Reduction 51
3.3 Variability Analysis 52
3.3.1 Single-Pointing Variability 55
3.3.2 Full Variability Analysis 56
3.3.3 Notes on Variables Found 61
3.4 Transient Search 66
3.4.1 Efficacy of Source-finding Algorithms 66
3.4.1.1 `sfind` (*MIRIAD*) 68
3.4.1.2 *SExtractor* 69
3.4.1.3 `SAD` (*AIPS*) 71
3.4.1.4 `IMSAD` (*MIRIAD*) 74
3.4.1.5 *Aegean* 78
3.4.1.6 Summary of results from the efficiency tests 82
3.4.2 Transient Candidate Search 82
3.5 Discussion and Conclusions 84
3.5.1 Comparison of variability with previous surveys 84
3.5.2 Limits on transient areal density and rate 86
3.5.3 Future Radio Surveys 88

Acknowledgments 90

4 The Caltech NRAO Stripe 82 Survey (CNSS) Paper I: The Pilot Radio Transient Survey In 50 deg^2 96

Abstract 97

4.1 Introduction 98
4.2 The Survey 99
4.2.1 Radio Observations 99

4.2.2 Optical Observations . . . 101
4.3 Radio Data Processing . . . 102
4.3.1 Near-Real-Time Processing . . . 103
4.3.2 Final Processing . . . 105
4.3.2.1 Calibration . . . 105
4.3.2.2 RFI . . . 106
4.3.2.3 Imaging . . . 107
4.3.2.4 Source Catalogs . . . 109
4.3.2.5 Data Release . . . 111
4.4 Optical Data Processing . . . 111
4.5 Radio Variables and Transients . . . 111
4.5.1 Near-Real-Time Search . . . 112
4.5.2 Search for Variables and Transients after Final Data Processing . . . 113
4.5.3 Transients On Timescales $<$1 Week . . . 117
4.5.3.1 VTC225411-010651: AGN flare . . . 117
4.5.4 Transients On Timescales $<$1 Month . . . 118
4.5.4.1 VTC223612+001006: RS CVn flare . . . 118
4.5.4.2 VTC225707-010238: Flaring Type-I QSO . . . 120
4.5.5 Transients On Timescales $<$1.5 Year . . . 120
4.5.5.1 VTC224730+000008: Flaring AGN . . . 120
4.5.6 Transients On Timescales $\lesssim$20 Years . . . 120
4.5.6.1 VTC233002-002736: Renewed activity of Type-II QSO . . . 120
4.5.7 Transients Found Serendipitously . . . 122
4.5.7.1 VTC221515-005028: Extreme variability of flat-spectrum AGN . . . 124
4.5.7.2 VTC230241+003450: Flare from dKe Star . . . 125
4.6 Optical Properties of Radio Sources . . . 125
4.7 Summary & Discussion . . . 129
4.7.1 Comparison of variability with previous surveys . . . 131
4.7.2 Transient Rates . . . 132

5 The Caltech NRAO Stripe 82 Survey (CNSS) Paper II: On-The-Fly Mosaicing Methodology 151

Abstract 152

5.1 Introduction . . . 153
5.1.1 OTFM Theory . . . 153
5.1.2 Design of OTFM Observations for the Jansky VLA . . . 157
5.2 Planning of Dynamically-Scheduled OTFM Survey Observations . . . 157

5.3 Observations . . . 159
5.4 RFI . . . 159
5.5 Near Real Time Processing . . . 163
5.6 Final Processing . . . 164
5.7 Comparison Between Epochs . . . 164
5.8 Summary & Conclusions . . . 168

6 The Caltech NRAO Stripe 82 Survey (CNSS) Paper III: Prime Candidates for Slow Radio Transients 170

Abstract 171

6.1 Introduction . . . 172
6.2 The Selection of Prime Slow Radio Transients . . . 172
6.2.1 VTC0141+00 and VTC0303-00 . . . 174
6.2.2 VTC0309+01 . . . 176
6.2.3 VTC2040-00 . . . 180
6.3 **Other Similar Transient Candidates and False Alarm Probability** . . . 180
6.4 **Summary & Discussion** . . . 181

7 Summary and Future Directions 184

A B- and A-Type Stars in the Taurus-Auriga Star Forming Region 190

Abstract 191

A.1 INTRODUCTION . . . 192
A.2 DATA COLLECTION AND ANALYSIS . . . 195
A.2.1 OVERVIEW . . . 195
A.2.2 COMPILING THE LIST OF CANDIDATE EARLY-TYPE STARS AND ANCILLARY DATA . . . 196
A.2.3 SELECTION OF CANDIDATE MEMBERS OF TAURUS . . . 200
A.2.3.1 DISTANCE CRITERION AND METHODS . . . 201
A.2.3.2 KINEMATIC CRITERIA AND METHODS . . . 203
A.2.3.3 RESULTS OF CANDIDATE SELECTION . . . 205
A.2.4 FOLLOW-UP SPECTROSCOPY . . . 207
A.2.5 MODELLING THE DUST EMISSION WITH *DUSTY* . . . 209
A.3 INDIVIDUAL EARLY TYPE OBJECTS PLAUSIBLY ASSOCIATED WITH TAURUS . . . 215
A.3.1 IC 2087 . . . 218
A.3.2 72 Tau . . . 220

A.3.3 V892 Tau . . . 221
A.3.4 HD 282276 . . . 221
A.3.5 HD 29647 . . . 222
A.3.6 HR 1445 . . . 223
A.3.7 τ Tau . . . 224
A.3.8 AB Aur and HD 31305 . . . 224
A.3.9 HD 26212 . . . 225
A.3.10 HD 27659, HD 283815 . . . 226
A.4 SUMMARY & CONCLUSION . . . 226

Acknowledgments **229**

B Study of X-ray emission from the old open cluster, M67 **254**

Abstract **255**
B.1 INTRODUCTION . . . 256
B.2 ARCHIVAL DATA AND DATA PROCESSING . . . 257
B.2.1 X-ray Data . . . 257
B.2.2 Data Processing . . . 257
B.2.3 X-ray Images . . . 259
B.2.4 SOURCE DETECTION . . . 259
B.3 IDENTIFICATION OF X-RAY SOURCES . . . 260
B.3.1 X-ray Counterparts from ROSAT and Chandra . . . 260
B.3.2 Optical Counterparts . . . 260
B.3.3 Members of M67 and Source Classification . . . 262
B.3.4 Chance Identification . . . 266
B.3.5 Background sources . . . 266
B.4 SPECTRAL AND TIMING ANALYSIS . . . 267
B.4.1 Spectral Fitting and Luminosities . . . 267
B.4.2 Hardness Ratios . . . 270
B.4.3 X-ray Variability . . . 270
B.5 NOTES ON INDIVIDUAL CLASSES OF X-RAY SOURCES IN M67 . . . 274
B.5.1 RS CVn / similar binaries . . . 274
B.5.1.1 Luminosity functions of RS CVn-type systems . . . 275
B.5.2 Algol Systems . . . 275
B.5.3 Contact Binaries . . . 275
B.5.4 Cataclysmic Variables . . . 276

B.5.5 Blue and Yellow Stragglers, Peculiar Stars 277
B.5.6 New Member NX75 and Other Members 278
B.6 SUMMARY 278

List of Figures

1.1 The phase space of radio transients. This plot shows two quantities, peak luminosity and the evolution timescale, among the several that characterize the phase space. Slant dashed lines are lines of constant brightness temperature. Slow transients are generally defined as having timescales larger than one second. The points in gray are previously-known radio transients. Some of the most noteworthy slow transients from the CNSS survey are marked in blue. Note that for some the extragalactic transients detected in CNSS, the timescales are not very well constrained, and the timescales marked here denote lower limits. Also note that for some of previously-known transients, such as flare stars, only the short timescale structure in their light curves has been considered. 3

1.2 In the shock-in-jet model for AGN flaring, electrons behind shocks propagating down the jet are responsible for radio emission. The synchrotron radiation evolves in three stages depending on the dominant emission-loss mechanism of the electrons: inverse Compton, synchrotron, and adiabatic. Figure courtesy: M. Türler, Astronomy Department of the University of Geneva. . . 5

1.3 Radio light curves of 3C 273 (grey points) decomposed into a series of seventeen synchrotron outbursts (Türler et al. 2000). The best-fit light-curve is shown by solid lines, the emission from from the outer jet is shown by long-dashed lines, the decay of all outbursts peaking before 1979 is represented by short-dashed lines, and the seventeen superimposed outbursts are denoted by dotted lines. 6

1.4 Schematic diagram of the supernova blastwave interacting with the CSM (Weiler et al. 2002; Stockdale et al. 2007). The radio emission originates just behind the blastwave. 7

1.5 *Top*: Type II supernovae light curves from Weiler et al. (2002): (1) SN1979C (left) at 14.9 GHz (crossed circles, solid line), 4.9 GHz (open squares, dash-dot line), and 1.5 GHz (open stars, dotted line); and (2) SN1980K (right) at 4.9 GHz (open squares, solid line), and 1.5 GHz (open stars, dashed line). *Bottom*: A compilation of light curves of SN Ib/c supernovae in the local universe at 8.46 GHz from Soderberg et al. (2010). Local type Ib/c supernovae with well studied radio emission (grey) exhibit lower luminosities and peak at later times, indicating smaller sizes and lower mean expansion velocities. The radio emission from most local type Ib/c supernovae is below the detection threshold (3σ upper limits shown as grey triangles). Reprinted by permission from Macmillan Publishers Ltd: Nature (Soderberg et al. 2010), copyright 2010. 9

1.6 A schematic picture of the GRB fireball model. See §1.1.1.3 for details. Figure credit: J. Valesco. 10

1.7 A compilation of beamed GRB light curves from Chandra & Frail (2012) at 8.5 GHz. Observer-frame long-duration GRBs are shown on the left while rest-frame short-duration GRB light curves are shown to the right. The red thick solid line represents the mean light curve for log GRBs. The pink shaded area is the 75% confidence interval for the long GRBs. 10

1.8 *Left*: Differential and cumulative (inset) distributions of the time when OA peak (blue solid line) and of the duration of the OA emission (red dashed line). *Right*: Cumulative flux distribution of OA at GHz and MHz observing frequencies (color codes as shown in the legend). Figure taken from Ghirlanda et al. (2014) 11

1.9 *Left*: Radio light curves of BNS merger events from the numerical simulations of Piran et al. (2013). The afterglow is generated by interaction of the dynamically ejected sub-relativistic outflows from different combinations of BNS masses. 1 cm^{-3} circum-merger environment density and a distance of 300 pc are assumed . The shaded region represents the period dominated by mildly relativistic outflows, not included in the simulations. *Right*: Same as the left panel, except for 0.1 cm^{-3} circum-merger environment density. 12

1.10 *Left*: A schematic diagram of the tidal disruption of a solar-mass star by a supermassive black hole (Rees 1988). The star approaching the black hole on a parabolic orbit at a pericenter distance r_T is distorted and spun up before being tidally disrupted. Almost half of the mass of the star going into the debris escapes on hyperbolic orbits. The gravitationally bound debris orbits the black hole on elliptical orbits. *Right*: The geometry and emission regions for Swift J1644+57 as suggested by Bloom et al. (2011). Shocked, circularized fallback mass sets up a temporary accretion disk with inner radius equal to 3 times the Schwarzschild radius (for a non-spinning BH). A two-sided relativistic jet starts at the time of accretion and travels through the interstellar region surrounding the black hole. Emission from the accretion disk is Compton up-scattered giving rise to the observed X-rays. A possible analogy of Swift J1644+57 to be a scaled-down version of a blazar impulsively fed by the tidal disruption of a Sun-like star is proposed. From Bloom et al. (2011). Reprinted with permission from AAAS. 13

1.11 Radio light curves of Swift 1644+57 from Zauderer et al. (2013). The solid lines represent a synchrotron emission model described in Zauderer et al. (2013). 13

1.12 Close binaries may undergo magnetic reconnection events between magnetospheres. Figure taken from Dulk (1985). 15

1.13 *Upper left*: Count rate and hardness light curves of the black hole binary, GX 339-4, during its 2002-03 outburst (Belloni et al. 2005). *Upper right*: The hardness-intensity diagram for the GX 339-4 outburst. At the beginning of the outburst (A->B), the system is in the hard state with emission dominated by non-thermal processes in a very hot, optically thin, plasma ("corona"). The radio emission observed in this state is believed to be entirely produced by a steady jet. When the system reaches high luminosities (B->C), it transitions into the soft state, in which discrete super-luminal ejections occur. In the soft state (C->D), the spectrum is dominated by thermal emission from an optically thick accretion disc, and the radio/IR emission is strongly reduced, suggesting the disappearance / fading of the jet component. At the end of the outburst (D->A), the accreting system turns back to the hard state, with the reappearance of the radio/IR emission (but without super-luminal ejection). Figure courtesy: S. Markoff, J. Miller-Jones, R. Fender. 16

1.14 Two examples of XRB flares observed in the radio and X-rays (Fender et al. 2004). The top panels show observations for GRS 1915+105 and the lower panels show XTE J1859+226 observations. The panels on the left indicate the behavior of these flares in the L_{radio}–L_X plane while the panels to the right indicate thier behavior in the radio. 18

1.15 Radio and optical light curve of the dwarf nova, SS Cyg, from Körding et al. (2008). Reprinted with permission from AAAS. 19

1.16 Radio light curves for SGR 1806-20 from Cameron et al. (2005). The best-fit broken power-law models are indicated by lines. The first break in the spectrum defines the boundary between the regions A and B. Region B, the period of steep light curve decline, is shaded gray. The second break in the GHz spectrum defines the boundary between the regions B and C. Reprinted by permission from Macmillan Publishers Ltd: Nature (Cameron et al. 2005), copyright 2005. . . 20

1.17 *Top*: Radio flaring and quiescent emission from the brown dwarf LP944-20 found by Berger et al. (2001). The three panels show light curves at three different epochs. Squares indicate emission at 8.5 GHz while circles represent 4.9 GHz emission. Solid and dashed lines represent a simple exponential model fit to the flaring light curves. Reprinted by permission from Macmillan Publishers Ltd: Nature (Berger et al. 2001), copyright 2001. *Bottom*: Periodic pulses of radio emission from the brown dwarf TVLM 513-46546 (Hallinan et al. 2007) correlated with the spin period of 1.96 h. The total intensity (Stokes I) and the circularly polarized (Stokes V) radio emission at 8.44 GHz are shown. The pulses are 100% polarized, with right circularly polarized emission appearing as positive peaks and the left circularly polarized emission appearing as negative peaks in Stokes V. 21

1.18 *Top*: The multi-frequency radio light curves of two novae, V1500 Cyg (left) and 1723 Aql (right), considered in Roy et al. (2012). The best fit Hubble flow model (dashed lines) shows that late-time data agree with the standard model of expanding thermal ejecta. *Bottom*: The multi-frequency light curve of nova V959 Mon (Chomiuk et al. 2014) consistent with a expanding thermal ejecta model. Reprinted by permission from Macmillan Publishers Ltd: Nature (Chomiuk et al. 2014), copyright 2014. 22

3.1 Hexagonal grid of six pointings (crosses), each pointing separated $12'$ from its nearest neighbor. The $34' \times 34'$ (black square) region represents the extent of the final image from the Miller et al. (2008) data release. $15'$-circles (grey) corresponding to the 50% beam attenuation in different pointings are also shown. The $60' \times 60'$ background image is from NVSS. 52

3.2 A histogram of the signal-to-noise ratio (SNR) of the sources in the DR2 catalog. 54

3.3 Variability plot for the point sources in the Miller et al. DR2 catalog, shown separately for all pointings. The peak flux density is denoted by the symbol size. The red dashed line represents the 4σ level for the appropriate number of degrees of freedom (one less the number of epochs in each pointing) for each pointing. The number of epochs in each pointing lies between 7 and 9. 56

3.4 χ^2 normalized by its value at the 4σ level, plotted against the modulation index, m, for sources in the Miller et al. DR2 catalog using peak fluxes from all pointings, and corrected with empirically-derived beam attenuation profile. The 4σ level is different for different sources, depending on the number of epochs in which they are present. The mean peak flux density is denoted by the symbol size. Filled circles indicate significant variables (lying above a normalized χ^2 of unity). 58

3.5 Light curves of the variable sources from Miller et al. DR2 catalog listed in Table 3.3. Filled symbols represent the flux densities considered for variability analysis (i.e. where $\theta < 12'$). Flux densities in epochs where a source lies within the 50% power circle of the beam (i.e. where $\theta \lesssim 15'$) are plotted for reference as open symbols. The error bars take into account the background rms, primary beam correction, and bandwidth smearing (no taper). 59

3.6 $2.2'' \times 2.5''$ GEMS (all sources except ID 337) and GOODS-S (ID 337) F606W ACS-WFC image cutouts of variable sources found in this work. The red error ellipses denote the radio source positions from Miller et al. (2013), shift-corrected to the HST source positions. All the positional uncertainties are 1σ (see § 3.3.2 and Table 3.4). 62

3.7 *Spitzer*/IRAC color-color diagram for the mid-infrared counterparts of the variable sources (filled circles). For comparison, the radio sources from AEGIS20 (Willner et al. 2012) are also shown (unfilled circles). The AGN selection region in the upper-right corner, bounded by the dashed lines, is from Donley et al. (2012). Curves represent the colors of three template spectral energy distributions (E: elliptical galaxy; Sbc: spiral galaxy; AGN) from Assef et al. (2010) as redshift increases from 0 to 3. The redshift-dependent color-coding is — blue: $z \leqslant 0.5$, green: $0.5 < z \leqslant 1.1$ and red: $z > 1.1$. 64

3.8 Completeness of the catalogs generated by different source-finding algorithms. Results for a background mesh-size (rmsbox) of 20 beamwidths, wherever specifiable, are shown. For `IMSAD` and *Aegean*, the results are for the histogram option and csigma=$1\sigma_{\rm cmap}$ respectively. See §3.4.1 for the definition of completeness used here. The decreasing completeness beyond $SNR \sim 50$ is due to deblending of multiple components of extended sources. The inset shows only the region where SNR is between 4 and 10. Smoothing over every 75 data points has been done before plotting. Note the low-number statistics for sources with SNR $\gtrsim$70 as implied by Figure 3.2. 72

3.9 The completeness (top) and reliability (bottom) of the catalogs generated by different source-finding algorithms. See §3.4.1 for the definitions of completeness and reliability used in this work. Results for a background mesh-size (rmsbox) of 20 beamwidths are shown. For `IMSAD`, these results are for the histogram option. For sfind, we have used α=10, whereas for *SExtractor*, `SAD`, `IMSAD` and *Aegean*, detection threshold of 3σ. Only those sources which are $\geqslant 5\sigma$ have then been selected from the respective catalogs prior to comparison with the DR2 catalog. The inset shows only the region where SNR is between 4 and 10. Smoothing over every 75 data points has been done before plotting. Note the low-number statistics for sources with SNR $\gtrsim$70 as implied by Figure 3.2. 75

3.10 Examples of 5σ and brighter sources detected by various source-finding algorithms in the DR2 image. Top panel: blended components ($30''$ cutouts centered on $03^{\rm h}32^{\rm m}32.2^{\rm s}$,$-28^\circ03'09.4''$), middle panel: source with sidelobes ($20''$ cutouts centered on $03^{\rm h}32^{\rm m}06.1^{\rm s}$,$-27^\circ32'35.8''$), bottom panel: region with a relatively large rms (12 μJy) at the corner of the image ($3'$ cutouts centered on $03^{\rm h}31^{\rm m}19.4^{\rm s}$,$-27^\circ32'55.6''$). The logarithmic flux density scale shown in each panel has units of Jy. The ellipses have major and minor axes and position angles according to the parameters reported by the respective algorithms. 76

3.11 The SNR of sources found by different source-finding algorithms relative to their SNR in the DR2 catalog. Smoothing over every 75 data points has been done before plotting. Note the low-number statistics for sources with SNR $\gtrsim$70 as implied by Figure 3.2. 76

3.12 Results of the completeness (middle) and reliability (bottom) tests on the Hancock et al. simulated image. Matching radius of $15''$ was used to find counterparts. Input parameters to the source-finding algorithms are same as those given in Figure 3.9. Here, the completeness and reliability within each SNR bin are plotted (see §3.4.1), which makes these diagrams different from the ones given in Hancock et al. (2012). For reference, the histogram of the simulated sources is also shown (top). The completeness at SNR$\sim$70 dropping below 90% is a result of highly-blended sources. 77

3.13 Normalized 1.4 GHz differential radio source counts for persistent sources from de Zotti et al. (2010) and the normalized areal density of transients (or limits) as a function of the flux density for various surveys at this frequency. Bannister et al. (2011a) survey at 0.84 GHz is colored differently than the other surveys. Most of the surveys are upper limits (wedge symbols) and the sampled phase space is shown by the grey shaded area. Upper limits from Frail et al. (1994) and Bower & Saul (2011) do not explore any new part of the phase space (non-grey area), and hence have been left out of this diagram. Our upper-limit is labeled as "E-CDFS". Three surveys have transient detections so far, 2σ error bars for which are shown according to Gehrels (1986). Note that Thyagarajan et al. (2011) and Bannister et al. (2011a) may have identified a few strong variables as transients (see §3.5.2), which would make their detections move downward on this plot. The black solid line is the model for AGNs and star-forming galaxies from Condon (1984). Lines of constant areal density are shown as blue dotted lines. The horizontal dashed lines are estimates for the areal density for known and expected classes of long-duration radio transients taken directly from Frail et al. (2012). The areal density for Swift J1644+57-like tidal disruption events has been modified according to Berger et al. (2012) to reflect their true rate at 1.4 GHz. Upper limits from the ASKAP-VAST surveys are estimated to be an order of magnitude or more below the rate of orphan gamma-ray burst afterglows, and having a rms sensitivity ranging between 10 μJy and 0.5 mJy. 85

4.1 Setup of target pointings for a part of region R1 of the Jansky VLA survey. The circles indicate primary beam FWHM at the mean frequency of 2.9 GHz, and the pointing numbers are labelled. Nearest neighbors are separated by $15'$. See §4.2.1 for details on the pointing setup. . 100

4.2 Setup of pointings for the PTF survey. The dashed and solid lines indicate the footprint of the different pointings. The PTF field IDs for the pointings are shown at the bottom right corner of the respective footprints. The shaded regions indicate the missing CCD. 102

4.3 Log of PTF observations. MJD / Gregorian date is on the x-axis and PTF field ID is on the y-axis. Each point corresponds to an observation. The first three Jansky VLA epochs (Table 5.1) are shown at the top for reference. See §4.2.2 for details. 103

4.4 Demonstration of gain compression in the data. *Top*: Gain amplitudes derived for the gain calibrator J2323-0317 observed during the survey epoch 14Jul2012 (E1R2; blue circles) correlate well with the rms noise (green 'plus' symbols) in the pointings (scans). The gain amplitudes and the rms have been arbitrarily normalized. Note that the scan number is a proxy for time. *Bottom*: Calibrated and normalized amplitude of J2323-0317 (scan number 157) observed during the 23Jul2012 (E3R2) survey epoch. RR and LL correlations are shown in light blue and dark blue respectively. There is large RFI in the LL correlation of SPW 5 (between 2.65 and 2.75 GHz), which has affected the gains in the other spectral windows as well. The inset shows a zoom-in for SPW 9 (known to be RFI-free), where the gains in the LL correlation are seen to differ from the RR by almost 10% (the latter is assumed to have the true or expected gain). . . 107

4.5 The primary beam response at the lowest (blue dashed line), highest (green dot-dashed) and reference (solid red) frequencies. 108

4.6 The survey area having the rms noise (flat sky) less than or equal to the given sensitivity. . . . 109

4.7 The Y-shaped imaging artifact discovered in the first 1.5 hours of observations for the 24Aug2012 (E3R1) epoch. The image of a bright source before and after the calibration desribed in §4.3.2.3. 109

4.8 *Left*: Histograms of the peak flux densities in epoch E2 of sources in the PSC and integrated flux densities for all sources in E2CAT. *Right*: PTF R band and the SDSS (Stripe 82 co-add) r band magnitudes of the optical sources considered in this work. The SDSS histogram between magnitudes 15–21 is higher than the PTF histogram due to multiple entries of sources in SDSS in this magnitude range. 110

4.9 A histogram of the variability statistic, V_s, for sources in the PSC. After the application of the corrections to the flux densities mentioned in §4.5, V_s agrees with the expected distribution, Student's t. 114

4.10 The variability statistic, V_s, as a function of the modulation index, m, for sources in the PSC for the various timescales considered in this work. The dashed red lines indicate our selection criteria for variables. Filled gray circles denote sources that are not variable while red circles have been selected as variables. The sizes of the circles indicate the mean flux densities of the sources in the two epochs being compared. We find 30, 21, and 30 variable sources on timescales of one week, one month, and 1.5 years respectively, amounting to a total of 142 variable sources. The upper x-axis in each of the three panels represents the fractional variability as given by equation 4.3. See §4.5 for details. 115

4.11 A comparison of the 3 GHz peak flux densities of sources in the PSC with the 1.4 GHz peak flux densities from the FIRST (top) and VLA-Stripe 82 (bottom) surveys. these two surveys (Figure 4.11). Triangles denote upper limits to the peak flux density. Red color denotes sources selected as variable candidates by our search criteria. See §4.5.2 for details. 116

4.12 Radio continuum spectrum of VTC225411-010651 at two follow-up epochs (blue circles and green squares). The 3σ upper limit at 1.4 GHz from Hodge et al. (2011) is shown in red. The measurements from the four survey epochs are shown in grey. The first two epochs have spectral indices of -1.68 ± 0.95 and 0.39 ± 0.68 within the S band respectively and are indicated by grey crosses joined by straight lines between the two frequencies used for spectral index measurement. See §4.5.3.1 for details. 118

4.13 *Top*: The radio image cutouts from three epochs, E1, E2 and E3, showing VTC223612+001006 and a comparison 0.5 mJy persistent source. The transient is detected with an SNR of 9 in the first epoch, and is below SNR of 4 in the other two epochs. The colorbar to the right has units of Jy. *Bottom*: The continuum-normalized optical spectrum of VTC223612+001006 observed with ESI at KeckII on 13 Sep 2012. The spectrum has been binned with 20 data points in each bin. We classify this star as a late G to early K subgiant or giant. See §4.5.4.1 for details. . . 119

4.14 *Top*: The radio continuum spectrum of VTC225707-010238 at two follow-up epochs (blue circles and green squares). The 3σ upper limit at 1.4 GHz from Hodge et al. (2011) is shown in red. The measurements from the first three survey epochs are shown in grey. See §4.5.4.2 for details. *Bottom*: The optical spectrum of VTC225707-010238 observed with LRIS at KeckI on 18 Aug 2012. The spectrum is typical of a blue quasar. We derive a redshift of 1.56. 121

4.15 *Top*: The multi-frequency continuum spectrum of VTC233002-002736. Archival photometry is shown as filled red circles. The 3σ upper limit at 1.4 GHz from the FIRST survey and the upper limit from WISE W4 filter are shown as red arrows. Blue circles and green squares indicate the first and second follow-up observations. Black dashed and dotted lines are average spectra for radio-loud and radio-quiet quasars from Elvis et al. (1994). The *inset* shows the zoom-in of the follow-up radio continuum spectra from the three epochs. Red triangles show data from the third follow-up epoch, and the measurements from the four survey epochs appear in grey. *Bottom*: The optical spectrum of VTC233002-002736 observed with DIEMOS at KeckII on 14 Sep 2012. The y-axis is flux in arbitrary units. Broad emission lines indicate a quasar at a redshift of 1.65. See §4.5.6.1 for details. 123

4.16 The radio continuum spectrum of VTC221515-005028 at the follow-up epoch 29May2014 (red triangles). The 3σ upper limit from the FIRST survey is shown with the red arrow and the detection from the Hodge et al. (2011) survey is marked by a red circle. he measurements from the four survey epochs are shown in grey. See §4.5.7.1 for details. 124

4.17 The number of optical matches for the radio sources in E2CAT for different matching radii. Solid lines indicate the matching process carried out using the actual radio source positions and the dot-dashed lines indicate background matches found by offsetting the radio source positions by $1'$ in an arbitrary direction. Blue and green lines show radio versus SDSS and PTF matching respectively. 126

4.18 Optical counterparts of persistent (blue) and variable (green) radio sources in the PSC. The x-axis is r-band magnitude from SDSS. The top panel gives the completeness of the radio-optical cross-matching, the middle panel shows histograms of persistent and variable radio sources with optical counterparts, and the bottom panel plots the radio flux densities versus optical magnitudes. The approximate limiting magnitudes for PTF (per-epoch; $R = 21$ mag.) and SDSS (Stripe 82 co-add; $r = 23.5$ mag.) are shown as red dashed lines. 127

4.19 Light curves of the 8 spectroscopically-confirmed supernovae found in the PTF survey. Each supernova is represented by a unique color. Optical photometric data from PTF and follow-up observations are shown as solid lines. The 3σ radio upper limits from the JVLA survey (four epochs) are shown as downward-pointing triangles. For PTF12gzk, the radio detection (red circle and errorbar) and 3σ upper limits (downward-pointing red arrows) at 5 GHz from (Horesh et al. 2013) are also marked. See §4.6 for details. 128

4.20 Venn diagram showing the number of persistent as well as variable optical sources from PTF and radio sources from the PSC. The sets plotted here are not to scale. 129

4.21 Well-sampled optical light curves of radio variable sources from SDSS (showing variability on timescales of years) and PTF (inset; showing variability on timescales of weeks). For SDSS, the u-, r-, and z-band light curves are shown as blue, red, and magenta circles with errorbars respectively. For PTF, the R band light curve is shown. The title of the inset is based on whether the source is classified as a variable through our variability criteria. See §4.6 for more details. The y-axis in each plot is the magnitude and the x-axis is the Modified Julian Date (MJD). Note that MJDs 51000, 54000, 56100, and 56200 correspond to Jul 1998, Sep 2006, Jun 2012, and Oct 2012 respectively. 130

4.22 *Top*: The phase space of slow extragalactic transients. The panel shows the upper limits to the transient rates from previous radio surveys (colored wedges; 95% confidence), the rates derived from radio transient detections (2σ errorbars), and the expected transient rates. All observed quantities are color-coded according to the observing frequency. The solid gray line is the rate claimed by Bower et al. (2007), plotted for reference. The upper limit to the extragalactic transient rate from our pilot survey (this work) and the phase space probed by the full CNSS survey are shown as thick green wedges. The phase space probed by the VLA Sky Survey all-sky tier (VLASS) is also shown. The solid red line denotes the source counts from the FIRST survey, and the dashed red line denotes the approximate counts for strong variables at 1.4 GHz (1% of the persistent sources). *Bottom*: The Galactic transient phase space. Symbols have similar meanings as in the top panel. Black solid lines denote the source counts from the FIRST and the MAGPIS 1.4 GHz surveys. The source counts for variable Galactic sources approximated from Becker et al. (2010) are shown as a blue dashed line. The transient rate for active binaries resulting from our pilot survey is shown by the green errorbar and the upper limit for the rate of all other classes of Galactic transients is denoted by a thick green wedge. See §4.7.2 for more details. 135

5.1 The OTFM smeared beam as a function of the slew of the antennas in arcmin within each scan (i.e. slew of the antennas between each change of correlator phase center). In other words, it shows the fractional change in the flux density with respect to the true flux density when only a single, time invariant, primary beam correction is applied to each scan. See equations 5.11–5.13 for details. 156

5.2 OTFM observation planning for dynamic scheduling. This plot shows the azimuth and elevation simulated for one of our observing blocks. The assumed starting position of the antennas is 0^o in right ascension and declination, corresponding to AZ$\simeq 100^o$ and EL$\simeq 10^o$ at the specified start LST. The AZ and EL of the antennas through the observation is denoted by the blue line. Tertiary and secondary calibrators are denoted by magenta and green circles respectively. The gain calibrator source is represented by red circles, and the flux and polarization calibrators, 3C48 and 3C84, are denoted by black circles. The known Clarke belt satellites (courtesy of Vivek Dhawan, NRAO) and their orbits on the sky are shown as thin colored lines. See §5.2 for details. 158

5.3 OTFM observations carried out on 21 Dec 2013. Black arrows represent the motion of antennas on the sky. Discontinuity in the arrows implies a gain calibrator or a secondary calibrator observation. Typically, groups of two OTFM stripes were interspersed with calibrator scans. The gray shaded area is the 22.5 deg^2 region observed in a single observing block on 21 Dec 2013. The red circle denotes the FWHM beam at 3 GHz. See §5.2 and §5.3 for details. 160

5.4 Raw spectra (2–4 GHz) of the gain calibrator source, J2212+0152, from the 21 Dec 2013 epoch, i.e. phase vs. channel (upper frame in the top and bottom panels) and amplitude vs. channel (lower frame in each panel) for the RR and LL polarizations (top panels and bottom panels respectively). All baselines and all pointings of the gain calibrator source have been combined to produce these plots. Note the large-amplitude RFI in the SPWs 2 and 3, and the distorted phased in SPWs 14–16. 162

5.5 The mosaic from the final processing of the CNSS data from the 21 Dec 2013 epoch (top), having a median rms noise is 85 μJy. The mosaic shown at the bottom is from the pointed observations carried out on 18 Aug 2012. Apart from the differences in imaging resulting from different UV coverages and non-uniform rms noise for the pointed observations, these two mosaics agree quite well with each other. 165

5.6 Cutouts of a "bright" (300 mJy; top panels) source and of sources with moderate flux densities (several mJy; bottom panels). The panels on the left are from the pointed observations carried out on 18 Aug 2012, and those on the right are from the 21 Dec 2013 OTFM observations. . . 166

5.7 Same as Figure 5.6, but for an extended source (top panels) and for "faint" (sub-mJy; bottom panels) sources. 166

5.8 The mean absolute deviation (MAD) of source flux densities between OTFM observations from the 21 Dec 2013 epoch and pointed observations from the 18 Aug 2012 epoch are shown as blue points. The comparison between OTFM observations from two epochs is also shown (red points). Only point sources with SNR$>$10 have been considered here. For reference, we show the MAD expected from purely Gaussian image noise (dashed line), 10% fractional variability of all sources (dot-dashed line), and from the Gaussian noise and true source variability as seen by Ofek et al. (2011) (dotted line). See §5.7 for details. 167

6.1 A log N - log S diagram showing the large, unexplored, part of the phase space of slow radio transients explored by the three-epoch CNSS survey. Based on expected rates (dashed black lines) this survey is capable of discovering rare extragalactic phenomena such as radio supernovae, jetted tidal disruption events, and binary neutron star merger events. The region of the phase space explored by past surveys resulting in non-detection of transients are shown as wedges, while the rates calculated from transient detections in blond surveys are marked as errorbars. The color coding is according to observing frequency. The persistent source counts from the FIRST survey are shown as the red solid line. 173

6.2 The predicted peak spectral luminosity vs. evolution time scale at 3 GHz for the different classes of extragalactic radio transients detectable in the CNSS survey. White zones correspond to optically thin sources, while gray zones represent sources that are expected to be optically thick before maximum light and optically thin afterwards. Also shown is the detectability distance for these events in our survey. The blue shaded box corresponds to the region occupied by the radio transient VTC0141+00. The blue and green shaded boxes correspond to the region occupied by VTC0303-00. 175

6.3 SDSS cutouts and radio continuum spectra of the two BNS merger candidates, VTC0141+00 and VTC0303-00, from follow-up observations carried out in May 2014. These two transients are undetected in the FIRST survey (3σ upper limit of 0.4 mJy from mean epoch 1999) and appear to have evolution timescales of several months. 177

6.4 *Top*: Deep Keck/MOSFIRE infrared Ks-band images at the locations of VTC0303-00 and VTC0141+00 (marked by the red circles having $0.5''$radius) taken in October 2014. The sources are not detected with limiting magnitudes of Ks=22.8 and Ks=19.1 respectively. Sources marked with green ellipses are $>5\sigma$ sources from SExtractor. These observations rule out a background AGN hypothesis to a high significance and make the association of these transients with the spiral arms of the galaxies more likely. *Bottom*: The ratio of the 1.4 GHz and near-IR K band flux densities plotted against the 1.4 GHz radio spectral luminosity. These quantities are plotted for VTC0303-00 and VTC0141+00 as pink dashed lines (note that these are lower limits along the y-axis) assuming that these transients are not associated with galaxies in the local Universe and that their distance is unknown. A compilation of GPS and CSS sources from O'dea (1998) are also shown. Based on the trend displayed by the O'dea (1998) sources, we are able to rule out the association of VTC0303-00 and VTC0141+00 with background AGN at redshifts $z<0.5$ and $z<3$ respectively. 178

6.5 VTC0309+01, a likely tidal disruption event discovered in our JVLA survey of the Stripe 82 region. The top panel shows the optical spectrum consistent with a star-forming galaxy at 170 Mpc (z=0.04; inset shows the image cutout with the radio source being coincident with the nucleus of this galaxy) from SDSS and the lower panel shows the evolution of the radio continuum spectrum in two follow-up epochs. The non-detection in the FIRST survey (3σ upper limit of 0.4 mJy at 1.4 GHz) and the evolution of the peak of the spectrum to lower frequencies advocates the TDE nature of this source. 179

6.6 Follow-up radio spectrum of VTC2040-00, the intermediate polar AE Aqr, from February 2014 detected in outburst in our Stripe 82 survey. The flat spectrum indicates a jet as a viable explanation. If a jetted outflow is detected for AE Aqr through our proposed VLBA observations, then it would be the first direct evidence that white dwarfs can harbor jets. 181

7.1 A transient candidate, GMRT J022041.0-010411.4, from our pilot 100 deg^2 survey. It is associated with a broadline AGN at a redshift of 0.34. The radio source is undetected in the TGSS epoch from Aug 2010, but is detected in our two epochs from 2014. The flux densities of the candidate in these three observations are $<$36 mJy (3σ upper limit), 77$\pm$10 mJy and 88$\pm$10 mJy respectively, while the flux densities of a nearby comparison source, lying to the lower right of the transient candidate in the image cutouts shown above, are fairly stable (<20% fractional variability in flux density). 188

A.1 Spitzer mosaic of IRAC and MIPS images of Taurus. Color coding: 8 (blue), 24 (green), and 160 (red) μm. Four bright and large nebulous objects illuminated by B stars are evident in this mosaic. They have been marked with large circles and are associated with: (i) top-middle: HD 282276, (ii) top-right: V892 Tau (Elias 1), (iii) bottom-middle: HD 28149 (72 Tau), and (iv) middle-left: HD 29647. Two fainter and weaker nebulae are marked with smaller circles and are associated with: (v) top-middle: HD 28929 (HR 1445), (vi) middle-left: IC 2087. 194

A.2 Areal extent of the Spitzer Taurus Legacy Survey (green) and SDSS spectroscopic observations by Knapp et al. (2007) (red symbols) overlaid on a mosaic of the Taurus region at 100μm from the *IRAS* Sky Survey Atlas. 198

A.3 2MASS color-color (left panels) and color-magnitude (right panels) diagrams for the early-type candidate stars considered in this work. 2MASS objects with contamination flags set and error in J,H,K_s magnitudes greater than 0.1 were rejected from the plots. The mean error in J,H,K_s magnitudes is about 0.02, which is smaller than the size of symbols used. *Top panels*: O,B stars from SIMBAD. In the color-color diagram, two of these stars lie outside the range plotted: V892 Tau (Elias 1) and IC 2087-IR, having $(H-K_s, J-H) = (1.23, 1.73), (1.78, 2.62)$ respectively. *Middle panels*: Stars of spectral-type A and earlier from Knapp et al. (2007) are shown in blue. The B stars proposed by Rebull et al. (2010) are shown in red. Note that the area covered by these surveys is less than that represented in the top and bottom panels. *Bottom panels*: Left: 2MASS objects with color-coding as follows. Blue: stars with magnitude $K_s < 8$, green: $8 < K_s < 9$, red: $9 < K_s < 10$. Right: All 2MASS objects are in blue, and those selected as possible O,B stars using the photometric selection criterion (described in §A.2.2) are shown in red. *All panels*: The reddening vector (magenta) from Rieke & Lebofsky (1985) is used. Intrinsic colors and magnitudes of main-sequence stars (from Table 5 of Kraus & Hillenbrand 2007) are shown as a thick black curve (magenta curve in the bottom panel color-color diagram). The thick black, dashed curve in color-magnitude diagrams is the same curve, but displaced along the luminosity axis to denote the apparent magnitude of main sequence stars at 140 pc. The thin black, dashed straight line in the color-color diagrams represents the color-selection criterion applied to the 2MASS objects (see section A.2.2). The thin grey solid line in color-magnitude diagrams represents the reddening vector passing through the position of an A0V star at a distance of 140 pc. The location of the six B stars illuminating bright IR nebulae are shown as cyan circles with two of the stars having very similar, near-zero, colors. . 199

A.4 Distances to stars in Taurus measured via VLBI, from Table A.2; the star T Tau is not shown since it lies south of the region of interest. Background image is velocity-coded ^{12}CO map from Goldsmith et al. (2008). The LSR velocities are color-coded as blue: 3–5 km s^{-1}, green: 5–7 km s^{-1}, red: 7–9 km s^{-1}. 200

A.5 Comparison of spectroscopic distances calculated in this work with those published in past literature. 202

A.6 *Upper panel*: Proper motions of the candidate early-type stars shown as a cloud plot with blue indicating objects selected from 2MASS; green, SIMBAD; cyan, the B stars proposed by Rebull et al. (2010), and red: O,B,A stars from Knapp et al. (2007). The "+" symbols at the bottom-left corner denote the mean errors for each sample. The mean proper motion of Taurus groups considered in this paper (see Section A.2.3.2) are shown as black symbols The hatched reference circle indicates the area where the χ^2 probability of membership is greater than 1% with respect to the mean proper motion of Taurus. 51 stars from our list of candidate early-type stars have proper motions consistent with Taurus groups. *Lower panel*: Vector diagram showing the proper motion of all the stars tested for membership. Those which satisfy the proper motion criterion P($\chi^2 > 1\%$) are shown in red. Positions of the stars are indicated by the circles, whose sizes are based on the spectroscopic parallax distance of the respective stars (key given at the bottom). Red circles denote stars satisfying our distance criterion for Taurus member selection (within an uncertainty of 15 pc). 206

A.7 Radial velocity versus *SDSS* i-band magnitude for the early-type stars selected from Knapp et al. (2007). The y-axis has been rescaled to show only the stars with RV between $\pm$50 km s^{-1}. The mean RV of accepted members of Taurus (Luhman et al. 2009), 15.8 km s^{-1}, is shown with a black horizontal line. The neighboring red lines denote the region $9.8 \leq RV \leq 17.5$, our RV-member selection criterion. No concentration at the Taurus velocity is seen, and among those stars satisfying this RV criterion, most are too faint to be probable members of Taurus. . 207

A.8 Equivalent widths of various absorption lines measured in the grid of B-type spectral standard stars (luminosity class V only) that were observed for comparison with the Taurus candidate early-type stars. 210

A.9 Normalized optical spectra obtained at the Palomar 200-inch Hale telescope. The upper set of stars comprise the grid of B-type spectral standard stars used for assigning spectral types to the program stars (lower set of spectra). All spectra have an arbitrary offset along the ordinate. Note the hydrogen emission lines or line cores in HD 283751, HD 283637, V892 Tau, and AB Aur. Approximately half of the program stars have diffuse interstellar band signatures: a narrow absorption at 6614 Å and a broader shallow feature at 4428 Å. The feature labeled as Li I6708Å in the right panel is probably anomalous as this line is not expected to be present in these early-type young stars, and especially not in the spectral standards (including our white dwarf flux standard which is not shown); we suspect a possible terrestrial atmosphere source, perhaps associated with the Geminid meteor shower; this hypothesis is supported by lack of absorption at this wavelength in the two spectra towards the bottom of the sequence that were taken on a different night from all others. 211

A.10 Modelling the SEDs (black data points) of some sources having far-infrared excess using *DUSTY*. For each of the sources, the attenuated blackbody representing the star is the grey dashed line, the contribution from the thermal and scattered emission components from the associated dust slab are shown as red and green dashed lines, respectively, and the blue solid line represents the total model output. Photometric points with error bars are shown; the circles represent BVR photometry that is reported without errors. *72 Tau*: A dust slab having 40 K temperature at the boundary closest to 72 Tau roughly reproduces the SED. *HD 29647 Tau*: Two slab components are required to reproduce the SED, one chosen to have a dust temperature of 500 K to reproduce the 10μm silicate feature, and another one at about 45 K. *HD 282276*: Two dust slabs, having inner-edge temperatures of 200 K and 35 K are required to faithfully reproduce the SED. *HD 31305*: The inner-edge dust temperature was found to be 350 K. 212

A.11 Cutouts of the IC 2087 region. Left-to-right are: B, R images from the Palomar Observatory Sky Survey (POSS-I) and J, H images from 2MASS (Row 1), Ks band from 2MASS, and IRAC channels 3.6μm, 4.5μm, 5.8μm (Row 2), IRAC 8μm, and MIPS images 24μm, 70μm, and 160μm (Row 3). The red circle in the POSS-I B band image has a diameter of 1 arcmin, for scale. 215

A.12 Same as Figure A.11 but for 72 Tau. 215

A.13 Same as Figure A.11 but for V892 Tau / Elias 1. 216

A.14 Same as Figure A.11 but for HD 282276. 216

A.15 Same as Figure A.11 but for HD 29647. 216

A.16 Same as Figure A.11 but for HR 1445. 217

A.17 Spectral energy distributions (SEDs) of those sources exhibiting infrared nebulae in Figure A.1 plus the candidate early-type stars we conclude are probable members of Taurus based on our assessment of distance and kinematics. Infrared excess is apparent in many objects. This may be due to the presence of a circumstellar disk associated with a pre-main sequence stars, to a debris disk in a somewhat older main sequence star, to a dusty atmosphere in the case of an evolved giant star, or to a chance superposition of a hot star with a nearby diffuse cloud. For comparison, an example of the chance-superposition case is also shown in the lower right panel: the Pleiades member Maia, whose SED exhibits an apparent infrared excess. The data sources include GALEX (ultraviolet), NOMAD (optical, *BVR*), 2MASS-PSC (near-infrared, JHK_s), *Spitzer*, AKARI and IRAS (mid-far infrared), and SCUBA (sub-mm). Photometric error bars are generally smaller than the symbol size; circles denote photometry lacking uncertainty (usually values from NOMAD). The dashed line in each panel represents a blackbody at 140 pc characterized by the effective temperature and radius of the star whose SED is represented in that panel. No correction for reddening has been applied though the existence of reddening can be inferred from the location of short wavelength photometry well below the nominal blackbody. 218

A.18 Estimation of the isochronal age of some of B stars showing infrared reflection nebulae and τ Tau. Isochrones are from Girardi et al. (2002). Horizontal errorbars represent the error in the 2MASS magnitudes and vertical errorbars represent the uncertainty in the distance ($128 < d < 162$pc). Blue markers are plotted using the reddening parameters from literature, while red markers represent values derived using $R_V = 3.1$ and the Cardelli et al. (1989) reddening. . 219

B.1 A $45' \times 45'$image of M67 from the Digital Sky Survey. The footprints of the Chandra ACIS observation (dashed white boxes; van den Berg et al. 2004), ROSAT observations (dashed white circles; Belloni et al. 1993, 1998), and the XMM–Newton observations used in this work (red; aimpoints marked by crosses) are overlayed. 257

B.2 The >10 keV PN light curves for the two XMM-Newton observations of M67, ID 0109461001 (blue) and ID 0212080601 (green). The latter has enormous soft proton flaring, and the count-rate threshold of 40 counts per second used to define the good time interval is shown with the red line. 258

B.3 $V/B-V$ color-magnitude diagram of X-ray members in M67 known till date, and listed in Table B.3. Members from this work, from Belloni et al. (1998) and those from van den Berg et al. (2004) are plotted as black filled filled circles, red squares and green open circles respectively. Numbers specified in these respective colors are the IDs of sources in the respective catalogs (NX, RX and CX). Sources from WEBDA, from Yadav et al. (2008) with membership probability greater than 80%, and all EIS sources are plotted in grey. Note that the $B-V$ colors for main sequence stars of spectral types A0, F0, G0, K0, M0, and M8 are 0.0, 0.3, 0.6, 0.8, 1.4, and 2.0 respectively (Johnson 1966). 263

B.4 Spectral fitting for sources having PN countrate greater than 100 (NX1–8). For each source, the top panel shows the binned background-subtracted normalized countrate (black points with error bars), the best-fit single-/multi-component spectrum (green), and the individual spectral components (dashed black curves), while the bottom panel shows the residual-to-noise ratio. For best-fit parameters, see Table B.4 268

B.5 Hardness ratios (see §B.4.2) of the 75 unique sources detected in the XMM observations. Sources identified as M67 members, non-members, and sources with no optical counterparts (also suggested as non-members in §B.3.3) are shown as cyan circles, green crosses, and grey squares respectively. The weighted mean error bars are shown to the left hand side of the plot, representative of sources in each of the three classes. Note that these error bars are just for guiding the eye, and the actual uncertainties (see Table B.2) depend on countrate. Note that the members NX 36 and NX 75 have large uncertainties in their hardness ratios ($\sim$0.6), and appear to be outliers with respect to the clustering of M67 members in the lower right hand corner of the plot. The expected hardness ratios for three kinds of spectra, power-law (P(Γ)), blackbody (BB), and collisionally-ionized plasma (APEC), are shown as black circles joined by black lines (dashed, dotted and solid lines respectively). Each black dot marks a unique value of temperature (in case of BB or APEC) or a power law index. the hardness ratios have been calculated for Γ=1, 2, and 4 in the case of power law; T=0.03, 0.1, and 0.3 keV for BB; and T=0.3, 1, and 3 keV for APEC. For each type of spectrum, one point has been labeled. These were calculated using WebPIMMS using Galactic hydrogen column density of 2.2×10^{20} cm^{-2}. 271

B.6 The light curves for sources having 100 or more counts in PN (MOS1 for NX6). The background-subtracted light curves are in blue and the background-only light curves are in grey. Countrate (counts per second) is on y-axis and time in hours is along the x-axis. The time bin size is set to 300 s for NX1 and 450 s for the rest in order to get $>$30 counts in each bin. Whether a source is variable or not according to the χ^2 test is denoted on the upper left side. See §B.4.3 for details. 272

B.7 Variability of X-ray members of M67 on 5-month (top) and 4-year (bottom) timescale shown using plots of the X-ray luminosities of sources in Obs ID 0109461001 versus X-ray luminosities in van den Berg et al. (2004) (top) and those in Obs ID 0212080601 (bottom) respectively. The solid red line marks equal luminosities in either quantity plotted, and the red dotted (dashed) lines denote variability of a factor of 2 (5). See §B.4.3 for details. Note that the implied X-ray luminosities in the 0.2–7.0 energy band are used. 273

B.8 The X-ray luminosity functions for RS CVn-type sources in different star clusters. The sensitivity threshold for different star clusters below which the source counts are incomplete are shown at the bottom. See §B.5.1.1 for details. 276

List of Tables

1.1 Summary of Slow Radio Transient Phenomena at 1–6 GHz Frequencies 23
1.2 Telescope Specifications 27

2.1 Summary of OVRO 40-m Observations at 15 GHz 40

3.1 List of survey pointings 52
3.2 Observing Epochs 53
3.3 Variables among Miller et al. DR2 sources 60
3.4 Radio Positional Offsets wrt. Optical HST Catalogs 61
3.5 Completeness and Reliability of `sfind` catalog 80
3.6 Completeness and Reliability of *SExtractor* catalog 80
3.7 Completeness and Reliability of `SAD` catalog 81
3.8 Completeness and Reliability of `IMSAD` catalog 81
3.9 Completeness and Reliability of *Aegean* catalog 81

4.1 Summary of the Jansky VLA Observations 101
4.2 Summary of the radio transient and variable sources found in this work 144
4.3 Summary of the radio follow-up observations of variable and transient sources reported in this work 150

5.1 Log of Jansky VLA observations used in this work 159

6.1 Prime candidates for slow radio transients and other similar but low-priority objects 182

A.1 Number of O,B stars known to SIMBAD towards Taurus (central rectangle) and neighboring regions of equivalent area in coordinates of Galactic latitude and Galactic longitude. 234
A.2 Distances to known Taurus members measured through VLBI techniques. 234
A.3 List of candidate early-type stars with sections separating various selection methods. 235
A.4 Spectral types derived through new spectroscopy. 251
A.5 Physical parameters derived through model atmosphere fitting. 252
A.6 Final list of early-type stars showing indications of membership with Taurus. 253

B.1 XMM-Newton data on M67 258

B.2 Summary of EPIC detections in the field of M67. For each source we give the XMM-Newton source ID (NX), coordinates (α_{J2000}, δ_{J2000}), uncertainty in the coordinates ($\delta_{\alpha,\beta}$), PN total counts (counts) and countrate (ctr) in the total energy band (0.2–7 keV), hardness ratios (HR), ROSAT and Chandra counterparts (RX and CX from Belloni et al. and van den Berg et al. respectively), the distance between the EPIC source position and the optical counterpart (d_{XO}), membership in M67 (Y/N: Yes/No, from Yadav et al.; n: no from multiwavelength data) and comments. The superscript ^{a} on the source ID denotes that the corresponding counts, countrate, and hardness ratios are from the MOS1 detector due to the source being in one of the gaps of the PN CCD. 261

B.3 Summary of X-ray members of M67. The *top panel* shown members among the sources that were detected in XMM-Newton observations (this work) and classified as members in Vereshchagin et al. (2014), The *middle panel* shows members detected in Chandra van den Berg et al. (2004), while the *lower panel* lists members from ROSAT Belloni et al. (1998). The source IDs from this work, from Belloni et al. and van den Berg et al. are given in columns 1–3, the optical counterpart and its spectral type are listed in columns 4–5, X-ray luminosity in column 6, the orbital period and ellipticity in columns 7–8, and source classification is in column 9. See §B.3.3 for details. 264

B.4 The best-fit parameters and goodness-of-fit for the spectral fitting performed on sources NX1–8. The hydrogen column was held fixed and was calculated as described in §B.4.1. The columns are: (1) source ID; (2) single-multi-component model used for fitting along with photoelectric absorption; (3), (4) temperatures of the two APEC components used to fit spectra of member stars of M67, (5) ratio of the emission measures of the two APEC components; (6), (7) power-law index and blackbody temperature used for fitting non-members; (8) hydrogen column supplied to the photoelectric absorption model; (10) energy conversion factor (ECF=Rate/Flux; see §B.4.1); and (11) the reduced χ^2 of the fit and the degrees of freedom (dof; equal to the number of channel groups minus one). The corresponding fits are shown in Figure B.4. Note that NX6 fitting was done on MOS1. 269

Chapter 1

Introduction

Within our constantly changing Universe, transient phenomena are ubiquitous. These phenomena occur on a wide gamut of timescales, ranging from practically infinitesimal to a Hubble time[1]. Within this infinite realm, a Ph.D. student can study only a very minute, insignificant, portion. Here, I endeavor to study radio transient phenomena at GHz frequencies occurring on timescales between minutes and decades for reasons indicated below.

Time domain astronomy has always been and continues to be a subject of fascination. In the distant past transient phenomena such as eclipses and supernovae were observed and recorded[2]. Recently, the Astro 2010 decadal review has placed time domain at the forefront of discovery (Lazio et al. 2009). While in the past observations and data recording were done with minimal use of gadgets, technology has become the very driver for the exploration of the dynamic Universe today. Owing to the rapidly progressing CCD technology, optical astronomy has enjoyed large fields of view and high angular resolution, and as a result dedicated experiments (e.g. Carnegie Supernova Project, KAIT Supernova Search, Palomar Transient Factory, Pan-STARRS, etc.) for transient search have excelled for a long time. Synoptic survey instruments in the X-ray and γ-rays (e.g. Swift, Fermi) have given a similar rich yield of transients at higher frequencies. Despite the large surveys dedicated to pulsar search, exploration of the dynamic radio sky lags far behind the optical, X-rays and γ-rays. The search for slow radio transients has especially been hindered by the computational challenges and small fields of view associated with radio interferometers[3]. In fact, most of what we currently know about slow radio transients comes from the radio follow-up of objects discovered at higher frequencies. As a result, the rates of radio transients, the false positive foreground relevant for future radio counterpart searches to gravitational wave sources, the beaming angle jets in GRBs, are poorly constrained. Lastly, majority of the past blind surveys, carried out with radio interferometers, have suffered from low yield of slow transients, ambiguous transient classifications, and contamination by false positives (e.g. Bower et al.

[1] The smallest timescales currently measured for astrophysical transient phenomena are nanosecond giant pulses from the Crab pulsar. Phenomena occurring on timescales of millions of years include the formation of stars, the switching on and switching off of AGN jets, etc. Processes such as the appearance and disappearance of bars in the discs of galaxies or mergers of galaxies resulting in intense starbursts occur on much longer timescales, comparable to the Hubble time.

[2] Now a subject of archeoastronomy.

[3] Radio interferometers offer high angular resolution and are ideal for slow transient search.

2007; Bannister et al. 2011a; Thyagarajan et al. 2011; Frail et al. 2012; Mooley et al. 2013). Through this Ph.D. thesis I aim at addressing these issues by systematically exploring the dynamic radio sky for slow transient phenomena using the newly refurbished Karl G. Jansky Array (VLA).

The organization of this thesis is as follows. In the current chapter I introduce the reader to slow radio transients and describe the physical processes that drive these phenomena (§1.1), give an account of slow transient searches in literature (§1.2), describe the capabilities of the Karl G. Jansky array and its relevance for slow transient searches (§1.3), and enumerate the goals of this thesis (§1.4). The second chapter describes a collaborative radio follow-up effort, carried out early on in my Ph.D., to study a target of opportunity, Swift J1644+57 (published as Zauderer et al. 2011). Swift J1644+57 was the first non-thermal tidal disruption event, i.e. disruption of a star by a black hole leading to an outflow (jet), to be discovered. The estimated rates make such TDEs one of the most commonly-occurring extragalactic transients in the radio sky, and this fact raises a profound question: why weren't such transients found in previous radio surveys? The third chapter explores an archival approach to slow transient search through a narrow and deep survey in the Extended Chandra Deep Field South region with the legacy VLA (published as Mooley et al. 2013a). The fourth chapter reports a unique study of the dynamic radio sky through a joint radio and optical survey of 50 $\deg^2$ of the SDSS Stripe 82 region (Mooley et al. 2015a, ApJ, submitted). This survey was a pilot for the survey of the entire, 270 $\deg^2$, Stripe 82 region, called the Caltech-NRAO Stripe 82 Survey (CNSS). The CNSS survey was carried out using a new observing mode at the VLA, on-the-fly mosaicing (OTFM). The fifth chapter relates the OTFM survey methodology (Mooley et al. 2015c, in prep), which will be the basis for the VLA Sky Survey (VLASS) all-sky tier, which is currently in the planning phase. The sixth chapter reports some of the high-impact transients that have been discovered in the CNSS survey (Mooley et al. 2015d, in prep). Finally, the seventh chapter summarizes the thesis and gives some promising avenues for future slow radio transient search experiments. There are two appendices reporting some other work done during the Ph.D., but unrelated to slow radio transients (Mooley et al. 2013b; Mooley et al. 2015b, MNRAS, accepted).

For clarity and bookkeeping purposes I define transients, here at the beginning of my thesis, as events occurring for some period of time and then disappearing forever (non-recurring transients) or repeating sporadically / at regular intervals (recurring transients or variables).

1.1 Slow Radio Transient Phenomena And Physical Mechanisms for Transient Emission

In Figure 1.1, I show the wide gamut of transient phenomena detectable at radio frequencies, spanning 20 orders of magnitude or more in timescale and luminosity. It is evident that radio transients span a wide range of timescales and luminosities. In this figure, the points in gray represent the radio transients that have been previously found. Fast transient searches have been primarily carried out in spectral domain via single dish

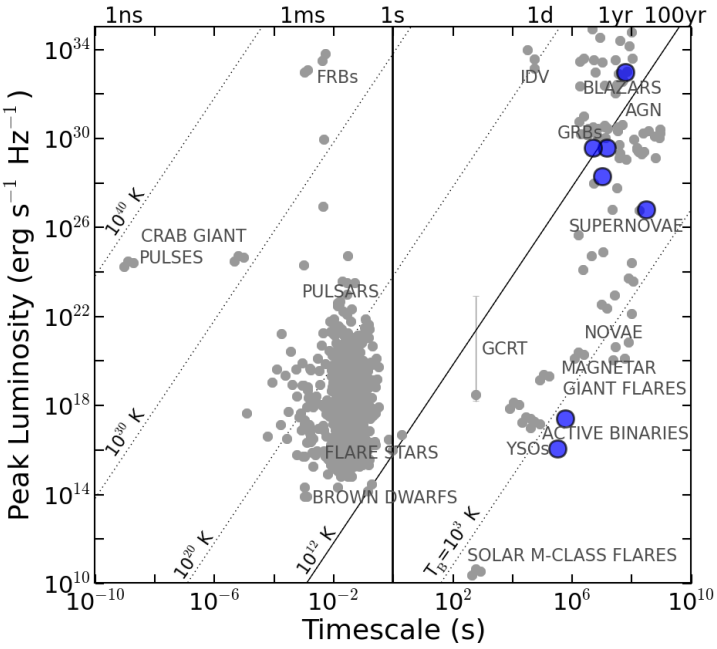

Figure 1.1: The phase space of radio transients. This plot shows two quantities, peak luminosity and the evolution timescale, among the several that characterize the phase space. Slant dashed lines are lines of constant brightness temperature. Slow transients are generally defined as having timescales larger than one second. The points in gray are previously-known radio transients. Some of the most noteworthy slow transients from the CNSS survey are marked in blue. Note that for some the extragalactic transients detected in CNSS, the timescales are not very well constrained, and the timescales marked here denote lower limits. Also note that for some of previously-known transients, such as flare stars, only the short timescale structure in their light curves has been considered.

experiments, while slow transient searches are typically done in image data, usually limited to integration times of one second or more. Hence, slow radio transients are generally defined as transients evolving on timescales longer than one second. I have also marked (in blue) some of the most noteworthy slow transients from the CNSS survey (reported in Chapters 4 and 6) in Figure 1.1. Slow radio transients allow us to study the environments and objects associated with extreme magnetic fields, relativistic outflows, the coupling between accretion discs and jets, black hole spin, and other exotic phenomena capable of producing gravitational waves. A summary of the known classes of slow transients at GHz frequencies is given in Table 6.1. Below, I provide a compilation of the physical processes responsible for each class of transient.

1.1.1 Extragalactic Phenomena

1.1.1.1 Active Galactic Nuclei

Galaxies containing an actively accreting supermassive black hole with or without a jet are called AGN. Owing to the nature of synchrotron emission, only those AGN which have a jet are detectable at radio frequencies. AGN variability in the radio can be extrinsic or intrinsic.

Extrinsic variability (see, for example, Walker 1998) arises from propagation effects and requires a very small angular size ($\sim \mu$as) for the radio source. Small phase changes ($\ll \pi^c/2$) introduced by the ISM over the first Fresnel zone defines the weak scattering regime, while the wavefront being highly corrugated on scales smaller than the first Fresnel zone defines the strong scattering regime. In the strong scattering regime (phase changes $\gg \pi^c/2$ introduced by the ISM), two types of variability are expected for point sources: slow, broad-band changes, and fast, narrow-band variations. The former is called refractive interstellar scintillation (RISS; since it can be understood in terms of lenses and ray-optics), while the latter is known as diffractive interstellar scintillation (DISS; since it is an interference phenomenon). Variability at frequencies at or below a few GHz ($\nu = \nu_0$) is thought to be dominated by RISS and not by intrinsic changes in the source (Gaensler & Hunstead 2000; Ofek et al. 2011). Since interstellar scintillation is strongest toward compact sources, we expect samples of variables to be dominated by flat-spectrum AGN, as appears to be the case (Condon et al. 1979; Gaensler & Hunstead 2000). For RISS, the amplitude of variability is small (less than a few ten percent), but for DISS, the variability amplitude can be much higher ($\sim$100%). In general, the amplitude and timescale of variability for ISS are both functions of frequency. The variability amplitude and timescale for RISS are proportional to $(\nu/\nu_0)^{0.5}$ and $(\nu_0/\nu)^2$ respectively (Walker 1998). For DISS, the timescale is proportional to (ν/ν_0). Extreme scattering events are instances where DISS is the cause for strong variability. At GHz frequencies the ISS variability timescale is generally $<$10 days (e.g. Ofek et al. 2011).

The basic model explaining intrinsic AGN variability in the radio is the shock-in-jet model (Marscher & Gear 1985; Türler et al. 2000; Fromm et al. 2011, 2014). In this model, the flaring processes in AGN are described through the propagation of a shock waves down the jet flow. VLBI observations reveal moving structures, or blobs, along the jets interpreted as shock waves. Electrons behind the shock are accelerated. They emit synchrotron radiation and radio spectrum evolves following three stages depending on the dominant emission-loss mechanism of the electrons. Initially, when the blob is close to the core, inverse-Compton scattering is the dominant loss mechanism. After the blob moves away, synchrotron losses take over, until finally, adiabatic losses dominate over the other two. A schematic diagram of the shock-in-jet model is presented in Figure 1.2. Intrinsic variability on long timescales (several years or more) can take place during phases of enhanced accretion in the AGN (e.g. Kunert-Bajraszewska et al. 2006, 2010; Czerny et al. 2009, Mooley et al. 2015a, ApJ, submitted), or, in blazars, due to jet-precession (e.g. Perucho et al. 2012; Lister et al. 2013; Chen et al. 2013). The radio light curves portraying the intrinsic variability of the quasar 3C 273 decomposed into individual outbursts using the shock-in-jet model (Türler et al. 2000) are shown in Figure 1.3.

1.1.1.2 Supernovae

Supernovae (SNe) are among the most energetic transient phenomena in the Universe, releasing $\geq 10^{51}$ erg in a few seconds with shock speeds ranging from 5,000 km s^{-1} to $\sim$3c/4 km s^{-1} (for the extreme Type Ic SN 1998bw; Kulkarni et al. 1998). While early and late-time optical emission in supernovae results from

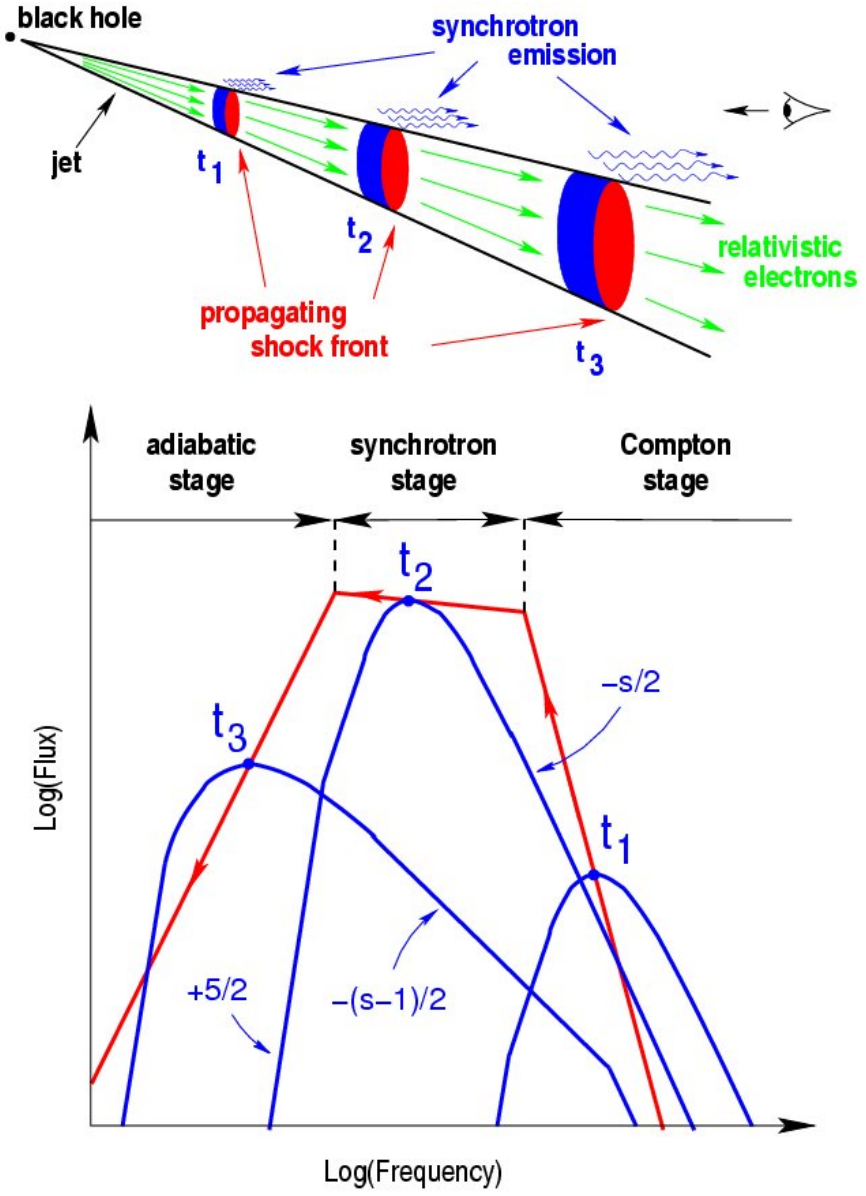

Figure 1.2: In the shock-in-jet model for AGN flaring, electrons behind shocks propagating down the jet are responsible for radio emission. The synchrotron radiation evolves in three stages depending on the dominant emission-loss mechanism of the electrons: inverse Compton, synchrotron, and adiabatic. Figure courtesy: M. Türler, Astronomy Department of the University of Geneva.

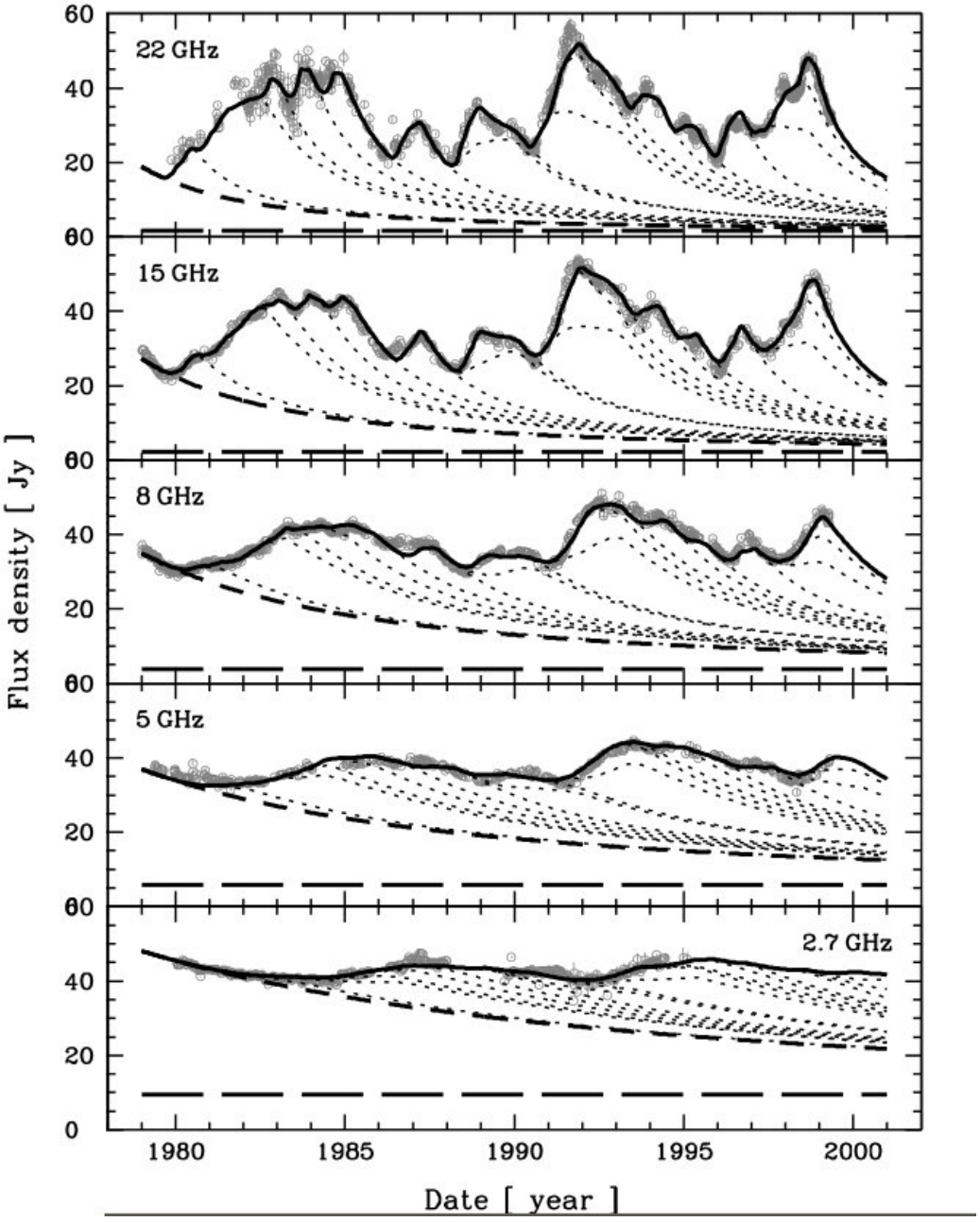

Figure 1.3: Radio light curves of 3C 273 (grey points) decomposed into a series of seventeen synchrotron outbursts (Türler et al. 2000). The best-fit light-curve is shown by solid lines, the emission from from the outer jet is shown by long-dashed lines, the decay of all outbursts peaking before 1979 is represented by short-dashed lines, and the seventeen superimposed outbursts are denoted by dotted lines.

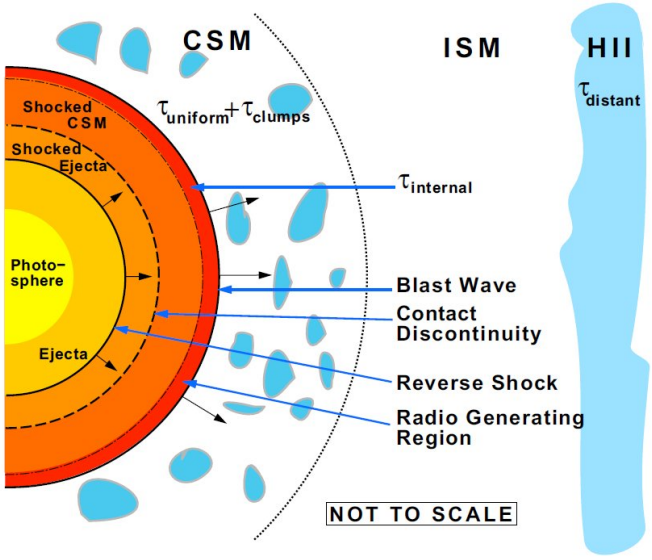

Figure 1.4: Schematic diagram of the supernova blastwave interacting with the CSM (Weiler et al. 2002; Stockdale et al. 2007). The radio emission originates just behind the blastwave.

prompt emission and decay of radioactive elements respectively (on timescales ranging from days to years), only the afterglow is detectable in the radio. A schematic diagram of the afterglow is presented in Figure 1.4. During the afterglow, the supernova blastwave interacts with a relatively high-density circum-stellar medium (CSM) that has been ionized and heated by the initial UV/X-ray flash (Chevalier et al. 1982a). The evolution timescale is a function of the density of the CSM, and is typically days to months (at 8 GHz) or years to decades (1.4 GHz). All known radio SNe appear to share common properties of (a) non-thermal synchrotron emission with high brightness temperature; (b) a decrease in absorption with time, resulting in a smooth, rapid turn-on, first at shorter wavelengths and later at longer wavelengths; (c) a power-law decline of the flux density with time at each wavelength after maximum flux density (optical depth$\sim$1) is reached at that wavelength; and (d) a final, asymptotic approach of spectral index to an optically thin, non-thermal, constant negative value (Weiler et al. 2002). The radio light curves can be used to model the SN blastwave interaction with the CSM and obtain several micro-physical parameters relevant to the SN-CSM system. These include the mass-loss rate from the SN progenitor prior to explosion as well as the density and clumpiness of the CSM (Chevalier et al. 1982a,b; Weiler et al. 1986; Sramek & Weiler 2003) .

There are two types of SNe based on the progenitor, type Ia (thermonuclear detonation of white dwarfs) and types Ib/Ic/II (resulting from the core-collapse of massive stars). While no radio emission has yet been detected from type Ia SNe (Panagia et al. 2006; Hancock et al. 2011; Chomiuk et al. 2012), 75% of detected radio SNe are type II and 25% are type Ib/Ic. Type II SNe are thought to be the deaths of stars between 8M$\odot$ and 40M$\odot$, while type Ib/Ic SNe are generally thought to be exploding Wolf-Rayet stars (M$>$ 40M$\odot$; Conti et al. 1983; Humphreys et al. 1985) or lower mass stars in interacting-binary systems (Uomoto 1986). The radio luminosities of radio SNe range between 10^{22} and 10^{28} erg s^{-1} Hz^{-1} (Weiler et al. 2002), while in the

optical the absolute V-band magnitudes are $-15 < M_V < -18$. Example radio light curves of SNe are given in Figure 1.5.

1.1.1.3 Beamed Afterglows from Long and Short γ-ray Bursts and their Orphan Counterparts

The prompt γ-ray (sub-MeV) emission in long GRBs lasts for several seconds and has a soft spectrum. Short GRBs on the other hand give prompt γ-ray emission lasting for less than one second and they have a hard spectrum. Long GRBs come from the deaths of massive, rapidly rotating stars. However, the exact nature of short GRB progenitors is unknown; the characteristics of the host galaxies and the energetics of the bursts suggest that and they arise from compact star mergers (neutron stars or black holes).

The fireball model (Figure 1.6) has become quite popular for explaining the electromagnetic emission seen in GRBs. A fine review of this model can be found in Piran (1999). The short-timescale structure in the GRB light curves suggests that the angular size of the emitting regions is extremely small, which is interpreted as being associated with jets with extremely narrow opening angles ($\theta_{\rm jet} <$ few degrees). Shortly after the formation of the central engine, γ-rays are produced via internal shocks and collisions within the ultra relativistic outflow. Internal shocks are not capable of converting all the energy of the relativistic outflow to radiation or thermal energy. The remaining kinetic energy will most likely dissipate via external shocks produced upon collision with the ISM. This external shock produces an "afterglow" resulting in radiation across the electromagnetic spectrum from X-rays to radio (see also Meszaros & Rees 1997). The discovery of several such afterglows confirms the fireball picture. The external shock is known to produce a forward shock and also a reverse shock, as indicated by the modeling of GRB afterglow light curves (e.g. Perley et al. 2014). The jet opening angle can be estimated from the jet break time, i.e. the time when afterglow light curves steepen due to the Lorentz factor becoming approximately $1/\theta_{\rm jet}$ (e.g. Rhoads 1997). The radio light curves of beamed GRBs compiled by Chandra & Frail (2012) are shown in Figure 1.7.

During the afterglow phase, the bulk Lorentz factor decreases with time while the beaming angle of the emitted radiation increases. If a GRB is observed off-axis, i.e. with a viewing angle that is larger than $\theta_{\rm jet}$, then the prompt burst of γ-ray will be undetected. However, the afterglow emission (in the optical, infrared and radio bands) can be detected after a certain time, when the beaming angle of the radiation becomes large enough to intercept the line of sight. Such a transient is called an Orphan Afterglow (OA) in the case of a long GRB and a binary neutron star (BNS) merger in the case of a short GRB. These transients are without any γ-ray counterpart, detectable at optical, infrared, and radio frequencies[4]. However, if the ISM is very dense, then the optical signal will be highly attenuated, giving access only via infrared and radio waves.

Radio signals from OAs and BNS mergers have not been discovered so far, although there exist published works predicting the expected radio signal through simulations. Through a population synthesis code, Ghirlanda et al. (2014) study the emission properties of OAs at GHz and sub-GHz frequencies. They find that OAs reach their emission peak on year-timescales and their duration is of a similar timescale. However, this

[4] At late times, the X-ray emission is much too faint.

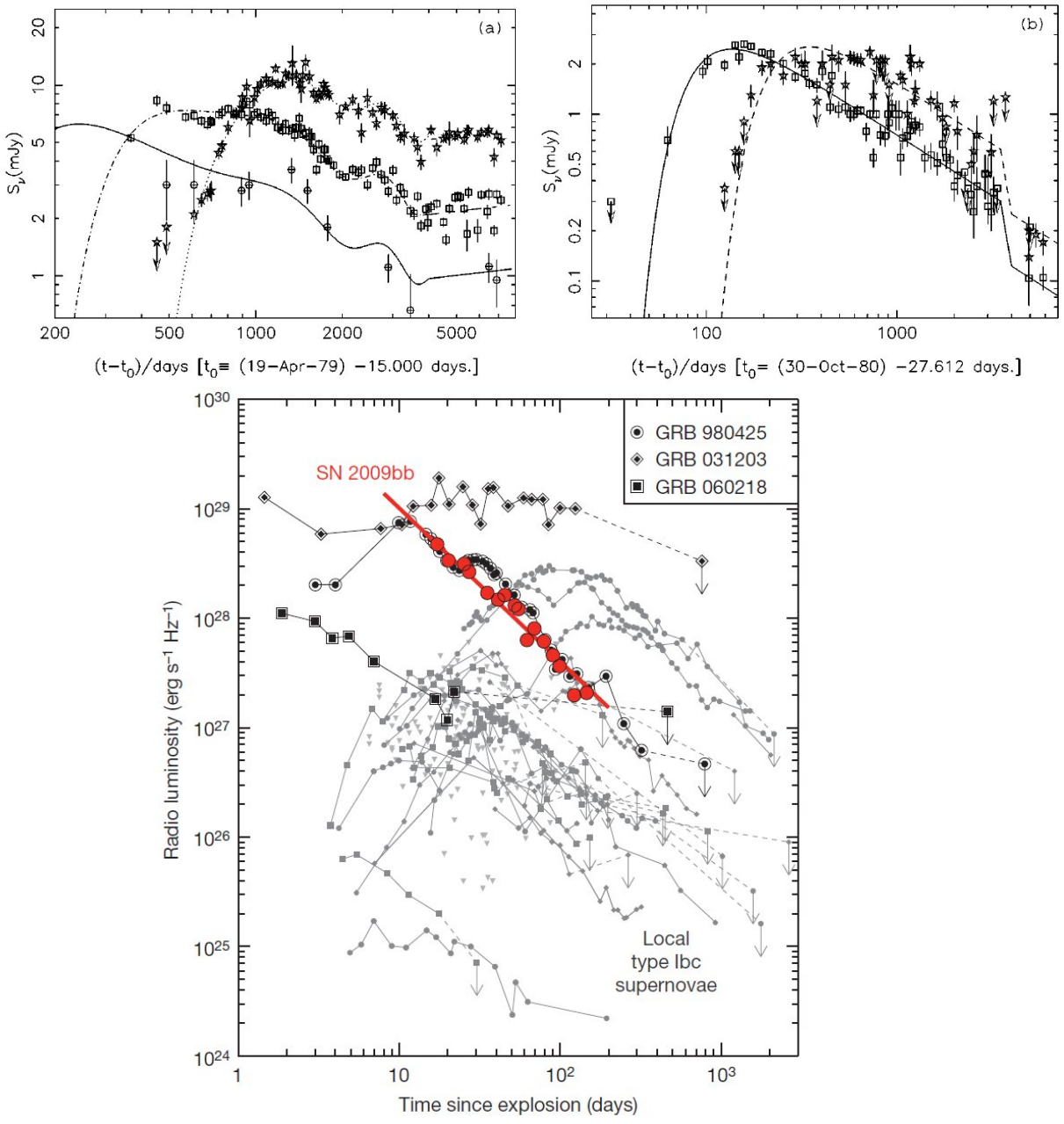

Figure 1.5: *Top*: Type II supernovae light curves from Weiler et al. (2002): (1) SN1979C (left) at 14.9 GHz (crossed circles, solid line), 4.9 GHz (open squares, dash-dot line), and 1.5 GHz (open stars, dotted line); and (2) SN1980K (right) at 4.9 GHz (open squares, solid line), and 1.5 GHz (open stars, dashed line). *Bottom*: A compilation of light curves of SN Ib/c supernovae in the local universe at 8.46 GHz from Soderberg et al. (2010). Local type Ib/c supernovae with well studied radio emission (grey) exhibit lower luminosities and peak at later times, indicating smaller sizes and lower mean expansion velocities. The radio emission from most local type Ib/c supernovae is below the detection threshold (3σ upper limits shown as grey triangles). Reprinted by permission from Macmillan Publishers Ltd: Nature (Soderberg et al. 2010), copyright 2010.

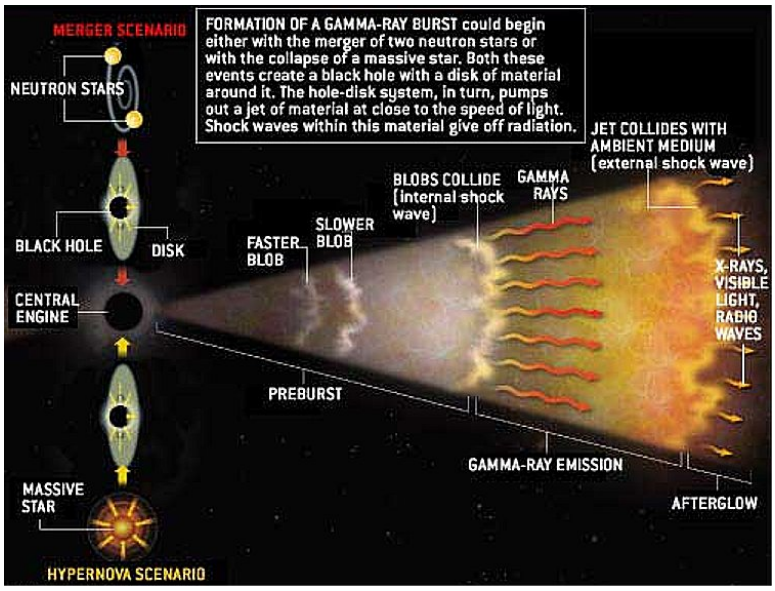

Figure 1.6: A schematic picture of the GRB fireball model. See §1.1.1.3 for details. Figure credit: J. Valesco.

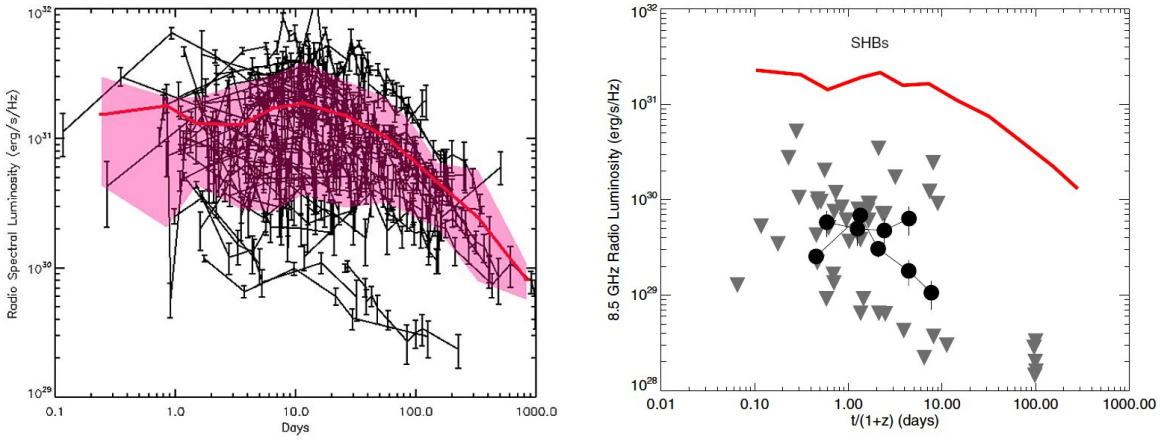

Figure 1.7: A compilation of beamed GRB light curves from Chandra & Frail (2012) at 8.5 GHz. Observer-frame long-duration GRBs are shown on the left while rest-frame short-duration GRB light curves are shown to the right. The red thick solid line represents the mean light curve for log GRBs. The pink shaded area is the 75% confidence interval for the long GRBs.

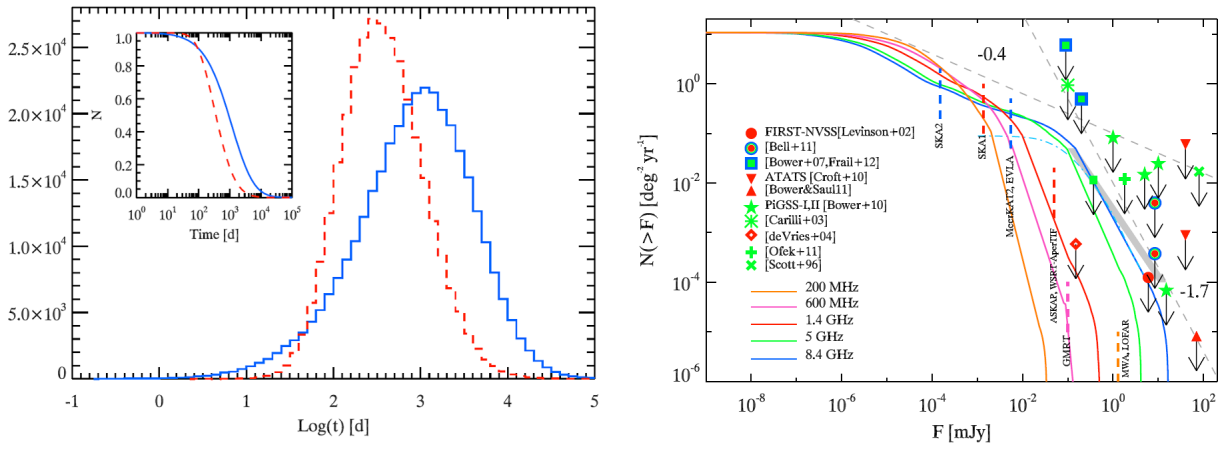

Figure 1.8: *Left*: Differential and cumulative (inset) distributions of the time when OA peak (blue solid line) and of the duration of the OA emission (red dashed line). *Right*: Cumulative flux distribution of OA at GHz and MHz observing frequencies (color codes as shown in the legend). Figure taken from Ghirlanda et al. (2014)

is dependent on the frequency of observations: the evolution is faster at higher frequencies. The evolution timescale and the rates for OAs expected from the Ghirlanda et al. study is given in Figure 1.8.

BNS mergers are sources of gravitational waves (GWs) that are also expected to give observable electromagnetic (EM) counterparts. Piran et al. (2013) present numerical simulations to study the EM signals from the dynamically ejected sub-relativistic material in BNS mergers. While in the infrared to ultraviolet wavelengths the outflows are expected to produce signals powered by radioactive decay evolving on day timescales, a long-lasting (timescales of more than a year at GHz and sub-GHz frequencies) radio counterpart is expected at radio frequencies on account of the interaction of the outflow with the surrounding matter (afterglow). The radio emission is expected to be dominant especially during the sub-relativistic phase of the ejecta. The expected radio signal from the numerical simulations is shown in Figure 1.9.

1.1.1.4 Non-thermal Tidal Disruption Events

If a star enters the tidal radius of the central supermassive black hole within a galaxy, then it is tidally disrupted. Whether any EM radiation is emitted as a result of the disruption depends on the mass of the black hole, M_{BH}. If M_{BH} is less than $\sim 10^8$ $M_\odot$, then the tidal radius,

$$R_T \simeq R_* \left(\frac{M_{BH}}{M_*}\right)^{1/3} \simeq 6 \times 10^{13} \text{ cm } M_{BH,8}^{1/3} \rho_*^{-1/3} \tag{1.1}$$

is larger than the Schwarzschild radius,

$$R_{Sch} = \frac{2GM_{BH}}{c^2} = 1.5 \times 10^{13} \text{ cm } M_{BH,8} \tag{1.2}$$

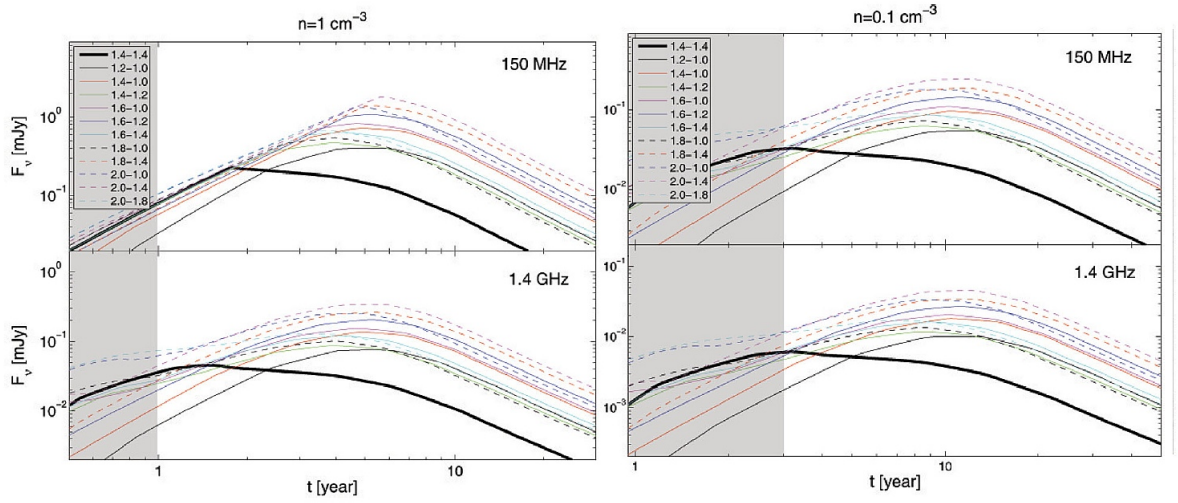

Figure 1.9: *Left*: Radio light curves of BNS merger events from the numerical simulations of Piran et al. (2013). The afterglow is generated by interaction of the dynamically ejected sub-relativistic outflows from different combinations of BNS masses. 1 cm^{-3} circum-merger environment density and a distance of 300 pc are assumed . The shaded region represents the period dominated by mildly relativistic outflows, not included in the simulations. *Right*: Same as the left panel, except for 0.1 cm^{-3} circum-merger environment density.

then the star is disrupted outside the event horizon, giving rise to EM radiation. Otherwise, the star is swallowed wholly by the black hole, leading to no transient emission. Assuming that $R_{\rm T}$ is larger than $R_{\rm Sch}$ (for a Sun-like star, this happens if $M_{\rm BH,8} < 7$), a star approaching the $R_{\rm T}$ acquires a quadrupole distortion leading to faster spinning up. This results in the disrupted material having a certain velocity spread, and half of the debris escaping on hyperbolic orbits around the black hole. The other half of the debris is gravitationally bound to the black hole on an elliptical orbit. The infall rate for a solar-type star is given by (Rees 1988),

$$\dot{M}(t) \simeq 25\, M_{\rm BH,8}^{-1/2} \left(\frac{t}{t_i}\right)^{-5/2} \tag{1.3}$$

where t_i is the infall time of the most tightly-bound debris. Radiation due to the loss of gravitational potential energy is the dominant heating mechanism and imparts temperatures of a few times 10,000 K in the inner parts of the accretion disk. Due to blackbody emission, this gives a bright transient at ultraviolet wavelengths. Due to high viscosity, the luminosity cannot permanently remain as high as the Eddington luminosity, $L_{\rm Edd}$. The luminosity eventually falls off as $t^{-5/2}$.

In some cases TDEs can give rise to jets, although the necessary conditions for jet launching in TDEs is not well understood. Such a transient is detectable in the radio and referred to as a non-thermal tidal disruption event (TDE). The first such case was discovered in March 2011, when Swift J1644+57 was detected as a rapidly flaring source by the Swift Burst Alert Telescope. This event was initially thought to be a GRB, was later found to be consistent with the tidal disruption event launching a jet that was relativistically beamed towards the Earth. Based on observational data in the first two days following the event, Bloom et al. (2011) suggested a possible analogy of Swift J1644+57 to be a scaled-down version of a blazar impulsively fed by

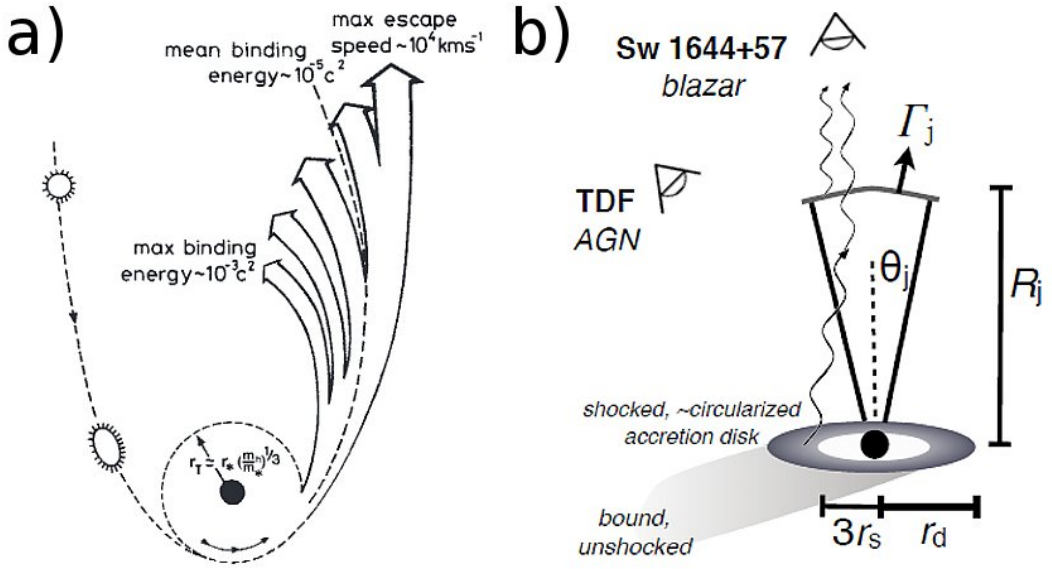

Figure 1.10: *Left*: A schematic diagram of the tidal disruption of a solar-mass star by a supermassive black hole (Rees 1988). The star approaching the black hole on a parabolic orbit at a pericenter distance r_T is distorted and spun up before being tidally disrupted. Almost half of the mass of the star going into the debris escapes on hyperbolic orbits. The gravitationally bound debris orbits the black hole on elliptical orbits. *Right*: The geometry and emission regions for Swift J1644+57 as suggested by Bloom et al. (2011). Shocked, circularized fallback mass sets up a temporary accretion disk with inner radius equal to 3 times the Schwarzschild radius (for a non-spinning BH). A two-sided relativistic jet starts at the time of accretion and travels through the interstellar region surrounding the black hole. Emission from the accretion disk is Compton up-scattered giving rise to the observed X-rays. A possible analogy of Swift J1644+57 to be a scaled-down version of a blazar impulsively fed by the tidal disruption of a Sun-like star is proposed. From Bloom et al. (2011). Reprinted with permission from AAAS.

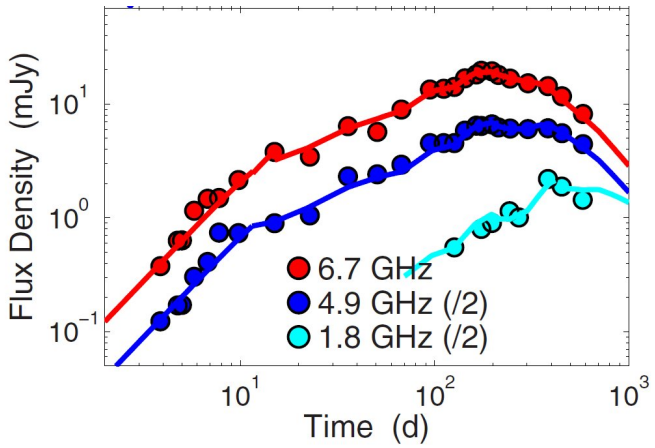

Figure 1.11: Radio light curves of Swift 1644+57 from Zauderer et al. (2013). The solid lines represent a synchrotron emission model described in Zauderer et al. (2013).

the tidal disruption of a Sun-like star. As the relativistic outflow plows through the circum-nuclear material (CNM), the electrons behind the shock front emit synchrotron radiation detectable at radio frequencies. The radio flux density depends on the density of the CNM. In the case of Swift J1644+57, extensive radio follow-up observations have been used to derive the energetics of the transient and the density of the CNM. To date, only two TDEs have been detected as radio transients, possibly suggesting that a majority do not have a super-Eddington phase and do not give rise to powerful jets. The radio light curves of the only TDE with detailed radio follow-up, Swift J1644+57, are shown in Figure 1.11.

1.1.2 Galactic Phenomena

1.1.2.1 Active Stars

Flaring phenomena on stars, resulting in transient radio emission, arises from the reconnection of magnetic fields. See Dulk (1985); Bastian et al. (1998) for reviews on this topic. Much of the flaring radio radiation is due to individual electrons being accelerated during such reconnection events. In some circumstances there can be very efficient conversion of electron energy into some natural wave mode of the plasma, such as electron-cyclotron waves (transverse, electromagnetic waves) or Langmuir waves (longitudinal, electrostatic waves). The characteristic frequencies of the plasma harboring these waves are typically $< 10^{10}$ Hz; the principal characteristic frequencies are the electron plasma frequency, $\nu_p \approx 9$ kHz$\sqrt{n_e/1\ \mathrm{cm}^{-3}}$, and the electron-cyclotron frequency, $\nu_c \simeq 3$ GHz $(B/1000\ G)$. Coherent radio bursts which have been detected from the Sun and other dwarf stars.

Rapid rotation gives rise to large magnetic fields, thus inducing frequent flaring phenomena. The ability to generate strong magnetic fields depends on the presence of a convective envelope. Rapidly rotating young stars of spectral type F, G, K, and M are therefore known to be active stars.

1.1.2.2 Active Binaries

There is an alternative way to enhance the rotation in stars: tidal interaction. Stars in binary systems which can tidally interact with each other can therefore become active even though they may not be young. This results in active coronae and chromospheres similar to active stars, and the emission mechanism is also similar. RS CVn-type systems are examples of active binaries of this type. For close binary systems, the magnetospheres of the components may collide and undergo reconnection events resulting in transient radio emission (Figure 1.12).

1.1.2.3 X-ray Binaries

X-ray binaries (XRBs) are accreting binaries that are luminous in X-rays. The acceptor is a compact star, i.e. a black hole (BH), a neutron star (NS), or a white dwarf (WD). There are two known classes of XRBs based on the mass of the donor star. Low mass X-ray binaries (LMXBs) consist of a BH or NS acceptor with a

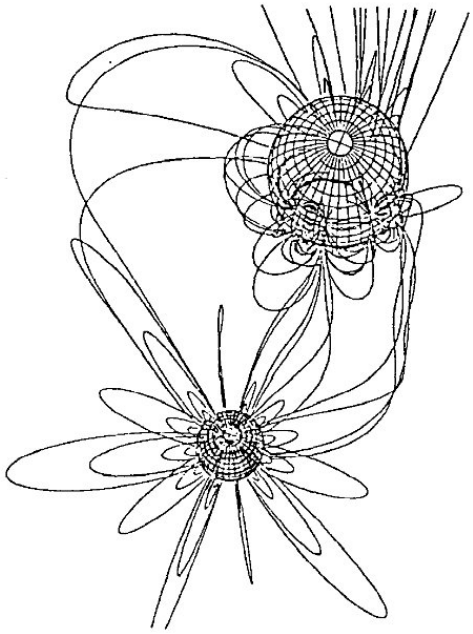

Figure 1.12: Close binaries may undergo magnetic reconnection events between magnetospheres. Figure taken from Dulk (1985).

donor star that has a lower mass than the acceptor. The donor may be a main-sequence star, a red giant, or a WD. High mass X-ray binaries (HMXBs) usually have a massive donor star, i.e. with spectral type O or B.

Accretion onto neutron stars is similar to that onto black holes (e.g, Psaltis 2006), with some notable difference arising due to the presence of a solid surface for neutron stars. Occasionally, XRBs undergo outbursts, lasting for a few months to a year, owing to global changes in the accretion disk, the corona, and the jets. The outburst is characterized by two distinct phases: the "hard state" and the "soft state", according to the hardness of the X-ray spectrum. During the hard state, occurring at the rise and decay of the outburst, the bolometric luminosity of the source is dominated by non-thermal emission. This may be synchrotron or inverse Compton emission from the jet and/or corona. During the soft state, occurring at the luminous outburst phase, the dominant emission mechanism is thermal (from the accretion disk). When XRBs are in outburst, the flux across the entire electromagnetic spectrum rises by several orders of magnitude (McClintock & Remillard 2006). The different hardness states versus the intensity of emission is shown in Figure 1.13.

The radio emission arises primarily from the jets. For a short summary of the radio transient emission observed from XRBs, see Corbel et al. (2015). Observations of Galactic black holes have shown two forms of jets associated with the hard and soft accretion states: 1) the slowly-varying, partially self-absorbed, compact jets having a flat or slightly inverted radio spectrum and radio luminosities of $\sim 10^{20}$ erg s^{-1} Hz^{-1} observed in the hard state (Corbel et al. 2000; Fender et al. 2000; Dhawan et al. 2000; Stirling et al. 2001), and 2) the strongly variable, transient, jets having an optically thin radio spectrum detected during the transition from the hard to the soft state (Corbel et al. 2004; Fender et al. 2004). Radio emission from jets interacting

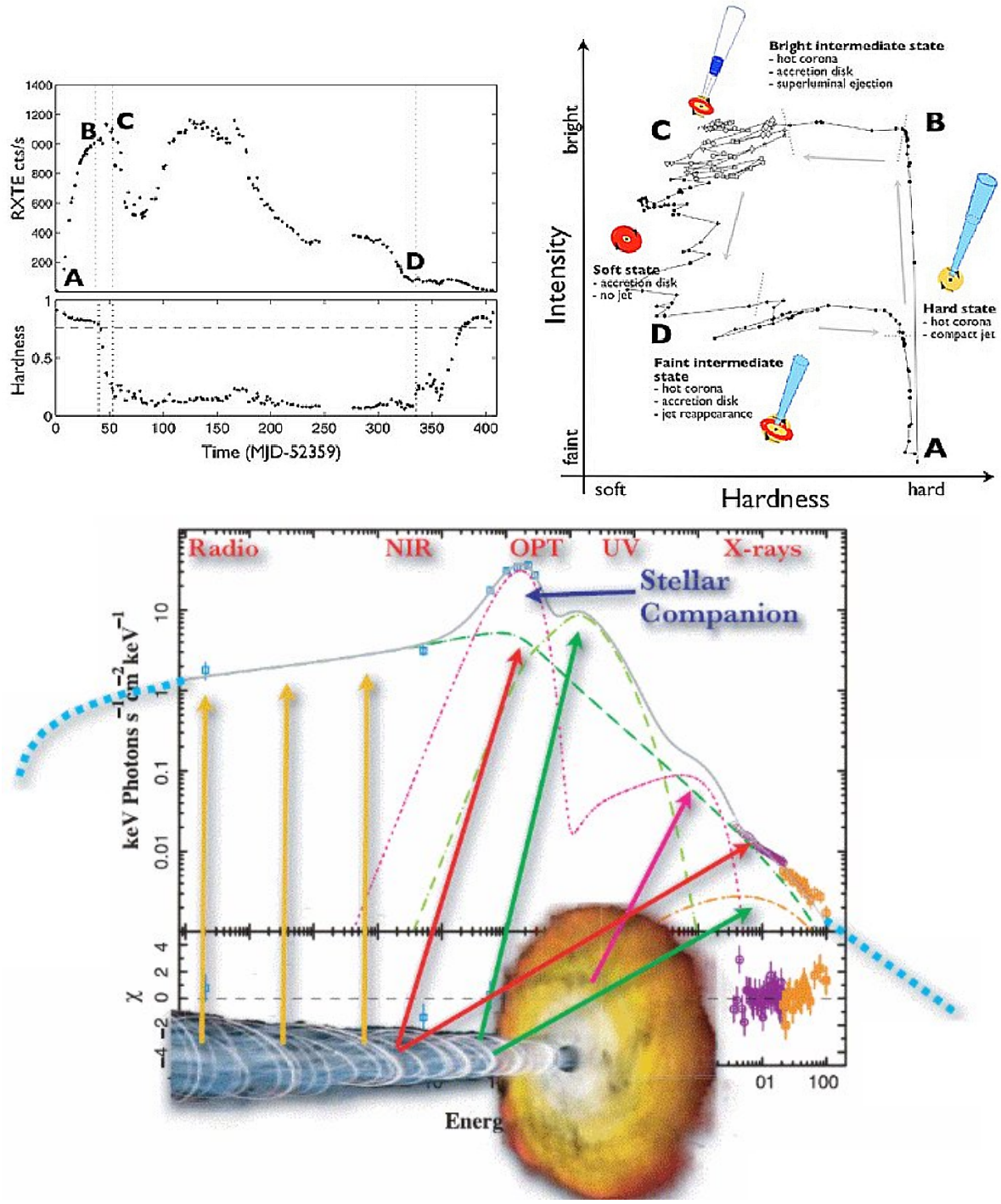

Figure 1.13: *Upper left*: Count rate and hardness light curves of the black hole binary, GX 339-4, during its 2002-03 outburst (Belloni et al. 2005). *Upper right*: The hardness-intensity diagram for the GX 339-4 outburst. At the beginning of the outburst (A->B), the system is in the hard state with emission dominated by non-thermal processes in a very hot, optically thin, plasma ("corona"). The radio emission observed in this state is believed to be entirely produced by a steady jet. When the system reaches high luminosities (B->C), it transitions into the soft state, in which discrete super-luminal ejections occur. In the soft state (C->D), the spectrum is dominated by thermal emission from an optically thick accretion disc, and the radio/IR emission is strongly reduced, suggesting the disappearance / fading of the jet component. At the end of the outburst (D->A), the accreting system turns back to the hard state, with the reappearance of the radio/IR emission (but without super-luminal ejection). Figure courtesy: S. Markoff, J. Miller-Jones, R. Fender.

with the ambient medium can also be detected as large-scale lobes (Gallo et al. 2005), or as faint, transient, hot spots (Corbel et al. 2002). Typically, the sub-GHz radio emission will peak a few days to weeks later and at lower fluxes (by an order of magnitude or more) compared to the emission at GHz frequencies. The radio light curves of two magnetars captured in outburst, GRS 1915+105 and XTE J1859+226, are shown in Figure 1.14.

1.1.2.4 Cataclysmic Variables

Cataclysmic variables (CVs) are binary systems consisting of a white dwarf primary and a mass transferring secondary. The accretion disk may be prone to instability leading to dwarf nova outbursts, where a small fraction of the disk material falls onto the white dwarf, leading to radiation from the loss of gravitational potential energy. Brighter and less frequent outbursts resulting from hydrogen fusion reactions on the surface of the white dwarfs are called "novae" (see §1.1.2.8). Sometimes, the accretion process may continue for extended periods of time such that the white dwarf mass comes close to the Chandrasekhar limit, thus igniting carbon fusion and triggering a Type Ia supernova explosion (see §1.1.1.2).

Cataclysmic variables (CVs), such as the recurrent nova RS Oph (Rupen et al. 2008) and the dwarf nova SS Cyg (Körding et al. 2008) have shown evidences for synchrotron emission at radio frequencies, which has been interpreted as jetted outflows. However, the brightness temperatures of the radio emission are not inconsistent with thermal or cyclotron emission processes. There is a possibility of multiple emission mechanisms being at play.

Persistent jets are also thought to occur in nova-like variables (Körding et al. 2011) in a regime of steady high mass transfer rate (e.g. Potter & Balbus et al. 2014). The non-magnetic dwarf nova, SS Cyg, repeatedly exhibits radio outbursts associated with its disc instability outburst cycle (Körding et al. 2008). The outbursts in dwarf novae are described by a thermal-viscous instability in the accretion disc, leading to enhanced mass transfer lasting for days to weeks. CVs provide an important link in understanding how accretion is coupled to the outflow. The radio and optical light curve of the dwarf nova SS Cyg are shown in Figure 1.15.

1.1.2.5 Pulsars

While the intrinsic radio luminosity of normal rotation-powered pulsars is expected to be steady, their emission is affected by interstellar scintillation. The largest variability is seen for the nearest pulsars since in that case the number of scattering centers is small. The typical timescale for scintillation is $\sim$1 minute at 20 cm (e.g. Walker 1998). Occasionally, pulsars also show long-term variations in their mean pulse energies by a factor of 10 or more (e.g. Rankin et al. 1974; Lyne et al. 1975; Levinson et al. 2002).

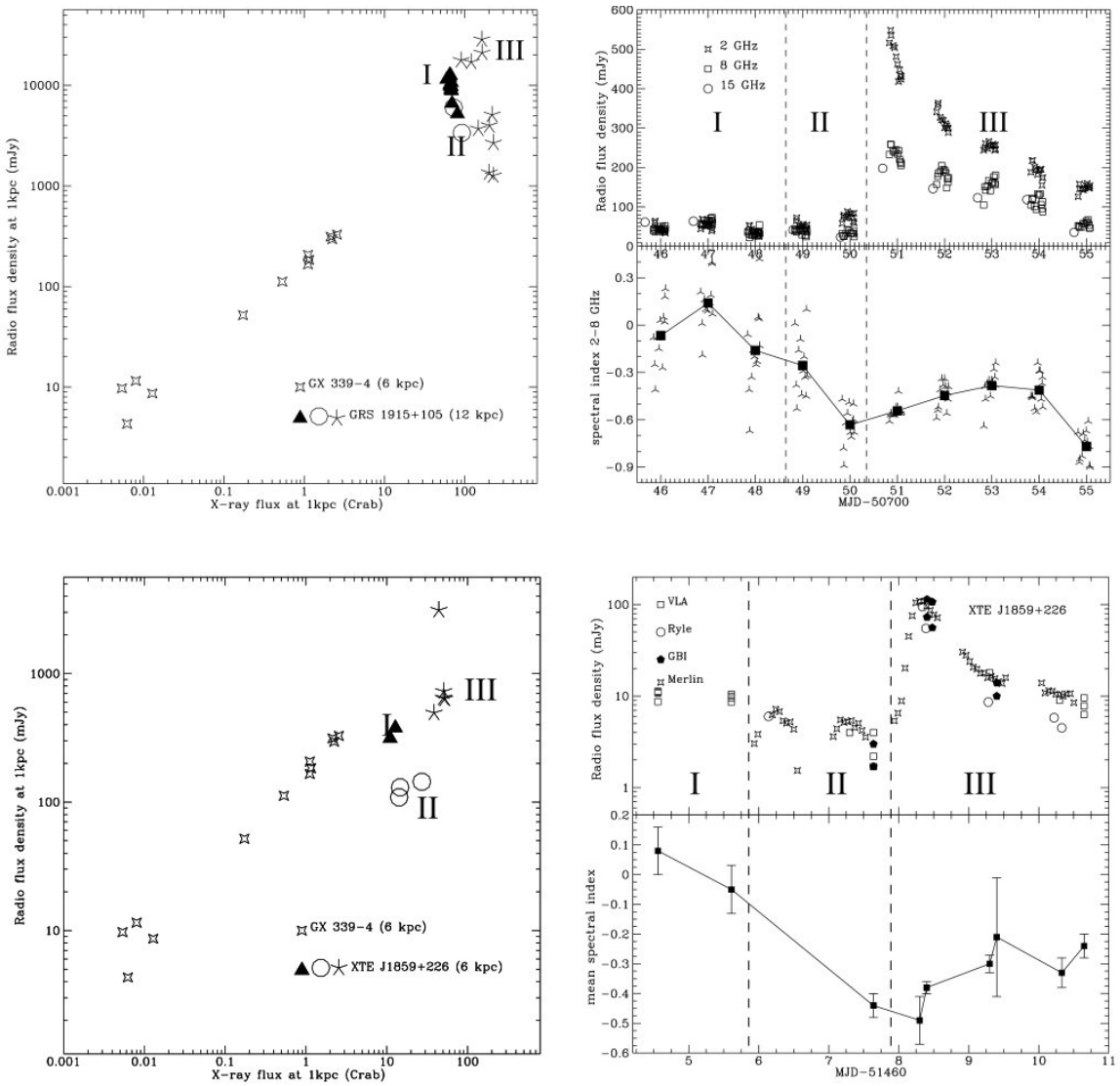

Figure 1.14: Two examples of XRB flares observed in the radio and X-rays (Fender et al. 2004). The top panels show observations for GRS 1915+105 and the lower panels show XTE J1859+226 observations. The panels on the left indicate the behavior of these flares in the L_{radio}–L_X plane while the panels to the right indicate thier behavior in the radio.

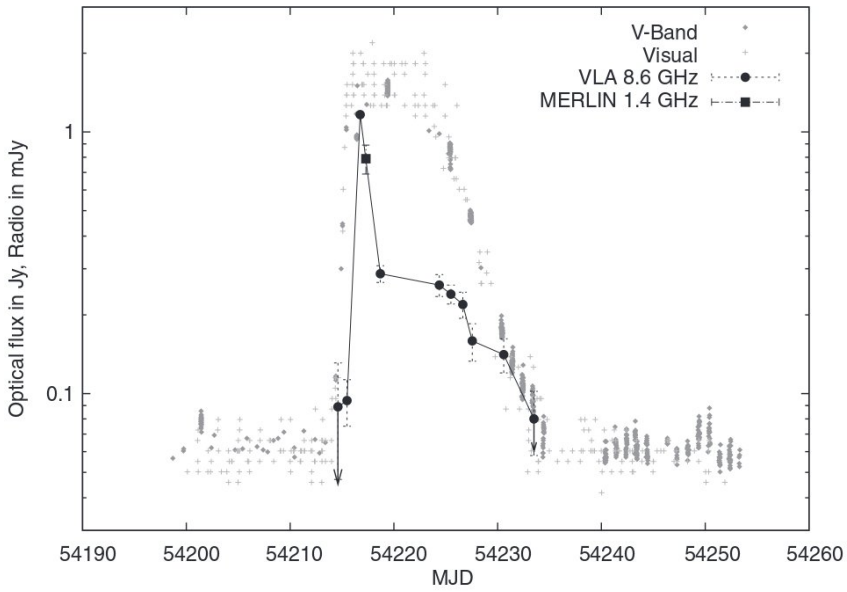

Figure 1.15: Radio and optical light curve of the dwarf nova, SS Cyg, from Körding et al. (2008). Reprinted with permission from AAAS.

1.1.2.6 Magnetars

Magnetars are isolated neutron stars having field strengths of $>10^{13}$ G. They occasionally undergo giant flaring episodes probably due to magnetic reconnection events. These giant magnetar flares are associated with transient radio emission, short bursts of gamma-rays, and mildly-relativistic ejecta. SGR 1806-20 is an exemplar, which underwent a large outburst on 27 Dec 2004. The associated radio flare reached a peak flux density of over 100 mJy at 1.4 GHz, and gave rise to relativistic ejecta (Gaensler et al. 2005; Cameron et al. 2005; Fender et al. 2006) Transient radio emission arising from the flare is shown in Figure 1.17.

1.1.2.7 Brown Dwarfs

Brown dwarfs are known to exhibit flaring phenomena attributed to gyrosynchrotron emission and radio "pulses" arising from electron-cyclotron emission traversing the line of sight over a rotation cycle of these objects (Berger et al. 2001; Hallinan et al. 2007). With μJy-level sensitivities, it is possible to detect such pulses from brown dwarfs up to a distances of tens of pc. The pulsing emission, thought to be due to electron-cyclotron emission similar to that from Jupiter, is periodic and circularly polarized. The period corresponds to the rotation period of the brown dwarfs, so active regions on the brown dwarfs are envisaged. The flux density drops off precipitously beyond the cyclotron frequency at the surface of the dwarf, $\nu_c \simeq 3$ GHz $(B/1000\ G)$, where B is the surface magnetic field. Thus, GHz observations of brown dwarfs allow us to accurately measure and study extreme magnetic fields, $\sim$kG strength, a regime inaccessible to other methods. The radio flaring light curves of the brown dwarf LP944-20 (Berger et al. 2001) and the pulsing light curves of TVLM 513-46546 (Hallinan et al. 2007) are shown in Figure 1.17.

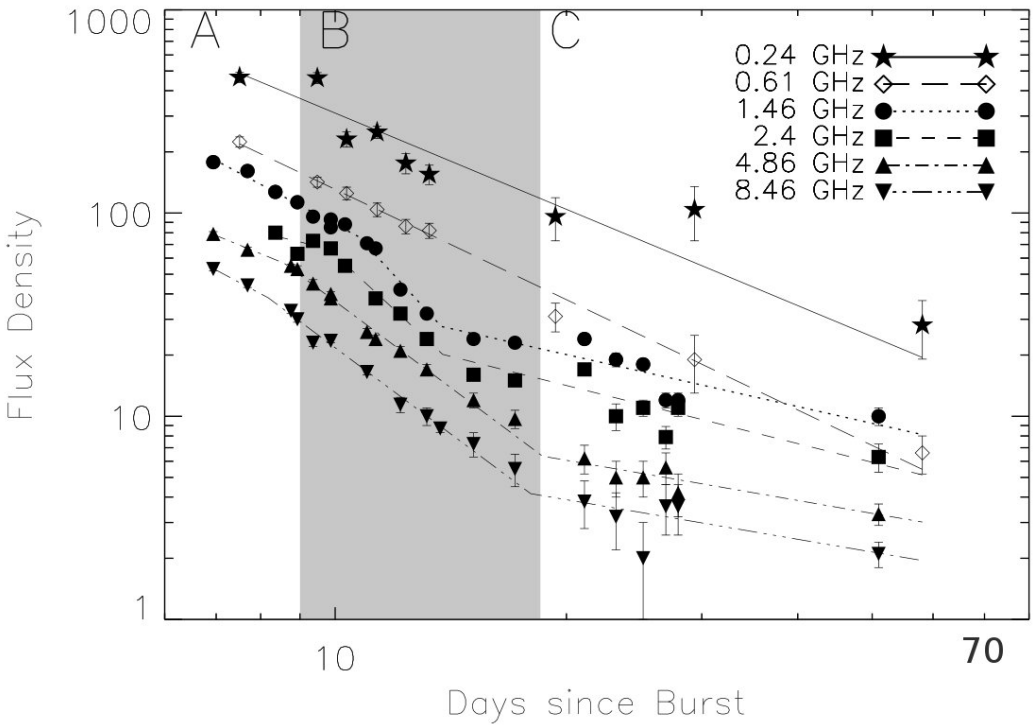

Figure 1.16: Radio light curves for SGR 1806-20 from Cameron et al. (2005). The best-fit broken power-law models are indicated by lines. The first break in the spectrum defines the boundary between the regions A and B. Region B, the period of steep light curve decline, is shaded gray. The second break in the GHz spectrum defines the boundary between the regions B and C. Reprinted by permission from Macmillan Publishers Ltd: Nature (Cameron et al. 2005), copyright 2005.

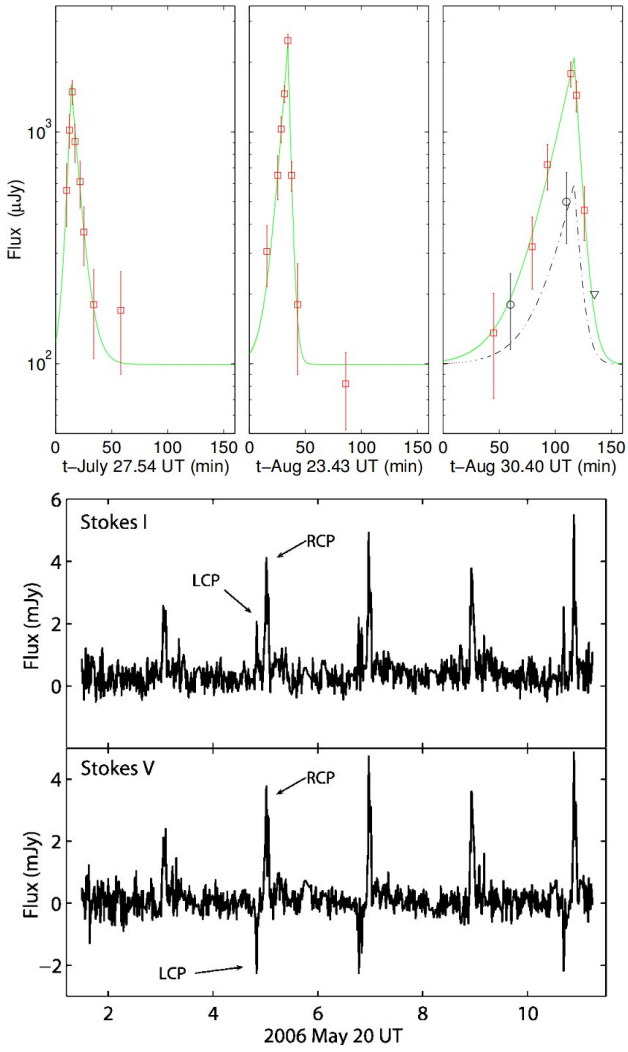

Figure 1.17: *Top*: Radio flaring and quiescent emission from the brown dwarf LP944-20 found by Berger et al. (2001). The three panels show light curves at three different epochs. Squares indicate emission at 8.5 GHz while circles represent 4.9 GHz emission. Solid and dashed lines represent a simple exponential model fit to the flaring light curves. Reprinted by permission from Macmillan Publishers Ltd: Nature (Berger et al. 2001), copyright 2001. *Bottom*: Periodic pulses of radio emission from the brown dwarf TVLM 513-46546 (Hallinan et al. 2007) correlated with the spin period of 1.96 h. The total intensity (Stokes I) and the circularly polarized (Stokes V) radio emission at 8.44 GHz are shown. The pulses are 100% polarized, with right circularly polarized emission appearing as positive peaks and the left circularly polarized emission appearing as negative peaks in Stokes V.

1.1.2.8 Novae

Novae occur in CVs when the density and temperature at the bottom of the accumulated hydrogen layer become high enough to ignite hydrogen fusion reactions, thus convert the hydrogen layer rapidly to helium. They are brighter and less frequent than dwarf novae. While thermal emission is the dominant component of radio emission in novae (Seaquist & Bode 2008; Chomiuk et al. 2014), a significant number of novae exhibit non-thermal, synchrotron, emission associated with collimated bipolar and jet-like outflows (e.g., RS Oph: O'Brien et al. 2006; Rupen et al. 2008). Late-time emission might arise due to the shock interaction with the ISM or ejecta. The radio light curves of three novae, V1500 Cyg, 1723 Aql, and V959 Mon, are shown in Figure 1.18.

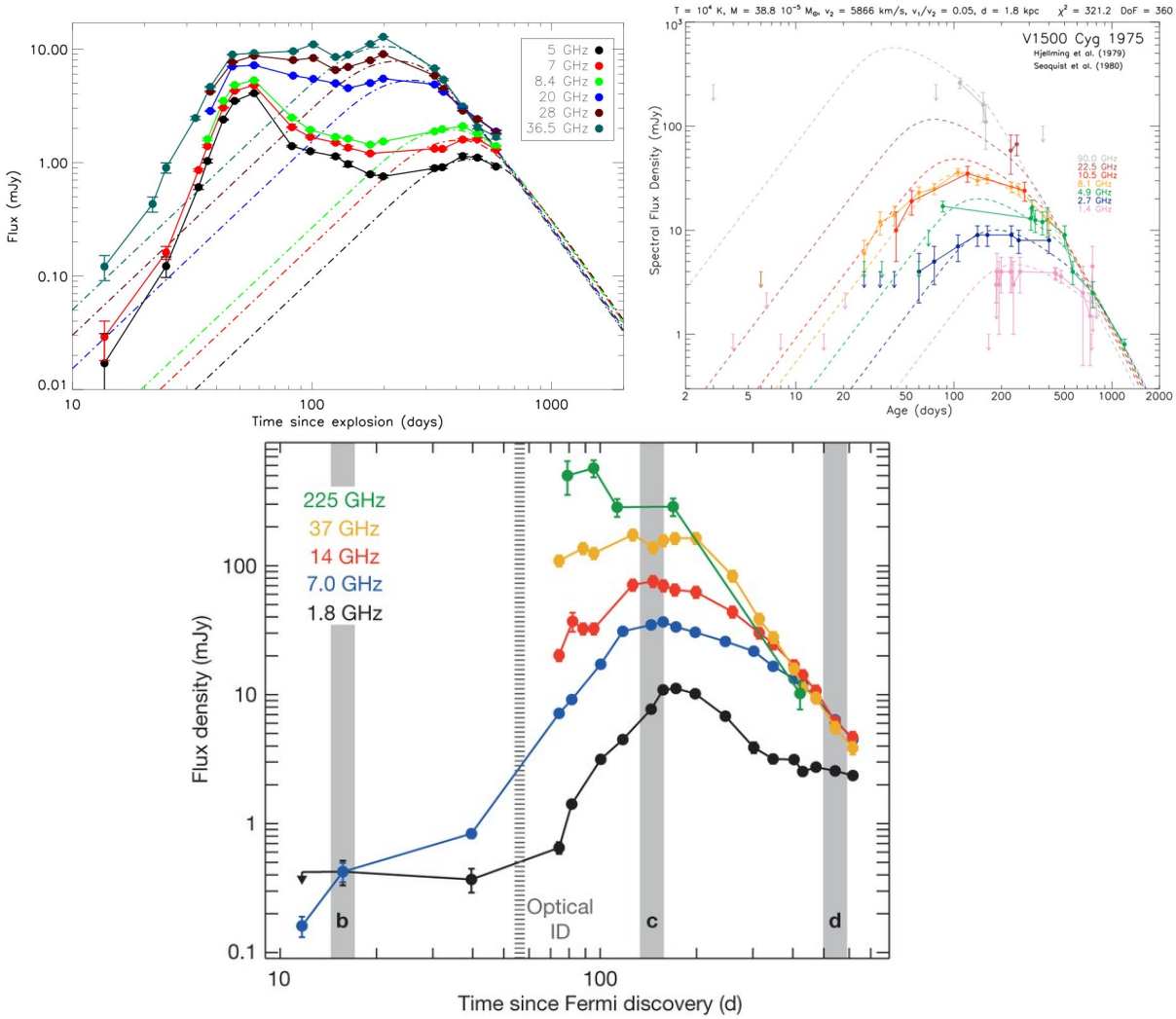

Figure 1.18: *Top*: The multi-frequency radio light curves of two novae, V1500 Cyg (left) and 1723 Aql (right), considered in Roy et al. (2012). The best fit Hubble flow model (dashed lines) shows that late-time data agree with the standard model of expanding thermal ejecta. *Bottom*: The multi-frequency light curve of nova V959 Mon (Chomiuk et al. 2014) consistent with a expanding thermal ejecta model. Reprinted by permission from Macmillan Publishers Ltd: Nature (Chomiuk et al. 2014), copyright 2014.

Table 1.1: Summary of Slow Radio Transient Phenomena at 1–6 GHz Frequencies

No	Object	Variability Process	Location	Timescale		Peak Luminosity		Rate (>0.3 mJy)	Ref.
				Radio	Optical	Radio (erg s^{-1} Hz^{-1})	Optical (erg s^{-1})	(deg^{-2})	
				Extragalactic					
1	AGN	a) Quiescent	Nuclear	years – decades	years	10^{27}–10^{34}	10^{42}–10^{47}	0.6	1–7
		b) Shock-in-jet	”	days – years	—	10^{27}–10^{34}	—	1.25	6–10
		c) ISS	”	minutes – days	—	—	—	60	11–13
		d) ESE	”	months	—	—	—	0.001	14–15
		e) Jet-precession	”	years	—	—	—	unknown	16–17
2	SN-II/Ib/c	Shocked CSM	Traces SF	months – decades	days – months	10^{25}–10^{29}	10^{41}–10^{43}	0.04 (II), 6×10^{-6} (Ib/c)	18–23
3	SN-Ia	Shocked CSM	Non-nuclear	days – weeks	days – months	$\lesssim10^{23}$	10^{39}–10^{43}	$<10^{-5}$	23–28
4	Long-GRB	Shocked CSM / Jet	Traces SF	days – years	days – months	10^{29}–10^{31}	10^{43}–10^{47}	6×10^{-5}	29
	OA	Shocked CSM	Traces SF	weeks – years	days?	10^{29}–10^{30}	10^{43}–10^{46}	7×10^{-4}	30–32
5	Short-GRB	Shocked CSM / Jet	Non-nuclear	days – years?	days	$\sim10^{25}$	$10^{39} \sim 10^{41}$	$<10^{-6}$	33–35
	BNS merger	Shocked CSM	Non-nuclear	weeks – years	days	$10^{22} \sim 10^{25}$	$10^{39} \sim 10^{40}$	2×10^{-4}	31,36–37
6	TDE	Shocked CNM / Jet	Nuclear	years?	months – years?	$10^{30} \sim 10^{31}$	$10^{42} \sim 10^{44}$	0.005	31,38–40
	Off-axis TDE	Shocked CNM	Nuclear	years?	unknown	$\sim10^{30}$	unknown	0.01	31
7	AIC	Shocked CSM	Non-nuclear	months	day	unknown	$\sim 10^{39}$	6×10^{-5}	70–72
				Galactic					
1	Active star	Flaring (magnetic)	Isotropic	hours – days	seconds – hours	10^{12}–10^{15}	$10^{30} \sim 10^{33}$	0.02	7,41–44
2	Active binary	Flaring (magnetic)	Isotropic	hours – days	hours – days	10^{14}–10^{22}	$< 10^{33} \sim 10^{34}$	0.01	7,41,43,46
3	X-ray binary	Mass accretion / flare	GP	days – weeks	minutes – hours	$10^{20} \sim 10^{21}$	$\sim10^{35}$	0.005	7,44,46–50
4	CV	Dwarf nova / jet	GP	hours – days	days – weeks	$10^{16} \sim 10^{17}$	$10^{33} \sim 10^{35}$	0.001	44,51–54
5	YSO	Mass accretion / flare	GP	hours – weeks	hours – weeks	10^{16}–10^{18}	$10^{31} \sim 10^{34}$	<0.05	7,41,55
6	Pulsar	Scattering	GP	weeks – months	—	$10^{15} \sim 10^{17}$	—	0.003	44,56,57
7	Magnetar	Flaring (magnetic)	GP	weeks	unknown	$\sim10^{20}$?	unknown	<0.05	7,58–60
8	Brown Dwarf	Pulsing (magnetic)	Isotropic	seconds – hours	seconds – hours	$10^{13} \sim 10^{14}$	$\sim10^{24}$	<0.05	7,61,62
9	Novae	Ejecta / Shocked CSM	GP	years	days – months	$\sim 10^{20}$	10^{38}–10^{40}	<0.05	23,63–65
10	GCRT	Unknown	Unknown	minutes – years	unknown	unknown	unknown	unknown	66–69

References: [1]Aller et al. (1999), [2]Valtaoja et al. (1992), [3]Arshakian et al. (2012), [4]Hovatta et al. (2008), [5]Padovani et al. (2011), [6]Woo & Urry (2002), [7]this work, [8]Teraesranta et al. (1998), [9]Mooley et al. (2013), [10]Türler et al. (2000), [11]Dennett-Thorpe & de Bruyn (2002), [12]Lovell et al. (2008), [13]Ofek et al. (2011), [14]Fiedler et al. (1994), [15]Murphy et al. (2013), [16]Lister et al. (2013), [17]Chen et al. (2013), [18]Weiler et al. (2002), [19]Stockdale et al. (2009), [20]Soderberg et al. (2010), [21]Gal-Yam et al. (2006), [22]Berger et al. (2003), [23]Kasliwal (2012), [24]Boffi & Branch (1995), [25]Panagia et al. (2006), [26]Hancock et al. (2011), [27]Chomiuk et al. (2012), [28]Perez-Torres et al. (2014), [29]Chandra & Frail (2012), [30]Ghirlanda et al. (2014), [31]Metzger et al. (2015), [32]Cenko et al. (2013), [33]Hjorth et al. (2005), [34]Tanvir et al. (2013), [35]Fong et al. (2014), [36]Nakar & Piran (2011), [37]Piran et al. (2013), [38]Zauderer et al. (2011), [39]Cenko et al. (2012), [40]Zauderer et al. (2013), [41]Güdel (2002), [42]Kovari et al. (2007), [43]AAVSO, [44]Thyagarajan et al. (2011), [45]Henry & Newsom (1996), [46]Augusteijn et al. (1992), [47]Motch et al. (1989), [48]Miller-Jones et al. (2004), [49]Miller-Jones et al. (2012), [50]Williams et al. (2013), [51]Körding et al. (2008), [52]Mooley et al. (2015), in prep., [53]Groot et al. (2015), in prep., [54]Patterson et al. (2011), [55]Findeisen et al. (2013), [56]Levinson et al. (2002), [57]Huguenin et al. (1973), [58]Gaensler et al. (2005), [59]Cameron et al. (2005), [60]Fender et al. (2006), [61]Hallinan et al. (2007), [62]Harding et al. (2013), [63]Chomiuk et al. (2012b), [64]Roy et al. (2012), [65]Kantharia et al. (2007), [66]Hyman et al. (2002), [67]Hyman et al. (2005), [68]Hyman et al. (2007), [69]Hyman et al. (2009) [70]Piro & Kulkarni et al. (2013), [71]Metzger et al. (2009), [72]Darbha et al. (2010)

Notes: (1) Location refers to the position within the host galaxy where the transient class is expected to be concentrated. (2) Timescale refers to the approximate time duration for which the flux density of a transient is within an order of magnitude of the flux density at the peak of the light curve. (3) The transient rates (instantaneous snapshot rates) are compiled from a variety of sources. In some cases, a $N\propto S^{-3/2}$ scaling has been applied to find the rate above the 0.3 mJy flux density threshold. The expected uncertainty / scatter in the rate is between 10–50%. (4) Variability of the quiescent AGN emission refers to the sustained change in the quiescent flux density level. (5) Extrinsic variability phenomena considered here, viz. interstellar scattering (ISS) and extreme scattering events (ESEs), are discussed only in the context of AGN. While the rates of these events are dominated by AGN, they could very well affect any class of compact sources such as pulsars. (6) Orphan afterglows (OAs) and binary neutron star (BNS) mergers refer to the orphan counterparts of beamed long- and short-GRBs respectively. (7) TDE rates assume Swift J1644+57-like events. The deg^{-2} rates quoted here for on- and off-axis TDEs have been calculated using the (logarithmic) mean of the Gpc^{-3} yr^{-1} rate from Metzger et al. (2009) and that implied by the two on-axis TDEs discovered till date: Swift J1644+57 and Swift J2058+05 (Zauderer et al. 2011; Cenko et al. 2012).

1.2 Exploration of the Dynamic Radio Sky In Literature

Existing transient surveys have already explored, to some extent, the dynamic radio sky with a wide range of sensitivities, angular resolution, and cadences. I am maintaining a revised list of transient surveys online[5].

There have been a number of wide field surveys of the sky at 1.4 GHz. Frail et al. (1994) imaged a much larger field at 1.4 GHz toward a gamma-ray burst with the Dominion Radio Astrophysical Observatory synthesis telescope, making daily measurements for two weeks and then on several single epochs for up to three months. No transients were identified on these timescales, and no sources above a peak flux density limit of 3.5 mJy were seen to vary by more than 4σ. A systematic search for transients was made between the two largest radio sky surveys, Faint Images of the Radio Sky at Twenty-Centimeters (FIRST; Becker et al. 1995) and NVSS (Condon et al. 1998) by Levinson et al. (2002). Nine transient candidates were identified. Follow-up observations of these established that only one was a genuine transient — a likely radio supernova in NGC 4216 (Gal-Yam et al. 2006; Ofek et al. 2010). Carilli et al. (2003) used a deep, single VLA pointing at 1.4 GHz toward the Lockman hole. They found that only a small fraction, $<2\%$, of radio sources above a peak flux density limit of 0.1 mJy are highly ($>50\%$) variable on 19 day and 17 month timescales. No transients were identified. de Vries et al. (2004) used the VLA to image a region, toward the South Galactic cap, twice on a seven-year timescale. No transients were found above a limit of 2 mJy. Transients reported by Bower et al. (2007) were found to be due to rare imaging artifacts, except one which could be a true transient. Bright (>1 Jy), short-lived, transients reported by the Nasu 1.4 GHz survey (Matsumura et al. 2009, Kida et al. 2008) were also not confirmed to be true (email correspondence). Croft et al. (2010, 2011) argued that these transients are not real because their implied event rate cannot be reconciled with their own survey unless this population has a sharp cutoff at flux densities below 1 Jy. Croft et al. (2010, 2011) presented results from the Allen Telescope Array Twenty-centimeter Survey (ATATS). They surveyed 690 deg^2 of an extragalactic field on 12 epochs. They compared the individual images with their combined image and the combined image with the NRAO VLA Sky Survey (NVSS; Condon et al. 1998). No transients were found above a peak flux density limit of 40 mJy in the combined image, with respect to the NVSS survey (Croft et al. 2010). In addition, no transients were found in the individual epochs above a peak flux density of about 100 mJy (Croft et al. 2011). A comprehensive survey at 0.8 GHz was reported by Bannister et al. (2011). They surveyed 2776 deg^2 south of declination -30 deg over a 22 year period. Out of about 30,000 sources they identified 53 variables and 2 transient sources. One of these transients is associated with a nearby galaxy, suggested as a long GRB afterglow, and the other is a known microquasar. Bower & Saul (2011) reported a transient search in the fields of the VLA calibrators in which no transients were found. These findings at sub-mJy levels are consistent with the several previous 1.4 GHz studies at higher flux density thresholds. Thyagarajan et al. (2011) analyzed the 8444 deg^2 of the FIRST survey and found only 0.5% (1627/279407) of sources above 1 mJy varied significantly on timescales of minutes to years. Ofek & Frail (2011) do a two-epoch comparison

[5]http://www.tauceti.caltech.edu/kunal/radio-transient-surveys/index.html

of FIRST and NVSS point sources brighter than 5 mJy and find that only 0.1% (43/4367) vary by more than 4σ over timescales ranging from about 300 to 1700 days. Recently, Mooley et al. (2013) found that only a small fraction (7/599 = 1.2%) of the point sources in the ECDFS region showed any significant variability on day-week-month timescales. Evidently, the sub-milliJansky radio sky at 1.4 GHz is not highly variable.

There have also been several blind transient surveys carried out at frequencies above 1.4 GHz. Two surveys at 5 GHz have specifically targeted the Galactic plane. Taylor and Gregory (1983) and Gregory and Taylor (1986) used the NRAO 91-m telescope to image an approximately 500 $\deg^2$ region from Galactic longitude $l = 40$ deg to $l = 220$ deg with Galactic latitude $|b| \leq 2$ deg in 16 epochs over a 5-year period. They identified one transient candidate which underwent a 1 Jy flare but for which follow-up VLA observations showed no quiescent radio counterpart (Tsutsumi et al. 1995). They also claimed tentative evidence for a separate Galactic population of strong variables comprising 2% of their sources. Support for this comes from Galactic survey of Becker et al. (2010), who find about one half of their variable source sample (17/39), or 3% of all radio sources in the Galactic plane, undergo strong variability on 1-year and 15-year baselines. We note that the surface density of radio sources in the Galactic plane is only slightly higher ($\approx 20\%$) than at high Galactic latitudes (Helfand et al. 2006; Murphy et al. 2007). In a five year catalog of radio afterglow observations of 75 γ-ray bursts, Frail et al. (2003) found several strong variables at 5 and 8.5 GHz, but no new transients apart from the radio afterglows themselves. At 3.1 GHz Bower et al. (2010) report a marginal detection of one possible transient (4.3σ) in a 10 $\deg^2$ survey of the Boötes extragalactic field. Bell et al. (2011) searched for radio transients in the fields of the VLA phase calibrators at 1.4 GHz, 4.9 GHz, and 8.5 GHz. Based on their survey parameters (Table 1), we estimate that their 95% confidence surface density upper limit on transients brighter than 8 mJy in 1.4 GHz, 4.9 GHz, and 8.5 GHz are 0.19 $\deg^{-2}$, 0.13 $\deg^{-2}$, and 0.50 $\deg^{-2}$, respectively.

One of the largest variability survey of its kind was carried out using the 7-beam receiver on the NRAO 91-m telescope (Scott 1996; Gregory et al. 2001). The sky between 0 deg and 75 deg in declination was surveyed over two 1-month periods between Nov 1986 and Oct 1987 (Condon, Broderick & Seielstad 1989; Becker et al. 1991; Condon et al. 1994; Gregory et al. 1996). The final catalog, made by combining both the 1996 and 1997 epochs, contained 75,162 discrete sources with flux densities > 18 mJy. Long term variability information was available for the majority of the sources by comparing the mean flux densities between the 1986 and 1987 epochs. Scott (1996) carried out a preliminary analysis of the long-term measurements and identified 146 highly variable sources, or $<1\%$ of the cataloged radio sources. Eight possible transients in the Scott (1996) list appear in either 1986 or 1987 but are undetected in the other epoch ($< 2\sigma$). Two sources are previously identified variables from the Gregory and Taylor (1986) survey, while six are flagged as possible false positives due to confusion by nearby bright sources. One source (B150958.3+103541) was 9 ± 6 mJy in 1986 and 75 ± 7 mJy in 1987 but it is in both the FIRST and NVSS source catalogs. There are therefore no long-term transients identified in the Scott (1996) survey.

In summary, the radio sky is relatively quiet compared with the the optical, X-ray and γ-rays sky. The

fraction of strong variables among the persistent radio sources less than a few percent from flux densities of 0.1 mJy to 1 Jy. The rates of transients is at least a factor of ten lower than this. Variability at frequencies at or below a few GHz is thought to be dominated by propagation effects (i.e. refractive interstellar scintillation) and not by intrinsic changes in the source (Gaensler & Hunstead 2000; Ofek et al. 2011). Since interstellar scintillation is strongest toward compact sources, we expect samples of strong variables to be dominated by flat-spectrum AGN, as appears to be the case. We may then hypothesize that the fraction of strong variables may change with decreasing flux densities as radio source counts transition from being dominated by AGN to galaxies dominated by star formation. There is a (weak) trend of spectral *flattening* with decreasing flux density (Randall et al. 2012).

1.3 An Improved Interferometer: the Karl G. Jansky Array

The Very Large Array ("Legacy" VLA) was designed and built in the 1970s as an imaging radio interferometer. Located in west-central New Mexico, the Legacy VLA comprised of 27 25-meter dishes with the ability to observe in four frequency bands with a maximum bandwidth of 100 MHz per polarization. Refurbishment of the Legacy VLA into the Karl G. Jansky Array (VLA or JVLA; Perley et al. 2011) began in 2001 and was completed by 2012. New capabilities of this interferometer over the Legacy VLA include: bandwidths between 1–16 GHz in each polarization continuum sensitivity frequency resolution improvement by more than a factor 10, and five times more frequency coverage (1–50 GHz). Unlike the Legacy VLA, the upgraded VLA possesses frequency agility essential for precise RFI excision and characterization of the broadband radio spectra of detected transients. It has a much improved snapshot multi-frequency UV coverage; imaging artifacts and contamination by sidelobes (Bower et al. 2007; Frail et al. 2012) are no longer major impediments in transient search.

The capabilities of the VLA with respect to the SKA pathfinder facilities are given in Table 1.2. Survey speed (SS), normalized here to the VLA L band, is a useful figure of merit for inter-comparison of survey capabilities of long duration transients and is expressed as,

$$\mathrm{SS} \propto \mathrm{BW} \times \Omega(\mathrm{A}_e/\mathrm{T}_{sys})^2 \tag{1.4}$$

where BW is the bandwidth, Ω is the field of view, A_e is the total collecting area times the aperture efficiency ϵ_e, and T_{sys} is the antenna system temperature (Cordes 2008). Generally expressed units of deg^2 hr^{-1}, the survey speed is a measure of the area on the sky that a telescope can cover per unit time, for a given rms noise. This can be easily verified by combining the radiometer equation ($\sigma_T = T_{sys}/\sqrt{BW\ \tau}$) and the system equivalent flux density (SEFD = $2kT_{sys}/A_e$). The relative survey speeds in Table 1.2 are only approximate since some of the system parameters for MeerKAT and ASKAP have not been confirmed with on-the-sky testing. Likewise, we have assumed that radio frequency interference (RFI) limits the L-band VLA bandwidth

to only 50% of its maximum BW. Larger fractions are achievable in the more extended array configurations and with better RFI excision of the data. For VLA S-band, we assume a conservative BW value of 1350 MHz. Despite these uncertainties, it is clear from Table 1.2 that to within factors of a few, the VLA is a powerful wide-field imaging facility, at par with the SKA pathfinders.

Table 1.2: Telescope Specifications

Telescope	BW (MHz)	Ω (deg^2)	D (m)	N	ϵ_e	T_{sys} (K)	SS
VLA L-band	512	0.25	25	27	0.5	26	1.0
VLA S-band	1350	0.06	25	27	0.7	28	1.1
ASKAP	300	30	12	36	0.8	50	4.6
Apertif	300	8	25	13	0.75	70	1.3
MeerKAT	750	1	13.5	64	0.7	30	4.1

Notes– Here BW is bandwidth in MHz, Ω is the field of view in deg^2, D is the antenna diameter in meters, N is the number of antennas in the array, ϵ_e is the aperture efficiency, T_{sys} is the system temperature in Kelvin, and SS is the survey speed normalized to the VLA L band. Latest specifications for MeerKAT (correspondence with B. Fanaroff) suggest T_{sys}=22.5 K and SS=7.2.

The new capabilities of the VLA also bring in new challenges such as large data rate from the interferometer and substantial increase in data processing time. This thesis aims at greatly reducing the processing time through a custom-developed calibration and imaging pipeline. This pipeline (Bourke, Mooley & Hallinan 2014, ASPC, 485, 367) was originally developed by Stephen Bourke in AIPSLite. I have made modifications to and optimized this pipeline in order to enable the fully-automated rapid processing of the large volumes of VLA data. AIPSLite (Bourke et al. 2013, Experimental Astronomy, 36, 59) is a python module that allows the execution of AIPS tasks as executable files. The interface used is ParselTongue (Kettenis et al. 2006, ASPC, 351, 497) and AIPSLite additionally depends on the Obit package developed by Bill Cotton. The pipeline follows, in general, the procedures outlined in Chapter E of the AIPS Cookbook[6]. In brief, the data is first loaded with the Obit task BDFIn; band edges, and to a larger extent IF edges, are then flagged with the task UVFLG; sub-bands that are irreparably corrupted by RFI are entirely flagged aso using the task UVFLG; after flagging, FRING, BPASS, SETJY, CALIB, GETJY, and CLCAL are used to derive the delay, bandpass, and complex gain solutions; polarization calibration is performed using the tasks RLDLY, PCAL, and RLDIF as detailed in section 7 of Chapter E in the AIPS Cookbook; RFLAG is used to flag all target pointings and the flags are applied using the UVCOP task; the derived calibration is applied and the calibrated dataset is produced with the SPLAT task; finally the calibrated UV data is saved to disk using the task FITTP. During the pipeline process several diagnostic plots are generated to assess the quality of the calibration: bandpass solutions, antenna gains as a function of time, calibrated spectrum of the gain calibrator, and calibrated amplitude versus phase plots of the gain calibrator per pointing.

Later in this thesis I describe the near-real-time CNSS survey that we have carried out at S band in the

[6]http://www.aips.nrao.edu/cook.html

B array configuration with the VLA. The VLA S band offers maximum survey speed, and a wide bandwidth to allow for RFI excision in frequency space and for measuring the spectral indices of radio transients. Additionally, observations in the S band improve the sensitivity towards transients in their optically thick, rising phase, over observations carried out at lower frequencies. This is critical for rapid multiwavelength follow-up, since the emission at higher frequencies generally peaks earlier and evolve faster.

1.4 Goals of this Thesis

The primary objectives of this thesis are: (1) to characterize the dynamic radio sky in terms of timescale, flux density, and areal density; apart from giving us an insight into the explosive universe; this work will also help us understand the false-positive foreground for future searches for the radio counterparts of gravitational-wave (GW) sources; (2) answer key problems such as the rate of transients (TDEs, obscured supernovae, binary neutron star mergers, etc.) and the beaming factor of GRBs; (3) statistical study of variable sources which will be essential for our understanding of radio emission from AGNs; (4) to develop a software infrastructure for the rapid processing of VLA data and near-real-time radio transient search; (5) establish the VLA as an efficient survey and follow-up facility (especially in terms of variable and transient sources); and (6) inform the best search strategy to transient surveys planned for WSRT/Apertif, ASKAP and MeerKAT.

Bibliography

Abazajian, K. N., Adelman-McCarthy, J. K., Ag ueros, M. A., et al. 2009, ApJS, 182, 543

Aller, M. F., Aller, H. D., Hughes, P. A., et al. 1999, ApJ, 512, 601

Annis, J., Soares-Santos, M., Strauss, M. A., et al. 2011, arXiv:1111.6619

Arshakian, T. G., Leon-Tavares, J., Böttcher, M. et al. 2012, A&A, 537, 32

Augusteijn, T., Karatasos, K., Papadakis, M., et al. 1992, A&A, 265, 177

Bannister, K. W., Murphy, T., Gaensler, B. M., Hunstead, R. W., & Chatterjee, S. 2011, MNRAS, 412, 634

Bannister, K. W., Murphy, T., Gaensler, B. M., Hunstead, R. W., & Chatterjee, S. 2011, Erratum, July 2011

Bastian, T. S., Benz, A. O. & Gary, D. E. 1998, ARA&A, 36, 131

Belloni, T., Homan, J., Casella, P., 2005, A&A, 440, 207

Ben-Ami, S., Gal-Yam, A., Filippenko, A. V., ey al. 2012, ApJ, 760, 33

Benz, A. O., Güdel, M. 1994, A&A, 285, 621

Berger, E., Ball, S., Becker, K. M., 2001, Nature, 410, 338

Philip R. B. & Keith D. R. 2003, Data reduction and error analysis for the physical sciences, 3rd ed., Boston, MA: McGraw-Hill, ISBN 0-07-247227-8

Bloom, J. S., Giannios, D., Metzger, B. D., et al. 2011, Science, 333, 203

Bloom, J. S., Richards, J. W., Nugent, P. E., et al. 2012 PASP, 124, 1175

Boffi, F. R. & Branch, D. 1995, PASP, 107, 347

Bonzini, M., Mainieri, V., Padovani, P. et al. 2012, ApJS, 203, 15

Booth, R. S., & Jonas, J. L. 2012, AfrSk, 16, 101

Bourke, S., Mooley, K., Hallinan, G. 2014, ASPC, 485, 367

Bovy, J., Hogg, D. W., Roweis, S. T. 2009, ApJ, 700, 1794

Bower, G. C., Saul, D., Bloom, J. S., Bolatto, A., Filippenko, A. V., Foley, R. J., & Perley, D. 2007, ApJ, 666, 346

Cameron, P. B., Chandra, P., Ray, A., et al. 2005, Nature, 434, 1112

Carilli, C. L., Ivison, R. J., & Frail, D. A. 2003, ApJ, 590, 192

Cenko, S. B., Krimm, H. A., Horesh, A., et al. 2012, ApJ, 753, 77

Chandra, P. & Frail, D. A., 2012, ApJ, 746, 156

Chen, X., Rachen, J. P., LÃşpez-Caniego, M., et al. 2013, A&A, 553, 107

Chevalier 1982a, ApJ, 258, 302

Chevalier 1982, ApJ, 259, L85

Chomiuk, L., Soderberg, A. M., Moe, M., et a. 2012, ApJ, 750, 164

Chomiuk, L., Krauss, M. I., Rupen, M. P., et al. 2012, ApJ, 761, 173

Chomiuk, L., Linford, J. D., Yang, J. et al. 2014, Nature, 514, 339

Condon, J. J., Ledden, J. E., Odell, S. L., & Dennison, B. 1979, AJ, 84, 1

Condon, J. J., Cotton, W. D., Greisen, E. W., et al. 1998, AJ, 115, 1693

Conti et al. 1983, ApJ, 274, 302

Corbel, S., Fender, R. P., Tzioumis, A. K., et al. 2000, A&A, 359, 251

Corbel, S., Fender, R. P., Tzioumis, A. K., et al. 2002, Science, 298, 196

Corbel, S., Fender, R. P., Tomsick, J. A., Tzioumis, A. K., & Tingay, S. 2004, ApJ, 617, 1272

S. Corbel, J. C. A. Miller-Jones, R. P. Fender, et al. 2015 arXiv:1501.04716v2

Cordes, J. M. 2008, Frontiers of Astrophysics: A Celebration of NRAO's 50th Anniversary, 395, 225

Croft, S., Bower, G. C., Ackermann, R., et al. 2010, ApJ, 719, 45

Cutri, R. M., Wright, E. L., Conrow, T. et al. 2012, WISE Rept

Czerny, B., Siemiginowska, A., Janiuk, A., et al. 2009, ApJ, 698, 840

Dawson, K. S., Schlegel, D. J., Ahn, C. P., et al. 2013, AJ, 145, 10

Dehnen, W. 1998, AJ, 115, 2384

de Vries, W. H., Becker, R. H., White, R. L., & Helfand, D. J. 2004, AJ, 127, 2565

Dhawan, V., Mirabel, I. F., & Rodriguez, L. F. 2000, ApJ, 543,37

Dulk, G. A. 1985, ARA&A, 23, 169

El Bouchefry, K. & Cress, C. M. 2007, Astronomische Nachrichten, 328, 577

Elvis, M., Wilkes, B. J., McDowell, J. C. et al. 1994, ApJS, 95, 1

Evans, C. R. & Kochanek, C. S. 1989, ApJ, 346, 13

Fender, R. P., Pooley, G. G., Durouchoux, P., Tilanus, R. P. J., & Brocksopp, C. 2000, MNRAS, 312, 853

Fender, R. P., Belloni, T. M., & Gallo, E. 2004, MNRAS, 355, 1105

Fender, R. P. et al . 2006, MNRAS, 367, L6

Findeisen, K., Hillenbrand, L., Ofek, E., et al. 2013, ApJ, 768, 93

Frail, D. A., Kulkarni, S. R., Ofek, E. O., Bower, G. C., & Nakar, E. 2012, ApJ, 747, 70

Frail, D. A., Kulkarni, S. R., Berger, E., & Wieringa, M. H. 2003, AJ, 125, 2299

Frail, D. A., Kulkarni, S. R., Hurley, K. C., Fishman, G. et al. 1994, ApJ, 437, 43

Fromm, C. M., Perucho, M., Ros, E., et al. 2011, A&A, 531, 95

Fromm, C. M., Fuhrmann, L., & Perucho, M, 2014, arXiv1412.7194

Gallo, E., Fender, R., Kaiser, C., et al . 2005, Nature, 436, 819

Gaensler, B. M., & Hunstead, R. W. 2000, PASA, 17, 72

Gaensler, B. M., Kouveliotou, C., Gelfand, J. D., et al . 2005, Nature, 434, 1104

Gehrels, N., Ramirez-Ruiz, E., Fox, D. B. et al. 2009, ARA&A, 47, 567

Ghirlanda, G., Burlon, D., Ghisellini, G., et al. 2014, PASA, 31, 22

Güdel, M. 2002, ARA&A, 40, 217

Hallinan, G., Bourke, S., Lane, C., et al. 2007, ApJ, 663, 25

Hancock, P. J., Gaensler, B. M. & Murphy, T., 2011, ApJ, 735, 35

Hancock, P. J, Murphy, T., Gaensler, B. M, Hopkins, A., & Curran, J. R 2012, MNRAS, 422, 1812

Harding, L. K., Hallinan, G., Boyle, R. P., et al. 2013, ApJ, 779, 101

Henry, G. W. & Newsom, M. S 1996, PASP, 108, 242

Hodge, J. A., Becker, R. H., White, R. L., Richards, G. T. & Zeimann, G. R. 2011, AJ, 142, 3

Hodge, J. A., Becker, R. H., White, R. L., Richards, G. T., 2013, ApJ, 769, 125

Hog, E., Fabricius, C., Makarov, V. V. 2000, A&A, 355, 27

Horesh, A., Kulkarni, S. R., Corsi, A., et al. 2013, ApJ, 778, 63

Hovatta, T., Nieppola, E., Tornikoski, M, et al. 2008, A&A, 485, 51

Hovatta, T., Pavlidou, V., King, O. G., et al. 2014, MNRAS, 439, 690

Huguenin, G. R., Taylor, J. H., Helfand, D. J., et al. 1973, ApJ, 181, 139

Humphreys, Nichols & Massey 1985, AJ, 90, 101

Huynh, M. T., Jackson, C. A., Norris, R. P., Fernandez-Soto, A. et al. 2008, AJ, 135, 2470

Huynh, M. T., Hopkins, A. M., Lenc, E., et al. 2012, PASA, 29, 229

Hyman, S. D., Lazio, T. J. W., Kassim, N. E., 2002, AJ, 123, 1497

Hyman, S. D., Lazio, T. J. W., Kassim, N. E., et al. 2005, Nature, 434, 50

Hyman, S. D., Lazio, T. J. W., Roy, S., et al. 2006, ApJ, 639, 348

Hyman, S. D., Roy, S., Pal, S., et al. 2007, ApJ, 660, 121

Hyman, S. D., Wijnands, R., Lazio, T. J. W., et al. 2009, ApJ, 696, 280

Ivezic, Z., Menou, K., Knapp, G. R., et al. 2002, AJ, 124, 2364

Johnson, D. R. H., Soderblom, D. R. 1987, AJ, 93, 864

Johnston, S., Taylor, R., Bailes, M., et al. 2008, Experimental Astronomy, 22, 151

Kantharia, N. G., Anupama, G. C., Prabhu, T. P., et al. 2007, ApJ, 667, 171

Kasliwal, M. M. 2012, PASA, 29, 482

Kesden, M., 2012, PhRvD, 85, 4037

Kharchenko, N. V., Roeser, S. 2009, VizieR Online Data Catalogs

Körding, E., Rupen, M., Knigge, C., et al. 2008, Science, 320, 1318

Körding, E. G., Knigge, C., Tzioumis, T., & Fender, R. 2011, MNRAS, 418, L129

Kovari, Zs., Vilardell, F., Ribas, I., et al. 2007, Astronomische Nachrichten, 328, 904

M. Kunert-Bajraszewska, A. Marecki,, and P. Thomasson, et al. 2006, A&A 450, 945

M. Kunert-Bajraszewska, M. P. Gawronnski, A. Labiano & A. Siemiginowska, et al. 2010 MNRAS 408, 2261

Laher, R. R., Surace, J., Grillmair, C. J., Ofek, E. O., et al. 2014, arXiv:1404.1953L

Law, N. M., Kulkarni, S. R., Dekany, R. G., et al. 2009, PASP, 121, 1395

LaMassa, S. M., Urry C. M., Cappelluti, N. et al. 2013, MNRAS, 436, 3581

Lawrence, A., Warren, S. J., Almaini, O. et al. 2007, MNRAS, 379, 1599

Lazio, J., Bloom, J. S., Bower, G. C., Cordes, J., Croft, S., Hyman, S., Law, C., & McLaughlin, M. 2009, astro2010: The Astronomy and Astrophysics Decadal Survey, 2010, 176

Lazio, J. W., Kimball, A., Barger, A. J. et al. 2014, PASP126, 196

Levinson, A., Ofek, E. O., Waxman, E. & Gal-Yam, A., 2002, ApJ, 576, 923

M. L. Lister, M. F. Aller, H. D. Aller, et al. 2013,146, 120

Levinson, A., Ofek, E. O., Waxman, E., & Gal-Yam, A. 2002, ApJ, 576, 923

Lyne, A. G., & Thorne, D. J. 1975, MNRAS, 172, 97

Macquart, J.-P. 2014, arXiv1406.5790

Marscher, A. P. & Gear, W. K. 1985, ApJ298, 114

Mason, B. D.; Wycoff, G. L.; Hartkopf, W. I. 2001, AJ, 122, 3466

Mateos, S., Alonso-Herrero, A., Carrera, F. J., et al. 2012, MNRAS426, 3271

McConnell, N. J. & Ma, C.-P. 2013, ApJ, 764, 184

McClintock, J. E. & Remillard, R., A. 2006, in Compact stellar X-ray sources. Ed. Walter Lewin & Michiel van der Klis. Cambridge Astrophysics Series, No. 39. Cambridge, UK: Cambridge University Press

McMahon, R. G., White, R. L., Helfand, D. J. & Becker, R. H., 2002, ApJS, 143, 1

Meszaros, P. & Rees, M. J. 1997, ApJ, 476, 232

Michelson, P. F., Atwood, W. B., Ritz, S. et al. 2010, Reports on Progress in Physics, 73, 7

Miller-Jones, J. C. A., Sivakoff, G. R., Altamirano, D., et al. 2012, MNRAS, 421, 468

Miller-Jones, James C. A., Blundell, Katherine M., et al. 2004, ApJ, 600, 368

Mooley, K. P., Frail, D. A., Ofek, E. O., et al. 2013, ApJ, 768, 165

Motch, C., Pakull, M. W., Mouchet, M., Beuermann, K., et al. 1989, A&A, 219, 158

Murphy, T., Chatterjee, S., Kaplan, D. L., et al. 2013, PASA, 30, 6

O'Brien, T. J., Bode, M. F., Porcas, R. W., et al . 2006, Nature, 442, 279

O'Dea, C. P. 1998, PASP, 110, 493O

Ofek, E. O., Frail, D. A., Breslauer, B., et al. 2011, ApJ, 740, 65O

Oosterloo, T., Verheijen, M., & van Cappellen, W. 2010, ISKAF2010 Science Meeting

Padovani, P., Miller, N., Kellermann, K. I., 2011, ApJ, 740, 20

Panagia, N., Van Dyk, S. D., Weiler, K. W., et al. 2006, ApJ, 646, 369

Patterson, J. 2011, MNRAS, 411, 2695

Perez-Torres, M. A., Lundqvist, P., Beswick, R., et al. 2014, arXiv:1405.4702

Perley, R. A., Chandler, C. J., Butler, B. J., & Wrobel, J. M. 2011, ApJ, 739, L1

Perley, D. A., Cenko, S. B., Corsi, A, et al. 2014, ApJ, 781, 37

M. Perucho, Y. Y. Kovalev, A. P. Lobanov, et al. 2012, ApJ, 749, 55

Piran, T. 1999, Physics Reports 314, 575

Piran, T., Ehud N., & Stephan R., 2013, MNRAS, 430, 2121

Polletta, M., Tajer, M., Maraschi, L., et al. 2007, ApJ, 663, 81

Potter, W. J. & Balbus, S. A. 2014, MNRAS, 441, 681

Psaltis, D. 2006, in Compact stellar X-ray sources. Ed. Walter Lewin & Michiel van der Klis. Cambridge Astrophysics Series, No. 39. Cambridge, UK: Cambridge University Press

Rahmer, G., Smith, R., Velur, V., et al. 2008, SPIE, 7014, 163

Rau, A., Kulkarni, S. R., Law, N. M., et al. 2009, PASP, 121, 1334

Randall, K. E., Hopkins, A. M., Norris, R. P., et al. 2012, MNRAS, 2478

Rankin, J. M., Payne, R. R., & Campbell, D. B. 1974, ApJ, 193, L71

Randall, K. E., Hopkins, A. M., Norris, R. P., et al. 29012, MNRAS, 421, 1644

Rau, U. & Cornwell, T. J. 2011, A&A, 532, 71

Rees, M. J. 1988, Nature, 333, 523

Rhoads, J.E., 1997, ApJL, 487, L1

Richards, J. L.; Max-Moerbeck, W., Pavlidou, V., et al. 2011, ApJS, 194, 29

Roy, N., Chomiuk, L., Sokoloski, J. L., et al. 2012, BASI, 40, 293

Rupen, M. P., Mioduszewski, A. J. & Sokoloski, J. L. 2008, ApJ, 688, 559

Seaquist, E. R. & Bode, M. F. 2008, Cambridge University Press (Classical Novae), 14

Smith, A. M., Lynn, S., Sullivan, M., et al. 2011, MNRAS, 412, 1309

Smolcic, V., Schinnerer, E., Scodeggio, M., et al. 2008, ApJS, 177, 14

Snellen, I. A. G., Schilizzi, R. T., Bremer, M. N., et al. 1999, MNRAS, 307, 149

Soderberg, A. M., Chakraborti, S., Pignata, G., et al. 2010, Nature, 463, 513

Sramek & Weiler 2003, Lecture Notes in Physics, 598, 145

Stirling, A. M., Spencer, R. E., de la Force, C. J., et al . 2001, MNRAS, 327, 1273

Stockdale et al. 2007, ApJ, 671,1, 689

Stockdale, C., Weiler, K. W., Panagia, N., et al. 2009, Astro2010, 288

Student, 1908, Biometrika 6, 1

Teraesranta, H., Tornikoski, M., Mujunen, A., et al. 1998, A&AS, 132, 305

Thyagarajan, N., Helfand, D. J., White, R. L., & Becker, R. H. 2011, ApJ, 742, 49

Tingay, S. J., Goeke, R., Bowman, J. D., et al. 2013, PASA, 30, 7

Torres, C. A. O., Quast, G. R., da Silva, L. 2006, A&A, 460. 695

Türler, M., Courvoisier, T. J.-L. & Paltani, S., 2000, A&A, 361, 850

Uomoto 1986, ApJ, 310, L35

Valtaoja, E., Terasranta, H., Urpo, S., et al. 1992, A&A, 254, 80

van Haarlem, M. P., Wise, M. W., Gunst, A. W et al. 2013, A&A, 556, 2

Vernstrom, T., Scott, D., Wall, J. V., et al. 2014, MNRAS, 440, 2791

Voges, W., Aschenbach, B., Boller, T. 1999, A&A, 349, 389

Walker, M. A., 1998, MNRAS, 294, 307

Weiler et al. 1986, ApJ, 301, 790

Weiler, K. W., Panagia, N., Montes, M. J., et al. 2002, ARA&A, 40, 387

White, R. L., Becker, R. H., Helfand, D. J. & Gregg, M. D. 1997, ApJ, 475, 479

Woo, J.-K., Urry, C. M. 2002, ApJ, 579, 530

Wright, E. L., Eisenhardt, P. R. M. et al. 2010, AJ, 140, 1868

Zauderer, B. A., Berger, E., Soderberg, A. M., et al. 2011, Nature, 476, 425

Zauderer, B. A., Berger, E., Margutti, R., et al. 2013, ApJ, 767, 152

Mooley, K. P., Hillenbrand, L. A., Rebull, L. et al. 2013, ApJ, 768, 165

Kulkarni, S. R., Frail, D. A., Wieringa, M. H., 1998, Nature, 395, 663

Chapter 2

The Birth of a Relativistic Outflow in the Unusual γ-ray Transient, Swift J164449.3+573451

This chapter is adapted from a previous publication: Zauderer, A., Berger, E., Soderberg, A. M., …, Mooley, K. P., et al. 2011, Nature, 476, 425.

Abstract

Active galactic nuclei (AGN), powered by long-term accretion onto central supermassive black holes, produce relativistic jets with lifetimes of $\gtrsim 10^6$ yr that preclude observations at birth. Transient accretion onto a supermassive black hole, for example through the tidal disruption of a stray star, may therefore offer a unique opportunity to observe and study the birth of a relativistic jet. On 2011 March 25, the *Swift* γ-ray satellite discovered an unusual transient source (Swift J164449.3+573451) potentially representing such an event. Here we present the discovery of a luminous radio transient associated with Swift J164449.3+573451, and an extensive set of observations spanning centimeter to millimeter wavelengths and covering the first month of evolution. These observations lead to a positional coincidence with the nucleus of an inactive galaxy, and provide direct evidence for a newly-formed relativistic outflow, launched by transient accretion onto a 10^6 $M_\odot$ black hole. While a relativistic outflow was not predicted in this scenario, we show that the tidal disruption of a star naturally explains the high-energy properties, radio luminosity, and the inferred rate of such events. The weaker beaming in the radio compared to γ-rays/X-rays, suggests that radio searches may uncover similar events out to redshifts of $z \sim 6$.

2.1 Introduction

Upon the discovery of Swift J164449.3+573451 (Burrows et al. 2011), and the identification of a galaxy at a redshift of $z = 0.354$ (Levan et al. 2011) within the *Swift* X-ray localization region ($1.4''$ radius), we initiated radio observations of the transient on 2011 March 29.36 UT with the Expanded Very Large Array (EVLA) at a frequency of 5.8 GHz and discovered an unresolved source with a flux density of 310 ± 7 μJy. Astrometric matching demonstrated that the radio source coincides with the galaxy nucleus (Figure 2.1), subsequently confirmed with other data (Levan et al. 2011). A follow-up EVLA observation 0.9 d later revealed that the source brightened to 530 ± 10 μJy, thereby conclusively linking the X-ray/γ-ray transient and the galaxy for the first time. The galaxy exhibits no evidence for an active nucleus (Levan et al. 2011), and the lack of previous γ-ray/X-ray activity (Burrows et al. 2011) argues against an AGN flare origin.

2.2 Archival Data and Followup Radio Observations

We carried out additional observations at multiple frequencies spanning $1-345$ GHz with several cm- and mm-wave facilities. The spectral energy distribution (SED) in this frequency range on 2011 March 30 UT ($\Delta t \approx 5$ d) is well described by a power law with $F_\nu \propto \nu^{1.3\pm0.1}$ up to $F_\nu(345\,\mathrm{GHz}) = 35 \pm 1$ mJy. The steep power law requires self-absorbed synchrotron emission. The weak near-infrared (NIR) variability (Levan et al. 2011) indicates $F_\nu(2.5\,\mu\mathrm{m}) \approx 0.1$ mJy, while the lack of optical variability leads (Levan et al. 2011) to an upper bound of $F_\nu(0.64\,\mu\mathrm{m}) \lesssim 2$ μJy. The SED therefore peaks in the millimeter band, with a best-fit rest-frame peak frequency and flux density of $\nu_p \approx 6 \times 10^{11}$ Hz and $F_{\nu,p} \approx 80$ mJy, respectively (Figure 2.2). The non-detection of optical variability requires significant rest-frame extinction of $A_V \gtrsim 3$ mag, further supporting a nuclear origin. Subsequent SEDs at $\Delta t \approx 10$, 15, and 22 d exhibit significant evolution, with $\nu_p \propto t^{-1.3}$ and $F_{\nu,p} \propto t^{-0.8}$ (Figure 2.2).

2.3 15 GHz Followup Observations With the OVRO 40-m Telescope

We observed Swift J164449.3+573451 with the Owens Valley Radio Observatory (OVRO) 40-meter telescope at a frequency of 15 GHz beginning 2.82 d after the X-ray trigger (see Table 1). The 40-m telescope is equipped with a dual-beam Dicke-switched receiver with two symmetric, off-axis beams (each 2.5 arcmin full-width at half-maximum) separated azimuthally by 12.95 arcmin. The receiver has a 2.5 GHz noise-equivalent reception bandwidth. We used sky switching, alternating the source between the two beams to reduce atmospheric and ground pickup, and to account for the non-identical nature of the two beams. The flux scale is derived from observations of 3C286 and Baars et al. (1977), with about 5% uncertainty. The summary of the OVRO 40-m observations are given in Table 2.1. We note that daytime measurements of Swift J164449.3+573451 lead to consistently discrepant flux densities, most likely due to increased thermal

Table 2.1: Summary of OVRO 40-m Observations at 15 GHz

UT Date	Δt (d)	F_ν (mJy)
Mar 31.37	2.82	2.36±1.14
Apr 1.34	3.80	3.17±1.17
Apr 8.36	10.82	8.06±0.95
Apr 10.36	12.82	7.65±0.90
Apr 12.33	14.79	7.45±0.80
Apr 12.41	14.87	6.60±1.22
Apr 15.35	17.81	10.54±0.93
Apr 19.33	21.79	11.99±1.03
Apr 21.36	23.82	9.55±1.04

emission from the ground. These discrepant measurements lead to a large Lorentz factor of $\Gamma \gtrsim 10$, while from our synchrotron model of the radio emission we get $\Gamma \simeq 1.2$.

2.4 Discussion

For synchrotron sources there is a well-defined minimum energy (Readhead 1994), achieved near equipartition between the fractional energies in the relativistic electrons (ϵ_e) and magnetic fields (ϵ_B). This condition defines (Chevalier 1998) the equipartition radius: $\theta_{\rm eq} = 110\, d_{\rm L,Mpc}^{-1/19} F_{\nu,\rm p,mJy}^{9/19} \nu_{\rm p,GHz}^{-1}$ μas. From the March 30 UT SED we find $\theta_{\rm eq} \approx 1$ μas ($r_{\rm eq} \approx 1.5 \times 10^{16}$ cm) and hence mildly relativistic expansion with a Lorentz factor of $\Gamma \approx 2$. A more detailed model (Kumar & Narayan 2009) that accounts for relativistic effects leads to a similar result, $r_{\rm eq} \approx 1 \times 10^{16}$ cm and $\Gamma \approx 1.2$. From the observed SED temporal evolution we find that the source continues to expand relativistically with nearly constant velocity. Extrapolating the linear trend in radius we find a formation epoch in the range 2011 March 23–26 UT, in excellent agreement with the initial γ-ray detection on 2011 March 25 UT. This provides independent evidence for a newly-formed relativistic outflow.

An angular size of a few μas will inevitably lead to variability in the low frequency radio emission due to interstellar scintillation, with the amplitude of modulation depending on the ratio of the source size, θ_s, to the Fresnel scale, θ_F (Goodman & Narayan 2006). For the line of sight to Swift J164449.3+573451 the maximum modulation ($m_p \approx 1$) is expected at $\nu_0 \approx 10$ GHz (Cordes & Lazio 2002), for $\theta_s \approx \theta_F \approx 1$ μas. The observed modulation inferred from our detailed radio light curves is tens of percent at $5-7$ GHz and a few percent at 15 GHz (Figure B.6), leading to a projected radius of $\theta_s \approx 5$ μas, or $\Gamma \approx 5$. This provides independent evidence for a relativistic outflow. Our radio observations with Very Long Baseline Interferometry (VLBI) at a frequency of 22 GHz place an upper bound on the size of $r \lesssim 0.8$ pc, consistent with the synchrotron and scintillation analyses, and providing an upper bound on the lifetime of the event of $\lesssim 1.7$ yr for an expansion with $\Gamma \approx 2$.

The mean X-ray luminosity during the four radio epochs exceeds the synchrotron peak by a factor of $\sim 10^3$ and therefore requires a distinct origin (Figure 2.2). One potential mechanism to generate the large X-ray luminosity is inverse Compton (IC) scattering of radio synchrotron photons by the relativistic electrons (synchrotron self-Compton: SSC), but from the relativistic model we find a predicted SSC X-ray luminosity of only $\approx 2 \times 10^{45}$ erg s^{-1}. Similarly, although order of magnitude variations in brightness are seen in the X-rays, our detailed radio light curves do not reveal coincident variations as would be expected for SSC (Figure B.6). We therefore conclude that the X-ray emission is dominated by a distinct, and more compact emission region, most likely at the base of the outflow.

Having established the birth of a relativistic outflow, coincident with the nucleus of the host galaxy, we briefly describe a model to power the outflow through transient accretion (Bloom et al. 2011) onto a supermassive black hole (SMBH). The host galaxy luminosity, $M_B \approx -18.2$ mag, implies (Greene & Ho 2007) a modest SMBH mass of $\sim 10^5 - 10^6$ M$_\odot$. The duration of the bright early phase in the X-ray light curve, $\sim 10^5$ s, coincides with the debris fallback time for a solar-mass star tidally disrupted at a pericenter distance $R_p \sim 13(M_{\rm SMBH}/10^6\,{\rm M}_\odot)^{-5/6}$ Schwarzschild radii. The most bound stellar debris is expected to feed the black hole at an initial rate of $\sim (\frac{1}{2}{\rm M}_\odot)/10^5$ (Strubbe & Quataert 2009). With a radiative efficiency of $\gtrsim 1\%$ at $\sim R_p$, this can account for the observed X-ray luminosity. However, this luminosity is $\sim 10^3$ times the Eddington limit for a $\sim 10^6$ M$_\odot$ black hole, leading inevitably to a highly collimated outflow, the origin of the radio-emitting relativistic outflow found here.

2.5 Conclusions

We conclude with several key implications of our results. First, our initial estimate of the energy, $E_K \approx 3 \times 10^{50}$ erg at $\Delta t \approx 22$ d, corresponds to the Eddington luminosity of a 10^6 M$_\odot$ black hole, lending support to the tidal disruption scenario, and suggesting that the X-ray/γ-ray emission is collimated by a factor of $\sim 10^3$. Long-term radio monitoring will test this result by providing precise beaming-independent calorimetry (Frail, Waxman & Kulkarni 2000; Shivvers & Berger 2011) of the true energy release. Continued radio observations will also uniquely probe the density structure near a previously-dormant supermassive black hole as the ambient medium is swept up by the relativistic outflow. From the existing data we find $n_e \propto {\rm r}^{-2.4}$. Second, with continued expansion we expect that VLBA observations will resolve the radio source on a timescale of ~ 2 yr, and directly confirm the relativistic expansion; from the observed flux density evolution we predict a peak of a few mJy at several GHz on this timescale, within the reach of the VLBA. Third, from the detection of a single such event in 6 years of *Swift* operations we infer a rate of ~ 0.1 Gpc^{-3} yr^{-1}, much lower than the predicted (Wang & Merritt 2004) tidal disruption rate of $\sim 10^2 - 10^3$ Gpc^{-3} yr^{-1}, or upper limits from current radio surveys (Bower 2011) of $\lesssim 10^3$ Gpc^{-3} yr^{-1}. This suggests that the properties of Swift J164449.3+573451 are exceedingly rare; if due to jet collimation, the implied beaming fraction is $\sim 10^3$, consistent with the ratio of the observed X-ray luminosity to the Eddington limit and the radio-inferred

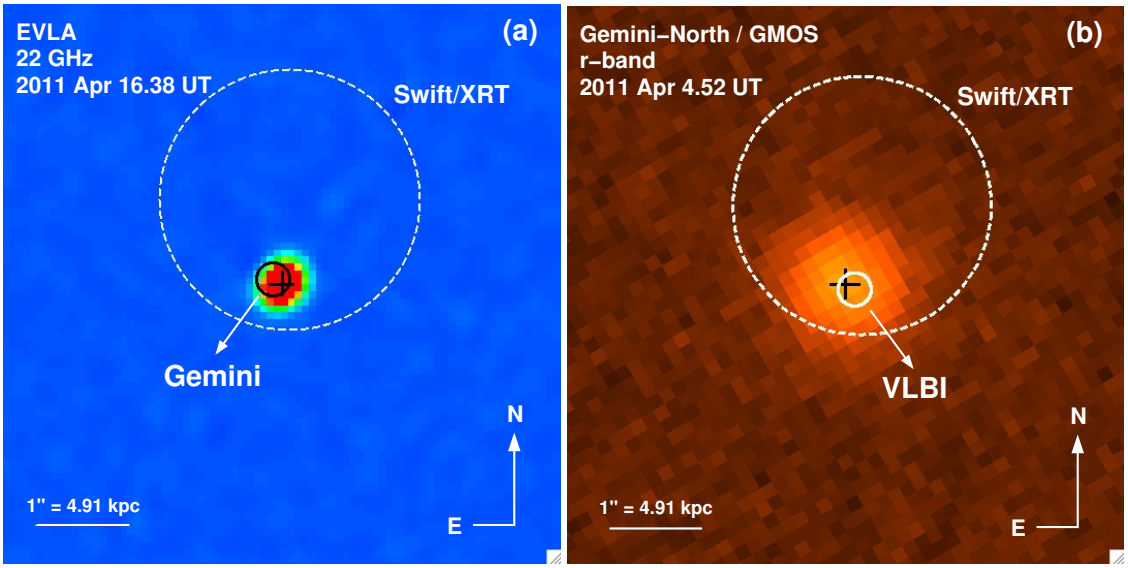

Figure 2.1: Radio and optical images of Swift J164449.3+573451 and its host galaxy reveal a positional alignment between the transient and the center of the galaxy. (a) The radio image is from the EVLA at a frequency of 22 GHz. The most precise radio position, from VLBI is α_{J2000} =16 44 49.93130, δ_{J2000} =+57 34 59.6893 ($\pm$0.1 mas; see SI). (b) The optical *r*-band image was obtained on 2011 April 4.52 UT with the Gemini-North 8-m telescope, and has been astrometrically aligned to the Two Micron All Sky Survey (2MASS) catalog using 14 common objects with a resulting root-mean-square uncertainty of 0.13 arcsec in each coordinate (68% confidence level). The galaxy optical centroid is located at α_{J2000} =16 44 49.942, δ_{J2000} =+57 34 59.74 ($\pm$0.01 arcsec). The *Swift*/XRT error circle (large white circle), with a radius of 1.4 arcsec (90% confidence level), contains the galaxy, but cannot be used to locate the X-ray transient position within it. On the other hand, the radio position relative to the astrometric solution of the Gemini image has an uncertainty of only 0.18 arcsec (68% confidence level; this uncertainty is dominated by the astrometric match of the optical image to the 2MASS catalog, not by the radio position itself) and leads to an offset of 0.11 ± 0.18 arcsec, corresponding to a physical scale of 0.5 ± 0.9 kpc at $z = 0.354$. The radio transient position is therefore consistent with an origin in the nucleus of the host galaxy. (a) The radio centroid is marked by cross-hairs, while the galaxy optical centroid (with an uncertainty of 0.18 arcsec due to 2MASS astrometric solution) is marked by the small black circle. (b) The galaxy optical centroid is marked by cross-hairs, while the radio position (with an uncertainty of 0.18 arcsec due to 2MASS astrometric solution) is marked by the small white circle.

energy. Finally, past searches for tidal disruption events (Komossa & Bade 1999; Gezari et al. 2008; Croft et al. 2011) have focused on the expected bright optical/UV and soft X-ray emission (Strubbe & Quataert 2009), but the large optical extinction and associated soft X-ray absorption in Swift J164449.3+573451 suggest that radio observations may provide a cleaner signature. This is particularly true if the X-ray/γ-ray emission is beamed by a factor of $\sim 10^3$. With the EVLA and the Atacama Large Millimeter Array, similar events are detectable to $z \sim 6$.

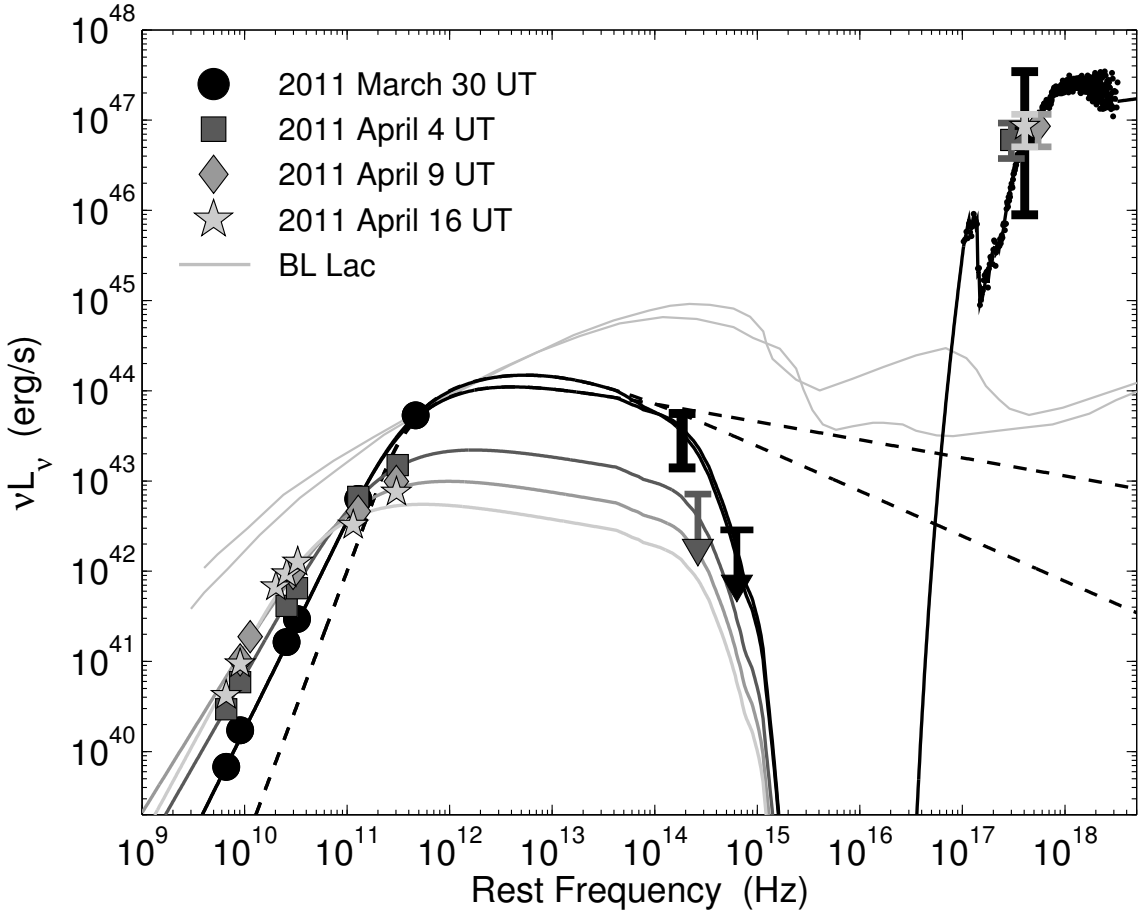

Figure 2.2: Spectral energy distributions (SEDs) of Swift J164449.3+573451 from radio to X-rays point to synchrotron emission from a relativistic outflow. Our radio observations cover decimeter to millimeter wavelengths at 5, 10, 15, and 22 d after the initial γ-ray detection. The NIR luminosity on March 30 can only be constrained within a factor of five due to the unknown contribution from the host galaxy; on April 4 the NIR upper limit is inferred from a *Hubble Space Telescope* imageLevan et al. (2011). Only an upper bound is available on the optical luminosity (black triangle) due to the lackLevan et al. (2011) of variable emission. The flux in the soft X-ray band is highly variable on March 30, but is more quiescent at 10, 15, and 22 d (extrema marked by vertical bars and mean brightness by solid symbols with points at 10 and 15 d shifted slightly in frequency for clarity). The radio, NIR, and optical data are well modeled by an evolving synchrotron spectrum (solid lines) with a large rest-frame optical extinction of $A_V \gtrsim 3$ mag. The synchrotron curves for the March 30 SED are for two values of the synchrotron cooling frequency: $\nu_c \approx 2 \times 10^{13}$ Hz (steeper optically thin slope) and $\nu_c \gtrsim 2 \times 10^{18}$ Hz (shallower optically thin slope). This model cannot explain the large X-ray luminosity, which remains nearly constant while the radio spectrum is evolving strongly. A representative model for the X-ray spectrum (data=black dots; model=black line) includes power-law ($F_\nu \propto \nu^{0.9}$) and blackbody ($kT \approx 1$ keV) components with significant absorption ($N_H \approx 2 \times 10^{22}$ cm^{-2}), in agreement with the large optical extinction. Shown for comparison is the SED of the canonical blazar BL Lac in two separate states (varying in peak frequency and flux of the synchrotron component), normalized to the luminosity of Swift J164449.3+573451 at 345 GHz. The blazar SED provides a poor match.

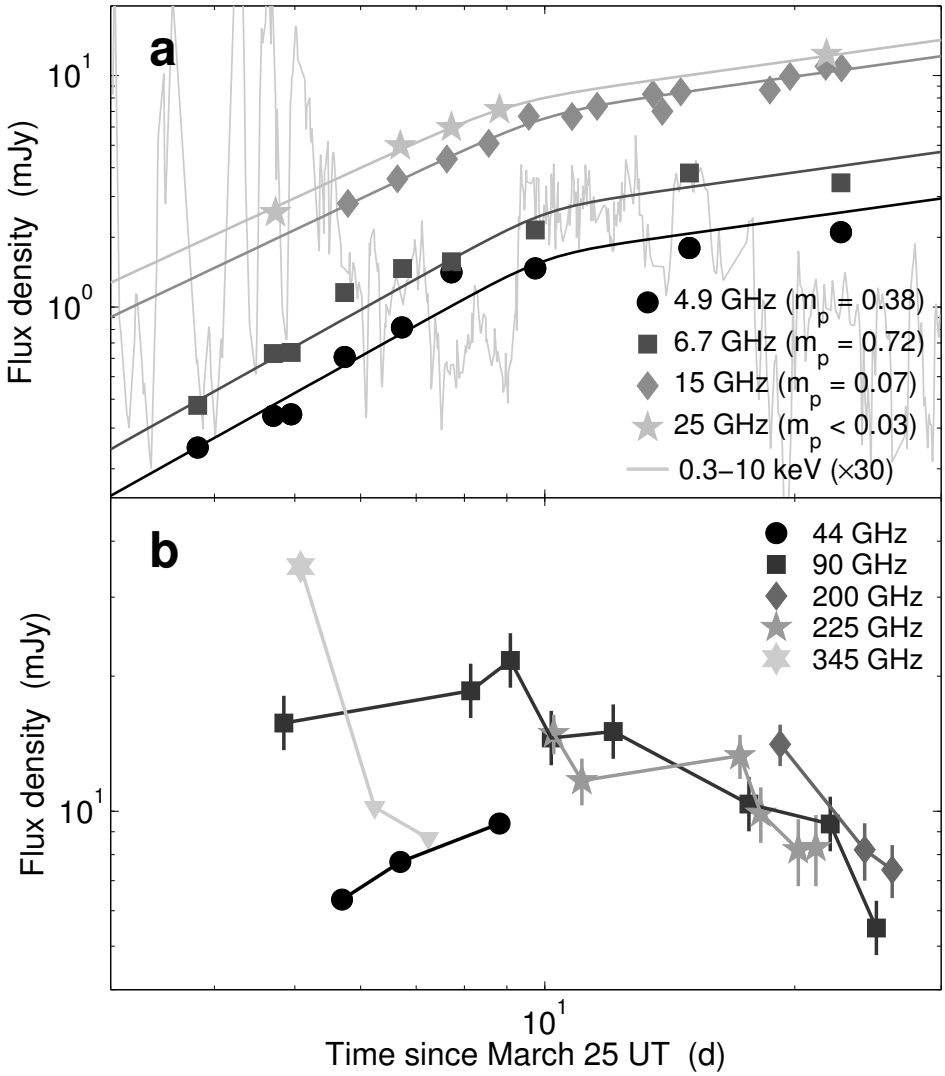

Figure 2.3: Radio light curves of Swift J164449.3+573451 at $5-345$ GHz reveal interstellar scintillation. (a) Light curves at $5-25$ GHz (error bars are smaller than symbols; see SI). These data are from the EVLA, the AMI Large Array, and the OVRO 40-m telescope. The lines are broken power law fits to the $5-25$ GHz light curves, using March 25 as the initial time. The low frequency light curves exhibit significant interstellar scintillation, with the strongest modulation at 6.7 GHz. To calculate the expected interstellar scintillation we use the NE2001 Galactic Free Electron Density ModelCordes & Lazio (2002). For the line of sight to Swift J164449.3+573451 ($l = 86.7111$, $b = 39.4415$) the scattering measure is 2.2×10^{-4} kpc m$^{-20/3}$. With a scattering screen distance of ~ 1 kpc the transition from weak to strong scattering occursGoodman & Narayan (2006) at $\nu_0 \approx 10$ GHz, while the Fresnel scale is $\theta_{F,0} \approx 1$ μas (sizes are given as radii). At frequencies above ν_0 the modulation index is given by $m_p \propto (\nu/\nu_0)^{-17/12} (\theta_s/\theta_{F,0})^{-7/6}$. For frequencies below ν_0 refractive scintillation leads to $m_p \propto (\nu/\nu_0)^{17/30} (\theta_s/\theta_r)^{-7/6}$, where the refractive scale is $\theta_r = \theta_{F,0}(\nu/\nu_0)^{-11/5}$. Comparing these results to the observed modulation we infer a size of $\theta_s \approx 5$ μas. Also shown is the *Swift* X-ray light curveBurrows et al. (2011) binned on a timescale of 15 min and multiplied by a factor of 1.3×10^{10} to fit on the same flux density scale as the radio data. The strong X-ray variability during the first 10 d is not accompanied by similar order of magnitude fluctuations in the radio bands, pointing to a distinct origin for the radio and X-ray emission. (b) Light curves at $44-345$ GHz from the EVLA, CARMA, and the SMA (error bars are one standard deviation). These frequencies are mainly in the decline phase and therefore provide information on the peak of the synchrotron spectrum (Figure 2.2). Upper limits at 345 GHz are marked by triangles.

Bibliography

Begelman, M. C., Blandford, R. D. & Rees, M. J. Theory of extragalactic radio sources. Reviews of Modern Physics 56, 255

Hills, J. G. Possible power source of Seyfert galaxies and QSOs. Nature 254, 295

Rees, M. J. Tidal disruption of stars by black holes of 10 to the 6th-10 to the 8th solar masses in nearby galaxies. Nature 333, 523

Burrows, D. N. et al. Discovery of the Onset of Rapid Accretion by a Dormant Massive Black Hole. Submitted to Nature.

Bloom, J. S., Giannios, D., Metzger, B. D., Cenko, S. B., Perley, D. A. et al. A relativistic jetted outburst from a massive black hole fed by a tidally disrupted star. ArXiv:1104.3257

Levan, A. J., Tanvir, N. R., Cenko, S. B., Perley, D. A., Wiersema, K. et al. An extremely luminous panchromatic outburst from the nucleus of a distant galaxy. ArXiv:1104.3356

Berger, E., Levan, A., Tanvir, N. R., Zauderer, A., Soderberg, A. M. et al. GRB 110328A / Swift J164449.3+573451: Radio-optical/NIR astrometry. GRB Coordinates Network, Circular Service 1854, 1

Readhead, A. C. S. Equipartition brightness temperature and the inverse Compton catastrophe. Astrophys. J. 426, 51

Chevalier, R. A. Synchrotron Self-Absorption in Radio Supernovae. Astrophys. J. 499, 810

Kumar, P. & Narayan, R. GRB 080319B: evidence for relativistic turbulence, not internal shocks. Mon. Not. R. Astr. Soc. 395, 472

Baars, J. W. M., Genzel, R., Pauliny-Toth, I. I. K., & Witzel, A. 1977, A&A, 61, 99

Goodman, J. & Narayan, R. Fitting Formula for Flux Scintillation of Compact Radio Sources. Astrophys. J. 636, 510

Cordes, J. M. & Lazio, T. J. W. NE2001.I. A New Model for the Galactic Distribution of Free Electrons and its Fluctuations. ArXiv:0207156

Greene, J. E. & Ho, L. C. A New Sample of Low-Mass Black Holes in Active Galaxies. Astrophys. J. 670, 92

Strubbe, L. E. & Quataert, E. Optical flares from the tidal disruption of stars by massive black holes. Mon. Not. R. Astr. Soc. 400, 2070

Frail, D. A., Waxman, E. & Kulkarni, S. R. A 450 Day Light Curve of the Radio Afterglow of GRB 970508: Fireball Calorimetry. Astrophys. J. 537, 191

Shivvers, I. & Berger, E. A Beaming-Independent Estimate of the Energy Distribution of Long Gamma-Ray Bursts: Initial Results and Future Prospects. Astrophys. J. in press, 2011.

Wang, J. & Merritt, D. Revised Rates of Stellar Disruption in Galactic Nuclei. Astrophys. J. 600, 149

Bower, G. C. Constraining the Rate of Relativistic Jets from Tidal Disruptions Using Radio Surveys. Astrophys. J. 732, 12

Komossa, S. & Bade, N. The giant X-ray outbursts in NGC 5905 and IC 3599:() hfill Follow-up observations and outburst scenarios. *Astr. Astrophys. 343, 775*

Gezari, S., Basa, S., Martin, D. C., Bazin, G., Forster, K. et al. UV/Optical Detections of Candidate Tidal Disruption Events by GALEX and CFHTLS. Astrophys. J. 676, 944

Cenko, S. B., Bloom, J. S., Kulkarni, S. R., Strubbe, L. E., Miller, A. A. et al. PTF10iya: A short-lived, luminous flare from the nuclear region of a star-forming galaxy. ArXiv:1103.0779

Acknowledgements The EVLA and VLBA are operated by the NRAO, a facility of the NSF operated under cooperative agreement by AUI. The SMA is a joint project between the SAO and the ASIAA, and is funded by the Smithsonian Institution and the Academia Sinica. CARMA development and operations are supported by the NSF under a cooperative agreement, and by the Associates of the California Institute of Technology, the University of Chicago, and the states of California, Illinois, and Maryland. The AMI arrays are supported by the University of Cambridge and the STFC. This work is partially based on observations with the 100-m telescope of the MPIfR at Effelsberg. This work made use of data supplied by the UK Swift Science Data Centre at the University of Leicester.

AuthorContributions B.A.Z. and E.B. designed and coordinated the radio observations and analysis among all instruments reported here. B.A.Z. and D.A.F. performed EVLA observations, data reduction and analysis. G.R.P. observed the source with the SMA, and along with N.A.P. reduced and analysed the SMA observations. CARMA observations were set up, reduced and analysed by B.A.Z., J.M.C. and S.R.K. Fast-response CARMA observations were facilitated by N.H.V. and T.L.C., with the first CARMA observation made by S.S. and C.L.H.H. R.C. implemented and analysed MMT and Gemini optical observations. K.M. performed observations with the OVRO 40-m telescope and analysed results, with advice from S.R.K., A.C.S.R., J.R., M.S. and W.M-M. G.G.P. performed observations with the AMI Large Array and analysed the results. A.M.S., A.B., M.F.B. and M.P.R. planned observations with the VLBA and the MPIfR. A.B. reduced the VLBI data. R.M. analysed and modelled the X-ray data. A.L., R.N. and E.N. provided the theoretical model for a tidal disruption event. The paper was put together by B.A.Z. and E.B., with the primary text written by E.B. and portions of Supplementary Information written by E.B., B.A.Z., R.C., K.M. and A.B. D.B.F. provided feedback on the manuscript. All authors discussed the results and commented on the manuscript.

Chapter 3

Sensitive Search For Radio Variables And Transients In The Extended Chandra Deep-Field South

This chapter is previously published as: Mooley, K. P., Frail, D. A., Ofek, E. O., et al. 2013, ApJ, 768, 165.

Abstract

We report on an analysis of the Extended Chandra Deep Field South (E-CDFS) region using archival data from the Very Large Array, with the goal of studying radio variability and transients at the sub-mJy level. The 49 epochs of E-CDFS observations at 1.4 GHz sample timescales from one day to 3 months. We find that only a fraction (1%) of unresolved radio sources above 40 μJy are variable at the 4σ level. There is no evidence that the fractional variability changes along with the known transition of radio source populations below one milliJansky. Optical identifications of the sources show that the variable radio emission is associated with the central regions of an active galactic nucleus or a star-forming galaxy. After a detailed comparison of the efficacy of various source-finding algorithms, we use the best to carry out a transient search. No transients were found. This implies that the areal density of transients with peak flux density greater than 0.21 mJy is less than 0.37 deg^{-2} (at a confidence level of 95%). This result is approximately an order of magnitude below the transient rate measured at 5 GHz by Bower *et al.* (2007) but it is consistent with more recent upper limits from Frail *et al.* (2012). Our findings suggest that the radio sky at 1.4 GHz is relatively quiet. For multi-wavelength transient searches, such as the electromagnetic counterparts to gravitational waves, this frequency may be optimal for reducing the high background of false positives.

3.1 Introduction

For more than four decades the largest science yield of variable and transient radio emission has come from single-dish radio telescopes, which have surveyed the sky for pulsed and periodic emission from pulsars and related phenomena on typical timescales of seconds to milliseconds. In contrast, interferometric imaging surveys, which are best-suited to probe timescales ranging from seconds, hours and days, have only just begun. There are a limited number of surveys of these so-called *long duration* transients and variables at frequencies of 1–10 GHz, each with a different sensitivity, cadence and field-of-view (Ofek et al. 2011; Bell et al. 2011). Fully exploring this phase space is one of the main science drivers for a new generation of synoptic radio imaging facilities, such as ASKAP (Johnston et al. 2008) and Apertif/WSRT (Oosterloo et al. 2010), that are being built in the coming years (see also Lazio et al. 2009).

Our knowledge of the variable GHz sky is especially lacking at sub-milliJansky flux density levels. For *persistent* sources there is a well-known flattening of the Euclidean-normalized radio source counts below about 1 mJy, corresponding to a change in the radio source populations. This flattening is likely due to the emerging importance of star forming galaxies and low-luminosity active galactic nuclei (AGNs) at redshifts of order unity (Condon 2007; Seymour et al. 2008; Smolčić et al. 2008; Padovani 2011; Condon et al. 2012). Thus, while the variability studies above milliJansky levels are dominated by radio-loud AGNs with compact, flat-spectrum components (Sadler et al. 2006; Lovell et al. 2008), variability at these deeper flux density levels may probe new source populations.

There are indications that the mJy transient sky is exciting. Over the last decade astronomers have detected transient decimetric emission from a variety of sources: transient, bursting and pulsed radio emission from magnetars (Cameron et al. 2005; Gaensler et al. 2005; Camilo et al. 2006), short-lived radio afterglows of short-duration gamma-ray bursts (Fox et al. 2005), emission from (a transient) jet in a dwarf nova (Körding et al. 2008), a new population of sub-relativistic supernovae (Soderberg et al. 2010), a mysterious population of bursting radio sources (Hyman et al. 2005, 2009), and relativistic outflows from tidal disruption events (Zauderer et al. 2011; Cenko et al. 2012). However, with few exceptions, most of what we know about the transient radio sky has come via radio follow-up of objects identified by synoptic telescopes at optical, X-ray or gamma-ray wavelengths. Clearly, this titillating trove of (serendipitous) discoveries call for systematic exploration of the decimetric sky on timescales of minutes and longer.

A ready source of archival data for searching for sub-milliJansky transients and variables comes from deep continuum imaging surveys of the GHz radio sky undertaken to study the extragalactic radio source populations. Many such surveys have been carried out, reaching noise levels of 4–10 μJy and with arcsecond resolution (e.g. Schinnerer et al. 2007; de Zotti et al. 2010). In order to reach these deep flux density limits, it is standard to observe these fields for many epochs with a cadence that samples timescales of days, weeks and months. An added benefit is that these deep surveys are accompanied by rich multi-wavelength continuum datasets and optical/infrared spectroscopic measurements. Thus the counterpart of any unusual variable or

transient source can be readily identified and its redshift determined.

In this paper we present a search for transients and variables at sub-milliJansky flux density levels using data taken as part of a deep radio continuum survey toward a region known as the Extended Chandra Deep Field-South (E-CDFS; Miller et al. 2008). In §3.2 we describe the original survey and our re-reduction of the data. In §3.3 we describe how the variability light curves for 599 point sources were extracted. The transient search is described in §3.4. The interpretation and implication of these results for radio source variability and transients is discussed in §3.5.

3.2 Observations and Data Reduction

The E-CDFS is an intensely studied region having a plethora of multi-wavelength data available (viz. X-ray, ultraviolet, optical, infrared and radio; see Miller et al. 2008, and references therein). Here, we use data from the radio survey undertaken by Miller et al. (2008)[1]. The observations were made at a frequency of 1.4 GHz, using the National Radio Astronomy Observatory (NRAO) VLA in its A configuration (Project code AM 889). A hexagonal grid of six pointings was made, with each pointing separated $12'$ from its nearest neighbor (see Table 3.1 and Figure 3.1). All the observations were carried out in 2007 between June 15 and September 23. Only a single pointing was observed for each epoch. Each epoch was a 5-hr track centered on 03:30 LST[2]. There were a total of 49 epochs, with a combined allocation of 245 hrs (see Table 3.2). The total number of epochs for each pointing $N_{\rm ep}$ is given in Table 3.1. For more details about the specifics of the observational setup see Miller et al. (2008).

The original purpose of these data was to average together all pointings and epochs in order to create a deep (σ_{rms} = 5–8 μJy) continuum image of the E-CDFS. In order to explore variability and to search for transients, we needed to work with the single epoch, single pointing images instead. Despite this, many of the data reduction steps that we followed were similar to Miller et al. (2008). We summarize the process here, pointing out slight differences. All calibration and imaging was carried out in the Astronomical Image Processing System (*AIPS*) package[3].

The calibrated *uv* data for each epoch were imaged and deconvolved separately. In order to image the entire field-of-view at full resolution, we created 37 different facets in a flys-eye pattern. Each of the 37 facets was an image of 1024^2 pixels with a $0.5''$ pixel size offset from one another. There were another 23-25 outlier fields 128^2 pixels each made of cataloged bright radio sources outside the primary beam of each pointing but within a 2° radius.

The *AIPS* task `IMAGR` was used to deconvolve each image to the rms noise level. In order to have a consistent set of images, we applied a Gaussian taper to the (30% level) of 100 kλ and 70 kλ in the u and

[1] In the past, radio observations of this field have also been carried out by Kellerman et al. (2008), Afonso et al. (2006), and Norris et al. (2006).

[2] This is of great benefit to variability studies, which are otherwise plagued by changes in the observing setup.

[3] http://www.aips.nrao.edu/

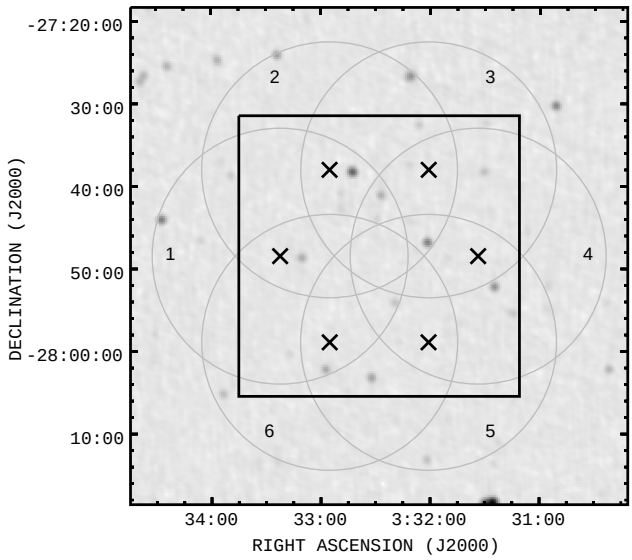

Figure 3.1: Hexagonal grid of six pointings (crosses), each pointing separated $12'$ from its nearest neighbor. The $34' \times 34'$ (black square) region represents the extent of the final image from the Miller et al. (2008) data release. $15'$-circles (grey) corresponding to the 50% beam attenuation in different pointings are also shown. The $60' \times 60'$ background image is from NVSS.

Table 3.1: List of survey pointings

Pointing ID	R.A. (J2000.0)	Dec. (J2000.0)	$N_{\rm ep}$
ECDFS1	03 33 22.25	–27 48 30.0	7
ECDFS2	03 32 55.12	–27 38 03.0	9
ECDFS3	03 32 00.88	–27 38 03.0	8
ECDFS4	03 31 33.75	–27 48 30.0	8
ECDFS5	03 32 00.88	–27 58 57.0	9
ECDFS6	03 32 55.12	–27 58 57.0	8

$N_{\rm ep}$ is the number of epochs per pointing.

v directions to the visibility data, and we restored the final images to a synthesized beam of $2.8'' \times 1.6''$ (position angle$\simeq 0^\circ$). After deconvolution, the 37 facets for each epoch were combined using the *AIPS* task `FLATN` to form a single 5120^2 pixel image $42.7'$ across. A correction for the attenuation from the primary beam was not applied at this stage in order that the images used in analysis had uniform noise statistics across the entire image. The rms noise σ_{rms} for each epoch is given in Table 3.2.

3.3 Variability Analysis

The source catalog we used to investigate variability was taken from the second data release (DR2; Miller et al. 2013) of Miller et al. (2008). This catalog was generated by combining all the data from Tables 3.1 and 3.2 to make a single deep $34' \times 34'$ image with a typical sensitivity of 7.4 μJy. Miller et al. (2013) identified sources using the *AIPS* task `SAD` down to 4σ, and then inspected the residual map to identify missed sources as well as accepted sources which were poorly fit by `SAD`. These missing sources were then added to the

Table 3.2: Observing Epochs

Epoch	Date (UT)	Pointing	σ_{rms} μJy bm^{-1}
1	2007 Jun. 15	ECDFS2	26.3
2	2007 Jun. 24	ECDFS3	28.0
3	2007 Jun. 25	ECDFS4	28.6
4	2007 Jul. 01	ECDFS6	25.9
5	2007 Jul. 06	ECDFS5	29.2
6	2007 Jul. 12	ECDFS1	26.6
7	2007 Jul. 13	ECDFS2	26.6
8	2007 Jul. 14	ECDFS3	25.5
9	2007 Jul. 15	ECDFS4	26.4
10	2007 Jul. 16	ECDFS5	26.8
11	2007 Jul. 17	ECDFS6	26.1
12	2007 Jul. 19	ECDFS1	26.0
13	2007 Jul. 20	ECDFS2	34.2
14	2007 Jul. 21	ECDFS3	26.0
15	2007 Jul. 22	ECDFS4	25.3
16	2007 Jul. 23	ECDFS5	27.8
17	2007 Jul. 24	ECDFS6	27.5
18	2007 Jul. 26	ECDFS5	31.8
19	2007 Jul. 27	ECDFS2	27.2
20	2007 Jul. 28	ECDFS3	30.5
21	2007 Jul. 29	ECDFS4	27.1
22	2007 Jul. 30	ECDFS1	28.0
23	2007 Aug. 02	ECDFS6	27.0
24	2007 Aug. 03	ECDFS1	27.4
25	2007 Aug. 04	ECDFS2	26.7
26	2007 Aug. 05	ECDFS3	25.9
27	2007 Aug. 06	ECDFS4	29.1
28	2007 Aug. 09	ECDFS5	31.2
29	2007 Aug. 10	ECDFS6	30.0
30	2007 Aug. 11	ECDFS1	31.9
31	2007 Aug. 13	ECDFS2	31.3
32	2007 Aug. 14	ECDFS3	31.5
33	2007 Aug. 16	ECDFS4	30.8
34	2007 Aug. 17	ECDFS5	45.7
35	2007 Aug. 18	ECDFS6	28.6
36	2007 Aug. 21	ECDFS1	29.1
37	2007 Aug. 23	ECDFS2	30.9
38	2007 Aug. 25	ECDFS3	30.8
39	2007 Aug. 26	ECDFS4	29.8
40	2007 Aug. 28	ECDFS5	33.9
41	2007 Aug. 31	ECDFS6	29.3
42	2007 Sept. 06	ECDFS2	30.9
43	2007 Sept. 07	ECDFS3	29.3
44	2007 Sept. 08	ECDFS4	29.3
45	2007 Sept. 09	ECDFS5	28.9
46	2007 Sept. 10	ECDFS6	30.2
47	2007 Sept. 11	ECDFS1	30.4
48	2007 Sept. 12	ECDFS5	37.9
49	2007 Sept. 23	ECDFS2	31.6

preliminary source list. Further flagging and follow-up was done in order to produce a modified source list in which all sources with peak flux density greater than 5 times the local rms noise (i.e. 5σ), were fit using the *AIPS* task `JMFIT`. Also, the effect of bandwidth smearing on sources within the six individual pointings was assessed using `JMFIT`, and the resolution information was thus preserved in the output catalog. Lastly, the sources in the DR2 catalog were compared with the catalog of Kellerman et al. (2008).

The DR2 catalog contains almost twice as many sources (883 vs. 464) compared to the first data release (see Miller et al. 2013, 2008) owing to a more careful data reduction. Of the 883 sources in the DR2 catalog we created a point-source-only catalog of 736 objects used for exploring variability. With this careful approach outlined above, we expect the Miller et al. DR2 catalog to contain all real sources above 5σ (however, see §3.4.1).

We thus justify our use of the DR2 catalog for investigating the variability of the sub-milliJansky population. In §3.4 we use both the DR2 image and its source catalog as a testbed for different source-finding algorithms. The signal-to-noise ratio (SNR) of sources in the DR2 catalog is shown in Figure 3.2.

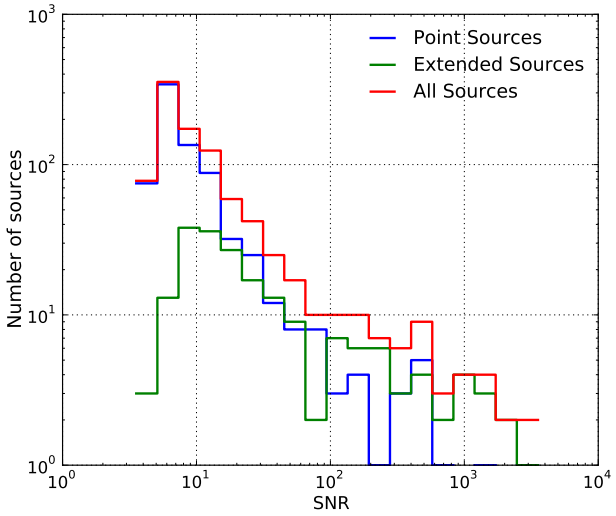

Figure 3.2: A histogram of the signal-to-noise ratio (SNR) of the sources in the DR2 catalog.

It is important to quantify the uncertainty in the peak flux density when analyzing variability of sources in different epochs. Following Thyagarajan et al. (2011), we attribute this uncertainty primarily to a combination of four[4] causes: (i) local image rms noise, (ii) uncertainty in the primary beam, (iii) flux density calibration amplitude, (iv) pointing errors. Let us denote the measured peak flux density of a source in epoch i by f_i, such that the primary beam correction is $b = b(\theta)$, where θ is the angular distance of the source from the phase center. We wish to calculate the uncertainty in the quantity (f_i/b). The image local noise (Δf_i) scales as $\Delta f_i/b$. If we denote the fractional uncertainty in the beam as ϵ_b and that in the flux density calibration

[4]Far out in the primary beam, orthogonally polarized beams can be far offset on the sky, making amplitude calibration difficult. For short observations, the effects of this "beam squint" can be much larger than all other uncertainties combined. However, these offsets tend to average out when observations are made over sufficiently long times. Since the VLA's beam squint is oriented almost exactly East-West (Cotton & Perley 2010), our observational setup is optimal for averaging out the effects of beam squint.

amplitude by ϵ_c, then the corresponding errors scales as $(f_i/b)\epsilon$. We adopt a value of 4% for ϵ_c, intermediate between the conservative estimate of Thyagarajan et al., 5%, and the one quoted by Ofek et al. (2011), 3%. The typical pointing error ($\Delta\theta$) of a VLA antenna is between 10″–20″. The resultant uncertainty scales as $(f_i/b^2)(-db/d\theta)\Delta\theta$. All these four error terms, added in quadrature, would give the total uncertainty, σ_i, in the peak flux density corrected for the primary beam attenuation. However, as shown below, the pointing-related error term is much smaller than the rest, and hence can be neglected. Thus,

$$\sigma_i = \frac{1}{b}\sqrt{\Delta f_i^2 + f_i^2(\epsilon_b^2+\epsilon_c^2)} \tag{3.1}$$

Polynomial coefficients (and the associated error) that express the average angular dependence of b can be found in the AIPS task PBCOR, while measurements of the VLA beam power response to beyond the first null are given in Cotton & Perley (2010). Using the beam response profile from Cotton & Perley , we can estimate the error terms (i)–(iv) above for a typical source in the DR2 catalog, having measured flux density of 300 ± 30 μJy. If the source lies at the half-power radius ($\theta = 15'$), then these correction factors are about 10%, 4%, 4% and 1% of the primary-beam-corrected flux density (570 μJy) respectively. The pointing-related uncertainty is thus negligible.

In light of Ofek et al. (2011), we use two measures of variability (see also Scheers 2011), the modulation index defined as the standard deviation divided by the mean,

$$m = \frac{1}{\bar{f}}\sqrt{\frac{1}{\mathrm{N}-1}\sum_{i=1}^{N}(f_i-\bar{f})^2}, \tag{3.2}$$

and the χ^2,

$$\chi^2 = \sum_{i=1}^{N}\frac{(f_i-\bar{f})^2}{\sigma_i^2}, \tag{3.3}$$

where N is the number of epochs, and $\bar{f}$ is the mean flux density of the source over all the epochs considered for the variability analysis. In these two equations, the primary beam correction is implicit in f_i and $\bar{f}$. χ^2 gives a measure of the deviation from stochastic epoch-to-epoch fluctuations in the peak flux density, and we define "significant variability" beyond a level[5] of 4σ. The modulation index indicates the strength of variability, i.e. the fractional variation of the peak flux density.

3.3.1 Single-Pointing Variability

A variability analysis was carried out on each pointing in Table 3.1 separately. Peak flux densities were measured for all point sources in the DR2 catalog brighter than 40 μJy and within a 15′ radius of the pointing centers (i.e. the 50% response radius of the primary beam of the VLA antennas; see also Figure 3.1). This approach has the merit of being simple and robust. Since the angular distance of a source from its pointing

[5]For Gaussian noise, 4σ corresponds to a probability of about 1/16,000, while the number of measurements in our variability analysis (several to tens of epochs multiplied by a few hundred sources) ranges from about 1,500 to 15,000.

center is constant, the accuracy of the correction for the primary beam attenuation $b(\theta)$ is unimportant. The modulation index and χ^2 measures of variability are insensitive to a constant $b(\theta)$.

The limitation of this approach is that the resulting light curves are constructed for only 7–9 epochs. Many of our investigated point sources are found in multiple pointings and therefore light curves can be constructed with many more epochs, resulting in higher cadence over the full 100 days of observing. A full variability analysis of this kind is carried out in §3.3.2.

In Figure 3.3 we show variability plots (i.e. χ^2 vs. m) for the DR2 sources in each of the six pointings. There are approximately 175 sources per pointing. Some of the bright (> 3 mJy) sources show significant variability but with only low modulation indices ($\sim$10%). We define strong variables as sources having $m > 0.5$ (i.e. higher than 50% fractional variability). Only two genuine variables were found in this single-pointing analysis; no strong variables were found (Table 3.3, upper panel).

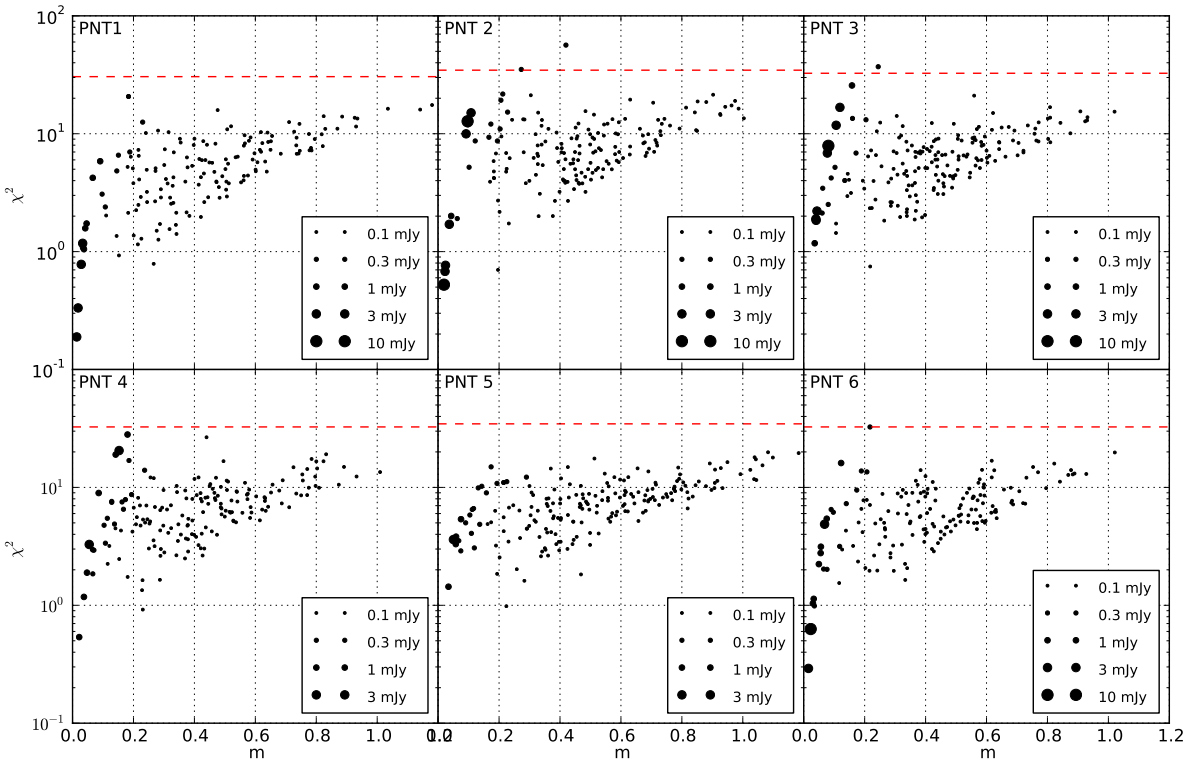

Figure 3.3: Variability plot for the point sources in the Miller et al. DR2 catalog, shown separately for all pointings. The peak flux density is denoted by the symbol size. The red dashed line represents the 4σ level for the appropriate number of degrees of freedom (one less the number of epochs in each pointing) for each pointing. The number of epochs in each pointing lies between 7 and 9.

3.3.2 Full Variability Analysis

In order to undertake variability analysis using data from all the epochs, the single-epoch peak flux densities were required to be corrected for (i) bandwidth-smearing, and (ii) the primary beam response, as any given

source will lie at different angular distance from the phase center in different pointings. We applied bandwidth smearing correction from the approximation given in Bridle & Schwab (1989) (Eqn. 13-19 therein).

There were two choices for the primary beam profile — one derived as the empirical beam profile for VLA-FIRST (Thyagarajan et al. 2011), and the other found in the AIPS task `PBCOR`. To test which of these profiles best represented our data, we adopted the following approach. We first normalized the peak flux densities of > 300 μJy sources from all epochs using their peak flux density from the DR2 catalog and plotted them as a function of distance from the pointing center. The resultant beam profile matched with the VLA-FIRST profile better than the one from `PBCOR` (to within 1%, but only for $\theta < 12'$; scatter of 6.5%). Hence we used the former beam profile for our primary beam correction, $b(\theta)$; the associated error (ϵ_b), was also taken from Thyagarajan et al. (2011). Thus, for a reliable all-epoch variability analysis, we restricted our search to the point sources in the DR2 catalog which were located within $12'$ from the pointing centers of their respective epochs. This also appears to be the radius beyond which our bandwidth- smearing approximation starts to break down. Thus, for example, a source located at $\alpha = 03^{\rm h}33^{\rm m}00^{\rm s}$ and $\delta = -28^\circ 00' 00''$ would be present in pointings 6, 5, and 1, but not in 2,3, and 4 because the separation between the source and the centers of pointings 2,3, and 4 is larger than 12 arcmin. Further, as we did with the single-pointing variability (§3.3.1), we restricted our analysis to sources whose mean flux density was brighter than 40 μJy. This full variability analysis was carried out on 599 point sources.

Depending on the number of pointings in which a source is present, this analysis allowed us to exploit the higher cadence over the entire duration of the observing program. The resulting light curves are now more densely sampled with 15–26 epochs, rather than the 7–9 epochs for the single-pointing variability case. In Figure 3.4 we show variability plots for the DR2 sources, taking into account all the epochs.

Seven significant variables were found via this procedure, but no strong variables ($m > 0.5$). Both of the variables identified in the single-pointing analysis in §3.3.1 are also seen here. The results of the variability study are given in Table 3.3 and the light-curves for the significant variables are shown in Figure 3.5. We can compare our variability criteria with the Carilli et al. (2003) measure for variability, i.e. $V_c = (S_1 - S_2)/S$, where S_1 and S_2 are the maximum and minimum flux densities respectively observed, and S is their mean. This measure of variability for the seven variable sources found in this work are listed in Table 3.3.

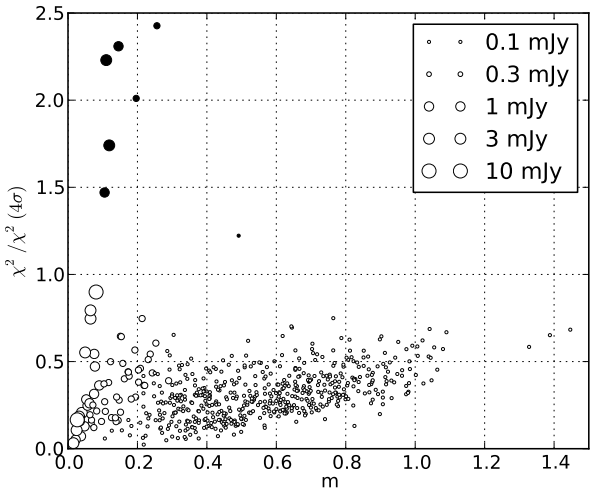

Figure 3.4: χ^2 normalized by its value at the 4σ level, plotted against the modulation index, m, for sources in the Miller et al. DR2 catalog using peak fluxes from all pointings, and corrected with empirically-derived beam attenuation profile. The 4σ level is different for different sources, depending on the number of epochs in which they are present. The mean peak flux density is denoted by the symbol size. Filled circles indicate significant variables (lying above a normalized χ^2 of unity).

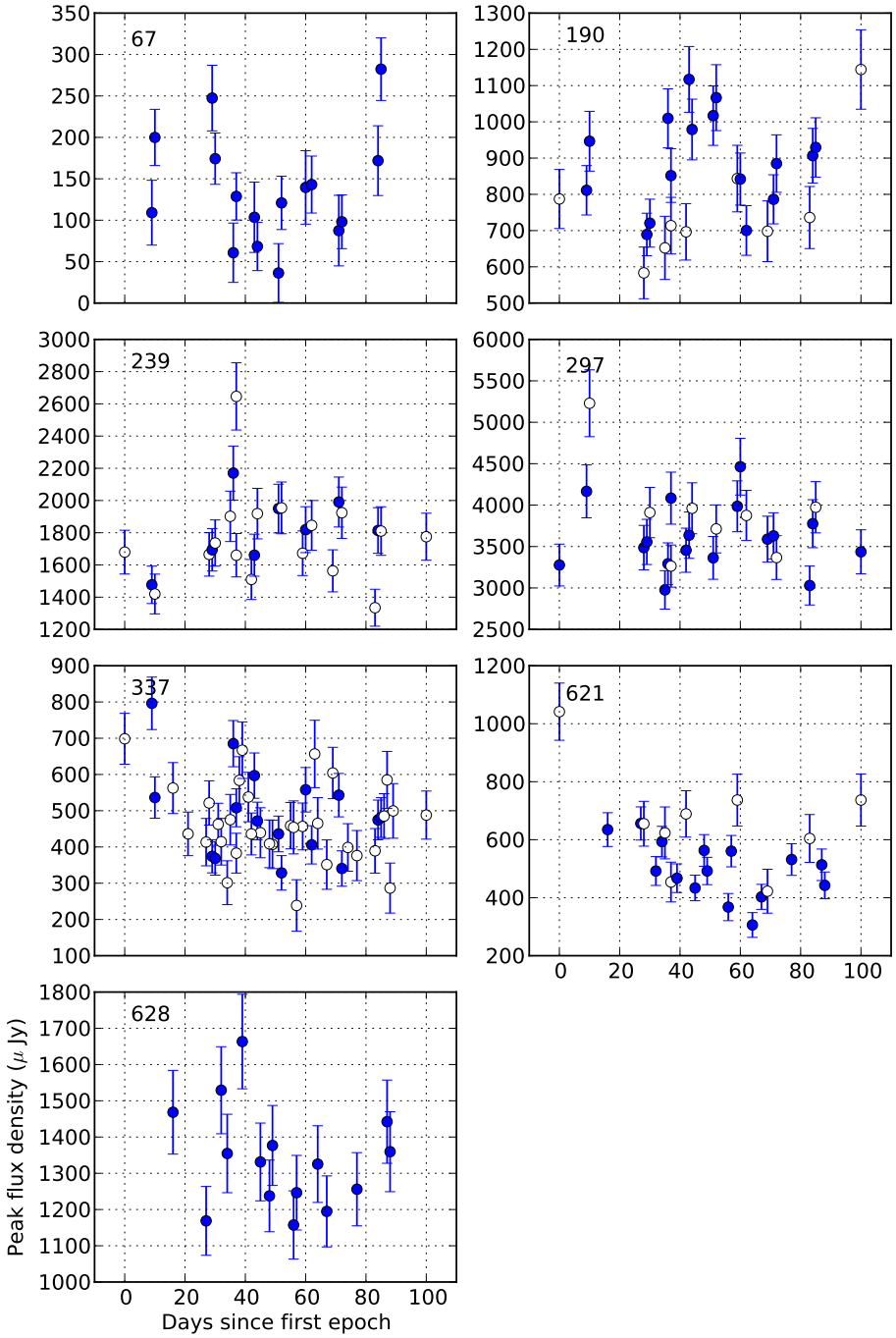

Figure 3.5: Light curves of the variable sources from Miller et al. DR2 catalog listed in Table 3.3. Filled symbols represent the flux densities considered for variability analysis (i.e. where $\theta < 12'$). Flux densities in epochs where a source lies within the 50% power circle of the beam (i.e. where $\theta \lesssim 15'$) are plotted for reference as open symbols. The error bars take into account the background rms, primary beam correction, and bandwidth smearing (no taper).

Table 3.3: Variables among Miller et al. DR2 sources

ID	α_{J2000} (h, m, s)	δ_{J2000} (°, ′, ″)	$\overline{f}$ (μJy)	m	V_c (%)	N_{ep}	z	log $\overline{L}_R$ (cgs)	α_R	α_{IR}	M_R (mag)	Energy Source
Single Pointing Analysis												
337	03 32 18.03	−27 47 18.8	558 ± 14	0.26	76	8						
621	03 33 15.00	−27 51 51.3	663 ± 22	0.23	93	9						
Full Variability Analysis												
67	03 31 27.07	−27 44 09.9	136 ± 9	0.50	181	16	1.005	30.6	+0.23	> -3.8	−21.04	SF+AGN
190	03 31 52.13	−27 39 26.6	891 ± 12	0.15	48	16	2.296	32.1	−0.35	> -1.3	−22.07	AGN
239	03 32 00.85	−27 35 57.1	1822 ± 27	0.12	38	8	0.266	30.5	−0.30	> -2.3	−17.26	SF+AGN
297	03 32 11.66	−27 37 26.3	3600 ± 36	0.11	41	17	0.605	31.5	+0.89	−0.9	−23.98	AGN
337	03 32 18.03	−27 47 18.8	494 ± 11	0.26	95	16	0.734	30.8	−0.08	> -3.4	−22.69	SF+AGN
621	03 33 15.00	−27 51 51.3	497 ± 10	0.20	70	15	1.107	31.2	+0.24	> -3.4	−20.71	SF+AGN
628	03 33 16.74	−27 56 30.4	1341 ± 16	0.11	38	15	0.685	31.2	−0.40	−2.2	−21.21	SF+AGN

Notes– (1) ID is the source-ID as given in the Miller et al. DR2 catalog. (2) $\overline{f}$ refers to the mean flux density corrected for the primary beam and bandwidth smearing. (3) V_c is the Carilli et al. (2003) variability criteria as described in § 3.3.2. (4) Redshift z is according to Bonzini et al. (2012) or Treister et al. (2009). The redshifts of ID 67, ID 239 and ID 297 as per the COMBO-17 survey catalog (Wolf et al. 2004) are 0.548, 0.947 and 1.574 respectively. (4) The 1.4 GHz spectral luminosity (erg s^{-1} Hz^{-1}) is $\overline{L}_R = 4\pi d_l^2 \bar{f}/(1+z)$, where the luminosity distance d_l assumes cosmological parameters from Komatsu et al. (2011). (5) The spectral indices ($S \propto \nu^{\alpha}$) between 1.4 GHz and 5.5 GHz and between 24 μm and 70 μm are tabulated as α_R and α_{IR} respectively. In the absence of a 70 μm counterpart, a 3σ upper limit to the flux density at this wavelength is considered. Note that the 1.4 GHz and 5.5 GHz measurements are non-simultaneous. (6) The absolute R-band magnitude M_R has been calculated using the redshift z and the apparent magnitude from the NASA/IPAC Extragalactic Database. (7) The energy sources within the galaxy as indicated by the radio and mid-to-far-infrared properties are listed in the last column. SF: star-formation, AGN: active galactic nucleus (see §3.3.3).

In order to undertake multiwavelength identifications we had to align the reference frames of all the data sets. The radio and optical source positions were brought to the same reference frame by calculating the radio-source position offsets with respect to *Hubble* Space Telescope source positions from GOODS-S (Giavalisco et al. 2004) and the GEMS (Rix et al. 2004). Optical counterparts (from these two HST catalogs) were searched toward radio sources within $1''$. Only point-like sources having a single counterpart were chosen. A histogram of the offsets of these counterparts in right ascension ($\Delta\alpha = \alpha_{\rm radio} - \alpha_{\rm optical}$) and declination ($\Delta\delta = \delta_{\rm radio} - \delta_{\rm optical}$) was then computed to find the most-likely offset (peak of the histogram). The associated error was taken to be the standard deviation about this most-likely offset added in quadrature with the cataloged mean positional error of the radio source. In addition to the Miller et al. (2013) DR2 catalog, we repeated this procedure for other radio-source catalogs in the E-CDFS region, viz. Kellerman et al. (2008), Norris et al. (2006), and Afonso et al. (2006) using $\geqslant 5\sigma$ sources. The computed radio vs. optical positional offsets along with the mean positional errors listed in the respective radio catalogs are shown in Table 3.4.

Table 3.4: Radio Positional Offsets wrt. Optical HST Catalogs

	arcsec	(1)	(2)	(3)	(4)
	σ_α	~ 0.1	0.37	0.31	[b]
	σ_δ	~ 0.1	0.57	0.58	[b]
GEMS	$\Delta\alpha$	0.18 ± 0.31	0.15 ± 0.45	-0.09 ± 0.41	-0.17 ± 0.40[a]
	$\Delta\delta$	-0.32 ± 0.32	-0.34 ± 0.53	-0.20 ± 0.44	0.11 ± 0.30[a]
GOODS	$\Delta\alpha$	-0.20 ± 0.23	0.15 ± 0.42[a]	0.03 ± 0.44[a]	-0.10 ± 0.39[a]
	$\Delta\delta$	0.22 ± 0.28	-0.18 ± 0.37[a]	0.03 ± 0.44[a]	-0.18 ± 0.33[a]

Column headers– (1) Miller et al. (2013), (2) Kellerman et al. (2008)
(3) Norris et al. (2006), (4) Afonso et al. (2006)
Notes– (a) Few ($\leqslant 15$) sources available to calculate the offsets.
(b) Positional uncertainty not mentioned in catalog; assumed to be $0.1''$.
(c) All offsets are in arcseconds.

3.3.3 Notes on Variables Found

An important question that we can address is whether the variability at sub-milliJansky levels is dominated by normal star-forming galaxies or by AGN. For AGN-dominated samples above 1 mJy, variability at frequencies of a few GHz or below is thought to be dominated by propagation effects (i.e. refractive interstellar scintillation) and not by intrinsic changes in the source (Gaensler & Hunstead 2000; Ofek & Frail 2011). For a disk galaxy we expect there to be steady emission from diffuse synchrotron emission and the sum of all supernovae. Intrinsic variability can be induced by (i) a stellar explosion (supernova, low-luminosity gamma-ray burst), and (ii) nuclear radio emission (AGN). Mapping the radio emission to the center of the galaxy would favor (ii) whereas if the radio emission is mapped to the disk then (i) is favored.

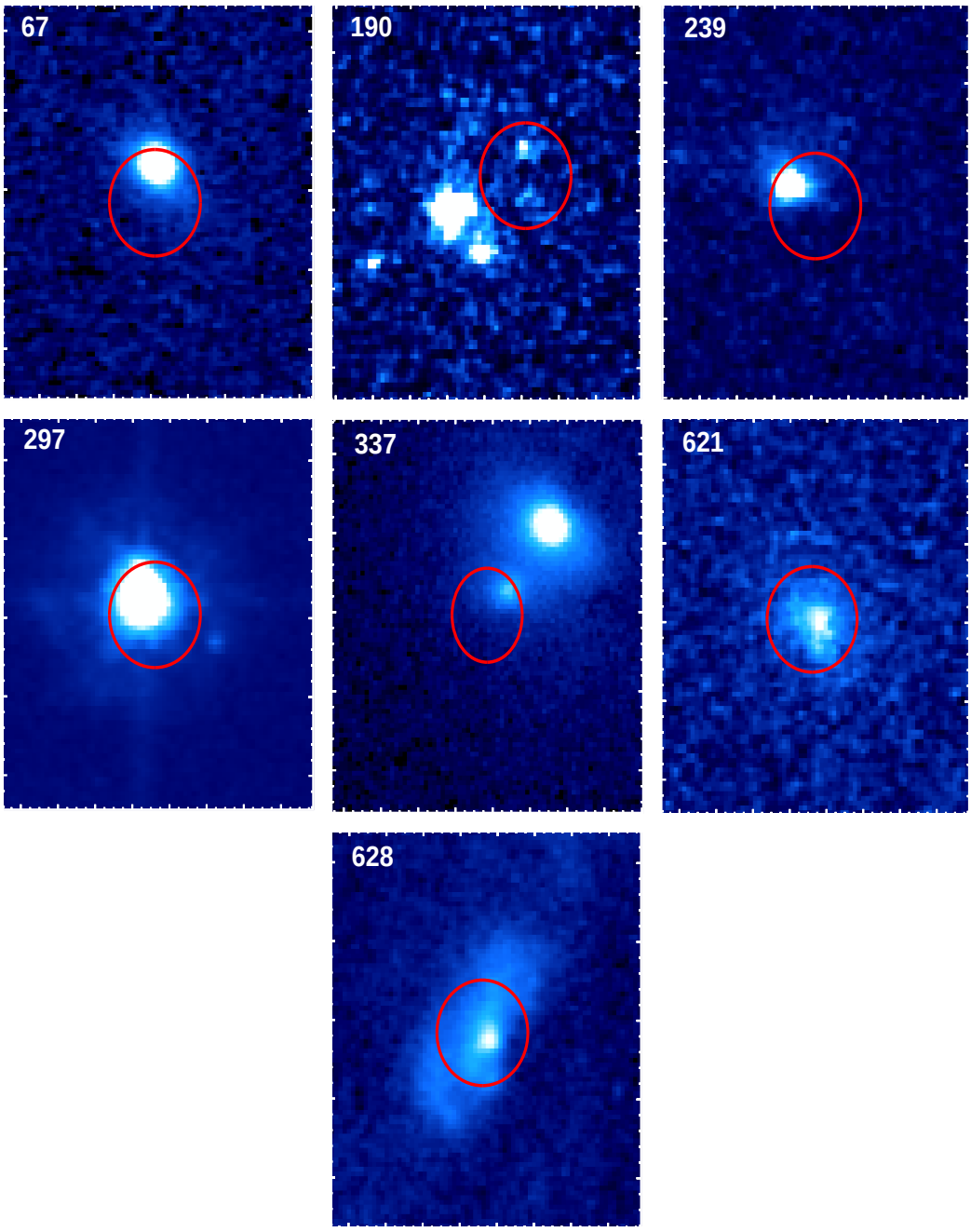

Figure 3.6: $2.2'' \times 2.5''$ GEMS (all sources except ID 337) and GOODS-S (ID 337) F606W ACS-WFC image cutouts of variable sources found in this work. The red error ellipses denote the radio source positions from Miller et al. (2013), shift-corrected to the HST source positions. All the positional uncertainties are 1σ (see § 3.3.2 and Table 3.4).

To this end, we overplotted radio source positions of the seven variables given in Table 3.3 on HST image cutouts from GOODS-S and the GEMS projects (Figure 3.6). All of the radio sources have an optical counterpart on these HST images. The redshifts of these objects vary from 0.3 to 2.3. Thus, the post-offset radio source-position uncertainties lie between 1.4 and 2.7 kpc. Within most error ellipses, there is a centrally compact source, suggesting that this is the source of the variable emission. Light-curves of the variable sources are given in Figure 3.5. Detailed notes on each of these objects are given below, and key physical parameters are listed in Table 3.3. All of the variable sources have luminosities in excess of 10^{30} erg s^{-1} Hz^{-1}, where the luminosity functions of AGNs and star-forming galaxies intersect (Condon 2002). Most of the variable sources have a roughly flat spectrum between 1.4 GHz and 5.5 GHz suggesting the presence of AGN. Note that the spectral indices between 1.4 GHz and 5.5 GHz are based on non-simultaneous measurements having different resolutions. Additionally, mid-infrared colors, far-infrared spectral indices, and mid-to-far-infrared luminosities indicate that most of the variable sources reside in star-forming galaxies. In Figure 3.7 we show the mid-infrared color-color diagram for the variable sources using *Spitzer*/IRAC photometry from the SIMPLE survey catalog (Damen et al. 2011). The Donley et al. (2012) AGN selection region is overplotted. For comparison, the colors of the radio sources from the AEGIS20 sample (Willner et al. 2012) are shown along with those of three template spectral energy distributions (SEDs) — an elliptical galaxy, an Sbc galaxy, and an AGN — from Assef et al. (2010). This figure along with the far-infrared flux densities identify two variables with AGNs and the rest as star-forming galaxies.

Summarizing, the high-resolution optical images together with photometric information from radio and mid-to-far-infrared suggest that variability arises from the central regions of an AGN or star-forming galaxy.

ID 67: This source has a mean 1.4 GHz flux density of 136 ± 9 μJy and shows the strongest variation among all seven variables. Two flaring bursts are evident from the light curve (Figure 3.5), one of them lasting for about 25 days, and the flux density of the other increasing by at least a factor of 2.5 in 12 days. This source also appears in the Kellerman et al. 1.4 GHz catalog, where its flux density is 90 ± 16 μJy. The photometric redshift of z=1.005 (Bonzini et al. 2012) implies a mean radio luminosity of $\log L_R = 30.6$ erg s^{-1} Hz^{-1}. The radio spectral index (defined as α where $S_\nu \propto \nu^\alpha$) between 1.4 GHz and 5.5 GHz is +0.23 (Huynh et al. 2012). The morphology of the host galaxy as seen from the HST image appears to be that of a bright, compact nucleus surrounded by faint extended structure. The half-light radius of the galaxy according to the *GALFIT* parameters from the GEMS catalog is 620 ± 10 pc. The K-corrected[6] mid-to-far-infrared spectral luminosities derived from the FIDEL and GOODS (Magnelli et al. 2009, 2011), and SIMPLE *Spitzer* surveys are $\nu L_\nu(5.8\ \mu\text{m}) = 6.6 \times 10^8$ L$_\odot$ and $\nu L_\nu(24\ \mu\text{m}) < 5.4 \times 10^{10}$ L$_\odot$. By comparing these quantities with the Chary & Elbaz (2001) template SEDs (see Figure 4 of that paper) and from the *Spitzer*/IRAC color-color diagram (Figure 3.7), we interpret that the host galaxy is star-forming.

Taken together, the radio luminosity, radio spectral index, optical morphology and mid-to-far-infrared

[6]For the 5.8 μm and 24 μm luminosities, the K-correction has been applied based on the 8 μm and 70 μm flux densities. In the absence of a 70 μm detection, the 3σ upper limit has been used.

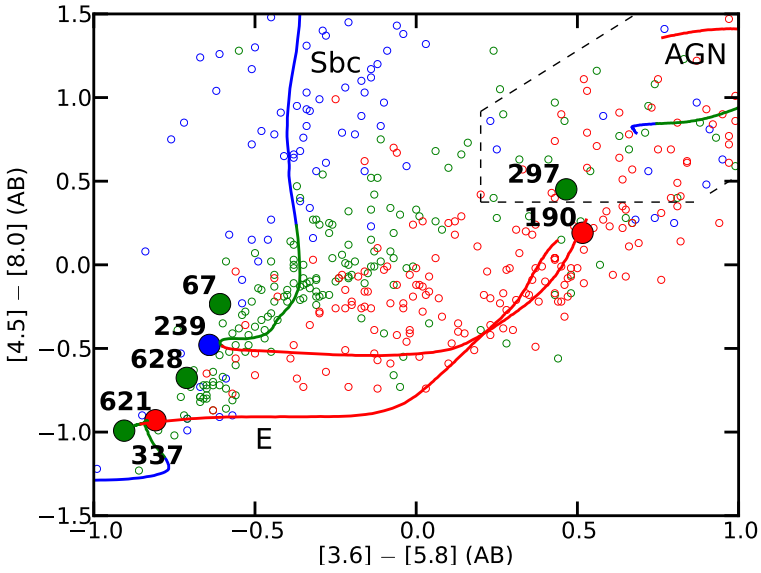

Figure 3.7: *Spitzer*/IRAC color-color diagram for the mid-infrared counterparts of the variable sources (filled circles). For comparison, the radio sources from AEGIS20 (Willner et al. 2012) are also shown (unfilled circles). The AGN selection region in the upper-right corner, bounded by the dashed lines, is from Donley et al. (2012). Curves represent the colors of three template spectral energy distributions (E: elliptical galaxy; Sbc: spiral galaxy; AGN) from Assef et al. (2010) as redshift increases from 0 to 3. The redshift-dependent color-coding is — blue: $z \leqslant 0.5$, green: $0.5 < z \leqslant 1.1$ and red: $z > 1.1$.

flux densities argue that ID 67 is a star-forming galaxy harboring a low-luminosity AGN.

ID 190: This source has a mean 1.4 GHz flux density of 891 ± 12 μJy. The light curve appears to fluctuate between high and low flux density states on a timescale of order 20 days. This source is also found in the Kellerman et al. and Norris et al. catalogs where the flux density is 970 ± 30 and 810 ± 19 μJy respectively, and a spectral index of –0.6 between 1.4 and 4.8 GHz. The 5.5 GHz flux density from Huynh et al. is 555 ± 17 μJy, for which we derive a spectral index of –0.35. The photometric redshift of z=2.296 (Bonzini et al. 2012) implies a mean radio luminosity of log L_R = 32.1 (cgs). The HST image of this galaxy as seen in Figure 3.6 shows that the radio source is offset from the brightest emission in the field. On the basis of its departure from the radio-FIR correlation, Norris et al. classify this source as an AGN. The radio and far-infrared spectral indices (Table 3.3) and mid-infrared colors (Figure 3.7) are consistent with this identification. Note that between 24 μm and 70 μm, a spectral index greater than −1.5 is representative of AGNs (e.g. Condon 2002).

ID 239: This source has a mean 1.4 GHz flux density of 1822 ± 27 μJy. This source is also found in the Kellerman et al. and Norris et al. catalogs where the flux density is 2030 ± 43 and 1640 ± 20 μJy respectively. Its light-curve shows a gradual increase in flux density, over a period of about 50 days, followed by an equally gradual decline. The radio spectral index between 1.4 GHz and 5.5 GHz is –0.30. This slope is more consistent with AGNs than star-forming galaxies which are expected to have $\alpha \simeq -0.8$. The redshift z=0.266 (Treister et al. 2009) implies a mean radio luminosity of log L_R = 30.5 (cgs). The HST cutout

(Figure 3.6) reveals just a bright nucleus surrounded by faint extended structure, the half-light radius being 3.2 ± 0.5 kpc. The K-corrected mid-to-far-infrared spectral luminosities, $\nu L_\nu(5.8\ \mu\text{m}) = 3.6 \times 10^8\ \text{L}_\odot$ and $\nu L_\nu(24\ \mu\text{m}) < 1.0 \times 10^9\ \text{L}_\odot$, and the mid-infrared colors (Figure 3.7) show that the host is a star-forming galaxy.

Taken together, the radio luminosity, radio spectral index, optical morphology and mid-to-far-infrared flux densities argue that ID 239 is a star-forming galaxy harboring a low-luminosity AGN.

ID 297: This source has a mean 1.4 GHz flux density of 3.60 ± 0.04 mJy. Huynh et al. (2012) measure a 5.5 GHz flux density of 12.25 mJy, implying a spectral index of +0.89. One the basis of this steep positive spectral index, Huynh et al. (2012) suggest that this is part of a class of Gigahertz Peaked Spectrum (GPS) sources, thought to be a young AGN. The redshift z=0.605 (Treister et al. 2009) implies a mean radio luminosity of log L_R = 31.5 (cgs). ID 297 appears to be a stochastically varying source with no specific trend in its light-curve (Figure 3.5). The radio position is consistent with a bright, unresolved HST source. On the basis of departure from radio-FIR correlation Norris et al. classify this source as an AGN. The mid-infrared colors (Figure 3.7) and far-infrared spectral index (Table 3.3) are consistent with this identification.

ID 337: This source has a mean 1.4 GHz flux density of $494 \pm 11\ \mu$Jy. From its radio light-curve, ID 337 appears to have repeated outbursts roughly every 25d. The flux density of this source in the Miller et al., Kellerman et al., Norris et al. and Afonso et al. catalogs is 439 ± 8, 524 ± 14, 380 ± 16, and $404 \pm 34\ \mu$Jy respectively, and a spectral index of −0.2 between 1.4 and 4.8 GHz. The 5.5 GHz flux density from Huynh et al. is $443 \pm 20\ \mu$Jy, for which we derive a spectral index of −0.08. The photometric redshift of z=0.734 (Vanzella et al. 2008) implies a mean radio luminosity of log L_R = 30.8 (cgs).

The HST image (Figure 3.6) shows that the optical counterpart to the radio source is actually associated with the fainter (or more extincted) galaxy among a group of two closely separated galaxies. This has lead to some confusion over the correct optical identification. VLA observations carried out in 1999–2001 and 2007 (Kellerman et al. and Miller et al. respectively) suggest that the radio counterpart is the fainter galaxy. ATCA observations carried out in 2003–2004 (Norris et al. and Afonso et al.) suggest the bright galaxy as the optical counterpart. Our optical-radio frame tie summarized in Table 3.4 supports the fainter optical source as the likely radio counterpart. The spectral index and radio luminosity argue that ID 337 is a low-luminosity AGN. Afonso et al. state that the bright radio source is a luminous star-forming galaxy, possibly part of a merging system. Comparison of the K-corrected spectral luminosities, $\nu L_\nu(5.8\ \mu\text{m}) = 4.0 \times 10^9\ \text{L}_\odot$ and $\nu L_\nu(24\ \mu\text{m}) < 1.1 \times 10^{10}\ \text{L}_\odot$, with the Chary & Elbaz (2001) SED templates and Desai et al. (2007), together with the mid-infrared colors (Figure 3.7) advocate the star-forming nature of the host galaxy.

ID 621: This source has a mean 1.4 GHz flux density of $497 \pm 10\ \mu$Jy. The first epoch in its light-curve reveals an initial brightening of the source followed by a decline and subsequent small-amplitude variations. The maximum flux density is close to 400% of the quiescent flux density of about 300 μJy. The Miller et al., Kellerman et al., and Norris et al. catalogs list the flux density of this source as 494 ± 10, 565 ± 17, $450 \pm 18\ \mu$Jy respectively, and a spectral index of −0.1 between 1.4 and 4.8 GHz. The 5.5 GHz flux density

from Huynh et al. is 689 ± 16 μJy, for which we derive a spectral index of 0.24. The photometric redshift of z=1.107 (Bonzini et al. 2012) implies a mean radio luminosity of log L_R = 31.2 (cgs).

The HST image reveals a bright nucleus surrounded by diffuse emission. The half-light radius is $\sim$3 kpc. The radio position is consistent with the nuclear source. Taken together, the radio luminosity, spectral index and optical morphology argue that ID 621 is an AGN. Additionally, the K-corrected 5.8 μm luminosity of 5.0×10^9 $L_\odot$, the 24 μm luminosity upper limit of 6.8×10^{10} $L_\odot$, and the mid-infrared colors (Figure 3.7) suggest that this is also a star-forming galaxy.

ID 628: This source has a mean 1.4 GHz flux density of 1.34 ± 0.02 mJy. The light-curve indicates a steady increase of the quiescent emission to maximum flux density, followed by a steady decline. The Miller et al., Kellerman et al., and Norris et al. catalogs list the flux density of this source as 1.07 ± 0.02, 1.33 ± 0.03, and 0.90 ± 0.02 μJy. The 5.5 GHz flux density from Huynh et al. is 0.78 ± 0.02 μJy, for which we derive a spectral index of -0.40. The photometric redshift of z=0.685 (Norris et al. 2006) implies a mean radio luminosity of log L_R = 31.2 (cgs).

The HST image reveals a bright nucleus surrounded by disk-like diffuse emission, the half-light radius being $\sim$10 kpc. The radio position is consistent with the nuclear source. On the basis of departure from radio-FIR correlation Norris et al. classify this source as an AGN, which is consistent with our flat radio spectral index and radio luminosity. Additionally, the K-corrected 5.8 μm luminosity of 3.0×10^9 $L_\odot$, the 24 μm luminosity of 3.7×10^{10} $L_\odot$, and the mid-infrared colors (Figure 3.7) suggest that this is a normal star-forming or a starburst galaxy. Taken together, the radio and mid-to-far-infrared properties along with the optical morphology argue that ID 628 is an AGN embedded within a star-forming galaxy.

3.4 Transient Search

For our transient search, we are interested in identifying those point sources which show up above the flux density limit for a short amount of time (corresponding to one or more epochs depending on the cadence), and remain below the limit in all other epochs. It is therefore important to reliably distinguish noise from real transients (which will determine how well we can reject false positives), and to avoid the rejection of transients as noise (reducing the number of true negatives). Thus, characterizing the effectiveness of source-finding algorithms in terms of reliability and completeness is crucial. Another motivation for characterizing source-finding algorithms is to find the optimum parameter values for use in transient searches.

In the following subsections we begin by the testing the efficacy of existing source-finding algorithms (§3.4.1). We then apply some of the better-performing algorithms on the E-CDFS epochs (§3.4.2).

3.4.1 Efficacy of Source-finding Algorithms

Recently, quantitative tests have been carried out on the reliability and completeness of source-finding algorithms (Huynh et al. 2011; Hancock et al. 2012). Of these many publicly available software packages,

`sfind` and `IMSAD` in *MIRIAD*, *Aegean*, *SExtractor*, and *Selavy*, these studies found that `sfind` and *Aegean* produce the most reliable catalogs.

The analysis of Huynh et al. (2011) and Hancock et al. (2012) was carried out on two simulated data sets. (i) The ASKAP simulation is a $4^\circ \times 4^\circ$ image of a full continuum observation with critically-sampled beams in the 6-km ASKAP configuration. Its pixel-scale is $2.75''$ and the rms noise is about 35 mJy, which varies across the field. 16 idealized beams one degree apart, spaced in a rectangular grid, mimic the effect of the phased-array feed. The image contains $\sim$7.7 million sources having flux densities greater than 1 μJy from the S^3-semi-empirical extragalactic simulation (Wilman et al. 2010). (ii) For the Hancock et al. simulation, a sky image was created as a 4801^2 pixel image 8° across with a $6''$ pixels sampling a $30''$ beam and an rms noise of 25 μJy. Sources were injected at random positions with angular sizes (with random position angles) from $0''$ to $52''$ and with source number counts distributed with peak flux densities as $N(S) \propto S^{-2.3}$ such that 15,000 sources having fluxes densities $> 1\sigma$ are present in the image.

With our E-CDFS dataset we are able to carry out a similar analysis using real data with all its attendant residual calibration and imaging errors. A comparison of real and simulated data could be informative. While simulations are useful in determining which source-finding algorithm work best in general, they do not explore the parameter space of the algorithm thoroughly. Hence they may not provide optimum parameter values for a transient search on a specific dataset. The deep field of the E-CDFS is well suited for this comparison. The 4096^2 pixel image is $34'$ across with a $0.5''$ pixels sampling a synthesized beam of $2.8'' \times 1.6''$ (position angle$\simeq 0^\circ$) and an rms noise 7.4 μJy. As outlined in §3.3, great care was taken in constructing the DR2 source catalog so we can be assured of its completeness and reliability (see also Figure 3.2).

In what follows, we will use the DR2 catalog and the deep E-CDFS image to test various source-finding algorithms for completeness and reliability for different input parameters. We use the terms "real sources" and "false sources" as being those sources present in the DR2 catalog, and those that are not, respectively[7]. Whether a source detected by a source-finding algorithm has a counterpart in the DR2 catalog is determined by searching for DR2 sources within $1''$ from the source position. Following Huynh et al. (2011), we define two additional terms, "completeness", as the fraction of real sources detected by a source-finding algorithm, and "reliability", as the fraction of detected sources which are real. Note that in Figures 3.8, 3.9 and 3.12, we plot the completeness and reliability within contiguous SNR bins, unlike Huynh et al. (2011) and Hancock et al. (2012) where, for a given SNR, the plots represent the completeness and reliability for sources greater than or equal to that SNR. For source-finding algorithms employing a probabilistic approach of drawing a pixel from the background and thus calculating false-detection rate (FDR), FDR + Reliability = 100%.

[7]Even though the DR2 catalog was constructed with great care, it is likely that $\sim$1 genuine source was missed and a handful of spurious sources added (perhaps not truly spurious, but `SAD` sources at 4σ bumped up to 5σ by the `JMFIT` task in *AIPS*). Recall that according to Eddington bias, more sub-5σ sources get bumped up than 5σ get bumped down.

3.4.1.1 `sfind` (*MIRIAD*)

In its default mode, `sfind`[8] incorporates a statistically robust method for detecting source pixels, called "False Discovery Rate", or FDR. In the FDR algorithm, detected sources are drawn from a distribution of pixels with a robustly known chance of being falsely drawn from the background. Contiguous, monotonically decreasing adjacent pixels from the FDR-selected ones, are used for fitting 2-D elliptical Gaussians to the sources. Thus, the fraction of expected false sources is more reliably determined than in sigma-clipping criteria (see methods below). Details of the FDR method can be found in Hopkins et al. (2001). The run-time for `sfind` searching for sources down to 5σ in the DR2 image is about 20 seconds. For all the tests carried out on `sfind`, MIRIAD version 4.2.3 (optimized for CARMA; CVS Revision 1.11, 2011/04/26) was used.

Here, we explore the completeness and reliability of `sfind` by tweaking the two relevant parameters: (i) *alpha* (α), the percentage of probable background pixels that can be accepted in the analysis, and (ii) *rmsbox*, the size of the smoothing box used for estimating the background and the standard deviation of the image. Table 3.5 lists the parameter values tested.

In general, completeness of `sfind` increases, and its reliability decreases (Table 3.5) with increasing α, as expected for an FDR algorithm. Also, both these quantities increase with *rmsbox*. The rise in completeness and reliability is precipitous (between 5% and 20%) as *rmsbox* is increased from 5 to 10 beamwidths, after which it flattens off. There is a slight decrease in the reliability as *rmsbox* is increased from 20 to 50 beamwidths. 10 beamwidths can then be interpreted as the minimum box size for determining the background rms noise without significant contribution from the sources themselves, whereas 50 beamwidths would correspond to the size where the calculated rms starts deviating significantly from the true local rms. However, in the case of bright sources in the field, these *rmsbox* limits might be somewhat larger. Completeness and reliability are $\sim$88% for α=10 and *rmsbox*=20, but better reliability (by a few percent) can be obtained at an equal expense of completeness by using α=5 or 2. Further decrease in α substantially decreases the completeness without any significant improvement in the reliability. Thus, we determine the optimum values for the input parameters to be $5 \leqslant \alpha \leqslant 10$ and $10 \leqslant$ *rmsbox* $\leqslant 50$ beamwidths. For the FDR algorithm, we expect the reliability to be $1-\alpha$. However, `sfind` reliability is lesser than this expected value by a few percent, due to the acceptance of sidelobes of bright sources and fitting of extended sources with multiple elongated and overlapping (unphysical) components. To some extent, the acceptance of these false sources can be reduced by choosing a lower value of α. Some examples of the components fit by `sfind` to different kinds of sources in different environments in the DR2 image are shown in Figure 3.6. In general, compared to other source-finding algorithms excepting `SAD`, `sfind` has a better reliability for a given completeness, and vice-versa (Tables 3.5–3.9; see also §3.4.1.3 for a note on the efficacy of `SAD`). These findings are consistent with the tests carried out on simulated images (Huynh et al. 2011). In the ASKAP simulation, the reliability of the `sfind` catalog is rather flat with respect to α, whereas, for the Hancock et al. simulation it decreases by several percent as α increases from 0.1 to 10 (Huynh et al. 2011). In the latter, *rmsbox*=20 is found to give

[8] www.atnf.csiro.au/computing/software/miriad/doc/sfind.html

slightly better reliability than *rmsbox*=20. For the $\sim$3–10σ sources in these simulations, the completeness for α=5 is greater than that for α=0.1 by 5–10%. They do not explore the completeness for α=10 and *rmsbox* other than 10 beamwidths.

Figure 3.8 shows the completeness of the `sfind` catalog as a function of the SNR of the detected sources for different values of the input parameter α. The reduction in completeness beyond SNR$\sim$20 is due to missed or badly-fit components of extended sources. The completeness for optimum values of input parameters is shown in the upper panel of Figure 3.9, which shows that `sfind` reaches 100% completeness at a much lower SNR than other algorithms. The lower panel of Figure 3.9 shows the reliability. Curiously, there is a dip in the reliability between SNRs of 6 and 10. Point sources strewn across the DR2 image but primarily located near its edges (in regions of increased rms; see the lower panel of Figure 3.10 for example), which are absent in the DR2 catalog and detected by `sfind`, are responsible for this reduced reliability. Some of these sources get rejected from the `sfind` catalog when a lower value of α or *rmsbox* is used, indicating that they are either not genuine sources on the sky or are sources at a lower SNR. Indeed, other algorithms find some of these sources to be at a much reduced SNR between 3 and 5. The results of (Hancock et al. 2012) also show a dip in the `sfind` reliability, although centered on SNR$\sim$15. Figure 3.11 compares the SNR of sources detected by `sfind`, with those of the counterparts from the DR2 catalog. The largely increased SNR reported for sources at or below 6σ in the DR2 catalog, and largely reduced SNR for sources above $\sim$100σ, is anomalous. Although for SNR above 100 the discrepancy is likely to be due to overlapping components fit to extended sources, all the above observations indicate that the SNR reported by `sfind` is somewhat different from that reported by other algorithms. Sources with 6<SNR<10 in the `sfind` catalog clearly have over-estimatated (upto 100%) peak flux densities and different dimensions than what would be expected by inspecting the cutouts of these sources. Thus, fitting of sources rather than differently-reported rms is the cause of the SNR descrepancy, at least at these low SNRs. The solution of this issue is possibly in correctly setting the *fdrpeak* and *psfsize* input parameters which allow reasonable measurements of sources close to the threshold. Since there are not many sources in our data having SNR $\gtrsim$70 (Figure 3.2), the suggested trend in completeness, reliability and measured SNR in this domain should be treated with caution.

3.4.1.2 *SExtractor*

SExtractor[9] is a source-finding program widely used in optical astronomy, and is particularly oriented towards the reduction of large-scale galaxy-survey data, as well as sparsely- to moderately-crowded stellar fields. It analyzes the image in two passes such that, in the first pass, a background map is made, and in the second, background-subtraction, filtering and thresholding is done on-the-fly. Detected sources are then deblended and CLEANed before performing photometry. The run-time for *SExtractor* searching for sources down to 5σ in the DR2 image is about 2 seconds. For all the tests carried out here, the latest release of *SExtractor* (version 2.8.6, 09-Apr-2009) has been used.

[9] www.astromatic.net/software/sextractor

We adopted a strategy of searching for sources down to Nσ (N=3,5,6,7,10, as set using the *DETECT_THRESH* parameter in *SExtractor*) and then selecting the ones $\geqslant 5\sigma$ prior to the comparison with the DR2 sources. Two input parameters (apart from possibly *DEBLEND_NTHRESH*, *BACK_FILTTHRESH* and *CLEAN_PARAM*, which we have not tested) are expected to affect the completeness and reliability of the *SExtractor* catalog. First, the mesh-size, which determines the size of the box used for background rms estimation, is specified by *BACK_SIZE*, and second, the size of the median filter (*BACK_FILTERSIZE*) applied to the background grid used for smoothing large artifacts in the image.

In Table 3.6, we list the completeness and reliability as a function of these parameters. Note that in this table, in order to reflect the true completeness for the specified detection threshold, the completeness values of the *SExtractor* catalog for 6σ, 7σ and 10σ thresholds have been normalized by the percentage of sources in the DR2 catalog which are beyond these thresholds respectively. Thus, the completeness at any threshold is expected to be 100% if all the DR2 sources beyond that threshold are detected by *SExtractor*. The general trend observed is that, with increasing detection threshold, the completeness of *SExtractor* is fairly steady, but its reliability increases. However, for 5σ and 6σ detection thresholds, the completeness is rather low ($\sim$75% or lower). Choosing higher detection thresholds such as 7–10σ does not seem to improve the completeness substantially. This is due several factors through which the source-finding in *SExtractor* seems to be different from the conventionally-used algorithms in radio astronomy. Firstly, for any given source, the reported peak flux density decreases as the detection threshold is raised, although there is not much of a change in the reported rms. Hence, the SNR of sources close to the detection threshold decreases so as to be rejected by *SExtractor*. Choosing a 3σ threshold usually gives the correct peak flux density. This is also the reason why searching down to 3σ and selecting sources at the desired, higher threshold, increases the completeness (although with the side effect of reduced reliability). The explanation for such an effect is hinted by the fact that the dimensions of the fitted sources decrease (this effect is quite significant for sources with SNR$<$10) with increasing detection threshold, implying that the number of source pixels considered in the fitting process depends on the threshold. Secondly, several DR2 sources having SNR$<$10 and detected by other source-finding algorithms (excepting `IMSAD`), are not detected at all by *SExtractor*, not even at a reduced SNR. This might be due the differences in the fitting process rather than discrepant rms. Lastly, for some extended sources, positions of the components reported by *SExtractor* are at least a few synthesized beams away from the positions given in the DR2 catalog; the latter almost always agree with the positions reported by other sources-finding algorithms (again, with the exception of `IMSAD`; see §3.4.1.4 for anomalies associated with `IMSAD`). The completeness peaks at a background mesh-size of 5 beamwidths used with 3x smoothing, whereas reliability appears to increase steadily or remain constant with increasing mesh-size. *BACK_FILTERSIZE* is not seen to change either the completeness or reliability much. *SExtractor* does not seem to achieve a high completeness and reliability ($>$85%) simultaneously for any given set of values for the input parameters. For reliability of $>$ 90%, we see that completeness $<$ 80%. Beyond a detection threshold of 6σ, the reliability is quite good, yet less than 100% owing primarily to the acceptance of sidelobes and the

fitting of extended sources handled differently. Nevertheless, the highest reliability for *SExtractor* is better than the catalogs of other algorithms (except, maybe SAD), and hence it is best for cases where reliability is strongly favored over completeness. In such a case, we recommend setting the detection threshold to about 10σ, along with a large enough value for *BACK_SIZE*. Tests on *SExtractor* with the ASKAP and Hancock et al. simulations (Huynh et al. 2011) suggest that the reliability is almost constant for mesh-size between 10 and 100 beamwidths, but increases with the detection threshold. They find that the completeness generally decreases or remains constant as mesh-size increases, but its change with respect to detection threshold is not explored. Our results are thus broadly consistent with the tests on the simulated images.

The upper-left panel of Figure 3.8 shows the completeness of *SExtractor* sources as a function of their SNR in the DR2 catalog for mesh-size of 20 beamwidths and different values of the detection threshold. The completeness for optimum input parameter values is shown in the upper panel of Figure 3.9. *SExtractor* approaches 100% completeness faster than IMSAD, but slower than the other algorithms. This is possibly related to the approach used for determining source pixels. The decrease in completeness beyond SNR$\sim$20 can be attributed to the extended-source components being reported differently than other algorithms, as mentioned above. The lower panel of Figure 3.9, which shows the *SExtractor* reliability in relation with other source-finding algorithms, reveals that this algorithm gives quite unreliable results for SNR$\lesssim$10. These low-SNR false sources are all point sources located near the edges of the DR2 image, where the rms is somewhat large (12 μJy), but the rms reported by *SExtractor* is quite small (7–8 μJy). This scenario is presented in the image cutouts in Figure 3.10, which also illustrate the ability of *SExtractor* to find sources with different morphologies located in different environments. Figure 3.11 shows the SNR of sources detected by *SExtractor*, in comparison with the corresponding sources in the DR2 catalog. For SNR$\leqslant$30, the peak flux density of *SExtractor* sources sfind,SExtractor is generally less than that of the DR2 catalog sources, suggesting that the difference in the calculated peak flux density (and to a smaller extent, the associated uncertainty) is responsible for the observed departure of the *SExtractor* SNR from the DR2 SNR.

3.4.1.3 SAD (*AIPS*)

The "Search and Destroy" (SAD[10]) algorithm finds all the pixels above a specified threshold (typically a multiple of the rms noise, which is assumed to be Gaussian) in the image, and merge contiguous pixels above the threshold into islands. The strength and size of each island is then estimated, followed by least squares Gaussian fitting of each island (if rms residual is too high, then multiple Gaussian fits may be applied). However, note that Gaussian statistics may not be a good model for the distribution of values in pixels well above zero flux density on account of thermal noise, and calibration and imaging artifacts (Cotton & Peters 2011). The run-time for SAD searching for sources down to 5σ in the DR2 image is about 2 minutes. Additionally, to prepare the background rms image, the task RMSD takes $\sim$15 minutes. For all the tests carried out on SAD, 31DEC11 *AIPS* was used.

[10] www.aips.nrao.edu/cgi-bin/ZXHLP2.PL?SAD

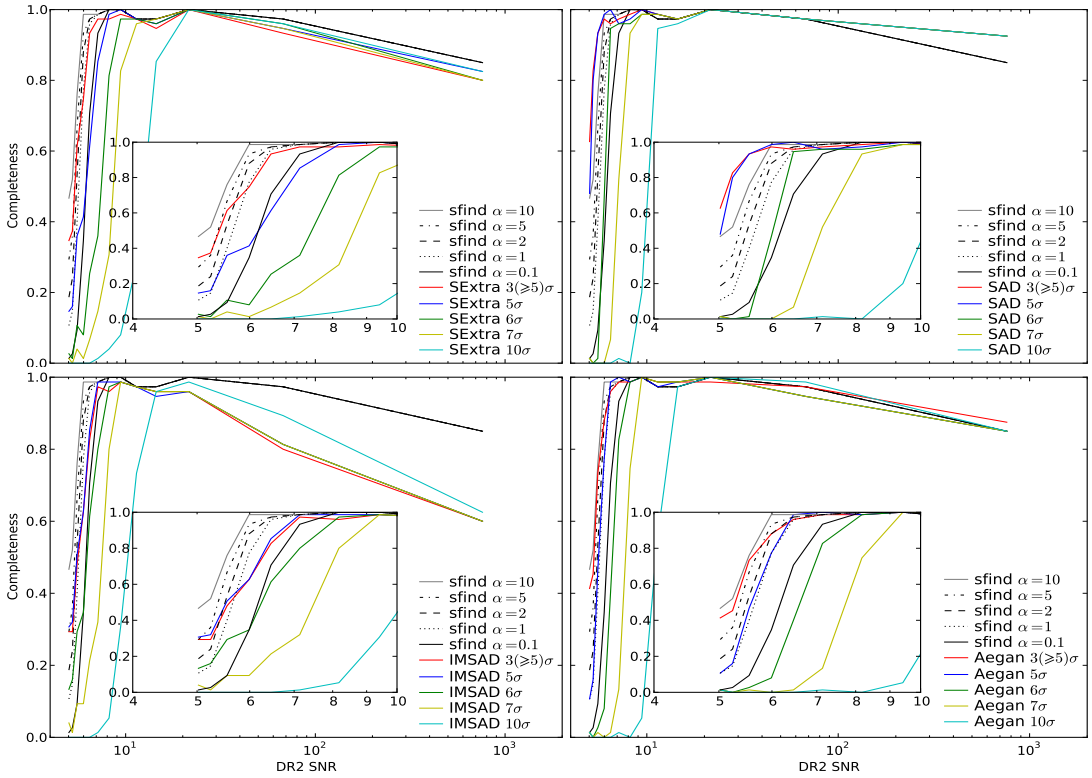

Figure 3.8: Completeness of the catalogs generated by different source-finding algorithms. Results for a background mesh-size (rmsbox) of 20 beamwidths, wherever specifiable, are shown. For `IMSAD` and *Aegean*, the results are for the histogram option and csigma=1$\sigma_{\rm cmap}$ respectively. See §3.4.1 for the definition of completeness used here. The decreasing completeness beyond $SNR \sim 50$ is due to deblending of multiple components of extended sources. The inset shows only the region where SNR is between 4 and 10. Smoothing over every 75 data points has been done before plotting. Note the low-number statistics for sources with SNR $\gtrsim$70 as implied by Figure 3.2.

SAD has several input parameters which affect the number of sources detected. Here, we test the effect of the detection SNR (*CPARM*), rms threshold, flux residual threshold (*DPARM*,*GAIN*), and the size of rms box (*IMSIZE*). The parameter *DPARM*(3) (along with *GAIN* added in quadrature) specifies the upper limit for the rms in the fitting box, while *DPARM*(7) and *GAIN* specify the upper limit on the residual flux in the fitting box. *GAIN* thus defines the fraction of the source flux which is acceptable in the residual image. By default, SAD uses the entire image to find the rms. We used the *AIPS* task RMSD to prepare rms images using mesh-sizes (specified by the *IMSIZE* parameter) of 5, 10, 20, and 50 beamwidths. Although a decremental search in SNR (via *CPARM*) is recommended in the SAD help file, we found that such a search results in multiple sources being fit to a single genuine source during each iteration, especially when the source is extended. Hence, we rejected this recommendation. As in the case of *SExtractor*, we searched for sources down to Nσ. Note that in SAD, the errors in the flux density are determined by theory from the image rms (actnoise keyword in the image header).

In Table 3.7, we list the completeness and reliability of the SAD catalog for different values of the input parameters. We held the input parameters *DPARM*(3) and *DPARM*(7) fixed at 1000 and 1 (in units of Jy beam^{-1}) respectively in order to get optimum completeness (without significant loss of reliability, as we found later, but possibly at the expense of correct SNR of the detected sources). Due to these large input values, we did not find any change in the results with the *GAIN* parameter. However, we found that reliability can be traded for completeness by setting smaller values for *DPARM*(7) and *GAIN*. In general, the completeness and reliability of SAD increase with the detection threshold. Completeness increases with mesh-size. So does reliability, though this quantity decreases significantly as the mesh-size is increased from 20 to 50 beamwidths, similar to sfind. Our inspection of the rms image for a mesh-size of 50 beamwidths reveals that there are a few pockets where the rms is rather low ($\sim$1 μJy). A profusion of false sources (or very low-SNR sources reported to have an SNR above the threshold) detected in these pockets are responsible for the markedly reduced reliability for the case of mesh-size equal to 50 beamwidths. Search with actnoise usually performs at least a few percent worse in terms of completeness and reliability than using mesh-size of 20 beamwidths. Curiously, the completeness and reliability of SAD is $>$90% for a wide range of input parameters tested. We determine the optimum values of input parameters to be 10–20 beamwidths mesh-size and 6–7σ detection threshold. Searching down to 3σ followed by selection of sources greater than 6–7σ may improve completeness to some extent. Huynh et al. (2011) and Hancock et al. (2012) have not tested SAD on simulated images.

The completeness of SAD with respect to detection SNR and for different detection thresholds is shown in the upper-right panel of Figure 3.8, which depicts the high level of completeness close to the threshold and rapid increase with SNR compared to the other algorithms. The upper panel of Figure 3.9 plots the SAD completeness for optimum input parameters. Due to missed sources throughout the SNR spanned, the completeness is seen to hover close to unity, but not quite getting to 100%. The source-rejection criteria based on 2-D Gaussian fitting in SAD, defined by the several elements of the *DPARM* input array, is the likely

cause for such such missed sources. The lower panel of Figure 3.9 shows the reliability for the optimum values input parameters. As with the case of completeness, the reliability seems to hover close to unity. SAD provides the best reliability for sources SNR$\lesssim$20, beyond which, sfind gives better results. Departure of the reliability from unity for a wide range of SNR values is due to the fitting of different components to extended sources. Some examples of how SAD fits different kinds of sources in the DR2 image, in comparison with other algorithms, is shown in Figure 3.10. Figure 3.11 shows the SNR of sources detected by SAD, in comparison with that of their counterparts in the DR2 catalog. Usually the SNRs agree with each other, but any disagreement between the two is due to the reported uncertainty in the peak. The peak flux densities reported by SAD match those in the DR2 catalog quite well.

There is a possibility that the superior completeness and reliability of SAD may be due simply because the DR2 catalog, against which we are doing all of our comparisons, was constructed from SAD. However, the construction of the DR2 catalog involved much more than running SAD (see §3.3 for more details). In any case, an independent check using simulated sources is warranted. In Figure 3.12, we compare the completeness and reliability of SAD with other source-finding algorithms on the Hancock et al. (2012) simulated image. We find a similar superior behavior of SAD.

3.4.1.4 IMSAD (*MIRIAD*)

IMSAD[11] computes the image rms noise by fitting a Gaussian to the image histogram, then searches for contiguous pixels (islands) which are above some cutoff and fits the islands with Gaussian components. For fitting, the routine from the *MIRIAD* task imfit is used, whereas the island detection is based on the *AIPS* task SAD. IMSAD can also be used in a mode where the threshold background noise is user-specified. The run-time for this source-finding algorithm searching for sources down to 5σ in the DR2 image is about 2 seconds. We used IMSAD version 8-May-98 from MIRIAD 4.2.3 (optimized for CARMA) to carry out these tests.

As before, we searched for sources down to Nσ (specified via the *clip* parameter), and then selected $\geqslant 5\sigma$ sources. The completeness and reliability were tested using the histogram mode (*noplt*,*hist* options set) as well as the user-specified mode (only the *noplt* option set; rms of 8 μJy used) for background-rms determination.

The results of these tests on IMSAD are given in Table 3.8. The *noplt*,*hist* mode usually performs better than the *noplt* mode at least by a few percent in terms of completeness, whereas the latter mode gives better completeness, again by a few percent. For achieving completeness and reliability of 80% or more, the detection threshold needs to be $\geqslant 6\sigma$. Hence, the optimum use of IMSAD would be in this SNR cutoff regime, and the mode in which it is used will depend upon whether completeness or reliability is preferred. Searching down to 3σ followed by rejection of sources below the desired threshold might give better completeness. The reason for the low completeness at a detection threshold of 5σ is that several DR2 sources (which are

[11] www.atnf.csiro.au/computing/software/miriad/doc/imsad.html

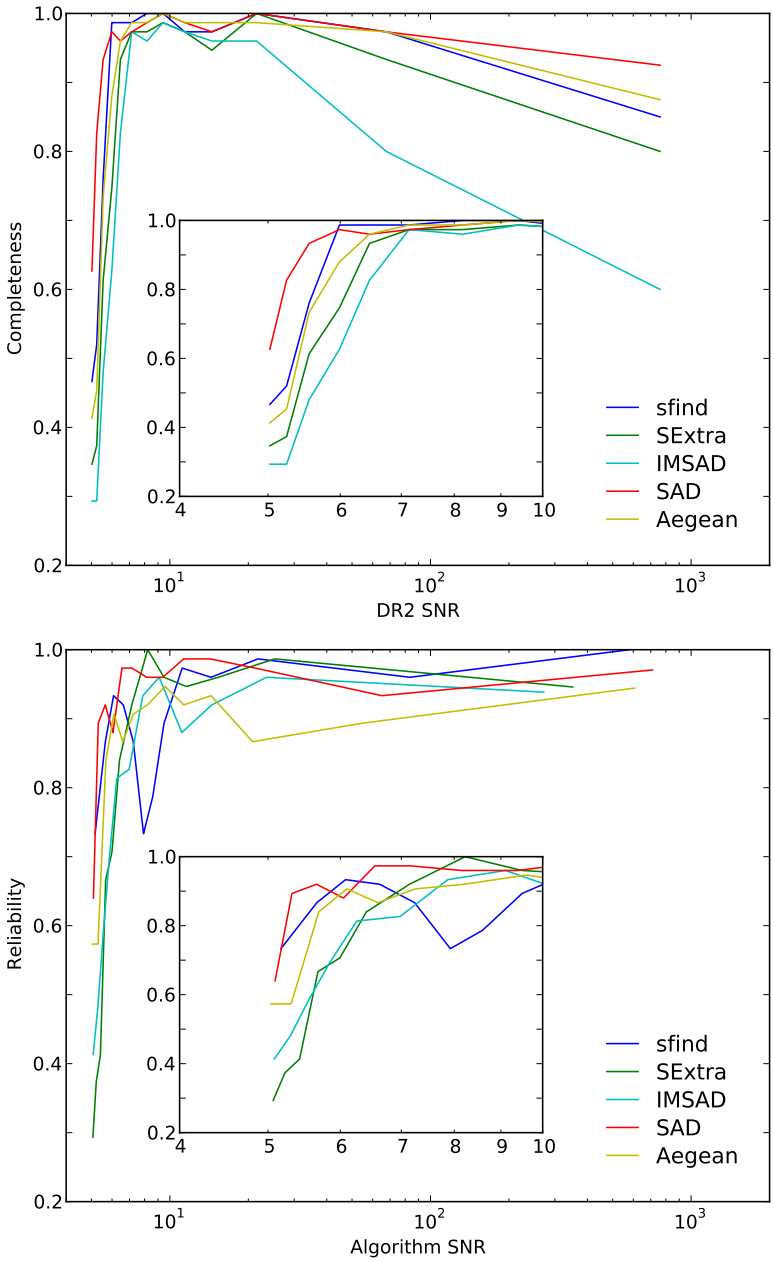

Figure 3.9: The completeness (top) and reliability (bottom) of the catalogs generated by different source-finding algorithms. See §3.4.1 for the definitions of completeness and reliability used in this work. Results for a background mesh-size (rmsbox) of 20 beamwidths are shown. For `IMSAD`, these results are for the histogram option. For sfind, we have used α=10, whereas for *SExtractor*, `SAD`, `IMSAD` and *Aegean*, detection threshold of 3σ. Only those sources which are $\geqslant 5\sigma$ have then been selected from the respective catalogs prior to comparison with the DR2 catalog. The inset shows only the region where SNR is between 4 and 10. Smoothing over every 75 data points has been done before plotting. Note the low-number statistics for sources with SNR $\gtrsim$70 as implied by Figure 3.2.

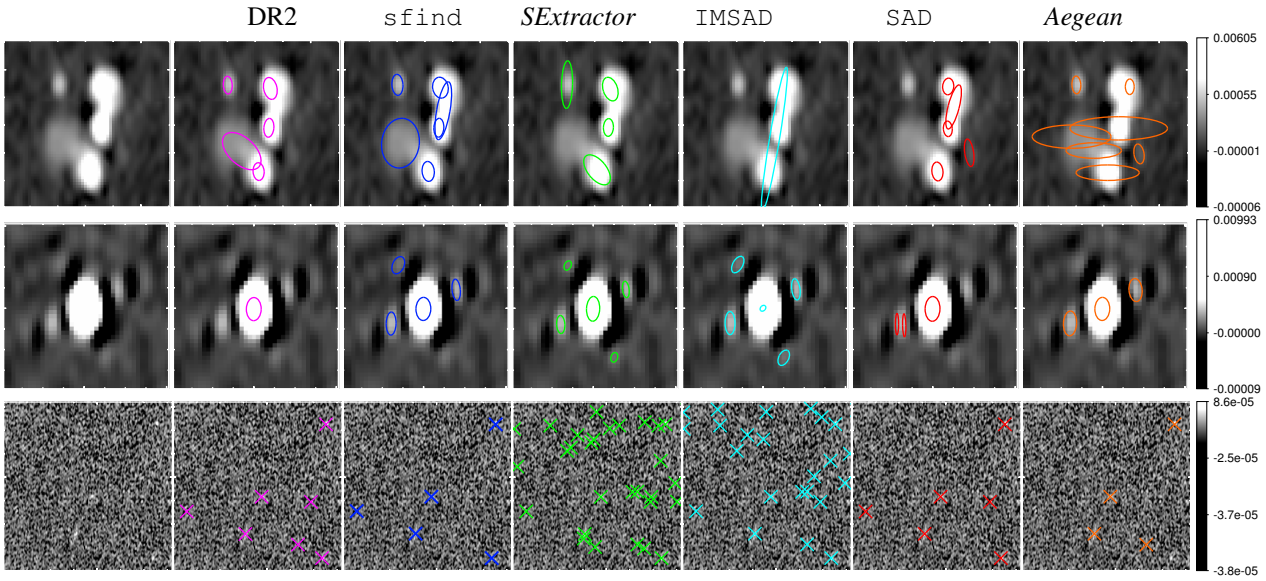

Figure 3.10: Examples of 5σ and brighter sources detected by various source-finding algorithms in the DR2 image. Top panel: blended components ($30''$ cutouts centered on $03^{\rm h}32^{\rm m}32.2^{\rm s}$,$-28°03'09.4''$), middle panel: source with sidelobes ($20''$ cutouts centered on $03^{\rm h}32^{\rm m}06.1^{\rm s}$,$-27°32'35.8''$), bottom panel: region with a relatively large rms (12 μJy) at the corner of the image ($3'$ cutouts centered on $03^{\rm h}31^{\rm m}19.4^{\rm s}$,$-27°32'55.6''$). The logarithmic flux density scale shown in each panel has units of Jy. The ellipses have major and minor axes and position angles according to the parameters reported by the respective algorithms.

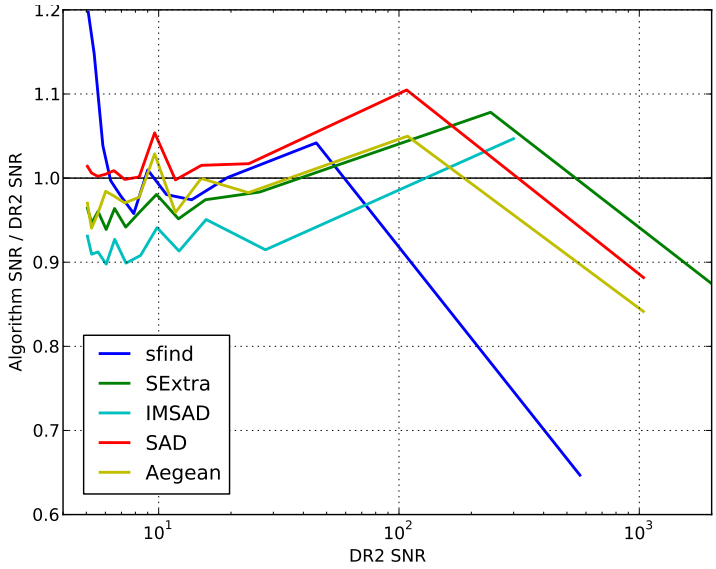

Figure 3.11: The SNR of sources found by different source-finding algorithms relative to their SNR in the DR2 catalog. Smoothing over every 75 data points has been done before plotting. Note the low-number statistics for sources with SNR $\gtrsim$70 as implied by Figure 3.2.

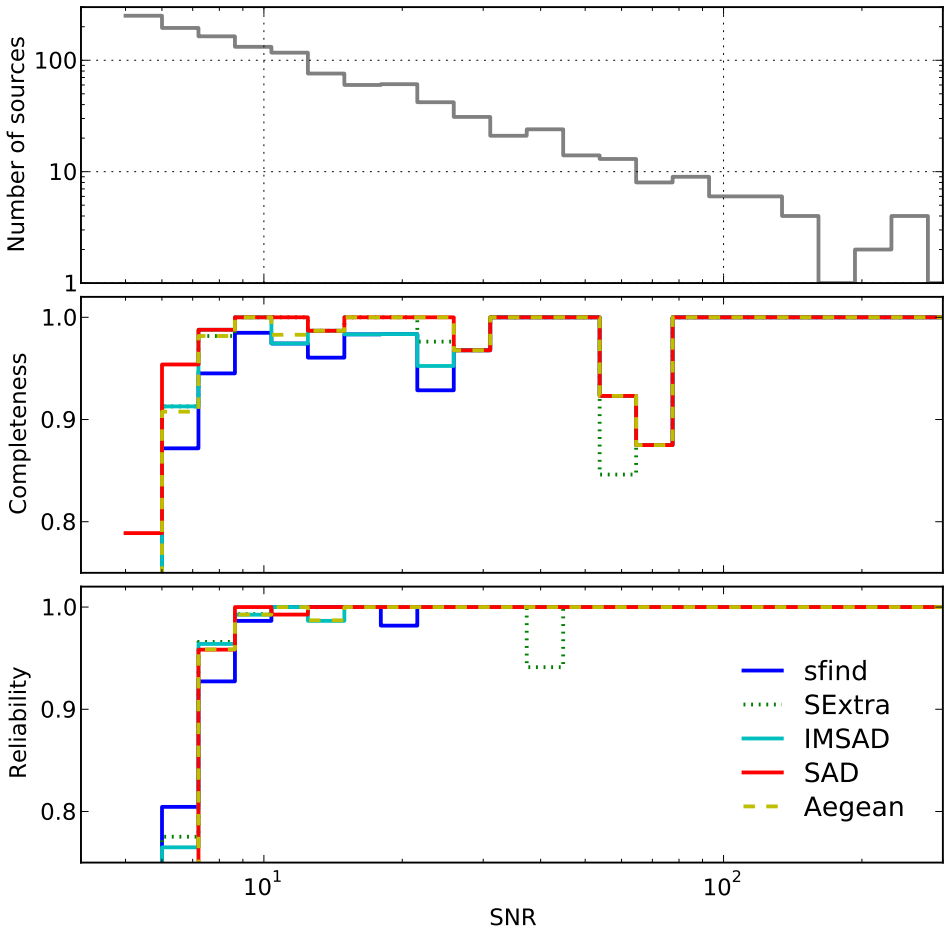

Figure 3.12: Results of the completeness (middle) and reliability (bottom) tests on the Hancock et al. simulated image. Matching radius of 15″ was used to find counterparts. Input parameters to the source-finding algorithms are same as those given in Figure 3.9. Here, the completeness and reliability within each SNR bin are plotted (see §3.4.1), which makes these diagrams different from the ones given in Hancock et al. (2012). For reference, the histogram of the simulated sources is also shown (top). The completeness at SNR∼70 dropping below 90% is a result of highly-blended sources.

.

detected by `sfind`, `SAD` and *Aegean*) close to this threshold are not detected by `IMSAD`, not even at a reduced SNR. The reliability at this threshold is also rather low. This can be attributed to several false point sources detected near the edges of the DR2 image, which are mainly low-SNR features mistaken to be high-SNR due to incorrect assumption of the local rms. Since `IMSAD` does not give the rms for each detected source, one needs to assume this quantity (a constant equal to 8 μJy in our case), and thus, the SNR calculated in regions of increased rms, e.g. regions close to the edge of the DR2 image, is expected to be erroneous. By using an rms image to find the local rms, this false-detection problem can be tackled. Another issue related to false sources is that `IMSAD` does not reject a single sidelobe. All the sidelobes are reported as (genuine) sources. Thus, with respect to false sources detected in noisy regions, missed sources, and sidelobe recognition, `IMSAD` behaves like *SExtractor*. The sources detected by `IMSAD` in some of these scenarios are shown in the image cutouts in Figure 3.10. Hancock et al. (2012) tested `IMSAD` on a simulated image and found that its completeness and reliability is lower than other source-finding algorithms. However, through our tests on the DR2 image, it appears that `IMSAD` has a competitive performance if used with detection thresholds higher than 5σ.

The completeness of the `IMSAD` catalog as a function of the detection SNR is shown in the lower left panel of Figure 3.8. The upper panel of Figure 3.9 shows the `IMSAD` completeness for optimum input parameters. Several sources having $10<\text{SNR}<20$ as well as $\text{SNR}\gtrsim100$, which are detected by other source-finding algorithms, are not detected by `IMSAD`. This is due to the inability of this algorithm to individually fit blended sources and components of extended sources; `IMSAD` tends to fit one elongated source for all components (see upper panel of Figure 3.10). In Figure 3.9, the reliability of this algorithm is plotted for the optimum input parameters. `IMSAD` shows reduced reliability between SNRs of 10 and 20, beyond which the reliability roughly flattens off at the 95% level. The reason for this reduced reliability is two-fold. First, several point sources detected close to the edge of the DR2 image have integrated flux densities less than their peak by a factor of a few, clearly indicating unphysical fitting of sources. These false sources can easily be rejected by using a peak-to-integrated flux density ratio criterion. Second, `IMSAD` does not break up islands into components as mentioned above, resulting in extended source positions to be substantially different from those listed in the DR2 catalog. This was also found in the tests carried out by Hancock et al. (2012), which resulted in several false detections. Figure 3.11 shows the SNR of `IMSAD` sources compared with their counterparts in the DR2 catalog. The assumed constant rms as well as the somewhat lower peak flux density reported by `IMSAD` (for extended sources) are responsible for the lower SNR with respect to DR2 sources.

3.4.1.5 *Aegean*

Aegean[12] uses the *FloodFill* algorithm, which separates the foreground pixels from the background and groups them into islands. These "islands" are then passed on to the source characterization stage. Each island of pixels is fit with multiple Gaussian components. The number of components to be fit is determined

[12] www.physics.usyd.edu.au/%7Ehancock/index.php/Programs/Aegean

from a surface-curvature map (cmap), derived from the input image with a Laplacian transform. *Aegean* thus performs a well-constrained multiple Gaussian fitting. A detailed description of *Aegean* and its implementation can be found in Hancock et al. (2012), where the authors demonstrate this source-finding algorithm on a simulated image to produce catalogs for better reliability and completeness than other source finding algorithms. The run-time for *Aegean* searching for sources down to 5σ in the DR2 image is about 4 minutes (using two CPU cores). We used *Aegean* r706 (25-Jul-2012 release) for testing this source-finding algorithm.

We tested the effect of the parameters: (i) *innerclip* (*seedclip*) and *outerclip* ($floodclip$), and (ii) *csigma* on the completeness and reliability of the *Aegean* catalog. innerclip defines the sigma clipping (lower limit) which is used for the detection ("seeding") of islands, whereas outerclip defines that used for reporting ("flooding") the islands in the catalog. *csigma* is the sigma clipping parameter for the curvature map. Note that the r706 version of *Aegean* uses an immutable mesh-size of 20 beamwidths. We used $innerclip = outerclip$ for our tests. Setting the innerclip to 1σ lower than outerclip gives results alike equating these two clipping parameters, while using a 1σ lower outerclip than innerclip seems to give a few percent better completeness and a slightly reduced reliability.

Our results for *Aegean* are given in Table 3.9. *csigma* does not have a significant effect on either the completeness or reliability. As with our tests on other source-finding algorithms, we searched for sources down to Nσ. The best completeness and reliability require a 7σ or higher detection threshold. Using a 3σ detection threshold followed by the selection of greater than 7σ might give better completeness at the cost of reliability. Surprisingly, the completeness and reliability are not $>$95%, as seen in the tests with the Hancock et al. (2012) simulated image. This is because *Aegean* performs well with isolated point sources, but not quite with extended or blended ones. For extended sources, *Aegean* tends to fit some of the components at unexpected locations and with quite elongated Gaussians (the fitting-error flag is also set for these components). Numerous small (but unphysical; size equal to the synthesized beam) components are also reported for several extended sources. Since Hancock et al. (2012) have demonstrated that *Aegean* successfully fits all the components of blended simulated sources, we think that diffuse components and imaging artifacts such as negative sidelobes adversely affect the curvature map produced by this source-finding algorithm, which in turn determines the sources reported. An example of such a case is given in the upper panel of Figure 3.10. Note that in the latest release of Aegean (r808; 13-Feb-2013) this situation is somewhat improved, since some of the elongated components from r706 are reported with more realistic source sizes (and also without any fitting-error flags), and relatively fewer small-size components are fit.

Figure 3.8 shows the completeness of the *Aegean* catalog as a function of SNR of sources in the DR2 catalog, and the upper panel of Figure 3.9 shows the completeness for *csigma*=$1\sigma_{\rm cmap}$, and searching for sources down to 3σ. *Aegean* completeness appears to be quite good except for sources below 7σ in the DR2 catalog, which are detected at a decreased SNR (below 5) and hence rejected from the catalog, and for a few components of extended sources above $\sim$$100\sigma$, which are reported to have positions not matching those in the DR2 catalog. The decreased SNR reported for 5–7σ sources is due to a slightly decreased peak

Table 3.5: Completeness and Reliability of `sfind` catalog

rmsbox	α				
(beamwidths)	10	5	2	1	0.1
Completeness					
5	80.9%	77.8%	74.3%	72.4%	61.9%
10	85.7%	83.7%	79.1%	75.9%	65.5%
20	88.4%	84.5%	81.2%	77.8%	67.8%
50	89.1%	85.7%	82.1%	78.4%	68.0%
Reliability					
5	78.8%	84.9%	90.6%	93.1%	96.4%
10	86.8%	91.6%	95.2%	95.6%	97.4%
20	88.7%	92.5%	95.3%	96.0%	96.4%
50	87.5%	91.4%	93.8%	94.8%	95.3%

Notes– Only $\geqslant 5\sigma$ sources have been selected from the `SFIND` catalogs prior to comparison with the DR2 catalog.

Table 3.6: Completeness and Reliability of *SExtractor* catalog

BACK_SIZE	DETECT_THRESH				
(beamwidths)	3($\geqslant$5)	5	6	7	10
Completeness*					
5	82.2%	72.1%	76.8%	79.1%	77.9%
5 + 3×smoothing	83.4%	73.7%	78.7%	80.0%	79.0%
5 + 10×smoothing	83.3%	73.0%	78.4%	80.0%	79.0%
10	81.7%	71.4%	76.9%	78.7%	78.2%
10 + 3×smoothing	82.1%	71.1%	76.7%	79.1%	77.6%
10 + 10×smoothing	81.7%	71.2%	76.4%	78.6%	77.6%
20	81.6%	70.6%	75.9%	78.6%	77.6%
50	81.3%	70.2%	75.3%	78.0%	77.3%
Reliability					
5	70.4%	87.5%	95.1%	96.3%	97.0%
5 + 3×smoothing	72.4%	89.0%	96.1%	97.2%	97.4%
5 + 10×smoothing	72.2%	89.5%	96.1%	97.2%	97.4%
10	75.2%	90.8%	96.2%	96.5%	97.4%
10 + 3×smoothing	75.8%	90.1%	96.2%	97.0%	97.4%
10 + 10×smoothing	75.6%	90.2%	96.2%	96.9%	97.4%
20	77.0%	90.3%	96.4%	96.9%	97.4%
50	78.1%	91.1%	96.5%	96.9%	97.4%

Table 3.7: Completeness and Reliability of `SAD` catalog

IMSIZE	CPARM				
(beamwidths)	3(⩾5)	5	6	7	10
Completeness*					
5	77.8%	75.5%	80.0%	83.7%	78.4%
10	89.9%	88.7%	93.1%	92.1%	93.4%
20	93.4%	92.2%	95.9%	95.4%	97.1%
50	95.9%	94.8%	96.5%	95.8%	97.1%
actnoise‡	87.4%	86.7%	95.2%	96.7%	95.7%
Reliability					
5	88.1%	89.0%	97.3%	99.1%	99.3%
10	91.2%	93.0%	97.4%	97.4%	96.6%
20	92.5%	93.9%	96.7%	96.9%	97.0%
50	85.1%	87.3%	88.1%	88.6%	92.1%
actnoise‡	58.2%	60.2%	86.6%	94.6%	96.4%

Notes– ‡Search using the `actnoise` keyword in the FITS header (=7.465E-06 JY/BM).

Table 3.8: Completeness and Reliability of `IMSAD` catalog

options	clip				
	3(⩾5)	5	6	7	10
Completeness*					
noplt‡	75.7%	73.9%	78.1%	84.2%	79.3%
noplt,hist	75.4%	76.5%	91.1%	90.5%	90.6%
Reliability					
noplt‡	77.4%	83.7%	95.3%	96.5%	96.8%
noplt,hist	78.2%	79.2%	91.7%	95.8%	96.2%

Notes– ‡Clipping level is manually entered as the appropriate multiple of the background rms chosen to be 8 μJy.

Table 3.9: Completeness and Reliability of *Aegean* catalog

csigma	innerclip = outerclip				
(cmap rms)	3(⩾5)	5	6	7	10
Completeness*					
0.5	86.1%	78.7%	83.8%	86.1%	85.8%
1.0	86.3%	78.5%	84.2%	86.4%	85.8%
2.0	88.2%	78.5%	84.5%	86.8%	85.5%
Reliability					
0.5	86.2%	91.6%	91.6%	92.1%	91.7%
1.0	84.9%	90.6%	90.5%	90.5%	91.1%
2.0	83.4%	91.0%	91.2%	91.4%	89.9%

Notes– *The fraction of sources in the DR2 catalog which are $\geqslant 6\sigma$, 7σ and 10σ are 73.0%, 58.1% and 37.7% respectively. Completeness for these detection thresholds has been normalized accordingly. A detection threshold of 3(⩾5) implies a search down to 3σ followed by the selection of only those source that are greater than 5σ.

flux density and a slightly increased rms with respect to the DR2 catalog. Figure 3.9 plots the reliability using *csigma*=1$\sigma_{\rm cmap}$, and searching for sources down to 3σ. The significant deviation of reliability from unity for SNR>10 sources, results from the several (false) small-size, and elongated components reported for extended sources, as mentioned above. Figure 3.11 shows the SNR of sources detected by *Aegean*, in comparison with the corresponding sources in the DR2 catalog. The disagreement in SNR for 5–7σ sources in the DR2 catalog has been explained above. For SNR>200 sources, the peak flux densities agree quite well between the Aegean and DR2 catalogs, but the rms reported by Aegean is consistently higher, which causes the disagreement at the high-SNR end of the diagram.

3.4.1.6 Summary of results from the efficiency tests

We find remarkable differences between algorithms in terms of components fitted for extended sources, side-lobe rejection, and point sources detected in regions where the rms is appreciably larger than the mean rms. Our results for completeness and reliability are broadly similar to those of Huynh et al. (2011) and Hancock et al. (2012). For applications that need both completeness as well as reliability, `sfind` and *Aegean* are good. Additionally, we found that the `SAD` algorithm within the widely available *AIPS* package had a better performance. `IMSAD` also gives a good completeness and reliability for detection thresholds $\geqslant 6\sigma$. For transient searches, reliability takes preference over completeness, since false positives are likely to consume follow-up resources. Most transient projects are likely to be searching in near real-time. However, in this particular project we were fortunate to have a deep reference image that was more than three times deeper than the single-epoch images. This allowed us to study reliability with real (rather than synthetic) datasets. From Figure 3.9, we see that the reliability of `sfind` is better than that of *SExtractor*, `IMSAD` and *Aegean* except for SNR near 8. However, the best reliability is provided by `SAD`.

3.4.2 Transient Candidate Search

Using the best-performing source finding algorithms from §3.4.1.6 and their optimum parameter values, we carried out a search for transient radio sources over all epochs. We ran `sfind`, `SAD`, `IMSAD` and *Aegean* on single-epoch images and obtained 49 single-epoch catalogs for each algorithm. We required that any potential transient candidate identified in the single-epoch catalog obey the following constraints.

1. The source is not found in the reference catalog (within 2″) of persistent sources. The reference catalog was constructed similar to DR2 but the sources were selected up to the 20% power point of the beam (i.e. $\theta < 21.5'$ radius) of each pointing rather than the 34′ interior region shown in Figure 3.1.
2. The source is at least a 7σ detection.
3. Is a genuine point-like source, i.e. it has
   (a) $0.9 < S_{int}/S_{peak} < 1.5$

(b) $a < 2.8'' \times 1.5$, $b < 1.6'' \times 1.5$

(a =major axis, b =minor axis; recall that the synthesized beam is $2.8'' \times 1.6''$)

4. The source is at least 20 synthesized beams (20 $\times$ geometric mean of FWHMs; $42''$) away from the nearest:

   (a) bright source (> 500 μJy), so that any sidelobe emission is rejected

   (b) extended source

The multiplicative factor of three-halves used in the selection of point sources, as well as the distance of 20 beamwidths used for constraining the proximity from bright and extended sources, is somewhat arbitrary, but is based on several iterations of our transient search code and inspection of the cutouts of the resulting transient candidates. By investigating how the major axes of sources increase with their distance from the pointing center, we found that $\theta \simeq 21.5'$ appears also to be the threshold beyond which bandwidth smearing coupled with our constraints on the major (and minor) axes start rejecting genuine point sources.

Due to the large number of synthesized beams searched ($n = 1.8 \times 10^7$) in this dataset, there is a modest probability that a transient candidate is due to noise[13]. We thus carried out an analysis similar to Frail et al. (2012) (see Appendix A of that paper) to determine the SNR above which the probability of having the highest value of n Gaussian random numbers is $\leqslant 1\%$. This corresponds to an SNR of 6.1. However, following the recommendation of Frail et al. (2012) to have a higher SNR cutoff when the noise was not strictly Gaussian, we chose 7σ as the lower limit for finding transients.

The search method outlined above may miss transients which are bright enough to be present in the reference catalog. Therefore, we also searched (with similar constraints as above) for sources which are detected in the reference catalog of persistent sources and detected in only one of the single-epoch catalogs.

For `sfind`, we adopted the parameters α=10 and *rmsbox*=20 for transient search. We found five candidates which are present only in a single epoch above the 7σ detection threshold. They also show up in the reference catalog. However, all of these candidates seem to be variable but persistent, and are detected at a low SNR ($\sim$3–5σ) in other epochs. Thus we do not find any transient with `sfind`.

For *Aegean*, we used a clipping level of 7σ and a curvature-map cutoff of 1σ. We discarded all the transients corresponding to islands which were too small to give a 6-parameter Gaussian fit (sources with flag 10000 or 00100 set) since otherwise we were dealing with a large number of transients. Using these constraints, we found one candidate which is present in the reference catalog and is a persistent source detected at a largely reduced SNR in other epochs. Accordingly, *Aegean* does not yield any transients.

For `SAD`, we searched for sources down to 3σ with an rmsbox of 20 beamwidths, and used the input parameters *DPARM*(3), *DPARM*(7)=(1000,1) to ensure optimum completeness and reliability based on our efficiency test. We do not find any transients with `SAD`.

[13] From theory we know that the statistics of beam values of interferometric maps should follow a Gaussian distribution.

With IMSAD, we searched for sources down to 7σ with the histogram option set. The several sources found to be transient candidates, are only variables at our detection limit, as evident through visual inspection of the images. Thus, there are no transients reported by IMSAD.

3.5 Discussion and Conclusions

In this paper we have explored the time-domain properties of a 1.4 GHz survey made toward the Extended Chandra Deep Field South (E-CDFS) region. Six mosaic pointings toward E-CDFS were taken in 49 separate epochs over a period of three months. Single-epoch images allow us to explore the transient and variable radio sky at sub-milliJansky levels on timescales of days, weeks and months. We will now use these data to assess the degree of variability (§3.5.1) and the transient rate (§3.5.2) of the radio sky, and predict what will be seen by future wide-field surveys (§3.5.3).

3.5.1 Comparison of variability with previous surveys

We found in our study that only a small fraction ($7/599 = 1.2^{+1.2}_{-0.7}\%$) of the point sources in the E-CDFS showed any significant variability on day-week-month timescales. Evidently, the sub-milliJansky radio sky at 1.4 GHz is not highly variable. The only previous sub-mJy study at 1.4 GHz was from a single deep pointing toward the Lockman Hole. With sampling timescales of 19 days, Carilli et al. (2003) found less than 2% of sources above 0.1 mJy to be highly variable.

Our findings at sub-mJy levels are consistent with the several previous 1.4 GHz studies at higher flux density thresholds. Thyagarajan et al. (2011) analyzed the 8444 deg^2 of the FIRST survey and found only 0.5% (1627/279407) of sources above 1 mJy varied significantly on timescales of minutes to years. Frail et al. (1994) imaged a 2° region toward a gamma-ray burst on timescales of 1-96 days and found that fewer than $\sim$1% of the sources above a flux density of 3.5 mJy were strongly variable. de Vries et al. (2004) imaged a 120.2 deg^2 area of Sloan Digital Sky Survey Stripe 82 finding $\leqslant$1.4% (123/9086) of the radio sources to be strongly variable (i.e. $>4\sigma$) above flux densities of 2 mJy on a 7 year timescale. Ofek & Frail (2011) do a two-epoch comparison of FIRST and NVSS point sources brighter than 5 mJy and find that only 0.1% (43/4367) vary by more than 4σ over timescales ranging from about 300 to 1700 days. Bannister et al. (2011a,b) analyzed 22 years and 2775 deg^2 of MOST observations at 0.84 GHz and found only 0.17% (53/29730) strong variables above 14 mJy on timescales of days to minutes to years. Finally, Croft et al. (2011) used the Allen Telescope Array to survey a 690 deg^2 area at 1.4 GHz. They compared their catalog to the NVSS, finding that 0.1% (6/4408) of the sources were highly variable on a timescale of 15 years.

In Figure 3.13 we plot the differential source counts for the persistent radio sky at 1.4 GHz, normalized in the usual way by the Euclidean rate (Huynh et al. 2005). The steep evolution of the AGN with decreasing flux density is apparent, as is the flattening of the source counts near 1 mJy. The fractional variability appears to be low, at a level of one percent, among the sources greater than 100 μJy.

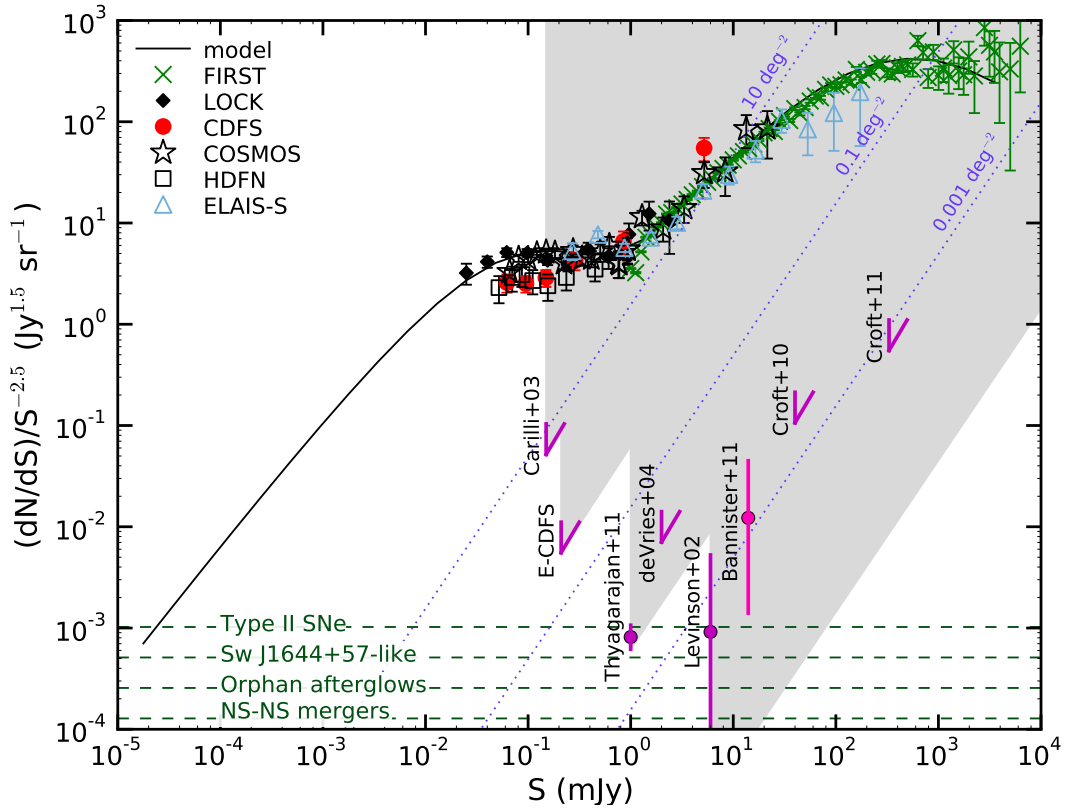

Figure 3.13: Normalized 1.4 GHz differential radio source counts for persistent sources from de Zotti et al. (2010) and the normalized areal density of transients (or limits) as a function of the flux density for various surveys at this frequency. Bannister et al. (2011a) survey at 0.84 GHz is colored differently than the other surveys. Most of the surveys are upper limits (wedge symbols) and the sampled phase space is shown by the grey shaded area. Upper limits from Frail et al. (1994) and Bower & Saul (2011) do not explore any new part of the phase space (non-grey area), and hence have been left out of this diagram. Our upper-limit is labeled as "E-CDFS". Three surveys have transient detections so far, 2σ error bars for which are shown according to Gehrels (1986). Note that Thyagarajan et al. (2011) and Bannister et al. (2011a) may have identified a few strong variables as transients (see §3.5.2), which would make their detections move downward on this plot. The black solid line is the model for AGNs and star-forming galaxies from Condon (1984). Lines of constant areal density are shown as blue dotted lines. The horizontal dashed lines are estimates for the areal density for known and expected classes of long-duration radio transients taken directly from Frail et al. (2012). The areal density for Swift J1644+57-like tidal disruption events has been modified according to Berger et al. (2012) to reflect their true rate at 1.4 GHz. Upper limits from the ASKAP-VAST surveys are estimated to be an order of magnitude or more below the rate of orphan gamma-ray burst afterglows, and having a rms sensitivity ranging between 10 μJy and 0.5 mJy.

Comparing the variability properties at 1.4 GHz of our sub-mJy population with those at higher flux densities, we find no obvious change in the *fraction* of strong variables. This is despite the fact that radio-loud AGN (which dominate at milliJansky levels) diminish in importance as radio-quiet AGN and star forming galaxies begin to populate the radio sky at lower flux densities, the latter constituting about 50% of the sub-milliJansky radio sky (Smolčić et al. 2008; Padovani 2011). On the other hand, in a sample of brightness temperature-limited radio sources, it would be expected that the variability of ultra-compact sources due to scintillation would increase with decreasing flux density.

Our optical identifications for the seven radio variables show a mix of AGN and star-forming galaxies. Six of these are consistent with a nuclear source based on the carefully matched astrometry. There is no evidence from this sub-mJy sample that we are seeing a new source of variable radio emission such as supernovae, gamma-ray bursts, etc. that would be expected to be offset from the nucleus.

Radio variability appears to be a strong function of frequency. The best study to compare to this one is the 5 GHz survey of Ofek et al. (2011), since it used a similar observing cadence and the identical statistical measures of variability. In this case it was found that $\sim$30% of point sources brighter than 1.5 mJy at 5 GHz were variable.

Some caution is warranted in comparing fractional variability between different experiments. Differences in the cadence, integration time, duration, and angular resolution will have a tendency of reducing the variability amplitude. For example, the low angular resolution of some surveys may have the effect of reducing the strong variability from compact radio sources embedded in diffuse emission. This current survey with a synthesized beam of $2.8'' \times 1.6''$ has the highest angular resolution of any previous variability survey (see Ofek et al. 2011).

Another factor to consider is that the degree of variability which can be detected in a given experiment, as measured by the modulation index m, is a function of the signal-to-noise ratio. A source in our present survey would have to have a mean flux density of 1 mJy in order to detect a 10% modulation, while at the 5σ limit of the DR2 catalog ($\sim$40 μJy) a source would have to have $m \geqslant 1.5$ in order to be identified as a significant variable. No strong variables (i.e. $m > 0.5$) were identified in our survey, but only the about 90 sources in the DR2 catalog are bright enough ($\geqslant$126 μJy) to have been identified as a strong variable. In either case the fraction of significant or strong variables is less than a few percent of the sample.

The most robust conclusion that can be drawn is that the variable radio sky at 1.4 GHz appears to be relatively quiet with only a fraction of a percent of sources varying substantially over a wide range of flux densities and timescales.

3.5.2 Limits on transient areal density and rate

We searched our multi-epoch data for transients but found none. The search was conducted on each image out to a radius of $21.5'$ from the pointing center. The single-epoch area out to that radius is 0.40 deg^2, or a total area of 20 deg^2 for all 49 epochs. However, the sensitivity of the VLA antennas is not uniform across

this area. The primary beam response is well-described by a Gaussian with a half-width to half-maximum of $15'$, falling to 20% response at our search radius of $21.5'$. At the pointing center the 7σ flux density limit was approximately 210 μJy for each epoch.

In order to calculate a limit on the areal density of any putative transient population we follow Ofek et al. (2011) and parameterize the source number-count function as a power law of the form

$$\kappa(>S) = \kappa_0 (S/S_0)^{-\gamma}, \tag{3.4}$$

where S is the peak flux density, $\kappa(>S)$ is the sky surface density of sources brighter than S, κ_0 is the sky surface density of sources brighter than S_0, and γ is the power law index of the source number-count function. We assume, for simplicity, a homogeneous source distribution in Euclidean Universe so $\gamma = 3/2$. The one-sided 2-σ upper limit on the areal density is three events (Gehrels 1986). Therefore, using Equation C5 in Ofek et al. (2011) we find that the 2σ upper limit on areal density to a flux limit of 210 μJy is 18.0 deg^{-2} per epoch. Given that we have 49 epochs the 2σ upper limit on the areal density is $\kappa(>0.21\,\mathrm{mJy}) < 0.37\,\mathrm{deg}^{-2}$. We can further estimate an upper limit on the transient rate assuming a duration $t_{\rm dur}$ less than the shortest time between epochs of $\Re(>0.21\,\mathrm{mJy}) < 268(t_{\rm dur}/0.5\,\mathrm{day})^{-1}\ \mathrm{deg}^{-2}\,\mathrm{yr}^{-1}$.

Our upper limit on the areal density of transient sources at sub-milliJansky levels can be compared with the predictions based on previous surveys. The Bower et al. (2007) survey is a useful benchmark since their areal density dominates all known classes of transients. Adopting their measured two epoch rate of $\kappa(>0.37\,\mathrm{mJy}) = 1.5\,\mathrm{deg}^{-2}$ and assuming a Euclidean source distribution (i.e. $\gamma = 3/2$) we predict $\kappa(>0.21\,\mathrm{mJy}) = 3.5\,\mathrm{deg}^{-2}$ at the flux density limit of our current survey.

An alternative way to look at our results is to compare our null detection to the expected number of Bower et al. transients expected in our dataset. We use the parameterization of Fender & Bell (2011) for the predicted Bower et al. transient rate as a function of flux density,

$$\log\left(\frac{\kappa}{\mathrm{deg}^{-2}}\right) = -1.5\,\log\left(\frac{S_\nu}{\mathrm{Jy}}\right) - 5.13 \tag{3.5}$$

where κ is the snapshot rate, and S_ν denotes the detection threshold of the observations at the pointing center (i.e. $7\sigma = 210$ μJy). Integrating both sides of equation 3.5 over the azimuthal angle and in θ out to $21.5'$ we get about 0.42 transients per epoch, if the Bower et al. (2007) transients are real. Since we have 49 epochs, we expect to have about 21 Bower et al. transients in our E-CDFS dataset.

Our search on the E-CDFS field suggests that the areal density of radio transients is an order of magnitude or more below the rate measured by Bower et al. (2007) (i.e. $<0.37\ \mathrm{deg}^{-2}$ vs. $3.5\,\mathrm{deg}^{-2}$). Alternatively, we find a 2σ upper limit of <3 transients while the predicted number is $\sim$21 transients. Our work therefore appears to support that of Frail et al. (2012), which found from a re-analysis of the Bower et al. data, that the transient rate was as much as an order of magnitude smaller than previously reported. This conclusion would be more robust if the spectral index of the putative transient population was better known. Ofek et al.

(2010) was able to use other surveys to constrain the spectra index $\alpha > 0$ (where $S_\nu \propto \nu^\alpha$). Since the Bower et al. (2007) rates were derived based on observations made mostly at 5 GHz, our only data provide strong constraints for $0 \leqslant \alpha \leqslant 1.1$. A population of optically thick $\alpha \simeq 5/2$ sources with a rate similar to that of Bower et al. (2007) would be undetected in our 1.4 GHz E-CDFS fields.

Many of the same variability surveys discussed in §3.5.1 were also sensitive to transients. Superposed on the radio source-count plot of Figure 3.13 are the results of several of these transients surveys. Light grey shaded areas represent the transient phase space covered by each of the surveys, white space represents open phase space for future narrow-deep or wide-shallow surveys. With few exceptions most of these transient surveys result in upper limits. Also shown are the normalized areal density of several known and expected classes of long-duration radio transients, based on Frail et al. (2012). The nominal rates for the putative Bower et al. (2007) sources are about two orders of magnitude above the tidal disruption or Sw J1644+57-like objects. Thyagarajan et al. (2011) define a transient as having either a single detection in the analyzed epochs, or the highest flux density 5 times greater than the next highest one (detection/upper-limit). Thus, Thyagarajan et al. (2011) and 2-epoch surveys like Bannister et al. (2011a) may identify a strong variable as a true transient, which will move the source-count of detected transients lower in Figure 3.13.

3.5.3 Future Radio Surveys

There are several facilities built or under construction that will be capable of synoptic imaging at 1.4 GHz. All of these facilities have the exploration of the time domain as part of their core science programs. The Australian Square Kilometer Array Pathfinder (ASKAP) and the Apertif instrument on the Westerbork Synthesis radio Telescope (WSRT) will be using focal plane array technology to instantaneously image an instantaneous field of view (FoV) of 30 deg^2 and 8 deg^2, respectively (Murphy et al. 2012; Oosterloo et al. 2010). South Africa is building MeerKAT, an array of 64 13.5-m diameter dishes, with a FoV of 1 deg^2 at 1.4 GHz (Booth et al. 2009). Finally, there is the newly refurbished Karl G. Jansky Array (VLA) has 27 25-m dishes with a FoV of 0.25 deg^2 at 1.4 GHz (Perley et al. 2011).

We list the capabilities of each of these telescopes in Table 1.2. It is clear from this table that, to within factors of a few, these are all powerful wide-field imaging facilities.

To illustrate the survey capabilities and compare them to what we currently know about the transient and variable radio sky, we will use the example of a electromagnetic counterpart search for gravitational waves. For a good overview of the topic of EM-GW searches, and the main issues, we refer the reader to Metzger & Berger (2012) and Nissanke et al. (2011).

Long-duration radio emission has been predicted to originate from the merger of a neutron star binary from several sources including the merger shock (Kyutoku et al. 2012), afterglow emission from the beamed outflow in the relativistic and non-relativistic phases (Metzger & Berger 2012), and from quasi-isotropic, mildly relativistic outflows ejected during the merger (Nakar & Piran 2011; Piran et al. 2012). All of these mechanisms depend on the amount of energy put into shocked material and the density of the ambient

medium. Predicted flux densities and timescales therefore vary over a wide range. We take as an example the detection of a signal with a peak flux density of 100 μJy. Such a signal might be expected to occur for an ambient medium with a density of 0.1 cm^{-3} on day timescales for a merger shock, or on year-long timescales for mildly relativistic ejecta. We note that if short duration gamma-ray bursts are the dominant population of neutron star mergers, then the predicted radio signal would be difficult to detect with the telescopes in Table 1.2, given the the canonical energy and ambient density inferred for this population (Fong et al. 2012; Metzger & Berger 2012).

The median sky localization of a gravitational-wave source will be 60 deg^2 with a three-element GW network, and 7 deg^2 with a five- element GW network (Nissanke et al. 2011). With such large error boxes, the main challenge for the identification of a EM-GW counterpart will be to distinguish it from the foreground of false positives. Optical-only searches for EM-GW counterparts are expected to be overwhelmed by false positives at the required depth of 22-23 mag and special strategies are required (Nissanke et al. 2011). However, as we have shown from this paper, the radio sky at 1.4 GHz is relatively quiet. Integrating the differential source counts in Figure 3.13 using the fit from Huynh et al. (2005), we estimate that the number of *persistent* radio sources above 100 μJy to be 910 deg^{-2}. We have estimated that the fraction of strong variables, on a wide range of timescales, is likely to be one percent or less, or 9 strong variables per square degree. Further, the radio variables that we have seen to date have all been nuclear sources (§3.3.3). Such variable or transient sources could be easily rejected as EM-GW counterparts since significant offsets are predicted from the host galaxy based on binary neutron-star population synthesis models and measurements from short-hard gamma-ray bursts (Belczynski et al. 2006; Fong et al. 2010). Lastly, the number of unrelated transients is also expected to be much less. Our derived limit on the transient areal rate of $\kappa(> 0.21\,\mathrm{mJy}) < 0.37\,\mathrm{deg}^{-2}$ translates to a $<$1.1 deg^{-2} at 100 μJy (§3.5.2) for a Euclidean distribution. The limit on the *known* transient populations is even smaller (Frail et al. 2012).

We believe that the multi-wavelength approach which we have taken here should inform future searches. For the radio variables that we found in the E-CDFS, we were able to identify the source of the emission using optical images and spectra (§3.3.3). A similar strategy could be employed to identify false-positives for the small number of radio variables or transient sources identified in EM-GW counterpart searches. Whether this approach will ultimately lead to a robust EM-GW counterpart detection is uncertain, but in terms of characterizing the variables, minimizing false-positives and getting an early sense on the nature of transients, we suggest that joint radio-optical searches will be fruitful for exploring the dynamic sky.

Acknowledgments

M. Kunal wishes to thank Rick Perley, Eric Greisen, Sanjay Bhatnagar, Andrea Petric, Margherita Bonzini, Bill Cotton, and Paul Hancock for useful discussions. We thank the anonymous referee for useful comments. The National Radio Astronomy Observatory is a facility of the National Science Foundation operated under cooperative agreement by Associated Universities, Inc. SRK's research in part is supported by NASA and NSF. This research has made use of NASA's Astrophysics Data System, Vizier and NED.

Bibliography

Afonso, J., Mobasher, B., Koekemoer, A., Norris, R. P., Cram, L. 2006, AJ, 131, 1216

Assef, R. J., Kochanek, C. S., Brodwin, M., et al. 2010, ApJ, 713, 970

Bannister, K. W., Murphy, T., Gaensler, B. M., Hunstead, R. W., & Chatterjee, S. 2011, MNRAS, 412, 634

Bannister, K. W., Murphy, T., Gaensler, B. M., Hunstead, R. W., & Chatterjee, S. 2011, Erratum, July 2011

Belczynski, K., Perna, R., Bulik, T., et al. 2006, ApJ, 648, 1110

Bell, M. E., Fender, R. P., Swinbank, J., et al. 2011, MNRAS, 415, 2

Berger, E., et al. 2001, Nature, 410, 338

Berger, E., Zauderer, A., Pooley, G. G. et al. 2012, ApJ, 748, 36

Bonzini, M., Mainieri, V., Padovani, P., et al. 2012, ApJS, 203, 15

Booth, R. S., de Blok, W. J. G., Jonas, J. L., & Fanaroff, B. 2009, arXiv:0910.2935

Bower, G. C., & Saul, D. 2011, ApJ, 728, L14

Bower, G. C., Saul, D., Bloom, J. S., Bolatto, A., Filippenko, A. V., Foley, R. J., & Perley, D. 2007, ApJ, 666, 346

Bridle, A. H., & Schwab, F. R. 1989, ASPC, 6, 247

Burke-Spolaor, S., Bailes, M., Ekers, R., Macquart, J.-P., & Crawford, F., III 2011, ApJ, 727, 18

Burrows, D. N., Kennea, J. A., Ghisellini, G., et al. 2011, Nature, 476, 421

Cameron, P. B., et al. 2005, Nature, 434, 1112

Camilo, F., Ransom, S. M., Halpern, J. P., Reynolds, J., Helfand, D. J., Zimmerman, N., & Sarkissian, J. 2006, Nature, 442, 892

Carilli, C. L., Ivison, R. J., & Frail, D. A. 2003, ApJ, 590, 192

Cenko, S. B., Krimm, H. A., Horesh, A., et al. 2012, ApJ, 753, 77

Chary, R., & Elbaz, D. 2001, ApJ, 556, 552

Condon, J. J., Cotton, W. D., Fomalont, E. B., et al. 2012, ApJ, 758, 23

Condon, J. J., 2007, Astronomical Society of the Pacific Conference Series, 380, 189

Condon, J. J., Cotton, W. D., Broderick, J. J., 2002, AJ, 124, 675

Condon, J. J., 1984, ApJ, 284, 44

Cordes, J. M. 2008, Frontiers of Astrophysics: A Celebration of NRAO's 50th Anniversary, 395, 225

Cotton, W. D. & Perley, R. 2010, OBIT Development Memo Series No. 17, ftp://ftp.cv.nrao.edu/NRAO-staff/bcotton/Obit/EVLABeam.pdf

Cotton, W. D. & Peters, W. 2011, OBIT Development Memo Series No. 25, ftp://ftp.cv.nrao.edu/NRAO-staff/bcotton/Obit/FDR.pdf

Croft, S., Bower, G. C., Keating, G., Law, C., Whysong, D., Williams, P. K. G., & Wright, M. 2011, ApJ, 731, 34

Damen, M., Labbé, I., van Dokkum, P. G., et al. 2011, ApJ, 727, 1

Desai, V., Armus, L., Spoon, H. W. W., et al. 2007, ApJ, 669, 810

Donley, J. L., Koekemoer, A. M., Brusa, M. et al. 2012, ApJ, 748, 142

Fender, R. P., & Bell, M. E. 2011, Bulletin of the Astronomical Society of India, 39, 315

Fong, W., Berger, E., Margutti, R., et al. 2012, ApJ, 756, 189

Fong, W., Berger, E., & Fox, D. B. 2010, ApJ, 708, 9

Fox, D. B., et al. 2005, Nature, 437, 845

Frail, D. A., Kulkarni, S. R., Ofek, E. O., Bower, G. C., & Nakar, E. 2012, ApJ, 747, 70

Frail, D. A., Kulkarni, S. R., Berger, E., & Wieringa, M. H. 2003, AJ, 125, 2299

Frail, D. A., Kulkarni, S. R., Hurley, K. C., Fishman, G. et al. 1994, ApJ, 437, 43

Gaensler, B. M., et al. 2005, Nature, 434, 1104

Gaensler, B. M., & Hunstead, R. W. 2000, PASA, 17, 72

Gehrels, N. 1986, ApJ, 303, 336

Giavalisco, M., Ferguson, H. C., Koekemoer, A. M., et al. 2004, ApJ, 600, 93

Hancock, P. J, Murphy, T., Gaensler, B. M, Hopkins, A., & Curran, J. R 2012, MNRAS, 422, 1812

Hallinan, G., et al. 2007, ApJ, 663, L25

Hankins, T. H., Kern, J. S., Weatherall, J. C., & Eilek, J. A. 2003, Nature, 422, 141

Hopkins, A. M., Miller, C. J., Connolly, A. J., et al. 2002, AJ, 123, 1086

Huynh, M. T., Jackson, C. A., Norris, R. P., & Prandoni, I. 2005, AJ, 130, 1373

Huynh, M., Hopkins, A., Norris, R., et al. 2012, PASA, 29, 229

Huynh, M. T., Hopkins, A. M., Lenc, E., et al. 2012, arXiv:1208.6306

Hyman, S. D., Lazio, T. J. W., Kassim, N. E., Ray, P. S., Markwardt, C. B., & Yusef-Zadeh, F. 2005, Nature, 434, 50

Hyman, S. D., Wijnands, R., Lazio, T. J. W., Pal, S., Starling, R., Kassim, N. E., & Ray, P. S. 2009, ApJ, 696, 280

Ibar, E., Ivison, R. J., Biggs, A. D., et al. 2009, MNRAS, 397, 281

Johnston, S., Taylor, R., Bailes, M., et al. 2008, Experimental Astronomy, 22, 151

Kellermann, K. I., Fomalont, E. B., Mainieri, V., et al. 2008, ApJS, 179, 71

Komatsu, E., Smith, K. M., Dunkley, J. et al. 2011, ApJS, 192, 18K

Körding, E., Rupen, M., Knigge, C., Fender, R., Dhawan, V., Templeton, M., & Muxlow, T. 2008, Science, 320, 1318

Kyutoku, K., Ioka, K., & Shibata, M. 2012, arXiv:1209.5747

Lazio, J., Bloom, J. S., Bower, G. C., Cordes, J., Croft, S., Hyman, S., Law, C., & McLaughlin, M. 2009, astro2010: The Astronomy and Astrophysics Decadal Survey, 2010, 176

Levinson, A., Ofek, E. O., Waxman, E., & Gal-Yam, A. 2002, ApJ, 576, 923

Lovell, J. E. J., et al. 2008, ApJ, 689, 108

Magnelli, B., Elbaz, D., Chary, R. R., et al. 2011, å, 528, 35

Magnelli, B., Elbaz, D., Chary, R. R., et al. 2009, å, 496, 57

Mainieri, V., Kellermann, K. I., Fomalont, E. B., Miller, N., et al. 2008, ApJS, 179, 195

McLaughlin, M. A., et al. 2006, Nature, 439, 817

Metzger, B. D., & Berger, E. 2012, ApJ, 746, 48

Miller, N. A., Fomalont, E. B., Kellermann, K. I., Mainieri, V., Norman, C., Padovani, P., Rosati, P., & Tozzi, P. 2008, ApJS, 179, 114

Miller, N. A., Bonzini, M., Fomalont, E. B., et al. 2013, ApJS, 205, 13

Murphy, T., Chatterjee, S., Kaplan, D. L., et al. 2012, arXiv:1207.1528

Nakar, E., & Piran, T. 2011, Nature, 478, 82

Nissanke, S., Kasliwal, M., Georgieva, A. 2013, ApJ, submitted

Norris, R., P., Afonso, J., Appleton, P. N., et al. 2006, AJ, 132, 2409

Ofek, E. O., Breslauer, B., Gal-Yam, A., Frail, D., Kasliwal, M. M., Kulkarni, S. R., & Waxman, E. 2010, ApJ, 711, 517

Ofek, E. O., & Frail, D. A. 2011, ApJ, 737, 45

Ofek, E. O., Frail, D. A., Breslauer, B., et al. 2011, ApJ, 740, 65

Oosterloo, T., Verheijen, M., & van Cappellen, W. 2010, ISKAF2010 Science Meeting,

Padovani, P. 2011, MNRAS, 411, 1547

Perley, R. A., Chandler, C. J., Butler, B. J., & Wrobel, J. M. 2011, ApJ, 739, L1

Piran, T., Nakar, E., & Rosswog, S. 2012, arXiv:1204.6242

Rix, H-W., Barden, M., Beckwith, S. V. W. et al., 2004, ApJS, 152, 163

Sadler, E. M., et al. 2006, MNRAS, 371, 898

Scheers, B. 2011, “Transient and Variable Radio Sources in the LOFAR Sky”, PhD thesis, University of Amsterdam.

Schinnerer, E., et al. 2007, ApJS, 172, 46

Seymour, N., et al. 2008, MNRAS, 386, 1695

Smolčić, V., et al. 2008, ApJS, 177, 14

Soderberg, A. M., et al. 2010, Nature, 463, 513

Thyagarajan, N., Helfand, D. J., White, R. L., & Becker, R. H. 2011, ApJ, 742, 49T

Treister, E., Virani, S., Gawiser, E., et al. 2009, ApJ, 693, 1713

Vanzella, E., Cristiani, S., Dickinson, M., et al. 2008, A&A, 478, 83

de Vries, W. H., Becker, R. H., White, R. L., & Helfand, D. J. 2004, AJ, 127, 2565

Welch, J., Backer, D., Blitz, L., et al. 2009, IEEE Proceedings, 97, 1438

Willner, S. P., Ashby, M. L. N., Barmby, P., et al. 2012, ApJ, 756, 72

Wilman, R. J., Jarvis, M. J., Mauch, T., Rawlings, S. Hickey, S., 2010, MNRAS, 405, 447

Wolf, C., Meisenheimer, K., Kleinheinrich, M., et al. 2004, å, 421, 913

Zauderer, B. A., Berger, E., Soderberg, A. M., et al. 2011, Nature, 476, 425

de Zotti, G., Massardi, M., Negrello, M., & Wall, J. 2010, A&A Rev., 18, 1

Chapter 4

The Caltech NRAO Stripe 82 Survey (CNSS) Paper I: The Pilot Radio Transient Survey In 50 deg^2

This chapter is submitted for publication to ApJ as: Mooley, K. P., Hallinan, G., Bourke, S., et al. 2015

Abstract

We have commenced a multi-year program, the Caltech-NRAO Stripe 82 Survey (CNSS), to search for radio transients with the Jansky VLA in the Sloan Digital Sky Survey Stripe 82 region. The CNSS will deliver five epochs and an eventual deep combined map and catalogs, at a frequency of 3 GHz and spatial resolution of $3''$, over the entire $\sim$270 deg^2 of Stripe 82. This first paper presents the results from an initial pilot survey of a 50 deg^2 region of Stripe 82, involving four epochs spanning logarithmic timescales between one week and 1.5 years, with the combined map having median rms noise of 35 μJy. This pilot survey enabled the development of the hardware and software for rapid data processing, as well as transient detection and follow-up, necessary for the full 270 deg^2 survey. Data editing, calibration, imaging, source extraction, cataloging and transient identification were completed in a semi-automated fashion within six hours of completion of each epoch of observations, using dedicated computational hardware at the NRAO in Socorro, and custom-developed data reduction and transient detection pipelines. Classification of variable and transient sources relied heavily on the wealth of multi-wavelength legacy survey data in the Stripe 82 region, supplemented by repeated mapping of the region by the Palomar Transient Factory (PTF). $3.9^{+0.5}_{-0.9}$% of the few thousand detected point sources were found to vary by greater than 30%, consistent with similar studies at 1.4 GHz and 5 GHz. Multiwavelength photometric data and light curves suggest that the variability is mostly due to shock-induced flaring in the jets of AGN. Although this was only a pilot survey, we detected two bona fide transients, associated with an RS CVn binary and a dKe star. Comparison with existing legacy survey data (FIRST, VLA Stripe 82) revealed additional highly variable and transient sources on timescales between 5–20 years, largely associated with renewed AGN activity. The rates of such AGN possibly imply episodes of enhanced accretion and jet activity occurring once every $\sim$40,000 years in these galaxies. We compile the revised radio transient rates and make recommendations for future transient surveys and joint radio-optical experiments.

4.1 Introduction

Owing to rapidly advancing detector technology and faster computing speeds, optical and high energy astronomy have enjoyed a synoptic survey capability[1] for over a decade. A rich discovery phase space has been revealed through synoptic experiments such as the Fermi Gamma-Ray Satellite (Michelson et al. 2010), the Swift Gamma-Ray Burst Alert Mission (Gehrels et al. 2009), and optical imagers such as the Catalina Real-Time Transient Survey (CRTS), the Panoramic Survey Telescope Rapid Response System (Pan-Starrs), and the Palomar Transient Factory (PTF; Kasliwal 2012).

The known slow radio transient sources highlight that radio observations trace high energy particles; arise in locations of high magnetic field; and probe the interaction of fast outflows with the surrounding medium. They are complementary to optical and high energies in that they are not affected by extinction and the emission from fast outflows is often not as narrowly beamed; providing reliable calorimetry and the true rates of cosmic explosions.

In recognition of these discovery opportunities, a new generation of centimeter wavelength facilities have been built or are underway. These include the Karl G. Jansky Array (Jansky VLA; Perley et al. 2011), ASKAP (Johnston et al. 2008), MeerKAT (Booth et al. 2012), and Apertif/WSRT (Oosterloo et al. 2010). The upgraded Jansky VLA is the first operational interferometer with the survey speed to routinely detect the extragalactic explosive population with modest time allocation. Unlike the legacy VLA, the Jansky VLA possesses frequency agility essential to characterize the broadband radio spectra of detected transients. It has a much improved snapshot multi-frequency UV coverage; imaging artifacts and contamination by sidelobes (Bower et al. 2007; Frail et al. 2012) are no longer major impediments in transient search. Furthermore, unlike the SKA pathfinders, the Jansky VLA has the spatial resolution to allow the accurate localization within a host galaxy (nuclear vs non-nuclear) necessary to rule out the AGN activity that dominates the extragalactic transient and variable population.

To date, there have been rather few radio surveys dedicated to slow variables and transients[2], and they all have a number of limitations. The majority of these surveys were single, multi-epoch interferometric pointings with a limited field of view and as a result the number of variables and transients is low (e.g. Carilli et al. 2003; Mooley et al. 2013). Existing wide-area surveys are either based on archival data or the data reduction and candidate source identification was carried out significantly delayed from the observing dates. This approach has drawbacks since without near-real-time data reduction and multi-wavelength follow-up, the candidate lists contain ambiguous transient classifications (Thyagarajan et al. 2011; Bannister et al. 2011a,b).

We note that wide field, shallow surveys are superior to narrow field, deep surveys, since they have the advantage of bringing the detectable population of transients closer in distance, thus improving the ability

[1] We refer to a "synoptic survey" here as a blind survey (as opposed to a targeted survey) sampling a large part of the sky (tens of square degrees or more) with a cadence of days to weeks.

[2] http://www.tauceti.caltech.edu/kunal/radio-transient-surveys/index.html

to find optical/infrared counterparts and to characterize host galaxies and/or progenitors. In appendix A we show mathematically that wide and shallow surveys are ideal for radio transient searches.

In this paper we present a 50 deg^2 sub-mJy Jansky VLA survey at 3 GHz for slow transients and variables that was designed to address some of the limitations of past surveys. This survey, carried out in the SDSS Stripe 82 region, was a prototype survey to demonstrate the fast imaging capabilities of the VLA, and to develop near real-time data processing, source identification, and transient search. Another unique aspect of this radio survey is that it was undertaken with a contemporaneous high-cadence optical survey with the PTF so that a direct comparison could be made of the dynamic radio and optical skies.

Technical details of the radio and the optical surveys are given in §4.2. The calibration, RFI flagging, imaging and source cataloging of the Jansky VLA data carried out in near-real-time as well as during the final careful processing is described in §4.3. §4.4 details the optical data processing for the contemporaneous survey with the PTF. A description of the radio transient search on timescales less than one week, one month, 1.5 years and longer timescales is provided in §4.5. A subset of the radio variable and transient sources representative of the full sample found in the pilot radio survey are discussed in detail in §4.5. The optical counterparts of radio sources from the JVLA survey, and the optical variability of the radio transients from §4.5, are studied in §4.6 using photometry from PTF and SDSS. §4.6 also gives a brief discussion of the optical transients found in PTF independently of the radio survey. A summary of the results from our joint radio-optical experiment and their implications are discussed in §B.6.

4.2 The Survey

4.2.1 Radio Observations

The Caltech-NRAO Stripe 82 Survey (CNSS) was designed to: 1) logarithmically sample timescales roughly between one week and one year, 2) have a high survey speed (which is a function of the bandwidth and the antenna system temperature), 3) have a relatively high angular resolution to facilitate a precise location of transients, 4) be carried out in a part of the sky where ample multiwavelength archival data were available so as to enable the identification of host galaxies or progenitors of the radio transients, 5) find non-thermal transients relatively early-on in their evolution, and 6) be wide and sensitive enough to potentially detect or place strong constraints on binary neutron star (BNS) mergers and orphan long-duration gamma-ray burst afterglows (OAs),

For the pilot survey, we chose a $\sim$50 deg^2 region in SDSS Stripe 82 with similar characteristics. The region had to satisfy other scheduling constraints in the radio and optical, so we specifically chose the region bounded in right ascension by 329.127°and 353.158°, and in declination by -1.132°and +1.167°, approximately. Observations were carried out across four epochs with the Jansky VLA in B array configuration and S-band was chosen to maximize survey speed. To maximize the continuum imaging sensitivity, the observ-

ing setup chosen was: Wideband Interferometric Digital Architecture (WIDAR) correlator with 16 spectral windows, 64 2-MHz-wide channels each to get 2 GHz of total bandwidth centered on 3.0 GHz, and 1-sec integrations.

The first three epochs were observed under the project code 12A-371 between Jul–Aug 2012. Due to telescope scheduling constraints, each of these epochs was divided into two nights of observing of 7 hours each. All the six 7-hour observing blocks were centered on 23h local sidereal time (LST). We refer to the three epochs as E1/2/3 and the regions observed on the two nights of the first epoch as R1 and R2 respectively. *Observations were carried out at the same LST in the three epochs in order to minimize systematic effects associated with sidelobes and beam squint.* Each of the regions, R1 and R2, was divided into 485 pointings arranged in a hexagonal mosaic pattern (Figure 4.1), optimized using the *makeschedule* task in CASA written by Andreas Brunthaler. In order to maximize the volume probed by our survey, we compromised on uniform-sensitivity coverage, placing neighboring pointings at $\geqslant 15'$. The mosaic is therefore not precisely hexagonal close packed[3]. Nearest neighbors having the same declination are separated by $15'$, and those having offset in declination are $\sqrt{15'^2+7.5'^2} = 16.8'$ apart. During each night of observing, one 39-second snapshot observation was obtained at each of the 485 target pointings. J2212+0152 and J2323-0317 were chosen as the phase calibrators for the two regions respectively, and 3C48 as the flux and bandpass calibrator. The phase calibrator was observed every 15 minutes. A summary of the first three observing epochs is given in Table 5.1.

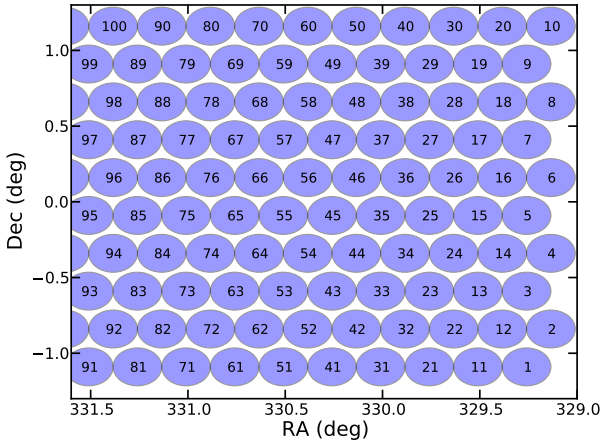

Figure 4.1: Setup of target pointings for a part of region R1 of the Jansky VLA survey. The circles indicate primary beam FWHM at the mean frequency of 2.9 GHz, and the pointing numbers are labelled. Nearest neighbors are separated by $15'$. See §4.2.1 for details on the pointing setup.

The fourth epoch (E4) was observed under the project code 13B-370, and is essentially a co-addition of three epochs of observation carried out between Nov 2013 and Feb 2014. For these observations, we

[3]Although epochs E1–E3 do not have uniform sensitivity across the survey region, the final CNSS survey is designed to have uniform RMS noise.

Table 4.1: Summary of the Jansky VLA Observations

No.	Date (UT)	Epoch/ Reg.	Array config.	RA range (deg)	rms (μJy)	Obs. mode	phase calib.	LST (h)
1	2012 Jul. 13	E1R1	B	329.127 – 341.143	71	STD	J2212+0152	19.5 – 02.5
2	2012 Jul. 14	E1R2	B	341.143 – 353.158	61	STD	J2323-0317	19.5 – 02.5
3	2012 Aug. 15	E2R2	B	341.143 – 353.158	52	STD	J2323-0317	19.5 – 02.5
4	2012 Aug. 18	E2R1	B	329.127 – 341.143	52	STD	J2212+0152	19.5 – 02.5
5	2012 Aug. 23	E3R2	B	341.143 – 353.158	58	STD	J2323-0317	19.5 – 02.5
6	2012 Aug. 24	E3R1	B	329.127 – 341.143	55	STD	J2212+0152	19.5 – 02.5
7	2013 Dec. 20	E4R5	B	346.000 – 355.000	93	OTF	J2323-0317	23.5 – 02.5
8	2013 Dec. 21	E4R3	B	328.000 – 337.000	96	OTF	J2212+0152	18.6 – 21.6
9	2013 Dec. 22	E4R4	B	337.000 – 346.000	96	OTF	J2212+0152	19.1 – 22.1
10	2014 Jan. 13	E4R3	B	328.000 – 337.000	95	OTF	J2212+0152	19.8 – 22.8
11	2014 Jan. 18	E4R5	B	346.000 – 355.000	102	OTF	J0016-0015	23.3 – 02.3
12	2014 Jan. 19	E4R4	B	337.000 – 346.000	95	OTF	J2212+0152	19.8 – 22.8
13	2014 Feb. 08	E4R3	BnA	328.000 – 337.000	96	OTF	J2212+0152	19.3 – 22.3
14	2014 Feb. 09	E4R4	BnA	337.000 – 346.000	96	OTF	J2212+0152	19.3 – 22.3
15	2014 Feb. 09	E4R5	BnA	346.000 – 355.000	92	OTF	J0016-0015	23.3 – 02.3

Note: The rms noise tabulated for epochs E1, E2, and E3 are before correcting the pointings for the primary beam. For the flat-sky rms noise, see Figure 4.6. For epoch E4, the rms noise for the individual sub-epochs from the near-real-time processing are tabulated. See Figure 4.6 for the rms noise of the final E4 co-add.

took advantage of On-The-Fly mosaicing (OTF[4]), available as a Resident Shared Risk Observing (RSRO) capability of the Jansky VLA. In the OTF mode, data was taken while the telescopes were slewing at a speed of $1'$ per second along right ascension, and the correlator phase center being stepped every four seconds. In each observing block, 9° in right ascension and 2.5° in declination centered on 0° were observed to get a total areal coverage of 22.5 deg^2. Observations were carried out with the telescopes moving in a zig-zag basket-weave pattern on the sky: slewing 9° in decreasing right ascension along a constant declination strip at -1.25°, then stepping up in declination by $10.6'$ and slewing along increasing right ascension, and so on. Covering 2.5° along declination required 15 such zig-zag strips offset by $10.6'$ in declination from nearest neighbors. This observing plan is designed to yield 2025 four-second-long scans, and a mosaic with a uniform rms noise of $\sim$80 μJy across 22.5 deg^2. Since these observations were carried out as part of a proposal to observe 270 deg^2 of SDSS Stripe 82, the details will be provided in a later publication (Mooley et al. 2015, in prep). In this paper, we will be interested only in the region bounded in right ascension by 329.127° and 353.158°, and in declination by -1.132° and +1.167°. A summary of the fourth epoch of observations is given in Table 5.1.

4.2.2 Optical Observations

The optical survey, designed to be contemporaneous with the radio survey, was carried out with the 1.2-meter (48-inch) Samuel Oschin Telescope at the Palomar Observatory as part of the Palomar Transient Factory (PTF; Rahmer et al. 2008; Rau et al. 2009; Law et al. 2009). PTF uses a large field camera (CFH12k)

[4]https://science.nrao.edu/facilities/vla/docs/manuals/opt/otf

consisting of a 6×2 array of 2048×4096 pix^2 CCDs out of which one CCDs are inactive. The camera subtends $\sim$7.2 deg^2 on the sky. The 50 deg^2 survey region was covered in 14 pointings with each pointing overlapping by about 50% with its adjacent one (necessitated by one inactive CCD). The footprints of the 14 pointings (fields) are shown in Figure 4.2.

The PTF observations of the 50 deg^2 region were carried out between 25 June 2012 and 25 September 2012. The survey was done primarily in the R-band, but g-band observations are available for some of the nights. The Stripe 82 fields were dynamically queued with the other PTF program fields, such that the frequency of observing was determined by the priorities of different PTF fields and the weather. As a result, each PTF field was observed a maximum of five times each night. The log of PTF observations of Stripe 82 carried out as part of our coordinated program is shown in Figure 4.3. Standard exposure time per frame is 60 seconds, yielding 3-sigma limiting magnitudes of 20.5 and 21 in the R- and g-band respectively.

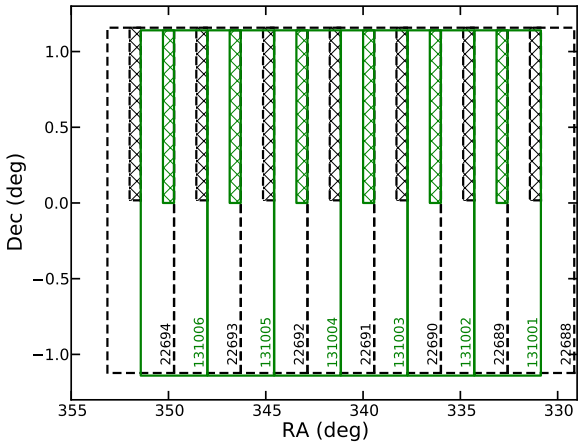

Figure 4.2: Setup of pointings for the PTF survey. The dashed and solid lines indicate the footprint of the different pointings. The PTF field IDs for the pointings are shown at the bottom right corner of the respective footprints. The shaded regions indicate the missing CCD.

4.3 Radio Data Processing

With the new wideband system in place for the Jansky VLA, the data rates are quite large, and this poses a computational challenge in terms of rapid data processing needed for triggered transient follow-up. The size of each of our observation blocks (listed in Table 5.1) is about 250 GB, and to enable near-real-time data processing, dedicated computational hardware was set in place at the NRAO in Socorro. In general, the calibration, source cataloging and transient search was carried out over a single cluster node at Socorro, and the imaging was distributed across multiple (up to six) cluster nodes. All this processing was done using a custom-developed, semi-automated AIPSLite/Python-based pipeline developed at Caltech (e.g. Bourke et al. 2014). Details of the near-real-time data processing are given in §4.3.1. After the completion of all observing

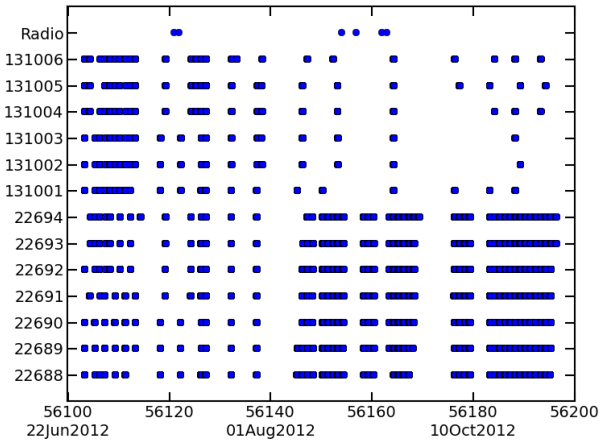

Figure 4.3: Log of PTF observations. MJD / Gregorian date is on the x-axis and PTF field ID is on the y-axis. Each point corresponds to an observation. The first three Jansky VLA epochs (Table 5.1) are shown at the top for reference. See §4.2.2 for details.

epochs, a more detailed calibration and imaging of the raw data was carried out using CASA[5] (§4.3.2).

4.3.1 Near-Real-Time Processing

For each observing block, the data were downloaded onto the NRAO lustre file system (typical download time of 20 min) immediately after they appeared on the VLA archive (only several minutes lag after the completion of the observations). Next, the raw data was calibrated on a single cluster node using AIPS/Obit tasks accessed via ObitTalk, ParselTongue and AIPSLite. The calibration part of the pipeline follows the procedures outlined in Chapter E of the AIPS Cookbook. The first three spectral windows (SPWs), spanning 2.00–2.38 GHz in frequency, and as well as the last three SPWs, spanning 3.62–4.00 GHz, were completely flagged. Calibration as per the prescription is carried out on a per-SPW basis and almost always failed for many of these SPWs. This was caused by strong satellite-induced RFI in these bands which was not automatically removed by RFLAG. Therefore, to speedup the data processing and meet the goal of rapid follow-up, we flagged these SPWs. For the fourth epoch, we recognized that the first SPW was recoverable with minor manual flagging and the entire SPW was not flagged.

Post-calibration imaging was carried out somewhat differently for the first three epochs and the fourth epoch, since different observing modes were used. For the first three epochs, the derived calibration was applied to each pointing during imaging. The imaging stage of the pipeline was distributed over 16 cores across two cluster nodes such that, at any point in time, 16 pointings were being imaged simultaneously using the AIPS task IMAGR. CLEANing was done with 800 iterations per pointing and natural weighting. For each pointing, the CLEANed 4096×4096 pix^2, 0.58 $''$pix^{-1} images, uncorrected for the primary beam to

[5]http://casa.nrao.edu/. Although calibration and imaging was seen to be faster in AIPSLite than in CASA, the latter was preferred due to the user-friendliness of plotting the data and the availability of wide-band wide-field imaging algorithms. Through our tests, no significant difference is seen in the quality of data calibrated using either software.

get a uniform rms noise across the image, were sub-imaged to 2048×2048 pix^2 using the AIPS task SUBIM. After the imaging of each observing block, the 485 single-pointing sub-images were copied over to a local machine at Caltech, where the source cataloging and transient detection part of the pipeline was run. The thermal noise in each pointing is expected to be $\sim$50 μJy, and our automated flagging produced data which is within 10% of this value, except for E1 where larger RFI as present. For source-finding, the use of the *sfind* algorithm from MIRIAD was motivated by the short runtime and reasonable completeness and reliability of catalogs (Huynh et al. 2012; Hancock et al. 2012; Mooley et al. 2013). We cataloged all sources above the 5σ threshold and used these for the variability and transient search described in detail in §4.5.1.

The imaging for the fourth epoch was carried out with the CASA task *clean* after the calibrated data from AIPSLite were exported into UVFITS format and then imported into CASA as measurement sets. Before the imaging step, we clipped the visibility amplitudes of all SPWs at a threshold determined by the SPW with the least RFI. For each SPW, a RFI-proxy value was calculated as the sum of the mean and three times the standard deviation of the scalar-averaged amplitude. The clipping amplitude was then chosen to be the least of the RFI-proxy values. We carried out tests on several pointings to ensure that this clipping threshold was robust and did not alter the flux densities and spectral indices of sources. After the clipping of visibility amplitudes, all 4-second-long scans, which have unique phase centers, were imaged individually. Imaging was distributed over 60 cores across five cluster nodes such that, at any given time, 60 pointings were being imaged simultaneously using the CASA task *clean*. CLEANing was done with 500 iterations per scan and natural weighting with a *cyclefactor* of 4.5 chosen to mitigate imaging artifacts. A common $3''$ circular restoring beam was chosen to facilitate the co-addition of scans in the image plane. 2800×2800 pix^2, $0.75''$ pix^{-1} images, uncorrected for the primary beam, were produced and then sub-imaged to 1700×1700 pix^2 using the image analysis toolkit in CASA. 1700 pixels corresponds to 20% of the primary beam at 3 GHz. The CASA images were exported to FITS format and combined into a mosaic using the AIPS task *FLATN* after correcting for the primary beam. The mean rms noise is $\sim$95 μJy while the theoretically expected value is 80 μJy. The increased rms noise is likely due to low-level RFI and joint-deconvolution not being incorporated during the CLEANing process. Sources beyond 5σ were found using RMSD and SAD tasks in AIPS to get reasonably complete and reliable catalogs (Mooley et al. 2013). Once all the E4 observations were complete, the images were combined using the AIPS task *COMB* to make a final E4 mosaic. This mosaic was used to carry out a deeper variability and transient search with respect to epoch E2, the FIRST survey, and the VLA Stripe 82 survey (§4.5).

Since computing time required for the various stages of data processing and transient search are critical for any near-real-time search, we briefly describe this aspect here. Data I/O is the rate-determining factor in our near-real-time data processing. As a result, the processing time is a strong function of the percentage of free disk space on the NRAO lustre file system at Socorro which hosted the data-processing for our survey. For the first three epochs, the lustre had 75% free disk space, and the calibration, imaging, cataloging and transient search for each observing block, covering 25 deg^2 over 485 pointings or scans and amounting to

250 GB of visibility data, required about 4.5 hours, 0.5 hours, 0.5 hours, and 0.5 hours respectively. Thus, we were able to detect transient candidates within six hours from the completion of observations. This fast turnaround allowed same-night triggering of optical follow-up and also rapid broadband radio follow-up, which are crucial for understanding transients that evolve on relatively short timescales. For the fourth epoch, the lustre had 15–20% free disk space and imaging problem was much more lengthy owing to the 2025 scans to be imaged. The calibration and imaging for each observing block within E4, which had 250 GB of visibility data and covered a 22.5 deg^2 area on the sky, required 12 hours and 3 hours respectively, while the transient search was completed in 1 hour.

4.3.2 Final Processing

During the near-real-time processing, the data editing and source identification (§4.3.1) was not done optimally in order to enable rapid follow-up of interesting radio transient candidates. Also, some problems with a small subset of the data were discovered after the near-real-time processing. Specifically, 1) the automated RFI algorithm and manual flagging likely excised both terrestrial interference and valid astronomical data, 2) the gain calibration for several pointings was affected by strong satellite signals, and 3) a subset the initial calibrated data suffered from a systematic phase distortion (§4.3.2.3). Thus, following the completion of the observing epochs E1, E2 and E3, we carried out a more detailed processing of the raw data using CASA. Epoch E4 was not subjected to final detailed processing; calibrated data from the near-real-time processing was directly used for analysis.

4.3.2.1 Calibration

The final calibration was carried out using the NRAO calibration pipeline (pipeline version 1.2.0 implemented in CASA 4.1), modified to accommodate manual flagging and additional calibration diagnostic plots, and to bypass Hanning smoothing. The calibration was done with two iterative runs of the pipeline. Diagnostic plots for the flux and gain calibrators (plots of the gain calibration tables and calibrated phases and amplitudes) from the initial run were used to determine visibilities with incorrect amplitude and/or phase calibration or bad calibrator data. Antenna-, baseline-, correlation-, SPW-, and time-based manual flagging of the flux and gain calibrators was incorporated in the second run to remove these visibilities. Especially, five SPWs having frequencies between 2.12–2.38 GHz and 3.62–4.00 GHz, for which the amplitude and phase calibration failed in most instances, were manually flagged before calibration. After the second iteration of the NRAO calibration pipeline followed by imaging, two issues persisted: 1) the amplitude gain solutions were not stable as a function of time likely due to RFI-induced non-linearities in the signal chain (see §4.3.2.2), and 2) Y-shaped imaging artifact in the first 95 scans of the 24Jul2012 epoch, indicating bad raw phase data for the gain calibrator (see §4.3.2.3).

4.3.2.2 RFI

Since Stripe 82 is close to the Clarke belt, radio observations are prone to severe RFI from satellites in geostationary and geosynchronous (GSO) orbits. The RFI in the frequency range 3.62–4.00 GHz is low-level in amplitude, but it distorts the phase information quite significantly. Those data that are irreparably affected are flagged for our final reduction. GSO satellites seen by the Jansky VLA have not been individually characterized in terms of downlink frequencies and polarizations, and our target data could potentially be affected.

The derived calibration also shows instability in the form of sporadically varying amplitude gains from the gain calibrator. This effect is pronounced in those gain calibrator scans that are severely affected by RFI. In epochs E1, E2 and E3, where the observations were carried out over the same LST range (§4.2.1), the aberration in gain is reproducible within a specific LST range. This suggests that the aberrant amplitude gains occur at a particular range of azimuth: between 124° and 255° for region R1 (J2212+0152 used as gain calibrator) and between 135° and 220° for region R2 (gain calibrator J2323-0317). The scans of the southern calibrator, J2323-0317, are more severely affected than those of J2212+0152 due to the proximity of the former to the Clarke belt. The upper panel of Figure 4.4 shows the normalized gain amplitudes for J2323-0317 and the normalized rms noise in the target pointings as a function of the observing scan number (as a proxy for time). It is evident that the amplitude gains are correlated with the rms noise of the target pointings, suggestive of anomalous gain values. Our analysis of the calibrated data is complicated by the fact that, although the RFI is localized to typically a single SPW, amplitude gains in SPWs that are free from RFI are also significantly affected (irrespective of the baseband in which the RFI is present; lower panel of Figure 4.4). We refer to this as "gain compression". The "compression" signifies that the amplitude gain values are reduced with respect to their true values and result in increased rms noise in the target fields. Initial assessment attributes the aberrant gains with non-linearities in the amplification stage in the analog signal chain somewhere upstream from the correlator caused by the the high power of the satellite signals. However, this hypothesis has not been thoroughly tested.

We devised a fix for the gain compression in the gain calibrator scans by altering the amplitude gain calibration table generated by the NRAO calibration pipeline. Towards the end of each epoch there is a time interval lasting several minutes where the gains are relatively stable and close to unity (to within a few percent). We therefore applied constant amplitude gains of unity for the duration of each epoch, and for all epochs. With this correction, the rms noise values for epochs E1, E2 and E3 are more stable with time and are usually within 10% of the thermal noise. The spread in the baseline-based amplitude gains in the stable time duration is <0.05, and hence we estimate that this correction will affect the true amplitudes of the target sources by $<5\%$. *Given that gain calibrators in the vicinity of the Clarke belt are susceptible to gain compression, we have avoided using such gain calibrators for the final CNSS survey.* Accordingly, there is no indication of severe gain compression in the gain calibrator scans from epoch E4. While the gain compression in the gain calibrator scans has a relatively straightforward workaround, the effect of gain compression on

the target pointings, if present, is much more challenging to deduce. We investigate the possible issue of gain compression in target fields in §4.5.

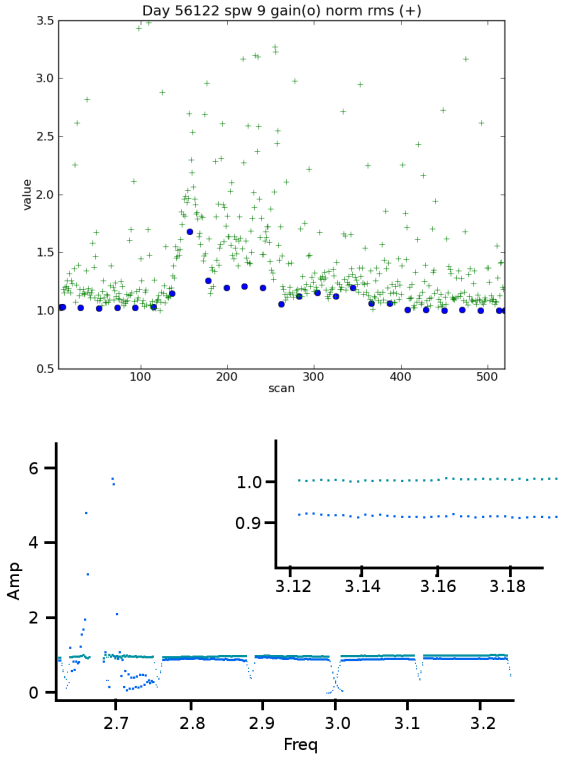

Figure 4.4: Demonstration of gain compression in the data. *Top*: Gain amplitudes derived for the gain calibrator J2323-0317 observed during the survey epoch 14Jul2012 (E1R2; blue circles) correlate well with the rms noise (green 'plus' symbols) in the pointings (scans). The gain amplitudes and the rms have been arbitrarily normalized. Note that the scan number is a proxy for time. *Bottom*: Calibrated and normalized amplitude of J2323-0317 (scan number 157) observed during the 23Jul2012 (E3R2) survey epoch. RR and LL correlations are shown in light blue and dark blue respectively. There is large RFI in the LL correlation of SPW 5 (between 2.65 and 2.75 GHz), which has affected the gains in the other spectral windows as well. The inset shows a zoom-in for SPW 9 (known to be RFI-free), where the gains in the LL correlation are seen to differ from the RR by almost 10% (the latter is assumed to have the true or expected gain).

4.3.2.3 Imaging

After calibration of the data using the NRAO pipeline, we derived and applied a single phase-only self calibration solution to every pointing containing a source brighter than 10 mJy in the near-real-time image. The model for the self calibration was constructed by making a preliminary image with 100 clean iterations using the CASA task *clean*. Self calibration solutions were allowed to break at spectral window and scan boundaries. Each self calibrated pointing was then imaged by cleaning within the 1% power point of the primary beam of the lowest frequency, 2.0 GHz, using natural weighting in the *clean* task in CASA, choosing

a cellsize of 0.6″, and 500 clean iterations to minimize clean bias. We also chose a *cyclefactor*[6] of 4.5 to avoid imaging arifacts. Basic quality checks were made by visually inspecting the images for each pointing. Using Briggs weighting with a *robust* parameter of zero, we re-imaged those pointings in which imaging artifacts persisted. All the 4800×4800 pix^2 cleaned single-pointing images at 2.8 GHz were then sub-imaged to 2400×2400 pix^2. 2400 pixels corresponds to 42%, 15% and 1% of the power point of the primary beam at 2.0 GHz, 2.8 GHz and 3.63 GHz respectively (Figure 4.5). The median synthesized beam obtained for all three epochs is $3.1'' \times 2.0''$, except for E1R1, where the median synthesized beam size is $3.8'' \times 2.1''$ likely due to increased RFI. The mean rms noise per epoch is given in Table 5.1. The cumulative plot for rms noise (flat sky) as a function of survey area is shown in Figure 4.6. For epochs E2 and E3, more than 90% of the survey area has rms noise lower than 105 μJy, while for E4 it is better than 75 μJy. Epoch E1, having rms noise of 130 μJy or better over 90% of the survey area, is severely affected by low-level RFI compared to other epochs. Note that, for the first three epochs, neighboring pointings are quite far apart and do not contribute significantly to the sensitivity of the overlap region. Hence, single pointings were imaged separately and treated independently during the source finding step.

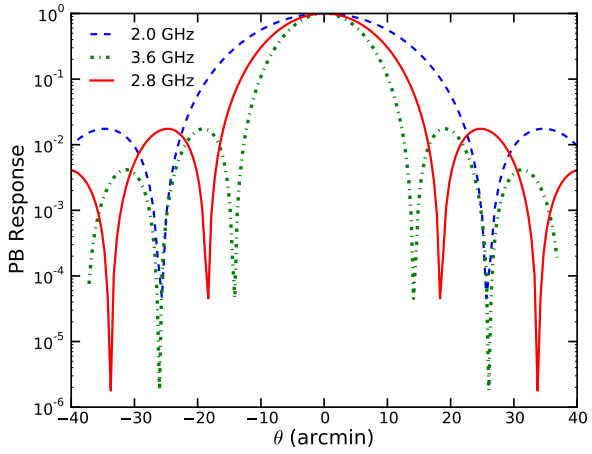

Figure 4.5: The primary beam response at the lowest (blue dashed line), highest (green dot-dashed) and reference (solid red) frequencies.

For the 24Aug2012 (epoch E3, region R1) epoch, the first 1.5 hours of observations have been affected by a systematic phase distortion. About 80 target pointings and six phase calibrator (J2212+0152) scans have been thus affected. When the calibrated data is imaged, the phase distortion manifests as a three-pronged artifact such that point sources appear extended along three axes characteristic of the Y-shape of the VLA configuration (left panel of Figure 4.7). We looked at the phase gain solutions per antenna derived from one of the affected phase calibrator scans and plotted it as a function of x- and y-positions (east-west and north-south) of the respective antennas in the array. The center of the array has higher gain phase (degrees) than

[6]The *cyclefactor* parameter determines the number of minor cycles carried out between successive major clean cycles. A large *cyclefactor* value thus minimizes the confusion between sidelobes and true sources during minor cycles that may sometimes result in strong line or spike-shaped imaging artifacts.

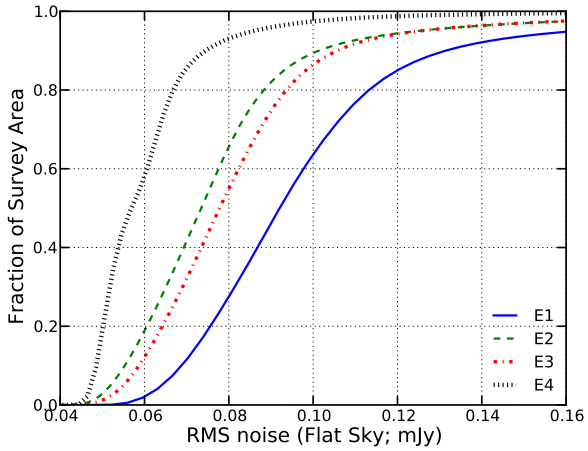

Figure 4.6: The survey area having the rms noise (flat sky) less than or equal to the given sensitivity.

the arms, and along the arms, it decreases monotonically, in general. This is equivalent to a bowl-shaped or lenticular phase screen above the array. The exact cause of the phase distortion is unknown, but it may arise due to RFI, unfavorable weather, the ionosphere, or some internal error in the antenna phase recording. While the true phases can be restored through self calibration, not all our affected pointings have bright sources to facilitate this. Therefore, for the affected pointings, we used the corresponding phases and amplitudes from the 18Jul2012 (epoch E2, region R1) observations as a model for self calibration. The image of a bright source after such a calibration is applied, is shown in the right panel of Figure 4.7.

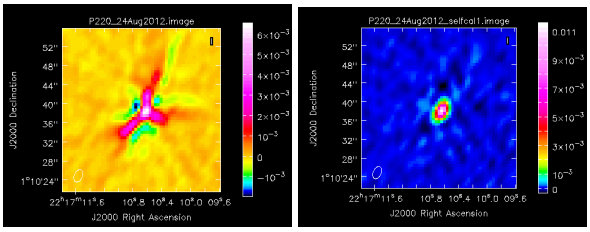

Figure 4.7: The Y-shaped imaging artifact discovered in the first 1.5 hours of observations for the 24Aug2012 (E3R1) epoch. The image of a bright source before and after the calibration desribed in §4.3.2.3.

4.3.2.4 Source Catalogs

The AIPS task RMSD was used to create an rms image for each individual pointing for epochs E1, E2 and E3, and the resulting background images were supplied as input to SAD. Source-finding was then carried out with SAD to find sources with SNR>5. For sources present in adjacent pointings, only the catalog entries were retained in which the sources are closest to their respective pointing centers. Thus, the cataloged sources are within $9'$ (within 40% of the 2.8 GHz primary beam) from their nearest pointing centers. Approximately 10^9 synthesized beams span the images from our 4-epoch survey, from which we expect 500, 2, and <1 noise

peaks above 5σ, 6σ, and 7σ respectively. While we used 5σ source catalogs for the near-real-time transient search, we followed the recommendations of Frail et al. (2012), to filter our new source catalogs and keep only SNR$>$7 sources during the final processing. With the goal of variable and transient search in mind, we further retained only probable point sources[7]. The resulting catalogs from each epoch were then merged into a single point-source catalog (PSC).

In many cases, it was found that the peak flux densities of sources in the PSC, as reported in the original SAD catalogs, was not in agreement with the peak flux densities as seen in the images. Since accurate peak flux densities are critical for any variability and transient search, we replaced the SAD peak flux density values for all objects in the PSC with the corresponding peak pixel values in the single-epoch images. The uncertainties in the peak flux densities of sources in the PSC were taken directly from their corresponding counterparts in the SAD catalogs or by measuring the image rms noise in the vicinity of the sources. The flux densities of all sources in the PSC and their associated uncertainties were corrected for the primary beam at 2.8 GHz using parameters from the PBCOR task in AIPS. The PSC thus contains peak flux densities and the uncertainties of 3652 point sources having SNR$>$7 in any one of the four epochs. The histogram in the left panel of Figure 4.8 shows the distribution of flux densities from epoch E2 of sources in the PSC. We used this PSC for our variability and transient search (§4.5).

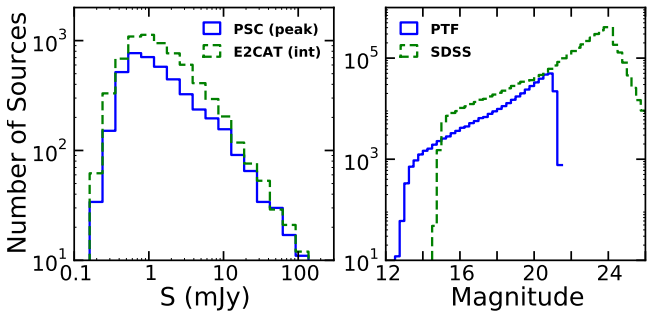

Figure 4.8: *Left*: Histograms of the peak flux densities in epoch E2 of sources in the PSC and integrated flux densities for all sources in E2CAT. *Right*: PTF R band and the SDSS (Stripe 82 co-add) r band magnitudes of the optical sources considered in this work. The SDSS histogram between magnitudes 15–21 is higher than the PTF histogram due to multiple entries of sources in SDSS in this magnitude range.

[7]Sources having the ratio of their integrated flux densities to peak flux densities less than 1.5 were selected as probable point sources. During this step of filtering the source catalogs, we also rejected probable false positives associated with imaging artifacts in the vicinity of bright sources. Sources in the catalog that were elongated by a factor of 2.5 larger than the ratio of the major axis to minor axis of the convolved beam were rejected. All cataloged objects within $1.6'$ of $>$10 mJy sources were rejected, retaining the $>$10 mJy sources themselves. In order to filter out false positives with flux densities greater than 10 mJy, all cataloged objects within $1.6'$ of $>$50 mJy sources were rejected, retaining the $>$50 mJy sources themselves. This reduces our transient search area by less than one square degree, but gets rid of almost most false positives. Some sidelobes identified as such by eye, were also rejected from the source catalogs. This false positive rejection step eliminates 438 objects out of 4205 unique objects in our list of probable point sources. Additional 35 sources were discarded as being resolved after manual inspection of a subset of images from our survey.

4.3.2.5 Data Release

As part of a preliminary data release[8], we provide to the astronomical community single-epoch images and our PSC for the four epochs of radio observations of the survey region. Additionally, we release a 5σ catalog (E2CAT) of sources from epoch E2. E2CAT consists of 6846 sources after a preliminary elimination of false positives (probable sidelobes) as done with the PSC, and described in §4.3.2.4. The histogram of the integrated flux densities recorded in E2CAT are shown in the left panel of Figure 4.8. The final data release, consisting of calibrated UV data, a deep mosaic made from the co-addition of all four epochs, and a deep source catalog, will be done in a later publication (Horesh et al., in prep).

4.4 Optical Data Processing

The PTF near-real-time reduction and transient search was carried out using a pipeline hosted at the Lawrence Livermore Berkeley Laboratory. Transient search was done by subtracting an older reference (deep co-add) image from the new observations. For further details on the PTF near-real-time operations, see §2.1 of Smith et al. (2011). The Stripe 82 data processed with the IPAC pipeline (Laher et al. 2014) and photometrically calibrated (Ofek et al. 2012) was used to make light curves reported in this work. The processed data and catalogs are available online at the NASA/IPAC Infrared Science Archive[9] as part of PTF first data release. The histogram of the R band magnitudes of PTF sources considered in this work are shown in the right panel of Figure 4.8. The distribution of r band magnitudes from the SDSS Stripe 82 co-add catalog are also given in Figure 4.8.

4.5 Radio Variables and Transients

In this paper we use the terms “variables” and “transients” somewhat interchangeably, making note of the fact that the processes listed in the summary table in Chapter 1 are all transient processes. Here, we use our four survey epochs to carry out two-epoch transient searches on different timescales. We are thus probing variability on all timescales that are approximately larger than the duration of each observation (40 seconds per pointing in our case) but less than the separation between the two epochs being compared. Accordingly, in the text below, we refer to a transient search on a “timescale of X days” synonymously with ”timescale less than X days“, but note that in the transients summary table given in Chapter 1, we refer to the precise “timescale of evolution” since the evolution of the light curves of these transients has been well studied through high-cadence targeted observations.

One of the primary goals of our survey was to understand the transient phenomena on timescales of one week, one month, and one year. For this purpose, we performed a two-epoch comparison of flux densities of

[8] http://tauceti.caltech.edu/cnss
[9] http://irsa.ipac.caltech.edu/applications/ptf

sources in our survey using the PSC from §4.3.2.4. Since radio interferometric noise is Gaussian distributed (e.g. Condon et al. 1998), we can compare the flux densities of a source between two epochs with the statistic $(S_1 - S_2)/\sqrt{\sigma_1^2 + \sigma_2^2} = \Delta S/\sigma$ under the null hypothesis that they are drawn form the same distribution (and hence the source is non-variable between the two epochs that are being compared). From statistical theory we know that this quantity is distributed according to the Student-t distribution (Student 1908; Bevington & Robinson 2003). We define a source as being a variable if the t-statistic lies beyond the 95% confidence interval[10], i.e. if,

$$V_s = \left| \frac{\Delta S}{\sigma} \right| \geqslant 4.3 \tag{4.1}$$

The choice of the confidence interval was motivated by the need for high reliability of the variable sources found, while making a possible compromise on the completeness. This issue of completeness and reliability is taken into account while calculating the rates of variable sources in §4.7.1. For the two-epoch comparison of variables selected using equation 4.1, we use the modulation index as the measure of variability.

$$m = \frac{\Delta S}{\overline{S}} \tag{4.2}$$

where $\overline{S}$ is the mean of the flux densities, $S_1 \pm \sigma_1$ and $S_2 \pm \sigma_2$, in the two epochs being compared. We note that the definition of modulation index used here is proportional to the one used by Mooley et al. (2013), but larger by a factor of $\sqrt{2}$. The modulation index is related to the fractional variability, $f_{\rm var}$, by the following equation.

$$m = 2 \times \frac{S_1/S_2 - 1}{S_1/S_2 + 1} = 2 \times \frac{f_{\rm var} - 1}{f_{\rm var} + 1} \tag{4.3}$$

4.5.1 Near-Real-Time Search

Initially, during the near-real-time transient and variability search, we used variability statistic V_s (equation 4.1), and further selected sources with fractional variability larger than 50%. As soon as a new epoch was observed, it was compared with all previous epochs. Among $\sim$6000 sources in our near-real-time 5σ single-epoch catalogs, we found $\sim$500 to be variables. We note here, beforehand, that following the final data processing, we found that most of these candidates were falsely identified as variable due the RFI-induced amplitude calibration problem identified in § 4.3.2.2.

The shortlist of follow-up candidates was generated from the near-real-time catalogs. For further filtering of variable candidates, we used multiwavelength archival data and PTF, and inspected the radio image cutouts by eye. It turned out that the PTF data were not very useful for this purpose. As we show in §4.6, there is

[10]For two degrees of freedom this corresponds to a Gaussian probability of more than $\pm 4\sigma$. For the Gaussian distribution, 4σ corresponds to a probability of about 1/16,000, while the number of measurements in our variability analysis (few thousand point sources multiplied by four epochs) is about 15,000. For our variability analysis we could have used the χ^2 statistic as previous studies have done (e.g. Ofek et al. 2011; Mooley et al. 2013), but for cases where the number of degrees of freedom are small, Student's t is preferred. See also chapter 4 and appendix C of Bevington & Robinson (2003).

little overlap between variable radio sources and sources that vary in the optical, and almost all these jointly variable sources are AGN. Optical spectra from the SDSS BOSS program (Dawson et al. 2013) were especially useful in filtering our list of candidates. In general, for those radio transients having BOSS spectra, we filtered out sources showing AGN features in their optical spectra. WISE colors were also used to eliminate possible AGN. Preference was given to sources that are undetected in archival radio data.

We also compared our catalogs with those from past surveys at 1.4 GHz, viz. FIRST (White et al. 1997) and VLA Stripe 82 (Hodge et al. 2011), to select $\sim$10 sources with implied spectral indices more than 2.5 or less than -2.5 between 3 GHz and 1.4 GHz. This was motivated by the search for transients such as supernovae and tidal disruption events (Swift J1644+57-like; Zauderer et al. 2011; Zauderer et al. 2013) which evolve on a timescale of years. However, most of these candidates turned out to be either GPS sources or flaring AGN (see below).

Our final list of candidates for follow-up consisted of 20 objects that displayed a factor of two or more fractional variability between any two epochs, or were new bright sources compared with previous surveys at 1.4 GHz.

4.5.2 Search for Variables and Transients after Final Data Processing

After correcting for the aberrant complex gains during the final data processing (§4.3.2), we carried out a careful search for variables and transients bearing in mind the possibility of gain compression (§4.3.2.2) in the target fields. To maintain consistency during our variability and transient search, we only compared epochs E1, E3, and E4 with epoch E2 in order to probe variability on timescales of one month, one week, and 1.5 years respectively. Note that among the first three epochs, E2 was the least affected by RFI.

For each source in the PSC, we calculated the statistical quantity V_s using equation 4.1. There appeared to be a small deviation of this statistic from the expected distribution (Student's t distribution). This may be a result of low-level gain compression in the target fields. Although the epoch-to-epoch flux densities are not significantly discrepant, we addressed this issue by applying small, relative, corrections to the ratios of and the differences in the flux densities of sources between the two epochs being compared.

For the one-week and one-month comparison, we made multiplicative corrections of 7%$\pm$4% (median value with standard deviation) to the ratios of flux densities and additive corrections of 20 μJy $\pm$ 50 μJy to the differences in the flux densities of sources in the PSC. These corrections were derived for the two-epoch comparisons by plotting the ratios and differences of flux densities of sources as a function of time of observation and demanding the ratios and differences to be centered at unity and zero respectively. During the comparison between epochs E4 and E2, we found it necessary to make two independent sets of corrections to the ratios of flux densities. In the first set, multiplicative corrections of 3%$\pm$4% were seen to be correlated with the declination of the sources. This discrepancy of flux densities in epoch E4 with respect to epoch E2 is a result of the the OTF survey design and the near-real-time imaging process. During the OTF observations carried out for epoch E4, the primary beam moved by $4'$ within every scan; this was not accounted for in the

imaging step. The resulting fractional change in flux density of a source depends on its position in the primary beam. This effect is manifested as a sinusoidal pattern when the flux density ratios are plotted as a function of source declinations. The second set of corrections consist of multiplicative corrections of 4%±4% to the ratios of flux densities and may be attributed to gain compression. Additive corrections of 10 μJy $\pm$ 30 μJy were applied to the differences in the flux densities between epochs E4 and E2. With the application of these small, first-order, corrections we ensure to not over-fit the data and remove real variability in flux densities of the sources in the PSC. The histograms showing the resultant distributions of the variability statistic, V_s, is shown in Figure 4.9. It is evident that, after the corrections, V_s agrees well with the Student's t distribution.

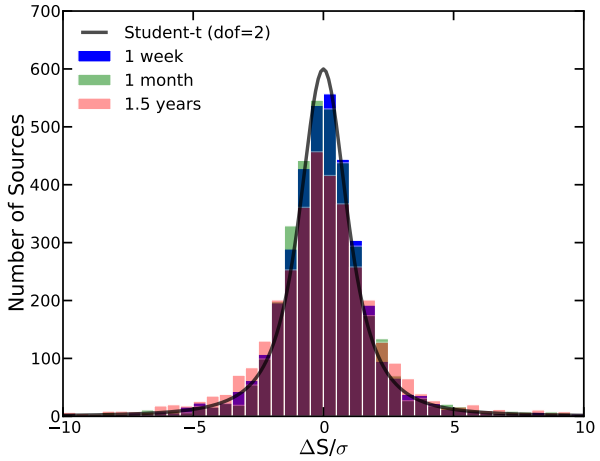

Figure 4.9: A histogram of the variability statistic, V_s, for sources in the PSC. After the application of the corrections to the flux densities mentioned in §4.5, V_s agrees with the expected distribution, Student's t.

To determine additional sources of artificial variability, we ran further intensive tests with manual flagging and imaging. We found variations of up to a few percent in the flux densities of sources just by choosing different values for the input parameters to the CASA *clean* task. Specifically, these parameters are: cleaning iterations (*niter*) and Taylor terms (nterms). We also noticed variations by changing the values provided to the *clipminmax* parameter in the *flagdata* task. Additionally, we know that the flux density absolute calibration (we used 3C48 as the flux density standard calibrator in our survey) is usually accurate to only 3–5% (e.g. Ofek et al. 2011; Thyagarajan et al. 2011; Mooley et al. 2013).

All in all, due to gain compression and other possible causes of artificial variability mentioned above, we adopt a conservative criterion for selection of our variable sources: fractional variability greater than 0.3 ($|m| > 0.26$). Our final variability selection criteria are $V_s \geqslant 4.3$ and $|m| > 0.26$. The plots of the V_s versus m for sources in the PSC after applying the corrections mentioned earlier in this subsection are shown in Figure 4.10.

We thus find 142 variables among 3652 sources in our PSC, or, in other words, about 3.8% of the sample has fractional variability more than 30% on timescales <1.5 years. The number of point sources varying

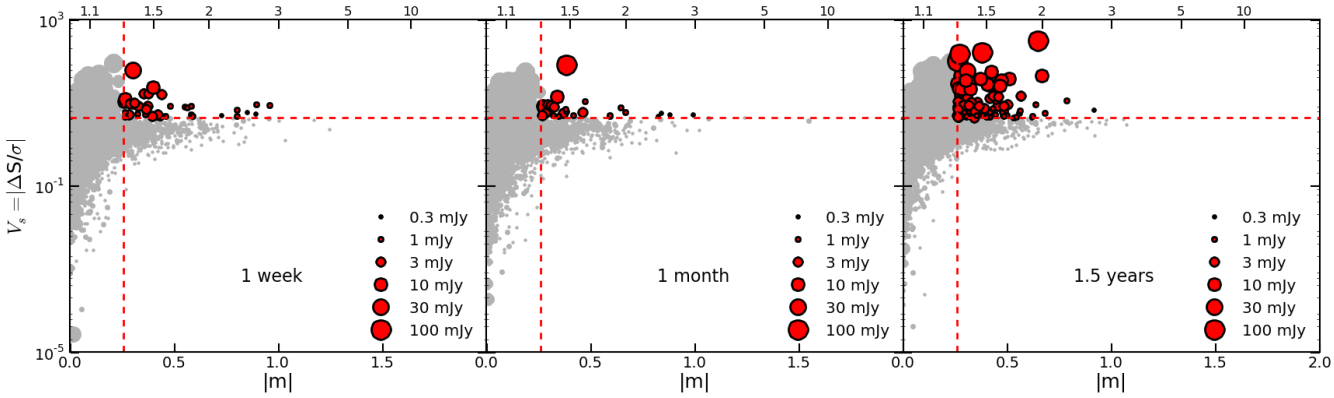

Figure 4.10: The variability statistic, V_s, as a function of the modulation index, m, for sources in the PSC for the various timescales considered in this work. The dashed red lines indicate our selection criteria for variables. Filled gray circles denote sources that are not variable while red circles have been selected as variables. The sizes of the circles indicate the mean flux densities of the sources in the two epochs being compared. We find 30, 21, and 30 variable sources on timescales of one week, one month, and 1.5 years respectively, amounting to a total of 142 variable sources. The upper x-axis in each of the three panels represents the fractional variability as given by equation 4.3. See §4.5 for details.

on week, month, and 1.5 year timescales are 38, 28, and 96 respectively, or 1.0%, 0.8% and 2.6% respectively. These sources are listed in Table 4.2. A glance at Figure 4.9 suggests that the variability statistic, V_s, comparing epochs E2 and E4 (probing variability on a timescale of 1.5 years) deviates from the Student's t distribution in the tail. This may be due to some calibration errors from the near-real-time processing that we have not tried correcting for, and therefore the fraction of variables on a 1.5-year timescale, 2.6%, is likely an upper limit.

Since our 50 deg^2 survey region contains rich archival data from the FIRST and VLA-Stripe 82 surveys, we extended our transient search to timescales of up to $\sim$20 years. We compared the 3 GHz peak flux densities of sources in the PSC with the 1.4 GHz peak flux densities from these two surveys (Figure 4.11). The mean spectral index[11], $\alpha_{\rm mean}$, appears to be between -0.5 and -1, as expected (e.g. Randall et al. 2012). With the view of finding only the extreme variable and transient candidates, we searched beyond implied spectral indices of -1 ± 2.5 (i.e. less than -3.5 or greater than 1.5) with respect to the FIRST survey, and beyond -0.5 ± 2.5 with respect to the VLA-Stripe 82 survey. The threshold of ±2.5 in spectral index is somewhat arbitrary; it is motivated by our need for filtering out most of the sources and selecting only a few, extreme, objects. This search has resulted in 12 unique objects. Two candidates are resolved out (closely-separated radio lobes) in our data; one candidate is identified as such due to its erroneously absent in VLA-Stripe 82 catalog (but present in the image); one candidate, VTC220456-000147, is identified as a variable also on a timescale of 1 month; and another candidate lies outside of our $\sim$50 deg^2 region of interest, so no FIRST counterpart was selected for matching. Accordingly, out of the eight genuine candidates, seven have been listed in Table 4.2 in the timescale $<$20 years section.

[11] We define the spectral index, α, as $S \propto \nu^{\alpha}$.

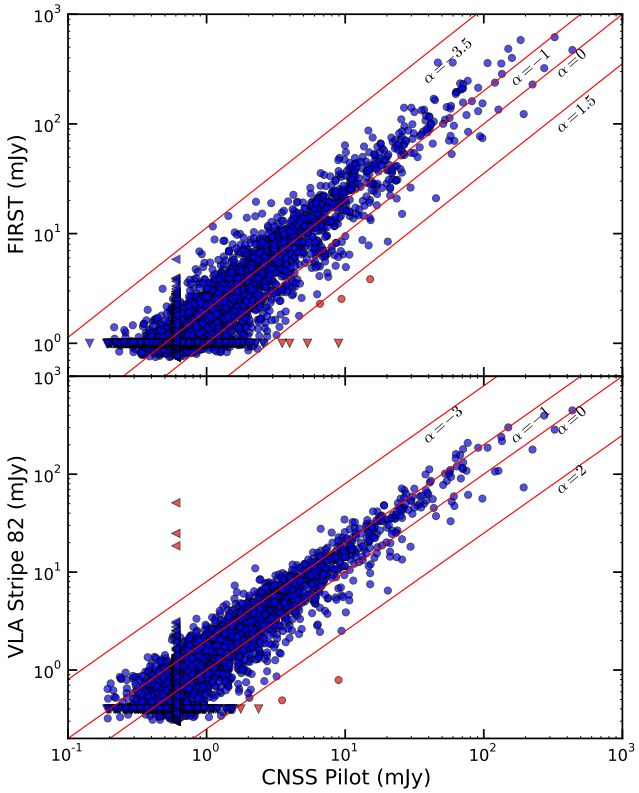

Figure 4.11: A comparison of the 3 GHz peak flux densities of sources in the PSC with the 1.4 GHz peak flux densities from the FIRST (top) and VLA-Stripe 82 (bottom) surveys. these two surveys (Figure 4.11). Triangles denote upper limits to the peak flux density. Red color denotes sources selected as variable candidates by our search criteria. See §4.5.2 for details.

Below, we discuss five candidates[12] in detail, that are meant to be broadly representative of our complete sample of 142 variables and transients. Additionally, we discuss about two transients found serendipitously. A summary of all the variable and transient sources found in this work is given in Table 4.2, and a summary of radio follow-up observations is given in Table 4.3.

4.5.3 Transients On Timescales <1 Week

4.5.3.1 VTC225411-010651: AGN flare

This variable source has flux densities 0.649±0.064, 0.782±0.050, 0.299±0.056, and 0.289±0.050 mJy in epochs E1 to E4, and in the first two epochs it has spectral indices -1.68 ± 0.95 and 0.39 ± 0.68 respectively at 3 GHz. At the location of VTC225411-010651, the 1.4 GHz flux densities from the FIRST and Hodge et al. (2011) surveys are 0.30 ± 0.17 and 0.12 ± 0.10 mJy, respectively. To investigate further, we obtained follow-up observations of this object between 1–15 GHz in two epochs (on 02 Sep and 17 Sep 2012; 10 days and 25 days respectively after the epoch E3R2) with the VLA. The continuum radio spectra are shown in Figure 4.12. The first follow-up observation reveals a flat spectrum source in the 2–15 GHz frequency range. The second observation indicates a spectrum peaked at about 1.5 GHz with the optically thin part having a spectral index of -0.99 ± 0.16. The spectrum is flat beyond 4 GHz. Sub-mm (100 GHz) follow-up observations on 09 Sep 2012 with CARMA[13] gave a non-detection with a 3σ upper limit of 2.1 mJy.

There is no optical counterpart in PTF, but a faint SDSS DR7 (Abazajian et al. 2009) source having $r \simeq 23.3$ mag. lies $1.8''$ away from the radio source position of VTC225411-010651. The photometric redshift from SDSS is 0.64 ± 0.14. Assuming a 1.4 GHz quiescent flux density of 0.2 mJy, we can calculate the radio-to-optical flux density ratio for the host galaxy to be $log(S_{1.4\mathrm{GHz}}/S_g) = 2.1$, which is typical of radio-loud AGN (e.g. Padovani et al. 2011). WISE colors ($W1-W2 = 0.37 \pm 0.29$ mag, $W2-W3 = 3.90 \pm 0.51$ mag) of the host galaxy are consistent with a LINER / (U)LIRG / spiral galaxy (Cutri et al. 2012; Wright et al. 2010).

The flat spectrum of this source in the first follow-up epoch indicates a jet with unresolved knots. Assuming a 3 GHz quiescent flux density of 0.3 mJy, we obtain of radio luminosity of $5.3 \pm 2.5 \times 10^{23}$ erg s^{-1} Hz^{-1} at the SDSS photometric redshift. It is thus likely that this source is a low-luminosity radio-loud AGN, in which case, the peaked spectrum in the second follow-up epoch can be naturally explained as an intrinsic AGN flaring phenomenon. The flaring spectrum in Figure 4.12 is reminiscent of the shock-in-jet model that has been extensively used to explain flaring in bright quasars (Marscher & Gear 1985; Türler et al. 2000; Fromm et al. 2011). The strong variability of VTC225411-010651 in the S band between epochs E2 and E3 of our survey indicates that the flares in this AGN evolve on a timescale of less than one week. We note that current radio variability surveys are primarily focused towards the monitoring of blazars and bright

[12] We adopt the following naming convention for our variable and transient sources: VTC*hhmmss+ddmmss*, where "VTC" stands for "VLA transient candidate" and the right ascension and declination are both rounded at the least significant digit.

[13] All CARMA data were reduced with MIRIAD and VLA follow-up data with the NRAO CASA pipeline 1.2.0

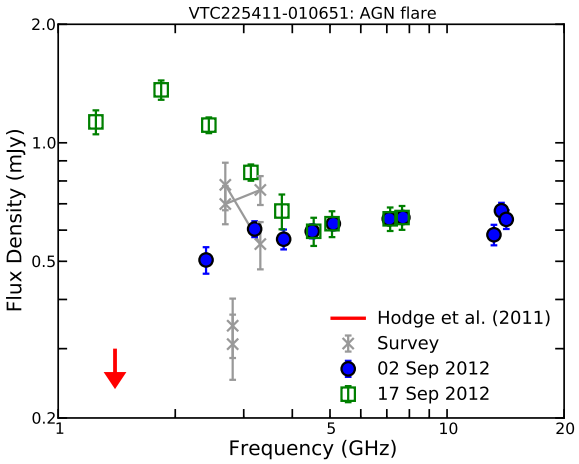

Figure 4.12: Radio continuum spectrum of VTC225411-010651 at two follow-up epochs (blue circles and green squares). The 3σ upper limit at 1.4 GHz from Hodge et al. (2011) is shown in red. The measurements from the four survey epochs are shown in grey. The first two epochs have spectral indices of -1.68 ± 0.95 and 0.39 ± 0.68 within the S band respectively and are indicated by grey crosses joined by straight lines between the two frequencies used for spectral index measurement. See §4.5.3.1 for details.

quasars, where the flares at GHz frequencies evolve typically on timescales of a few months (e.g. Hovatta et al. 2008; Richards et al. 2011), and that VTC225411-010651 presents the first ever direct evidence of shocks propagating down the jet in sub-mJy AGN on a relatively short timescale.

4.5.4 Transients On Timescales <1 Month

4.5.4.1 VTC223612+001006: RS CVn flare

VTC223612+001006 is detected as a transient on 13 Jul 2012 (epoch E1, regions R1). The peak pixel values at the location of the transient in epochs E1–E4 are 0.804±0.086, 0.271±0.071, 0.179±0.073, 0.100±0.058 mJy respectively. The image cutouts near the source location for the three epochs are shown in Figure 4.13. A comparison source about $1.5'$ away from this transient candidate has relatively stable peak flux densities, 0.605, 0.584, and 0.553 mJy in epochs E1–E3 respectively, indicating that the variability of the candidate is secure. In the FIRST and Hodge et al. (2011) surveys, the peak pixel values at the location of the transient candidate are 0.13 ± 0.11 and 0.16 ± 0.06 mJy respectively.

The nearest optical counterpart of VTC223612 is the 10th V-band magnitude star HD 214129 ($\sim 1''$ away), documented as a K0IV star by Torres et al. (2006), and as a G5/6III star by Kharchenko & Roeser (2009). HD 214129 is a known visual binary and possibly a triple stellar system (e.g. Mason et al. 2001), and has been detected in the X-rays by ROSAT (1RXS J223612.5+001008; Voges et al. 1999). HD 214129 is saturated in PTF and SDSS, precluding the study of optical variability of this Galactic radio transient. We obtained an optical spectrum for this star using the Echelle spectrograph (ESI) at KeckII on 13 Sep 2012, which suggests a spectral type similar to K0IV. The spectrum does not show any strong emission lines within our spectral

coverage between 4000–10000 Å. Figure 4.13 shows the binned optical spectrum between 4000–7000 Å. The narrow absorption line profiles and absence of Lorentzian wings indicate that the star is a subgiant or a giant. Fitting a blackbody to the photometric data from the SDSS, NOMAD and WISE catalogs gives an effective temperature of 5000 ± 200 K.

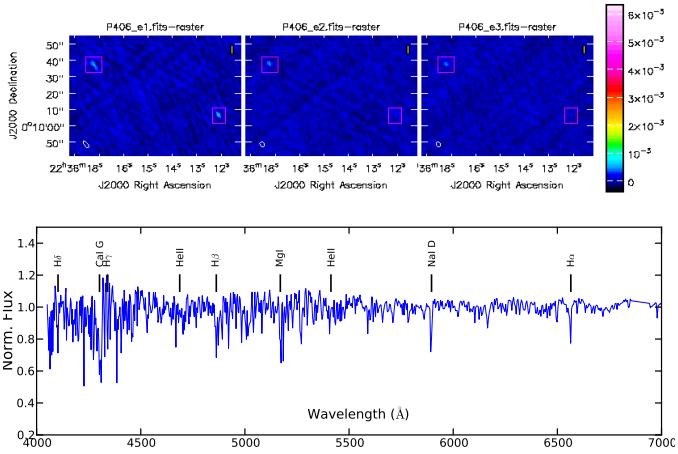

Figure 4.13: *Top*: The radio image cutouts from three epochs, E1, E2 and E3, showing VTC223612+001006 and a comparison 0.5 mJy persistent source. The transient is detected with an SNR of 9 in the first epoch, and is below SNR of 4 in the other two epochs. The colorbar to the right has units of Jy. *Bottom*: The continuum-normalized optical spectrum of VTC223612+001006 observed with ESI at KeckII on 13 Sep 2012. The spectrum has been binned with 20 data points in each bin. We classify this star as a late G to early K subgiant or giant. See §4.5.4.1 for details.

If this were a main sequence star, it would have a photometric parallax distance of $d \sim 65$ pc, while if it is a giant, $d \sim 700$ pc. A sub-giant can have any value between these extremes. An independent constraint on the distance comes from the space velocity. Using the proper motion and radial velocity, $\mu_\alpha, \mu_\delta = 127.3, -39.4$ mas yr^{-1} and $v_r = -3.3$ km s^{-1} (Hog et al. 2000; Torres et al. 2006), we can calculate the space velocity (heliocentric) for $d \sim 65$ pc and $d \sim 700$ pc as $v \sim 40$ and $v \sim 440$ km s^{-1} respectively (Johnson et al. 1987). Typically for stars we expect heliocentric space velocities between 0–100 km s^{-1} (e.g. Dehnen 1998). Therefore, we expect $40 < d \lesssim 160$. Here, we adopt a distance of 100 pc.

We used a 1 keV collisionally-excited plasma (APEC) model and an absorbing Galactic hydrogen column of $N_H = 5.05 \times 10^{20}$ cm^{-2} (derived from the *nh* task in *HEASoft*) to convert the ROSAT/PSPC countrate from 1RXS (0.23 counts s^{-1}) in the 0.1–2.4 keV energy band to an unabsorbed flux of 3.2×10^{-12} erg cm^{-2} s^{-1} using WebPIMMS[14]. This corresponds to an X-ray luminosity of 3.8×10^{30} erg s^{-1} at 100 pc. The X-ray luminosity, the X-ray-to-optical flux ratio of 1.4×10^{-3}, and the spectral type all suggest that HD 214129 is an RS CVn-type binary. Accordingly, we expect the quiescent 3 GHz radio luminosity of the transient to be $L_R \lesssim 10^{15\pm1}$ erg s^{-1} Hz^{-1} (Benz & Güdel 1994; Güdel 2002, ; however, strictly speaking, their L_X-L_R relationship is valid for 5 GHz flux density). From epoch E4 we get the 3σ upper limit on the quiescent 3

[14]https://heasarc.gsfc.nasa.gov/cgi-bin/Tools/w3pimms/w3pimms.pl

GHz flux density of this transient as 2.4×10^{15} erg s^{-1} Hz^{-1}. Using a distance of 100 pc, we can estimate the flaring radio luminosity in epoch E1 as 1.1×10^{16} erg s^{-1} Hz^{-1}. From the binarity, the optical spectrum, radio and X-ray luminosities, X-ray hardness ratios from ROSAT, and the X-ray-to-optical flux ratio, we conclude that this radio transient is a flare from an active binary system.

4.5.4.2 VTC225707-010238: Flaring Type-I QSO

VTC225707-010238 is a persistent but variable source with flux densities 0.609±0.074, 1.218±0.069, 0.911±0.065, and 1.165±0.055 mJy in the four epochs of our survey. The spectral indices within the S band for the first three epochs are 1.93 ± 1.42, 1.16 ± 0.53 and 1.64 ± 0.82. The 1.4 GHz peak flux densities from the FIRST and Hodge et al. (2011) surveys are 0.17 ± 0.14 and 0.17 ± 0.07 mJy respectively. We followed up this transient with the VLA on 01 Sep 2012 (2–15 GHz) and 17 Sep 2012 (1–4 GHz). The continuum radio spectra are shown in the top panel of Figure 4.14. Both follow-up spectra are peaked at a few GHz. On 01 Sep 2012, the peak is 2.5 mJy at 7 GHz, while the 17 Sep 2012 spectrum is likely peaked at 3 GHz with a flux density of 1.5 mJy. This might suggest that this object is a flaring Gigahertz-peaked spectrum (GPS; young AGN) source. Sub-mm (100 GHz) follow-up observations on 09 Sep 2012 with CARMA gave a non-detection with 3σ supper limit of 2.1 mJy.

The optical counterpart of VTC225707-010238 is a blue point source in SDSS having $r = 20.1$ mag. The optical light curve from PTF shows intra-day small amplitude (sub-magnitude) variability. Follow-up spectroscopy with KeckI LRIS on 18 Aug 2012 (bottom panel of Figure 4.14) shows that this is a quasar at a redshift of 1.56. We therefore conclude that this transient is a flaring type-I quasar.

4.5.5 Transients On Timescales <1.5 Year

4.5.5.1 VTC224730+000008: Flaring AGN

VTC224730+000008 is a variable source with flux densities 284.2±1.2, 272.9±0.8, 260.3±1.0, and 535.2±0.4 mJy in the four epochs of our survey. Its 1.4 GHz peak flux densities from the FIRST and VLA-Stripe 82 surveys are 317.1 ± 0.1 mJy and 388.7 ± 0.1 mJy respectively. The optical counterpart of VTC224730+000008 is a blue quasar, classified as a BL Lac-type object. Blazar-like optical variability is indeed evident in the PTF and SDSS photometric data. Optical spectra from the SDSS BOSS program indicate that the redshift is z$\sim$1. Given this information, we conclude that VTC224730+000008 is an intermediate-redshift blazar.

4.5.6 Transients On Timescales $\lesssim$20 Years

4.5.6.1 VTC233002-002736: Renewed activity of Type-II QSO

This is a transient with respect to the FIRST survey. Its flux density is 5.540±0.159, 5.342±0.143, 5.725±0.147, 5.342±0.071 mJy in our four survey epochs, E1–E4, with spectral indices 1.42 ± 0.23, 0.86 ± 0.22, and

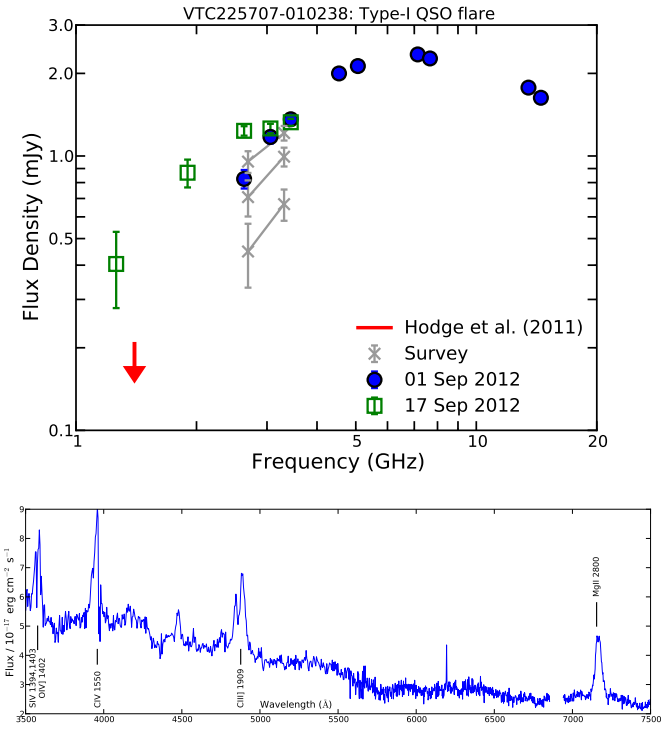

Figure 4.14: *Top*: The radio continuum spectrum of VTC225707-010238 at two follow-up epochs (blue circles and green squares). The 3σ upper limit at 1.4 GHz from Hodge et al. (2011) is shown in red. The measurements from the first three survey epochs are shown in grey. See §4.5.4.2 for details. *Bottom*: The optical spectrum of VTC225707-010238 observed with LRIS at KeckI on 18 Aug 2012. The spectrum is typical of a blue quasar. We derive a redshift of 1.56.

0.63 ± 0.21 in epochs E1–E3, within the S band. The flux density in the FIRST survey at the location of VTC233002-002736 is 0.34 ± 0.13 mJy (mean epoch 1999.2). This implies an order of magnitude or more increase in flux density at 1.4 GHz over the past decade, and relatively stable flux density at 3 GHz over the past 2 years. We obtained follow-up observations with the VLA (1–15 GHz) on 01 Sep 2012, 17 Sep 2012, and 29 May 2014. These observations reveal a Gigahertz-peaked spectrum source with an optically thick spectral index of 2.1 between 1–3 GHz. On 01 Sep 2012, the spectrum peaks at 5 GHz with a flux density of about 10 mJy, and the optically thin spectral index is −0.6 between 7–15 GHz. In the 29 May 2014 observations, spectral flattening is observed between 2–15 GHz with respect to 01 Sep 2012 and the spectral peak appears to be at 3 GHz, suggesting a significant evolution in the spectrum beyond 3 GHz. The radio continuum spectra from the survey and follow-up observations are shown in the inset of the top panel of Figure 4.15. Follow-up observations from CARMA at 100 GHz on 09 Sep 2012 give a detection at 2.3 ± 0.7 mJy.

The SDSS counterpart of VTC233002-002736 is a reddish point source with $r = 21.3$ mag. The detection in the PTF is only marginal, and no meaningful optical variability information can be obtained. The SDSS light curve between 1998–2008 reveals sub-magnitude variability, typical of AGN, on shortest timescales of a few weeks. VTC233002-002736 also has an X-ray counterpart in XMM-Newton (LaMassa et al. 2013). The multi-frequency continuum spectrum of VTC233002-002736 is shown in the top panel of Figure 4.15. The optical to mid-infrared part of the spectrum agrees well with a type-II quasar template from Polletta et al. (2007). A comparison between the radio and optical flux densities indicates that this is a radio loud quasar. We obtained a follow-up optical spectrum on 14 Sep 2012 with DIEMOS at Keck II (Figure 4.15, bottom panel). The spectrum shows broad CIII] and MgII spectral lines allowing us to calculate the redshift, $z = 1.65$.

From the nature of the radio spectrum, the timescale of its evolution, and the nature of the host galaxy, we conclude that VTC233002-002736 is due to renewed jet-activity from a type-II radio loud quasar, where the GPS spectrum is indicative of a young jet. The order-of-magnitude increase in flux density with respect to the FIRST survey could be indicative of an enhanced accretion phenomenon leading to an intensified jet. The flattening of spectral index at GHz frequencies between 2012 and 2014 may imply cessation in the increased accretion episode and/or the interaction of the jet with the circum-nuclear material in the host galaxy.

4.5.7 Transients Found Serendipitously

This subsection describes two transients that were found while manually inspecting archival radio images and analyzing our 5σ source catalogs. Being below the significance threshold, our variability criteria are not able to recover them. These two exemplars highlight the possibility that there are many more transients in our pilot survey data than have been reported in this work.

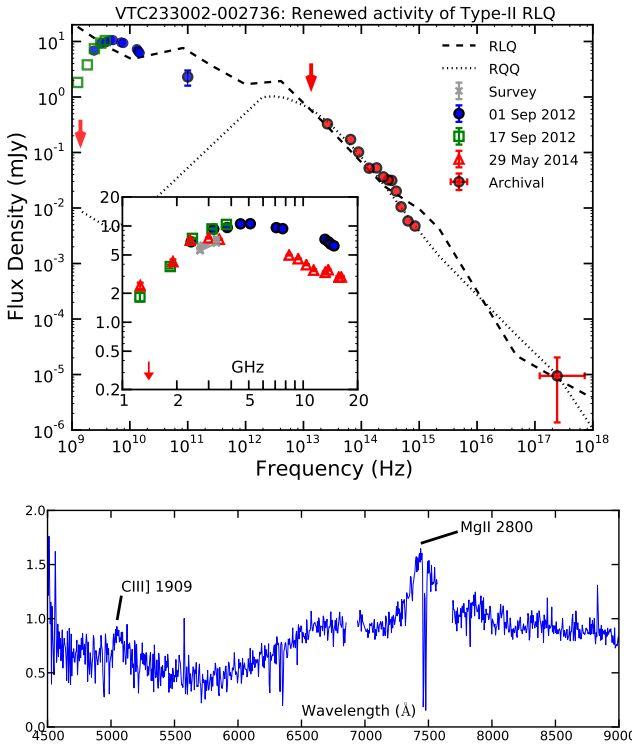

Figure 4.15: *Top*: The multi-frequency continuum spectrum of VTC233002-002736. Archival photometry is shown as filled red circles. The 3σ upper limit at 1.4 GHz from the FIRST survey and the upper limit from WISE W4 filter are shown as red arrows. Blue circles and green squares indicate the first and second follow-up observations. Black dashed and dotted lines are average spectra for radio-loud and radio-quiet quasars from Elvis et al. (1994). The *inset* shows the zoom-in of the follow-up radio continuum spectra from the three epochs. Red triangles show data from the third follow-up epoch, and the measurements from the four survey epochs appear in grey. *Bottom*: The optical spectrum of VTC233002-002736 observed with DIEMOS at KeckII on 14 Sep 2012. The y-axis is flux in arbitrary units. Broad emission lines indicate a quasar at a redshift of 1.65. See §4.5.6.1 for details.

4.5.7.1 VTC221515-005028: Extreme variability of flat-spectrum AGN

VTC221515-005028 has flux densities 2.568±0.086, 1.989±0.062, 1.780±0.071, 1.750±0.057 mJy and spectral indices 0.24 ± 0.30, 0.03 ± 0.31, 0.68 ± 0.38, and -0.45 ± 0.72 in epochs E1–E4 of our survey. It is absent in the FIRST survey (mean epoch 1996.1), where the flux density at that location is 0.25 ± 0.10 mJy, but present in the 1.4 GHz Stripe 82 survey catalog (Hodge et al. 2011) with a peak flux density of 0.79 mJy. For the transient search on timescales $\lesssim$20 years (§4.5.6) we assumed the upper limit to the flux density in FIRST as 1 mJy, and hence did not recovered this source as a transient using our spectral index criterion. We carried out radio follow-up observations with the VLA (1–15 GHz) on 29 May 2014. The radio continuum spectrum are shown in Figure 4.16. The source appears to have a flat spectrum between 1–5 GHz and a spectral index of −1.1 between 5–15 GHz.

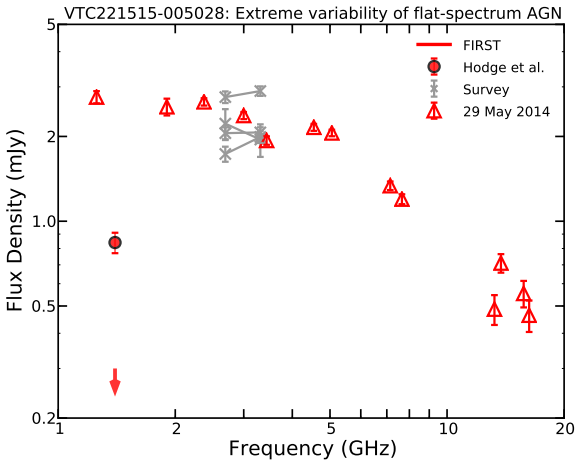

Figure 4.16: The radio continuum spectrum of VTC221515-005028 at the follow-up epoch 29May2014 (red triangles). The 3σ upper limit from the FIRST survey is shown with the red arrow and the detection from the Hodge et al. (2011) survey is marked by a red circle. he measurements from the four survey epochs are shown in grey. See §4.5.7.1 for details.

The optical counterpart of VTC221515-005028 is a faint red galaxy having $r \simeq 20.8$ mag. From the PTF light curve it is seen to exhibit stochastic variability with a maximum amplitude of one magnitude in the R band, and having a shortest timescale of about three days. The SDSS light curve between 1999–2008 reveals sub-magnitude variability and intermittent flares with amplitudes upto $r = 2$ mag on $\sim$1 day timescale. The photometric redshift from SDSS is 0.37. The radio-to-optical flux density ratio for the host galaxy, $R = log(S_{1.4\mathrm{GHz}}/S_g) \simeq 2.8$, and the radio luminosity at 1.4 GHz, 9.0×10^{29} erg s^{-1} Hz^{-1}, suggest a low-luminosity radio-loud AGN. We thus conclude that VTC221515-005028 is an extremely variable flat-spectrum AGN.

4.5.7.2 VTC230241+003450: Flare from dKe Star

VTC230241+003450 is detected as a 6σ source on 15 Aug 2012 (epoch E2, regions R2) and is not detected in the other epochs. The peak pixel values at the location of this transient in epochs E1–E4 are 0.090 ± 0.078, 0.422 ± 0.069, 0.046 ± 0.076, and 0.127 ± 0.065 mJy respectively. In the FIRST and Hodge et al. (2011) surveys, the peak pixel values at the location of the transient candidate are 0.13 ± 0.11 and 0.16 ± 0.06 mJy respectively. The optical counterpart of this transient is a 11th magnitude star, SDSS J230241.41+003450.2, classified as a K4Ve star by Torres et al. (2006). There is no evidence for binarity. Fitting a blackbody to the photometric data from SDSS, the NOMAD catalog, and WISE gives an estimate of the effective temperature, 3800 ± 500 K, and the distance, 70 ± 20 pc (assuming the radius of a main sequence star). SDSS J2302+00 derive a $v \sin(i)$ of 85 km s^{-1}. This star has a ROSAT counterpart, 1RXS J230240.3+003453, $17''\pm12''$ away, whose hardness ratios are consistent with those of a coronal emitter. We used a 1 keV APEC model in WebPIMMS to convert the ROSAT/PSPC countrate to a flux of 1.1×10^{-12} erg cm^{-2} s^{-1} in the 0.1–2.4 keV energy band. The X-ray-to-optical flux ratio is 0.002, and the X-ray luminosity at a distance of 70 pc is 6.4×10^{29} erg s^{-1}, both values being consistent with a dKe star. The quiescent 3 GHz radio luminosity of VTC230241+003450 can therefore be estimated as $6.4 \times 10^{14\pm1}$ erg s^{-1} Hz^{-1} (Benz & Güdel 1994; Güdel 2002). This can be compared with the flaring luminosity, 5.9×10^{15} erg s^{-1} Hz^{-1}. We conclude that this transient is a flare from a dKe star.

4.6 Optical Properties of Radio Sources

PTF carried out a concurrent optical survey which resulted in the identification of a few hundred thousand sources per epoch down to a limiting magnitude of R$\simeq$21 mag[15]. Our radio survey further benefits from the presence of SDSS deep co-add images containing more than a million objects over the 50 deg^2 to r$\simeq$23.5 mag (Annis et al. 2011). To find optical counterparts of radio sources we followed the procedure from (Hodge et al. 2011). We matched each source in the E2CAT with the SDSS and PTF catalogs using a $15''$ matching radius, and selected only the nearest match. To understand the false matching rate, we repeated the search by offsetting the radio source positions by $1'$ in an arbitrary direction. The resulting number of matches as a function of the matching radius is plotted as a histogram in Figure 4.17. Based on these results we choose a matching radius of $1''$ for SDSS and $1.5''$ for PTF to achieve a false matching rate of less than 3% and completeness better than 85%. The PTF source positions for the faintest objects are known to have a larger scatter than theoretically expected, and hence the larger matching radius of $1.5''$ is reasonable. Using these matching radii, we found the optical counterparts of sources in the PSC. The corresponding matching fraction in SDSS as a function of the r-band magnitude is shown graphically in Figure 4.18. 49% of the radio sources in the PSC have an optical counterpart down to the SDSS r-band limit[16]. Hodge et al. (2011), using the

[15]Note that, for the 60-second snapshots taken by PTF, the CCDs are saturated at $\sim$10–11 mag. This represents the lower limiting magnitude of the optical study carried out here.

[16]If all the radio sources (components) from the E2CAT are matched with SDSS sources, then the completeness is much lower, $\sim$35%.

deep co-added SDSS images (limit i∼23.5 mag), found a matching ratio (within a 1″ radius) of 44.4%. For radio variable sources, we found a somewhat higher matching fraction of 63% (Figure 4.18), which is also in agreement with Hodge et al..

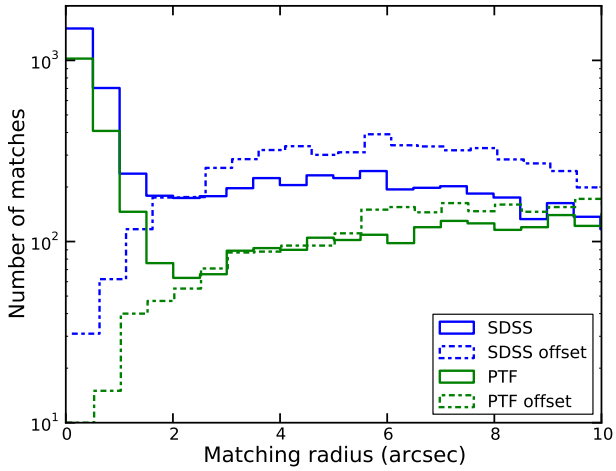

Figure 4.17: The number of optical matches for the radio sources in E2CAT for different matching radii. Solid lines indicate the matching process carried out using the actual radio source positions and the dot-dashed lines indicate background matches found by offsetting the radio source positions by 1′ in an arbitrary direction. Blue and green lines show radio versus SDSS and PTF matching respectively.

The modest optical matching rate in our medium-wide, medium-deep survey was not unexpected. Ivezic et al. (2002) compared the SDSS (limit r∼22 mag) and the FIRST (5σ ∼1 mJy) surveys over in 1230 deg^2 of the sky and matched about 30% of the 108,000 FIRST radio sources. McMahon et al. (2002) looked at the 382,892 FIRST sources in the north Galactic cap and looked for optical matches using the APM scans of POSS-I plates (R∼20 mag, B∼21.5 mag) for a 18% identification rate (70,000 sources). The optical match rate improves substantially in deep, narrow surveys. For example, Huynh et al. (2008) use Australia Telescope Compact Array (ATCA) data taken toward the Hubble Deep Field (HDF) at 20 cm, 11 cm, 6 cm and 3.6 cm, establishing a 66% matching of optical counterparts to I=23.5 mag. There is a strong color dependence, with the matching rate increasing from the blue to the near infrared (El Bouchefry & Cress 2007; Smolcic et al. 2008). Match rates approach 100% with the use of deep infrared data (Bonzini et al. 2012).

The near-real-time optical transient search carried out via image subtraction during the three-month high-cadence PTF observations resulted in approximately 8 million detections. Following standard practice, about 0.9 million of these (corresponding to only ∼50,000 unique optical sources) were identified in machine learning software as unlikely to be image subtraction artifacts, and further filtering was carried out using several stringent selection criteria (such as: at least two detections within one hour, no coincidence with stellar counterparts or AGN, etc.) and automated classifiers (Bloom et al. 2012). This was followed by human inspection of the subtracted images, light curves, and automated classifications, and the list was narrowed down to 193 candidates for further follow-up. Out of the 193 candidates, only 10 sources were ultimately

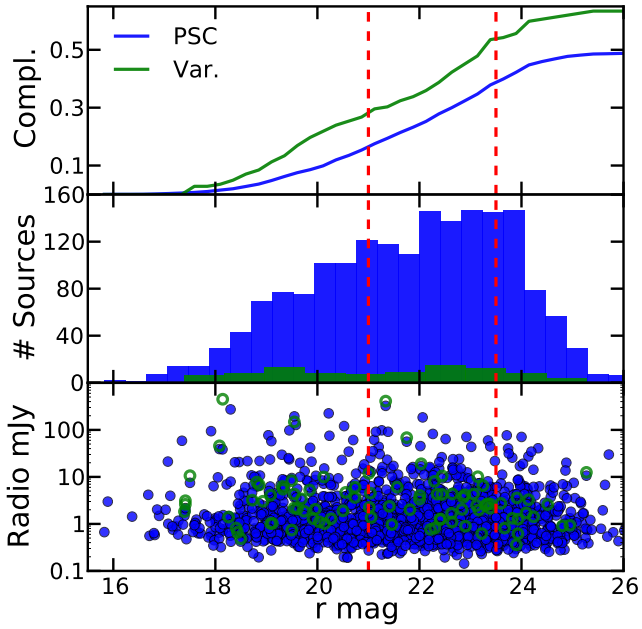

Figure 4.18: Optical counterparts of persistent (blue) and variable (green) radio sources in the PSC. The x-axis is r-band magnitude from SDSS. The top panel gives the completeness of the radio-optical cross-matching, the middle panel shows histograms of persistent and variable radio sources with optical counterparts, and the bottom panel plots the radio flux densities versus optical magnitudes. The approximate limiting magnitudes for PTF (per-epoch; $R = 21$ mag.) and SDSS (Stripe 82 co-add; $r = 23.5$ mag.) are shown as red dashed lines.

followed up spectroscopically, among which are 8 confirmed supernovae, PTF12gzk (SN Ic, z=0.014), 12jaa (IIb, 0.024), 12giy (Ia, 0.029), 12hwb (Ia, 0.056), 12hmx (Ia, 0.085), 12iet (II, 0.095), 12ild (Ia, 0.17), and 12itq (Ia, 0.22). The multiwavelength observations of PTF12gzk have been discussed at length by Ben-Ami et al. (2012); Horesh et al. (2013). In Figure 4.19 we plot the optical light curves of these eight supernovae as well as the upper limits to their spectral luminosity in the radio. The radio non-detections are in accordance with the expected flux densities of Type II, Ic and Ia supernovae. The radio detection and subsequent non-detections of PTF12gzk from Horesh et al. are also shown for reference, and these data emphasize the need for deep radio observations for optically-bright supernovae such as the ones generally found by PTF. After all the survey observations were complete, we compiled optical light curves of sources using the catalogs hosted at IPAC (§4.4). In order to enable robust variability search, we selected only those optical sources having more than 16 reliable observations (unflagged in SExtractor) and R band magnitudes between 10 and 23. There are 402,747 such sources in the PTF database with the 90% completeness of this sample corresponding to approximately an R band limiting magnitude of 21. 802 (0.2%) of these sources have counterparts in the PSC (i.e. 22% of the PSC sources have optical counterparts). 13,667 (3.4%) are optical variables[17]. Only 42 radio sources have optical variable counterparts among the sample of 3652, while only two of these are variable also in the radio. Thus, given the limiting magnitude of R=21 mag. in optical and our source detection threshold of $\sim$0.5 mJy in the radio, we find that the overlap between optical variables and radio variable sources is extremely small. These demographics are succinctly presented in a Venn diagram in Figure 4.20.

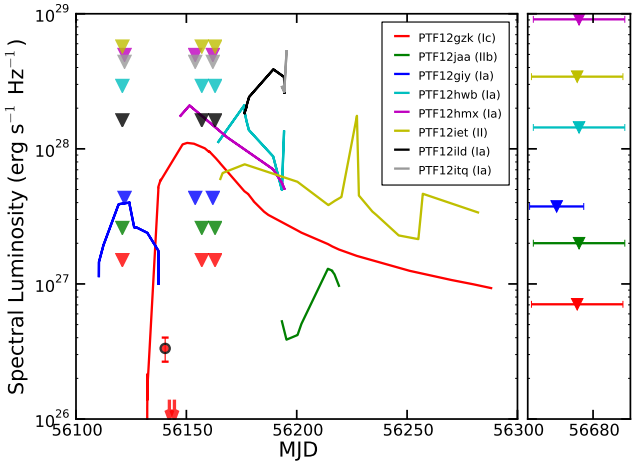

Figure 4.19: Light curves of the 8 spectroscopically-confirmed supernovae found in the PTF survey. Each supernova is represented by a unique color. Optical photometric data from PTF and follow-up observations are shown as solid lines. The 3σ radio upper limits from the JVLA survey (four epochs) are shown as downward-pointing triangles. For PTF12gzk, the radio detection (red circle and errorbar) and 3σ upper limits (downward-pointing red arrows) at 5 GHz from (Horesh et al. 2013) are also marked. See §4.6 for details.

[17]Given the optical light curves, sources having a χ^2 probability is less than 1 in 500,000 and variability >30%, i.e. a standard deviation of >0.28 mag. were selected as optical variables. These criteria were designed to be similar to the radio variability criteria.

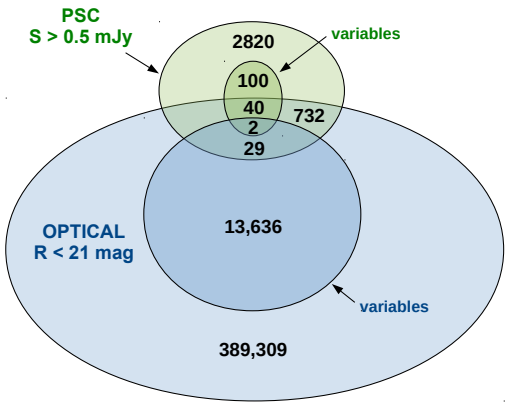

Figure 4.20: Venn diagram showing the number of persistent as well as variable optical sources from PTF and radio sources from the PSC. The sets plotted here are not to scale.

Here we are less concerned about optical-only transients and will focus instead on the optical variability properties of the radio transients and variables. A study of optical-only variables and transients from synoptic surveys is better done elsewhere in literature (e.g. Drake et al. 2009; Rau et al. 2009). We have obtained photometric data from PTF and SDSS after searching for counterparts as described above. A compilation of the optical light curves of the radio variable sources is given in Figure 4.21. Majority of the PTF light curves reveal sub-magnitude variability, while the SDSS light curves show gradual sub-magnitude or magnitude-level variability on timescales of years. This is characteristic of AGN, where fluctuations in the accretion rate or other causes give rise to optical variability on a wide range of timescales. Coupled with radio variability information, it seems likely that all of these sources are AGN.

4.7 Summary & Discussion

We have carried out a dedicated radio transient survey in a 50 deg^2 region of the SDSS Stripe 82. This survey is a pilot for the Caltech-NRAO Stripe 82 Survey (CNSS), a multi-epoch survey of 270 deg^2 of Stripe 82, which is currently underway. The pilot observations were carried out with the Jansky VLA between 2–4 GHz over four epochs spaced logarithmically in time, i.e. having cadences of one week, one month, and 1.5 years. The median rms noise per epoch is between 50 μJy and 90 μJy. With this pilot we have successfully demonstrated the near-real-time calibration, imaging, and transient search capability with the Jansky VLA data. We have found 142 sources displaying fractional variability beyond 30%, almost all of which are likely to be due to shocks in AGN jets based on radio follow-up observations, radio variability and spectral indices, and multi-wavelength archival data. We have also found two bona fide radio transients associated with Galactic objects, a flare from an RS CVn binary and a dKe flare. Comparison of our pilot survey data with the FIRST and VLA Stripe 82 surveys has (unexpectedly) revealed a few additional, highly variable and transient, sources on timescales of 5–20 years. These sources, most of which are either previously-

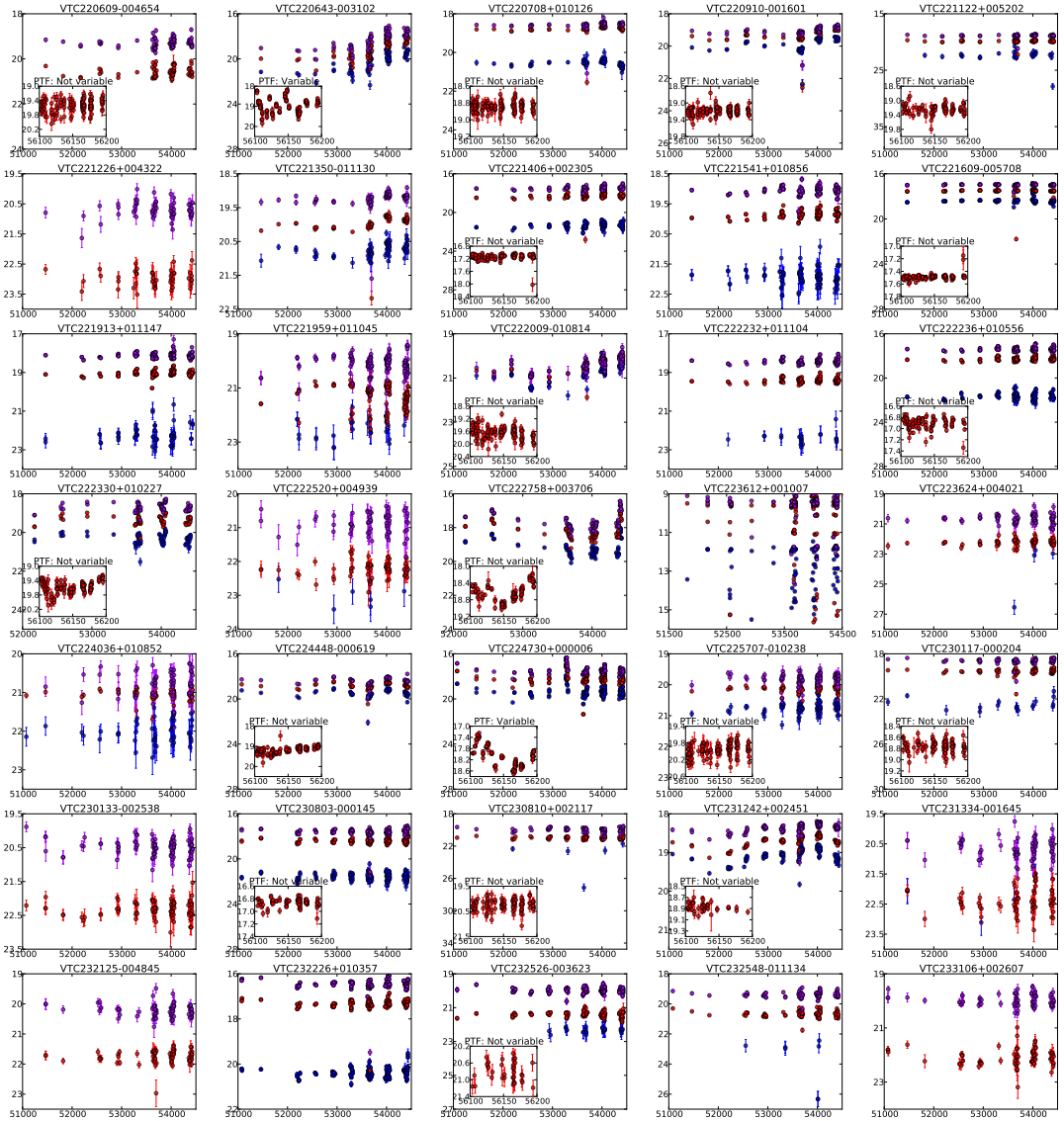

Figure 4.21: Well-sampled optical light curves of radio variable sources from SDSS (showing variability on timescales of years) and PTF (inset; showing variability on timescales of weeks). For SDSS, the u-, r-, and z-band light curves are shown as blue, red, and magenta circles with errorbars respectively. For PTF, the R band light curve is shown. The title of the inset is based on whether the source is classified as a variable through our variability criteria. See §4.6 for more details. The y-axis in each plot is the magnitude and the x-axis is the Modified Julian Date (MJD). Note that MJDs 51000, 54000, 56100, and 56200 correspond to Jul 1998, Sep 2006, Jun 2012, and Oct 2012 respectively.

known radio sources or have optical AGN hosts, are likely associated with renewed AGN activity. Two other transients, found serendipitously, suggest that there are many more such objects in this dataset than we have found through our transient selection criteria. We encourage the astronomical community to take advantage of the data from this pilot radio survey (see §4.3.2.5 for the data release website) for finding these hidden transients or for other science.

A high-cadence optical survey using PTF was carried out over three months, contemporaneous with the first three epochs of the radio survey. The motivation behind this joint survey was the selection of radio transients for rapid follow-up, preliminary classification of radio variables and transients based on optical light curves, and a direct comparison of the dynamic radio and optical skies. As noted by previous radio and optical studies, 20% of the persistent radio sources have an optical counterpart above the PTF limiting magnitude of 21, while 50% have counterparts above the SDSS limiting magnitude of 23.5 in the red filter. We have found primarily slowly-evolving radio transients, and, within the sensitivity limits of our PTF and pilot JVLA survey, very little overlap between the optical and radio variable skies. Only 0.05% of the radio point sources and $<$0.001% of the optical sources are variable at both frequencies. The fraction of strong variables per square degree of the radio decimetric sky is at least an order of magnitude smaller than those in the optical sky. We will now use the radio data to assess the degree of variability and the transient rate of the radio sky, and make recommendations for future surveys.

4.7.1 Comparison of variability with previous surveys

We found only a small fraction ($142/3652 = 3.9^{+0.5}_{-0.9}$%) of the point sources varying by $>$30% on week-month-year timescales. Majority of these are variable only on a 1.5 year timescale, and as described in §4.5.2, this variability fraction is to be taken as the upper limit. Several previous studies at 1.4 GHz (Frail et al. 1994; de Vries et al. 2004; Croft et al. 2010; Bannister et al. 2011a,b; Thyagarajan et al. 2011; Mooley et al. 2013) have shown that the fraction of variables on timescales between minutes and years, and flux densities between 0.1 mJy and 100 mJy, is $\sim$1% or less. Similar to these studies[18], we see that the 3 GHz sky is not highly variable on timescales longer than a few days. Radio follow up observations, optical and radio light curves, and multiwavelength archival data of the radio variable sources suggest that almost all of these are shock-related flaring in the jets of AGN.

Our choice of modulation index for measuring variability and selection threshold introduces a bias towards sources with large flux densities. A source in the PSC would have to have a mean flux density of 1.4 mJy in order to detect a 30% fractional variability, while at the 7σ source detection limit of of $\sim$0.5 mJy, a source would have to have $|m| > 3/4$ ($f_{\rm var} >$120%) in order to be identified as a significant variable. Fifteen strong variables (i.e. sources having $|m| > 2/3$, or $f_{\rm var} >$100%) were identified in our survey, but only 3000 sources in the PSC are bright enough ($>$0.55 mJy) to have been identified as a strong variable. We can therefore conclude that the fraction of strong variables is less than one percent.

[18] see http://tauceti.caltech.edu/kunal/radio-transient-surveys.html for a description of past variability studies

Radio variability appears to be a strong function of timescale. Ofek et al. (2011) found that $\sim$30% of point sources brighter than 1.5 mJy at 5 GHz were variable, with majority of the sources varying on timescales $<$10 days. This variability is primarily small amplitude (modulation indices of less than 0.2); only $\sim$0.3% of the sources in Ofek et al. have larger variability amplitude on timescales less than two years. The variability fraction that we find on week-month timescales in our pilot survey is in good agreement with this value. Large fraction of variables and small variability amplitude on short timescales was also found earlier by the MASIV survey (Lovell et al. 2008) conducted at 5 GHz. Recently, Hodge et al. (2013) compared the 1.4 GHz Stripe 82 survey with FIRST and found that $\sim$12% (6% per epoch $\times$ 2 epochs) of the sources vary by $>$30% on timescales between 7 years and 22 years, majority of which are AGN. It is possible that some of the Hodge et al. (2013) variables are solely due to angular resolution differences between the VLA-Stripe 82 and FIRST surveys. Indeed, Becker et al. (2010) and Bannister et al. (2011a) find that the fraction of variables on similar timescales is a few percent or less.

Radio variability (especially extrinsic) is expected to have a frequency dependence, but this has not been extensively studied. We can only use the results of past blind surveys to conclude that the fraction of strong variables is less than a few percent between frequencies of 1 GHz and 5 GHz, between flux densities of $\sim$0.3 mJy and $\sim$100 mJy, and over a wide gamut of timescales (between one day and several years).

In our pilot survey, we found a single AGN, VTC233002-002736, with flux density $>$3 mJy at 1.4 GHz, that appears to have increased in flux density by more than a factor of ten over the past 15 years. Similar objects may have been found by Bannister et al. (2011a,b) in the SUMSS survey (e.g. J201524-395949 or J060938âĹŠ333508). It is likely that such phenomena are a result of episodes of enhanced accretion leading to increased jet activity (see Kunert-Bajraszewska et al. 2006; Czerny et al. 2009; Kunert-Bajraszewska et al. 2010; Elitzur et al. 2014; Keel et al. 2014; LaMassa et al. 2015, for discussions of possibly related phenomena). Assuming a timescale of $\sim$20 years for an enhanced accretion episode, and given that fact that 50 deg^2 of the sky has $\sim$2000 AGN with flux density $>$3 mJy (White et al. 1997; Hopkins et al. 2001), we can estimate the period of occurrence of such episodes over the lifetime of an AGN: $\sim$40,000 years.

4.7.2 Transient Rates

We searched our four-epoch dataset for transients and found only a single source in the PSC (VTC223612+001006; RSCVn) that was present in one epoch and absent in the rest. Our transient search was carried out over a single-epoch area of $\sim$52 deg^2, but the sensitivity is not uniform across this area. For the first three epochs, our transient search was conducted on single-pointing images out to a radius ($r_{\rm max}$) of $\sim 8'$ from the pointing center. Although the fourth epoch has fairly uniform rms noise, comparison with the first three epochs for transient search diminishes the significance of the added sensitivity for this epoch. We can approximate the transient rate larger than a threshold flux density, $\kappa(> S)$, using the formulation from Appendix C of Ofek et al. (2011). We use a Gaussian primary beam response with half-width at half-maximum ($r_{\rm HP}$) of $7.5'$.

$$\kappa(>S) = \kappa_0 (S/S_0)^{-3/2}$$
$$\kappa_0 = \frac{3N_b \ln(2)}{2\pi r_{\rm HP}^2}(1 - e^{-3r_{\rm max}^2 \ln(2)/r_{\rm HP}^2}) \quad (4.4)$$

The 2σ upper and lower limits for the number of transient events, N_b, in 50 deg^2 given that we found one event are 5.683 and 2.3×10^{-2} (Gehrels 1986). Since the mean rms noise (flat sky) for the first three epochs of our survey is 70 μJy, we use a 7σ detection threshold of 0.5 mJy. For RS CVn variables (active binaries) we calculate a rate of $\kappa(>0.5$ mJy$)=0.0081^{+0.0381}_{-0.0079}$ events deg^{-2}. For all other types of transients we derive an upper limit of $\kappa(>0.5$ mJy$)<0.024$ events deg^{-2}.

The logN-logS plots for Galactic and extragalactic slow radio transients are shown in Figure 4.22. The top panel shows the upper limits to the transient rates[19] derived from previous radio surveys (colored wedges), the rates derived from radio transient detections (errorbars), and the theoretically-expected / empirically-estimated transient rates (dashed gray lines; see the transients summary table from Chapter 1 for more details). It should be noted that the expected transient rates are not sharp lines but are probability surfaces in the logN-logS diagram with the "most-probable" rates reported as dashed lines. The dashed line labeled "TDE" is for Swift J1644+57-like Zauderer et al. (2011); Zauderer et al. (2013) events. Upper limits from a few radio surveys which do not probe any new part of the phase space are not shown in this figure. All observed quantities are color-coded according to the observing frequency. The solid gray line is the rate claimed by Bower et al. (2007), plotted for reference. The upper limit from our pilot survey and the phase space probed by the full CNSS survey are shown as thick green wedges. The phase space probed by the VLA Sky Survey all-sky tier (VLASS) is shown as a thin green wedge. The source counts from the FIRST survey are represented by the solid red line, and the dashed red line denotes 1% of these persistent sources, representing strong variable sources at 1.4 GHz (e.g. Mooley et al. 2013, and references therein). Bannister et al. (2011a,b) report only a single extragalactic transient, SUMSS J060938-333508, found to be a nuclear source from ATCA follow-up observations (Keith Bannister, private communication). Hence the transient rate is 7.5×10^{-4} events deg^{-2}. Thyagarajan et al. (2011) report 57 transients, but some of these are Galactic and others have indefinite classifications. Hence, we adopt a 95% confidence level upper limit of 71 transients. The lower panel of Figure 4.22 shows the Galactic transient phase space. Symbols have similar meanings as for the extragalactic plot (top panel). For reference, the source counts from the FIRST and the MAGPIS 1.4 GHz (White, Becker & Helfand 2005) surveys are denoted by black solid lines. The approximate source counts for variable Galactic sources from Becker et al. (2010) are denoted by the blue dashed line. The transient rate for active binaries derived from this work is shown by the green errorbar and the upper limit for all other classes of Galactic transients is denoted by a thick green wedge. It is evident from these logN-logS diagrams that our pilot survey is not sensitive and wide enough to discover extragalactic explosive transients,

[19] see http://www.tauceti.caltech.edu/kunal/radio-transient-surveys/index.html for more details

but it is already in the regime where stellar flares are expected.

Our contemporaneous optical survey with PTF allows us to make a direct comparison between the transient optical and radio skies. Within the limiting sensitivities of our experiment, the transient skies at these two frequencies appear to be quite distinct. In the three months of high-cadence PTF search, eight spectroscopically-confirmed supernovae were discovered, none of which were recovered in our radio survey. Conversely, three stellar flares were detected in the radio, but their optical counterparts are saturated in PTF. We thus conclude that future joint radio and optical searches, such as MeerKAT and MeerLICHT[20], may only be beneficial if shallow optical surveys are combined with deep radio surveys or vice versa, or if both surveys are deep (μJy-level sensitivity). We find that deep multiwavelength photometric data and spectroscopy are very important for host and progenitor classification of extragalactic radio transients, and this should inform future slow transient searches. Given the expensive radio observing time, we have attempted to distinguish between AGN and other transients based on optical light curves from PTF and SDSS. Although in the present study we have optical light curves only for a small fraction of our radio sources (due to the completeness of optical counterparts), we expect to have 100% completeness in the LSST era, when radio transient classification based on optical light curves may be a feasible approach.

The radio sky at frequencies of a few GHz appears to be quiet, with less than a percent of the persistent sources being strong variables. From the transients summary table provided in Chapter 1 of this thesis, we find that the rates for a majority of classes of slow radio transients is less than one transient per 10,000 persistent sources. We also find that the fraction of strong variables and explosive transients among persistent sources in the optical sky is similar to the radio. However, the large number of persistent optical sources per square degree of the sky (down to the limiting sensitivity of PTF, $R = 21$ mag., for example; see Figure 4.20) implies that the number of varying optical sources is much larger than the number of varying radio sources (down to the limiting sensitivity of our JVLA survey, $\sim$0.5 mJy). Accordingly, we conclude that the false positive foreground for future EM-GW searches is lower in the radio than in the optical[21].

The rates for extragalactic transients, like core-collapse supernovae and binary neutron star mergers, are significantly low (see the summary table in Chapter 1), and it is not surprising that we found none of these transients in our pilot radio survey. Surveys over large areas of the sky are thus motivated by the search for such exotica. Therefore, we recommend wide-field surveys like that of the entire $\sim$270 deg^2 of Stripe 82 with the Jansky VLA (the CNSS survey, which is currently underway), all-sky surveys like the VLA Sky Survey (VLASS; the all-sky tier has been recently approved), or similar surveys with ASKAP, MeerKAT, and WSRT/Apertif. Also, shallow radio surveys are preferred to deep surveys due to the added advantage of restricting the transient population to a low redshift space thus making optical counterpart search feasible.

Acknowledgemets: The authors extend sincere thanks to Joan Wrobel and other scheduling staff at the

[20] https://www.astro.ru.nl/wiki/research/meerlicht

[21] This statement holds even for optical and radio surveys that have the same limiting flux density, because the number of optical sources per square degree of the sky is expected to be larger than the number of radio sources. Note that the PTF limiting sensitivity of $R = 21$ mag. corresponds to 12μJy.

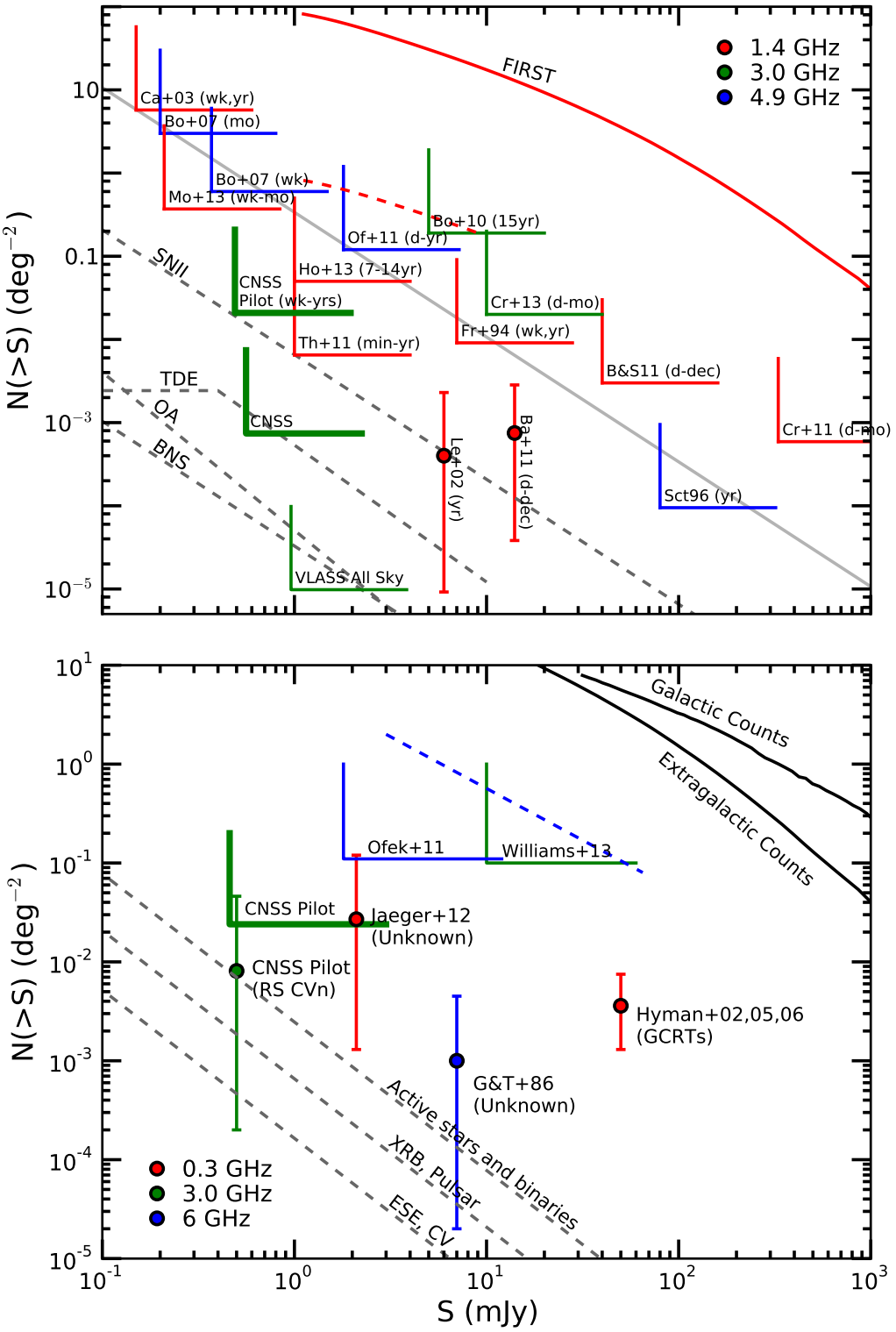

Figure 4.22: *Top*: The phase space of slow extragalactic transients. The panel shows the upper limits to the transient rates from previous radio surveys (colored wedges; 95% confidence), the rates derived from radio transient detections (2σ errorbars), and the expected transient rates. All observed quantities are color-coded according to the observing frequency. The solid gray line is the rate claimed by Bower et al. (2007), plotted for reference. The upper limit to the extragalactic transient rate from our pilot survey (this work) and the phase space probed by the full CNSS survey are shown as thick green wedges. The phase space probed by

NRAO in Socorro for extensive help with the scheduling of the VLA observations, and to James Robnett and other computing staff for their untiring assistance with the data storage and allocation of computing resources. The authors also wish to thank Luis Ho, Branimir Sesar, Eran Ofek, Sanjay Bhatnagar, Urvashi Rau, Kumar Golap, Vivek Dhawan, Craig Walker, Talvikki Hovatta, Tim Pearson, Anthony Readhead, Chuck Steidel, and Allison Strom for insightful discussions. The contribution of PTF collaboration members to optical data processing and optical follow-up observations relevant for this project is acknowledged. KPM is grateful to NRAO for the Grote Reber Fellowship, and to Yamini Jangir for going over this manuscript and providing useful suggestions. The National Radio Astronomy Observatory is a facility of the National Science Foundation operated under cooperative agreement by Associated Universities, Inc. SRK's research in part is supported by NASA and NSF. Some of the data presented herein were obtained at the W.M. Keck Observatory, which is operated as a scientific partnership among the California Institute of Technology, the University of California and the National Aeronautics and Space Administration. The Observatory was made possible by the generous financial support of the W.M. Keck Foundation. This research has made extensive use of ADS, CDS (Vizier and SIMBAD), NED, SDSS, and IRSA.

APPENDIX A

Given a total observing time T, we can either do a wide-shallow or a narrow-deep survey, where wide/narrow refers to the area covered, and shallow/deep refers to the sensitivity in terms of limiting flux density. To find which of these will explore the largest volume, consider two surveys, one which observes a single pointing for time T, and the other which observes N pointings with time T/N alloted for each pointing. We know that the limiting flux density (S_0), integration time (τ), maximum distance (d_0) and the total volume (V_0) probed by a survey are related as:

$$S_0 \propto \frac{1}{\sqrt{\tau}} \propto \frac{1}{d_0^2} \Rightarrow V_0 \propto d_0^3 \propto \tau^{3/4} \tag{4.5}$$

$$\therefore \frac{V_1}{V_2} = \frac{T^{3/4}}{N \times (T/N)^{3/4}} = \frac{1}{N^{1/4}} \tag{4.6}$$

Thus we see that the volume probed by a wide-shallow survey (V_2) is larger than that seen by a narrow-deep survey (V_1) by a factor of the number of pointings to the power of 1/4. However, note that since the distance probed in these two kinds of surveys goes as $d_1/d_2 = \sqrt{N}$. This means that if we want to probe transient populations concentrated at large distances (redshifts), it is best to do a narrow-deep survey. Also see Macquart (2014) for survey parameter optimization to maximize the yield of slow transients having well-defined distributions in space.

Bibliography

Abazajian, K. N., Adelman-McCarthy, J. K., Ag ueros, M. A., et al. 2009, ApJS, 182, 543

Aller, M. F., Aller, H. D., Hughes, P. A., et al. 1999, ApJ, 512, 601

Annis, J., Soares-Santos, M., Strauss, M. A., et al. 2011, arXiv:1111.6619

Arshakian, T. G., Leon-Tavares, J., Böttcher, M. et al. 2012, A&A, 537, 32

Augusteijn, T., Karatasos, K., Papadakis, M., et al. 1992, A&A, 265, 177

Bannister, K. W., Murphy, T., Gaensler, B. M., Hunstead, R. W., & Chatterjee, S. 2011, MNRAS, 412, 634

Bannister, K. W., Murphy, T., Gaensler, B. M., Hunstead, R. W., & Chatterjee, S. 2011, Erratum, July 2011

Ben-Ami, S., Gal-Yam, A., Filippenko, A. V., ey al. 2012, ApJ, 760, 33

Benz, A. O., Güdel, M. 1994, A&A, 285, 621

Philip R. B. & Keith D. R. 2003, Data reduction and error analysis for the physical sciences, 3rd ed., Boston, MA: McGraw-Hill, ISBN 0-07-247227-8

Bloom, J. S., Richards, J. W., Nugent, P. E., et al. 2012 PASP, 124, 1175

Boffi, F. R. & Branch, D. 1995, PASP, 107, 347

Bonzini, M., Mainieri, V., Padovani, P. et al. 2012, ApJS, 203, 15

Booth, R. S., & Jonas, J. L. 2012, AfrSk, 16, 101

Bourke, S., Mooley, K., Hallinan, G. 2014, ASPC, 485, 367

Bovy, J., Hogg, D. W., Roweis, S. T. 2009, ApJ, 700, 1794

Bower, G. C., Saul, D., Bloom, J. S., Bolatto, A., Filippenko, A. V., Foley, R. J., & Perley, D. 2007, ApJ, 666, 346

Becker, R. H., Helfand, D. J., White, R. L. & Proctor, D. D. 2010, ApJ, 140, 157

Berger, E., Kulkarni, S. R., Frail, D. A., & Soderberg, A. M. 2003, ApJ, 599,408

Cameron, P. B., Chandra, P., Ray, A., et al. 2005, Nature, 434, 1112

Carilli, C. L., Ivison, R. J., & Frail, D. A. 2003, ApJ, 590, 192

Cenko, S. B., Krimm, H. A., Horesh, A., et al. 2012, ApJ, 753, 77

Cenko, S. B., Kulkarni, S. R., Horesh, A., et al. 2013, ApJ, 769, 130

Chandra, P. & Frail, D. A., 2012, ApJ, 746, 156

Chen, X., Rachen, J. P., LÃşpez-Caniego, M., et al. 2013, A&A, 553, 107

Chomiuk, L., Soderberg, A. M., Moe, M., et a. 2012, ApJ, 750, 164

Chomiuk, L., Krauss, M. I., Rupen, M. P., et al. 2012, ApJ, 761, 173

Condon, J. J., Cotton, W. D., Greisen, E. W., et al. 1998, AJ, 115, 1693

Croft, S., Bower, G. C., Ackermann, R., et al. 2010, ApJ, 719, 45

Cutri, R. M., Wright, E. L., Conrow, T. et al. 2012, WISE Rept

Czerny, B., Siemiginowska, A., Janiuk, A.; Nikiel-WroczyÅĎski, B. & Stawarz, L. 2009, ApJ, 698, 840C

Darbha, S., Metzger, B. D., Quataert, E., et al. 2010, MNRAS, 409, 846

Dawson, K. S., Schlegel, D. J., Ahn, C. P., et al. 2013, AJ, 145, 10

Dehnen, W. 1998, AJ, 115, 2384

Dennett-Thorpe, J. & de Bruyn, A. G., 2002, Nature 415, 57

de Vries, W. H., Becker, R. H., White, R. L., & Helfand, D. J. 2004, AJ, 127, 2565

Drake, A. J., Djorgovski, S. G., Mahabal. A., et al. 2009, ApJ, 696, 870

Elitzur, M., Ho, L. C. & Trump, J. R. 2014, MNRAS, 438, 3340

El Bouchefry, K. & Cress, C. M. 2007, Astronomische Nachrichten, 328, 577

Elvis, M., Wilkes, B. J., McDowell, J. C. et al. 1994, ApJS, 95, 1

Fender, R. P. et al . 2006, MNRAS, 367, L6

Fiedler, R., Dennison, B., Johnston, K. J., et al. 1994, ApJ, 430, 581

Findeisen, K., Hillenbrand, L., Ofek, E., et al. 2013, ApJ, 768, 93

Fong, W., Berger, E., Metzger, B. D., et al. 2014, ApJ, 780, 118

Frail, D. A., Kulkarni, S. R., Ofek, E. O., Bower, G. C., & Nakar, E. 2012, ApJ, 747, 70

Frail, D. A., Kulkarni, S. R., Berger, E., & Wieringa, M. H. 2003, AJ, 125, 2299

Frail, D. A., Kulkarni, S. R., Hurley, K. C., Fishman, G. et al. 1994, ApJ, 437, 43

Fromm, C. M., Perucho, M., Ros, E., et al. 2011, A&A, 531, 95

Gaensler, B. M., Kouveliotou, C., Gelfand, J. D., et al . 2005, Nature, 434, 1104

Gal-Yam, A., Ofek, E. O., Poznanski, D., et al. 2006, ApJ, 639, 331

Gehrels, N. 1986, ApJ, 303, 336

Gehrels, N., Ramirez-Ruiz, E., Fox, D. B. et al. 2009, ARA&A, 47, 567

Ghirlanda, G., Burlon, D., Ghisellini, G., et al. 2014, PASA, 31, 22

GÃijdel, M. 2002, ARA&A, 40, 217

Hallinan, G., Bourke, S., Lane, C., et al. 2007, ApJ, 663, 25

Hancock, P. J., Gaensler, B. M. & Murphy, T., 2011, ApJ, 735, 35

Hancock, P. J, Murphy, T., Gaensler, B. M, Hopkins, A., & Curran, J. R 2012, MNRAS, 422, 1812

Harding, L. K., Hallinan, G., Boyle, R. P., et al. 2013, ApJ, 779, 101

Henry, G. W. & Newsom, M. S 1996, PASP, 108, 242

Hjorth, J., Watson, D., Fynbo, P. U. J., et al. 2005, Nature, 437, 859

Hodge, J. A., Becker, R. H., White, R. L., Richards, G. T. & Zeimann, G. R. 2011, AJ, 142, 3

Hodge, J. A., Becker, R. H., White, R. L., Richards, G. T., 2013, ApJ, 769, 125

Hog, E., Fabricius, C., Makarov, V. V. 2000, A&A, 355, 27

Hopkins, A. M., Miller, C. J., Connolly, A. J., et al. 2002, AJ, 123, 1086

Horesh, A., Kulkarni, S. R., Corsi, A., et al. 2013, ApJ, 778, 63

Hovatta, T., Nieppola, E., Tornikoski, M, et al. 2008, A&A, 485, 51

Hovatta, T., Pavlidou, V., King, O. G., et al. 2014, MNRAS, 439, 690

Huguenin, G. R., Taylor, J. H., Helfand, D. J., et al. 1973, ApJ, 181, 139

Huynh, M. T., Jackson, C. A., Norris, R. P., Fernandez-Soto, A. et al. 2008, AJ, 135, 2470

Huynh, M. T., Hopkins, A. M., Lenc, E., et al. 2012, PASA, 29, 229

Hyman, S. D., Lazio, T. J. W., Kassim, N. E., 2002, AJ, 123, 1497

Hyman, S. D., Lazio, T. J. W., Kassim, N. E., et al. 2005, Nature, 434, 50

Hyman, S. D., Lazio, T. J. W., Roy, S., et al. 2006, ApJ, 639, 348

Hyman, S. D., Roy, S., Pal, S., et al. 2007, ApJ, 660, 121

Hyman, S. D., Wijnands, R., Lazio, T. J. W., et al. 2009, ApJ, 696, 280

Ivezic, Z., Menou, K., Knapp, G. R., et al. 2002, AJ, 124, 2364

Johnson, D. R. H., Soderblom, D. R. 1987, AJ, 93, 864

Johnston, S., Taylor, R., Bailes, M., et al. 2008, Experimental Astronomy, 22, 151

Kantharia, N. G., Anupama, G. C., Prabhu, T. P., et al. 2007, ApJ, 667, 171

Kasliwal, M. M. 2012, PASA, 29, 482

Keel, W. C., Maksym, P., Bennert, V. N. et al. 2014, arXiv:1408.5159

Kesden, M., 2012, PhRvD, 85, 4037

Kharchenko, N. V., Roeser, S. 2009, VizieR Online Data Catalogs

Körding, E., Rupen, M., Knigge, C., et al. 2008, Science, 320, 1318

Kovari, Zs., Vilardell, F., Ribas, I., et al. 2007, Astronomische Nachrichten, 328, 904

Kunert-Bajraszewska, M., Marecki, A. & Thomasson, P. 2006, A&A, 450, 945

Kunert-Bajraszewska, M., GawroÅĎski, M. P., Labiano, A. & Siemiginowska, A. 2010, MNRAS, 408, 2261

Laher, R. R., Surace, J., Grillmair, C. J., Ofek, E. O., et al. 2014, arXiv:1404.1953L

LaMassa, S. M., Cales, S., Moran, E. C., et al. 2015, ApJ, 800, 144

Law, N. M., Kulkarni, S. R., Dekany, R. G., et al. 2009, PASP, 121, 1395

LaMassa, S. M., Urry C. M., Cappelluti, N. et al. 2013, MNRAS, 436, 3581

Lawrence, A., Warren, S. J., Almaini, O. et al. 2007, MNRAS, 379, 1599

Lazio, J., Bloom, J. S., Bower, G. C., Cordes, J., Croft, S., Hyman, S., Law, C., & McLaughlin, M. 2009, astro2010: The Astronomy and Astrophysics Decadal Survey, 2010, 176

Lazio, J. W., Kimball, A., Barger, A. J. et al. 2014, PASP126, 196

Levinson, A., Ofek, E. O., Waxman, E. & Gal-Yam, A., 2002, ApJ, 576, 923

Lister, M. L., Aller, M. F., Aller, H. D., et al. 2013, AJ, 146, 120

Lovell, J. E. J., Rickett, B. J., Macquart, J.-P., et al. 2008, ApJ, 689, 108

Macquart, J.-P. 2014, arXiv1406.5790

Marscher, A. P. & Gear, W. K. 1985, ApJ298, 114

Mason, B. D.; Wycoff, G. L.; Hartkopf, W. I. 2001, AJ, 122, 3466

Mateos, S., Alonso-Herrero, A., Carrera, F. J., et al. 2012, MNRAS426, 3271

McConnell, N. J. & Ma, C.-P. 2013, ApJ, 764, 184

McMahon, R. G., White, R. L., Helfand, D. J. & Becker, R. H., 2002, ApJS, 143, 1

Metzger, B. D., Piro, A. L., & Quataert, E. 2009, MNRAS, 396, 1659

Metzger, B. D., Williams, P. K. G. & Berger, E. 2015, arXiv150201350

Michelson, P. F., Atwood, W. B., Ritz, S. et al. 2010, Reports on Progress in Physics, 73, 7

Miller-Jones, J. C. A., Sivakoff, G. R., Altamirano, D., et al. 2012, MNRAS, 421, 468

Miller-Jones, James C. A., Blundell, Katherine M., et al. 2004, ApJ, 600, 368

Mooley, K. P., Frail, D. A., Ofek, E. O., et al. 2013, ApJ, 768, 165

Motch, C., Pakull, M. W., Mouchet, M., Beuermann, K., et al. 1989, A&A, 219, 158

Murphy, T., Chatterjee, S., Kaplan, D. L., et al. 2013, PASA, 30, 6

Nakar, E. & Piran, T. 2011, Nature, 472, 82

O'Dea, C. P. 1998, PASP, 110, 493O

Ofek, E. O., Laher, R., Law, N., et al. 2012, PASP, 124, 62O

Ofek, E. O., Frail, D. A., Breslauer, B., et al. 2011, ApJ, 740, 65O

Oosterloo, T., Verheijen, M., & van Cappellen, W. 2010, ISKAF2010 Science Meeting

Padovani, P., Miller, N., Kellermann, K. I., et al. 2011, ApJ, 740, 20

Panagia, N., Van Dyk, S. D., Weiler, K. W., et al. 2006, ApJ, 646, 369

Patterson, J. 2011, MNRAS, 411, 2695

Perez-Torres, M. A., Lundqvist, P., Beswick, R., et al. 2014, arXiv:1405.4702

Perley, R. A., Chandler, C. J., Butler, B. J., & Wrobel, J. M. 2011, ApJ, 739, L1

Piran, T., Nakar, E. & Rosswog, S. 2013, MNRAS, 430, 2121

Piro, A. L., & Kulkarni, S. R. 2013, ApJL, 762, 17

Polletta, M., Tajer, M., Maraschi, L., et al. 2007, ApJ, 663, 81

Rahmer, G., Smith, R., Velur, V., et al. 2008, SPIE, 7014, 163

Rau, A., Kulkarni, S. R., Law, N. M., et al. 2009, PASP, 121, 1334

Randall, K. E., Hopkins, A. M., Norris, R. P., et al. 29012, MNRAS, 421, 1644

Rau, A., Kulkarni, S. R., Law, N. M., et al. 2009, PASP, 121, 1334

Rau, U. & Cornwell, T. J. 2011, A&A, 532, 71

Richards, J. L.; Max-Moerbeck, W., Pavlidou, V., et al. 2011, ApJS, 194, 29

Roy, N., Chomiuk, L., Sokoloski, J. L., et al. 2012, BASI, 40, 293

Smith, A. M., Lynn, S., Sullivan, M., et al. 2011, MNRAS, 412, 1309

Smolcic, V., Schinnerer, E., Scodeggio, M., et al. 2008, ApJS, 177, 14

Snellen, I. A. G., Schilizzi, R. T., Bremer, M. N., et al. 1999, MNRAS, 307, 149

Soderberg, A. M., Chakraborti, S., Pignata, G., et al. 2010, Nature, 463, 513

Stockdale, C., Weiler, K. W., Panagia, N., et al. 2009, Astro2010, 288

Student, 1908, Biometrika 6, 1

Tanvir, N. R., Levan, A. J., Fruchter, A. S., et al. 2013, Nature, 500, 547

Teraesranta, H., Tornikoski, M., Mujunen, A., et al. 1998, A&AS, 132, 305

Thyagarajan, N., Helfand, D. J., White, R. L., & Becker, R. H. 2011, ApJ, 742, 49

Tingay, S. J., Goeke, R., Bowman, J. D., et al. 2013, PASA, 30, 7

Torres, C. A. O., Quast, G. R., da Silva, L. 2006, A&A, 460. 695

Türler, M., Courvoisier, T. J.-L. & Paltani, S., 2000, A&A, 361, 850

Valtaoja, E., Terasranta, H., Urpo, S., et al. 1992, A&A, 254, 80

van Haarlem, M. P., Wise, M. W., Gunst, A. W et al. 2013, A&A, 556, 2

Vernstrom, T., Scott, D., Wall, J. V., et al. 2014, MNRAS, 440, 2791

Voges, W., Aschenbach, B., Boller, T. 1999, A&A, 349, 389

Weiler, K. W., Panagia, N., Montes, M. J., et al. 2002, ARA&A, 40, 387

White, R. L., Becker, R. H., Helfand, D. J. & Gregg, M. D. 1997, ApJ, 475, 479

White, R. L., Becker, R. H. & Helfand, D. J. 2005, ApJ, 130, 586

Williams, P. K. G., Bower, G. C., Croft, S., et al. 2013, ApJ, 762, 85

Woo, J.-K., Urry, C. M. 2002, ApJ, 579, 530

Wright, E. L., Eisenhardt, P. R. M. et al. 2010, AJ, 140, 1868

Zauderer, B. A., Berger, E., Soderberg, A. M., et al. 2011, Nature, 476, 425

Zauderer, B. A., Berger, E., Margutti, R., et al. 2013, ApJ, 767, 152

Table 4.2: Summary of the radio transient and variable sources found in this work

VTC	α_{J2000}	δ_{J2000}	S_{E1}	S_{E2}	S_{E3}	S_{E4}	m	FIRST	Hodge et al.	r_{SDSS}	PTF	z_{spec}	log $\bar{L}_\nu$	Identification
	(deg)				(mJy)			(mJy)	(mJy)	(mag)			(erg cm^{-2} s^{-1})	
Timescale <1 week														
220210-000203	330.539900	-0.034252	2.079±0.109	1.064±0.077	1.862±0.083	1.382±0.059	-0.56	<0.50	...	...	...	...	...	AGN
220609-004654	331.536395	-0.781711	3.970±0.154	3.424±0.106	4.637±0.112	3.390±0.060	-0.33	1.83±0.14	1.47±0.07	20.7	nv	0.37	31.1	AGN
221122+005202	332.842184	0.867327	1.665±0.096	2.037±0.070	1.122±0.085	2.325±0.041	0.55	1.25±0.11	0.52±0.07	20.0	nv	0.31	30.7	AGN
221136+011142	332.898974	1.194886	3.420±0.077	3.128±0.054	4.383±0.064	2.368±0.061	-0.36	1.64±0.14	1.26±0.16	24.1	...	...	...	AGN
221226+004322	333.107130	0.722873	2.408±0.067	2.951±0.057	2.112±0.058	2.391±0.044	0.31	2.50±0.11	1.83±0.06	23.1	...	...	...	AGN
221406+002305	333.524900	0.384618	0.809±0.063	0.877±0.055	0.464±0.049	0.604±0.050	0.58	<0.51	<0.32	18.4	nv	0.15	29.5	AGN
221541+010856	333.921049	1.148981	1.425±0.081	1.041±0.053	1.664±0.063	1.213±0.059	-0.48	<0.69	0.68±0.09	19.9	...	0.32[a]	30.5	AGN
221713-002216	334.306166	-0.371232	1.376±0.088	1.320±0.068	1.783±0.071	1.027±0.053	-0.33	<0.53	1.14±0.07	23.8	...	...	...	AGN
221913+011147	334.805979	1.196250	1.015±0.085	1.442±0.063	0.539±0.074	1.007±0.047	0.90	1.05±0.14	0.82±0.07	19.1	...	0.20[a]	30.0	AGN
222009-010814	335.036567	-1.137346	4.386±0.096	3.873±0.071	5.565±0.081	4.895±0.061	-0.38	5.23±0.15	3.13±0.10	20.6	nv	...	...	QSO
222150-000325	335.460301	-0.056997	2.239±0.121	2.470±0.080	1.819±0.086	2.106±0.053	0.29	2.70±0.11	2.24±0.07	...	...	...	...	AGN
222232+011104	335.634687	1.184480	0.860±0.062	0.844±0.048	0.348±0.048	0.944±0.048	0.80	1.34±0.14	1.50±0.06	19.5	...	0.29	30.2	AGN
222236+010556	335.648844	1.098840	1.009±0.078	1.054±0.056	0.358±0.055	0.927±0.050	0.96	<0.72	0.53±0.05	18.4	nv	0.20	29.9	AGN
222330+010227	335.873148	1.040835	9.414±0.134	8.921±0.091	5.740±0.097	5.391±0.044	0.40	6.11±0.13	6.82±0.06	19.3	nv	...	...	QSO
222520+004939	336.331883	0.827551	3.807±0.115	3.500±0.090	5.326±0.085	4.273±0.054	-0.44	4.69±0.12	3.76±0.08	22.3	...	0.80[a]	31.9	AGN
222758+003706	336.992096	0.618294	48.766±0.240	39.161±0.160	51.889±0.155	45.320±0.095	-0.30	83.75±0.10	64.45±0.63	18.1	nv	...	...	QSO
223607+005259	339.028010	0.883015	0.951±0.068	0.941±0.056	1.319±0.055	0.940±0.053	-0.37	<0.50	0.62±0.05	...	...	...	...	AGN
223624+004021	339.099104	0.672614	0.886±0.071	0.955±0.055	0.595±0.060	0.828±0.052	0.43	<0.50	0.57±0.07	22.3	...	0.59[a]	30.9	AGN
224843-005459	342.178945	-0.916381	1.644±0.085	1.429±0.064	1.778±0.085	1.523±0.057	-0.27	<0.72	0.69±0.07	...	...	...	...	AGN
224922+001805	342.343018	0.301369	10.370±0.161	10.029±0.137	7.249±0.146	9.759±0.059	0.27	9.46±0.10	11.51±0.06	...	...	...	...	AGN
225411-010651	343.544297	-1.114119	0.644±0.063	0.782±0.050	0.300±0.056	0.300±0.052	0.85	<0.74	<0.60	...	...	...	...	AGN
230117-000204	345.322041	-0.034390	2.071±0.079	2.600±0.062	1.701±0.073	1.946±0.054	0.37	2.67±0.11	2.09±0.07	19.6	nv	0.28[a]	30.6	AGN
230133-002538	345.387209	-0.427294	0.676±0.082	0.392±0.073	0.876±0.079	0.524±0.052	-0.80	<0.61	0.34±0.06	...	...	0.84[a]	31.0	AGN
230556-001652	346.481658	-0.281193	1.071±0.091	0.900±0.074	1.371±0.079	1.031±0.064	-0.46	<0.51	0.89±0.17	...	...	...	...	AGN
230636-002609	346.649268	-0.435896	1.741±0.083	1.150±0.074	2.002±0.084	1.607±0.062	-0.58	1.71±0.11	1.48±0.09	...	...	...	...	AGN

230918+002642	347.324430	0.445083	0.472±0.068	0.350±0.055	0.716±0.065	0.433±0.065	-0.73	<0.50	<0.39	…	…	…	…	AGN
231437+003844	348.655518	0.645515	0.774±0.070	0.805±0.053	1.170±0.060	1.026±0.090	-0.42	<0.53	0.39±0.07	24.9	…	…	…	AGN
231444+004026	348.685137	0.673960	0.233±0.060	0.606±0.053	0.222±0.055	0.318±0.081	0.89	<0.53	0.34±0.06	23.9	…	…	…	AGN
231559-001205	348.994359	-0.201415	4.176±0.105	4.039±0.095	5.282±0.098	4.003±0.070	-0.31	4.90±0.10	4.21±0.05	23.1	…	…	…	AGN
231746-005355	349.441332	-0.898619	1.045±0.081	0.862±0.074	1.284±0.085	1.175±0.084	-0.44	<0.69	0.44±0.05	…	…	…	…	AGN
231942-004547	349.925567	-0.763046	3.373±0.088	4.311±0.076	3.093±0.085	3.372±0.074	0.29	4.36±0.14	3.89±0.06	23.9	…	…	…	AGN
232217+001252	350.569589	0.214481	0.933±0.096	0.700±0.078	1.226±0.084	1.081±0.060	-0.59	<0.49	…	…	…	…	…	AGN
232226+010357	350.606463	1.065718	3.082±0.193	2.164±0.131	3.145±0.168	3.577±0.093	-0.42	4.96±0.13	…	17.4	…	0.12	30.0	AGN
232634-010513	351.642405	-1.086815	2.481±0.129	1.565±0.121	2.239±0.128	2.241±0.086	-0.40	1.50±0.15	…	23.4	…	0.79[a]	31.5	AGN
232656-000438	351.734689	-0.077164	1.737±0.060	1.477±0.056	2.050±0.055	1.549±0.065	-0.37	1.09±0.10	…	24.1	…	…	…	AGN
232723-000507	351.843984	-0.085213	1.373±0.071	1.796±0.062	1.316±0.062	1.478±0.073	0.27	1.25±0.10	…	…	…	…	…	AGN
232933-004002	352.386845	-0.667239	8.785±0.165	9.301±0.143	6.812±0.149	12.592±0.086	0.26	6.93±0.14	…	22.4	…	…	…	AGN
233106+002607	352.774153	0.435175	0.841±0.054	0.644±0.044	0.922±0.047	0.648±0.057	-0.40	1.00±0.11	…	22.2	…	0.74	31.1	AGN
Timescale <1 month														
220127+001402	330.360610	0.233772	1.076±0.096	0.448±0.071	0.480±0.069	0.660±0.053	0.82	<0.49	…	23.9	…	…	…	AGN
220456-000147	331.232587	-0.029821	4.999±0.169	6.578±0.096	5.969±0.125	6.192±0.076	-0.27	2.29±0.11	2.45±0.26	…	…	…	…	AGN
220643-003102	331.680375	-0.517180	131.189±0.699	194.029±0.340	151.652±0.298	134.492±0.182	-0.39	122.89±0.13	73.21±0.76	19.5	V	…	…	QSO
220910-001601	332.293354	-0.267023	6.690±0.166	9.455±0.120	7.796±0.137	8.323±0.054	-0.34	8.39±0.10	5.78±0.06	19.5	nv	1.11	32.4	QSO
221308-010837	333.284558	-1.143507	0.921±0.075	0.376±0.057	0.614±0.067	0.711±0.059	0.84	<0.72	0.95±0.05	23.2	…	…	…	AGN
221350-011130	333.460186	-1.191627	1.540±0.120	0.835±0.086	1.083±0.101	1.139±0.052	0.59	<0.71	<0.28	20.0	…	1.96	32.0	QSO
221959+011045	334.994454	1.179204	4.827±0.104	3.679±0.081	3.710±0.107	4.981±0.052	0.27	4.62±0.14	3.42±0.07	21.0	…	0.84	31.9	QSO
222123-002509	335.345654	-0.419074	3.255±0.145	2.235±0.107	2.724±0.119	2.674±0.080	0.37	3.62±0.10	2.70±0.10	23.4	…	…	…	AGN
222942+003556	337.423504	0.598817	3.266±0.089	2.401±0.070	2.772±0.073	2.367±0.051	0.31	2.63±0.11	1.97±0.06	24.5	…	…	…	AGN
223317-005009	338.321408	-0.835723	1.977±0.093	1.344±0.068	1.448±0.066	1.344±0.066	0.38	1.80±0.14	1.27±0.06	…	…	…	…	AGN
223612+001007	339.050505	0.168559	0.804±0.086	0.271±0.071	0.179±0.073	0.098±0.057	0.99	<0.52	<0.39	…	…	…	…	RS CVn
224036+010852	340.150070	1.147826	2.005±0.070	2.729±0.054	2.411±0.056	1.686±0.057	-0.31	2.13±0.14	1.41±0.06	21.0	…	2.99	32.7	QSO
224448-000619	341.200443	-0.105397	8.637±0.086	6.604±0.074	5.485±0.079	6.716±0.064	0.27	6.90±0.10	7.21±0.07	18.9	nv	…	…	QSO
224657+005240	341.737102	0.877754	2.641±0.063	1.928±0.057	1.702±0.071	1.982±0.054	0.31	1.40±0.13	0.75±0.06	…	…	…	…	AGN
225649-005401	344.205944	-0.900221	1.935±0.086	1.397±0.074	1.364±0.077	1.480±0.059	0.32	1.63±0.14	1.74±0.06	…	…	…	…	AGN
225707-010238	344.280373	-1.043805	0.602±0.073	1.218±0.069	0.914±0.065	1.192±0.056	-0.68	<0.74	<0.39	20.1	nv	1.56	31.8	QSO

230236+005739	345.647977	0.960878	4.146±0.142	3.165±0.114	3.344±0.144	4.485±0.054	0.27	3.43±0.11	4.92±0.06	...	...	...	...	AGN
230803-000145	347.012572	-0.029111	0.376±0.058	0.698±0.053	0.453±0.056	0.351±0.062	-0.60	<0.52	<0.29	18.5	nv	0.15	29.5	AGN
230810+002117	347.039702	0.354644	1.200±0.063	1.771±0.055	1.322±0.061	0.903±0.078	-0.38	1.33±0.11	1.03±0.06	21.1	nv	0.40[a]	30.7	AGN
231242+002451	348.174063	0.414044	4.347±0.095	3.198±0.079	3.767±0.083	2.386±0.062	0.30	1.19±0.10	0.86±0.06	18.7	nv	1.90	32.5	QSO
231334-001645	348.390098	-0.279113	2.343±0.061	1.440±0.054	1.353±0.061	1.657±0.064	0.48	1.87±0.10	2.20±0.05	22.6	...	0.74	31.4	AGN
231455+002456	348.728453	0.415556	1.177±0.071	0.757±0.064	0.873±0.064	0.855±0.075	0.43	0.96±0.10	0.81±0.06	24.8	...	...	...	AGN
232125-004845	350.352737	-0.812522	2.527±0.072	1.829±0.065	1.822±0.068	1.905±0.071	0.32	1.94±0.14	...	21.8	...	0.58[a]	31.2	AGN
232526-003623	351.359745	-0.606393	2.039±0.092	2.672±0.075	2.098±0.078	2.535±0.076	-0.27	3.26±0.13	...	21.4	nv	0.63	31.4	AGN
232548-011134	351.451958	-1.192766	5.404±0.148	7.212±0.145	5.776±0.140	5.925±0.083	-0.29	6.21±0.14	...	20.7	...	0.46	31.5	AGN
Timescale <1.5 years														
215701+005124	329.252431	0.856537	0.923±0.074	1.142±0.052	0.811±0.059	0.764±0.043	0.40	1.06±0.10	...	22.9	...	0.57[a]	30.9	AGN
215732+010748	329.384654	1.130011	1.219±0.099	1.195±0.060	1.048±0.065	0.806±0.053	0.39	<0.78	...	19.1	nv	0.30	30.4	AGN
215929+004723	329.872536	0.789814	1.777±0.118	1.586±0.095	1.500±0.087	2.091±0.043	-0.27	1.52±0.11	...	...	...	...	...	AGN
215951+010041	329.963762	1.011278	1.405±0.102	1.375±0.075	1.300±0.074	2.005±0.044	-0.37	2.03±0.12	...	...	...	...	...	AGN
220005+002309	330.022192	0.385698	1.357±0.068	1.316±0.054	1.217±0.066	0.962±0.056	0.31	<0.51	...	...	...	...	...	AGN
220017-000134	330.072365	-0.026093	5.912±0.100	5.995±0.080	4.965±0.087	4.612±0.067	0.26	7.06±0.09	...	19.8	nv	0.61	31.7	QSO
220109+010124	330.288600	1.023416	12.343±0.147	11.386±0.107	11.627±0.096	15.358±0.049	-0.30	37.55±0.14	...	...	...	...	...	AGN
220110+002547	330.293140	0.429823	2.504±0.077	2.715±0.058	2.335±0.056	2.049±0.056	0.28	3.76±0.11	...	...	...	...	...	AGN
220221+001114	330.587782	0.187335	1.438±0.078	1.623±0.065	1.616±0.060	1.212±0.045	0.29	2.00±0.11	...	24.2	...	...	...	AGN
220445+005129	331.187680	0.857985	3.041±0.089	2.913±0.066	2.641±0.069	3.801±0.050	-0.26	4.76±0.13	3.10±0.15	...	...	...	...	AGN
220708+010126	331.784654	1.023799	7.029±0.173	6.286±0.122	6.481±0.131	8.313±0.053	-0.28	15.68±0.13	10.72±0.06	18.8	nv	2.91	33.2	QSO
220804+000556	332.018501	0.098983	6.253±0.163	5.422±0.118	5.585±0.128	7.053±0.058	-0.26	10.06±0.11	7.99±0.07	23.2	...	...	...	AGN
220904+004607	332.266020	0.768647	1.317±0.160	1.712±0.133	1.042±0.143	1.008±0.043	0.52	<0.51	1.00±0.05	...	...	...	...	AGN
221160-003139	332.998688	-0.527367	1.362±0.077	1.073±0.057	1.174±0.061	1.414±0.051	-0.27	2.10±0.10	2.12±0.05	23.9	...	...	...	AGN
221257-005711	333.235700	-0.953020	1.897±0.160	1.319±0.125	1.807±0.136	2.194±0.055	-0.50	3.51±0.15	2.83±0.06	...	...	...	...	AGN
221548-001031	333.948344	-0.175409	0.882±0.102	0.755±0.083	1.083±0.081	1.283±0.051	-0.52	1.30±0.10	1.36±0.06	22.6	...	0.54[a]	30.9	AGN
221609-005708	334.037121	-0.952234	9.000±0.158	7.481±0.149	7.805±0.149	11.971±0.064	-0.46	6.56±0.15	5.35±0.05	17.5	nv	2.40	33.2	QSO
221642-004904	334.174200	-0.817899	1.734±0.069	1.828±0.055	2.074±0.062	2.383±0.054	-0.26	1.24±0.15	2.46±0.06	22.8	...	0.69[a]	31.4	AGN
222038-001209	335.158511	-0.202623	1.916±0.205	1.596±0.157	1.922±0.158	2.574±0.047	-0.47	10.26±0.11	7.29±0.07	...	...	...	...	AGN
222109-001940	335.286275	-0.327789	0.959±0.125	0.907±0.095	0.892±0.105	1.563±0.061	-0.53	1.59±0.10	1.20±0.08	22.4	...	2.36	32.2	QSO

222127-001530	335.362235	-0.258239	1.779±0.121	1.720±0.085	1.558±0.085	2.316±0.055	-0.30	2.06±0.11	1.67±0.10	23.2	...	0.46[a]	31.0	AGN
222201-005008	335.505891	-0.835608	8.209±0.141	7.158±0.113	8.512±0.109	12.122±0.070	-0.51	5.56±0.15	4.02±0.07	20.1	nv	0.33[a]	31.4	AGN
222359+011148	335.997306	1.196745	1.044±0.116	1.006±0.087	1.118±0.084	1.478±0.054	-0.38	1.70±0.14	0.75±0.15	22.4	...	...	...	AGN
222443+002858	336.180822	0.482741	1.718±0.109	1.832±0.075	1.917±0.084	2.447±0.044	-0.29	2.12±0.11	1.52±0.06	19.5	nv	0.26[a]	30.5	AGN
222524-001837	336.348824	-0.310389	0.934±0.080	1.058±0.056	0.862±0.060	0.704±0.055	0.40	<0.55	1.11±0.06	...	...	...	...	AGN
222546+004038	336.439976	0.677156	1.572±0.069	1.607±0.060	1.667±0.060	1.146±0.060	0.34	2.18±0.10	2.92±0.07	...	...	...	...	AGN
222605-010441	336.521610	-1.078109	4.218±0.075	4.657±0.053	4.261±0.054	3.465±0.055	0.29	5.22±0.15	4.06±0.06	22.9	...	0.42[a]	31.3	AGN
222630-001248	336.625294	-0.213342	4.690±0.134	4.418±0.104	4.561±0.121	5.855±0.052	-0.28	10.75±0.11	7.66±0.07	...	...	...	...	AGN
222647+005211	336.694041	0.869751	359.852±0.879	324.569±0.639	362.536±0.610	433.361±0.246	-0.29	617.48±0.10	285.28±5.57	21.3	nv	2.26	34.7	QSO
222704+011055	336.766725	1.182021	1.665±0.150	1.488±0.098	1.302±0.090	2.291±0.065	-0.42	1.11±0.14	<3.06	17.4	...	0.06[a]	29.1	AGN
222907+001908	337.277758	0.318936	1.107±0.098	0.918±0.086	1.031±0.079	1.423±0.048	-0.43	1.51±0.11	0.91±0.06	...	nv	1.80	32.0	QSO
222930-000845	337.373252	-0.145791	3.183±0.141	3.171±0.106	3.020±0.100	4.163±0.059	-0.27	4.40±0.11	2.66±0.06	22.9	...	0.56[a]	31.5	AGN
223024+004334	337.598552	0.726077	1.417±0.082	1.180±0.069	1.210±0.066	1.586±0.047	-0.29	1.44±0.10	0.67±0.08	18.3	nv	0.13	29.7	AGN
223047+003160	337.694749	0.533246	2.088±0.153	1.877±0.122	1.881±0.126	2.860±0.047	-0.41	3.93±0.11	3.70±0.06	17.4	nv	0.09	29.7	AGN
223140+002305	337.917233	0.384585	0.775±0.092	0.641±0.071	0.616±0.068	1.125±0.057	-0.55	1.83±0.10	1.36±0.06	...	...	...	...	AGN
223225+003431	338.103745	0.575289	1.785±0.086	1.871±0.071	1.385±0.067	1.370±0.048	0.31	2.19±0.11	2.13±0.06	...	...	...	...	AGN
223409+010618	338.537649	1.105054	14.140±0.123	16.928±0.104	16.556±0.110	22.451±0.069	-0.28	27.15±0.13	24.37±0.24	22.0	...	...	...	AGN
223516-005849	338.817742	-0.980367	3.230±0.144	3.480±0.110	3.026±0.114	4.715±0.059	-0.30	2.91±0.15	4.54±0.06	19.1	nv	1.18	32.2	QSO
223908+003232	339.784225	0.542353	4.063±0.249	4.083±0.167	4.267±0.184	5.843±0.058	-0.35	3.83±0.10	4.01±0.08	19.3	nv	0.24[a]	30.9	AGN
224023-003555	340.096938	-0.598702	2.583±0.100	2.467±0.079	2.953±0.093	3.737±0.069	-0.41	5.67±0.13	3.17±0.08	18.9	nv	1.16	32.0	QSO
224628-001214	341.615430	-0.203797	56.423±0.343	56.155±0.291	55.536±0.307	73.059±0.112	-0.26	70.42±0.10	100.88±0.65	21.8	nv	0.55[a]	32.7	AGN
224730+000006	341.875813	0.001783	281.818±1.200	272.963±0.769	260.412±1.024	545.119±0.403	-0.67	322.29±0.10	397.62±2.48	18.1	V	0.97	34.1	QSO
224733+010817	341.885647	1.138013	1.415±0.061	1.364±0.053	1.202±0.065	0.973±0.054	0.34	1.78±0.14	0.86±0.09	...	...	...	...	AGN
224803+003959	342.013923	0.666301	7.771±0.131	6.594±0.099	6.750±0.111	9.238±0.068	-0.33	11.93±0.11	8.39±0.06	22.3	...	0.82[a]	32.2	AGN
225103+000156	342.760572	0.032354	2.359±0.126	2.126±0.114	2.042±0.119	3.040±0.060	-0.35	5.33±0.10	3.64±0.06	23.3	...	...	...	AGN
225307-010950	343.277710	-1.163845	2.320±0.079	2.124±0.060	2.011±0.071	1.464±0.053	0.37	1.39±0.14	1.73±0.07	20.5	nv	0.34	30.7	AGN
225438-001641	343.658007	-0.277990	3.564±0.080	3.759±0.072	3.375±0.077	2.759±0.074	0.31	2.92±0.11	3.52±0.09	22.0	...	0.38[a]	31.1	AGN
225510+002526	343.791849	0.423809	0.548±0.067	0.762±0.056	0.495±0.060	0.401±0.046	0.62	<0.53	0.42±0.07	...	...	...	...	AGN
225525-000956	343.854026	-0.165458	4.053±0.128	3.776±0.104	3.613±0.112	5.175±0.081	-0.31	6.19±0.10	4.77±0.12	22.6	...	0.71[a]	31.8	AGN
225621-004110	344.085666	-0.686069	0.982±0.107	1.318±0.091	0.960±0.098	0.866±0.050	0.41	1.22±0.15	0.94±0.07	21.5	nv	0.56	30.9	AGN

225934+010821	344.891408	1.139151	0.742±0.060	0.966±0.052	0.984±0.052	0.610±0.046	0.45	<0.69	<0.34	23.7	…	…	…	AGN
225936-003356	344.898924	-0.565593	2.109±0.128	1.989±0.110	1.844±0.124	2.683±0.066	-0.30	5.78±0.12	4.94±0.06	…	…	…	…	AGN
230112-002112	345.299432	-0.353462	1.611±0.108	1.523±0.084	1.484±0.087	2.122±0.070	-0.33	5.52±0.11	2.97±0.06	…	…	…	…	AGN
230132-010319	345.382529	-1.055362	2.802±0.106	2.772±0.091	2.890±0.106	4.338±0.056	-0.44	11.78±0.14	7.11±0.07	…	…	…	…	AGN
230158+000352	345.490838	0.064493	7.164±0.143	5.936±0.123	6.574±0.154	12.024±0.059	-0.68	5.38±0.11	5.02±0.07	23.1	…	…	…	AGN
230218-005817	345.576721	-0.971495	2.119±0.152	2.245±0.122	2.255±0.126	2.936±0.063	-0.27	14.39±0.15	10.93±0.09	…	…	0.91[a]	31.8	AGN
230334-004006	345.890039	-0.668195	3.817±0.155	3.400±0.120	3.223±0.140	4.479±0.070	-0.27	7.41±0.14	5.79±0.07	22.0	…	0.70[a]	31.7	AGN
230423-000417	346.096113	-0.071504	4.115±0.066	3.415±0.065	3.576±0.066	2.608±0.064	0.27	2.44±0.10	3.84±0.08	19.7	nv	1.05	32.0	QSO
230748+002213	346.950170	0.370314	4.502±0.083	4.657±0.069	4.229±0.077	2.940±0.103	0.45	7.68±0.10	6.26±0.06	22.4	…	0.71[a]	31.8	AGN
230847+010904	347.196936	1.151171	1.371±0.063	1.303±0.054	1.295±0.059	0.872±0.064	0.40	2.44±0.14	1.52±0.14	…	…	…	…	AGN
231014+002531	347.559929	0.425187	17.643±0.098	18.021±0.074	16.694±0.080	13.110±0.117	0.32	65.78±0.11	37.53±0.43	…	…	…	…	AGN
231210-003135	348.042870	-0.526485	2.677±0.073	2.661±0.070	2.580±0.079	1.596±0.098	0.50	5.86±0.10	5.50±0.07	23.3	…	…	…	AGN
231517+002630	348.822686	0.441566	3.696±0.080	3.709±0.065	3.481±0.065	2.853±0.100	0.26	8.88±0.10	9.35±0.06	…	…	…	…	AGN
231537-003726	348.902796	-0.623911	1.678±0.134	1.286±0.126	1.564±0.127	3.021±0.091	-0.81	2.05±0.14	1.20±0.06	…	nv	…	…	AGN
231542+002937	348.923546	0.493578	12.632±0.170	13.768±0.137	12.830±0.135	9.258±0.120	0.39	17.92±0.11	17.03±0.06	21.0	nv	1.35	32.8	QSO
231557+005001	348.986515	0.833474	1.945±0.095	2.160±0.082	2.012±0.089	1.516±0.069	0.35	<0.57	3.41±0.07	19.7	…	2.52	32.5	QSO
231713+000256	349.305229	0.048771	13.192±0.181	12.635±0.161	11.598±0.160	16.734±0.078	-0.28	31.86±0.11	27.90±0.20	…	…	…	…	AGN
231846-000755	349.690889	-0.131884	4.550±0.086	3.684±0.072	3.976±0.080	5.134±0.074	-0.33	4.18±0.11	3.14±0.06	19.5	nv	0.86	31.9	QSO
232025+002744	350.106120	0.462184	30.309±0.157	25.698±0.134	26.054±0.122	35.256±0.095	-0.31	35.98±0.10	21.68±0.27	…	…	2.89	33.8	QSO
232037+001335	350.153115	0.226407	0.771±0.081	0.957±0.062	0.788±0.070	0.542±0.066	0.55	<0.51	<0.39	…	nv	0.42[a]	30.5	AGN
232236-000712	350.650440	-0.119883	11.177±0.163	10.612±0.144	10.984±0.125	14.273±0.087	-0.29	24.53±0.10	…	25.3	…	…	…	AGN
232311-003122	350.794080	-0.522647	1.702±0.082	1.786±0.077	1.369±0.076	1.289±0.066	0.32	1.80±0.13	…	…	…	…	…	AGN
232324+003328	350.849824	0.557710	14.938±0.124	13.590±0.099	12.629±0.109	9.361±0.063	0.37	14.55±0.11	…	…	…	…	…	AGN
232656+000303	351.732481	0.050827	2.510±0.131	1.996±0.118	2.536±0.119	2.968±0.054	-0.39	0.93±0.10	…	23.6	…	…	…	AGN
232804+001904	352.017137	0.317754	7.877±0.090	6.876±0.079	6.344±0.100	4.273±0.067	0.47	6.15±0.10	…	21.6	…	…	…	AGN
233210-003101	353.043262	-0.516945	1.307±0.079	1.573±0.075	1.229±0.076	1.102±0.064	0.35	2.50±0.13	…	20.3	nv	0.45	30.8	AGN
233227-010443	353.111298	-1.078566	2.130±0.101	2.225±0.093	1.983±0.096	1.543±0.075	0.36	3.24±0.15	…	…	nv	0.26	30.5	AGN
233260-005129	353.249596	-0.857978	15.958±0.120	14.168±0.102	14.493±0.101	21.498±0.098	-0.41	45.33±0.13	…	…	…	…	…	AGN
233301-004501	353.255643	-0.750179	2.952±0.134	2.697±0.122	3.097±0.132	4.850±0.076	-0.57	6.75±0.14	…	…	…	…	…	AGN

Timescale <20 years

221650+005429	334.210170	0.908094	1.673±0.067	1.765±0.059	1.598±0.064	1.925±0.050	-0.09	<0.57	<0.31	21.4	nv	0.55[a]	31.1	AGN
221711+011038	334.294275	1.177200	14.097±0.108	15.139±0.081	13.095±0.077	18.508±0.057	-0.20	3.84±0.15	7.51±0.07	22.2	...	0.49[a]	32.0	AGN
221813-010344	334.554017	-1.062315	8.724±0.082	8.955±0.066	7.971±0.072	8.745±0.057	0.02	<0.72	0.79±0.10	...	...	...	...	AGN
223041-001644	337.672656	-0.278969	3.805±0.084	3.508±0.068	3.763±0.070	3.240±0.057	0.08	<0.53	0.49±0.06	...	...	...	...	AGN
223514-001425	338.806545	-0.240294	3.858±0.161	4.042±0.138	4.265±0.169	4.090±0.075	-0.01	10.45±0.11	8.36±0.10	...	...	0.14	30.3	AGN
230113-002941	345.306025	-0.494588	9.942±0.094	9.409±0.084	9.257±0.092	10.574±0.066	-0.12	2.54±0.13	2.51±0.06	...	...	...	...	AGN
233002-002736	352.507328	-0.460065	5.492±0.157	5.342±0.143	5.742±0.147	5.510±0.073	-0.03	<0.52	...	21.4	...	1.65	32.5	QSO
Serendipitous														
221515-005028	333.811588	-0.841078	2.569±0.086	1.989±0.062	1.778±0.071	1.787±0.058	0.11	<0.68	0.94±0.05	21.4	nv	0.44[a]	31.0	AGN
223634-003352	339.141345	-0.564383	0.114±0.150	0.897±0.123	0.373±0.122	0.394±0.069	0.78	<0.66	<0.63	...	...	...	...	RS CVn
230241+003450	345.672648	0.580639	0.090±0.078	0.422±0.069	0.046±0.076	0.127±0.065	1.61	<0.51	<0.28	...	...	...	...	dKe

(1) The PTF column lists the variability properties of the optical counterparts of the radio variable sources; V=variable, nv=not variable. See S4.6 for the definition of variability used for PTF sources in this work. (2) The z_{spec} column gives the spectroscopic redshift from SDSS. Values possessing a superscript 'a' represent photometric redshift estimates from SDSS. (3) For sources variable on multiple timescales, we place it in the smallest timescale section where the source shows significant variability. For example, VTC220456-000147 is picked up as a variable on timescales of <1 month and <20 years based on our selection criteria. It is placed in the <1 month timescale section in this table.

Table 4.3: Summary of the radio follow-up observations of variable and transient sources reported in this work

Obs. Date	Freq. (GHz)	S (mJy)	σ_S (mJy)
VTC225411-010651			
01 Sep 2012	2.4	0.504	0.039
01 Sep 2012	3.2	0.604	0.028
01 Sep 2012	3.8	0.569	0.033
01 Sep 2012	4.5	0.596	0.024
01 Sep 2012	5.1	0.623	0.023
01 Sep 2012	7.1	0.641	0.021
01 Sep 2012	7.7	0.646	0.021
01 Sep 2012	13.2	0.584	0.035
01 Sep 2012	13.8	0.672	0.032
01 Sep 2012	14.2	0.639	0.035
17 Sep 2012	1.2	1.130	0.079
17 Sep 2012	1.8	1.363	0.077
17 Sep 2012	2.4	1.109	0.051
17 Sep 2012	3.1	0.841	0.040
17 Sep 2012	3.8	0.671	0.068
17 Sep 2012	4.5	0.596	0.049
17 Sep 2012	5.1	0.623	0.047
17 Sep 2012	7.1	0.641	0.044
17 Sep 2012	7.7	0.646	0.045
VTC232939-004755			
01 Sep 2012	2.4	0.739	0.065
01 Sep 2012	3.0	0.701	0.048
01 Sep 2012	3.4	0.740	0.054
01 Sep 2012	4.8	0.778	0.027
01 Sep 2012	7.4	0.741	0.021
01 Sep 2012	13.5	0.598	0.026
01 Sep 2012	14.5	0.568	0.027
VTC233002-002736			
01 Sep 2012	2.4	6.846	0.095
01 Sep 2012	3.2	9.294	0.071
01 Sep 2012	3.8	9.641	0.108
01 Sep 2012	4.5	10.519	0.073
01 Sep 2012	5.1	10.558	0.071
01 Sep 2012	7.1	9.612	0.070
01 Sep 2012	7.7	9.381	0.073
01 Sep 2012	13.2	7.269	0.102
01 Sep 2012	13.8	6.836	0.097
01 Sep 2012	14.2	6.487	0.103
01 Sep 2012	14.8	6.217	0.098
17 Sep 2012	1.2	1.829	0.189
17 Sep 2012	1.8	3.791	0.179
17 Sep 2012	2.4	7.437	0.082
17 Sep 2012	3.1	9.327	0.067
17 Sep 2012	3.8	10.380	0.123
29 May 2014	1.3	2.396	0.179
29 May 2014	1.9	4.253	0.240
29 May 2014	2.4	7.095	0.188
29 May 2014	3.0	7.511	0.109
29 May 2014	3.4	7.272	0.094
29 May 2014	8.4	4.984	0.051
29 May 2014	9.4	4.562	0.053
29 May 2014	10.4	3.955	0.055
29 May 2014	11.4	3.474	0.081
29 May 2014	13.2	3.295	0.074
29 May 2014	13.8	3.505	0.070
29 May 2014	15.7	2.937	0.076
29 May 2014	16.3	2.949	0.076
VTC221515-005028			
29 May 2014	1.3	2.759	0.137
29 May 2014	1.9	2.549	0.175
29 May 2014	2.4	2.654	0.080
29 May 2014	3.0	2.373	0.069
29 May 2014	3.4	1.935	0.067
29 May 2014	4.5	2.155	0.061
29 May 2014	5.1	2.058	0.055
29 May 2014	7.1	1.337	0.047
29 May 2014	7.7	1.198	0.048
29 May 2014	13.2	0.487	0.059
29 May 2014	13.8	0.710	0.054
29 May 2014	15.7	0.554	0.060
29 May 2014	16.3	0.464	0.059

Chapter 5

The Caltech NRAO Stripe 82 Survey (CNSS) Paper II: On-The-Fly Mosaicing Methodology

Majority of the contents of this chapter will go into a paper in prep: Mooley, et al. (2015)

Abstract

Telescope slew and settle time can markedly lower the efficiency of wide-field surveys, especially for sensitive interferometers with small fields of view like the Jansky VLA. This overhead is significantly reduced by the use of on-the-fly mosaicing (OTFM) technique, where the the antennas are driven at a non-sidereal rate and visibilities are recorded continuously. OTFM markedly improves the efficiency for wide-field shallow surveys with the Jansky VLA, thus making it the ideal observing mode for multi-epoch transient surveys. This is critical for a systematic exploration the phase space of slow radio transients. Here, we present a subset of the Jansky VLA observations carried out with the OTFM technique as part of the Caltech-NRAO Stripe 82 Survey (CNSS). We report on the planning of these OTFM observations with dynamically-scheduled blocks, the latest imaging capabilities for OTFM developed within the Common Astronomy Software Applications (CASA) package, and the reliable reproducibility of flux densities of sources between two epochs observed with OTFM and between pointed observations and OTFM. Using the subset of our observations from the CNSS pilot and final surveys, we demonstrate that the wide-band and wide-field OTFM observations with the Jansky VLA can be imaged accurately, and that the OTFM technique offers a more efficient alternative to standard mosaicing for multi-epoch shallow surveys such as the CNSS and the VLASS.

5.1 Introduction

The modicum of radio surveys dedicated to slow transient search[1] highlight the rather low rates of these transients and hence the necessity of wide-field surveys. Recent near-real-time surveys (Ofek et al. 2011, Mooley et al. 2015, ApJ, submitted) with the Karl G. Jansky Array (Jansky VLA; Perley et al. 2011) have also stressed on the unique advantage of associating radio sources with optical counterparts (also see Frail et al. 2012). This tends to favor multi-epoch shallow surveys which bring the observable transient population closer in distance, improving the ability to find optical/infrared counterparts and to characterize host galaxies and/or progenitors. Radio transient searches therefore call for wide-field shallow surveys.

At centimeter wavelengths, the SKA pathfinders, viz. ASKAP (Johnston et al. 2008), MeerKAT (Booth et al. 2012) and Apertif/WSRT (Oosterloo et al. 2010), have been designed to have large numbers of small dishes and/or phased array feeds with wide fields of view and large survey speeds. Meanwhile, the Jansky VLA takes advantage of receiver upgrades that have enabled an order-of-magnitude increase in continuum sensitivity and in survey speed. The new on-the-fly mosaicing (OTFM[2]) observing mode of the Jansky VLA eliminates the slew and setup up overheads and is thus ideal for shallow very large mosaics.

Here, we present results from a subset of OTFM observations carried out as part of the Caltech-NRAO Stripe 82 Survey (CNSS). Specifically, we present the basic OTFM theory (§5.1.1), report on the design of OTFM observations for the Jansky VLA (§5.1.2) the planning of CNSS dynamically-scheduled blocks (§5.2), the CNSS observations carried out as part of the Resident Shared-Risk Observing program (§5.3), calibration and imaging of the OTFM data (§5.4,5.5,5.6), and comparison of source flux densities from two OTFM epochs of a 10 deg^2 region in SDSS Stripe 82 and with pointed observations (§5.7). Summary and conclusions are given in §B.6.

5.1.1 OTFM Theory

In this section we present the interferometric equations pertinent to OTFM. Most of the content presented here can be found in Pety & Rodriguez-Fernandez (2010). The measurement equation of interest in any interferometric wide-field imaging problem is,

$$V(u_p, \alpha_s) = \int_{\alpha_p} B(\alpha_p - \alpha_s)\, I(\alpha_p)\, e^{-i2\pi\alpha_p u_p}\, d\alpha_p \tag{5.1}$$

where V is the visibility function, u_p is the the spatial (uv) frequency with respect to the fixed phase center α_p, α_s is the sky coordinate, I is the sky brightness, and B the primary beam pattern. During OTFM, the

[1] We define slow transients in accordance with literature as those having timescales >1s. See http://tauceti.caltech.edu/stripe82/radio-transient-surveys.html for an up-to-date list of radio surveys aimed at exploring slow transient phenomena.

[2] https://science.nrao.edu/facilities/vla/docs/manuals/obsguide/modes/mosaicking

antennas slew on the sky during the integration time, and the above equation should be rewritten as,

$$V(\hat{u_p},\hat{\alpha_s}) = \frac{1}{\delta t}\int_{t_0-\delta t/2}^{t_0+\delta t/2}\left\{\int_{\alpha_p} B[\alpha_p-\alpha_s(t)]\, I(\alpha_p)\, e^{-i2\pi\alpha_p u_p(t)}\, d\alpha_p\right\} dt \tag{5.2}$$

$$\hat{u_p} = \frac{1}{\delta t}\int_{t_0-\delta t/2}^{t_0+\delta t/2} u_p(t)\, dt\ ,\ \ \hat{\alpha_s} = \frac{1}{\delta t}\int_{t_0-\delta t/2}^{t_0+\delta t/2} \alpha_s(t)\, dt \tag{5.3}$$

where δt is the integration time. To avoid phase errors (see D'Addario & Emerson 2010, for an analogous approach for estimating the coherence loss for a linear scan with a fixed phase center), it is necessary to ensure that $u_p(t)$ varies less than the distance associated with the tolerable aliasing ($d_{\rm alias}$) during the integration time. This demands the following condition.

$$\delta t \ll \frac{d_{\rm alias}}{d_{\rm max}\omega_{\rm earth}} \ \equiv\ \delta t \ll \frac{6900s}{\theta_{\rm alias}/\theta_{\rm syn}} \tag{5.4}$$

where $d_{\rm max}$ is the maximum baseline length, $\omega_{\rm earth}$ is the angular velocity of a spatial frequency due to the Earth rotation (7.3×10^{-5} rad s^{-1}), $\theta_{\rm alias}$ and $\theta_{\rm syn}$ are the angular values corresponding to the field of view giving a tolerable aliasing and the synthesized beam respectively. For a dynamic range of a few thousand, $\theta_{\rm alias}/\theta_{\rm fwhm} \simeq 5$ (Table 4 of Pety & Rodriguez-Fernandez 2010). Hence, and further using the CNSS S-band observations ($\theta_{\rm fwhm} \simeq 15'$, $\theta_{\rm syn} \simeq 2.5''$) we arrive at,

$$\delta t \ll \frac{1400s}{\theta_{\rm fwhm}/\theta_{\rm syn}} \simeq 4\ s \tag{5.5}$$

For the CNSS survey we have used an integration time of 0.5 s (§5.3). The motion of the primary beam across a finite region on the sky during the integration time necessitates the introduction of an "effective primary beam" ($B_{\rm eff}$). We can rewrite equation 5.2 in the following manner using $B_{\rm eff}$.

$$V(\hat{u_p},\hat{\alpha_s}) = \int_{\alpha_p} B_{\rm eff}(\alpha_p-\hat{\alpha_s})\, I(\alpha_p)\, e^{-i2\pi\alpha_p\hat{u_p}(t)}\, d\alpha_p \tag{5.6}$$

$$B_{\rm eff}(\alpha_p-\hat{\alpha_s}) = \frac{1}{\delta t}\int_{t_0-\delta t/2}^{t_0+\delta t/2} B(\alpha_p-\alpha_s(t))\, dt \tag{5.7}$$

The accuracy of the flux densities in the image is affected due to the use of the true primary beam instead of the effective primary beam. The relative error can be calculated as follows.

$$\frac{B_{\rm eff}(u)-B(u)}{B_{\rm eff}(u)} = 1-\frac{1}{{\rm sinc}(u\delta\alpha_s)} \tag{5.8}$$

where $\delta\alpha_s = v_{\rm slew}\delta t$, i.e. the product of the OTFM scan rate and the integration ("dump") time. Five dumps per primary beam gives a 1% accuracy in the image plane, while 15 dumps per primary beam gives 0.1% accuracy (Pety & Rodriguez-Fernandez 2010). For CNSS, 30 dumps per primary beam (at 3 GHz; 0.5 s dumps) were used, implying negligible error in the flux densities of sources due to the use of the true primary

beam instead of the effective one.

In a standard mosaicing procedure, adjacent pointings are weighted according to their rms noise such that the resulting flux density (S) at any location and the local rms noise (σ) in the mosaic are respectively given by the following equations.

$$S\sigma^2 = \frac{S_1/b_1}{(\sigma_1^2/b_1^2)} + \frac{S_2/b_2}{(\sigma_2^2/b_2^2)} + \ldots = \frac{S_1\ b_1}{\sigma_1^2} + \frac{S_2\ b_2}{\sigma_2^2} + \ldots \tag{5.9}$$

$$\frac{1}{\sigma^2} = \frac{1}{(\sigma_1^2/b_1^2)} + \frac{1}{(\sigma_2^2/b_2^2)} + \ldots = \frac{b_1^2}{\sigma_1^2} + \frac{b_2^2}{\sigma_2^2} + \ldots \tag{5.10}$$

where the subscripts denote the pointing number and b_i denote the primary beam correction. However in OTFM, the primary beam moves across some part of the sky within each pointing with a unique phase center. Unless the motion of the primary beam within the pointing (or scan) is taken into account, the flux densities are added linearly without any weighting, which might limit the dynamic range. Faster scanning rates are thus expected be more limiting in dynamic range. This can be demonstrated by OTFM observations of bright sources at various scan rates. While such test observations have already taken place, the dynamic range analysis will be carried out as future work. If the motion of the primary beam within each scan is neglected, then the flux densities of sources in the mosiac are also reduced with respect to their true flux densities (shown below). The thermal rms noise, however, continues to follow the radiometer equation.

Below we derive an expression for the fractional change (f) in the flux density of sources if the motion of the primary beam within a OTFM scan is neglected. The primary beam is given by,

$$b(x,y) = e^{-(x^2+y^2)/2\rho^2} \tag{5.11}$$

The fractional decrease in the flux density at a location x_0, y_0 in the image of the scan is given by (phase center is $x_0 = 0, y_0 = 0$),

$$f(x_0,y_0) = \frac{1}{\Delta x}\int_{x_0-\Delta x/2}^{x_0+\Delta x/2} b(x,y_0)\,\mathrm{d}x \tag{5.12}$$

$$= \frac{e^{-y_0^2/2\rho^2}}{\Delta x}\int_{x_0-\Delta x/2}^{x_0+\Delta x/2} e^{-x^2/2\rho^2}\mathrm{d}x$$

$$= \frac{\rho}{\Delta x}\sqrt{\frac{\pi}{2}}e^{-y_0^2/2\rho^2}\left[\mathrm{erf}\left(\frac{x_0+\Delta x/2}{\sqrt{2}\rho}\right) - \mathrm{erf}\left(\frac{x_0-\Delta x/2}{\sqrt{2}\rho}\right)\right] \tag{5.13}$$

where $\rho = FWHM/2.355$ is the standard deviation of the primary beam and Δx is the slew of the antennas in arcmin within each scan. $f(x_0,y_0)/b(x_0,y_0)$ then denotes the fractional change in the flux density with respect to the true flux density when only a single, time invariant, primary beam correction is applied to each scan. Figure 5.1 shows the $f(x_0,y_0)/b(x_0,y_0)$ as a function of the position in the image of a single scan.

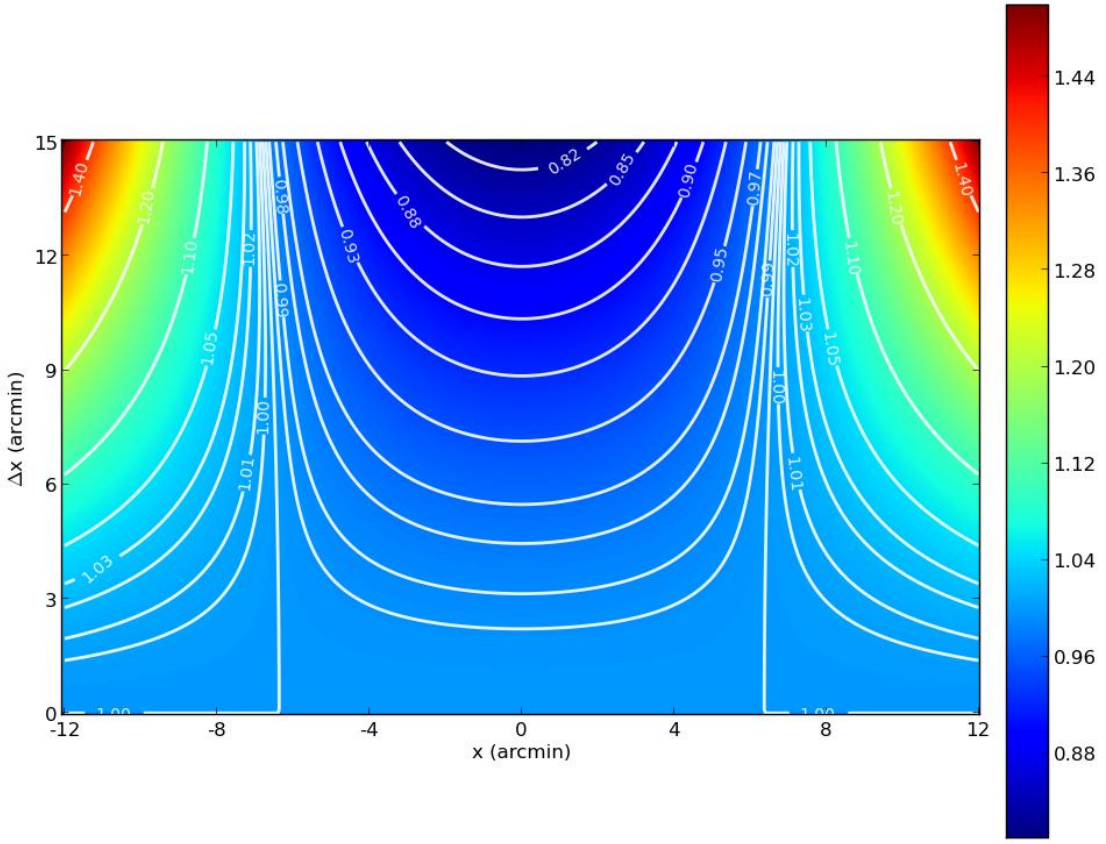

Figure 5.1: The OTFM smeared beam as a function of the slew of the antennas in arcmin within each scan (i.e. slew of the antennas between each change of correlator phase center). In other words, it shows the fractional change in the flux density with respect to the true flux density when only a single, time invariant, primary beam correction is applied to each scan. See equations 5.11–5.13 for details.

5.1.2 Design of OTFM Observations for the Jansky VLA

For OTFM observations, the antennas slew across a single stripe in right ascension along constant declination with a user-specified slew speed. In contrast to pointed observations, there is very little slew and settle overhead[3] since the antennas are in continuous motion over the stripe with only a small start-up ($\sim$10 s) at the start of each stripe. The phase center of the array is stepped at a user-specified intervals (typically timescales of a few seconds) in order to reduce phase smearing of the images. The interval over which the phase center remains unchanged constitutes a "scan". Over each scan, the phase center is set, by default, to be the coordinates where the antennas are pointing at the center of the scan. OTFM requires that, for fast scanning rates, the fundamental integration ("dump") times must be short (10% or less; see §5.1.1) compared to time it takes to cross the FWHM of the primary beam. Since the primary beam response pattern is moving with respect to the sky within each scan, the amplitudes must be corrected accordingly during the imaging stage. Note that for calibrator observations, standard pointed mode observations are used.

5.2 Planning of Dynamically-Scheduled OTFM Survey Observations

CNSS is meant to be a pathfinder for future wide-field surveys with the Jansky VLA, and it was observed with complete dynamic scheduling. With dynamic scheduling, only the local sidereal time (LST) constraints can be placed, and the exact time of observations cannot be predicted beforehand. This necessitated all our observing blocks to be self-contained with the standard calibrator observations. In order to determine the desirable LST ranges for our observations, we prepared a Python script[4] to simulate the position of the antennas in azimuth and elevation. This way the duration of observations, order of calibrator observations, maximum elevation of antennas, antenna wrap, proximity of sources to the Clarke belt, can be tracked and optimized. The script takes the coordinates of the calibrators, bounding box of the survey region, the slew speed for OTFM observations, the duration and order of calibrator/OTFM observations, and the start LST as input parameters. The algorithm for the simulator script is relatively straightforward:

1. Start the antennas at an arbitrary azimuth (AZ) and elevation (EL). Count the time and for each time increment check the user-specified order of scans for the following.

2. If a calibrator is to be observed next, then slew to the current AZ and EL of that calibrator source and track the source for the user-specified duration.

3. If OTFM observations to be carried out next, then slew to the required part of the survey region, then slew the antennas across a single stripe in right ascension along constant declination with a user-specified slew speed. Repeat the slew in adjacent stripes till the user-specified duration is complete.

[3] For the Jansky VLA, acceleration, slew rate, and settling time are 2.2 deg s^{-2}, 20 deg min^{-1} (elevation) and 40 deg min^{-1} (azimuth), 5–10 s respectively

[4] Plans of incorporating this script into CASA are currently underway.

Figure 5.2 shows the plot of the azimuth and elevation simulated for one of our scheduling blocks executed on 21 Dec 2013. The assumed starting location of the antennas is right ascension and declination of 0^o, corresponding to az$\simeq 100^o$ and el$\simeq 10^o$ at the specified start LST of 18h. The blue line denotes the motion of the antennas during the observation. At the beginning of the observation, the antennas slew to a tertiary calibrator (denoted by magenta circles), J2101+0341, which is observed once at the beginning and once towards the end of the observation. A secondary calibrator (denoted by green circles), J2136+0041, is then observed, followed by the gain calibrator (red circles), J2212+0152. The survey region is then observed with OTFM interleaved with phase calibrator observations. At the end of the scheduling block, the flux calibrator, 3C48, and the polarization calibrator, 3C84 are observed (black circles).

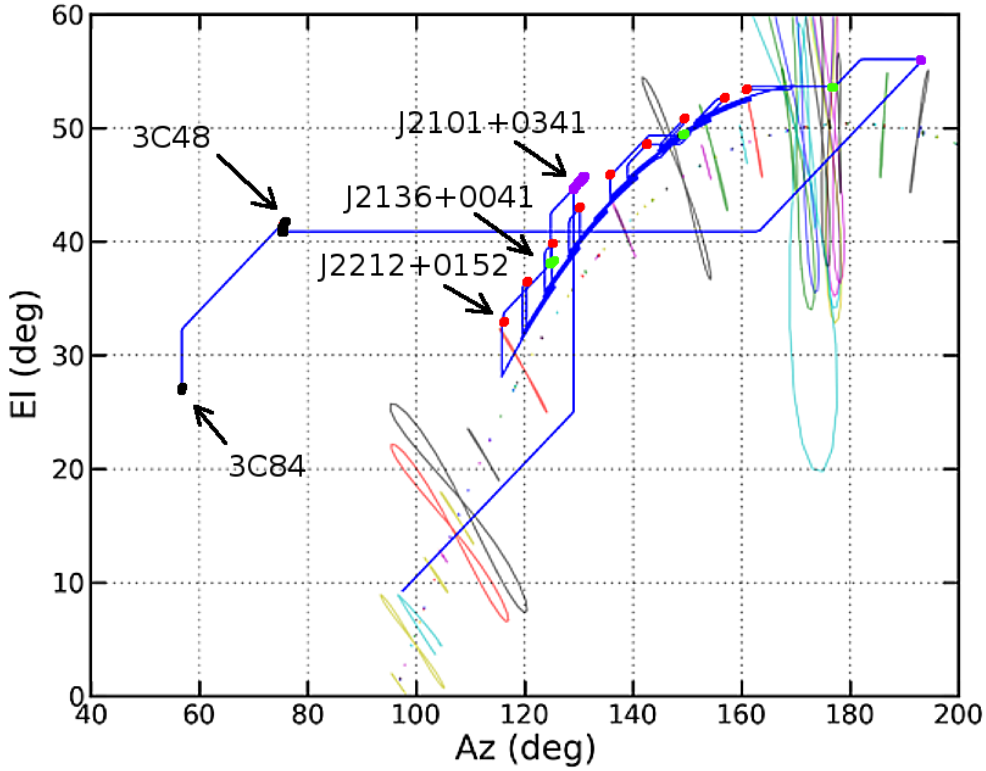

Figure 5.2: OTFM observation planning for dynamic scheduling. This plot shows the azimuth and elevation simulated for one of our observing blocks. The assumed starting position of the antennas is 0^o in right ascension and declination, corresponding to AZ$\simeq 100^o$ and EL$\simeq 10^o$ at the specified start LST. The AZ and EL of the antennas through the observation is denoted by the blue line. Tertiary and secondary calibrators are denoted by magenta and green circles respectively. The gain calibrator source is represented by red circles, and the flux and polarization calibrators, 3C48 and 3C84, are denoted by black circles. The known Clarke belt satellites (courtesy of Vivek Dhawan, NRAO) and their orbits on the sky are shown as thin colored lines. See §5.2 for details.

5.3 Observations

For the CNSS survey, observations were carried out with the Jansky VLA in B array configuration and S-band was chosen to maximize survey speed. To maximize the continuum imaging sensitivity, the observing setup chosen was: Wideband Interferometric Digital Architecture (WIDAR) correlator with 16 spectral windows, 64 2-MHz-wide channels each to get 2 GHz of total bandwidth centered on 3.0 GHz. In order to facilitate the search for fast transients and the correction of amplitudes for the primary beam response pattern as it moves with respect to the sky within each scan, we chose an integration time of 0.5 s (although for the latter 1 s integrations are sufficient). We observed independent 3 hr blocks, containing full calibration, and using dynamic scheduling. There were extra observations of calibrators from adjacent blocks included to help link the blocks. The on-source time was 2.25 hr, corresponding to a 33% overhead, mainly due to several calibrator observations. 3C48 was observed as the flux density and polarization angle calibrator while 3C84 was used as a low-polarization leakage calibrator. The OTFM scans comprising 15 stripes to cover the 2.5^o declination range, with each stripe covering 9^o (36 min) in right ascension. A scan rate of $1'$ s^{-1} was chosen to achieve a thermal noise of 80 μJy. The 15 stripes were separated in declination by $10.6'$(FWHM/$\sqrt{2}$) to obtain uniform rms noise over the survey region. Each stripe took 9.25 min to get 9 min on-source integration (3% scan overhead[5]). Typically, groups of two stripes were interspersed with calibrator scans. The correlator phase center was stepped every four seconds to avoid significant phase smearing of the images. This design of a single scheduling block yields 2025 four-second-long scans over a 22.5 deg^2 region. The setup of OTFM observations carried out on 21 Dec 2013 is shown in Figure 5.3. The log of observations used in this work is given in Table 5.1.

Table 5.1: Log of Jansky VLA observations used in this work

No.	Date (UT)	Array config.	RA range (deg)	rms (μJy)	Obs. mode	phase calib.	LST (h)
1	2012 Aug. 18	B	329.127 – 341.143	52	STD	J2212+0152	19.5 – 02.5
2	2013 Dec. 21	B	328.000 – 337.000	86	OTFM	J2212+0152	18.6 – 21.6
3	2014 Jan. 13	B	328.000 – 337.000	85	OTFM	J2212+0152	19.8 – 22.8

5.4 RFI

Since Stripe 82 is close to the Clarke belt, radio observations are prone to severe RFI from satellites in geostationary and geosynchronous (GSO) orbits. Two spectral windows (SPWs), between 2.125–2.375 GHz are severely and irreparably affected by RFI from the Satellite Digital Audio Radio Service (DARS) and satellite downlink. The RFI in the frequency range 3.62–4.00 GHz, which is also due to satellite downlink,

[5]In our pointed observations from 18 Aug 2012, we achieved a scan overhead of 14%. The on-source time for each pointing was 38 s, reaching a thermal noise of 48 μJy. For shallower surveys, the reduction in the overhead achieved with OTFM is expected to be significantly larger than with pointed observations.

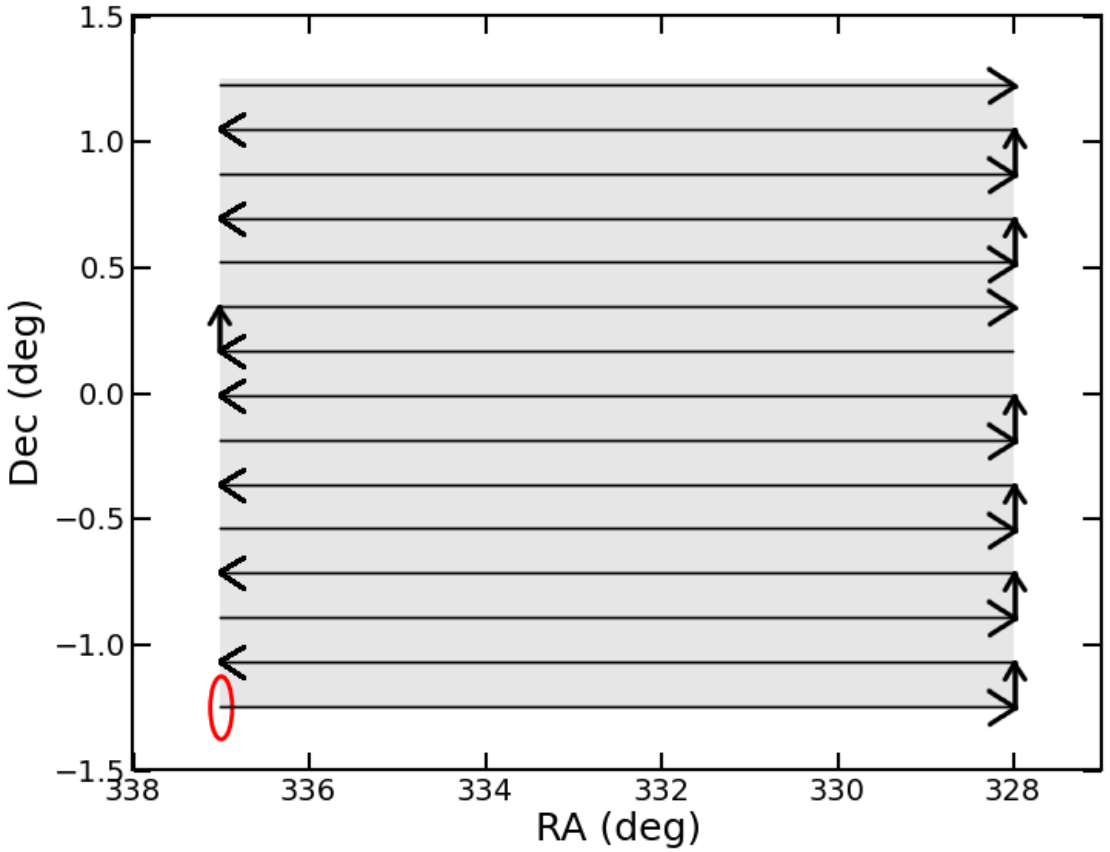

Figure 5.3: OTFM observations carried out on 21 Dec 2013. Black arrows represent the motion of antennas on the sky. Discontinuity in the arrows implies a gain calibrator or a secondary calibrator observation. Typically, groups of two OTFM stripes were interspersed with calibrator scans. The gray shaded area is the 22.5 deg^2 region observed in a single observing block on 21 Dec 2013. The red circle denotes the FWHM beam at 3 GHz. See §5.2 and §5.3 for details.

is low-level in amplitude, but it distorts the phase information quite significantly. GSO satellites seen by the Jansky VLA have not been individually characterized in terms of downlink frequencies and polarizations, but the orbits of some of these satellites are known (Figure 5.2). The RFI in the gain calibrator observations from the 21 Dec 2013 epoch is shown in Figure 5.4.

An anomalous effect of RFI on the gain values, called "gain compression", was seen in the gain calibrator observations by (Mooley et al. 2015, ApJ, submitted). This anomaly, where the amplitude gain values are reduced with respect to their true values, affects pointings that are very close to the Clarke belt (declination approximately between -3deg and -10deg). For the CNSS survey, we used gain calibrators far from the Clarke belt in order to avoid this gain compression issue. As expected, we do not find any evidence for gain compression in the gain calibrator observations in CNSS.

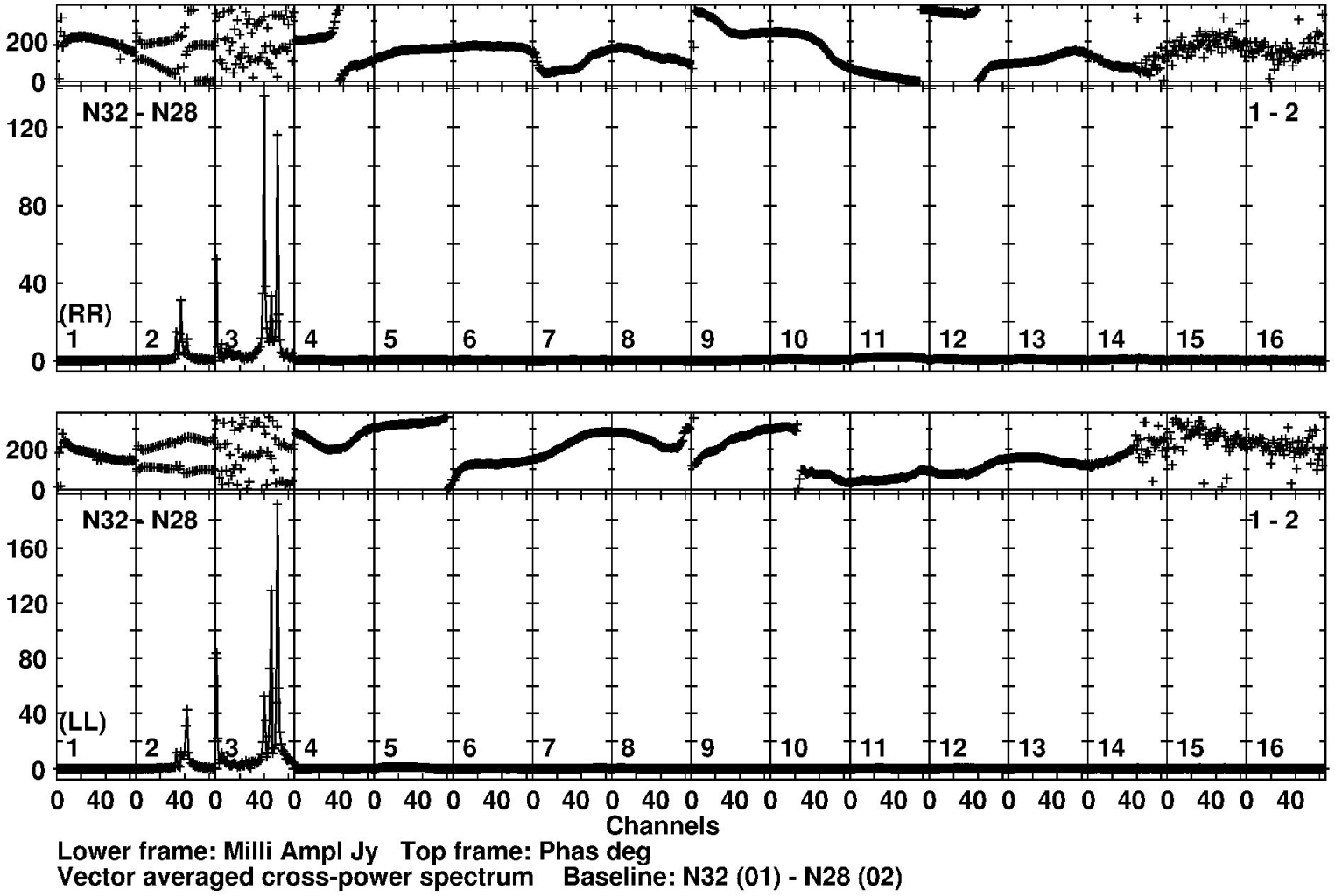

Figure 5.4: Raw spectra (2–4 GHz) of the gain calibrator source, J2212+0152, from the 21 Dec 2013 epoch, i.e. phase vs. channel (upper frame in the top and bottom panels) and amplitude vs. channel (lower frame in each panel) for the RR and LL polarizations (top panels and bottom panels respectively). All baselines and all pointings of the gain calibrator source have been combined to produce these plots. Note the large-amplitude RFI in the SPWs 2 and 3, and the distorted phased in SPWs 14–16.

5.5 Near Real Time Processing

For each observing block, the data were downloaded onto the NRAO lustre file system (typical download time of 20 min) immediately after they appeared on the VLA archive (only several minutes lag after the completion of the observations). The raw data was calibrated on a single cluster node using the AIPSLite pipeline described in Bourke et al. (2014). The calibration pipeline follows the procedures outlined in Chapter E of the AIPS Cookbook[6] with slight modifications as detailed below. First, the data is loaded with the Obit task BDFIn. Band edges, IF edges, and sub-bands 2 and 3 (2.12–2.38 GHz; found to be irreparably corrupted by RFI in all observations) are flagged using the task UVFLG. Sub-bands 14, 15, and 16 are also entirely flagged due to low-amplitude RFI from Clarke belt satellites causing the phase errors in majority of the scans. The pipeline then derives the delay, bandpass, and complex gain solutions using the FRING, BPASS, SETJY, CALIB, GETJY, and CLCAL tasks. RFLAG is used to flag all target pointings and the flags are applied using the UVCOP task. The derived calibration is applied and the calibrated dataset is produced with the SPLAT task. Finally, the calibrated UV data is saved to disk using the task FITTP. During the pipeline process several diagnostic plots are generated to assess the quality of the calibration: bandpass solutions, antenna gains as a function of time, calibrated spectrum of the gain calibrator, and calibrated amplitude versus phase plots of the gain calibrator per pointing. The calibration step required 8 hours for a single observing block.

The calibrated UVFITS data were imported into CASA as measurement sets. The imaging was carried out in a distributed fashion over 60 cores across five computer cluster nodes at the NRAO in Socorro. Before the imaging step, we clipped the visibility amplitudes of all SPWs at a threshold determined by the SPW with the least RFI. For each SPW, a RFI-proxy value was calculated as the sum of the mean and three times the standard deviation of the scalar-averaged amplitude. The clipping amplitude was then chosen to be the least of the RFI-proxy values. After the clipping of visibility amplitudes, all 2025 scans were imaged with CASA *clean* such that one core is assigned one scan. We used 500 iterations per scan and natural weighting with a *cyclefactor* of 4.5. A common $3''$ circular restoring beam was chosen to facilitate the coaddition of scans in the image plane. 2800×2800 pix^2, $0.75''$ pix^{-1} images, uncorrected for the primary beam, were produced and then sub-imaged to 1700×1700 pix^2 using the image analysis toolkit in CASA. 1700 pixels corresponds to 20% of the primary beam at 3 GHz. The CASA images were exported to FITS format and combined into a mosaic using the AIPS task *FLATN* after correcting for the primary beam. The imaging step required 3 hours for a single observing block. The median rms noise for the two OTFM epochs considered here, from 21 Dec 2013 and 13 Jan 2014, is 86 μJy, while the theoretically expected value is 80 μJy.

[6] http://www.aips.nrao.edu/cook.html

5.6 Final Processing

We carried out the RFI flagging and calibration using a custom-developed pipeline in CASA, which required $\sim$9 hours for a single observing block. The OTFM observations do not differ in the technique of calibration from normal, pointed, observations. Two spectral windows, between 2.12–2.38 GHz, are severely and irreparably affected by RFI, and was excised in all cases before the calibration. The RFI in the frequency range 3.62–4.00 GHz is low-level in amplitude, but it distorts the phase information quite significantly. Hence, the three spectral windows lying within this frequency range are flagged before calibration as well. To mitigate RFI, we also clipped the visibility amplitudes of all SPWs at a threshold determined by the SPW with the least RFI. For each SPW, a RFI-proxy value was calculated as the sum of the mean and three times the standard deviation of the scalar-averaged amplitude. The clipping amplitude was then chosen to be the least of the RFI-proxy values. Through tests, we ensure that this clipping threshold was robust and did not alter the flux densities and spectral indices of sources. For some SPWs, amplitude calibration errors were detected; such SPWs were flagged automatically in cases where the mean calibrated amplitude was larger than that in the SPW with the least RFI by the RFI-proxy value in the latter. Altogether, almost 35% of the data was flagged.

After RFI flagging and calibration, we derived and applied a single phase-only self calibration solution to every scan containing a source brighter than 10 mJy in the near-real-time image. Joint deconvolution incorporating wide-bandwidth AW-projection (Bhatnagar et al. 2013) with correction for the primary beam moving within each scan is an imaging mode ideal for OTFM imaging, but currently under development. This capability has been incorporated as task *tclean* in the CASA developer version; we have performed preliminary imaging tests using *tclean*, but additional tests are required in order to come up with final image products. Instead, we used an imaging strategy similar to that used in the near-real-time processing. The resulting mosaic, having a median rms noise is 85 μJy, is shown in the top panel of Figure 5.5.

The AIPS task RMSD was used to create an rms image of the mosaic and this was supplied as input to SAD. Source-finding was then carried out with SAD to find sources with SNR$>$5. These 5σ catalogs were used for our analysis (flux density comparison) presented in §5.7.

5.7 Comparison Between Epochs

Figure 5.5 shows 10 deg^2 mosaics from OTFM observations carried out on 21 Dec 2013 and standard pointed observations done on 18 Aug 2012. As reported in Mooley et al. (2015, ApJ submitted), the pointed observations were not designed to give a uniform rms noise over the survey region. Most of the differences seen in the mosaics from Figure 5.5 are due to the non-uniform sensitivity. Other differences arise from the UV coverage, but otherwise the mosaics agree quite well with each other. This is demonstrated by the image cutouts from the pointed and OTFM observations shown in Figures 5.6 and 5.7.

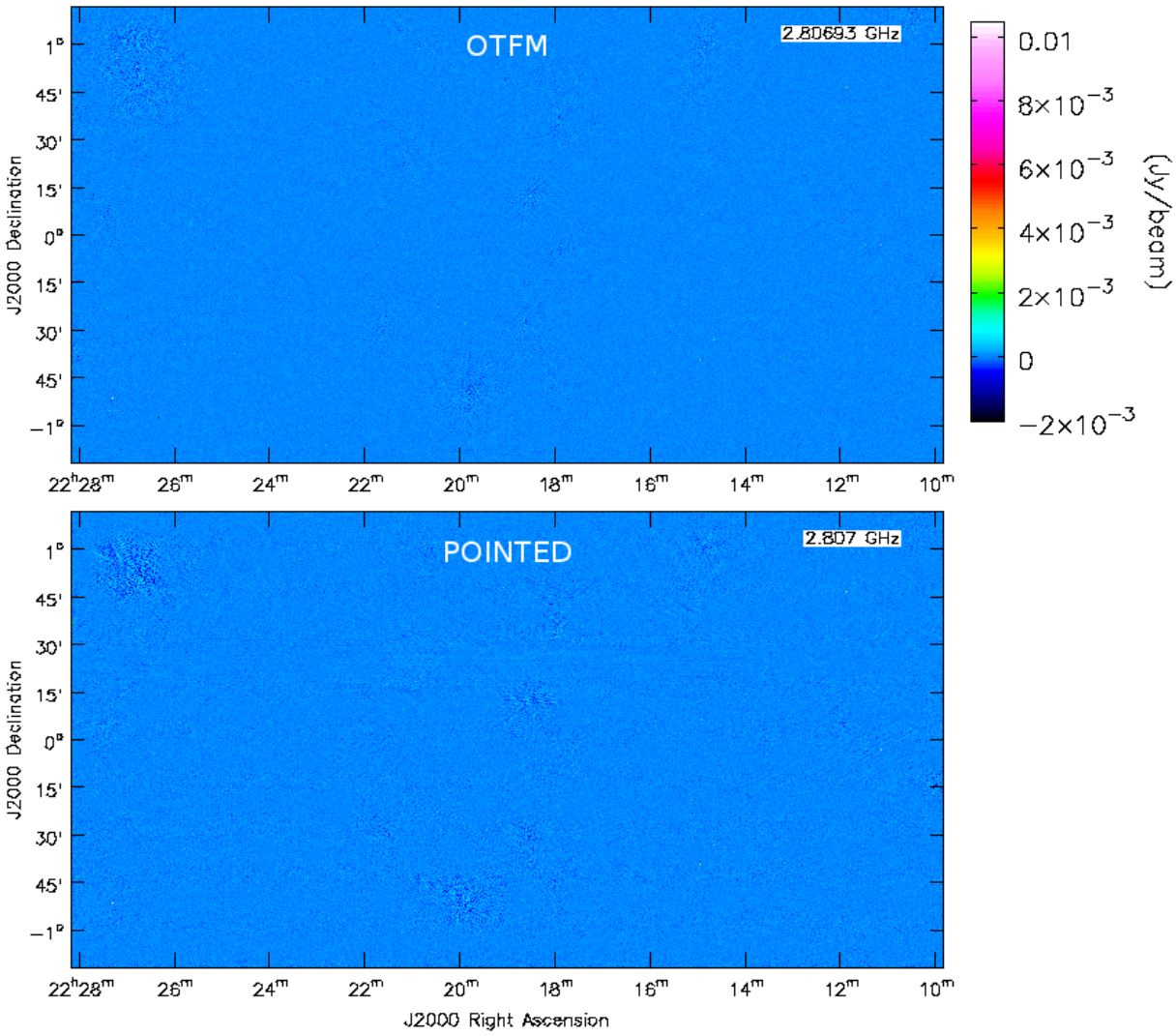

Figure 5.5: The mosaic from the final processing of the CNSS data from the 21 Dec 2013 epoch (top), having a median rms noise is 85 μJy. The mosaic shown at the bottom is from the pointed observations carried out on 18 Aug 2012. Apart from the differences in imaging resulting from different UV coverages and non-uniform rms noise for the pointed observations, these two mosaics agree quite well with each other.

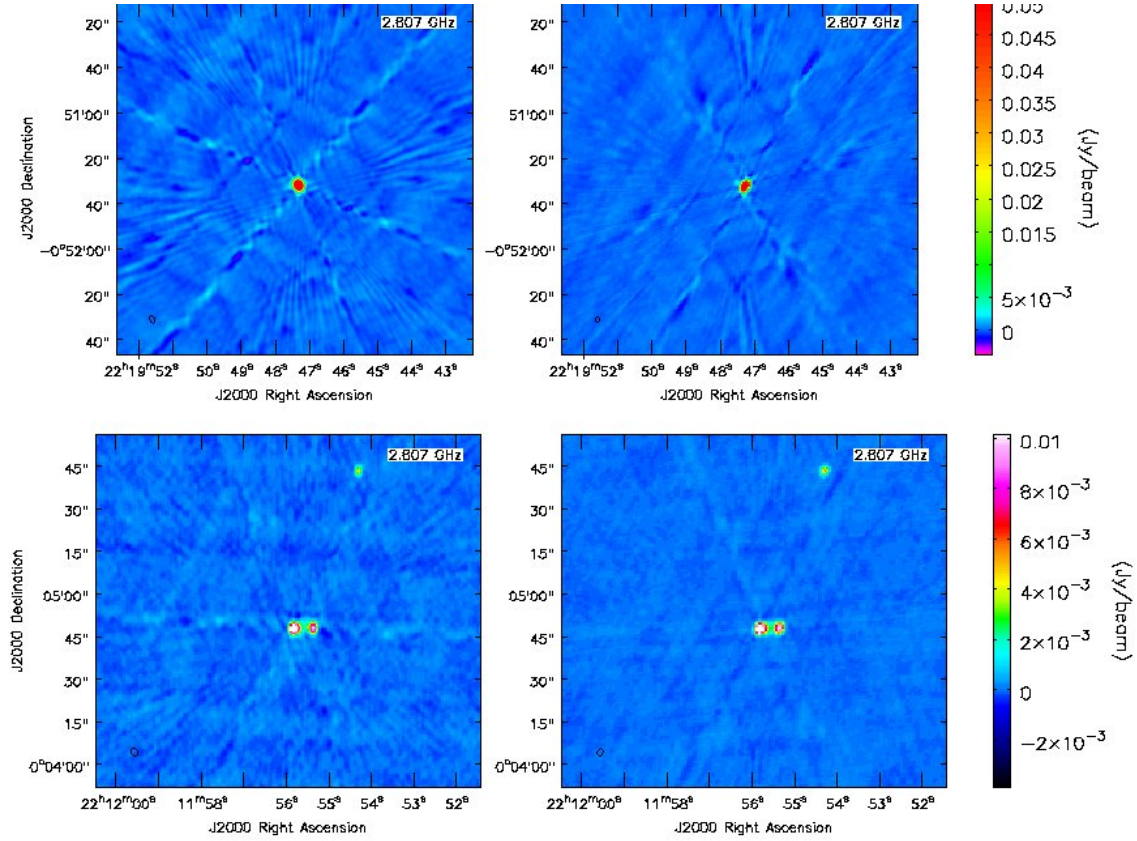

Figure 5.6: Cutouts of a "bright" (300 mJy; top panels) source and of sources with moderate flux densities (several mJy; bottom panels). The panels on the left are from the pointed observations carried out on 18 Aug 2012, and those on the right are from the 21 Dec 2013 OTFM observations.

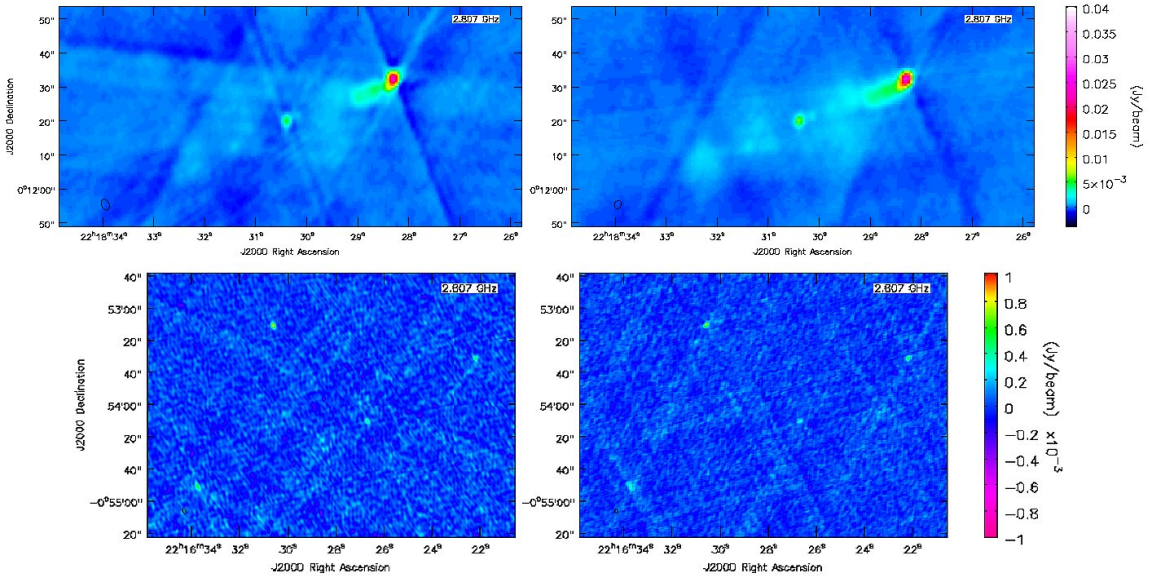

Figure 5.7: Same as Figure 5.6, but for an extended source (top panels) and for "faint" (sub-mJy; bottom panels) sources.

We compared the peak flux densities of all probable point sources[7] having SNR>10 between two OTFM epochs, and between pointed and OTFM observations (the 21 Dec 2013 epoch; Figure 5.8). We used the mean absolute deviation of flux densities between the two epochs as a measure of how accurately the source flux densities can be reproduced between two epochs. It is evident from these figures that the source flux densities are reproduced quite accurately in all cases except for sources having flux densities between 10–60 mJy. We note that, while the exact cause of this discrepancy has not been found yet, this "excess variability" is also seen when two epochs of pointed observations are compared with each other. Nevertheless, we can conclude from Figure 5.8 that the source flux densities are reproduced well within 10% between two OTFM observing epochs as well as between pointed observations and OTFM observations.

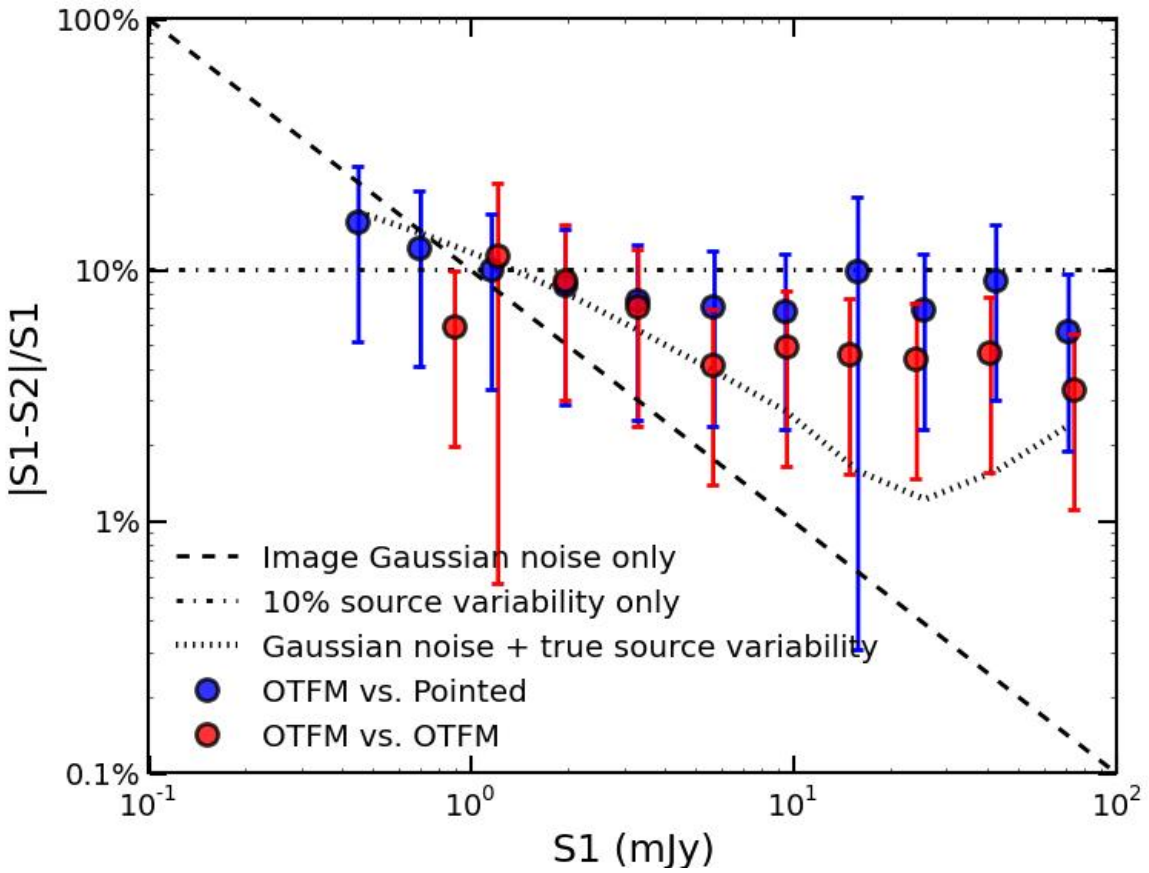

Figure 5.8: The mean absolute deviation (MAD) of source flux densities between OTFM observations from the 21 Dec 2013 epoch and pointed observations from the 18 Aug 2012 epoch are shown as blue points. The comparison between OTFM observations from two epochs is also shown (red points). Only point sources with SNR>10 have been considered here. For reference, we show the MAD expected from purely Gaussian image noise (dashed line), 10% fractional variability of all sources (dot-dashed line), and from the Gaussian noise and true source variability as seen by Ofek et al. (2011) (dotted line). See §5.7 for details.

[7]Selected as having the ratio of integrated to peak flux densities less than 1.2.

5.8 Summary & Conclusions

In this work we have presented a subset of Jansky VLA observations from the Caltech-NRAO Stripe 82 Survey (CNSS) carried out with OTFM technique, where the the antennas are driven at a non-sidereal rate and visibilities are recorded continuously. We find that, OTFM observations significantly reduce the slew-and-settle overheads as compared with pointed observations requiring on-source time of less than $\sim$30 s per pointing. Thus, for the Jansky VLA, OTFM substantially improves the efficiency for wide-field shallow surveys. We therefore encourage OTFM observations for science cases such as transient searches, requiring multiple shallow passes over wide areas on the sky. Through the use of newly-developed imaging techniques in the CASA package, we have also demonstrated that the flux densities of sources can be reliably and accurately reproduced not only between two epochs observed using OTFM, but also and between pointed observations and those observed with the OTFM technique.

We have many test observations (taken as part of the RSRO program at NRAO), utilizing different OTFM scan rates, that have not been analyzed. This data will be useful for understanding the imaging quality for different scan rates. Testing of the joint deconvolution mode in CASA incorporating wide-band AW projection and pointing tables is also left as future work.

Bibliography

Bhatnagar, S., Rau, U. & Golap, K. 2013, ApJ, 770, 91

Bourke, S., Mooley, K., Hallinan, G. 2014, ASPC, 485, 367

Booth, R. S., & Jonas, J. L. 2012, AfrSk, 16, 101

Frail, D. A., Kulkarni, S. R., Ofek, E. O., Bower, G. C., & Nakar, E. 2012, ApJ, 747, 70

Johnston, S., Taylor, R., Bailes, M., et al. 2008, Experimental Astronomy, 22, 151

Ofek, E. O., Frail, D. A., Breslauer, B., et al. 2011, ApJ, 740, 65O

Oosterloo, T., Verheijen, M., & van Cappellen, W. 2010, ISKAF2010 Science Meeting

Perley, R. A., Chandler, C. J., Butler, B. J., & Wrobel, J. M. 2011, ApJ, 739, L1

Pety, J. & Rodriguez-Fernandez, N. 2010, A&A, 517, A12

D'Addario, L. R. & Emerson, D. T. 2010, ALMA Memo 331

Chapter 6

The Caltech NRAO Stripe 82 Survey (CNSS) Paper III: Prime Candidates for Slow Radio Transients

Majority of the contents of this chapter will go into a paper in prep: Mooley, et al. (2015)

Abstract

The Caltech-NRAO Stripe 82 Survey (CNSS) is the first dedicated radio transient survey with the Karl G. Jansky Array (VLA) carried out in near-real-time. This 270 $\deg^2$ three-epoch survey, having a single-epoch rms noise of 80 μJy, is aimed at the systematic exploration of the dynamic radio sky on timescales between a few days and one decade. Four prime candidates for slow transients are reported here. Two of these radio transients are coincident with the spiral arms of local galaxies (z<0.05) and have radio spectral luminosities larger than those expected for radio supernovae. This therefore points to alternative possible causes, such as binary neutron star merger events, based on the expected rates. Another transient is coincident with the nucleus of a z=0.04 star-forming galaxy and is a promising candidate for a non-thermal tidal disruption flare. The final transient is a cataclysmic variable that is likely harboring a jet.

6.1 Introduction

Exploration of the dynamic radio sky lags far behind the optical and X-ray, where dedicated synoptic survey facilities are well established. For the first time, we are using the Karl G. Jansky Very Array (VLA) to systematically explore the radio sky for slow transient phenomena (timescales $>$1 second). Between November 2013 and March 2014 we carried out the Caltech-NRAO Stripe 82 Survey (CNSS), a sensitive 270 deg^2 dedicated radio transient survey. To enable near-real-time transient search, we performed rapid data editing, calibration, imaging, source cataloging, and catalog cross-matching using dedicated hardware at the NRAO in Socorro. The observations were done over three epochs, each having rms noise of $\sim$80 μJy, over a span of three months. This survey probes a large, unexplored, part of the phase space of slow radio transients, and is capable of discovering rare extragalactic transients such as radio supernovae, jetted tidal disruption events, and binary neutron star merger events (Figure 6.1). While past blind surveys dedicated to slow transient search have suffered from limitations such as delayed identification and follow-up observations, ambiguous transient classifications, and contamination by false positives due to imaging artifacts, our near-real-time survey eliminates these pitfalls. We note that, in literature, there exist only a few radio transients identified through blind surveys, and among these, there exists only a single definitive classification of an extragalactic transient: the radio supernova from Levinson et al. (2002) and Gal-Yam et al. (2006). In contrast, the CNSS represents a benchmark study committed to finding and unambiguously classifying extragalactic transients.

There is a rich yield ($\sim$40) of radio transients from the CNSS survey. Majority of these are associated with extreme AGN phenomena similar to those found in the CNSS pilot survey (Mooley et al. 2015, ApJ, submitted). However, among these interesting set of objects, are also four intriguing slow transients; three of these are extragalactic and one is a Galactic transient. These four transients, described in detail in this chapter, represent a small sample of the results from CNSS. At the same time, the discovery of these transients marks the culmination of this thesis. Additional VLA and VLBA observations have been awarded for the four, high-impact, transients and will occur shortly. This chapter presents an initial interpretation of these transients.

6.2 The Selection of Prime Slow Radio Transients

The Caltech-NRAO Stripe 82 Survey (CNSS) was carried out using the new on-the-fly (OTF) observing mode with the VLA. A description of the survey is provided in Chapter 5 of this thesis. After solving many of the RFI flagging, calibration, and imaging challenges associated with OTF, strong satellite RFI, and also with the wide bandwidths, we were able to confirm 28 genuine variable and transient candidates, varying in flux density by a factors of two or more, within our survey epochs. We have also selected 7 sources undetected in the FIRST (White et al. 1997) and VLA-Stripe 82 (Hodge et al. 2011) surveys, and having the 1.4 GHz flux densities varying by more than a factor of ten[1] with respect to these surveys. Through a meticulous selection

[1]From our S-band survey, we used the spectral index between 2 GHz and 4 GHz to find the expected 1.4 GHz flux density. A 3 GHz flux density threshold of 4 mJy was also used.

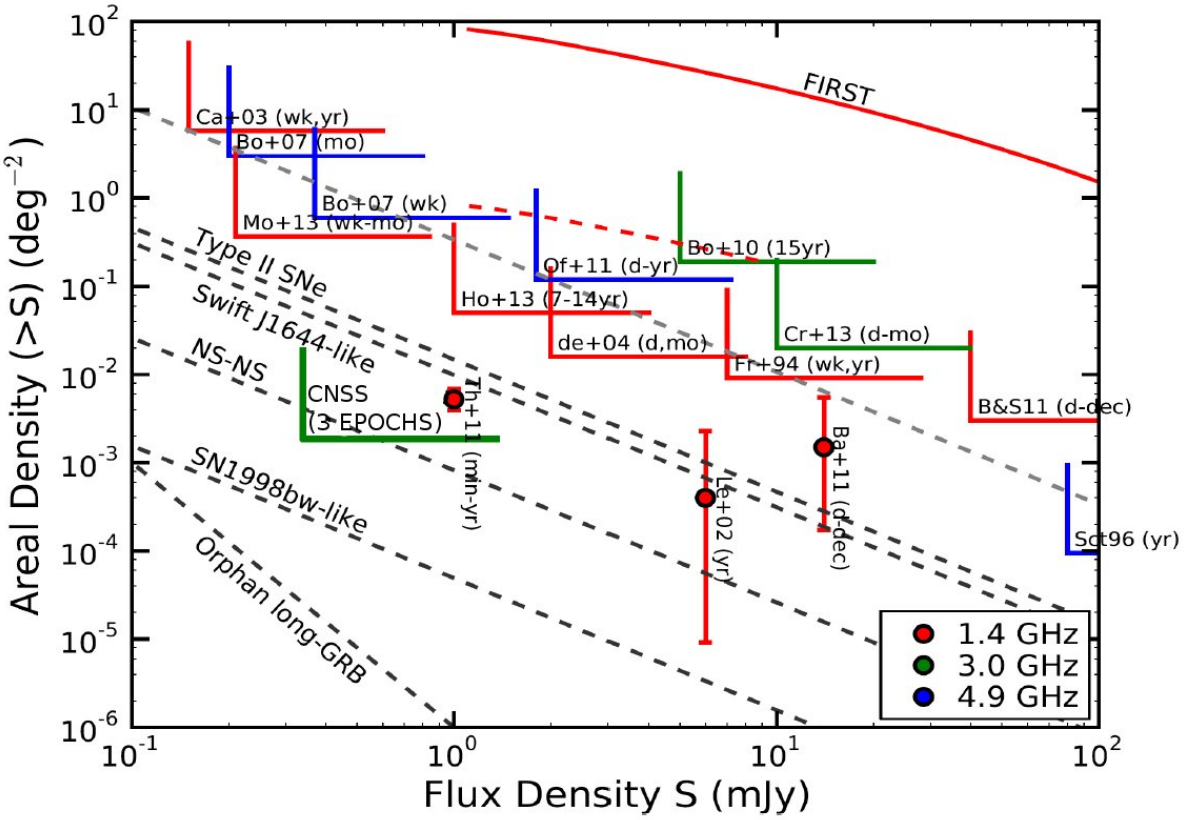

Figure 6.1: A log N - log S diagram showing the large, unexplored, part of the phase space of slow radio transients explored by the three-epoch CNSS survey. Based on expected rates (dashed black lines) this survey is capable of discovering rare extragalactic phenomena such as radio supernovae, jetted tidal disruption events, and binary neutron star merger events. The region of the phase space explored by past surveys resulting in non-detection of transients are shown as wedges, while the rates calculated from transient detections in blond surveys are marked as errorbars. The color coding is according to observing frequency. The persistent source counts from the FIRST survey are shown as the red solid line.

procedure and a detailed multi-wavelength follow-up program lasting several months, we have identified four unambiguous high-impact candidates. This intricate procedure was necessary to rule out false positive (imaging and calibration artifacts) and active galactic nucleus variability scenarios.

For finding our prime extragalactic transients, we selected all optical sources in SDSS Stripe 82 that had r-band magnitude of less than[2] 21, and cross-matched them with all the radio sources in our CNSS coadd catalog within $1'$ radius. This resulted in $\sim$900 matches and we inspected the corresponding optical image cutouts by eye to short list those radio sources that were located in proximity with a nearby galaxy[3]. We found five radio sources satisfying these criteria. One of them, VTC2346+01, is $10''$ offset from the center of a z=0.09 galaxy, but has a background source having a near-infrared K-band magnitude of 18.8 coincident with it. It has a flux density of 3 mJy at 1.4 GHz in our radio follow-up observations in 2014 as well as in the FIRST survey image from 1996, and hence does not qualify as a transient, Another source, VTC0115-00, is coincident with an intense star-forming region in a local starburst galaxy at z=0.006. A 3 GHz flux density of 1.1 mJy in CNSS (epoch 2014) and a 1.4 GHz flux density of 0.8 mJy in FIRST (epoch 1996) suggest that it is a very slowly evolving source, while the radio luminosity of 6×10^{26} erg cm^{-2} s^{-1} further advocates the nature of this source as a supernova remnant. The remaining three sources are intriguing extragalactic objects that are a subset of the 7 transients found by comparing CNSS with the FIRST and VLA-Stripe 82 surveys. Two of these transients, VTC0303-00 and VTC0309+01, are coincident with the spiral arms of local galaxies ($<$300 Mpc) and are excellent candidates for binary neutron star (BNS) mergers as indicated by their radio luminosities (Figure 6.2). These two sources appear to be not varying significantly on $\sim$month timescales and are likely old transients that are past peak luminosity. The third transient, VTC0141+00, is coincident with the nucleus of a z=0.04 star-forming galaxy and is a promising candidate for a non-thermal tidal disruption event (TDE).

Our fourth and final high-priority transient is a Galactic one: a cataclysmic variable (CV) that underwent a flaring episode and may harbor a jet. A summary of these transients is provided in Table 6.1.

6.2.1 VTC0141+00 and VTC0303-00

In VLA follow-up observations from May 2014 VTC0141+00 and VTC0303-00 have flux densities of 3–4 mJy at 1.4 GHz, while they are undetected in the FIRST survey (mean epoch 1999; 3σ upper limit of 0.4 mJy). The follow-up reveals a steep radio spectrum for VTC0303-00 and a Gigahertz-peaked spectrum for VTC0309+01. The radio follow-up spectra of the two transients is shown in Figure 6.3. Based on our survey and follow-up observations, VTC0303-00 and VTC0309+01 appear only slightly variable at frequencies of a few GHz on a timescale of four months. In the optical, VTC0141+00 and VTC0303-00 lie along the spiral arms of galaxies at redshifts 0.07 and 0.03 respectively. Their 3 GHz radio luminosities at these distances

[2]The magnitude has been used as a proxy for the distance. By selecting r$<$21 mag. galaxies we are ensuring the selection of local Universe galaxies (z$\lesssim$0.05) with $>$90% completeness. For reference, a typical Milky Way-like galaxy will have a magnitude of 17 and a LMC-like galaxy will have a magnitude of 24 at z=0.05.

[3]Angular size used as a crude proxy for distance.

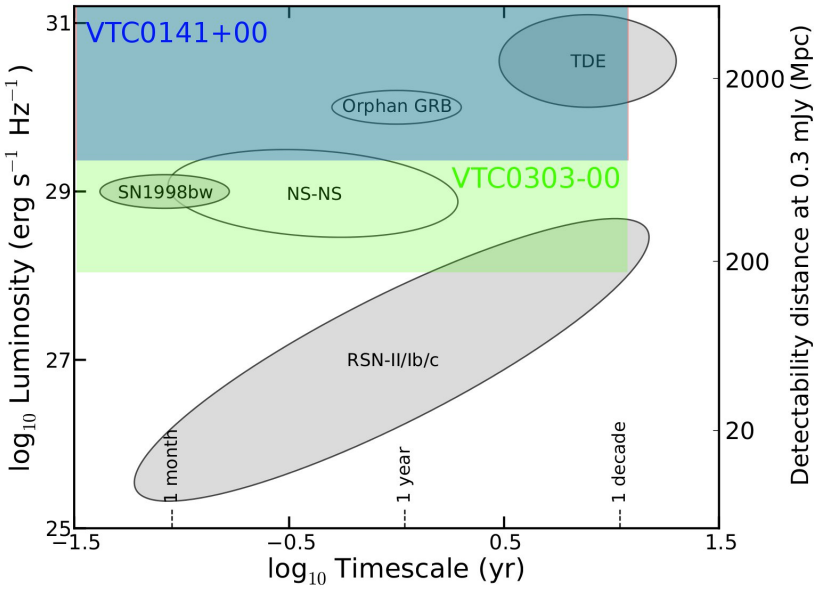

Figure 6.2: The predicted peak spectral luminosity vs. evolution time scale at 3 GHz for the different classes of extragalactic radio transients detectable in the CNSS survey. White zones correspond to optically thin sources, while gray zones represent sources that are expected to be optically thick before maximum light and optically thin afterwards. Also shown is the detectability distance for these events in our survey. The blue shaded box corresponds to the region occupied by the radio transient VTC0141+00. The blue and green shaded boxes correspond to the region occupied by VTC0303-00.

at the time of our radio follow-up observations are 3.6×10^{29} and 1.8×10^{28} erg s^{-1} Hz^{-1} respectively. The location of these transients within the host galaxies and their radio luminosities are consistent with radio supernovae (RSN), orphan long-duration GRB afterglows (OAs), BNS merger events. From Palomar Transient Factory data we see no evidence for an optical transient at the locations of VTC0303-00 and VTC0309+01 between 2009 and October 2014. Using deep infrared follow-up observations obtained from Keck/MOSFIRE in October 2014 along with radio-to-infrared flux ratios, we are able to rule out the association of these two transients with background AGN at redshifts z$<$0.5 and z$<$3 respectively (Figure 6.4). Independently, we can use the rates of extreme variability of AGN from Mooley et al. (2015, ApJ, submitted) to rule out the association of these transients with background AGN. Based on the rates[4] of extragalactic radio transients (Gal-Yam et al. 2006; Nakar & Piran 2011; Ghirlanda et al. 2014; Frail et al. 2012, Mooley et al. 2015, ApJ, submitted), the CNSS survey is likely to find a few RSN, one BNS merger event, and no OAs respectively. It is therefore possible that VTC0141+00 and VTC0303-00 are RSN or BNS merger events where the prompt emission counterparts were not detected in X-rays or γ-rays. The detection of radio emission from BNS mergers has implications on the search for radio counterparts to aLIGO sources and the jet beaming angle in short GRBs. The radio luminosity of VTC0303-00 is consistent with that of a RSN, but VTC0141+00 may be too bright to be explained by a RSN scenario (e.g. Weiler et al. 2002, Soderberg et al. 2010). VLBA observations of these two transients will be useful for constraining the size of the ejecta and hence constrain the date of merger / explosion.

6.2.2 VTC0309+01

This transient has a flux density of a few mJy at 1.4 GHz in the VLA follow-up observations carried out in May 2014, and was undetected in the FIRST survey (mean epoch 1995.7; 3σ upper limit of 0.4 mJy). We obtained radio follow-up observations of this transient in two epochs: April and June 2014. The radio follow-up spectra and the optical spectroscopic and imaging data (from SDSS) for VTC0309+01 is shown in Figure 6.5. Between these epochs, VTC0309+01 shows a peaked spectrum where the peak frequency evolves towards lower frequencies, possibly indicating synchrotron emission from a fast outflow interacting with the ambient medium. In the optical, VTC0309+01 coincides with the nucleus of a galaxy at a redshift of 0.04. Emission line ratios obtained from the optical spectrum of this host from the SDSS BOSS program suggest that it is a star-forming galaxy. The evolution in the radio spectrum and the association with the nucleus of a star-forming galaxy make this radio transient a strong TDE candidate similar to the non-thermal tidal Swift J1644+57 (Zauderer et al. 2011, 2013). The 3 GHz radio spectral luminosity of VTC0309+01 on June 2014 was 3.5×10^{29} erg s^{-1} Hz^{-1}, which is a factor of 30 lower than the peak spectral luminosity of Swift J1644+57.

[4] see http://www.tauceti.caltech.edu/kunal/radio-transient-surveys/index.html for a compilation of expected transient rates.

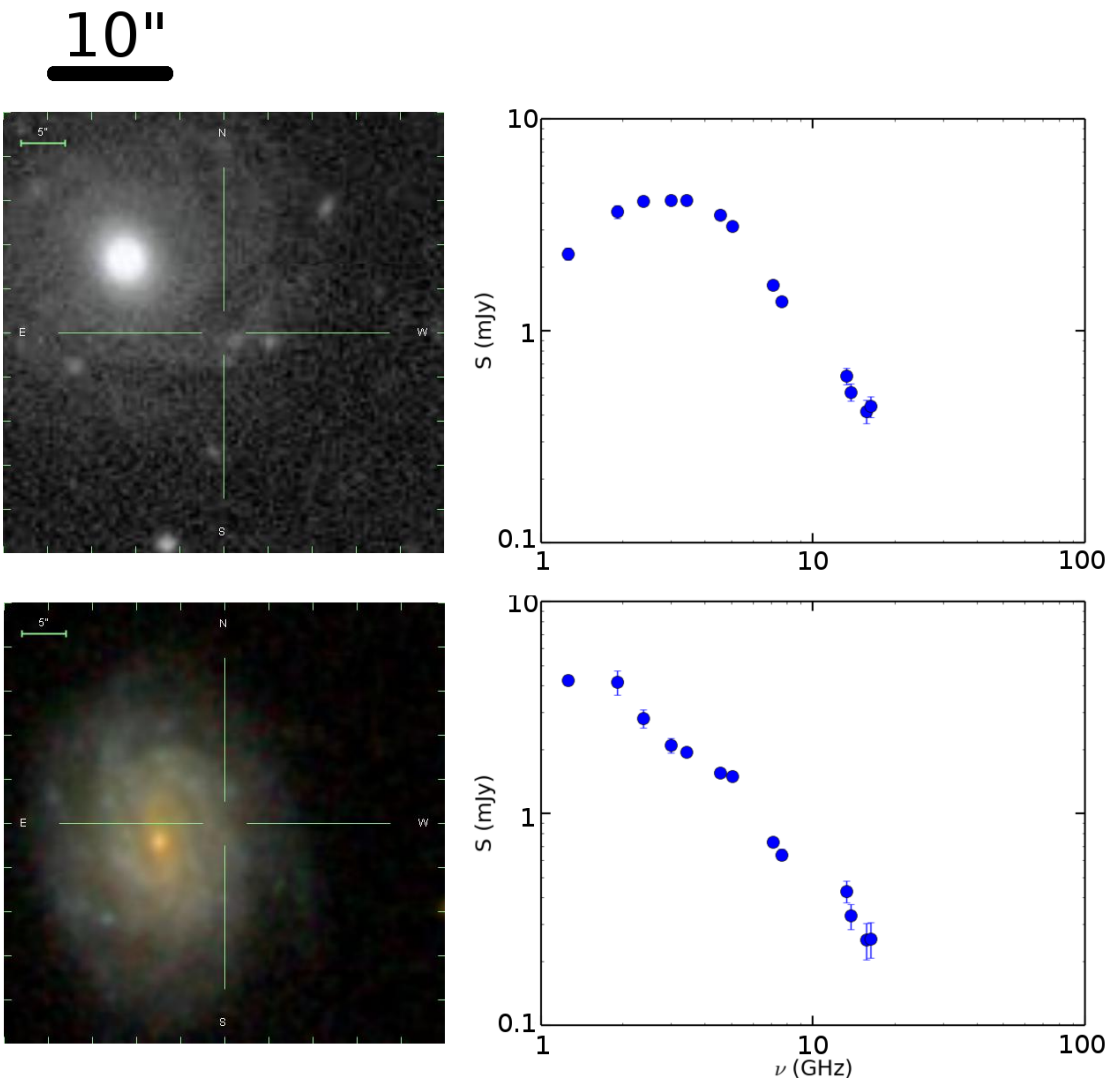

Figure 6.3: SDSS cutouts and radio continuum spectra of the two BNS merger candidates, VTC0141+00 and VTC0303-00, from follow-up observations carried out in May 2014. These two transients are undetected in the FIRST survey (3σ upper limit of 0.4 mJy from mean epoch 1999) and appear to have evolution timescales of several months.

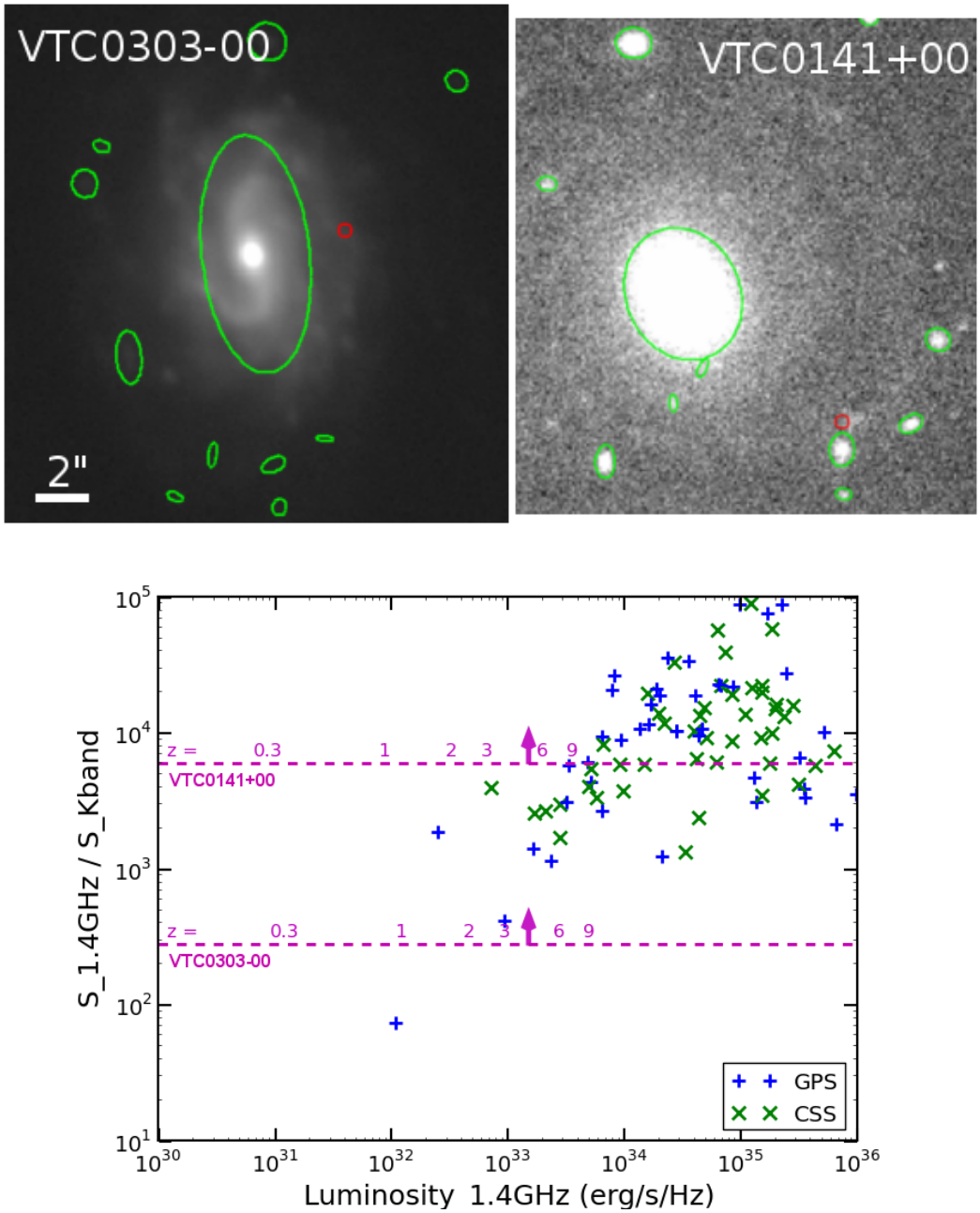

Figure 6.4: *Top*: Deep Keck/MOSFIRE infrared Ks-band images at the locations of VTC0303-00 and VTC0141+00 (marked by the red circles having 0.5″radius) taken in October 2014. The sources are not detected with limiting magnitudes of Ks=22.8 and Ks=19.1 respectively. Sources marked with green ellipses are $>5\sigma$ sources from SExtractor. These observations rule out a background AGN hypothesis to a high significance and make the association of these transients with the spiral arms of the galaxies more likely. *Bottom*: The ratio of the 1.4 GHz and near-IR K band flux densities plotted against the 1.4 GHz radio spectral luminosity. These quantities are plotted for VTC0303-00 and VTC0141+00 as pink dashed lines (note that these are lower limits along the y-axis) assuming that these transients are not associated with galaxies in the local Universe and that their distance is unknown. A compilation of GPS and CSS sources from O'dea (1998) are also shown. Based on the trend displayed by the O'dea (1998) sources, we are able to rule out the association of VTC0303-00 and VTC0141+00 with background AGN at redshifts z<0.5 and z<3 respectively.

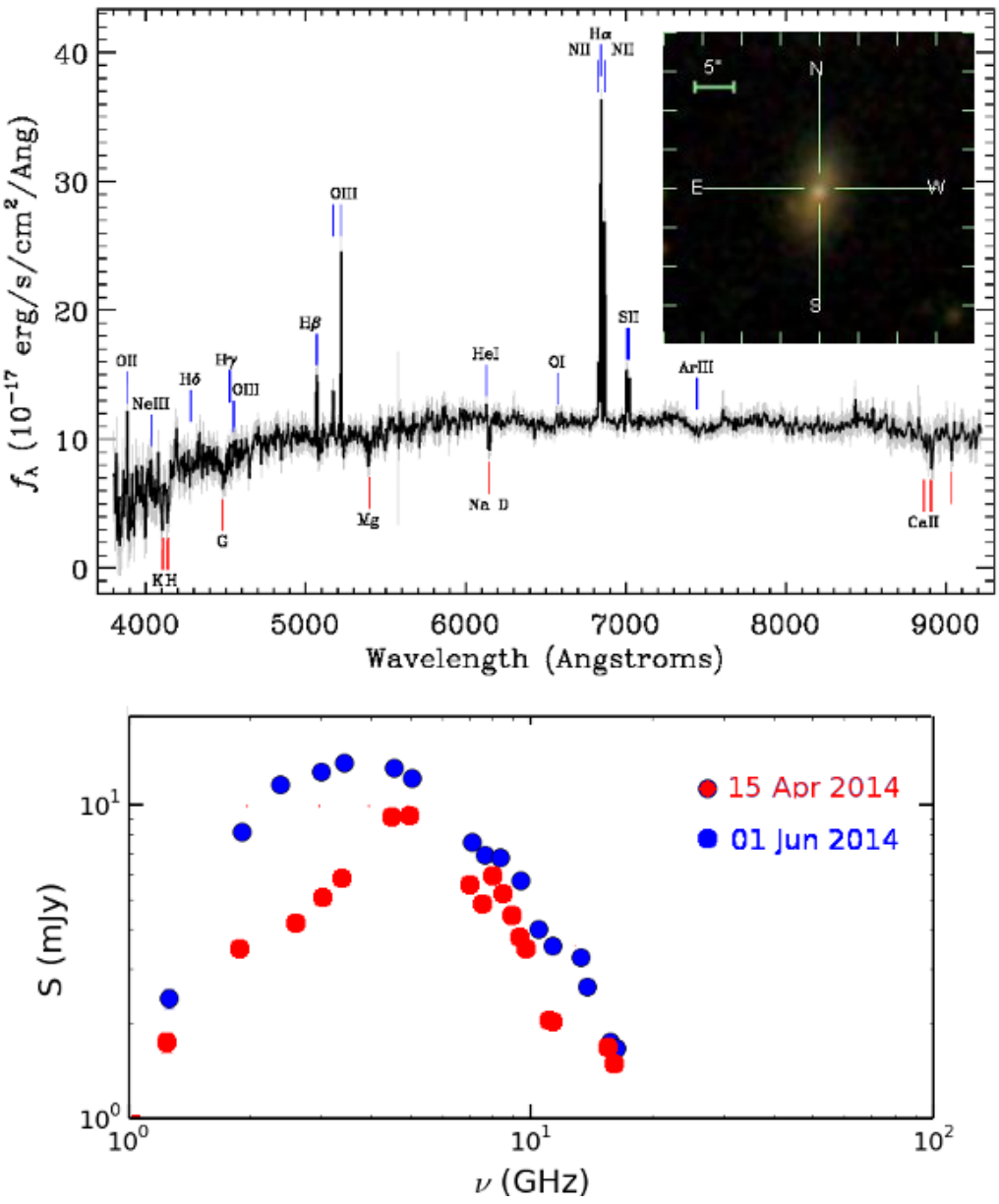

Figure 6.5: VTC0309+01, a likely tidal disruption event discovered in our JVLA survey of the Stripe 82 region. The top panel shows the optical spectrum consistent with a star-forming galaxy at 170 Mpc (z=0.04; inset shows the image cutout with the radio source being coincident with the nucleus of this galaxy) from SDSS and the lower panel shows the evolution of the radio continuum spectrum in two follow-up epochs. The non-detection in the FIRST survey (3σ upper limit of 0.4 mJy at 1.4 GHz) and the evolution of the peak of the spectrum to lower frequencies advocates the TDE nature of this source.

6.2.3 VTC2040-00

VTC2040-00 was detected as a flaring source in the first epoch of our survey in Jan 2014. The optical counterpart of this source is the CV: AE Aqr, an intermediate polar consisting of a white dwarf and a K4 main-sequence star. The white dwarf in this system has a spin period of 33 s, and is the most rapidly spinning white dwarf known till date. This CV is reasonably well-studied across the electromagnetic spectrum. However, past multi-frequency radio observations were sparsely sampled in time and did not have adequate spectral resolution. Power-law spectra were reported for the CV between 1–100 GHz (Bastian et al. 1988, Abada-Simon et al. 1993). The mechanism for radio emission suggested in literature is the propeller mechanism (Venter & Meintjes 2006, Meintjes & Venter 2005), where the material in the innermost regions of the accretion disc get ejected (propelled outward) instead of being accreted onto the white dwarf. This is due to the fact that the white dwarf is spinning much more rapidly than the innermost material in the accretion disc. We carried out follow-up radio observations with the VLA in February 2014, which reveal a flat-spectrum source below 5 GHz and a peaked spectrum at higher frequencies with a peak frequency of 10 GHz. The VLA follow-up spectrum of VTC2040-00 is shown in Figure 6.6. If blobs are expelled out one at a time by the propeller mechanism, the spectrum would be a self-absorbed synchrotron spectrum, $\nu^{2.5}$ at low frequencies. However, the flatness requires almost a continuous stream of blobs, or a jet. The nature of the spectrum thus suggests that a jetted outflow is quite a viable explanation (see also Deller et al. 2014, Russel et al. 2013). Through VLBA observations we aim at detecting a plausible jet structure in AE Aqr. We note here that, till date, there is no direct evidence of a CV harboring a jet. If a jetted outflow is detected for AE Aqr, then it would be the first direct evidence, through imaging, that white dwarfs can harbor jets.

6.3 Other Similar Transient Candidates and False Alarm Probability

As mentioned previously, we have found 7 transients by comparing the CNSS source catalog with the FIRST and VLA-Stripe 82 surveys. A summary of these transients is given in Table 6.1. Here we present a chance coincidence (i.e. false alarm) probability for these candidates to be co-located with a nearby galaxy. The SDSS BOSS catalog contains 8,000 galaxies in the Stripe 82 region having spectroscopic redshifts less than 0.05. Assuming a catalog completeness of 25%, we expect about 32,000 "local Universe" galaxies in Stripe 82. Our $1'$ criterion (see §6.2) implies a search area of 28 deg^2. The total area of Stripe 82 observed in CNSS is[5] 270 deg^2. The probability of having one source out of 7 lying within $1'$ of a nearby galaxy is therefore 28/270 $\times$ 7/10 = 7%, and the probability of having two such sources is 1%. This rather low probability of chance coincidence suggests that a (background) AGN scenario is unlikely for radio sources VTC0141+00, VTC0303-00, and VTC0309+01, and that these sources are likely associated with the optical galaxies near which they are located. The other transient candidates listed in Table 6.1 may be due to AGN phenomena and

[5]Since we have used 4 mJy as the flux density lower limit for selecting these transients, the mosaic rms noise, which varies between 47 μJy and 200 μJy (median of 55 μJy), does not affect our effective area probed, and the completeness is $\sim$100%.

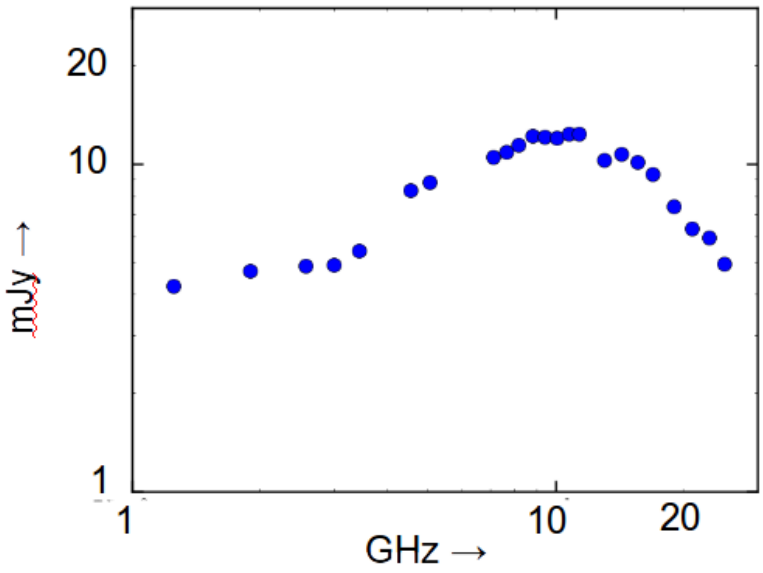

Figure 6.6: Follow-up radio spectrum of VTC2040-00, the intermediate polar AE Aqr, from February 2014 detected in outburst in our Stripe 82 survey. The flat spectrum indicates a jet as a viable explanation. If a jetted outflow is detected for AE Aqr through our proposed VLBA observations, then it would be the first direct evidence that white dwarfs can harbor jets.

are therefore low-priority.

6.4 Summary & Discussion

Through a meticulous selection procedure and detailed multi-wavelength follow-up observations we have narrowed down our CNSS transient candidate list to four high-impact transients. We have proposed for VLBA and VLA follow-up observations of these transients to better understand the nature of these objects and their evolution. We have two RSN and BNS merger candidates, VLBI observations will be important for constraining the size of the ejecta, which will directly constrain the plausible merger / explosion date. Considering ejecta speeds between 6,000 km s^{-1} (0.02c) and 60,000 km s^{-1} (0.2c), as appropriate for Type Ib/c supernovae and BNS mergers (Soderberg et al. 2010, Piran & Nakar 2011), the ejecta is expected to have an angular size between 0.6 mas and 6 mas assuming 10 years since explosion and a distance of 100 Mpc. VTC0309+01 is a tidal disruption flare candidate, and again, VLBI follow-up will be able to constrain the size of the jetted outflow, and hence constrain the date of disruption. Although less likely, some of these extragalactic transients could still be due to AGN phenomena that are not well studied (e.g. Kunert-Bajraszewska et al. 2006, 2010; Czerny et al. 2009). Through continued radio follow-up observations we will be able to distinguish between AGN and other transient classes. VTC2040-00 (AE Aqr), a cataclysmic variable, was detected as a flaring source in our survey, and its radio follow-up spectrum suggests a jetted

Table 6.1: Prime candidates for slow radio transients and other similar but low-priority objects

No.	Name	RA	Dec	Candidate Type*	S_{5GHz} (mJy; 2014.1 epoch)
			Prime Candidates		
1	VTC2040-00	20:40:09.22	-00:52:14.53	CV with jet	4.0
2	VTC0141+00	01:41:53.08	+00:37:18.7	BNS	3.8
3	VTC0303-00	03:03:49.98	-00:12:14.2	BNS / RSN	1.3
4	VTC0309+01	03:09:26.00	+01:14:57.9	TDE	9.0
			Other Candidates		
1	VTC2330-00	23:30:01.813	-00:27:36.53	AGN	7.0
2	VTC0208-00	02:08:27.060	-00:52:08.04	QSO	5.5
3	VTC0318+00	03:18:33.644	+00:26:35.97	unknown	4.2
4	VTC0345+00	03:45:26.003	+00:41:56.12	AGN?	4.1

*SN: radio supernova; BNS: binary neutron star merger; TDE: tidal disruption event

outflow as a possible explanation. VLA and VLBA follow-up observations of these transients have been approved. With the new VLA data we be able to get a measure of the power-law of decline and further constrain the progenitors (in the cases of VTC0141+00 and VTC0303-00), and the VLBA data will shed light on the ages of these high-impact transients.

Bibliography

Abada-Simon et al. 1993, ApJ, 406, 692

Bastian, D. & Chanmugam 1988, ApJ, 324, 431

Czerny, B., Siemiginowska, A., Janiuk, A.; Nikiel-Wroczynski, B. & Stawarz, L. 2009, ApJ, 698, 840C

Deller, A. T., et al. 2014, arXiv1412.5155

Frail, D. A., Kulkarni, S. R., Ofek, E. O., Bower, G. C., & Nakar, E. 2012, ApJ, 747, 70

Gal-Yam, A., et al. 2006, ApJ, 639, 331

Ghirlanda, G., Burlon, D., Ghisellini, G., et al. 2014, PASA, 31, 22

Kunert-Bajraszewska, M., Marecki, A. & Thomasson, P. 2006, A&A, 450, 945

Kunert-Bajraszewska, M., Gawronski, M. P., Labiano, A. & Siemiginowska, A. 2010, MNRAS, 408, 2261

Levinson, A., Ofek, E. O., Waxman, E., et al. 2002, ApJ, 576, 923

Meintjes & Venter 2005, 360, 573

Nakar, E. & Piran, T. 2011, Nature, 478, 82

O'Dea, C. 1998, PASP, 110, 493O

Russel, T. et al. 2014, MNRAS, 439, 1390

Soderberg, A. et al. 2010, Nature, 463, 513

Venter & Meintjes 2006, MNRAS, 366, 577

Weiler et al. 2002, ARA&A, 40, 387

White, R. L., Becker, R. H., Helfand, D. J. & Gregg, M. D. 1997, ApJ, 475, 479

Hodge, J. A., Becker, R. H., White, R. L., Richards, G. T. & Zeimann, G. R. 2011, AJ, 142, 3

Zauderer, A. et al. 2011, Nature, 476, 425

Zauderer, A. et al. 2013, ApJ, 767, 152

Chapter 7

Summary and Future Directions

Through this thesis, I have made the first attempt to explore the dynamic radio sky through sensitive and wide-field blind surveys with the Karl G. Jansky Array (VLA). I have used unique tools such as rapid calibration, imaging, source cataloging and transient search, employment of deep multiwavelength archival data, rapid multiwavelength follow-up, and contemporaneous optical surveys to study radio transients on timescales between one day and one decade. This thesis also includes a collaborative radio follow-up study of the discovery of the first non-thermal tidal disruption event, Swift J1644+57. The unifying feature of the research projects included herein is the study of slow transient phenomena. These studies were motivated by the opportunity for discovery, understanding the rates for slow radio variables and transients, the need for equipping the VLA with near-real-time an wide-field survey capabilities, and the direct comparison of the dynamic radio and optical skies.

Most of what was known about the transient radio sky before this thesis, especially about extragalactic transients, came from the radio follow-up of objects discovered at optical, X-ray or γ-ray wavelengths. The follow-up of Swift J1644+57 with the 40-m telescope at the Owens Valley Radio Observatory (OVRO), carried out early on in the Ph.D., represents one such effort (Chapter 2). The resulting publication (Zauderer et al. 2011) reports a collaborative radio follow-up effort. The conclusions of this work suggested a tidal disruption scenario with a relativistically beamed outflow (a jet with $\Gamma \sim 1$ and beaming fraction of $\sim 10^3$), and a density profile, $n_e \propto r^{-2.4}$, for the circum-nuclear environment of the host galaxy. The detection of a single such event in 6 years of Swift operations led to an estimate of ~ 0.1 Gpc^{-3} yr^{-1} for the rate of Swift J1644+57-like tidal TDEs. Such TDEs are therefore expected to be one of the most commonly-occurring extragalactic transients in the radio sky.

An initial study presented in this thesis (Chapter 3) is a sensitive search for radio transients in the Extended Chandra Deep Field South region, where archival Legacy VLA data from a narrow-deep survey at 1.4 GHz was used. The Caltech-NRAO Stripe 82 Survey (CNSS; Chapters 4, 5, and 6) was carried out are at 3 GHz, where the survey speed of the VLA is maximum. These surveys offer insights on the variability of radio sources at frequencies of a few GHz. It is found that only a small fraction, $\ll$1%, of the persistent radio sources beyond $\sim$100 μJy in the sky have fractional variability larger than 50% on timescales between one

day and several years. Multi-wavelength archival data, optical light curves and radio light curves of these variable sources indicate intrinsic AGN activity as being the cause of this variability. This is in agreement with the findings of previous radio surveys having mJy-level sensitivity, but most previous studies have been unable to identify intrinsic AGN variability from extrinsic. photometric data of the radio variable sources suggest that these are all shock-related flaring in the jets of AGN. The nature of extrinsic variability can be understood by comparing the results from our surveys with the findings of Ofek et al. (2011). The latter find that $\sim$30% of point sources brighter than 1.5 mJy at 5 GHz are variable, with majority of the sources varying on timescales $<$10 days. This variability is primarily small amplitude (modulation indices of less than 0.2), while only $\sim$0.3% of the sources in Ofek et al. have larger variability amplitude on timescales less than two years. This suggests that extrinsic phenomena (interstellar scintillation) manifests mainly as low-amplitude variability on timescales of several days or less. These findings agree with the expectations from refractive scintillation (Walker 1998).

The highlights of the CNSS are the transients that have been found from this survey. In the pilot survey (Chapter 4), a flare from an RS CVn binary system as well as a few rare AGN, showing renewed jet activity were found. The final survey had a candidate tidal disruption event, a flare from a cataclysmic variable, and two candidate radio supernovae / binary neutron star merger events (reported in Chapter 6). One of the first reliable estimates for the rates of such transients have come from this thesis, since many of the past surveys had ambiguous transient classification (e.g. Thyagarajan et al. 2011; Bannister et al. 2011). For all other classes of transients brighter than 0.5 mJy we are able to place a stringent upper limit of 0.004 events per deg^{-2}, an order of magnitude better as compared with previous surveys having similar sensitivities. A detailed follow-up of the transient candidates from the CNSS is in progress (Chapter 6), and will lead to advancement of our knowledge of the physics of these radio transients.

The CNSS has given an unbiased assessment of radio source variability and transient rates. These rates allow us to calculate the number of variables and transients expected in any survey with a given area and sensitivity, and hence the false positive foreground for future radio counterpart searches to gravitational wave (GW) sources.

The thesis has been instrumental for developing a near-real-time calibration, imaging, and transient search infrastructure for the VLA, and also for the planning and execution of wide-field sensitive surveys. Jointly with Stephen Bourke, I have developed a ready-to-deploy pipeline[1] to rapidly process the large volumes of VLA data and find transient candidates. A significant part of this thesis has been devoted to the commissioning of a new observing mode at the VLA, on-the-fly mosaicing (OTFM). OTFM has significantly reduced the overheads associated with wide-field shallow surveys, thus establishing the VLA as an efficient wide-field survey instrument. The VLA will continue to play an important role in future radio transient surveys.

The VLA Sky Survey (VLASS) is a direct application of the OTFM work and near-real-time transient

[1] based on AIPSLite and Python

search presented in this thesis. Recently, the All-Sky component of the VLASS[2], covering 34,000 deg^2 of the sky at S band in 3 epochs observed over several VLA configuration cycles, has been approved. The survey is meant to be a community resource, and it will have more an improved sensitivity, resolution, positional accuracy, etc. than previous "all-sky" radio surveys. OTFM has been chosen as the preferred observing mode for the All-Sky component and will utilize most of the observation planning and implementing techniques developed as part of this thesis. This thesis also places me in a unique position to use the VLASS for near-real-time transient search.

Despite the benchmark study carried out in this thesis, there is much work still to be done. Firstly, SKA pathfinder facilities such as ASKAP, MeerKAT, WSRT/Apertif, LOFAR, and MWA, have recently started or will soon start operating. Time domain is one of the primary drivers of these facilities, and many discovery opportunities are possible with these sensitive, wide-field, instruments using efficiently-designed surveys. Secondly, given that eventually the SKA and LSST will observe the sky concurrently, there is much interest in the astronomical community to explore the potential of joint radio and optical surveys. MeerLICHT[3] and MeerKAT are two such facilities under construction, and designed with the aim of concurrent observing. Joint radio and optical surveys may be a powerful technique to simultaneously understand prompt and afterglow emission in transients. Thirdly, future transient surveys will be able to survey large areas of the sky with a fast cadence, resulting in detailed light curves of variable and transient sources. Looking at each transient by eye will no longer be feasible, especially when the SKA and LSST come online. Machine learning will be necessary to automatically classify transients in this case. As a post-doctoral fellow in the Department of Surveys at Oxford University, I plan to work on many of these issues. I propose to take the near-real-time data processing and transient search techniques, developed as part of these thesis, to a new level, and to discover transients with the next generation of surveys carried out using the LOFAR, the MeerKAT, and MeerLICHT. I look forward to continued collaboration with Caltech, the owner of rich optical follow-up facilities, to this end. Lastly, a larger joy and motivation of studying transients is understanding the physics of these exotic objects. The whole new aspect of explaining the physical nature of newly-discovered radio transients awaits, but in addition to this, I would like to address intriguing questions associated with black-hole spin and the coupling between accretion discs and jets during my post-doc. These questions have been a topic debate for a long time, but the sensitivity of current telescopes and the accuracy of simulations is allowing us to understand this in much better detail than before. Summarizing the contents of this paragraph, ambitious surveys with powerful new radio and optical facilities, and carry transient astronomy into the SKA and LSST era.

There are other areas that need attention. In the advanced LIGO (aLIGO) era, gravitational wave (GW) sources will have poor localization, requiring surveys over large areas. Through this thesis, I have equipped the VLA with near-real-time survey capability over wide fields, so radio counterpart searches to GW sources

[2]The final proposal can be found at: https://safe.nrao.edu/wiki/pub/JVLA/VLASS/VLASS_final.pdf.
[3]https://www.astro.ru.nl/wiki/research/meerlicht.

are possible. A small amount of effort is needed to enable the VLA to take aLIGO triggers, carry out multi-epoch wide-field surveys over the localization regions, and to report possible radio counterparts. Also, the search for afterglows from binary neutron star mergers through dedicated radio surveys carried out independently of aLIGO will be very useful.

This thesis has shown that decimeter wavelengths reveal synchrotron events which evolve on significantly long timescales (weeks to years). There is a need to investigate the sky at centimeter frequencies ($\sim$10 GHz) where extragalactic transients evolve much faster. Additionally, meter-wavelength (30-300 MHz frequencies) observations are more likely to detect short-timescale coherent transients. This phase space is largely unexplored and has significant potential for discovery. I will briefly describe the GMRT survey[4], led by myself, that is being undertaken to significantly advance our knowledge of slow transients at MHz frequencies. This is part of a collaboration between Caltech and NRAO. Between November and December 2014 we carried out a pilot transient survey at 150 MHz in 100 deg^2 of SDSS Stripe 82 with the GMRT. For this dedicated transient survey, the first of its kind with the GMRT, the survey region was observed in two epochs separated by 1.5 months. After the completion of each observation the data were downloaded onto the computing cluster at the NRAO in Socorro with minimal lag. We developed a state-of-the-art calibration and imaging pipeline in AIPS/Obit using the SPAM recipe from Intema et al. (2009) in order to process the data in near-real-time. The data processing took 8 hours per pointing. Both, the calibration and imaging, were carried out through multi-core computing across two computer nodes, and calibrated images for the entire 100 deg^2 were produced within 16 hours. This was followed by source cataloging and transient search, which required one hour in total. Thus, once we had acquired the raw GMRT data, we were able to find transient candidates within 24 hours. We were able to reach a fairly uniform RMS noise of $\sim$5 mJy per epoch over 100 deg^2. Our observing frequency of 150 MHz was motivated by the availability of TGSS as a reference epoch for transient search. We used the TGSS to probe variability on a timescale of 4 years. For the second epoch, we additionally searched for transients on a timescales of 1.5 months by comparing it with the first epoch. We have found $\sim$20 variable and transient candidates varying by a factor of two or more in flux density on timescales less than four years. Preliminary assessment of these candidates using multiwavelength archival data suggests that they are all associated with AGN activity. One such candidate varying by a factor of three between the TGSS epoch and our December 2014 epoch is shown in Figure 7.1. Through our pilot survey we have demonstrated the wide-field and rapid imaging capabilities of the GMRT.

All together, the future looks bright and explosive (as explosive as a core-collapse supernova, figuratively speaking?) for the study of radio transient phenomena.

[4]The GMRT has recently been awarded a SKA Pathfinder status.

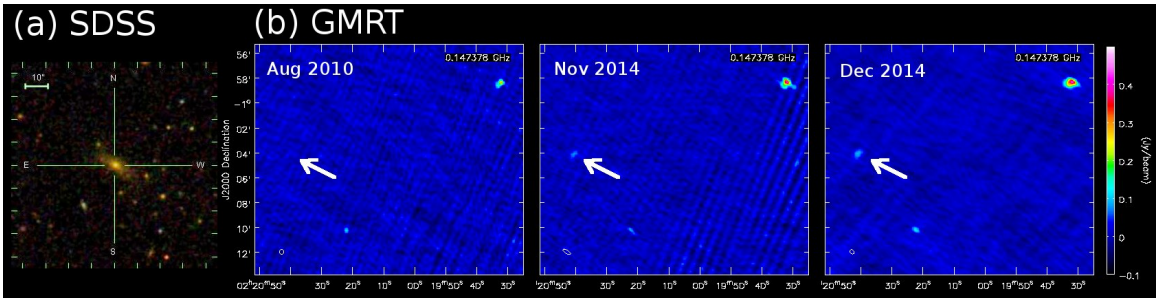

Figure 7.1: A transient candidate, GMRT J022041.0-010411.4, from our pilot 100 deg^2 survey. It is associated with a broadline AGN at a redshift of 0.34. The radio source is undetected in the TGSS epoch from Aug 2010, but is detected in our two epochs from 2014. The flux densities of the candidate in these three observations are $<$36 mJy (3σ upper limit), 77$\pm$10 mJy and 88$\pm$10 mJy respectively, while the flux densities of a nearby comparison source, lying to the lower right of the transient candidate in the image cutouts shown above, are fairly stable (<20% fractional variability in flux density).

Bibliography

Bannister, K. W., Murphy, T., Gaensler, B. M., Hunstead, R. W., & Chatterjee, S. 2011, MNRAS, 412, 634

Intema, H. et al. 2009, A&A, 501, 1185

Ofek, E. O., Frail, D. A., Breslauer, B., et al. 2011, ApJ, 740, 65O

Thyagarajan, N., Helfand, D. J., White, R. L., & Becker, R. H. 2011, ApJ, 742, 49

Walker, M. A. 1998, MNRAS, 294, 307

Zauderer, B. A., Berger, E., Soderberg, A. M., et al. 2011, Nature, 476, 425

Appendix A

B- and A-Type Stars in the Taurus-Auriga Star Forming Region

This chapter is previously published as: Mooley, K. P., Hillenbrand, L. A., Rebull, L., et al. 2013, ApJ, 771, 110.

Abstract

We describe the results of a search for early-type stars associated with the Taurus-Auriga molecular cloud complex, a diffuse nearby star-forming region noted as lacking young stars of intermediate and high mass. We investigate several sets of possible O, B and early A spectral class members. The first is a group of stars for which mid-infrared images show bright nebulae, all of which can be associated with stars of spectral type B. The second group consists of early-type stars compiled from (i) literature listings in SIMBAD; (ii) B stars with infrared excesses selected from the *Spitzer Space Telescope* survey of the Taurus cloud; (iii) magnitude- and color-selected point sources from the *Two Micron All Sky Survey*; and (iv) spectroscopically identified early-type stars from the *Sloan Digital Sky Survey* coverage of the Taurus region. We evaluated stars for membership in the Taurus-Auriga star formation region based on criteria involving: spectroscopic and parallactic distances, proper motions and radial velocities, and infrared excesses or line emission indicative of stellar youth. For selected objects, we also model the scattered and emitted radiation from reflection nebulosity and compare the results with the observed spectral energy distributions to further test the plausibility of physical association of the B stars with the Taurus cloud. This investigation newly identifies as probable Taurus members three B-type stars: HR 1445 (HD 28929), τ Tau (HD 29763), 72 Tau (HD 28149), and two A-type stars: HD 31305 and HD 26212, thus doubling the number of stars A5 or earlier associated with the Taurus clouds. Several additional early-type sources including HD 29659 and HD 283815 meet some, but not all, of the membership criteria and therefore are plausible, though not secure, members.

A.1 INTRODUCTION

The Taurus-Auriga molecular cloud complex (hereafter "Taurus") is the quintessential region of nearby recent star formation. It is characterized by low star-formation efficiency (Goldsmith et al. 2008) and the absence of high-mass young stars (Kenyon et al. 2008) and stands in contrast to more distant, massive, and dense star-forming environments like the Orion Molecular Clouds. Taurus lies at a mean distance of about 140 pc with a depth of 20 pc or more (Kenyon et al. 1994; Torres et al. 2007, 2012) and spans approximately 100 square degrees on the sky, or about a 25 pc diameter at this distance. The few times 10^4 $M_\odot$ cloud currently has over 350 known members, mainly substellar and low-mass stellar objects with $M < 0.5$ $M_\odot$, and only about 10 members identified with $M > 1.5$ $M_\odot$. Much effort over the past decade in Taurus has been directed towards completely defining the low-mass stellar and sub-stellar population.

A comprehensive review of Taurus is given by Kenyon et al. (2008). Major recent contributions to our knowledge include: (i) mapping of the molecular gas (Goldsmith et al. 2008; Narayanan et al. 2008) and dust (Lombardi et al. 2010; Palmeirim et al. 2013) comprising the cloud; (ii) determination of the distance of individual young star members through Very Long Baseline Interferometry (VLBI; Torres et al. 2009) parallaxes; (iii) improvement of the young stellar object census including new stellar and brown dwarf candidate members (Rebull et al. 2010; Luhman et al. 2009, 2010; Takita et al. 2010; Rebull et al. 2011) as well as new companions to already known objects (Kraus et al. 2011); (iv) measurement of proper motions using optical and VLBI techniques, (Torres et al. 2009; Luhman et al. 2009); (v) provision of evidence for mass segregation (Kirk & Myers 2011; Parker et al. 2011); and (vi) searches for outflows (Narayanan et al. 2012; Bally et al. 2012).

In particular, a *Spitzer* program directed at Taurus (Güdel et al. 2007, PI D. Padgett) produced large-scale multi-wavelength maps of the clouds. Photometry from this survey has improved our understanding of both the stellar/sub-stellar membership and the incidence of protoplanetary disks (Rebull et al. 2010). Motivating the investigation described in this paper are four large and two smaller reflected and/or scattered-light nebulae found in these mid- and far-infrared images, shown in Figure A.1.

Each of the large infrared nebulae is illuminated by a point source that is a known B or A0 star. Two of these, HD 28149 (72 Tau) and HD 29647, have been studied in the literature to date (e.g. Kenyon et al. 1994; Whittet et al. 2001, 2004), as background stars and used to derive the physical and chemical properties of the molecular cloud. One source, HD 282276, was unstudied until noted by Rebull et al. (2010, 2011) to have a mid-infrared excess. Finally, V892 Tau is a well-known Herbig Ae/Be type member of Taurus (Elias 1978) that also illuminates an optical reflection nebula — an original defining characteristic of the Herbig Ae/Be population. The two additional smaller infrared nebulae are likewise associated with early-type or high luminosity stars. HD 28929 = HR 1445 has been known as a chemically peculiar star (e.g. Wolff & Preston 1978) but has not otherwise distinguished itself in the literature. IC 2087 is associated with a known young stellar object (Elias 1978) and, like V892 Tau, illuminates an optical nebula. The nebular regions for

all six of these sources appear brightest at mid-infrared wavelengths; optical nebulosity is generally absent, but when apparent, is weaker except in the case of IC 2087.

The proximity of these early-type stars to cloud material, as evidenced by the mid-infrared nebulae, suggests that rather than being background stars as they have been traditionally considered, they may be heretofore unappreciated early-type members of Taurus. The association of these stars with prominent nebulosity is not, however, sufficient evidence that they are genuine members of Taurus. Instead, they could be stars of early type that are physically unassociated but fortuitously located with respect to either the Taurus molecular cloud complex itself or smaller patches of locally-enhanced density in the foreground or background interstellar medium (ISM). Reminiscent of this latter situation is the Pleiades star cluster, which is passing through and illuminating denser-than-average ISM that is physically unassociated with the stars themselves. In this contribution, we explore the evidence and attempt to distinguish between these two scenarios.

The earliest-type Taurus members are generally considered (Kenyon et al. 2008; Rebull et al. 2010) to be IC 2087-IR (estimated at B5 based on bolometric luminosity but a heavily self-embedded star with a continuum-emission optical spectrum), the binary system V892 Tau (Elias 1; a B8-A6 self-embedded Herbig Ae/Be star with a near-equal brightness companion), the triple system HD 28867 (B8 +2$\times$B9.5), AB Aur (A0e, a Herbig Ae/Be star), and HD 31648 (MWC 480; A2e, another Herbig Ae/Be star). There are no associated F stars [1] and the next earliest types are HP Tau/G2 (G0) and SU Aur (G2). Notably, almost all of these earliest-type members of Taurus harbor significant amounts of circumstellar material, the HD 28867 system [2] being the exception.

While no systematic investigation for high-mass stars associated with Taurus has been performed recently, there has been historical interest in early-type stars seen towards this canonically low mass star-forming region. Blaauw (1956) identified Casseiopeia-Taurus (hereafter Cas-Tau) as an OB association lying between 140 and 220 pc using the convergent-point method. There was ensuing debate concerning the relationship of the young Taurus-Auriga molecular cloud to the older Cas-Tau OB association, but it has now been resolved that they are unrelated in both space and age (see below). The first early type stars associated with the Taurus clouds was AB Aur, an original Ae/Be star associated with optical nebulosity (Herbig 1960), followed by the infrared-selected young stellar objects V892 Tau and IC 2087-IR (Elias 1978).

How many higher-mass stars should there be in Taurus? Using the number and distribution of the known low-mass T Tauri stars and the assumption that weak-lined T Tauri stars (WTTS) are far more numerous (as high as 10:1) than classical T Tauri stars (CTTS), Walter et al. (1988) argued from a sparse X-ray survey of Taurus with *Einstein* that there should be $\sim 10^3$ low-mass members of Taurus. The initial mass function (IMF) appropriate for young star clusters (Miller & Scalo 1979) would then predict the existence of tens of B-type members. The search for these B stars culminated with Walter & Boyd (1991) identifying 29 possible

[1] HD 283759 (F2–F3) and V410-Anon24 (F9–G3) have at various times been suggested as members, but both are well underluminous with respect to the other stars in this list if assumed to be at the same distance, and not particularly obscured.

[2] This source is to the south of the main Taurus-Auriga clouds, in the L 1551 region, and is not otherwise discussed in this paper; see Walter et al. (2003).

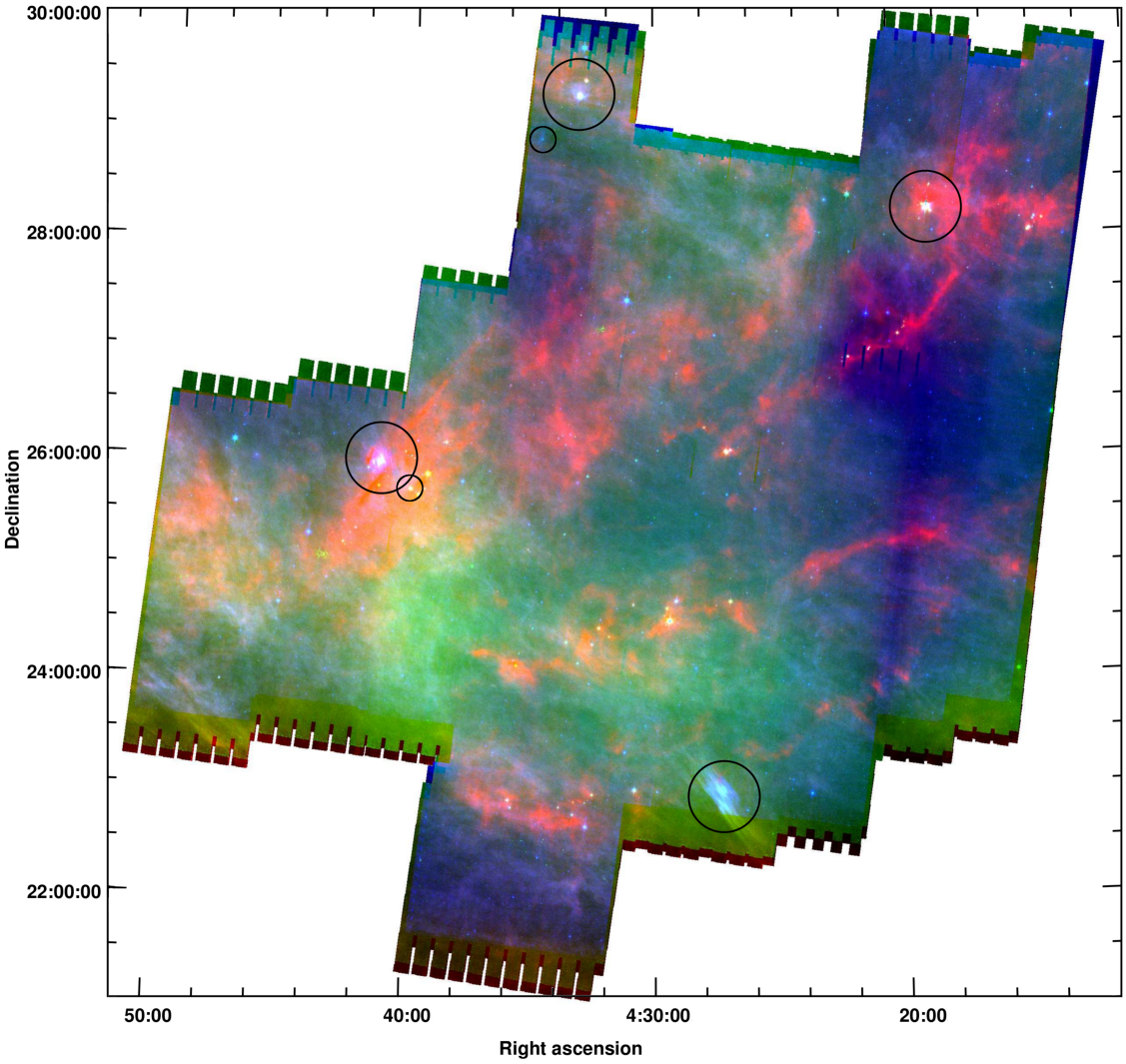

Figure A.1: Spitzer mosaic of IRAC and MIPS images of Taurus. Color coding: 8 (blue), 24 (green), and 160 (red) μm. Four bright and large nebulous objects illuminated by B stars are evident in this mosaic. They have been marked with large circles and are associated with: (i) top-middle: HD 282276, (ii) top-right: V892 Tau (Elias 1), (iii) bottom-middle: HD 28149 (72 Tau), and (iv) middle-left: HD 29647. Two fainter and weaker nebulae are marked with smaller circles and are associated with: (v) top-middle: HD 28929 (HR 1445), (vi) middle-left: IC 2087.

members of the Taurus-Auriga T association based on spectroscopic parallax and proper motion. However, the large number of low-mass Taurus member stars predicted by Walter et al. (1988) were not found in the proper-motion survey by Hartmann et al. (1991), who suggested that many of the stars found in the X-ray survey by Walter et al. (1988) belong to the older and more distant Cas-Tau group, and that the assumption of a uniform distribution of T Tauri stars is not correct. While Walter & Boyd (1991) had concluded that the Tau-Aur T association was related to the Cas-Tau OB association, de Zeeuw et al. (1999) showed that these are kinematically distinct groups and rejected the Walter & Boyd (1991) stars as Cas-Tau members.

Most subsequent publications on the Taurus-Auriga stellar population have focused on the low-mass stars. However, of relevance to the present study is that Whittet et al. (2004) proposed, on the basis of extinction and dust modelling, that HD 29647 (B9III) is located within a diffuse screen surrounding the dense molecular clump TMC-1 in Taurus. Also, Rebull et al. (2010) suggested that its infrared excess and spectroscopic parallax make HD 27659 (A0–A4V) a high-quality candidate member of Taurus, and that HD 282276 (B8V) and HD 283815 (A0V) are lower-quality, but plausible, candidate members. As the situation concerning associated early-type stars remains unclear, and considering the high level of interest in the membership and star-formation history of Taurus, a detailed investigation using the wealth of new information seems warranted.

This paper is organized as follows. In §A.2 we describe the process of compiling the list of early-type stars towards Taurus (§A.2.2) and testing these stars for membership (§A.2.3). Our literature survey showed that spectral typing and age estimation of some of the early-type stars was done decades ago with prism-based spectrometers, and so we considered the possibility that some have been assigned an incorrect spectral type. Additionally, we considered that some early-type stars could have been missed due to limits on the spatial extent or photometric depth of previous investigations. We spectroscopically followed up all probable members (§A.2.4). Given our initial motivation for this investigation, reflection/scattered-light nebulae toward several known B stars, we then describe the modelling procedure for the scattered/thermal dust emission in §A.2.5. Detailed discussion of our findings and results for individual objects are provided in §A.3. We conclude with a summary and discussion in §A.4.

A.2 DATA COLLECTION AND ANALYSIS

A.2.1 OVERVIEW

Working from the evidence of early-type members provided by the reflection/scattered-light nebulae and the recent suggestions of additional B and A0 type stars as plausible members, we carried out a new search for stars of spectral classes O–A0 associated with Taurus. The areal extent of our study is the region bounded by 4^h and 5^h in right ascension and 22°and 31°in declination. In galactic coordinates, this is roughly the region $(165,-20) \lesssim (l,b) \lesssim (180,-10)$. This boundary was chosen to include most of the dense cores in Taurus but

not to be so large as to obfuscate the search with unassociated early-type stars at different distances. The region south of the Taurus main cloud between 4.3^h and 4.9^h in right ascension and 16°and 20°in declination is also considered a part of the Taurus star-forming region, but is not included in this investigation.

We first looked at whether there is a concentration of early-type stars towards or away from the large patch of sky under consideration. A SIMBAD query for known O,B stars towards Taurus and eight neighboring regions of equal areal extent results in the distribution shown in Table A.1. There is a higher density of known early-type stars in the direction of the galactic plane as expected, and no particular bias of early-type stars at the longitude of Taurus compared to adjacent longitudes. Thus, from our study, we expect to find only a few known early-type stars, if any, that are genuinely associated with Taurus.

In order to compile the list of candidate early-type stars towards Taurus, we gathered multiwavelength photometric and spectroscopic data and images, and collected information from the literature. We then passed these stars through two membership tests: appropriate distance and appropriate kinematics. All candidates satisfying these two criteria were labeled as probable members of Taurus. These likely members along with other stars meeting some but not all of the criteria were followed up spectroscopically.

A.2.2 COMPILING THE LIST OF CANDIDATE EARLY-TYPE STARS AND ANCILLARY DATA

Four data sets were used to assemble a list of early-type stars towards the Taurus region: (i) previously identified O and B-type stars listed in SIMBAD; (ii) proposed B and early A stars with infrared excesses selected from the *Spitzer* survey of the Taurus cloud discussed in Rebull et al. (2010); (iii) photometrically-selected point sources from the *Two Micron All Sky Survey* (2MASS-PSC; Skrutskie et al. 2006); and (iv) spectroscopically identified early-type stars from the *S*loan Digital Sky Survey (*SDSS*) observations of the Taurus region (Finkbeiner et al. 2004) presented by Knapp et al. (2007). As illustrated in Figure A.2, there is only partial coverage of the total cloud region (see also Figure A.4) in each of *SDSS* and the Rebull et al. (2010) *Spitzer* surveys, and the overlap between the optical and infrared photometric surveys is also only partial. We now describe the collation of data from each of the four sources.

First, to select early-type stars from SIMBAD, we used the criterion query: $ra > 60$ & $ra < 75$ & $dec > 22$ & $dec < 31$ & $sptypes < A0$. This query (run in early 2011) resulted in 91 stars, three of which were listed twice with different names. We thus obtained 88 B stars and zero O stars through the SIMBAD database as candidates.

Second, potential Taurus members having early spectral types were taken from Tables 5 and 7 in Rebull et al. (2010). One of these, JH 225, also resulted from the SIMBAD search. Thus, the Rebull et al. (2010) paper added eight more stars with spectral types early A or B (O-type stars were absent). As noted above, the region covered by *Spitzer* does not encompass the whole region of our search (see Figure A.2).

Third, we selected from the 2MASS-PSC [3] objects satisfying the same coordinates constraint used in the SIMBAD query, having $K_s < 10$ mag with $> 5\sigma$ detection, and no contamination or quality flags set. The brightness threshold places an upper limit on the visual extinction for the selected stars. For example, a B8V star can have a maximum visual extinction of $A_V \simeq 37$ to be selected, since the absolute K-band magnitude for such a star is $M_{K_s} = 0.11$, the distance modulus at 140 pc is 5.73, and the reddening law for 2MASS magnitudes is $A_K = 0.112A_V$. Such a large value of extinction is much higher than the largest extinction observed for known Taurus members. The resulting 2MASS-PSC sample appears in the lower panels of Figure A.3. These objects were further filtered through the photometric color criterion: $J-H < 1.698(H-K_s+0.158)$ in order to select stars which, when translated backwards on the reddening vector in the $(J-H)/(H-K_s)$ color-color diagram, fall on the main-sequence earlier than spectral-type A0. For this procedure, we used intrinsic magnitudes from Kraus & Hillenbrand (2007), and the Rieke & Lebofsky (1985) reddening law, which is found consistent with reddening in the 2MASS photometric system (Maheswar et al. 2010). There is no a priori reason to believe that this color criterion unconditionally, due to one or more of the following reasons: (i) photometric errors could place stars within the reddening band employed in our selection; (ii) the reddening law (parametrized by R_V) is different for different lines of sight towards Taurus (e.g. Dobashi et al. 2005); (iii) stars of a given spectral type and luminosity class do not have unique photometric colors but tend to have a dispersion of astrophysical origin about the observed mean intrinsic value; (iv) additional emission of non-photospheric origin could change the $J-H$ and $H-K_s$ colors, possibly making late-type stars with infrared excesses look like earlier-type stars that are reddened; (v) stellar multiplicity is unaccounted for in our analysis. Nevertheless, using a more relaxed criterion is subject to the risk of selecting a large number of unreddened K and M-type stars which lie across the reddening vector defined by our photometric color criterion. Using our color criterion, we obtained 113 stars for further consideration. Fourteen of the stars selected in this manner were already present in the SIMBAD list of known early type stars (BD+23 607, HD 25487, V1137 Tau, HD 284228, HD 282240, HD 29259, 2MASS J04395574+2545020 = IC 2087-IR, HD 283845, HD 283952, HD 31353, HD 284941, HD 284012, HD 283751, HD 283794) and so we added 99 early-type candidates through this criterion, which we appended to the working list. We also add the famous star AB Aur at this point, which would pass our color selection criteria but is formally excluded from our analysis based on 2MASS-PSC flags present at K_s-band.

Last, we added to our early-type candidates list the stars from the Finkbeiner et al. (2004) survey belonging to our spatial region of interest which are classified as spectral class O, B, or A based on low-resolution *SDSS* spectra. Finkbeiner et al. chose the program stars for spectroscopy as those meeting one of two criteria: on the basis of red colors, as part of a survey seeking M-dwarfs, or as stars previously known as spectral class A or F, for use as reddening standards. As noted above, the region covered by *SDSS* does not encompass the whole Taurus cloud (see Figure A.2). Furthermore, there was no overlap between these candidates and those already selected above. We also considered a set of stars selected, similar to the 2MASS-PSC query described

[3] using the multi-object search form at the Infrared Science Archive http://irsa.ipac.caltech.edu/

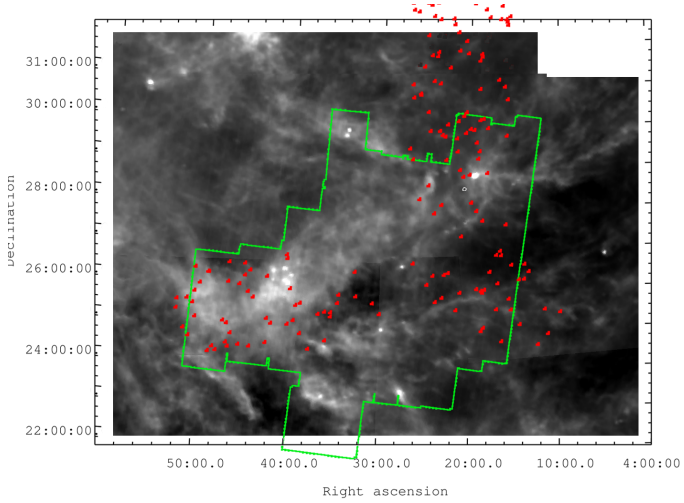

Figure A.2: Areal extent of the Spitzer Taurus Legacy Survey (green) and SDSS spectroscopic observations by Knapp et al. (2007) (red symbols) overlaid on a mosaic of the Taurus region at 100μm from the *IRAS* Sky Survey Atlas.

above, as those having $K_s < 10$ mag and blue colors within *SDSS*, specifically $u-g < 0$. This resulted in a short list of a few tens of objects, nearly all of which were known to SIMBAD already as early type stars (and thus included already among our first set of candidates), or as late type stars (with blue colors unexpectedly blue, likely indicative of hot companions).

In addition to stars in the four samples considered above, HD 31305 (A0V) is a star which we found in the vicinity of Taurus-Auriga due to its early spectral type and proximity to the well-known Taurus member AB Aur, though it is not within the area of the Spitzer maps of Taurus.

Our final list of early-type candidates for membership in the Taurus region of recent star formation thus consists of 329 stars. The color-color and color-magnitude diagrams for these stars, separated by the selection method, are shown in Figure A.3. We tested these objects for Taurus membership as described in the next subsection, after assembling the needed ancillary data.

For all objects in our list of candidate O, B, and A0 stars, we collected the following astrometric and photometric information. Proper motions were taken from the PPMXL catalog (Roeser et al. 2010), and trigonometric parallaxes from the Hipparcos catalog (Perryman & ESA 1997). B, V, and R magnitudes listed in the NOMAD-1 catalog (Zacharias et al. 2005), and J, H, K_s magnitudes from 2MASS-PSC were used. Radial velocity (RV, heliocentric) information was extracted from Gontcharov (2006) and Kharchenko et al. (2007) in that order of priority. For the *SDSS* stars which we chose from Finkbeiner et al. (2004), we used an A0 template to extract their radial velocities using the *SDSS* DR7 (Abazajian et al. 2009). In each of these catalogs, we searched for counterparts to our early-type candidate stars within 1 arcsec of the source position. In cases where two counterparts were found for a particular source, only the closest was considered. Finally, the spectral types were adopted from our own derivations for those stars which we followed-up

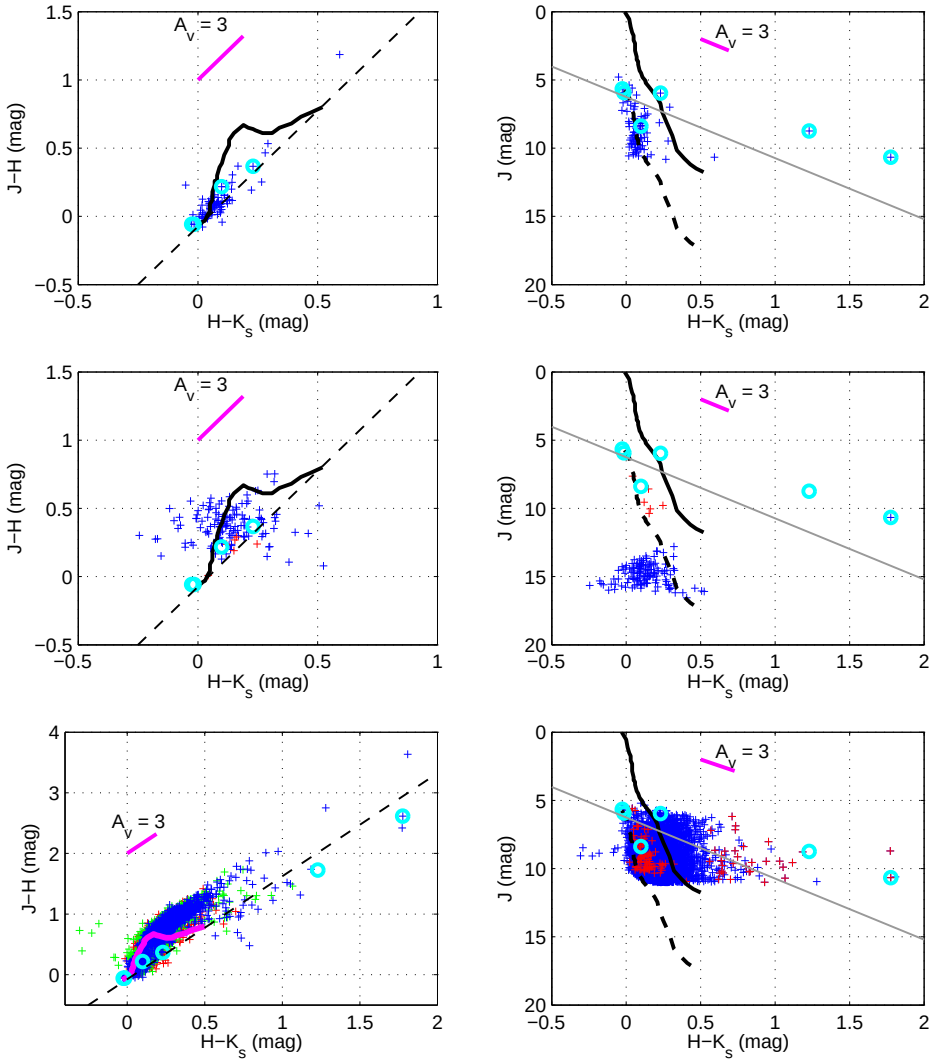

Figure A.3: 2MASS color-color (left panels) and color-magnitude (right panels) diagrams for the early-type candidate stars considered in this work. 2MASS objects with contamination flags set and error in J,H,K_s magnitudes greater than 0.1 were rejected from the plots. The mean error in J,H,K_s magnitudes is about 0.02, which is smaller than the size of symbols used. *Top panels*: O,B stars from SIMBAD. In the color-color diagram, two of these stars lie outside the range plotted: V892 Tau (Elias 1) and IC 2087-IR, having $(H-K_s, J-H) = (1.23, 1.73), (1.78, 2.62)$ respectively. *Middle panels*: Stars of spectral-type A and earlier from Knapp et al. (2007) are shown in blue. The B stars proposed by Rebull et al. (2010) are shown in red. Note that the area covered by these surveys is less than that represented in the top and bottom panels. *Bottom panels*: Left: 2MASS objects with color-coding as follows. Blue: stars with magnitude $K_s < 8$, green: $8 < K_s < 9$, red: $9 < K_s < 10$. Right: All 2MASS objects are in blue, and those selected as possible O,B stars using the photometric selection criterion (described in §A.2.2) are shown in red. *All panels*: The reddening vector (magenta) from Rieke & Lebofsky (1985) is used. Intrinsic colors and magnitudes of main-sequence stars (from Table 5 of Kraus & Hillenbrand 2007) are shown as a thick black curve (magenta curve in the bottom panel color-color diagram). The thick black, dashed curve in color-magnitude diagrams is the same curve, but displaced along the luminosity axis to denote the apparent magnitude of main sequence stars at 140 pc. The thin black, dashed straight line in the color-color diagrams represents the color-selection criterion applied to the 2MASS objects (see section A.2.2). The thin grey solid line in color-magnitude diagrams represents the reddening vector passing through the position of an A0V star at a distance of 140 pc. The location of the six B stars illuminating bright IR nebulae are shown as cyan circles with two of the stars having very similar, near-zero, colors.

spectroscopically (see section A.2.4), from Rebull et al. (2010) for stars listed in that paper, from SIMBAD, or from the ASCC-2.5 catalog (Kharchenko & Roeser 2009), in that order of preference. We also performed a thorough literature search, seeking relevant data not available through large catalogs.

A.2.3 SELECTION OF CANDIDATE MEMBERS OF TAURUS

Physical association of astronomical objects can be established through the combination of common location and common space motion, with not all six dimensions available for every star. The case at hand is that of a star forming region lying at a mean distance of 140 pc and having a depth and transverse extent of $\gtrsim 20$ pc. Although kinematics traditionally has been a robust mode of identification of cluster members, uncertainties in distance may lead to discrepant space velocities. Furthermore, the dispersion in the measured distance or kinematic quantities might be a significant fraction of their absolute values. With these challenges in mind, we chose the following filters to select (probable) members from our list of candidate early-type stars towards Taurus.

One set of criteria involved distance. Stars with trigonometric or spectroscopic parallax between 128 and 162 pc within 1σ errorbar were considered. Another set of criteria involved kinematics. From the probability associated with a calculated χ^2 statistic, stars having proper motion consistent with known members were selected. Finally, radial velocity (RV) was taken into account wherever available, considering as members stars with $9.8 \leq RV \leq 17.5$ km s^{-1}, which incorporates the mean radial velocities of all Taurus groups identified by Luhman et al. (2009) within 1σ uncertainty.

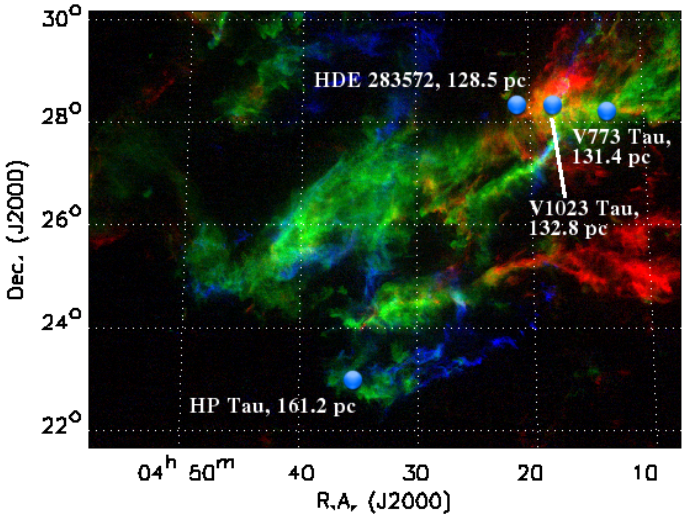

Figure A.4: Distances to stars in Taurus measured via VLBI, from Table A.2; the star T Tau is not shown since it lies south of the region of interest. Background image is velocity-coded ^{12}CO map from Goldsmith et al. (2008). The LSR velocities are color-coded as blue: 3–5 km s^{-1}, green: 5–7 km s^{-1}, red: 7–9 km s^{-1}.

A.2.3.1 DISTANCE CRITERION AND METHODS

Through VLBI measurements, the distances to five Taurus members are accurately known (see Table A.2 and for context Figure A.4). Taurus is at least as deep as it is wide (Torres et al. 2009), a few tens of parsecs in each direction. Based on this, we assume that Taurus occupies the region between 128 to 162 pc (i.e. $6.2 < \pi < 7.8$ milli-arcseconds on parallax). From our list of early-type candidate stars we chose candidate Taurus members such that both their Hipparcos and spectroscopic parallax distances, within 1σ error, were consistent with the above-stated distance criterion. van Leeuwen (2007) has effectively demonstrated the validity of the Hipparcos parallaxes (however, see below for an argument against in the case of HD 26212). We calculated the spectroscopic parallax distances for each of the six magnitudes (denoted by 'X' below) — B, V, R, J, H and K_s — using the definition,

$$d_X = 10^{(X - A_X - M_X)/5} \times 10 \tag{A.1}$$

where $A_X = [B-V-(B-V)_0] \cdot R_V \cdot (A_X/A_V)$, $R_V = 3.1$, and $(A_X/A_V) = a + b/R_V$. The parameters 'a' and 'b' are from Table 3 of Cardelli et al. (1989), and are the best-fit parameters to the average extinction law. M_V is from Schmidt-Kaler (1982), intrinsic colors, viz. $(B-V)_0$, $(V-R)_0$ are from Johnson (1966), and $(V-K)_0$, $(J-K)_0$, $(H-K)_0$ colors are from Koornneef (1983). The Koornneef magnitudes/colors were transformed into the 2MASS JHK_s system using transformations from Carpenter (2001). This intrinsic color and magnitude information for O, B and A-type stars were compiled from Schmidt-Kaler (1982), Johnson (1966), Koornneef (1983) and Carroll & Ostlie (2006). BVR reddening was determined using Cardelli et al. (1989) with $R_V = 3.1$, and JHK_s reddening using Rieke & Lebofsky (1985). Stars with missing luminosity class information were assumed to be dwarfs. Candidates having spectral types for which the intrinsic magnitudes and colors are missing in our compiled tables necessitated interpolation between the two adjacent spectral types.

We note that the difference in spectroscopic parallax calculated using alternate color tables such as those of Schmidt-Kaler (1982), Fitzgerald (1970), or Johnson (1966) is less than 0.5%. More modern empirical color references that include both dwarfs and giants are rare and possibly non-existent. However, considering the tables of Pickles (1998; based on synthetic photometry from stitched together spectrophotometric data) or Bessell et al. (1998; based on synthetic photometry from model atmospheres), the spectroscopic parallax differences are larger, but less than 3%. A more worrisome discrepancy lies in the absolute V-band magnitude, M_V, where the Pickles (1998) results differ from the Johnson (1966) values used in our compilation by 0.5 to 1 magnitudes, leading to 5–50% disagreement in the spectroscopic parallaxes. However, at least for B-type stars, the M_V from Johnson (1966) agrees with observations of well-studied stars (e.g. the 100 brightest stars [4]) better than does the Pickles (1998) scale; Bessell et al. (1998) do not quote M_V.

The error reported on the spectroscopic parallax distance is the standard deviation of the distances calculated using all of the six magnitudes. As well-tested empirical estimates of intrinsic colors involving R,J,H

[4] http://ads.harvard.edu/cgi-bin/bbrowse?book=hsaa&page=45

and K_s are not available for early-type giant stars, we calculate the distance to the luminosity class III stars using only B,V magnitudes and color. Other errors that could contribute but have not been accounted for include: (i) spectral type / luminosity classification error, (ii) error in apparent magnitudes, (iii) intrinsic colors are mean values and do not account for astrophysical spread within the luminosity classes, (v) error in choice of reddening model, (vi) presence of non-photospheric emission such as infrared excess. For points (i) and (ii) stated above, the manner in which these criteria impact the distance estimate can be understood quantitatively via the discussion provided in section 3.3 of Kenyon et al. (1994). Following that discussion, the 1σ error on spectroscopic parallax corresponding to quantities (i) and (ii) is roughly 30 pc at a spectral type of A0 with d = 140 pc. This uncertainty would then add to our quoted error appropriately taking into account equation A.1. Caution is thus advised in using the error bars quoted on spectroscopic distances, especially for giant stars.

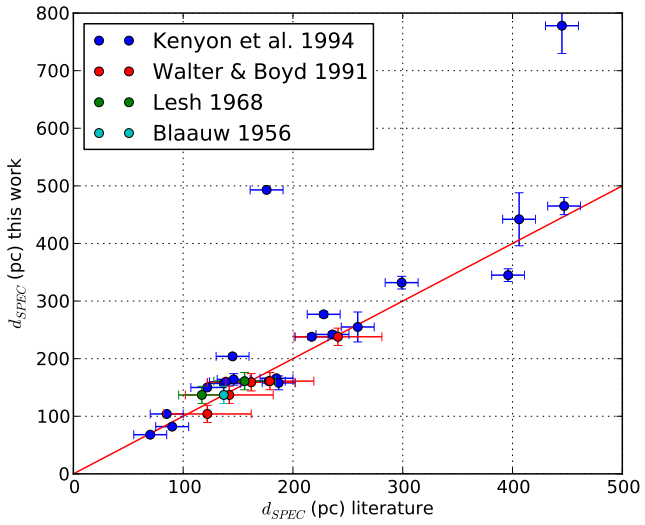

Figure A.5: Comparison of spectroscopic distances calculated in this work with those published in past literature.

Out of the 329 early-type candidates being tested for Taurus membership, the reddening and spectroscopic parallax distance can be calculated for 173 of them. In general, where there is overlap, the reddening values show good agreement with those stated in the literature. We compare our averaged spectroscopic parallax distances with those determined by Kenyon et al. (1994), Walter & Boyd (1991), Lesh (1968), and Blaauw (1956) in Figure A.5. For the majority of the objects, the spectroscopic parallax distances are in agreement within 1σ with those determined by *Hipparcos*. Notable exceptions are stars with very high reddening for which R_V (and possibly also the reddening law as a function of wavelength itself) would differ significantly from the value assumed here. Also, the method fails if the optical and/or near-infrared photometry is dominated by circumstellar rather than photospheric emission, or if the source is pre-main sequence rather than close to the main sequence; this latter condition is indeed the case for many of the later type stars selected in

the 2MASS part of the search.

In considering the appropriateness of the distance criterion we have adopted for testing the association with Taurus, which is that all stars must lie between 128 and 162 pc, a problem arises in the unknown 3-dimensional shape of the molecular cloud. The cloud may extend further along some lines of sight, or it may not have high enough density for current star formation along other lines of sight. A related problem in establishing membership is that, to the west of Taurus, there is another star-forming region along the line of sight extending behind Taurus: the Perseus molecular cloud at about 350 pc. The spectroscopic parallaxes of HD 282276 and HD 283677 suggest that they both lie closer to the Perseus cloud, though on the sky they are aligned with Taurus, not the Perseus cloud; these stars also have similar proper motion (see below). There have been suggestions of a bridge of molecular material connecting the Taurus-Auriga and Perseus regions (Ungerechts & Thaddeus 1987). The presence of the somewhat older Cas-Tau OB association along the line of sight also poses a potential contamination problem because its members span a range of at least 30 pc in distance (de Zeeuw et al. 1999) and perhaps as much as 80 pc, although it is securely behind the Taurus star-forming region.

A method for distinguishing chance superpositions, in addition to the distance criterion, is to look at the kinematics of the stars and the natal cloud. Consideration of proper motion and radial velocity of the stars helps in eliminating ambiguity, as discussed in the next sub-section.

A.2.3.2 KINEMATIC CRITERIA AND METHODS

The classical studies of proper motions of stars in the vicinity of the Taurus clouds are those of Jones & Herbig (1979) and Hartmann et al. (1991) with Ducourant et al. (2005) providing the latest catalog for Taurus. Kinematic membership probabilities are typically based on the convergent point method, which is used for regions that cover a large part of sky where the mean subgroup motion is changing as a function of position (this is a purely geometric effect). For regions less than a few degrees in size in the vicinity of comoving groups in Taurus, one can test the consistency of the proper motion of one star simply with respect to the mean motion of a group. Luhman et al. (2009) computed the mean proper motions and radial velocities of eleven distinct groups (occupying 1–10 deg^2 on the sky; see Table 8 of that paper) of Taurus members. Seven of these groups, specifically I-V, VIII and X, lie within our region of interest.

We checked the statistical consistency between the proper motion of the candidate early-type stars reported in Table A.3 and the proper motion of the closest kinematic group from Luhman et al. (2009) by estimating the χ^2 probability. The two components of proper motion, μ_α and μ_δ, can be understood as independent Gaussian variates drawn from a normal distribution parametrized by the mean (which can be estimated through the sample mean, i.e. the mean proper motion of the presently-known Taurus members) and the dispersion (likewise estimated as the dispersion of the sample of presently-known Taurus members). The sum of the square of these values will then be distributed according to the χ^2 distribution. Strictly speaking, these components are determined through the least-squares technique in proper-motion catalogs, and

are correlated (the complete covariance matrix is, for example, provided by the Hipparcos catalog). Here, we have calculated the quantity χ^2 using the definition $\sum_{i=1}^{k}(x_i-\bar{x})/\sigma_i^2$, where $i = 1, 2$, and x_i describes the components of proper motion. The uncertainties, however, are associated with not only the proper motion of individual stars, but also with the sample mean. Further, we have to incorporate the internal dispersion of the presently-known members of Taurus. We calculated the χ^2 statistic and the associated probability using equations A.2 and A.3, after de Zeeuw et al. (1999):

$$\chi^2_{\nu=2} = \frac{(\mu_\alpha - \mu_{\alpha,\mathrm{group}})^2}{(\sigma^2_{\mu_\alpha} + \sigma^2_{\mathrm{int}} + \sigma^2_{\mu_{\alpha,\mathrm{group}}})} + \frac{(\mu_\delta - \mu_{\alpha,\mathrm{group}})^2}{(\sigma^2_{\mu_\delta} + \sigma^2_{\mathrm{int}} + \sigma^2_{\mu_{\delta,\mathrm{group}}})} \tag{A.2}$$

$$P(\chi|\nu) = \frac{\chi^{(\nu-2)/2} e^{-\chi/2}}{2^{\nu/2}\,\Gamma(\nu/2)} \tag{A.3}$$

where $\mu_\alpha, \mu_\delta, \sigma_{\mu_\alpha}, \sigma_{\mu_\delta}$ denote the proper motion in right ascension and declination of the star being tested and their associated uncertainties. The quantities $\mu_{\mathrm{group}}, \sigma_{\mu_{\mathrm{group}}}, \sigma_{int}$ are the proper motion of the Taurus group closest to the star, its uncertainty, and the intrinsic dispersion of proper motion in the group (assumed to be 2 mas yr^{-1}). The denominator of each term is then the expected variance of the respective numerators. This method traditionally has been used to find "proper-motion members", but is partly biased toward stars having a large relative uncertainty in their proper motion which reduces the χ^2. We are able to calculate the χ^2 probability for all of the 329 early-type candidate stars being tested for Taurus membership.

The result of this proper motion analysis is illustrated in the upper panel of Figure A.6. The region allowed by our χ^2 probability membership criterion (set at $>1\%$) roughly corresponds to the shaded circular region. In the context of this figure, it is worthwhile to note that members of the background Cas-Tau OB association as listed by de Zeeuw et al. (1999) have μ_α ranging from a few mas yr^{-1} to 50 mas yr^{-1} (the mean is about 26 mas yr^{-1}), and μ_δ ranging from a negative few mas yr^{-1} to –40 mas yr^{-1} (mean is about −19 mas yr^{-1}; from the PPMXL catalog). Thus, a few of the stars studied herein are probably Cas-Tau members. A combined diagram showing the spectroscopic parallax distance and the proper motion of the early-type candidate stars is shown in the lower panel of Figure A.6.

The RV dimension was not included in the χ^2 analysis because this quantity is unknown for most stars. In cases where it is known, the uncertainties are generally quite large. Thus, as the second component of our kinematics investigation, we compared the RV of each of the early-type candidate member stars (where available and as reported in Table A.3) with that of the nearest Taurus group listed in Luhman et al. (2009). We chose as likely members the stars which, within 1σ, satisfied the criterion $9.8 \leq RV \leq 17.5$, corresponding to the range in the mean radial velocities of the Taurus groups. For the *SDSS*-selected early-type stars we show the radial velocities in Figure A.7. Most of the *SDSS*-selected stars satisfying the nominal RV-selection

criterion are too faint in the near-infrared to be probable members of Taurus.

A.2.3.3 RESULTS OF CANDIDATE SELECTION

The information in Table A.3 was used along with the procedures outlined above to arrive at the list of likely early-type members of Taurus. In all, 52 stars independently satisfy the proper motion membership criteria and 28 the distance membership criteria, with 18 satisfying both. However, not all sources have known values for all or any of the quantities we consider. As the samples of early-type stars under consideration were derived from four different sources, we discuss the details of our analysis as appropriate for each sample in what follows.

For the SIMBAD sample of known early-type stars and for the Rebull et al. infrared excess sample, spectral types exist in the literature. Also, we have followed up some of these stars spectroscopically ourselves in order to verify or revise their spectral classification. Fairly accurate spectroscopic parallax distances have thus been used to test the membership of these two sets of stars with Taurus. Radial velocity measurements also exist for some of these stars. We found that two stars, HD 28929 (B8V; also known as HR 1445) and HD 29763 (B3V; also known as τ Tau), satisfy all the tested criteria for membership of Taurus: parallax distance, proper motion, and radial velocity. V892 Tau (A0; also known as Elias 1) satisfies the first two criteria, leaving the third unknown due to insufficient information, but this star is already an accepted member of Taurus on the basis of its circumstellar disk attributes.

In the 2MASS photometric sample, accurate spectral classification is absent for many of the stars, and for these calculation of accurate spectroscopic parallax has not been possible. In this set of stars, twelve satisfy two criteria leaving the third criterion indeterminate due to insufficient information, while two stars satisfies all the criteria for membership of Taurus. However, many of these stars are late type T Tauri stars that are already known members of Taurus but selected by our methods because they have large enough near-infrared excesses to push them into the region of the 2MASS color-color diagram occupied by reddened earlier type stars. We note that the 2MASS search does select the mid-A stars HD 26212 and HD 31648 (along with AB Aur, if we ignore the 2MASS-PSC flag at K_s-band) as candidate early-type members, but finds no new B stars.

For the *SDSS* spectroscopic sample, the magnitude range precludes the availability of any *Hipparcos* parallax values, but since spectral types are available for many stars, spectroscopic parallaxes can be calculated. RV is also measured by the *SDSS* analysis pipeline. Some of the *SDSS*-selected stars satisfy the kinematic criteria (see Figures A.6 and A.7); however, they are under-luminous with respect to the expectations for reddened early type stars at the Taurus distance (see middle panels of Figure A.3) and indeed have much larger spectroscopic distance estimates (Table A.3). Most of these early-type stars are likely in the Galactic halo.

Finally, the spectroscopic parallax distance suggests that HD 31305 (located near AB Aur and discussed by Cody et al. (2013)) lies just beyond the distance range defined by our member-selection criterion ($<$10% in excess of the standard deviation among calculated d_{SPEC} values). Nevertheless, its proper motion conforms

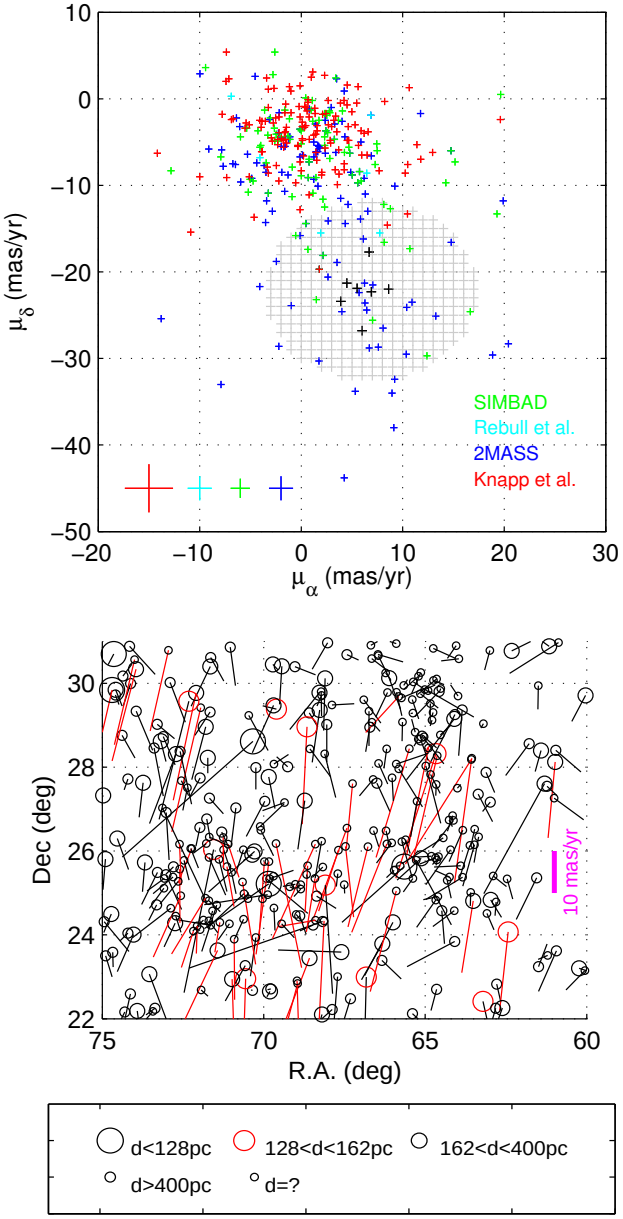

Figure A.6: *Upper panel*: Proper motions of the candidate early-type stars shown as a cloud plot with blue indicating objects selected from 2MASS; green, SIMBAD; cyan, the B stars proposed by Rebull et al. (2010), and red: O,B,A stars from Knapp et al. (2007). The "+" symbols at the bottom-left corner denote the mean errors for each sample. The mean proper motion of Taurus groups considered in this paper (see Section A.2.3.2) are shown as black symbols The hatched reference circle indicates the area where the χ^2 probability of membership is greater than 1% with respect to the mean proper motion of Taurus. 51 stars from our list of candidate early-type stars have proper motions consistent with Taurus groups. *Lower panel*: Vector diagram showing the proper motion of all the stars tested for membership. Those which satisfy the proper motion criterion P($\chi^2 > 1\%$) are shown in red. Positions of the stars are indicated by the circles, whose sizes are based on the spectroscopic parallax distance of the respective stars (key given at the bottom). Red circles denote stars satisfying our distance criterion for Taurus member selection (within an uncertainty of 15 pc).

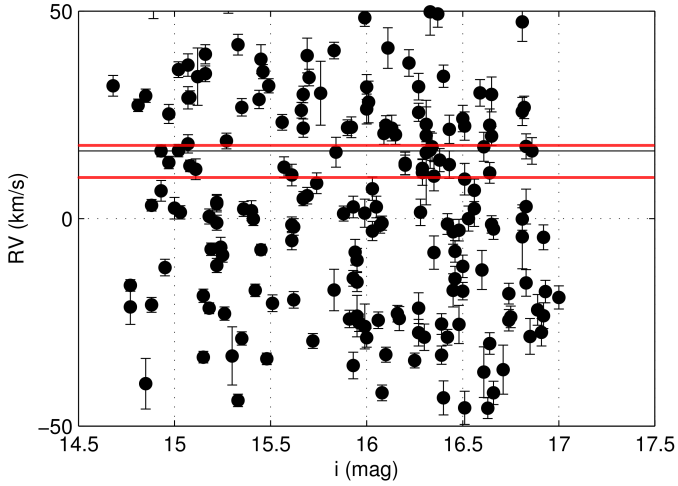

Figure A.7: Radial velocity versus *SDSS* i-band magnitude for the early-type stars selected from Knapp et al. (2007). The y-axis has been rescaled to show only the stars with RV between $\pm$50 km s^{-1}. The mean RV of accepted members of Taurus (Luhman et al. 2009), 15.8 km s^{-1}, is shown with a black horizontal line. The neighboring red lines denote the region $9.8 \leq RV \leq 17.5$, our RV-member selection criterion. No concentration at the Taurus velocity is seen, and among those stars satisfying this RV criterion, most are too faint to be probable members of Taurus.

with that of known Taurus members. Hence, we consider in what follows that this star could well be a member of Taurus.

In summary, we newly advocate the membership of two B-type stars (HD 28929 and HD 29763) and one A-type star (HD 26212) in Taurus using distance and kinematic arguments, and in addition find one A0-type star (HD 31305) to be a probable member (though it is not yet confirmed due to the lack of radial velocity information). Below, in section A.3, we discuss these stars in more detail and also revisit some of those which were rejected in the above procedures. After consideration of other evidence which might point towards their association with Taurus, we find several additional B and A0-type to be plausible Taurus members. In order to inform our further assessments regarding the likelihood of cluster membership, additional data on many of these stars were collected.

A.2.4 FOLLOW-UP SPECTROSCOPY

We performed follow-up spectroscopy of selected stars with an aim of (i) confirming or revising their spectral types based on temperature and surface gravity diagnostics, (ii) measuring radial velocities, and (iii) determining more precise stellar parameters so as to estimate ages. We obtained optical spectra for a subset of the Taurus early-type candidates which were found to satisfy several of our membership criteria, or which illuminated a nebula in the Spitzer image. Some of these sources appeared to be better candidates at the time we obtained the spectra than later re-analysis revealed. We also observed for comparison a grid of dwarf B stars from Abt et al. (2002). and, for calibration, RV standard stars and spectrophotometric standards.

The optical spectra were obtained at the Palomar 200-inch Hale telescope on 4 December 2010 using the Double Spectrograph (DBSP). The data have medium spectral resolution ($R \simeq 7800$ and 10419 in the blue and red channels respectively). We used a dichroic at 5500Å to split the optical light into blue and red channels with a 1200 lines mm^{-1} grating blazed at 4700Å, at a grating angle 34.92° on the blue side and 1200 lines mm^{-1}, 7100Å blaze, and 42.73° on the red side. The spectral range covered was $\sim 3480-5020$ Å at 0.55 Å pixel^{-1} (blue) and $\sim 6440-7110$ Å at 1.4 Å pixel^{-1} (red). For wavelength calibration we used an Fe-Ar lamp in the blue and a He-Ne-Ar lamp in the red. Spectra for two stars (HD 27659 and HD 26212) were taken on 2 September 2011 using a different configuration resulting in a much lower resolution and a larger wavelength coverage.

We reduced the data using the Image Reduction and Analysis Facility (IRAF) *ccdred* and *onedspec* packages. Spectra were extracted with the *apall* task after trimming, bias-subtraction, and flat-fielding of the images. The wavelength solution was then applied using *dispcor*. In the case of stars for which we had multiple short-exposure observations, the spectra were coadded using *scombine* to get a higher signal-to-noise ratio. We normalized all the spectra with *splot*.

For spectral typing the program stars, we measured the equivalent widths of several diagnostic absorption lines using *splot*, and then compared them with those of reference-grid stars (Figure A.8), guided by the graphics in Didelon (1982). The normalized spectra of the reference-grid stars and the program stars are shown in Figure A.9 with the reference types adopted from the literature and the program star types derived by us. We also compared our spectra with templates by Gray[5] and Morgan et al. (1943)[6]. The results of the spectroscopic analysis are given in Table A.4. Estimates for the effective temperature ($T_{\rm eff}$), projected rotational velocity ($v\cdot \sin i$) and the surface gravity (log g) and were made by fitting the spectra with templates from Munari et al. (2005). For the template spectra, the comparison grid resolution was 500–1000 K in $T_{\rm eff}$ and 0.5 in log g, while the grid in $v\cdot \sin i$ was: 0, 10, 20, 30, 40, 50, 75, 100, 150, 200, 250, and 300 km s^{-1}; hence, our derived values are no more accurate than this. Some stars have equally good fits between a higher temperature and gravity point, versus a lower temperature and gravity point one grid spacing away; in these cases we generally preferred the dwarf to the giant solution. The physical parameters derived from this fitting are given in Table A.5. In combination with the set of intrinsic stellar parameters discussed above, we thus derived a second set of spectral types for the stars that were spectroscopically followed up. These spectral types generally agree with those derived using equivalent widths in Table A.4. Due to the coarse spectral grid of templates and degeneracies involved in the fitting process, the spectral types derived from our equivalent width analysis usually take precedence over those derived from spectral fitting.

Unfortunately, radial velocity information could not be derived from our spectra at the expected performance of the instrument (given our care in taking source-by-source comparison lamp calibration frames), perhaps due to poorly understood flexure effects. We note that an error as small as 1 Å in the wavelength

[5]http://ned.ipac.caltech.edu/level5/Gray/Gray_contents.html
[6]http://ned.ipac.caltech.edu/level5/ASS_Atlas/MK_contents.html

calibration leads to an error of about 66 km s^{-1} at 4500 Å. Shifts of this order have been experienced between contiguous exposures while working with DBSP data. Due to our short exposure times, there are no sky lines in the blue part of the spectrum that could aid in more accurate wavelength calibration. While the red channel spectra have ample telluric absorption, too few photospheric absorption lines are available to provide a good fit. Hence, we defer the estimation of RV to a later time with another data set.

Notably, hydrogen emission lines or line cores are seen in HD 283751, HD 283637, V892 Tau, and AB Aur (see Figure A.9). While the emission properties of the last two stars in this list are well known, they have not been reported previously for the first two objects. Emission lines are often taken as a signature of activity associated with stellar youth, although evolved early-B type stars may exhibit a "Be phenomenon". We note that the derived spectral types of these emission-line objects are B5e and B9.5e, later than typical of evolved Be stars, but the infrared excesses detected by Rebull et al. (2010) are more typical of evolved Be stars than of young accretion disk systems. Neither star can be associated with Taurus by kinematic or distance arguments, and thus they appear to be interesting background interlopers.

A further note concerning the spectra is the appearance in Figure A.9 of what is likely diffuse interstellar band absorption at 6614 Å in about half of the program stars. Corresponding broad absorption at 4428 Å is also seen. There is excellent correlation between the presence of this feature and the spectroscopic parallax distance estimates reported in Table A.3. Distant stars have the absorption while closer stars do not. Notably, none of the stars we eventually conclude in this work to be associated with Taurus have these interstellar absorption features.

Finally, we call attention to ubiquitous absorption at 6708 Å, coincident with the Li I line seen in young low mass stars, that is seen in all of our spectra taken on 2010, December 4 (Figure A.9). The feature is not likely to be astrophysical and we suspect a (currently unexplained) terrestrial origin, perhaps related to a meteor shower.

A.2.5 MODELLING THE DUST EMISSION WITH *DUSTY*

In this section we consider the nebular structures associated with several of the early type sources and prepare to model in the next section their multiwavelength image morphology. Reflection nebulae appear bluish when illuminated by light from a nearby star on account of the scattering properties of dust. The star and the dust may be physically related, or the encounter between the star and a cloud of overdense interstellar medium may be by chance. Infrared emission is also associated with the illuminated clouds, due to the warm dust, but compared to, e.g., H II regions, the infrared luminosity is lower and there is a lack of radio emission.

DUSTY[7] solves the radiation transfer problem for a light source embedded in dust through an integral equation for the spectral energy density (Ivezic & Elitzur 1997). The code takes the following input parameters: type of external radiation source, dust composition, grain size distribution, dust temperature at the edge nearest to the external source, geometry of the cloud (spherical shell / planar slab), density profile, and the

[7]http://www.pa.uky.edu/ moshe/dusty/

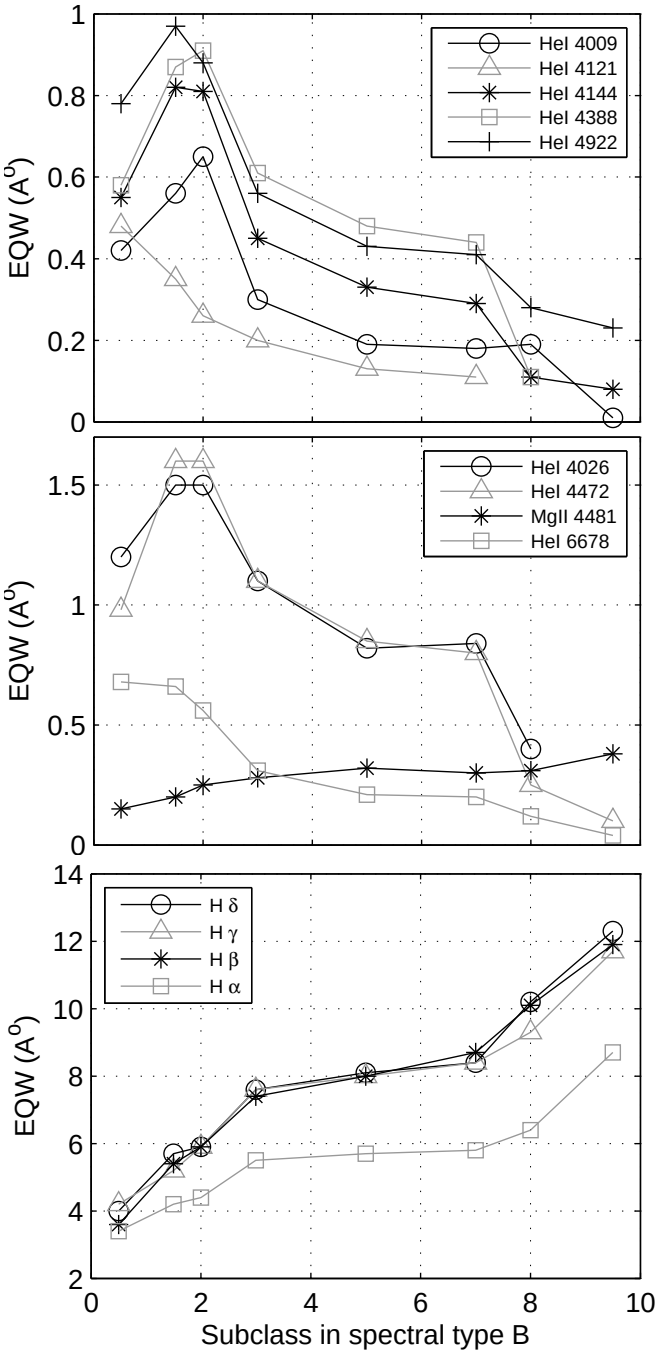

Figure A.8: Equivalent widths of various absorption lines measured in the grid of B-type spectral standard stars (luminosity class V only) that were observed for comparison with the Taurus candidate early-type stars.

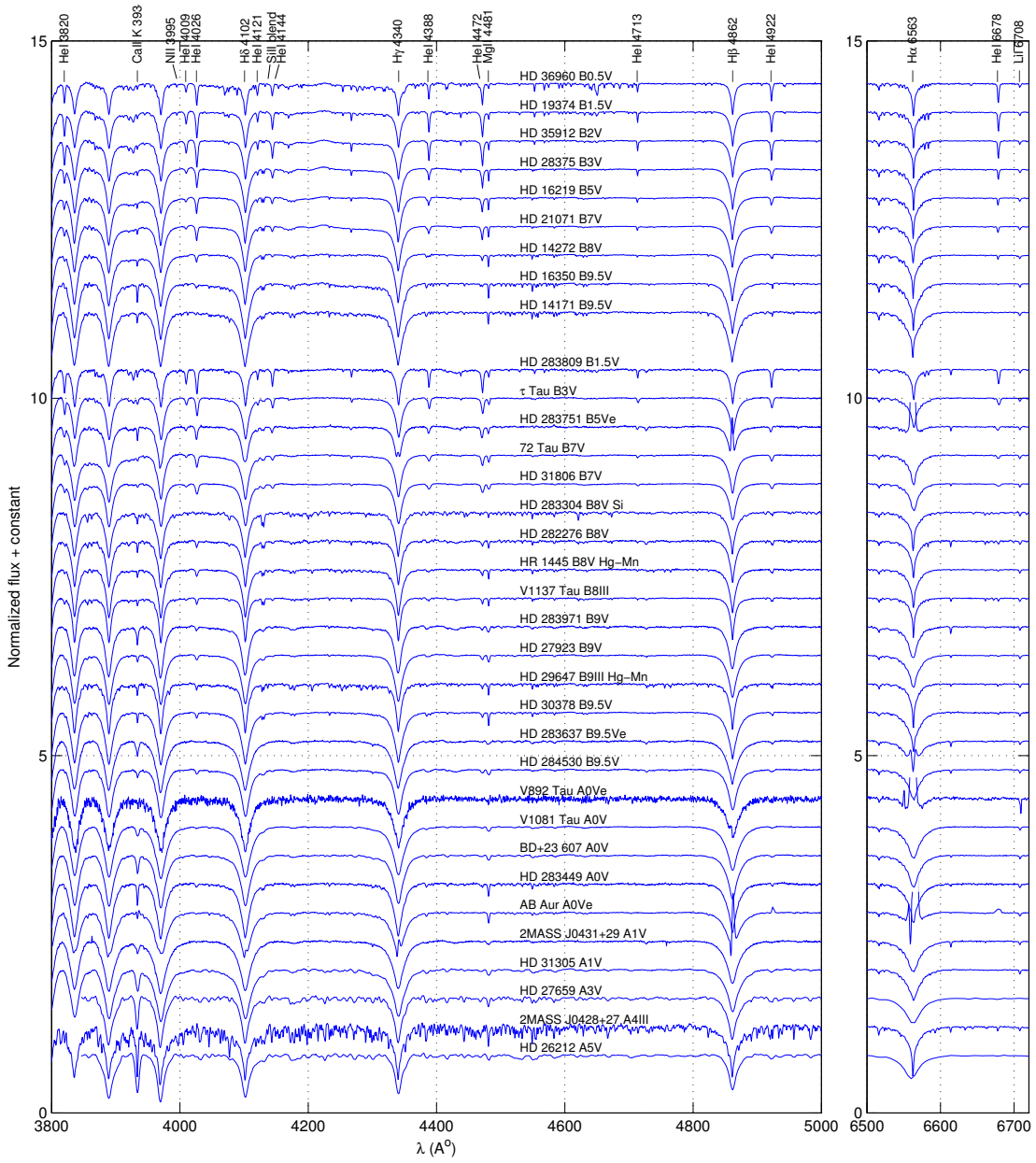

Figure A.9: Normalized optical spectra obtained at the Palomar 200-inch Hale telescope. The upper set of stars comprise the grid of B-type spectral standard stars used for assigning spectral types to the program stars (lower set of spectra). All spectra have an arbitrary offset along the ordinate. Note the hydrogen emission lines or line cores in HD 283751, HD 283637, V892 Tau, and AB Aur. Approximately half of the program stars have diffuse interstellar band signatures: a narrow absorption at 6614 Å and a broader shallow feature at 4428 Å. The feature labeled as Li I 6708Å in the right panel is probably anomalous as this line is not expected to be present in these early-type young stars, and especially not in the spectral standards (including our white dwarf flux standard which is not shown); we suspect a possible terrestrial atmosphere source, perhaps associated with the Geminid meteor shower; this hypothesis is supported by lack of absorption at this wavelength in the two spectra towards the bottom of the sequence that were taken on a different night from all others.

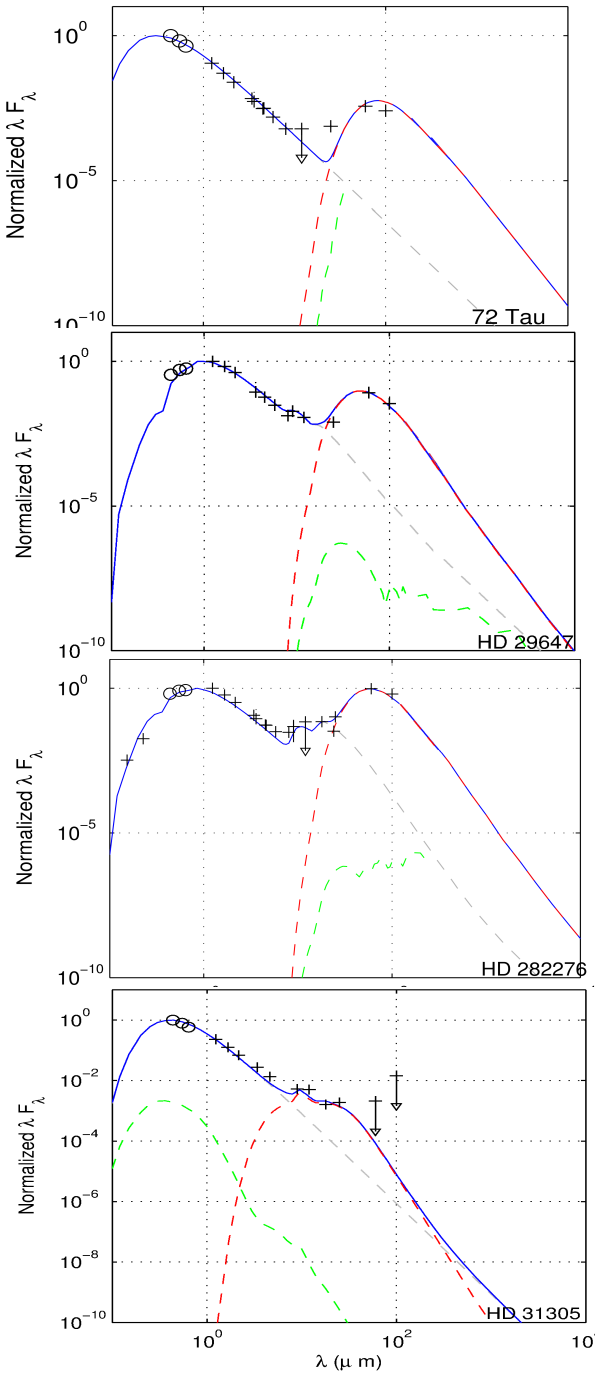

Figure A.10: Modelling the SEDs (black data points) of some sources having far-infrared excess using *DUSTY*. For each of the sources, the attenuated blackbody representing the star is the grey dashed line, the contribution from the thermal and scattered emission components from the associated dust slab are shown as red and green dashed lines, respectively, and the blue solid line represents the total model output. Photometric points with error bars are shown; the circles represent BVR photometry that is reported without errors. *72 Tau*: A dust slab having 40 K temperature at the boundary closest to 72 Tau roughly reproduces the SED. *HD 29647 Tau*: Two slab components are required to reproduce the SED, one chosen to have a dust temperature of 500 K to reproduce the 10μm silicate feature, and another one at about 45 K. *HD 282276*: Two dust slabs, having inner-edge temperatures of 200 K and 35 K are required to faithfully reproduce the SED. *HD 31305*: The inner-edge dust temperature was found to be 350 K.

optical depth. The dust temperature and optical depth together define the amount of radiation present at the edge of the photodissociation region. Ideally, given the dust properties and parameters of the illuminating star, the inner temperature of dust can be calculated giving us the separation from the star. Following Tielens (2005), we can calculate the dust temperature in a slab geometry as,

$$\begin{aligned}(T_d/Kelvin)^5 =& 2.7\times10^5\, G_0\, e^{-1.8A_V} \\ &+4.1\times10^{-4}\left[0.42-\ln(4.3\times10^{-4}\, G_0)\, G_0^{6/5}\right] \\ &+2.7^5 \end{aligned} \tag{A.4}$$

where A_V is the reddening caused by the slab. The assumption here is a simplistic model in which the absorption efficiency of the dust is directly proportional to the wavelength for $\lambda < \lambda_0 = 1000$ and is unity elsewhere; the dust size is $a = 1$ μm. G_0, the far-ultraviolet (FUV, $h\nu > 13.6$ eV) radiation field in terms of the average interstellar radiation field (1.6×10^{-3} erg cm^{-2} s^{-1}), is given by,

$$G_0 = 1.8\times\left(\frac{L_*}{100L\odot}\right)\left(\frac{\chi}{3.6\times10^{-4}}\right)\left(\frac{d}{0.02\text{ pc}}\right)^{-2} \tag{A.5}$$

where χ is the fraction of the star's luminosity (L_*) above 6 eV and d is the distance from the star with the normalization constant appropriate for a B8V star.

In the cases of interest here, the brightest part of the illuminated nebula is a few arcminutes wide, which, at a fiducial distance of 140 pc corresponds to $\sim$0.1 pc. For comparison, using the (Tielens 2005) formulation, the H II region expected for a constant density pure hydrogen region with electron number density n_e = 10^3 cm^{-3} surrounding a B0V star is 0.4 pc (and would produce detectable radio emission) while for a B5V or B8V star the Strömgren radius, $\mathcal{R}_s$, is about 0.03 pc or 0.02 pc respectively (and usually would not be detectable in the radio). Note that $\mathcal{R}_s \propto n_e$, so local overdensities can allow the photodissociation regions (PDRs) to exist closer to the star thus heating them to higher temperatures. Therefore, if a dust slab were located at a few hundredths of a parsec from a B8 dwarf, the FUV radiation field it would experience is $G_0 \simeq 2$. Using $A_V \simeq 1$ for the slab, we then get $T_d \sim 10$ K. However, this over-simplified picture overlooks important processes within PDRs such as cooling through trace species such as [OI] and [CII], and the inhomogeneities in the dust cloud as indicated by the changing morphology of the nebulae towards the B stars with wavelength.

Our calculations with *DUSTY* were conducted assuming a power-law grain size distribution according to the Mathis-Rumpl-Nordsieck model (Mathis et al. 1977). As expected, when the optical depth or the physical thickness of the simulated slab is reduced, the scattered and thermal components of the output flux both decrease. If the dust temperature is lowered, the thermal emission peak increases relative to the primary (scattered stellar flux) peak. Notably, the shape of the thermal bump flattens and broadens if the relative abundance of amorphous carbon to graphite increases, whereas increasing the relative abundance of silicates produces the broad 10 and 18 μm features.

We model the dust surrounding 72 Tau, HD 29647, HD 282276 and HD 31305 as slabs, and make an attempt to reproduce their SEDs using the *DUSTY* code. Our results appear in Figure A.10 and are discussed for the individual stars in the next section.

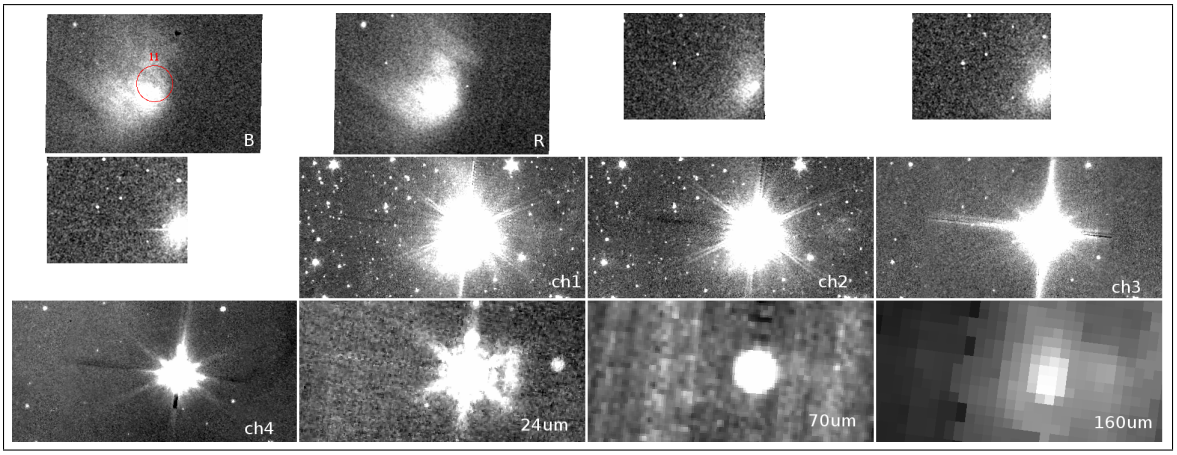

Figure A.11: Cutouts of the IC 2087 region. Left-to-right are: B, R images from the Palomar Observatory Sky Survey (POSS-I) and J, H images from 2MASS (Row 1), Ks band from 2MASS, and IRAC channels 3.6μm, 4.5μm, 5.8μm (Row 2), IRAC 8μm, and MIPS images 24μm, 70μm, and 160μm (Row 3). The red circle in the POSS-I B band image has a diameter of 1 arcmin, for scale.

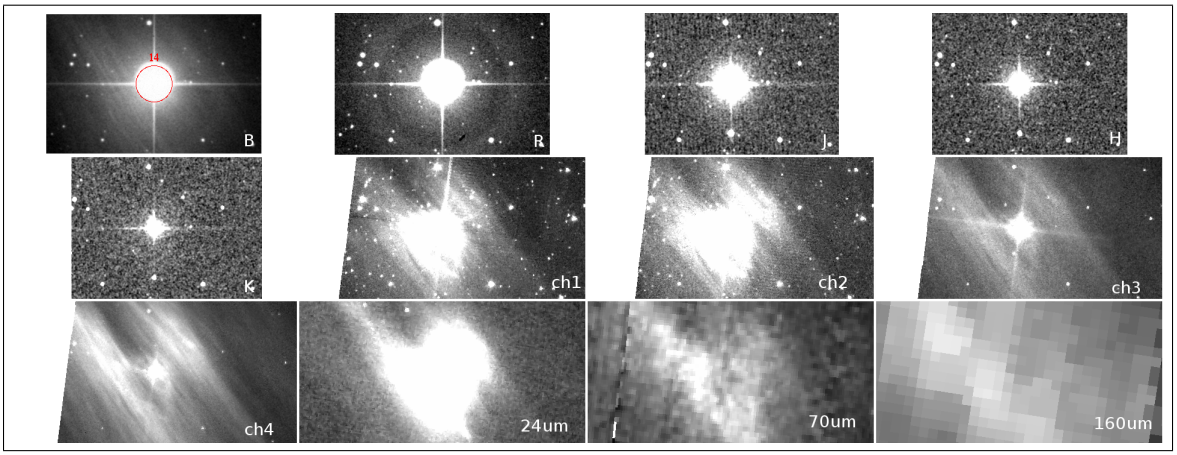

Figure A.12: Same as Figure A.11 but for 72 Tau.

A.3 INDIVIDUAL EARLY TYPE OBJECTS PLAUSIBLY ASSOCIATED WITH TAURUS

In this section we consider the collective set of plausible early-type members of Taurus based on the various lines of evidence for their physical association with the clouds.

Above we discussed the kinematic and distance evidence for association of HD 28929 (HR 1445), HD 29763 (τ Tau), HD 26212, and HD 31305 with Taurus. Additionally, the early type sources HD 31648, AB Aur, HD 27659, and HD 283815 have several lines of evidence that favor their association with Taurus but do not meet all of our stated criteria, mostly due to missing data.

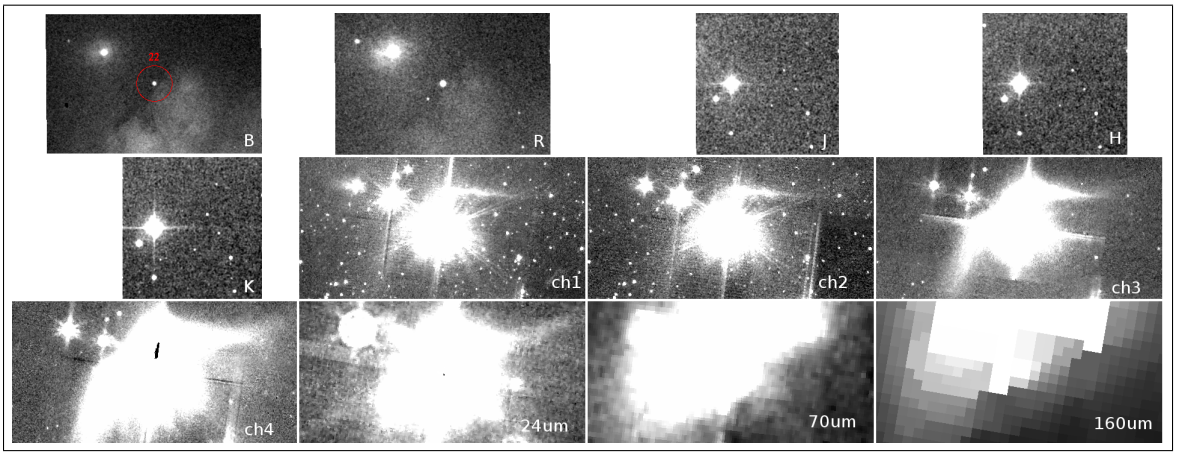

Figure A.13: Same as Figure A.11 but for V892 Tau / Elias 1.

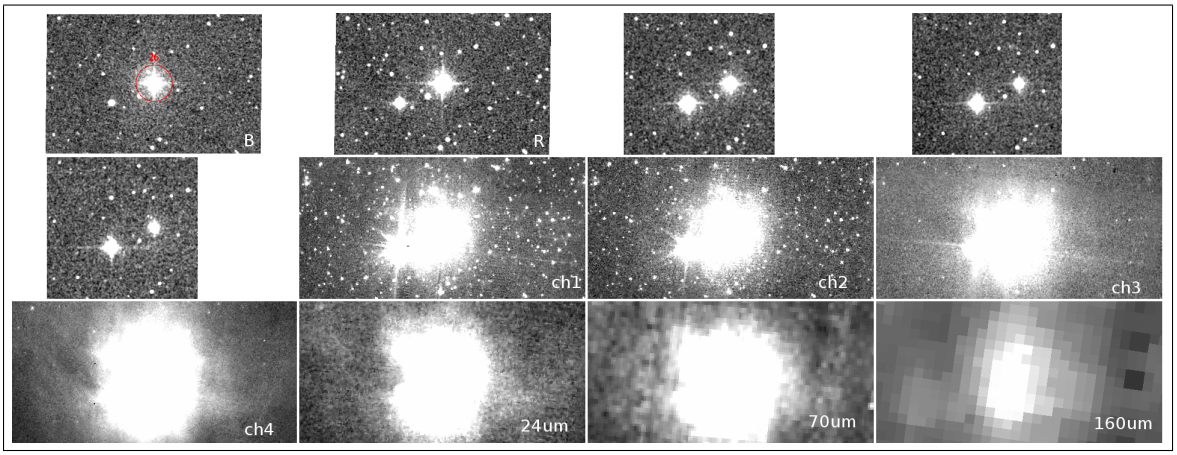

Figure A.14: Same as Figure A.11 but for HD 282276.

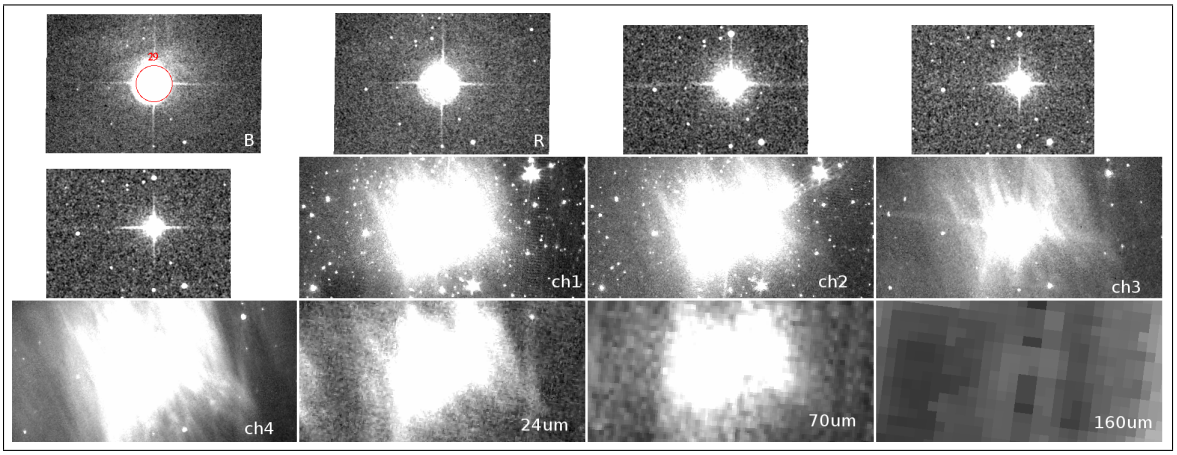

Figure A.15: Same as Figure A.11 but for HD 29647.

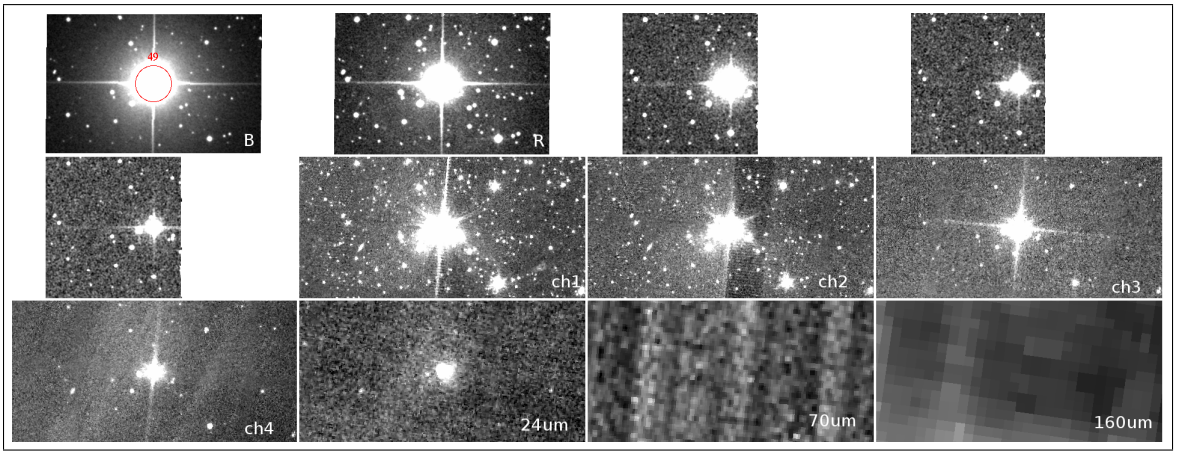

Figure A.16: Same as Figure A.11 but for HR 1445.

Further, within the footprint observed by Spitzer, six B-type stars (IC 2087-IR, 72 Tau, V892 Tau, HD 282276, HD 29647 and HR 1445) are seen in the multiband Spitzer images to illuminate mid-infrared reflection/scattered-light nebulae, not all of which can be kinematically associated with Taurus. As mentioned above, HR 1445 was also picked out by our distance and kinematic membership selection criteria. The nebular structure is illustrated in Figures A.11 – A.16. With the exception of IC 2087 which has a bright optical nebula, optical scattered light is weak or absent among our sample. Furthermore, there is relatively little extended emission in the near-infrared (J, H, K_s bands), with the wavelength of peak emission in the nebular regions typically being 8 or 24 μm. The morphologies of the nebulae are quite varied. They extend up to a few arcminutes and can appear circular or squarish, some of them being asymmetric and highly striated.

For both kinematically selected and nebular-selected objects, we constructed spectral energy distributions (SEDs) as shown in Figure A.17. We used the following data in making the SEDs: (i) sub-mm: SCUBA/Andrews & Williams (2005); (ii) infrared: *Spitzer*, 2MASS, AKARI, IRAS; (iii) optical/UV: NOMAD, GALEX. Counterparts within one arcsecond of the source were chosen, with the exception of IRAS counterparts.

As reviewed by Williams & Cieza (2011), for young pre-main sequence stars red *Spitzer*/IRAC colors indicate excess emission from circumstellar disks and envelopes, whereas excess emission at 24 μm but not in the shorter wavelength IRAC bands is indicative of a disk with an inner hole. At slightly later stages the dust is attributed to second generation 'debris' rather than primordial material. Infrared excess also could be attributed to dust shells around evolved stars, or illumination of nearby interstellar material, irrespective of any physical association of it with the star.

We also constructed various color-magnitude diagrams and overplotted isochrones (see Figure A.18) to assist in the assessment of stellar age, assuming that the distance of Taurus is appropriate for each source. The unknown stellar multiplicity and photometric error add substantial uncertainty to the stellar age estimate. Also, because of the rapid evolution of high mass stars, the age derived via isochrones is very sensitive to

the reddening correction, which is not insignificant, and which we have derived assuming a plausibly invalid constant R_V of 3.1. All these factors together preclude accurate determination of the stellar ages of our sample but we present the resulting color-magnitude diagram for completeness.

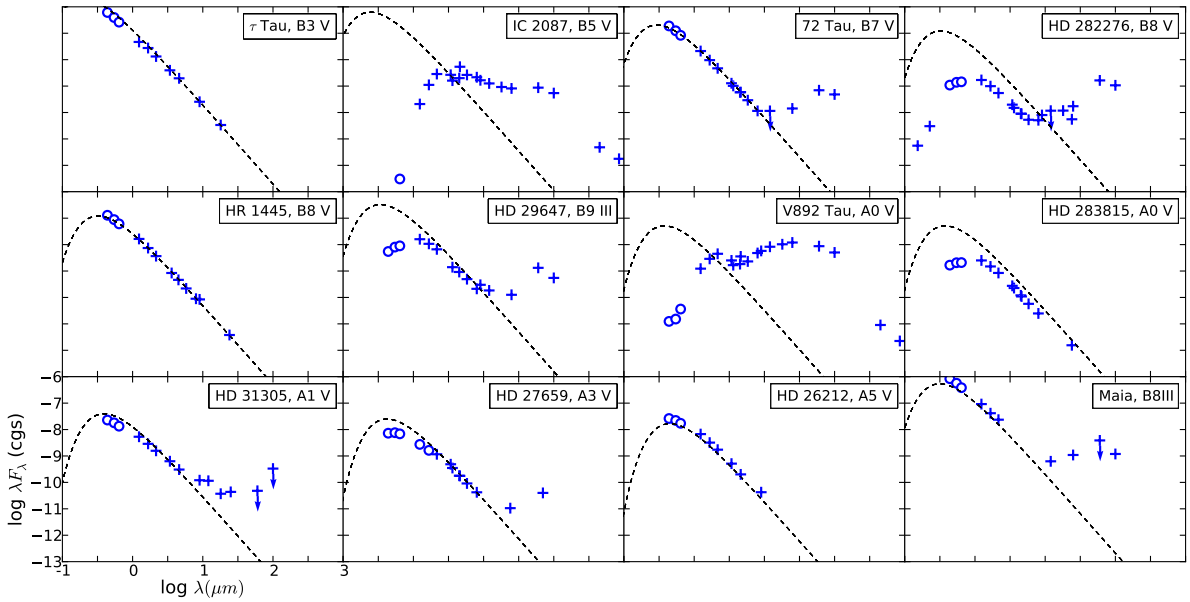

Figure A.17: Spectral energy distributions (SEDs) of those sources exhibiting infrared nebulae in Figure A.1 plus the candidate early-type stars we conclude are probable members of Taurus based on our assessment of distance and kinematics. Infrared excess is apparent in many objects. This may be due to the presence of a circumstellar disk associated with a pre-main sequence stars, to a debris disk in a somewhat older main sequence star, to a dusty atmosphere in the case of an evolved giant star, or to a chance superposition of a hot star with a nearby diffuse cloud. For comparison, an example of the chance-superposition case is also shown in the lower right panel: the Pleiades member Maia, whose SED exhibits an apparent infrared excess. The data sources include GALEX (ultraviolet), NOMAD (optical, *BVR*), 2MASS-PSC (near-infrared, JHK_s), *Spitzer*, AKARI and IRAS (mid-far infrared), and SCUBA (sub-mm). Photometric error bars are generally smaller than the symbol size; circles denote photometry lacking uncertainty (usually values from NOMAD). The dashed line in each panel represents a blackbody at 140 pc characterized by the effective temperature and radius of the star whose SED is represented in that panel. No correction for reddening has been applied though the existence of reddening can be inferred from the location of short wavelength photometry well below the nominal blackbody.

We now discuss our findings for individual sources, beginning with those illuminating nebulae in the *Spitzer* and then moving on to other candidates that we have assessed.

A.3.1 IC 2087

The IC 2087 nebula (Figure A.11) is brightest at optical wavelengths and is less prominent at *Spitzer* wavelengths, a unique illumination pattern among our sample. The SED (Figure A.17) of the associated point source (IC 2087-IR = IRAS 04369+2539 = Kim 1-41) is consistent with an early-type Class I – Class II young stellar object seen through ∼15 magnitudes of visual extinction. The foreground extinction is claimed

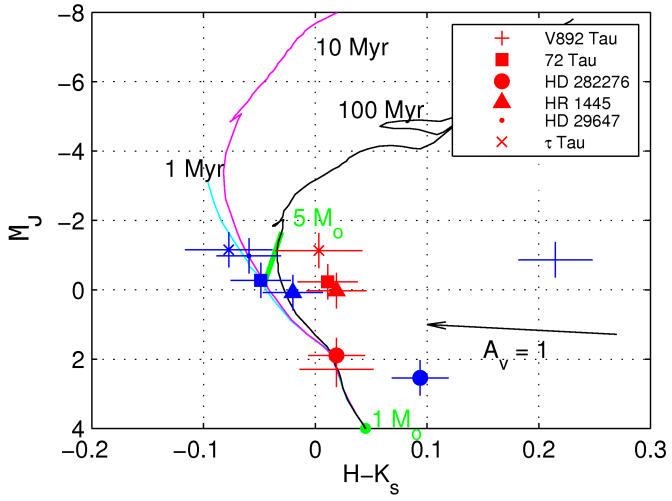

Figure A.18: Estimation of the isochronal age of some of B stars showing infrared reflection nebulae and τ Tau. Isochrones are from Girardi et al. (2002). Horizontal errorbars represent the error in the 2MASS magnitudes and vertical errorbars represent the uncertainty in the distance ($128 < d < 162$pc). Blue markers are plotted using the reddening parameters from literature, while red markers represent values derived using $R_V = 3.1$ and the Cardelli et al. (1989) reddening.

to be $A_V < 1$ (Frerking et al. 1982), and hence the majority of the extinction toward IC 2087-IR should be due to circumstellar material (Shuping et al. 2001).

This source is a known YSO member of Taurus. High veiling has precluded accurate determination of its spectral type but Elias (1978) classified it as B5 based on the bolometric luminosity. We were unable to derive a spectral type from either the *SDSS* spectrum or our own follow-up optical spectroscopy of this source. No spectroscopic parallax is possible given the vague spectral type. However it appears that a proper motion measurement exists for IC 2087-IR. White & Hillenbrand (2004) quoted a radial velocity of 22 ± 8 km s^{-1} but with the large error bar it is hard to tell whether the measurement is consistent with the RV membership criterion used herein; furthermore, the lines used may have been dominated by outflow kinematics rather than photosphere. Nonetheless, the source is currently an accepted member of Taurus, and based on multiwavelength information, we propose that an early spectral type of B5–B8 is most appropriate.

Rebull et al. (2010) confirmed that the source has a flat spectrum in the near-to-far-infrared, and report $L_{IR}/L_{total} = 0.41$. Weak molecular outflows, the presence of Herbig-Haro knots, mid-IR absorption features and associated reflection nebulosity provide additional evidence of the pre-main sequence nature of this object (e.g. Furlan et al. 2008). Hillenbrand et al. (2012) provide an extensive discussion of this source.

The nebula is apparently the result of complex radiative transfer of an emitting source seen through a three-dimensional, non-uniform distribution of circumstellar dust that both obscures the central source and produces significant amounts of scattered light asymmetrically distributed with respect to the infrared point source. We do not attempt to model the emission here, but see Hillenbrand et al. (2012) for an accretion disk

and weak envelope fit to the spectral energy distribution.

A.3.2 72 Tau

The nebula associated with 72 Tau (HD 28149) is brightest at about ~ 60 μm. It is prominent in all IRAS and *Spitzer* bands and is also discernible in blue optical bands. From the image cutouts (Figure A.12) it is evident that the optical depth of the associated nebula is quite different at different wavelengths in the infrared. The blue optical nebula appears to have been known by Cederblad (1946) and thus this feature should be referred to as Ced 34. The striated nebular morphology is similar to that observed for the Maia nebula, illuminated by the Pleiades stars. The SED (Figure A.17) of 72 Tau is consistent shortward of about 10 μm with an ideal blackbody having very low reddening, but there is a longer wavelength excess. The SED morphology is similar to that of Maia as well. Kalas et al. (2002) noted that 72 Tau is a Vega-like source associated with a gas overdensity, but no rigorous analysis was performed.

We arrive at a spectral classification of B7V for 72 Tau based on our follow-up spectroscopy. The Hipparcos distance to this star is 127 ± 12 pc while our estimate of spectroscopic parallax is 161 ± 3 pc. Walter & Boyd (1991) quoted a spectroscopic parallax distance of 179 pc and proposed that this star is a member of Taurus and the Cas-Tau OB association. The study by de Zeeuw et al. (1999) however does not acknowledge this star as a member of Cas-Tau association. Kenyon et al. (1994) found a similar distance of 178 pc based on a B5V spectral type. If the Hipparcos distance is accurate, 72 Tau would lie close to the nearer edge of the Taurus cloud whereas if the further distance estimates are correct the star is at the back edge of (our distance) or behind (literature distances) the cloud. Both the proper motion and the radial velocity of this star are consistent with the Taurus group (as defined by Luhman et al. 2009). We conclude that it is very likely that 72 Tau belongs to Taurus, although in the past (Whittet et al. 2001) the star has been considered a background source in studies of the Taurus clouds.

Previous age analysis in the literature (Westin 1985) suggested an age of 20 Myr based on ubvyβ photometry and theoretical stellar evolution models. From our spectral analysis, 72 Tau is clearly a main-sequence star which, after consideration of its spectral type, tells us that it is at least several Myr old and at most 170 Myr old; we are unable to place any further constraints on its age.

We were able to reproduce the SED with *DUSTY* using the parameters: (i) $T_{\rm eff} = 12,500$ K blackbody as the external radiation source; (ii) dust composition with silicates from Draine & Lee (1984) and amorphous carbon from Hanner (1988) in a ratio of 1:4 (however, output not very sensitive to this ratio so long as silicate fraction is less than 1); (iii) a 40 K dust temperature at the edge nearest to the external source; (iv) a 0.55 μm optical depth of 0.1 (corresponding to $A_V \simeq 0.1$). The resultant ratio of the dust contribution to the observed flux of the central star, a B7V-type blackbody, is about 1:200. This final model of the SED is shown in Figure A.10. Since the fraction of the observed flux contributed by dust emission is much less compared to that contributed by the central star itself, we conclude that the nebula is not a photodissociation region, and we do not expect any free-free emission (indicative of an ionizing front) from it.

A.3.3 V892 Tau

In the optical bands, V892 Tau (also known as Elias 1 or more properly Elias 3-1) appears to be a point source with an associated faint reflection nebula (Figure A.13). The nebular structure is brightest at about 24μm. Like IC 2087-IR, it is heavily reddened with a significant envelope component to its circumstellar environment. The SED (Figure A.17) is that of a Class I – Class II source. Rebull et al. (2010) report it as a flat-spectrum source in the near-to-far-infrared, having $L_{IR}/L_{total} = 0.089$. V892 Tau is a double-star system (Smith et al. 2005) with a circumbinary disk (Monnier et al. 2008).

This Herbig Ae/Be system is a well-accepted member of Taurus with reported spectral types ranging from B8 to A6. Our spectral type is B8.5V to ∼A0Ve. The optical spectrum also shows Balmer emission lines, further evidence of its youth and likely membership. Our derivation of the spectroscopic parallax distance for this star has a large uncertainty, possibly enhanced by reddening law uncertainties. The probability associated with the χ^2 analysis confirms that this source is a proper-motion member of Taurus. As for IC 2087-IR, the circumstellar environment is complex and we do not attempt to model the emission.

A.3.4 HD 282276

The nebula associated with HD 282276 (Figure A.14) is evident only in the *Spitzer*/IRAC and MIPS bands, and not in the 2MASS or shorter wavelength bands. The nebula appears to be circular and optically thick at *Spitzer* wavelengths. This source shows considerable infrared excess in its SED (Figure A.17) beyond 10 μm. The two peaks in the infrared excess suggest two different dust components from either two different radii or two different compositions contributing to the infrared emission.

Rebull et al. (2010) have classified HD 282276 as a pending member of Taurus which needs additional follow-up; they tentatively categorized it as a Class II YSO. The spectrum of this star is B8V in our analysis but it does not show any emission lines. Both the spectroscopic parallax distance and the proper-motion are inconsistent with Taurus. We estimated the reddening to be $A_V = 2.8$, and a spectroscopic parallax distance of 422 ± 52 pc, which means that it lies closer to the distance of Perseus than Taurus. We speculate that this star could be associated with the Perseus star forming region, which has a mean proper motion of about $\mu_\alpha = 5$ mas yr^{-1}, $\mu_\delta = -12$ mas yr^{-1} (de Zeeuw et al. (1999) and PPMXL catalog), quite consistent with the measured values for HD 282276. However, the derived distance is somewhat large, even for Perseus, and the star is offset to the east of the main Perseus cloud. There is no radial velocity measurement.

The fact that the star illuminates a reflection nebula in the infrared (see Figure A.1), suggests the presence of cloud material, perhaps associated with a low column density extension of the classical Perseus region. It is also possible that HD 282276 is similar to several Pleiades member stars, with the star randomly encountering a local overdensity in the interstellar medium.

The $\sim$ 3 arcmin-wide size of the nebula corresponds to a roughly 0.4 pc diameter structure at 420 pc. The H II region for a B8V star surrounded by a pure-hydrogen nebula would be about 0.02 pc in diameter

and as the two values are inconsistent (even if our distance estimate is wrong by a factor of 3), we believe that the nebula is not a PDR immediately surrounding the H II region. The SED shows two bumps in the infrared, indicative of contribution from two different dust components. We can reproduce this SED with *DUSTY* using the parameters for slab A: (i) a blackbody with T_{eff} = 11,400 K as the external radiation source; (ii) silicate grains from Draine & Lee (1984); (iii) a 200 K dust temperature at the edge nearest to the external source; (iv) a 0.55 μm optical depth of 1.4. The output of slab A summed with a 6:1 contribution from the star (blackbody) was fed into slab B, which was modeled to have the same dust composition and grain-size distribution of slab A, and a dust temperature as 35 K at the edge, with visual optical depth of 1.6. Together, the optical depth adds up to three, corresponding to $A_V \simeq 2.8$, approximately the average extinction through the Taurus dark cloud. The dust composition is only suggestive; the bump at 10μm is much too broad to guess the silicon abundance. However, noting that the increase of amorphous carbon abundance relative to silicon results in a broad spectral feature at $\sim 0.12\mu$m and flattening of the thermal bump, we expect the relative amorphous carbon content to be small. Also, this broad bump makes it difficult to interpret the temperature of slab A, and we note that the edge temperature for this slab can lie anywhere between 100 and 300 K.

A.3.5 HD 29647

Multi-wavelength images of HD 29647 (Figure A.15) clearly show striated nebulosity similar to that associated with Pleiades stars. Even the SED is similar to that of Maia, a Pleiades member; both are shown in Figure A.17. The source is frequently used in interstellar column density and extinction law studies, and has a rich literature.

HD 29647 is known as a heavily reddened Hg-Mn B6-7 IV or B8 III star. From our spectrum, we classify it as a B9 III spectral type and can confirm the presence of Hg absorption. Our analysis results in a spectroscopic parallax distance of 160 $\pm$ 1 pc, consistent with Taurus membership. However, as we do not have reliable estimates for the intrinsic colors of B-type giant stars, this distance estimate might have systematic error much greater than the quoted uncertainty. The Hipparcos parallax distance to HD 29647 is 177 ± 35 pc. Based on proper motion analysis, the star is probably a non-member. There is no radial velocity measurement; however, Adelman et al. (2001) make a statement that the radial velocity of the star "closely matches that of the foreground cloud" with unfortunately no quantitative detail given.

The fact that HD 29647 illuminates a bright infrared nebula is, however, a compelling reason to associate this star with the far side of Taurus. Whittet et al. (2004) argue that the visual extinction of 3.6 magnitudes for HD 29647 and 5.3 magnitudes toward an adjacent sightline suggests that this star lies within a diffuse cloud that is slightly beyond the molecular gas constituting TMC-1. These authors also mention the existence of infrared excess based on IRAS data as an argument for the proximity of HD 29647 to small grains associated with the cloud. A scenario in which HD 29647 was born from the Taurus cloud and ended up having different motion can be envisaged (for example, through ejection from a binary/multiple-star system). Given the relatively low space velocity as estimated from the small proper motion, however, this scenario seems unlikely.

Perhaps it was born from a cloud lying between the present-day Taurus and Perseus clouds. Being a giant star, an age between 90 Myr and 120 Myr as deduced from stellar evolution models, may be appropriate for this $\sim$5 $M_{\odot}$ star. We conclude that the nebulosity in this case is a situation similar to that of Pleiades stars.

Although we have argued that this source is probably not associated with Taurus, it does illuminate nebulosity and has a substantial infrared excess. We see on inspection of the SED that there is a broad silicate feature evident at 10μm, and another thermal bump at about 60μm. On modelling this emission with *DUSTY*, we find that two dust components are required to explain this. One produces the broad silicate feature, requiring dust temperature at the inner boundary between 400 and 2000 K. The cooler limit comes from a fit to the thermal bump of the dust continuum emission. The hotter temperature limit is defined by the fit of the SED to optical data points. We note that as dust evaporates somewhere between 1000 K and 2000 K depending on the exact composition (e.g. Duschl et al. 1996; Speck et al. 2000), dust temperatures at the upper end of the range become unphysical. We assume somewhat arbitrarily a 500 K temperature for the first component but the use of different temperatures within the range specified above does not affect the overall fit substantially. The second dust component is characterized by a temperature of about 45 K, which is defined by the peak of the thermal bump seen at tens of microns. To reproduce the SED as shown in Figure A.10 we used (i) a blackbody with $T_{\rm eff}$ = 10,900 K as the external radiation source; (ii) dust composition of silicates from Draine & Lee (1984) (with the output not very sensitive to the composition); (iii) dust temperature at the edge nearest to the external source: 500 K for slab A and 46.5 K for slab B; (iv) optical depth of 0.1 and 4 at 0.55μm for slabs A and B respectively (we need $\tau_A + \tau_B \simeq 4$, so that the total A_V for this star equals about 3.6). The output from slab A was passed as input to slab B and thus the overall output was calculated. To the output of slab B, another contribution from the output of slab A had to be added (in a 1:10 ratio) to the result of *DUSTY* in order to reproduce the observed flux.

A.3.6 HR 1445

The slight nebulosity associated with HR 1445 = HD 28929 is discernible only in the 8 and 24 μm bands, with a striated morphology evident at 8μm (Figure A.16). The SED (Figure A.17) does not reveal any infrared excess out to 24 μm and neither the star nor any nebular emission is seen at 70 and 160 μm.

HR 1445 is known as a peculiar star, an Hg-Mn main-sequence star of spectral type B8. Our spectral analysis also suggests a B8 (dwarf) star and we do see a weak Hg signature. The spectroscopic parallax distance is 136 ± 15 pc, and in good agreement with its Hipparcos parallax distance of 143 ± 17 pc. Walter & Boyd (1991) derived a spectroscopic parallax distance of 158 pc while Kenyon et al. (1994) found 137 pc. From our χ^2 probability test, we deduce secure proper motion membership. HR 1445 also has a radial velocity consistent with that of Taurus. The good agreement of the distance, proper motion, and radial velocity of this star with that expected for Taurus members provides strong support to the idea of HR 1445 being a Taurus member.

The age of this star, because it is main sequence, can be constrained only to less than a few hundred Myr,

within 1σ uncertainty. Westin (1985) quoted the age of this star as 60 Myr, in which case it would be an unlikely member of Taurus. HR 1445 is located toward a region of Taurus which is devoid of dense material along the line of sight. One might argue, to explain the nebulosity, that HR 1445 is located within a diffuse dust screen behind Taurus, just like HD 29647.

While HR 1445 shows hints of nebulosity, there is no infrared excess and because of the wide range of unconstrained parameter space allowed in the models we do not attempt a *DUSTY* model.

A.3.7 τ Tau

The τ Tau = HD 29763 region was not covered by any of the *Spitzer* surveys. However, examination of *WISE* image data reveals a compact, nebulous feature at 12 and 22 μm, similar to that observed for HR 1445. Also similar to the situation for HR 1445, the SED (Figure A.17) of τ Tau does not reveal any infrared excess out to 22 μm and the spectrum does not show the presence of any emission lines.

This source is a well-studied binary system composed of B and early A dwarfs (e.g. Cvetkovic & Ninkovic 2010). From our B3V spectral type we derive a spectroscopic parallax distance of 137 ± 9 pc. The Hipparcos parallax distance is 122 ± 13 pc. The value from Walter & Boyd (1991) is 142 pc. Both the proper motion and system radial velocity of τ Tau are consistent with Taurus group V (as defined in Luhman et al. 2009), towards which it lies. If it is a main-sequence star, as the spectrum indicates, then we can constrain the age as being $\lesssim 40$ Myr. Westin (1985) derived 20 Myr. Since the spectral type is so early τ Tau is plausibly coeval with the low mass T Tauri members of Taurus.

τ Tau also lies toward that region of Taurus which is devoid of dense material. A visual extinction of about 0.4 mag is derived. Only 1.6 degrees away from τ Tau is HP Tau/G2 which has had its distance accurately measured via VLBA at 161 pc, whereas we find 130 pc as the distance to the binary system; this would suggest a mainly line-of-sight separation of about 30 pc between the two stars. Indeed, HP Tau/G2 has higher reddening with $A_V = 2.6$ quoted by Rebull et al. (2010). We thus conclude the τ Tau is associated with the near side of the Taurus clouds.

As for HR 1445, given that τ Tau shows hints of nebulosity but no infrared excess, we do not attempt a *DUSTY* model.

A.3.8 AB Aur and HD 31305

AB Aur = HD 31293 is the prototypical Herbig Ae star with an assigned a spectral type of B9–A0e, consistent with our spectrum. It is a known member of Taurus with a Class II SED. We do not produce a model for this well-studied source.

HD 31305, though not part of the area mapped under the guise of the *Spitzer* Taurus Legacy Survey, was covered in the "C2D" (PI N. Evans) maps. The source is not associated with nebulosity in any mid-infrared, near-infrared, or optical wavelength. However, it came to our attention through its proximity to known early-

type member AB Aur. In the literature, HD 31305 mainly has been used as a reference star for variability studies of AB Aur and other nearby young stars, though itself turns out to be a variable (Cody et al. 2013).

We derive a spectral type of A1V with very little reddening ($A_V \simeq 0.1$) for HD 31305, and a spectroscopic parallax distance of 174 ± 11 pc. Although this star lies at 1σ just outside the formal distance range that we consider for Taurus membership, (up to 162 pc), the star is seemingly a good candidate for membership. A secure proper-motion membership probability is found, but no radial velocity measurements exist. Keeping these points in mind, we conclude that HD 31305 is likely a newly appreciated member of Taurus.

There is no nebulosity apparent but the SED shows infrared excess in the near-to-far infrared. Investigation of its SED relative to a range of *DUSTY* models tells us that the 10 μm silicate feature is probably strong, above the blackbody line, with the second thermal bump at a longer wavelengths broad and flat. This SED morphology indicates a similar abundance of silicon and amorphous carbon. The silicate feature remains significant if the edge temperature of the dust slab is set to lie between 100 and 500 K, but this is also dependent on the optical depth. We model this SED using the following parameters for a single slab. (i) blackbody with $T_{\rm eff}$ = 9,400 K (=A1V) as the external radiation source; (ii) silicate and graphite grains from Draine & Lee (1984) in a 10:1 ratio; (iii) a 350 K dust temperature at the edge nearest to the external source; (iv) 0.55 μm optical depth of 0.05. The contribution of the central star relative to the thermal and scattered dust emission is 4:1. The dust emission could equivalently be modeled using a 2-slab model to get a better fit, but this is not justified by the low extinction and the appearance of the nebula on 2MASS image cutouts.

A.3.9 HD 26212

HD 26212 also lies outside the region of the *Spitzer* Taurus Legacy Survey, but was not covered in C2D. Inspection of DSS, 2MASS, WISE and IRAS images does not reveal any nebulosity towards this star. It does not have any infrared excess out to 24 μm as evidenced by its SED (Figure A.17).

We arrived at a spectral classification of A5V for HD 26212. The corresponding spectroscopic parallax is 115 ± 4 pc which is in agreement (within the 2σ error) with both its larger Hipparcos parallax as well as the new Hipparcos reduction (van Leeuwen 2007), $d_{HIP} = 100^{+7.8}_{-6.7}$. The proper motion of this star is consistent with Taurus, which means that it is tangentially comoving with the members of this cloud. The mean radial velocity quoted in the literature is about 20 km s^{-1}, and within 1σ, agrees with that observed for Taurus members. The derived spectroscopic parallax yielded a visual reddening of $A_V = 0.16$. The low reddening and near distance suggests that HD 26212 lies in the outskirts of the L1498 region in Taurus. Since its spectrum suggests a main-sequence star and the spectral type is late, we can not meaningfully constrain the age.

HD 26212 shows neither significant infrared excess nor scattered light, and therefore cannot be modelled with *DUSTY*.

A.3.10 HD 27659, HD 283815

Both of these stars are listed as having spectral type A0 and as probable members of Taurus based on infrared excess by Rebull et al. (2010).

The multiwavelength image cutouts of HD 27659 show extended emission at 8μm. The object is seen to be fuzzy but somewhat compact beyond this wavelength, a feature which is similar to multi-wavelength image morphology of HR 1445 and τ Tau. HD 27659 also shows considerable infrared excess beyond 25 μm (Figure A.17). Rebull et al. (2010) find a Class II SED with $L_{IR}/L_{total} = 6 \times 10^{-4}$. Kenyon et al. (1994) classified HD 27659 as an A4V star and derived a spectroscopic parallax distance of d = 146 pc. Belikov et al. (2002) list HD 27659 as a member of the Perseus OB2 star forming complex, but its proper motion renders this improbable.

For HD 283815, there is no associated infrared nebulosity but Rebull et al. (2010) found the 8 μm to 24 μm flux ratio to indicate a Class III SED exhibiting a weak infrared excess, though this is not readily apparent from examination of the SED (Figure A.17). There is sparse literature for HD 283815.

In terms of spectroscopic parallax, HD 27659 has an implied distance based on our derivation of an A3 spectral type of 164 pc which matches our criteria of membership with Taurus. For HD 283815 we did not obtain a spectrum, but using the literature spectral type of A0 shows that it does not meet our distance criteria, as can be discerned from the underluminous SED of Figure A.17 when a 140 pc distance is assumed. In proper motion, however, the inverse is true with HD 27659 showing proper motion inconsistent with Taurus, but HD 283815 a high probability proper motion member. Radial velocity measurements exist for neither star.

Given the evidence, at present no strong statements can be made about the membership of either star. They could be early type members with peculiar motions, or background stars reddened due to the Taurus cloud. In both cases, there is some evidence for associated dust. HD 27659 has just two SED points within the region showing infrared excess, and we hesitate to attempt fitting of a unique model to it. HD 283815 shows neither significant infrared excess nor scattered light, and therefore cannot be modelled.

Of possible relevance is that lying only a quarter of a degree away from HD 27659 is HDE 283572, a Taurus member whose distance has been measured precisely by VLBA techniques. The implied distance between the two stars would be about 35 pc. From Figure A.4, the proximity with a high surface density part of the cloud is evident and there is significant reddening implied for the further star HD 27659.

A.4 SUMMARY & CONCLUSION

Early-type stars illuminating infrared nebulae found in *Spitzer* IRAC/MIPS maps of the Taurus-Auriga Molecular Cloud complex led us to carry out a more comprehensive search for early-type stars in this star-forming region. We compiled a list of 329 candidate early-type stars (see Table A.3) towards Taurus from (i) previously-known O, B stars listed by SIMBAD, (ii) proposed B stars from Rebull et al. selected to have infrared excess and followed up spectroscopically, (iii) stars from the *Two Micron All Sky Survey* Point Source Catalog se-

lected on the basis of photometric color, and (iv) early-type stars spectroscopically identified in the *Sloan Digital Sky Survey*. This set of stars was then tested against various membership criteria including distance, kinematics, and age criteria.

First, we provided accurate spectral type information for about 20 stars which were spectroscopically followed up from our initial sample at the 200-inch Hale telescope at the Palomar Observatory. This, along with the magnitudes available in the literature has helped in deriving spectroscopic parallax distances to the stars, accounting for extinction. Notably, the presence of several diffuse interstellar bands is well-correlated with the estimated distances; none of the stars we believe associated based on distance or kinematic arguments with the Taurus star forming region exhibit these features, which are seen in only more distant stars. Several of the spectra show emission lines which in two cases are associated with known young stellar objects and in the other two cases appear associated with background Be stars also exhibiting infrared excesses.

Hipparcos parallaxes and spectroscopic parallaxes were used to select stars between 128 and 162 pc, allowing for error. Proper motion membership was tested by calculating the χ^2 probability using the proper motion of various comoving groups in Taurus (defined by Luhman et al. 2009). Radial velocity, wherever available, has been compared with that of the previously-known members of Taurus. We have also specially considered all early-type sources illuminating nebulae, regardless of whether they meet the distance and kinematic criteria.

Our final assessment of membership is shown in Table A.6. Through this work, we have found three stars of spectral type B, and two of spectral type A to be newly-appreciated members of Taurus. Specifically, HR 1445 (HD 28929), τ Tau (HD 29763), 72 Tau (HD 28149), HD 31305, HD 26212 meet the kinematic and distance criteria while HD 27659, and HD 283815 show ambiguous kinematic and/or distance properties that make their membership plausible but not secure. Additional or improved space velocity information for these and several other stars could confirm their membership. These sources should be considered along with the currently accepted early-type members: IC2087-IR (B5-like luminosity but heavily self-embedded source with a continuum-emission optical and infrared spectrum), the binary system V892 Tau (Elias 1; a B8-A6 self-embedded Herbig Ae/Be star with a near-equal brightness companion), the triple system HD 28867 (B8 +2$\times$B9.5), AB Aur (A0e, a Herbig Ae/Be star), and HD 31648 (MWC 480; A2e, another Herbig Ae/Be star). While HD 28867 is located to the south of the main Taurus-Auriga clouds and therefore not recovered in our search, the other known early type members were recovered, although to varying degrees of security. Notably, more than half – but not all – of the stars listed above distinguish themselves through illumination of optical or infrared nebulae. Furthermore, two-thirds – but not all – of the stars have mid-infrared excesses which may be due to an extended nebula or to a more compact protoplanetary or later stage debris disk.

Among the stars with infrared reflection/scattered-light nebulae, two sources (HD 28149 = 72 Tau, and HD 29647) have been used as intrinsically bright background "candles" in studies of the molecular cloud's physical and chemical properties. In the case of 72 Tau, the kinematics and distance are both consistent with those of previously-known members of Taurus. While chance superposition with the Taurus cloud is

possible, this main-sequence star was probably born near its present environment and is truly associated with the cloud. Our assessment of HD 29647 suggests an object at similar distance to though just behind the Taurus cloud (the same conclusion was reached by Whittet et al. (2004)) and with different kinematics. Both HD 29647 and 72 Tau have nebulae which appear to be morphologically similar to the striated nebulosity toward the Pleiades stars Merope and Maia. The difference is that the Taurus nebulae under study here are much fainter and much less distinct at visible wavelengths than the Pleiades cases, probably due to the amount of foreground extinction or to the spectrum of incident radiation (and less likely due to the dust properties).

Another bright nebulous source, HD 282276 (northernmost circle in Figure A.1) is likely a B-type star lying background to Taurus and close to the distance of the Perseus star-forming region, although well east of it. The molecular material may also be at that further distance.

We modelled the nebular dust emission of a subset of interesting stars also showing infrared excess. The dust temperatures found via this study, which account for the thermal dust emission peaks in the SEDs, are usually about 45 K. In some cases (viz. HD 282276 and HD 29647) there is evidence of two dust components contributing to the infrared emission, where the higher-temperature component is between 100 K and 500 K. The distance between the nebulae and the early-type stars can be estimated by balancing the heating and cooling rates. However, the unknown composition, complicated morphology and the self-similar nature of the radiation transfer makes the problem very challenging. Nevertheless, the infrared excess tells us that the star is sufficiently close to the nebula to heat it. Kinematic information of the stars supplement this proximity information to help distinguish between association with the cloud and chance superposition.

We call attention to the fact that we have doubled the number of stars with spectral type A5 or earlier that can be associated with the Taurus Molecular Cloud. This includes the earliest type star claimed yet as a member of Taurus: the B3V star τ Tau. Nevertheless, the cloud still seems to be a factor of two short in early type members, considering a standard log-normal form for the initial mass function and given its low mass and brown dwarf population that numbers at least 350.

Acknowledgments

We acknowledge the contributions of Caer McCabe, Alberto Noreiga-Crespo, Sean Carey, Karl Stapelfeldt, Tim Brooke, Tracy Huard, and Misato Fukagawa in the production of the Spitzer maps that inspired this analysis. We thank John Carpenter, Varun Bhalerao, Eric Mamajek for their various suggestions and helpful advice. This research has made use of: the SIMBAD and VizieR online database services, IRAF distributed by the National Optical Astronomy Observatories, which are operated by the AURA under cooperative agreement with NSF, and the DUSTY code developed by Gary Ferland. FACILITIES: Spitzer, 2MASS, SDSS, WISE, Palomar 200-inch

Bibliography

Abazajian, K. N., Adelman-McCarthy, J. K., Agüeros, M. A., et al. 2009, ApJS, 182, 543

Abt, H. A., Levato, H., & Grosso, M. 2002, ApJ, 573, 359

Adelman, S. J., Snow, T. P., Wood, E. L., et al. 2001, MNRAS, 328, 1144

Andrews, S. M., & Williams, J. P. 2005, ApJ, 631, 1134

Bally, J., Walawender, J., & Reipurth, B. 2012, AJ, 144, 143

Belikov, A. N., Kharchenko, N. V., Piskunov, A. E., Schilbach, E., & Scholz, R.-D. 2002, A&A, 387, 117

Blaauw, A. 1956, ApJ, 123, 408

Cardelli, J. A., Clayton, G. C., & Mathis, J. S. 1989, ApJ, 345, 245

Carpenter, J. M. 2001, AJ, 121, 2851

Carroll, B. W., & Ostlie, D. A. 2006, An introduction to modern astrophysics, 2e., ed. Carroll, B. W. & Ostlie, D. A.

Cederblad, S. 1946, Meddelanden fran Lunds Astronomiska Observatorium Serie II, 119, 1

Cody, A. M., Tayar, J., Hillenbrand, L. A., Matthews, J., & Kallinger, T. 2013, AJ, 145, 79

Cvetkovic, Z., & Ninkovic, S. 2010, Serbian Astronomical Journal, 180, 71

de Zeeuw, P. T., Hoogerwerf, R., de Bruijne, J. H. J., Brown, A. G. A., & Blaauw, A. 1999, AJ, 117, 354

Didelon, P. 1982, A&AS, 50, 199

Dobashi, K., Uehara, H., Kandori, R., et al. 2005, PASJ, 57, 1

Draine, B. T., & Lee, H. M. 1984, ApJ, 285, 89

Ducourant, C., Teixeira, R., Périé, J. P., et al. 2005, A&A, 438, 769

Duschl, W. J., Gail, H.-P., & Tscharnuter, W. M. 1996, A&A, 312, 624

Elias, J. H. 1978, ApJ, 224, 857

Finkbeiner, D. P., Padmanabhan, N., & Schlegel, D. J. o. 2004, AJ, 128, 2577

Fitzgerald, M. P. 1970, A&A, 4, 234

Frerking, M. A., Langer, W. D., & Wilson, R. W. 1982, ApJ, 262, 590

Furlan, E., McClure, M., Calvet, N., et al. 2008, ApJS, 176, 184

Girardi, L., Bertelli, G., Bressan, A., et al. 2002, A&A, 391, 195

Goldsmith, P. F., Heyer, M., Narayanan, G., et al. 2008, ApJ, 680, 428

Gontcharov, G. A. 2006, Astronomy Letters, 32, 759

Güdel, M., Padgett, D. L., & Dougados, C. 2007, Protostars and Planets V, 329

Hanner, M. 1988, Grain optical properties, Tech. rep.

Hartmann, L., Stauffer, J. R., Kenyon, S. J., & Jones, B. F. 1991, AJ, 101, 1050

Herbig, G. H. 1960, ApJS, 4, 337

Hillenbrand, L. A., Knapp, G. R., Padgett, D. L., Rebull, L. M., & McGehee, P. M. 2012, AJ, 143, 37

Ivezic, Z., & Elitzur, M. 1997, MNRAS, 287, 799

Johnson, H. L. 1966, ARA&A, 4, 193

Jones, B. F., & Herbig, G. H. 1979, AJ, 84, 1872

Kalas, P., Graham, J. R., Beckwith, S. V. W., Jewitt, D. C., & Lloyd, J. P. 2002, ApJ, 567, 999

Kenyon, S. J., Dobrzycka, D., & Hartmann, L. 1994, AJ, 108, 1872

Kenyon, S. J., Gómez, M., & Whitney, B. A. 2008, in Handbook of Star Forming Regions, Volume I, ed. Reipurth, B., 405–+

Kharchenko, N. V., & Roeser, S. 2009, VizieR Online Data Catalog, 1280, 0

Kharchenko, N. V., Scholz, R., Piskunov, A. E., Röser, S., & Schilbach, E. 2007, Astronomische Nachrichten, 328, 889

Kirk, H., & Myers, P. C. 2011, ApJ, 727, 64

Knapp, G. R., Finkbeiner, D. P., Padmanabhan, N., & Schegel, D. J. 2007, in Bulletin of the American Astronomical Society, Vol. 38, Bulletin of the American Astronomical Society, 781–+

Koornneef, J. 1983, A&A, 128, 84

Kraus, A. L., & Hillenbrand, L. A. 2007, AJ, 134, 2340

Kraus, A. L., Ireland, M. J., Martinache, F., & Hillenbrand, L. A. 2011, ApJ, 731, 8

Lesh, J. R. 1968, ApJS, 17, 371

Loinard, L., Torres, R. M., Mioduszewski, A. J., et al. 2007, ApJ, 671, 546

Lombardi, M., Lada, C. J., & Alves, J. 2010, A&A, 512, A67

Luhman, K. L., Allen, P. R., Espaillat, C., Hartmann, L., & Calvet, N. 2010, ApJS, 186, 111

Luhman, K. L., Mamajek, E. E., Allen, P. R., & Cruz, K. L. 2009, ApJ, 703, 399

Maheswar, G., Lee, C. W., Bhatt, H. C., Mallik, S. V., & Dib, S. 2010, A&A, 509, A44

Mathis, J. S., Rumpl, W., & Nordsieck, K. H. 1977, ApJ, 217, 425

Miller, G. E., & Scalo, J. M. 1979, ApJS, 41, 513

Monnier, J. D., Tannirkulam, A., Tuthill, P. G., et al. 2008, ApJ, 681, L97

Morgan, W. W., Keenan, P. C., & Kellman, E. 1943, An atlas of stellar spectra, with an outline of spectral classification, ed. Morgan, W. W., Keenan, P. C., & Kellman, E.

Munari, U., Sordo, R., Castelli, F., & Zwitter, T. 2005, A&A, 442, 1127

Narayanan, G., Heyer, M. H., Brunt, C., et al. 2008, ApJS, 177, 341

Narayanan, G., Snell, R., & Bemis, A. 2012, MNRAS, 425, 2641

Palmeirim, P., André, P., Kirk, J., et al. 2013, A&A, 550, A38

Parker, R. J., Bouvier, J., Goodwin, S. P., et al. 2011, MNRAS, 412, 2489

Perryman, M. A. C., & ESA, eds. 1997, ESA Special Publication, Vol. 1200, The HIPPARCOS and TYCHO catalogues. Astrometric and photometric star catalogues derived from the ESA HIPPARCOS Space Astrometry Mission

Rebull, L. M., Koenig, X. P., Padgett, D. L., et al. 2011, ApJS, 196, 4

Rebull, L. M., Padgett, D. L., McCabe, C., et al. 2010, ApJS, 186, 259

Rieke, G. H., & Lebofsky, M. J. 1985, ApJ, 288, 618

Roeser, S., Demleitner, M., & Schilbach, E. 2010, AJ, 139, 2440

Schmidt-Kaler, T. 1982, The Physical Parameters of the Star, ed. K. Schaifers & H. H. Voigt

Shuping, R. Y., Chiar, J. E., Snow, T. P., & Kerr, T. 2001, ApJ, 547, L161

Skrutskie, M. F., Cutri, R. M., Stiening, R., & Weinberg, M. D. e. a. 2006, AJ, 131, 1163

Smith, K. W., Balega, Y. Y., Duschl, W. J., et al. 2005, A&A, 431, 307

Speck, A. K., Barlow, M. J., Sylvester, R. J., & Hofmeister, A. M. 2000, A&AS, 146, 437

Takita, S., Kataza, H., Kitamura, Y., et al. 2010, A&A, 519, A83+

Tielens, A. G. G. M. 2005, The Physics and Chemistry of the Interstellar Medium, ed. Tielens, A. G. G. M.

Torres, R. M., Loinard, L., Mioduszewski, A. J., & Rodríguez, L. F. 2007, ApJ, 671, 1813

—. 2009, ApJ, 698, 242

Torres, R. M., Loinard, L., Mioduszewski, A. J., et al. 2012, ApJ, 747, 18

Ungerechts, H., & Thaddeus, P. 1987, ApJS, 63, 645

van Leeuwen, F. 2007, A&A, 474, 653

Walter, F. M., Beck, T. L., Morse, J. A., & Wolk, S. J. 2003, AJ, 125, 2123

Walter, F. M., & Boyd, W. T. 1991, ApJ, 370, 318

Walter, F. M., Brown, A., Mathieu, R. D., Myers, P. C., & Vrba, F. J. 1988, AJ, 96, 297

Westin, T. N. G. 1985, A&AS, 60, 99

White, R. J., & Hillenbrand, L. A. 2004, ApJ, 616, 998

Whittet, D. C. B., Gerakines, P. A., Hough, J. H., & Shenoy, S. S. 2001, ApJ, 547, 872

Whittet, D. C. B., Shenoy, S. S., Clayton, G. C., & Gordon, K. D. 2004, ApJ, 602, 291

Williams, J. P., & Cieza, L. A. 2011, ARA&A, 49, 67

Wolff, S. C., & Preston, G. W. 1978, ApJS, 37, 371

Zacharias, N., Monet, D. G., Levine, S. E., et al. 2005, VizieR Online Data Catalog, 1297, 0

Table A.1: Number of O,B stars known to SIMBAD towards Taurus (central rectangle) and neighboring regions of equivalent area in coordinates of Galactic latitude and Galactic longitude.

0°			
	304	513	342
-10°			
	100	117	122
-20°			
	32	46	33
-30°			
	195°	180°	165°	150°

Table A.2: Distances to known Taurus members measured through VLBI techniques.

Star	α_{J2000} (h,m,s)	δ_{J2000} (°,′,″)	Distance (pc)	Ref.
HDE 283572	04 21 58.847	28 18 06.51	128.5 ± 0.6	1
V773 Tau	04 14 12.922	28 12 12.30	131.4 ± 2.4	2
V1023 Tau (Hubble 4)	04 18 47.037	28 20 07.32	132.8 ± 0.5	1
T Tau	04 21 59.434	19 32 06.42	146.7 ± 0.6	3
HP Tau/G2	04 35 54.152	22 54 13.46	161.4 ± 0.9	4

Refs: (1) Torres et al. (2007), (2) Torres et al. (2012), (3) Loinard et al. (2007), (4) Torres et al. (2009)

Table A.3: List of candidate early-type stars with sections separating various selection methods.

B#	Star	α	δ	$d_{\rm HIP}$	$d_{\rm SPEC}$	$\mu_\alpha cos\delta$	μ_δ	RV	SpT	Candidate?	
		(ICRS 2000, degrees)		(pc)		(mas/yr)		(km s^{-1})		d	μ/RV
					O,B, and A0 stars from SIMBAD						
1	HD 25063	60.036389	29.710836	⋯	195 ± 5	3.7 ± 0.9	-6.2 ± 0.8	⋯	B9	N	N/?
2	HD 25201	60.236744	23.201484	332^{+274}_{-103}	189 ± 5	-34.6 ± 15.2	-9.2 ± 15.2	13.8 ± 1.1	B9V	N/N	N/Y
3	HD 281490	60.871667	30.970278	⋯	792 ± 123	13.0 ± 1.6	-7.3 ± 1.7	⋯	B9/A3	N	N/?
4	BD+23 607	60.936736	23.620942	⋯	643 ± 94	5.1 ± 1.3	-9.7 ± 1.3	⋯	A0V	N	N/?
5	HD 25487	60.976316	28.125973	301^{+153}_{-76}	342 ± 32	1.9 ± 1.7	-18.1 ± 1.5	⋯	B8Ve+K0IV	N/N	Y/?
6	HD 283304	61.226290	27.545890	⋯	739 ± 69	-2.7 ± 1.3	-2.2 ± 1.3	⋯	B8V Si	N	N/?
7	HD 284130	61.487807	23.241767	⋯	943 ± 20	-2.4 ± 1.0	5.4 ± 1.0	⋯	B8	N	N/?
8	HD 283363	61.780708	28.560528	⋯	528 ± 25	6.4 ± 1.5	-7.6 ± 1.6	⋯	B9	N	N/?
9	HD 281679	62.320792	30.775956	185^{+85}_{-44}	373 ± 11	-8.1 ± 1.5	3.6 ± 1.2	⋯	B8	Y/N	N/?
10	HD 284179	62.785610	22.825372	⋯	745 ± 41	-1.2 ± 1.2	-4.3 ± 1.2	⋯	B8	N	N/?
11	HD 283507	62.969714	24.837432	⋯	405 ± 18	-3.0 ± 1.2	-4.2 ± 1.3	⋯	B9	N	N/?
12	HD 283449	63.112000	27.876861	⋯	1613 ± 652	-2.3 ± 1.8	-4.8 ± 1.8	⋯	A0V	N	N/?
13	HD 26571	63.213520	22.413458	316^{+113}_{-66}	159 ± 1	-3.0 ± 0.5	-10.9 ± 0.5	9.3 ± 3	B8III	N/Y	N/Y
14	HD 281815	63.852452	29.365851	⋯	548 ± 57	1.0 ± 1.6	-10.9 ± 1.6	⋯	B8	N	N/?
15	HD 281818	64.079170	29.256597	⋯	749 ± 67	7.1 ± 1.3	-12.2 ± 1.3	⋯	B8	N	N/?
16	HD 284228	64.085078	23.841866	⋯	839 ± 32	13.5 ± 1.2	-6.0 ± 1.2	⋯	B5	N	N/?
17	HD 283553	64.488019	24.577938	248^{+122}_{-62}	465 ± 15	-0.8 ± 0.7	-7.9 ± 0.7	⋯	B8	N/N	N/?
18	HD 281920	64.569998	29.807023	⋯	777 ± 69	6.5 ± 1.2	-6.0 ± 1.0	⋯	B5	N	N/?

19	V892 Tau	64.669250	28.320972	···	1697 ± 1548	10.9 ± 5.1	-29.7 ± 5.1	···	∼A0V	Y:	Y/?
20	HD 27405	65.126585	25.827451	229^{+71}_{-44}	242 ± 5	6.7 ± 1.4	-5.2 ± 1.5	···	B9	N/N	N/?
21	HD 283567	65.137783	28.652376	···	655 ± 44	-2.0 ± 1.5	-4.9 ± 1.6	···	B9	N	N/?
22	HD 27638	65.645598	25.629314	82^{+7}_{-6}	104 ± 2	17.4 ± 2.0	-13.3 ± 1.9	15.3 ± 3.4	B9V	N/N	N/Y
23	HD 27778	65.999008	24.300992	223^{+73}_{-44}	238 ± 5	8.0 ± 1.5	-12.7 ± 1.5	···	B3V	N/N	N/?
24	HD 284427	66.341599	23.389317	···	577 ± 56	-5.5 ± 1.2	-4.4 ± 1.2	···	B9V	N	N/?
25	HD 28149	66.822698	22.996337	127^{+13}_{-11}	161 ± 3	0.4 ± 0.5	-14.4 ± 0.5	7.3 ± 2.6	B7V	Y/Y	Y/Y
26	HD 284479	67.311975	22.478510	···	1153 ± 158	2.6 ± 1.5	-6.9 ± 1.5	···	B8V	N	N/?
27	HD 282151	67.424917	30.684083	···	771 ± 15	-3.1 ± 1.6	-1.3 ± 1.6	···	B9V	N	N/?
28	HD 28482	67.593513	23.588859	301^{+110}_{-64}	204 ± 1	18.0 ± 0.6	0.5 ± 0.6	···	B8III	N/N	N/?
29	HD 284487	67.879371	22.220857	···	1102 ± 177	3.4 ± 1.4	-2.5 ± 1.4	···	B9V	N	N/?
30	HD 282240	68.022275	30.967710	···	824 ± 31	4.1 ± 1.3	-6.3 ± 1.4	···	B9V	N	N/?
31	HD 283677	68.045575	29.015574	344^{+248}_{-102}	541 ± 15	0.0 ± 0.8	-8.9 ± 0.7	···	B5V	N/N	N/?
32	CoKu HK Tau G1	68.173333	24.317778	···	5976 ± 4466	37.7 ± 4.5	-11.1 ± 4.5	20 ± 4.5	B2	N	N/Y
33	HD 282276	68.267637	29.363863	···	422 ± 52	2.0 ± 1.6	-12.5 ± 1.7	···	B8V	N	N/?
34	2MASS J04335319+2414080	68.471667	24.235583	···	1244 ± 177	3.7 ± 1.6	-1.4 ± 1.6	···	B8	N	N/?
35	HD 282278	68.585583	29.297556	···	439 ± 30	-2.3 ± 1.3	-3.4 ± 1.4	···	B9	N	N/?
36	HD 28929	68.658299	28.961151	143^{+20}_{-16}	157 ± 3	1.3 ± 2.2	-23.2 ± 2.0	12.6 ± 2.2	B8V Hg-Mn	Y/Y	Y/Y
37	HD 283701	68.729070	27.203107	···	307 ± 3	1.9 ± 1.3	-11.6 ± 1.3	···	B8III	N	N/?
38	2MASS J04353218+2427069	68.884125	24.451944	···	1104 ± 201	-1.8 ± 4.6	-4.4 ± 4.6	···	B8	N	N/?
39	HD 283740	69.260698	28.011207	···	778 ± 48	3.0 ± 1.5	2.4 ± 1.5	···	B8V	N	N/?
40	HD 29259	69.438853	30.407638	667^{+2782}_{-298}	312 ± 10	0.6 ± 1.0	-9.1 ± 0.8	···	B9	N/N	N/?

41	HD 282380	69.715330	30.449740	···	287 ± 50	-1.4 ± 1.5	-1.3 ± 1.5	···	B8	N	N/?
42	HD 284583	69.777811	22.712064	···	1017 ± 25	1.0 ± 1.3	-0.2 ± 1.3	···	B5	N	N/?
43	HD 29450	69.806437	22.652255	429^{+340}_{-132}	345 ± 11	0.9 ± 0.8	-1.3 ± 0.7	-10.9 ± 2.6	B9	N/N	N/N
44	JH 225	69.916538	25.342850	···	540 ± 125	-11.6 ± 4.6	-8.3 ± 4.6	···	B9	N	N/?
45	HD 283794	69.964024	27.188951	···	428 ± 12	5.1 ± 1.2	-8.4 ± 1.3	···	B9V	N	N/?
46	IC 2087-IR	69.982292	25.750556	···	···	1.6 ± 5.9	-19.7 ± 5.9	···	B5	?	Y/?
47	HD 283772	70.246863	27.990404	···	519 ± 11	0.0 ± 1.3	-5.2 ± 1.3	···	B9V	N	N/?
48	HD 29647	70.283524	25.992765	177^{+43}_{-29}	160 ± 1	12.8 ± 0.9	-9.7 ± 0.7	···	B9III Hg-Mn	Y/Y	N/?
49	HD 29681	70.349520	22.676800	···	699 ± 18	0.4 ± 1.1	0.1 ± 1.1	···	B8V	N	N/?
50	HD 283809	70.353006	25.913469	···	695 ± 230	2.5 ± 1.6	-1.4 ± 1.7	···	B1.5V	N	N/?
51	HD 29763	70.561257	22.956926	123^{+13}_{-11}	137 ± 9	0.6 ± 0.2	-17.4 ± 0.2	12.3 ± 4.1	B3V	Y/Y	Y/Y
52	HD 283800	70.863805	27.026948	···	564 ± 42	1.3 ± 1.5	-9.1 ± 1.5	···	B8	N	N/?
53	HD 29935	70.975003	22.944410	90^{+11}_{-9}	175 ± 2	-0.5 ± 0.7	-15.8 ± 0.6	32 ± 4.8	A0V	N/N	Y/N
54	HD 283805	71.301213	26.453282	···	846 ± 17	-2.2 ± 1.4	-4.1 ± 1.4	···	B8V/A3	N	N/?
55	HD 30122	71.426948	23.627996	216^{+40}_{-29}	290 ± 1	9.8 ± 0.6	-17.3 ± 0.5	23.2 ± 2	B5III	N/N	Y/N
56	HD 282430	71.644099	30.615554	···	918 ± 97	-3.5 ± 1.7	-5.6 ± 1.7	···	B5	N	N/?
57	HD 282431	71.654007	30.404109	···	400 ± 16	5.1 ± 1.6	-9.5 ± 1.5	···	B9/A0	N	N/?
58	HD 282485	71.658884	29.317718	···	483 ± 16	4.1 ± 1.5	-5.6 ± 1.5	···	B9V	N	N/?
59	HD 283851	71.678804	27.261715	···	637 ± 46	-3.8 ± 1.2	-3.7 ± 1.2	···	B9V	N	N/?
60	HD 283836	71.729035	28.225371	···	336 ± 29	0.0 ± 1.3	-3.7 ± 1.3	···	B9	N	N/?
61	HD 283854	71.765792	26.765833	···	809 ± 29	-1.0 ± 1.4	-4.7 ± 1.4	···	B9V/A7	N	N/?
62	HD 283845	71.967880	27.744442	···	750 ± 23	2.9 ± 1.5	-4.7 ± 1.5	···	B3V	N	N/?
63	HD 30378	72.094763	29.773003	196^{+49}_{-33}	239 ± 5	6.1 ± 0.6	-25.6 ± 0.6	21.6 ± 3.5	B9.5V	N/N	Y/N
64	HD 30675	72.716687	28.314066	368^{+269}_{-109}	332 ± 11	7.2 ± 1.2	-16.6 ± 0.8	···	B3V	N/N	N/?

65	HD 283875	72.795560	25.622469	···	530 ± 63	2.1 ± 1.7	-1.7 ± 1.6	···	B8V	N	N/?
66	HD 282537	72.898060	30.021865	···	752 ± 16	-4.1 ± 1.6	-9.5 ± 1.6	···	B8	N	N/?
67	HD 283920	73.021685	26.917266	···	497 ± 3	-0.8 ± 1.7	-11.3 ± 1.7	···	B7III	N	N/?
68	HD 282548	73.297292	29.020944	···	999 ± 63	-4.7 ± 1.7	-3.4 ± 1.7	···	B9	N	N/?
69	HD 283952	73.318183	24.714376	···	765 ± 23	2.2 ± 1.3	-3.7 ± 1.3	···	B9V	N	N/?
70	HD 284874	73.364583	22.251722	···	793 ± 37	2.6 ± 1.0	-1.6 ± 1.0	···	B8	N	N/?
71	HD 31120	73.539369	23.066227	···	374 ± 28	-4.8 ± 1.1	-10.8 ± 1.1	···	B9V	N	N/?
72	HD 283932	73.677168	25.729056	···	442 ± 46	0.7 ± 1.5	-7.0 ± 1.4	···	B8V	N	N/?
73	HD 282653	73.945167	29.333056	···	670 ± 26	-4.4 ± 1.7	-9.3 ± 1.7	···	B9	N	N/?
74	HD 31353	74.029726	24.004623	···	294 ± 12	4.6 ± 1.2	-8.8 ± 1.3	···	B9	N	N/?
75	HD 282635	74.120904	29.994960	172^{+81}_{-42}	490 ± 21	2.0 ± 1.3	-5.4 ± 1.1	···	B8	Y/N	N/?
76	HD 282617	74.150050	30.882917	···	673 ± 51	-6.8 ± 1.7	-6.7 ± 1.7	···	B8	N	N/?
77	V722 Tau	74.205683	27.718514	···	2304 ± 583	1.0 ± 1.8	-2.6 ± 1.8	···	B3e	N	N/?
78	HD 283968	74.205773	24.043778	···	643 ± 103	2.3 ± 1.5	-1.9 ± 1.5	···	B9V	N	N/?
79	HD 284993	74.302100	22.159576	···	790 ± 44	2.4 ± 1.2	-3.9 ± 1.2	···	B9	N	N/?
80	HD 282633	74.362179	30.174772	···	581 ± 48	-2.4 ± 1.3	2.8 ± 1.3	···	B8V	N	N/?
81	HD 283971	74.382746	28.759850	···	859 ± 240	-3.5 ± 1.7	-5.4 ± 1.5	···	B9V	N	N/?
82	HD 284006	74.532658	26.298360	···	358 ± 30	-3.1 ± 1.5	-7.4 ± 1.4	···	B9	N	N/?
83	HD 282754	74.593708	29.722028	···	1033 ± 128	-1.0 ± 1.7	-2.3 ± 1.7	···	B9	N	N/?
84	BD+30 748	74.639620	30.697656	···	1202 ± 115	1.5 ± 1.3	-2.5 ± 1.3	7.2 ± 1.4	B1.5V	N	N/N
85	HD 284941	74.674310	23.585106	···	1011 ± 195	-0.1 ± 1.2	-3.5 ± 1.2	···	B9	N	N/?
86	HD 31679	74.719814	24.495712	379^{+498}_{-137}	378 ± 28	2.1 ± 0.9	-4.4 ± 0.8	···	B5	N/N	N/?
87	HD 284012	74.898442	25.807481	258^{+113}_{-60}	255 ± 26	0.7 ± 1.1	-7.3 ± 0.9	11 ± 2.5	B8	N/N	N/Y
88	HD 31806	74.973961	27.325604	138^{+52}_{-30}	232 ± 6	14.8 ± 1.6	-24.6 ± 1.7	···	B7V	Y/N	N/?

Additional B and early A stars proposed by Rebull et al. 2010 from infrared excess

89	HD 27659	65.727746	28.398614	···	164 ± 10	-23.7 ± 1.5	-17.8 ± 1.4	···	A3V	Y	N/?
90	HD 27923	66.329861	23.788020	194^{+101}_{-49}	277 ± 5	5.9 ± 1.1	-8.6 ± 1.1	···	B9V	Y/N	N/?
91	HD 283637	66.495250	27.617028	···	855 ± 279	-3.6 ± 1.7	-6.8 ± 1.7	···	B9.5V	N	N/?
92	2MASS J04285940+2736254	67.247550	27.607081	···	664 ± 147	1.7 ± 2.3	-15.5 ± 2.4	···	A4III	N	Y/?
93	2MASS J04313313+2928565	67.888075	29.482378	···	639 ± 144	-6.0 ± 5.1	0.3 ± 5.1	···	A1V	N	N/?
94	HD 284530	68.582858	23.447141	···	347 ± 9	7.1 ± 1.2	-15.5 ± 1.2	···	B9.5V	N	Y/?
95	HD 283751	69.353563	27.155458	···	1010 ± 85	6.1 ± 1.4	-1.9 ± 1.4	···	B5Ve	N	N/?
96	HD 283815	70.671592	24.688295	···	268 ± 40	8.7 ± 1.2	-20.4 ± 1.2	···	A0	N	Y/?

Additional early type candidates selected from 2MASS photometry

97	HD 25111	60.054439	23.149068	···	···	5.4 ± 1.1	-4.6 ± 1.1	···	A	?	N/?
98	HD 283286	60.959556	28.404501	···	420 ± 21	-6.9 ± 2.7	-5.19 ± 2.37	···	A2	N	N/?
99	04040178+2715454	61.007451	27.262593	···	···	-8.1 ± 5.6	-5.16 ± 4.98	···	?	?	N/?
100	HD 25554	61.160276	30.884204	207^{+70}_{-42}	280 ± 9	3 ± 1	1.97 ± 0.69	···	A0	N/N	N/?
101	HD 25620	61.208024	23.509276	···	176 ± 11	2.7 ± 1.1	-0.92 ± 1.01	···	F0	N	N/?
102	HD 25626	61.301075	27.609715	202^{+62}_{-38}	191 ± 3	16.7 ± 1	-26.23 ± 0.89	2 ± 1.8	A2	N/N	N/N
103	HD 25694	61.413234	28.395374	···	347 ± 15	1.6 ± 1.4	-5.01 ± 1.32	···	A0	N	N/?

10404055962+2956381	61.498439	29.943959	···	···	0.1 ± 1.7	-5.63 ± 1.47	···	?	?	N/?
105HD 283346	61.550881	25.362189	···	373 ± 32	5.7 ± 1.1	-9.94 ± 0.99	···	A2	N	N/?
106HD 26212	62.432002	24.072944	123^{+17}_{-14}	115 ± 4	2.4 ± 0.8	-18.81 ± 0.55	20.3 ± 3.9	A5V	Y/N	Y/Y
107HD 284189	62.614432	22.256375	···	289 ± 11	5.4 ± 1.1	-12.86 ± 1.02	···	A3	N	N/?
108HD 284191	62.819075	22.248622	···	374 ± 30	3.6 ± 1.2	-10.64 ± 1.11	···	A0	N	N/?
109HD 283467	62.988010	27.168309	···	648 ± 8	2.1 ± 1.5	-2.22 ± 1.33	···	A0	N	N/?
11004115969+3046563	62.998756	30.782361	···	···	1.4 ± 1.7	-4.64 ± 1.46	···	?	?	N/?
11104124695+2902138	63.195599	29.037144	···	···	0.7 ± 1.7	-1.05 ± 1.49	···	?	?	N/?
112HD 283457	63.356642	27.357025	···	···	-3.9 ± 1.2	-6.57 ± 1.07	···	···	?	N/?
113HD 283503	63.511797	24.813039	···	404 ± 68	3.2 ± 1.3	-17.16 ± 1.18	···	A7	N	Y/?
114FM Tau	63.556610	28.213672	···	808 ± 710	4.7 ± 2.4	-29.78 ± 2.11	···	K3	Y	Y/?
115CW Tau	63.570878	28.182714	···	236 ± 188	18 ± 5.1	-24.94 ± 4.5	···	K5V:e...	Y	Y/?
116HD 281820	64.102354	29.149663	···	···	12.9 ± 1.6	-14.5 ± 1.48	···	A	?	N/?
11704171672+2518050	64.319686	25.301403	···	···	-1.1 ± 2.3	-4.25 ± 2.08	···	?	?	N/?
118DD Tau	64.629677	28.274725	···	396 ± 326	6.7 ± 5.1	-25.28 ± 4.49	···	K6V:e...	Y	Y/?
119HD 284308	64.646193	22.701229	···	429 ± 40	1.6 ± 1.2	-5.07 ± 1.11	···	A3	N	N/?
120FR Tau	64.897754	28.456022	···	···	5.9 ± 5.5	-25.32 ± 4.84	···	···	?	Y/?
121HD 283568	65.094954	28.737826	···	688 ± 78	-5.9 ± 1.6	-6.58 ± 1.4	···	A0	N	N/?
122HD 284383	65.391471	22.119671	···	684 ± 28	-2.9 ± 1.3	-2.22 ± 1.2	···	A0V	N	N/?
123HD 283571	65.489190	28.443195	134^{+55}_{-30}	69 ± 29	9.1 ± 1.6	-25.94 ± 1.41	24.3 ± 1.9	F8V:e...	Y/N	Y/N
12404233478+2804292	65.894960	28.074773	···	···	-8.8 ± 2.4	2.56 ± 2.12	···	?	?	N/?
125FU Tau	65.897490	25.050747	···	118 ± 103	7.3 ± 4.5	-24.01 ± 4.08	···	M7.25	Y	Y/?
126HD 27787	66.113276	30.124556	···	380 ± 33	-3 ± 1.5	-7.35 ± 1.3	-24	A0V	N	N/N

1272MASS J04244457+2610141	66.185733	26.170592	···	254 ± 191	9.8 ± 4.5	-21.09 ± 4.04	···	M0	Y	Y/?
128JH 15	66.209223	26.482108	···	···	-1 ± 2.2	-3.94 ± 1.97	···	···	?	N/?
12904262631+2742225	66.609620	27.706273	···	···	3.8 ± 1.8	-3.9 ± 1.59	···	?	?	N/?
130HD 283625	66.715248	28.953061	···	527 ± 16	1.1 ± 1.4	-5.86 ± 1.23	···	A1V	N	N/?
131DG Tau	66.769586	26.104481	···	···	5.6 ± 1.7	-19.13 ± 1.53	···	GV:e...	?	Y/?
13204273688+2936338	66.903701	29.609408	···	···	-4.6 ± 1.7	-5.56 ± 1.48	···	?	?	N/?
133DH Tau	67.423219	26.549413	···	244 ± 198	9.3 ± 4.5	-21.56 ± 4.03	···	M0.5V:e	Y	Y/?
134IQ Tau	67.464609	26.112596	···	88 ± 56	-2.2 ± 4.8	-16.88 ± 4.04	···	M2	Y	Y/?
135DK Tau	67.684336	26.023512	···	76 ± 53	5.5 ± 2.4	-14.56 ± 2.16	···	M0V:e	Y	Y/?
1362MASS J04305028+2300088	67.709603	23.002469	···	···	3.9 ± 4.5	-40.32 ± 4.14	···	F1	N	N/?
137HD 28697	68.090832	25.185490	109^{+14}_{-11}	150 ± 2	-2 ± 0.6	-25.88 ± 0.54	···	A2	N/Y	N/?
138HD 282267	68.099987	30.118652	···	342 ± 7	0.4 ± 1.5	-12.46 ± 1.38	···	A2V	N	N/?
139HD 283688	68.108755	28.317406	···	145 ± 6	-3 ± 1.4	-10.39 ± 1.23	···	F5	Y	N/?
140FZ Tau	68.132328	24.334158	···	···	1.6 ± 4.5	-27.61 ± 4.1	···	···	?	Y/?
141HD 284484	68.192963	22.103749	···	287 ± 36	2.2 ± 1.5	-5.84 ± 1.39	···	A5	N	N/?
1422MASS J04325030+2942395	68.209596	29.710960	···	···	1.2 ± 5.1	-2.52 ± 4.43	···	···	?	N/?
1432MASS J04325316+2948046	68.221551	29.801318	···	···	-0.1 ± 6.7	-5.81 ± 5.81	···	···	?	N/?
144HD 282270	68.275192	29.778140	···	294 ± 8	8 ± 1.6	-8.77 ± 1.39	···	A1V	N	N/?
145HD 283718	68.366065	24.923085	···	693 ± 213	-5.5 ± 1.3	-2.9 ± 1.18	···	A3V/A0	N	N/?
146GK Tau	68.394029	24.351647	···	···	10.7 ± 13.2	-1.55 ± 12.3	···	K7	N	Y/?

147IS Tau	68.403326	26.163645	···	233 ± 158	11.9 ± 4.5	−22.53 ± 4.04	···	K7	Y	Y/?
148DL Tau	68.412898	25.344065	···	···	2.4 ± 4.5	−12.74 ± 4.07	···	GV:e...	?	Y/?
149HD 283684	68.570530	28.436188	···	392 ± 29	−5.7 ± 2.5	−6.68 ± 2.29	···	A7	N	N/?
150HQ Tau	68.947255	22.839317	···	···	6.5 ± 4.5	−19.81 ± 4.15	···	···	?	Y/?
151HP Tau	68.969924	22.906426	···	101 ± 79	−0.9 ± 10.3	−22.02 ± 9.49	···	K3	Y	Y/?
152HD 282334	69.033170	30.394761	···	686 ± 66	−5.5 ± 1.4	−1.9 ± 1.21	···	A0	N	N/?
153HD 29333	69.608312	29.387357	152^{+37}_{-25}	132 ± 7	3.7 ± 0.8	0.78 ± 0.7	···	A2	Y/Y	N/?
154DO Tau	69.619111	26.180440	···	···	−7.1 ± 4.6	−29.61 ± 4.13	···	GV:e...	?	Y/?
155HD 283739	69.682933	28.075829	···	251 ± 17	−4 ± 1.4	2.29 ± 1.24	···	A7	N	N/?
156HD 282387	69.695646	29.475297	···	282 ± 59	5.7 ± 1.6	−11.32 ± 1.39	···	A0	N	N/?
157GN Tau	69.837159	25.750568	···	138 ± 99	3.6 ± 4.6	−22.16 ± 4.14	···	M2.5	Y	Y/?
158HD 283746	69.842850	27.765421	···	292 ± 8	−1.7 ± 1.4	−7.52 ± 1.33	···	A3	N	N/?
159HD 29459	69.846455	25.218274	111^{+10}_{-9}	68 ± 3	18 ± 0.6	−10.68 ± 0.45	17.8 ± 3.1	A5Vn	N/N	N/Y
160HD 29631	70.245274	23.939795	···	···	1.5 ± 1.1	−9.23 ± 1.1	···	F	?	N/?
161HD 29646	70.332333	28.614989	103^{+10}_{-8}	82 ± 1	35.5 ± 0.3	−27.56 ± 0.44	25.3	A2V	N/N	N/N
16204415107+2914109	70.462775	29.236408	···	···	−5.2 ± 1.7	−8.38 ± 1.48	···	?	?	N/?
163HD 284648	70.572097	23.268516	···	428 ± 5	5.7 ± 0.9	−8.45 ± 0.83	···	A0	N	N/?
164DP Tau	70.657043	25.260368	···	205 ± 133	−3.7 ± 5.1	−19.63 ± 4.61	···	M0V:e	Y	Y/?
16504433905+2353578	70.912683	23.899431	···	···	−0.1 ± 1.5	−14.45 ± 1.37	···	?	?	Y/?
166HD 282424	71.037023	30.866020	···	···	−1.4 ± 1.6	−9.18 ± 1.37	···	···	?	N/?
16704454979+2442422	71.457514	24.711720	···	···	4.2 ± 2.3	−11.08 ± 2.09	···	?	?	N/?
168HD 30168	71.550277	26.035498	266^{+104}_{-58}	166 ± 4	8.2 ± 0.7	−34.14 ± 0.63	···	A0	N/Y	N/?
169HD 283868	71.778034	26.179319	···	16 ± 2	3.6 ± 1.4	−2.33 ± 1.26	30	K3pv/G6e	N	N/N
170HD 283823	71.796194	28.964173	···	406 ± 51	3.8 ± 1.6	−12.6 ± 1.4	···	A2	N	N/?

171HD 30309	71.865612	24.354856	···	398 ± 26	3 ± 1.4	-2.64 ± 1.28	···	A0/F5	N	N/?
172HD 284763	71.940583	22.685857	···	458 ± 46	-2 ± 1.5	-1.48 ± 1.38	···	F0	N	N/?
173DS Tau	71.952482	29.419766	···	98 ± 63	7.8 ± 2.7	-29.62 ± 2.35	0	K4V:e	Y	Y/N
174HD 283861	71.975276	26.560652	···	463 ± 12	1.1 ± 1.5	-4.47 ± 1.43	···	A0	N	N/?
175HD 30466	72.316676	29.571363	163^{+30}_{-22}	177 ± 5	8 ± 0.8	-28.18 ± 0.61	17	A0p	Y/N	N/Y
17604492661+2730388	72.360927	27.510755	···	···	1.3 ± 1.4	-5.41 ± 1.24	···	?	?	N/?
177HD 283842	72.548615	27.677257	···	···	-2 ± 1.7	-3.54 ± 1.51	···	A	?	N/?
178HD 283830	72.585658	28.377142	···	675 ± 154	-3.1 ± 1.7	-12.58 ± 1.5	···	A2	N	N/?
179HD 283885	72.743801	24.278521	···	343 ± 35	3.1 ± 1.5	-5.65 ± 1.37	···	A5	N	N/?
180UY Aur	72.947410	30.787076	···	115 ± 44	4.9 ± 2.3	-19.24 ± 2.06	18 ± 3	G5V:e...	Y	Y/Y
181HD 283945	73.028640	25.437055	···	515 ± 66	-4.4 ± 1.7	-8.31 ± 1.54	···	A2	N	N/?
182HD 283889	73.110373	28.729730	···	592 ± 65	-3.2 ± 1.6	-6.75 ± 1.4	···	A0	N	N/?
183BD+26 758	73.135736	27.027236	···	158 ± 12	-12.3 ± 1.5	-22.63 ± 1.34	···	A5	Y	N/?
184HD 283890	73.185411	28.619612	···	301 ± 48	-1.4 ± 1.7	-4.83 ± 1.49	···	A3	N	N/?
185HD 283941	73.289352	25.491105	···	487 ± 69	4.4 ± 1.5	-7.67 ± 1.44	···	A0	N	N/?
186HD 283893	73.392339	28.456354	···	616 ± 88	-2.5 ± 1.4	-11.43 ± 1.23	···	A0	N	N/?
187HD 284873	73.431141	22.178329	···	···	6.4 ± 1	-6.11 ± 0.93	···	A	?	N/?
188HD 283911	73.731551	27.630496	···	411 ± 57	1.1 ± 1.5	-8.24 ± 1.33	···	A2	N	N/?
189HD 31329	73.914289	22.187528	···	281 ± 17	-1.2 ± 0.9	-8.15 ± 0.93	···	A2	N	N/?
190HD 282624	73.997451	30.567085	152^{+63}_{-34}	451 ± 1	5.4 ± 1.4	-20.32 ± 0.95	23.2 ± 2.8	G2III	Y/N	Y/N
191HD 284989	74.128224	22.591051	···	775 ± 86	1.5 ± 1.4	-5.63 ± 1.38	···	A0	N	N/?
192HD 31581	74.581425	29.847393	···	194 ± 9	-1.7 ± 1.5	-3.9 ± 1.21	···	A2	N	N/?
193HD 31648	74.692775	29.843609	131^{+24}_{-18}	124 ± 32	5.6 ± 0.9	-21.16 ± 0.69	···	A3Ve/A2	Y/Y	Y/?
194HD 284946	74.893341	23.502550	···	479 ± 21	-1.8 ± 1.2	-5.04 ± 1.1	···	A0	N	N/?

195HD 284035	74.941567	24.314204	···	523 ± 61	−7 ± 5.9	−7.11 ± 5.65	···	A0	N	N/?

O,B,A stars from Knapp et al. *SDSS* data

19604095167+2520112	62.465271	25.336500	···	4389 ± 605	−1.6 ± 3.7	−4.8 ± 3.7	−0.1 ± 1.6	A0	N	N/N
19704111342+2447170	62.805889	24.788080	···	8576 ± 2737	0.3 ± 3.8	−3.3 ± 3.8	37.5 ± 3.2	A0	N	N/N
19804113476+2524136	62.894859	25.403830	···	12774 ± 2784	−3.7 ± 4.3	−2.5 ± 4.3	−2.5 ± 2.5	A0	N	N/N
19904122067+2430477	63.086201	24.513310	···	6397 ± 895	−2.0 ± 3.8	−3.9 ± 3.8	−7.4 ± 1.5	A0	N	N/N
20004132281+2620282	63.345039	26.341200	···	11426 ± 1981	1.3 ± 4.2	−6.2 ± 4.2	−1.1 ± 1.7	A0	N	N/N
20104135173+2631257	63.465488	26.523861	···	11234 ± 838	1.1 ± 4.4	−4.2 ± 4.4	69.9 ± 2.6	A0	N	N/N
20204135440+2609097	63.476631	26.152700	···	···	3.2 ± 3.9	−9.9 ± 3.9	64.2 ± 2.7	···	?	N/N
20304142194+2500478	63.591438	25.013350	···	8722 ± 1026	0.1 ± 4.3	−3.2 ± 4.3	−14.5 ± 3	A0	N	N/N
20404142864+2608046	63.619362	26.134621	···	7392 ± 1367	3.0 ± 3.8	−8.2 ± 3.8	2.3 ± 1.8	A0	N	N/N
20504152014+2629584	63.833901	26.499580	···	8897 ± 748	3.8 ± 4.1	−7.5 ± 4.1	25.6 ± 2.2	A0	N	N/N
20604152167+2522393	63.840290	25.377581	···	18112 ± 1920	10.3 ± 4.4	−5.3 ± 4.4	101.5 ± 5.1	B6	N	N/N
20704153610+2538570	63.900219	25.649200	···	···	7.4 ± 4.5	−0.3 ± 4.5	−66.4 ± 7.3	O	?	N/N
20804154968+3035156	63.957008	30.587580	···	20128 ± 6470	4.7 ± 5.5	−0.5 ± 5.5	62.6 ± 3.7	A0p	N	N/N
20904155589+2941428	63.982899	29.695271	···	14164 ± 7605	2.0 ± 4.4	2.7 ± 4.4	2.8 ± 2.6	A0	N	N/N
21004160013+2730051	64.000603	27.501440	···	5608 ± 403	−0.9 ± 4.3	0.9 ± 4.3	110.4 ± 2.6	A0	N	N/N
21104161037+3053487	64.043190	30.896900	···	14170 ± 5336	2.3 ± 4.6	−3.0 ± 4.6	−3 ± 2.3	A0	N	N/N
21204162411+2434450	64.100487	24.579250	···	7766 ± 575	6.0 ± 3.9	−3.8 ± 3.9	21.9 ± 1.9	A0	N	N/N
21304162961+2643589	64.123383	26.733021	···	10475 ± 1941	5.8 ± 4.0	−6.5 ± 4	31.8 ± 3.2	A0	N	N/N
21404163672+2650392	64.152969	26.844250	···	11636 ± 1775	1.4 ± 4.4	−3.7 ± 4.4	0 ± 3	A0	N	N/N
21504165196+2601449	64.216522	26.029141	···	12571 ± 2322	6.9 ± 4.3	−8.3 ± 4.3	26.8 ± 2.7	A0	N	N/N

21604170011+2522475	64.250412	25.379850	···	5729 ± 756	4.1 ± 3.9	1.6 ± 3.9	−10 ± 2.8	A0	N	N/N
21704170272+2644290	64.261322	26.741400	···	16618 ± 6674	−0.9 ± 4.2	−1.6 ± 4.2	−42 ± 1.9	A0	N	N/N
21804174593+2618579	64.441330	26.316080	···	12914 ± 2916	11.6 ± 4.2	−6.2 ± 4.1	−23.7 ± 2.6	A0	N	N/N
21904180495+2952363	64.520653	29.876770	···	5337 ± 739	0.4 ± 4.3	−1.0 ± 4.3	56.2 ± 2.9	A0	N	N/N
22004180763+2846201	64.531853	28.772261	···	···	−3.0 ± 4.3	2.4 ± 4.3	−8.2 ± 4	···	?	N/N
22104182140+2552023	64.589111	25.867371	···	13651 ± 2176	0.7 ± 4.5	−2.1 ± 4.5	19.9 ± 2.3	A0	N	N/Y
22204182615+2454459	64.608917	24.912741	···	6099 ± 481	4.1 ± 3.9	−0.7 ± 3.9	23.2 ± 1.9	A0	N	N/N
22304183386+2547250	64.641022	25.790310	···	7144 ± 1040	1.2 ± 3.9	−1.1 ± 3.9	40.5 ± 2	A0	N	N/N
22404183552+3006115	64.647987	30.103270	···	11840 ± 6382	5.1 ± 4.2	−3.7 ± 4.2	−28.9 ± 1.6	A0	N	N/N
22504183818+2735261	64.658989	27.590740	···	5840 ± 429	0.1 ± 4.3	−2.7 ± 4.3	93.5 ± 4.2	A0	N	N/N
22604184109+2449442	64.671127	24.828951	···	6709 ± 1285	5.4 ± 3.9	−6.5 ± 3.9	−28.6 ± 3.2	A0	N	N/N
22704184261+2550172	64.677528	25.838110	···	4135 ± 2695	4.5 ± 4.4	−1.5 ± 4.4	60.3 ± 2.2	A0	N	N/N
22804185780+3004129	64.740830	30.070339	···	7548 ± 2854	−2.8 ± 4.2	−1.0 ± 4.2	16.4 ± 1.5	A0	N	N/Y
22904185955+3050026	64.748200	30.834129	···	13418 ± 4181	−5.9 ± 4.7	−2.4 ± 4.7	17.3 ± 3.3	A0	N	N/Y
23004190128+2918288	64.755364	29.308020	···	17037 ± 6908	0.3 ± 4.7	−0.9 ± 4.7	−42 ± 2.8	A0	N	N/N
23104190952+2907266	64.789658	29.124069	···	10467 ± 2703	0.5 ± 4.4	−1.4 ± 4.4	−24.5 ± 2	A0	N	N/N
23204191436+2552469	64.809807	25.879721	···	7069 ± 461	3.8 ± 3.9	−0.2 ± 3.9	22.5 ± 2.3	A0	N	N/N
23304191985+2749395	64.832733	27.827740	···	···	−2.6 ± 4.3	−4.5 ± 4.3	37 ± 2.7	···	?	N/N
23404192106+2931069	64.837784	29.518650	···	5810 ± 1609	0.1 ± 4.3	−4.8 ± 4.3	−67 ± 1.5	A0	N	N/N
23504193853+2949396	64.910599	29.827740	···	···	−12.3 ± 5.8	−6.3 ± 5.8	−5.3 ± 2.2	0	?	N/N
23604195512+2801576	64.979652	28.032820	···	20143 ± 8223	−4.1 ± 5.0	−13.7 ± 5	49.8 ± 5.6	B9	N	N/N
23704200363+2950586	65.015122	29.849670	···	22508 ± 13749	−2.8 ± 4.4	1.1 ± 4.4	25.8 ± 3.4	A0	N	N/N
23804200803+2843222	65.033478	28.722879	···	5852 ± 1409	−3.4 ± 4.3	−2.6 ± 4.3	13.5 ± 1.5	A0	N	N/Y
23904203271+3015272	65.136299	30.257601	···	11597 ± 1905	2.5 ± 4.8	−5.1 ± 4.8	−15.5 ± 3.2	A0	N	N/N

24004203551+2945073	65.147903	29.752081	···	6242 ± 572	–4.8 ± 4.4	–3.4 ± 4.4	–21.6 ± 1.3	A0	N	N/N
24104204960+3010153	65.206642	30.170919	···	5912 ± 1380	4.0 ± 4.3	–3.2 ± 4.3	–1 ± 1.8	A0	N	N/N
24204205096+2840119	65.212318	28.670050	···	5659 ± 1353	1.2 ± 4.3	–1.7 ± 4.3	1.5 ± 1.6	A0	N	N/N
24304210068+2711172	65.252724	27.188320	···	15034 ± 10003	1.8 ± 3.8	–8.5 ± 3.8	–168.4 ± 2.2	A0	N	N/?
24404210658+2546557	65.277359	25.782129	···	16067 ± 2065	–9.8 ± 4.1	–15.4 ± 4.1	64 ± 2.8	B6	N	N/N
24504211397+2850064	65.308197	28.835079	···	12704 ± 3762	1.0 ± 4.7	3.1 ± 4.7	–45.6 ± 4	A0	N	N/N
24604212796+3002107	65.366501	30.036320	···	6888 ± 1080	–4.7 ± 4.2	–2.8 ± 4.2	–33.4 ± 1.4	A0	N	N/N
24704213150+2520399	65.381271	25.344431	···	4475 ± 673	2.7 ± 3.8	–3.2 ± 3.8	–11.3 ± 1.7	A0	N	N/N
24804213151+2917334	65.381310	29.292620	···	9353 ± 1500	0.6 ± 4.5	–0.1 ± 4.5	–1.6 ± 1.9	A0	N	N/N
24904213578+2936482	65.399117	29.613489	···	10898 ± 2482	–1.7 ± 4.5	–4.6 ± 4.5	–22.9 ± 2	A0	N	N/N
25004222582+2616149	65.607529	26.271099	···	13098 ± 3069	–1.3 ± 4.5	–3.3 ± 4.5	–11.5 ± 2.7	A0	N	N/N
25104224008+2957006	65.667023	29.950230	···	8232 ± 1932	–1.0 ± 4.4	1.4 ± 4.4	4.8 ± 1.7	A0	N	N/N
25204224882+2904442	65.703377	29.079029	···	14458 ± 3048	0.1 ± 5.0	–4.6 ± 5	–1.4 ± 2.1	A0	N	N/N
25304225306+2613188	65.721130	26.222340	···	···	–2.9 ± 4.4	–8.6 ± 4.4	–28.4 ± 4.3	0	?	N/N
25404225686+2939043	65.736900	29.651279	···	9610 ± 1149	–6.2 ± 4.6	2.3 ± 4.6	20 ± 2.1	A0	N	N/Y
25504230562+2538494	65.773392	25.647060	···	5550 ± 424	2.4 ± 3.8	–0.2 ± 3.8	1.9 ± 2.4	A0	N	N/N
25604231596+2941221	65.816551	29.689520	···	9546 ± 1035	8.9 ± 4.7	–8.6 ± 4.7	57.1 ± 2.4	A0	N	Y/N
25704231716+2757432	65.821480	27.962071	···	1417 ± 1307	–6.5 ± 4.3	–9.1 ± 4.3	34.9 ± 1.9	B9	Y:	N/N
25804233427+2947149	65.892807	29.787510	···	6340 ± 1232	–1.5 ± 4.3	–5.6 ± 4.3	12.7 ± 1.4	A0	N	N/Y
25904233438+3056585	65.893272	30.949650	···	3320 ± 420	4.8 ± 4.3	1.4 ± 4.3	–20.8 ± 1.8	A0	N	N/N
26004234983+2532157	65.957558	25.537720	···	11883 ± 2984	2.2 ± 4.2	–1.7 ± 4.2	49.3 ± 3.2	A0	N	N/N
26104240540+2744507	66.022369	27.747620	···	···	–0.3 ± 4.3	–5.5 ± 4.3	53.3 ± 2.8	···	?	N/N
26204240902+2611351	66.037521	26.193510	···	···	4.2 ± 3.9	–4.8 ± 3.9	–17.2 ± 5	0	?	N/N
26304243937+2946563	66.164047	29.782440	···	12882 ± 4098	3.2 ± 4.8	–5.9 ± 4.8	12.9 ± 2.4	A0	N	N/Y

26404244689+2826203	66.195351	28.439030	···	16870 ± 6801	0.7 ± 4.9	−4.7 ± 4.9	12.1 ± 2.3	A0	N	N/Y
26604245454+3014488	66.227280	30.246929	···	9024 ± 2583	−1.4 ± 4.3	−1.6 ± 4.3	−20.4 ± 2	A0	N	N/N
26704254650+2805257	66.443710	28.090530	···	10098 ± 1561	−2.5 ± 4.4	−4.9 ± 4.4	29.9 ± 4.2	B9	N	N/N
26804254749+3039409	66.447868	30.661350	···	10176 ± 3362	−3.3 ± 4.4	−6.1 ± 4.4	2.8 ± 2.6	A0	N	N/N
26904255111+3041231	66.462982	30.689720	···	5837 ± 1217	−6.7 ± 4.3	−1.8 ± 4.3	41.9 ± 2.5	A0	N	N/N
27004262320+2629082	66.596626	26.486160	···	···	−1.4 ± 3.9	−3.8 ± 3.9	15.9 ± 12.6	0	?	N/Y
27104263605+2904190	66.650147	29.072081	···	5375 ± 1263	−2.2 ± 4.3	−2.2 ± 4.3	−16.1 ± 1.4	A0	N	N/N
27204263695+3035247	66.654030	30.590200	···	9300 ± 1949	−4.4 ± 4.2	−3.0 ± 4.2	7.2 ± 2.8	A0	N	N/N
27304264332+3054283	66.680603	30.907900	···	6815 ± 1694	−2.3 ± 4.1	1.2 ± 4.1	18.7 ± 1.9	A0	N	N/Y
27404265712+2920054	66.737999	29.334990	···	4125 ± 496	0.0 ± 4.3	−8.3 ± 4.3	3.2 ± 1.4	A0	N	N/N
27504300090+2511506	67.503799	25.197390	···	11767 ± 4813	−0.1 ± 3.9	−2.1 ± 3.9	11.1 ± 3.1	A0	N	N/Y
27604304916+2527382	67.704887	25.460671	···	11299 ± 2639	0.4 ± 4.3	−3.1 ± 4.3	30.3 ± 3.2	A0	N	N/N
27704324026+2537105	68.167717	25.619631	···	9909 ± 1761	2.9 ± 4.2	−2.5 ± 4.2	92.8 ± 3.8	A0	N	N/N
27804325041+2613573	68.210083	26.232540	···	···	1.8 ± 3.8	−8.8 ± 3.8	−33.1 ± 7	···	?	N/N
27904343357+2538478	68.639870	25.646650	···	···	0.7 ± 3.8	−11.1 ± 3.8	41.1 ± 4.9	···	?	Y/N
28004344093+2526178	68.670540	25.438280	···	9457 ± 2601	−0.2 ± 3.9	−0.9 ± 3.9	13 ± 3.3	A0	N	N/Y
28104352460+2511584	68.852524	25.199591	···	···	0.6 ± 3.9	−0.4 ± 3.9	1.3 ± 3.4	···	?	N/N
28204352506+2505371	68.854431	25.093679	···	8742 ± 1788	1.9 ± 4.0	−1.8 ± 4	9.5 ± 3.8	A0	N	N/Y
28304355804+2429239	68.991859	24.490030	···	4305 ± 611	−2.0 ± 3.7	−2.1 ± 3.7	39.6 ± 2.3	A0	N	N/N
28404360432+2512256	69.018021	25.207150	···	7098 ± 1703	3.5 ± 3.7	−0.5 ± 3.7	83.4 ± 4	A0	N	N/N
28504364715+2508462	69.196533	25.146160	···	7047 ± 1224	−1.4 ± 3.9	−0.6 ± 3.9	21.8 ± 3.1	A0	N	N/N
28604374665+2415466	69.444412	24.262991	···	8970 ± 2523	−3.6 ± 3.9	−3.3 ± 3.9	−24.1 ± 2.9	A0	N	N/N
28704384454+2438388	69.685593	24.644190	···	···	−0.3 ± 3.8	−5.4 ± 3.8	16 ± 3.6	···	?	N/Y
28804384756+2524115	69.698174	25.403200	···	···	1.4 ± 3.8	−3.1 ± 3.8	34.2 ± 6.9	···	?	N/N

28904391699+2520299	69.820900	25.341660	···	···	−6.7 ± 3.8	2.0 ± 3.8	30.2 ± 7.7	···	?	N/N
29004393029+2457401	69.876183	24.961180	···	···	17.8 ± 3.8	−2.4 ± 3.8	11.9 ± 2.5	···	?	N/Y
29104400871+2451438	70.036377	24.862181	···	···	0.9 ± 3.8	2.5 ± 3.8	28.1 ± 5	···	?	N/N
29204402154+2629461	70.089851	26.496161	···	···	−3.5 ± 3.8	−6.1 ± 3.8	−21.3 ± 4.2	···	?	N/N
29304402572+2635205	70.107269	26.589060	···	···	−6.6 ± 3.8	5.4 ± 3.8	−26 ± 5.4	···	?	N/N
29404415750+2451568	70.489609	24.865770	···	···	−0.1 ± 4.0	1.5 ± 4	66.5 ± 3.5	···	?	N/N
29504422622+2459000	70.609337	24.983379	···	···	9.5 ± 4.0	−7.6 ± 4	22.7 ± 4.2	···	?	N/N
29604422916+2422346	70.621521	24.376360	···	···	2.6 ± 4.2	−4.8 ± 4.2	3.9 ± 1.9	···	?	N/N
29704423176+2601455	70.632378	26.029329	···	···	2.1 ± 4.0	−5.7 ± 4	2.5 ± 2.6	···	?	N/N
29804435975+2529297	70.998970	25.491650	···	···	−1.3 ± 4.3	−5.1 ± 4.3	1.5 ± 3.2	···	?	N/N
29904441407+2415542	71.058632	24.265110	···	12108 ± 5721	3.2 ± 4.2	−3.8 ± 4.2	31.7 ± 3	B9	N	N/N
30004442409+2609464	71.100418	26.162939	···	14445 ± 5743	−3.0 ± 4.7	−7.9 ± 4.7	6.8 ± 2.7	A0	N	Y/N
30104443402+2537401	71.141808	25.627850	···	···	−2.0 ± 4.3	−9.5 ± 4.3	54.6 ± 3.9	···	?	Y/N
30204445791+2601458	71.241364	26.029421	···	4464 ± 486	−2.1 ± 4.3	−5.3 ± 4.3	51.3 ± 1.8	A0	N	N/N
30304450067+2619327	71.252762	26.325800	···	9289 ± 1437	−0.1 ± 4.7	−7.3 ± 4.7	−17.3 ± 4	A0	N	Y/N
30404452569+2417505	71.357018	24.297430	···	11112 ± 3705	1.4 ± 4.4	−7.1 ± 4.4	24.1 ± 3.2	A0	N	Y/N
30504453199+2548133	71.383301	25.803770	···	···	−2.2 ± 4.3	−7.7 ± 4.3	89.7 ± 2.8	···	?	N/N
30604461962+2434148	71.581787	24.570881	···	···	1.3 ± 4.3	−4.1 ± 4.3	−23.5 ± 5	···	?	N/N
30704463405+2413551	71.641983	24.232010	···	11533 ± 1056	9.7 ± 4.9	1.3 ± 4.9	22.3 ± 3.4	B9	N	N/N
30804464411+2620004	71.683830	26.333450	···	3561 ± 2188	−6.0 ± 4.4	−2.3 ± 4.4	−7.9 ± 2.6	A0	N	N/N
30904464556+2550507	71.689850	25.847441	···	···	−4.6 ± 4.3	−9.0 ± 4.3	8.5 ± 2.5	···	?	N/Y
31004464746+2419597	71.697853	24.333281	···	6966 ± 1113	−2.5 ± 4.4	−2.8 ± 4.4	20.5 ± 2.6	A0	N	N/Y
31104464757+2448496	71.698288	24.813789	···	···	−3.2 ± 4.3	−2.6 ± 4.3	50.7 ± 2.5	···	?	N/N
31204471316+2452301	71.804802	24.875071	···	···	9.5 ± 4.4	−13.3 ± 4.4	−25.5 ± 4.6	···	?	Y/N

31304475295+2407358	71.970642	24.126699	···	14372 ± 3532	3.1 ± 4.8	-2.0 ± 4.8	14.1 ± 2.8	B9	N	N/Y
31404481479+2412522	72.061668	24.214569	···	12093 ± 1796	0.2 ± 5.1	-6.6 ± 5.1	-24.5 ± 2.6	A0	N	Y/N
31504484223+2405315	72.175957	24.092159	···	5295 ± 1494	3.4 ± 4.3	-8.7 ± 4.3	25.2 ± 2.3	B9	N	Y/N
31604485467+2603349	72.227799	26.059731	···	···	3.8 ± 4.3	-8.2 ± 4.3	-15.3 ± 2.3	···	?	Y/N
31704490164+2603474	72.256897	26.063191	···	···	-2.1 ± 4.3	-4.7 ± 4.3	-8.1 ± 3.1	···	?	N/N
31804495186+2546445	72.466042	25.779091	···	4478 ± 1063	-1.4 ± 4.3	-4.7 ± 4.3	18 ± 2.2	B9	N	N/Y
31904501677+2455582	72.569870	24.932921	···	···	7.7 ± 4.3	-14.6 ± 4.3	205.7 ± 3.1	···	?	Y/N
32004502462+2534113	72.602654	25.569889	···	···	-0.1 ± 4.3	-12.8 ± 4.3	39.3 ± 4.2	···	?	Y/N
32104502592+2609475	72.607941	26.163250	···	···	-0.5 ± 4.3	-9.7 ± 4.3	-8.8 ± 1.7	···	?	Y/N
32204503511+2516324	72.646263	25.275740	···	···	5.1 ± 4.4	-5.4 ± 4.4	2.4 ± 4.3	···	?	N/N
32304505387+2426576	72.724533	24.449440	···	7078 ± 1947	-1.5 ± 4.3	-3.9 ± 4.3	28.7 ± 2.2	A0	N	N/N
32404511381+2522599	72.807442	25.383381	···	6538 ± 1250	5.6 ± 4.3	-4.0 ± 4.3	12.4 ± 2.5	B9	N	N/Y
32504513070+2438129	72.877831	24.636990	···	3468 ± 296	10.7 ± 4.3	-7.0 ± 4.3	32 ± 2.5	A0	N	N/N
32604521892+2520501	73.078812	25.347281	···	5194 ± 884	4.8 ± 4.3	-3.0 ± 4.3	63.8 ± 2	A0	N	N/N
32704522135+2506498	73.088966	25.113840	···	9897 ± 2710	4.1 ± 4.4	-4.8 ± 4.4	26.4 ± 3.6	A0	N	N/N

Other stars

328HD 31305	73.950958	30.337911	···	174 ± 11	6.4 ± 1.7	-21.9 ± 1.6	···	A1V	N	Y/?
329HD 31293	73.941022	30.551191	139^{+22}_{-16}	121 ± 50	1.9 ± 0.9	-24.4 ± 0.7	8.9 ± 0.9	∼A0V	Y	Y/Y

(1) Error on d_{SPEC} is the standard deviation among distances calculated using B,V,R,J,H, and K magnitudes, as available, and underestimates true error values; see text. (2) Errors on other columns are taken from original references; see text. (3) Spectral types are from SIMBAD and Kharchenko et al. 2009 in the top three sections, with a slash (/) denoting any discrepancy between these two compilations, and from *SDSS* in the fourth section. In cases where we have derived new spectral types ourselves in this paper (see Table A.4), our types supersede those from the references. (4) Last two columns state whether or not (Y/N) the star is a probable Taurus member based on the two distance estimates (d), and the two kinematic assessments: proper motion (μ) and radial velocity (RV); see text.

Table A.4: Spectral types derived through new spectroscopy.

B#	Star	$\frac{SNR}{100}$	Equivalent Widths															Derived SpT
			Ca II K 3933.7	N II 3995.0	He I 4009.3	He I 4026.2	H_δ 4101.7	He I 4120.8	Si II 4128.1, 4130.9	He I 4143.7	H_γ 4340.4	He I 4387.9	He I 4471.5	MgII 4481.2	H_β 4862.3	He I 4921.9	H_α 6562.8	He I 6678.2	
Spectral Type Standards																			
	HD 36960	3.0	0.12	0.09	0.42	1.2	4.0	0.48	0.02	0.55	4.2	0.58	0.98	0.15	3.6	0.78	3.4	0.68	B0.5V
	HD 19374	2.6	0.15	0.08	0.56	1.5	5.7	0.35	0.08	0.82	5.2	0.87	1.6	0.20	5.4	0.97	4.2	0.66	B1.5V
	HD 35912	3.2	0.14	0.04	0.65	1.5	5.9	0.26	0.12	0.81	5.9	0.91	1.6	0.25	5.9	0.88	4.4	0.56	B2V
	HD 28375	2.6	0.13	0.01	0.30	1.1	7.6	0.20	0.21	0.45	7.6	0.61	1.1	0.28	7.4	0.56	5.5	0.31	B3V
	HD 16219	2.7	0.13	0.01	0.19	0.82	8.1	0.13	0.26	0.33	8.0	0.48	0.85	0.32	8.0	0.43	5.7	0.21	B5V
	HD 21071	2.7	0.14	<0.01	0.15	0.84	8.4	0.11	0.24	0.29	8.4	0.44	0.80	0.30	8.7	0.41	5.8	0.20	B7V
	HD 14272	1.7	0.19	···	<0.02	0.40	10.2	[a]	0.24	0.11	9.3	0.11	0.25	0.31	10.1	0.28	6.4	0.12	B8V
	HD 16350	1.9	0.57	···	···	[a]	12.3	[a]	0.26	0.08	17.8	[a]	0.10	0.38	11.9	<0.23	8.7	0.04	B9.5V
	HD 14171	1.7	0.29	···	···	···	14.6	[a]	0.30	[a]	13.0	···	0.023	0.33	13.6	[a]	9.4	[a]	B9.5V
O,B, and A0 stars from SIMBAD																			
50	HD 283809	1.8	0.24	0.09	0.70	1.4	4.9	0.35	0.10	0.86	4.9	0.90	1.4	0.27	5.0	0.93	3.8	0.64	B1.5-2V
51	τ Tau	2.4	0.29	0.01	0.43	1.2	8.2	0.21	0.15	0.56	7.9	0.72	1.0	0.27	7.8	0.68	5.6	0.38	B3V
25	72 Tau	3.1	0.12	0.02	0.16	0.82	9.8	>0.1	0.24	0.27	9.2	0.49	0.75	0.31	8.6	0.41	6.0	0.18	B7V
88	HD 31806	3.4	0.12	0.01	0.21	0.77	9.7	[a]	0.22	0.27	8.7	0.45	0.72	0.34	8.8	0.39	6.4	0.19	B7V
6	HD 283304	1.2	0.42	···	0.03	[a]	8.9	[a]	0.79	[c]	8.2	0.15	0.07	0.16	8.2	0.20	6.6	<0.05	B8V Si
33	HD 282276	1.4	0.28	0.02	0.05	0.31	8.9	[c]	0.41	0.09	8.2	[a]	0.29	0.26	8.0	0.24	6.5	0.12	B8V
36	HR 1445	2.3	0.19	[c]	0.04	0.41	9.6	[a]	0.30	0.13	9.1	<0.20	0.32	0.32	8.7	0.26	6.7	0.05	B8V
13	V1137 Tau	2.9	0.18	0.01	0.11	0.29	6.4	>0.05	0.37	0.11	5.9	<0.22	0.30	0.22	6.5	0.22	5.9	0.09	B8III
48	HD 29647	1.6	0.31	0.04	<0.1	0.24	8.7	[a]	0.34	0.09	7.8	<0.19	0.26	0.39	7.7	0.22	6.1	0.06	B9III
81	HD 283971	1.6	0.92	0.01	0.03	0.25	11.1	[a]	0.25	0.07	9.5	[a]	0.19	0.38	10.6	<0.22	7.9	<0.05	B9V
63	HD 30378	3.0	0.28	<0.01	0.01	0.24	13.6	[a]	0.24	0.06	13.0	<0.1	0.27	0.44	12.7	0.18	9.1	<0.05	B9.5V
4	BD+23607	2.3	1.1	<0.01	[c]	<0.01	16.6	[a]	[a]	[a]	14.0	[a]	0.08	0.38	13.9	<0.19	9.7	<0.02	A0V
12	HD 283449	1.2	0.75	[c]	[c]	0.23	14.3	[a]	0.26	<0.09	13.7	[c]	0.11	0.46	14.3	0.14	10.7	<0.05	A0V
53	V1081 Tau	3.1	0.59	[a,c]	[c]	0.11	16.8	[a]	[a]	0.01	16.8	[a]	0.13	0.37	15.8	<0.16	10.7	<0.03	A0V
19	V892 Tau	0.5	[a]	···	[c]	0.2	14	[c]	[c]	[c]	[b]	[c]	[c]	0.2	[b]	[c]	[b]	[c]	∼A0Ve
Early-type stars from Rebull et al. (2010)																			
95	HD 283751	1.5	0.39	0.49	0.26	0.82	8.0	0.13	0.23	0.36	[b]	0.50	0.79	0.32	[b]	0.31	[b]	0.21	B5Ve
90	HD 27923	2.3	0.24	[c]	0.04	0.33	12.9	[a]	0.18	0.07	11.8	<0.21	0.27	0.35	11.5	0.18	8.2	<0.05	B9V
91	HD 283637	1.6	0.91	[c]	0.1	<0.32	15.9	[a]	>0.04	[a,c]	13.7	[a]	0.1	0.37	13.6	0.22	[b]	0.1	B9.5eV
94	HD 284530	2.1	0.34	<0.01	[c]	0.30	13.6	[a]	0.30	0.09	11.7	<0.35	0.25	0.38	11.5	0.24	8.5	<0.07	B9.5V
93	2MASS0431+29	1.9	0.48	···	<0.03	[a]	16.6	[a]	[a]	[c]	17.2	[a/c]	<0.06	0.27	15.6	<0.24	10.9	<0.01	A1V
89	HD 27659	1.0	2.6	···	<0.19	⩽0.16	10.4	[a]	0.4	⩽0.19	10.4	<0.39	<0.23	0.47	11.6	<0.48	10.1	0.1	A3V
92	2MASS0428+27	0.3	3.5	[a]	<0.04	[c]	12	[a]	0.5	<0.2	12	[a]	<0.6	0.87	14	<0.11	9.6	0.14	A4III
Early-type stars selected using 2MASS colors																			
106	HD 26212	1.2	3.9	[a]	[a]	[a]	11.8	[a]	0.4	⩽0.16	8.9	<0.33	<0.21	0.41	9.0	⩽0.42	9.6	0.1	A5V
Other																			
328	HD 31305	1.8	1.7	···	[c]	<0.27	17.6	[a]	0.3	<0.09	16.3	<0.28	<0.16	0.46	15.0	<0.27	9.6	<0.02	A1V
329	AB Aur	2.4	[b]	···	···	···	···	···	0.2	···	···	···	···	0.40	···	···	[b]	[b]	A0Ve

B# is repeated from Table A.3. SNR is the signal-to-noise ratio of the obtained spectrum. Notes- (a) embedded in an adjacent absorption line, (b) emission line present within the absorption line, (c) hard to distinguish from noise.

Table A.5: Physical parameters derived through model atmosphere fitting.

Star	$T_{\rm eff}$ (K)	$v \cdot \sin i$ (km s^{-1})	log g (cgs)	SpT
HD 283809	21000	< 50	4.0	B2V
HD 29763 = τ Tau	18000	150	4.0	B3V
HD 283751	15000	50	4.0	B5V
HD 28149 = 72 Tau	14000	75	4.0	B7V
HD 31806	14000	100	4.0	B7V
HD 28929 = HR 1445	13000	< 50	4.0	B7V
HD 26571 = V1137 Tau	13000	< 50	3.5	B7III
HD 284530	12000	< 50	4.0	B7.5V
HD 283971	12000	50	4.0	B7.5V
HD 283304	12000	< 50	3.5	B8III
HD 282276	12000	< 50	3.5	B8III
HD 29647	11500	< 50	3.5	B8III
HD 27923	11000	< 50	4.0	B8.5V
AB Aur	11000	200	4.5	B8.5V
2MASS J04313313+2928565	11000	250	4.5	B8.5V
HD 31305	11000	150	4.5	B8.5V
HD 30378	11000	< 50	4.0	B8.5V
V892 Tau	11000	100	4.5	B8.5V
HD 29935 = V1081 Tau	11000	200	4.5	B8.5V
HD 283637	11000	50	4.0	B8.5V
BD+23 607	10000	< 50	4.0	A0V
HD 283449	10000	< 50	4.0	A0V
HD 27659	9000	< 50	3.5	A1III
2MASS J04285940+2736254	9000	< 50	3.5	A4III
HD 26212	8500	< 50	3.5	A5III

Table A.6: Final list of early-type stars showing indications of membership with Taurus.

B#	HD Number	Alt. Identifier	α_{J2000} (h,m,s)	δ_{J2000} ($^\circ$,$'$,$''$)	SpT	d_{HIP} (pc)	d_{SPEC} (pc)	$P(\chi^2)$ (%)	RV (km s^{-1})	Comments
Probable members based on our analysis of distance and/or kinematics										
51	HD 29763	τ Tau	04 42 14.70	22 57 24.9	B3V	123^{+13}_{-11}	137 ± 9	5.1	12.3 ± 4.1	
25	HD 28149	72 Tau	04 27 17.45	22 59 46.8	B7V	127^{+13}_{-11}	161 ± 3	2.4	7.3 ± 2.6	IR nebula; cool dust SED
36	HD 28929	HR 1445	04 34 37.99	28 57 40.1	B8V	143^{+20}_{-16}	157 ± 3	11.5	12.6 ± 2.2	Weak nebula
19	—-	V892 Tau	04 18 40.62	28 19 15.5	$\sim$B8.5–A0Ve	$\cdots$	†	25.7		IR nebula; Class I SED
329	HD 31293	AB Aur	04 55 45.85	30 33 04.3	A0Ve	139^{+22}_{-16}	120 ± 50	36.1	8.9 ± 0.9	Class II SED
328	HD 31305	IRAS 04526+3015	04 55 48.23	30 20 16.5	A1V	$\cdots$	174 ± 11	21.5		Cool dust SED
193	HD 31648	MWC 480	04 58 46.27	29 50 37.0	A3Ve	137^{+31}_{-21}	186 ± 48	18.8		Class II SED
106	HD 26212	—-	04 09 43.68	24 04 22.6	A5V	123^{+17}_{-14}		3.3	20.3 ± 3.9	
Candidates with several membership indicators but that are not secure distance and kinematic members										
46	—-	IC 2087-IR	04 39 55.75	25 45 02.0	B5-B8	$\cdots$		46.7		IR and visible nebula; Class I SED; member
96	HD 283815	—-	04 42 41.18	24 41 17.9	A0	$\cdots$	268 ± 40	12.8		Meets proper motion but not distance criteria
89	HD 27659	—-	04 22 54.66	28 23 55.0	A3V	$\cdots$	164 ± 10	< 0.1		Meets distance but not proper motion criteria; cool dust SED
Stars illuminating infrared nebulae but that can not be associated with Taurus based on distance and kinematic criteria										
33	HD 282276	—-	04 33 04.23	29 21 49.9	B8V	$\cdots$	422 ± 52	< 0.1		IR nebula; cool dust SED
48	HD 29647	IRAS 04380+2553	04 41 08.05	25 59 34.0	B9III	177^{+43}_{-29}	160 ± 1	< 0.1		IR nebula; cool dust SED

(1) B# is repeated from Table A.3. (2) SpT is the spectral type as revised in this work or from literature. (3) As noted elsewhere, error on d_{SPEC} corresponds to variance among calculations and underestimates the true error. (4) The probability of proper motion membership, $P(\chi^2)$, is as discussed in Section A.2.3.2. (5) The membership criteria used in this work are: $P(\chi^2) > 1\%$; $128 < d < 162$ pc within 1σ error; and $9.8 \leq RV \leq 17.5$ km s^{-1} wherever radial velocity is available. (6) For the † source V892 Tau, $d_{SPEC} = 1697 \pm 1548$ pc, but $d_B = 4720$ pc while $d_K = 135$ pc.

Appendix B

Study of X-ray emission from the old open cluster, M67

This chapter is submitted for publication as: Mooley, K. P. & Singh, K. P. 2015, MNRAS, accepted.

Abstract

We report on the X-ray analysis of the 4 Gyr-old open cluster, M67, using archival XMM-Newton data. The aim of this study was to find new X-ray members of M67, compile a revised list of X-ray members, and to use the updated member list for comparing the luminosity function of RS CVn-type systems in M67 with that in other star clusters. We have used two archival XMM-Newton observations, and find 21 X-ray members of M67 based on proper motion, including one new member. We also verified the membership of X-ray sources from previous ROSAT and Chandra observations of M67 based on the recent proper motion study by Vereshchagin et al. and compiled a revised list of M67 X-ray members consisting of 42 sources. Sixteen of these are known RS CVn sources or related binaries having orbital periods less than ten days, and near-circular orbits. We have also detected five contact binaries with orbital periods less than six hours, five yellow and blue stragglers, and two Algol-type systems. Fourteen members do not have any orbital information and cannot be definitively classified. Finally, we use the X-ray luminosity functions of RS CVn-type systems in M67 and other intermediate-to-old open clusters to discuss the distribution of such active binary systems in different clusters.

B.1 INTRODUCTION

Open clusters are useful for studying coeval and comoving populations of stars within the Galactic disk. X-ray studies of stars in open clusters offer an insight into their coronal activity and/or accretion phenomena. As clusters age, the spin down of stars causes X-ray emission to diminish in general, and thus, in the X-rays, revealing active coronae primarily from stars spun-up in binary systems (the age-rotation-activity correlation; e.g. Pallavicini 1989; Randich 1997; Gudel et al. 2004) or from systems undergoing accretion . Accordingly, X-rays from old (few Gyr or older) open clusters are unique probes of magnetically active (RS CVn, BY Dra, W UMa, FK Com, Algol) and mass-transfer (CVs, L/HMXBs) binary systems within the Galactic disk (Belloni et al. 1998; Verbunt 1999; van den Berg 2013).

Past studies of old open clusters, NGC 6791 ($\sim$8 Gyr; van den Berg et al. 2013), NGC 188 ($\sim$6 Gyr; Belloni et al. 1998), and M67 (Belloni et al. 1993, 1998; van den Berg et al. 2004), reveal that RS CVns, CVs, and subgiant stars dominate the X-ray emission, while peculiar objects such as blue and yellow stragglers, being rare, contribute to a lower extent.

M67 is a 4.2$\pm$0.6 Gyr-old open cluster at 850$\pm$30 pc having a small reddening value ($E_{B-V} \approx 0.04$) (Sarajedini et al. 1999; Yadav et al. 2008). On account of the extensive optical data available for M67, this cluster is well suited for study in X-rays. Proper-motion studies of M67 to establish cluster membership have been carried out by several groups (Sanders 1977; Girard et al. 1989; Zhao et al. 1993; Yadav et al. 2008; Vereshchagin et al. 2014). In this paper we use cluster membership information from Vereshchagin et al. (2014), a revised version of the Yadav et al. (2008) catalog reaching down to V$\sim$22 mag, containing 659 members. Two published X-rays studies of M67 exist. Belloni et al. (1993, 1998) presented ROSAT-PSPC observations covering $\sim$0.5 deg^2 of the M67 field, while van den Berg et al. (2004) analyzed Chandra-ACIS observations covering $\sim$0.1 deg^2 but with a limiting flux of about 40 times lower than the ROSAT observations.

Here, we present the results of two XMM-Newton observations of M67 having fields of view and limiting flux intermediate between the ROSAT and Chandra observations. The motivation of this study is to find new X-ray members of M67 and compare the X-ray luminosity function of RS CVn-type systems in M67 with that in other star clusters. The paper is organized as follows. In Section 2, we discuss the X-ray data and processing. The optical, ROSAT and Chandra counterparts of our X-ray sources are given in Section 3. The spectral hardness and variability analysis is in Section 4. Section 5 gives notes on individual classes of X-ray sources, and we conclude with a discussion in Section 6.

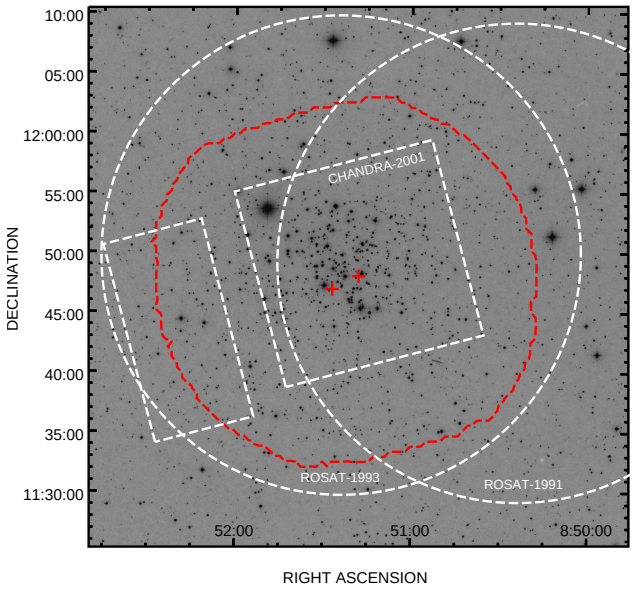

Figure B.1: A $45' \times 45'$image of M67 from the Digital Sky Survey. The footprints of the Chandra ACIS observation (dashed white boxes; van den Berg et al. 2004), ROSAT observations (dashed white circles; Belloni et al. 1993, 1998), and the XMM–Newton observations used in this work (red; aimpoints marked by crosses) are overlayed.

B.2 ARCHIVAL DATA AND DATA PROCESSING

B.2.1 X-ray Data

We used archival data for M67 from the XMM-Newton Science Archive (XSA). Two observations of M67 exist in the archive. Observation with ID 0109461001 was carried out in 2001 and ID 0212080601 in 2005. For both the observations, we used the European Photon Imaging Camera (EPIC, consisting of two MOS and one PN CCD arrays; Jansen 2001; Strüder et al. 2001; Turner et al. 2001). The first observation used the thin filter and data were acquired in the full frame mode, while the second used the thick filter and also acquired data in the full frame mode. The observation details are given in Table B.1. The merged XMM-Newton footprint for the two M67 observations are shown in Figure B.1. The footprints of previously published ROSAT and Chandra observations of M67 are also shown. Although the 3XMM pipeline products (Watson et al. 2014, in prep) are available, we manually reduced and inspected the data to use the latest calibration files and better control over the filtering, reduction and source selection process. We downloaded Observation data files (ODFs) from the XSA for further processing.

B.2.2 Data Processing

We processed the raw archival data with the SAS 13.5.0 and HEASoft 15.1 packages using the procedure outlined in the XMM-ABC and XMM-SAS guidebooks. In brief, we (i) generated the calibration information file using `cifbuild` task and downloaded the relevant calibration files from the XMM calibration archive,

Table B.1: XMM-Newton data on M67

Obs ID	0109461001	0212080601
Coordinates	08:51:26.99 11:46: 58.0	08:51:18.00 11:48:02.6
Start time (UT)	20 Nov 2001 23:56:16	08 May 2005 18:23:17
Stop time (UT)	21 Nov 2001 02:43:07	08 May 2005 22:23:28
Usable time (MOS1,MOS2,PN; ks)	9.42,9.42,6.80	5.70,5.70,5.70
Fiter, EPIC mode	Thin, Full frame	Medium, Full frame

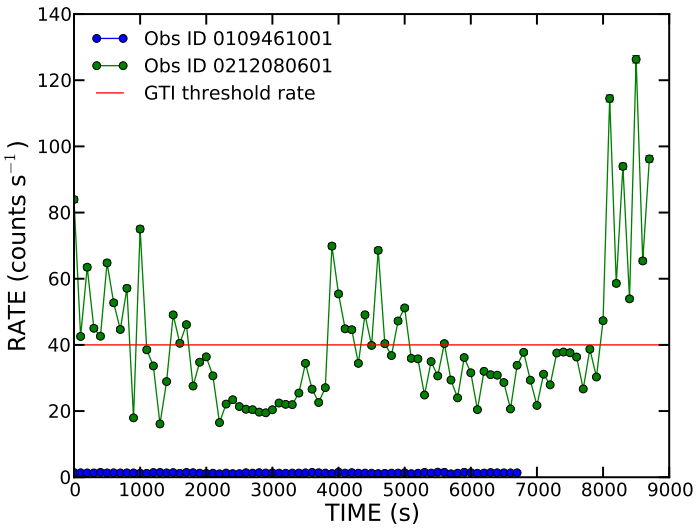

Figure B.2: The >10 keV PN light curves for the two XMM-Newton observations of M67, ID 0109461001 (blue) and ID 0212080601 (green). The latter has enormous soft proton flaring, and the countrate threshold of 40 counts per second used to define the good time interval is shown with the red line.

(ii) ran `odfingest` to compile housekeeping information on the ODFs, (iii) applied the calibration with the `emchain` and `epchain` tasks, (iv) filtered the MOS and PN event lists by selecting only the good events (*XMMEA_EM* and *XMMEA_EP* respectively). We then inspected the PN light curve above 10 keV; no evidence for soft-proton flaring was found for ID 0109461001, but ID 0212080601 was contaminated by significant flaring. To mitigate the flaring background in ID 0212080601, we chose a good time interval (GTI) where the PN countrate >10 keV was more than 40 counts per second. The >10 keV PN light curves for ID 0109461001 and ID 0212080601 along with the GTI countrate threshold for the latter is shown in Figure B.2. Using the GTI removes a large fraction of the major flaring events and reduces the background in the image by a factor of four. Note that the countrate threshold chosen for GTI is much larger than than the standard 0.4 counts per second, but is acceptable for the detection of point sources. ID 0212080601 was thus further filtered using the GTI.

B.2.3 X-ray Images

We produced images in three energy bands, a soft (S_X) band (0.2 – 0.5 keV), a medium (M_X) band (0.5 – 2.0 keV) and a hard (H_X) band (2.0 – 7.0 keV) band, for all three EPIC detectors using the `evselect` and `emosaic` tasks with the filtered MOS and PN event lists from §B.2.2 as input. Total energy band (0.2 – 7.0 keV) images for each detector were also produced. Although XMM-Newton is reasonably sensitive upto 10 keV, we restricted our images to 7 keV in order to enable easy comparison with the Chandra observation of M67 (van den Berg et al. 2004). During the imaging process, only events with (i) the *FLAG* keyword set to zero, (ii) *PATTERN* keyword less than or equal to 4 for PN and (iii) *PATTERN* keyword equal to zero for PN in the soft band were selected. The motivation for the latter is mainly the rejection of noise at the extremities of the PN detector along the detector Y-direction. This stricter requirement for *PATTERN* = 0 for PN in the soft band is also implemented in the 2XMM catalog (Watson et al. 2009), for example. Image binning was so chosen as to produce 600×600 pixel 4.35″pix^{-1} images.

B.2.4 SOURCE DETECTION

We used the `edetect_chain` script to simultaneously search for sources in the nine images (3 bands × 3 detectors) for each observation. The subroutine `edetect_chain` calls a series of tasks sequentially: (i) `expmap` to the calculate the exposure map for the input images using the attitude, vignetting, exposure, bad pixel information, (ii) `emask` produced a detector mask based on the exposure, (iii) `eboxdetect` was used in local mode to search for sources above a maximum likelihood (ML) of 5 simultaneously in all the input images in 5×5 pix boxes (pixels surrounding the boxes are used for background estimation), (iv) `esplinemap` removed the sources detected by `eboxdetect` from the input images to produce smoothed background maps through spline fits to the residual images, (v) `eboxdetect` was used in the map mode to find sources similar to the earlier `eboxdetect` call, except this time the background map was used, (vi) `emldetect` used the source locations from map mode `eboxdetect` to perform simultaneous ML point-spread function fits (Cruddace et al. 1988) to all input images and determine source parameters such as total counts, countrate, hardness ratios, etc. For `emldetect` we specified a ML detection threshold of six (similar to the 2XMM catalog; this corresponds to a 0.2% probability for Poissonian noise fluctuation to have caused the observed source counts). The hardness ratios (discussed in detail in §4.1) were calculated for the detected sources based on their countrate in different bands, and these are especially useful for characterizing weak sources for which spectral analysis was not possible.

For each observation, we combined the single-band and single-detector images into a single mosaic image using the `emosaic` task. We inspected the mosaics by eye and further used the hardness ratios of detected sources as well as the knowledge of their optical counterparts to reject one false positive in ID 0109461001 from the `emldetect` source list. Seventy two sources are detected in ID 0109461001 and 32 in ID 0212080601. Twenty nine sources are common between the two observations and three are unique

detections in ID 0212080601. The conversion of countrates to fluxes is described in §B.4. The minimum 0.2–7 keV flux of detected sources in the two observations is 1.6×10^{-15} and 4.8×10^{-15} erg cm^{-2} s^{-1} respectively. These correspond to X-ray luminosities of 1.4×10^{29} and 4.2×10^{29} erg s^{-1} respectively at the assumed distance of 850 pc to M67. The images in the total energy band were subjected to `esensmap` to find the median countrate corresponding likelihood threshold of six. Converting these to fluxes we get the median flux detection thresholds of 8.9×10^{-15} and 3.0×10^{-14} erg cm^{-2} s^{-1} in the 0.2–7.0 keV energy range for ID 0109461001 and ID 0212080601 respectively. Our final X-ray source catalog is given in Table B.2, which gives source parameters for the PN detector with countrate and total counts in the 0.2 – 7.0 keV band. The 1σ source position uncertainties range between $0.5''$and $4.0''$, the median uncertainty being $1.5''$.

B.3 IDENTIFICATION OF X-RAY SOURCES

In order to identify the X-ray sources found in both XMM-Newton observations of M67 with known classes of astronomical sources, we searched for optical and X-ray counterparts. Information from SIMBAD and infrared data from WISE were used as necessary in order to accurately classify sources (especially in case of AGN or foreground stars). All identifications were checked by eye. Counterparts from Yadav et al. (2008) were used to establish membership probabilities. Below, we describe the search for counterparts along with the identification process, and also give simple estimates of chance identification and expected background X-ray sources.

B.3.1 X-ray Counterparts from ROSAT and Chandra

Apart from XMM-Newton, M67 has been previously observed with ROSAT (Belloni et al. 1993, 1998) and Chandra (van den Berg et al. 2004) with flux detection thresholds of 9×10^{-15} and 2×10^{-16} erg cm^{-2} s^{-1} respectively (see Figure B.1 for coverage). We searched for counterparts of our XMM X-ray sources in these published catalogs. Out of the 61 X-ray sources detected by Belloni et al. (1998) with the ROSAT-PSPC, 44 are in the XMM field of view (fov), among which, 40 have one XMM counterpart within the positional error. van den Berg et al. (2004) detected 158 X-ray sources using the Chandra ACIS-I and ACIS-S detectors, out of which 153 Chandra sources lie within the XMM fov, out of which, 41 have a probable XMM counterpart. The X-ray counterparts are listed in column (8) and (9) of Table B.2.

B.3.2 Optical Counterparts

The most comprehensive and sensitive survey of M67 is the ESO Imaging Survey Pre-FLAMES (EIS; Momany et al. 2001), which contains objects with $11 \leq V \leq 23$. We cross-matched our X-ray source list with the to find the optical counterparts. Error in the optical source positions were taken to be $1''$, and these were added in quadrature with the X-ray source position uncertainties. This procedure gave unique EIS counter-

Table B.2: Summary of EPIC detections in the field of M67. For each source we give the XMM-Newton source ID (NX), coordinates (α_{J2000}, δ_{J2000}), uncertainty in the coordinates ($\delta_{\alpha,\beta}$), PN total counts (counts) and countrate (ctr) in the total energy band (0.2–7 keV), hardness ratios (HR), ROSAT and Chandra counterparts (RX and CX from Belloni et al. and van den Berg et al. respectively), the distance between the EPIC source position and the optical counterpart (d_{XO}), membership in M67 (Y/N: Yes/No, from Yadav et al.; n: no from multiwavelength data) and comments. The superscript ^{a} on the source ID denotes that the corresponding counts, countrate, and hardness ratios are from the MOS1 detector due to the source being in one of the gaps of the PN CCD.

(1) NX	(2) α_{J2000} ($^h\,^m\,^s$)	(3) δ_{J2000} ($^\circ\,'\,''$)	(4) $\delta_{\alpha,\beta}$ ($''$)	(5) counts	(6) ctr (c ks^{-1})	(7) HR HR1	HR2	(8) RX	(9) CX	(10) V (mag)	(11) $B-V$ (mag)	(12) d_{XO} ($''$)	(13) Mem	(14) Identification
Sources Detected in Obs ID 0109461001														
1	08:51:23.22	+11:48:25.9	0.4	291(19)	51(3)	0.63 ± 0.05	-0.84 ± 0.04	11	5	14.32	0.71	1.6	Y	E1740
2	08:51:38.40	+11:49:05.4	0.5	286(18)	53(3)	0.59 ± 0.06	-0.65 ± 0.05		2	20.79	0.15	1.2	n	E510; Gal,z$\sim$0.6
3	08:50:57.09	+11:46:07.6	0.5	208(19)	94(8)	0.39 ± 0.09	-0.50 ± 0.09	15	4	23.27	1.36	0.2	n	SDSSJ0850.95; AGN2,z$\sim$0.5
4	08:51:13.30	+11:51:39.5	0.6	169(14)	37(3)	0.68 ± 0.07	-0.91 ± 0.05	8	1	13.57	1.01	1.6	Y	E1708
5	08:51:23.78	+11:49:49.3	0.5	151(13)	28(2)	0.82 ± 0.06	-0.90 ± 0.05	10	6	11.44	0.90	0.1	Y	Y1289
6^a	08:51:18.64	+11:47:02.5	0.6	125(12)	14(1)	0.70 ± 0.08	-0.74 ± 0.07	13	9	12.67	0.74	1.1	Y	E1726
7	08:51:28.30	+11:41:27.4	0.7	123(12)	26(2)	0.55 ± 0.09	-0.56 ± 0.10		12	22.40	0.12	1.6	N	E2024
8	08:51:07.21	+11:53:02.0	0.6	118(16)	53(7)	0.70 ± 0.11	-0.65 ± 0.13	7	10	12.68	0.69	0.7	Y	E1687
9	08:51:51.35	+11:35:47.5	0.8	72(10)	28(3)	0.39 ± 0.13	-0.64 ± 0.14	59		20.99	0.66	2.0	n	E1907; QSO1
10	08:51:37.79	+11:50:56.6	0.8	68(9)	13(1)	0.58 ± 0.12	-0.90 ± 0.08	40	16	13.64	0.45	1.4	y	E1791; AH Cnc (F7V)
11	08:51:49.93	+11:49:52.0	0.9	67(9)	14(2)	0.39 ± 0.14	-0.68 ± 0.13	43	20	20.98	-0.05	0.9	N	E2757
12	08:50:52.70	+11:47:44.4	1.1	62(9)	19(2)	0.22 ± 0.16	-0.40 ± 0.17	49	21	21.86	0.27	1.4	n	E2183; AGN2
13	08:51:33.02	+11:34:11.9	1.3	62(9)	26(4)	0.74 ± 0.11	-0.77 ± 0.13	60		21.03	0.56	1.7	n	E2593; Gal
14	08:51:04.52	+11:55:28.1	0.8	61(9)	20(3)	0.72 ± 0.13	-0.45 ± 0.14	34	14	21.99	0.81	3.1	n	E2823; Gal
15	08:50:37.97	+11:47:09.3	1.2	54(9)	24(3)	0.72 ± 0.16	-0.18 ± 0.17	12		22.94	2.01	2.3	n	SDSSJ0850.63; AGN2
16	08:51:21.63	+11:52:37.5	0.9	52(8)	11(1)	0.64 ± 0.13	-1.00 ± 0.08	37	24	11.26	0.66	1.9	Y	Y1476
17	08:52:16.79	+11:48:31.0	1.1	50(8)	20(3)	0.69 ± 0.13	-0.83 ± 0.12	47	7	14.44	0.80	1.3	Y	E1857
18	08:51:03.86	+11:46:29.4	1.6	50(11)	20(4)	-0.04 ± 0.29	0.05 ± 0.30	14	13	21.21	0.36	1.0	N	E2153
19^a	08:51:37.27	+11:59:02.5	1.1	49(8)	12(2)	0.51 ± 0.14	-1.00 ± 0.08	31		11.62	0.06	1.3	N	E1787
20	08:51:28.12	+11:49:26.6	0.9	48(8)	8(1)	0.52 ± 0.15	-0.93 ± 0.10	45	19	12.84	0.41	1.4	Y	E1756
21	08:51:04.76	+11:45:56.3	1.1	47(8)	12(2)	0.87 ± 0.10	-1.00 ± 0.06		23	13.58	0.51	1.6	Y	E1569
22	08:51:17.71	+11:44:30.4	1.4	43(7)	8(1)	0.71 ± 0.13	-0.99 ± 0.05	17	15	15.49	0.84	0.8	Y	E1175
23	08:51:46.08	+11:49:49.9	0.9	42(7)	9(1)	0.62 ± 0.16	-0.67 ± 0.16		22	22.12	1.20	1.3	n	E2756; Gal
24	08:51:50.15	+11:46:05.9	1.4	41(7)	8(1)	0.61 ± 0.15	-1.00 ± 0.10	52	47	10.70	0.96	1.3	N	Y892
25	08:52:13.52	+11:46:21.1	1.7	39(8)	13(2)	0.72 ± 0.16	-0.81 ± 0.16	51		21.95	0.50	1.2	N	E2147
26	08:51:46.56	+11:52:01.7	1.2	36(7)	8(1)	0.38 ± 0.20	-0.60 ± 0.18		33	20.74	0.18	1.4	N	E600
27	08:51:07.92	+11:49:54.4	1.2	33(7)	7(1)	0.87 ± 0.13	-0.88 ± 0.13	42	17	15.68	0.86	2.5	Y	E2759
28	08:52:10.42	+11:47:12.7	1.6	33(7)	10(2)	0.41 ± 0.20	-0.55 ± 0.26			22.08	0.10	2.4	n	E2722; Gal
29	08:51:19.59	+11:52:10.5	1.2	32(10)	12(3)	0.66 ± 0.27	-0.89 ± 0.18	38	48	14.00	0.60	2.0	y	E1732; HX Cnc (G1V)
30	08:50:54.97	+11:56:50.3	1.5	28(6)	11(2)	0.47 ± 0.20	-1.00 ± 0.24		58	15.90	1.04	0.7	Y	E763
31	08:52:07.40	+11:52:07.1	1.4	27(6)	8(2)	-0.04 ± 0.24	-0.91 ± 0.23			21.30	0.77	0.6	n	E2952; Fore* ($\sim$M7V)
32	08:51:35.76	+11:47:59.7	1.1	25(6)	4(1)	0.77 ± 0.31	0.16 ± 0.26	48	31	22.38	0.34	1.7	n	E2190; Gal
33	08:51:36.03	+11:46:31.9	1.4	25(6)	4(1)	0.45 ± 0.24	-0.93 ± 0.15	50	49	12.79	0.63	2.0	Y	E1784
34	08:50:58.74	+11:51:36.3	1.4	25(6)	7(1)	0.29 ± 0.27	-0.61 ± 0.28	39	32	20.07	0.23	3.1	N	E1268
35	08:51:30.61	+11:50:45.6	1.7	24(6)	4(1)	0.56 ± 0.23	-0.84 ± 0.20		29					
36	08:51:31.43	+11:45:50.8	1.6	24(11)	10(5)	1.00 ± 0.71	0.14 ± 0.46	53	36	12.74	0.50	2.4	Y	E1581
37	08:51:20.83	+11:53:27.2	1.7	24(9)	13(5)	0.83 ± 0.31	-0.62 ± 0.34	4	3			0.8	N	E3205
38	08:51:52.93	+11:36:54.7	1.5	24(6)	8(2)	0.59 ± 0.22	-0.55 ± 0.26			21.91	0.85	2.0	N	E1929
39	08:52:07.44	+11:41:13.2	1.2	24(6)	8(2)	-0.29 ± 0.28	-0.07 ± 0.40	55		21.52	0.15	1.8	N	E2018
40	08:51:11.60	+11:50:29.5	1.5	23(6)	5(1)	1.00 ± 0.15	-0.37 ± 0.24							
41	08:51:30.47	+11:33:39.8	1.8	23(6)	10(2)	0.41 ± 0.23	-0.89 ± 0.25			22.07	0.00	2.4	n	E1866; AGN1
42	08:51:27.27	+11:46:55.1	1.5	23(6)	3(1)	-0.50 ± 0.33	0.23 ± 0.46	16	57	21.75	0.18	2.3	N	E2164
43	08:51:04.66	+11:42:19.3	2.2	22(6)	6(1)	0.53 ± 0.24	-0.91 ± 0.18							
44	08:51:27.13	+11:45:02.4	1.3	22(7)	5(1)	0.64 ± 0.26	-0.87 ± 0.29			22.83		3.9	n	E3674; Gal
45	08:51:24.69	+11:48:59.8	2.4	22(7)	3(1)	0.56 ± 0.29	-0.67 ± 0.27	46		13.24	0.60	3.9	Y	Y1212
46	08:51:16.99	+11:48:22.8	2.2	20(6)	3(1)	0.72 ± 0.27	-0.99 ± 0.15							
47	08:50:32.58	+11:53:54.3	3.1	20(6)	10(3)	1.00 ± 0.21	-0.42 ± 0.32							
48	08:50:57.55	+11:52:55.2	1.8	19(5)	6(1)	0.83 ± 0.25	-0.05 ± 0.30	36						
49	08:51:09.00	+11:50:44.4	1.6	19(5)	4(1)	-0.44 ± 0.80	0.88 ± 0.20		39	20.62	1.40	1.6	n	SDSSJ0851.14; Gal,z$\sim$0.4
50	08:51:06.38	+11:37:53.5	1.4	19(6)	19(7)	0.74 ± 0.26	-0.37 ± 0.40			20.36	0.27	2.3	N	E111
51	08:51:57.78	+11:45:46.1	1.8	18(5)	4(1)	0.81 ± 0.23	-0.66 ± 0.25			15.59	0.71	1.6	N	E1189
52	08:50:53.19	+11:59:24.6	2.6	17(5)	9(3)	0.35 ± 0.41	0.15 ± 0.38			22.17	0.00	2.6	n	E2436; QSO1,z$\sim$1
53	08:51:26.71	+11:56:10.5	1.8	16(5)	5(1)	1.00 ± 0.27	-0.79 ± 0.24		61	15.90	1.07	2.0	N	E742
54	08:51:27.02	+11:55:23.9	1.5	15(5)	4(1)	1.00 ± 0.29	0.44 ± 0.31	32	8	23.46	2.36	1.2	n	SDSSJ0851.45; AGN2,z$\sim$0.8
55	08:51:44.01	+11:48:49.7	1.8	15(5)	3(1)	0.93 ± 0.17	-0.77 ± 0.29		70	22.79	0.03	0.9	n	E2208; Gal
56	08:51:36.30	+11:44:43.8	2.3	15(5)	3(1)	0.56 ± 0.33	-1.00 ± 0.32		40					
57	08:52:05.18	+11:50:42.9	2.4	14(5)	4(1)	1.00 ± 0.21	0.21 ± 0.36							
58	08:51:38.40	+11:54:13.8	2.2	14(5)	3(1)	0.32 ± 0.34	-0.46 ± 0.41		71,149	21.42	0.57	0.9	N	E2807
59	08:50:56.41	+11:37:31.2	1.4	14(5)	6(2)	0.78 ± 0.42	0.28 ± 0.34			22.31		2.3	n	E3586; QSO2,z$\sim$0.7
60	08:51:47.73	+11:39:54.6	3.3	14(5)	4(1)	-0.01 ± 0.36	-0.81 ± 0.38							
61	08:51:38.72	+11:58:21.3	2.3	13(4)	4(1)	0.08 ± 0.39	-0.51 ± 0.44							
62	08:51:04.43	+11:41:51.6	1.9	12(4)	3(1)	0.58 ± 0.30	-1.00 ± 0.19	54		19.36	1.66	2.5	Y	E1498
63	08:51:01.48	+11:49:26.9	2.1	12(4)	3(1)	0.28 ± 0.36	-0.83 ± 0.34	44	68	14.82	0.72	1.9	N	E520
64	08:51:18.20	+11:50:15.3	2.5	11(4)	2(1)	0.94 ± 0.28	-1.00 ± 0.19	41	104	14.41	0.61	4.8	Y	E1723
65	08:51:42.75	+11:34:08.8	2.5	10(4)	5(2)	0.81 ± 0.26	-1.00 ± 0.18					1.6	n	E3280; AGN2,z$\sim$0.3
66^a	08:52:10.06	+11:55:28.1	1.6	10(5)	8(4)	0.45 ± 0.55	0.03 ± 0.59	33		17.24	1.73	1.1	n	E721; Fore* ($\sim$M7V)
67	08:51:25.87	+11:59:33.2	1.7	9(4)	5(2)	1.00 ± 1.38	0.68 ± 0.31						n	AGN2?
68	08:51:25.06	+11:57:48.4	4.2	9(4)	3(2)	0.50 ± 0.44	-0.80 ± 0.48							
69^a	08:51:26.29	+11:37:06.3	2.6	9(3)	1(0)	1.00 ± 0.51	0.46 ± 0.40							
70^a	08:50:56.52	+11:45:21.9	2.8	7(4)	1(0)	0.54 ± 0.57	-0.34 ± 0.61	24	53	20.27	0.34	1.1	N	E362
71	08:52:06.51	+11:53:24.4	2.9	4(3)	1(1)	1.00 ± 0.29	-1.00 ± 0.45							
72^a	08:52:17.03	+11:41:11.3	2.9	4(3)	1(1)	1.00 ± 0.75	-0.37 ± 0.65	56		16.85	1.81	2.1	N	E207
New Sources Detected in Obs ID 0212080601														
73	08:50:36.96	+11:54:05.8	1.6	31(9)	19(6)	0.66 ± 0.20	-0.48 ± 0.33	35		14.49	0.78	1.2	Y	E1475
74^a	08:51:28.80	+11:48:07.9	1.7	22(7)	4(1)	1.00 ± 0.13	-0.74 ± 0.28		41					
75	08:50:58.56	+11:48:05.0	1.9	17(9)	4(2)	-0.26 ± 0.59	-0.14 ± 0.92			15.81	0.80	2.2	Y	E4630

parts to 50 XMM sources. For sources absent in EIS, we searched for matches in the SDSS and Yadav et al. (2008) catalogs, thus finding 6 additional sources with optical counterparts. In this paper we refer to the EIS and Yadav et al. sources with the prefixes 'E' and 'Y' respectively, e.g. the optical counterparts of NX1 and NX5 are E1740 and Y1289 respectively. The optical counterparts, their V magnitudes, $B-V$ colors and the distance between the X-ray source and the optical counterparts are listed in columns (14), (10), (11), and (12) of Table B.2 respectively. Optical magnitudes and/or colors unavailable in the EIS or Yadav et al. catalogs were estimated from other catalogs on VizieR Catalog Service[1], wherever applicable. For SDSS counterparts, we converted u,g,r magnitudes to V magnitudes and $B-V$ colors using the transformations for stars from Jester (2005)[2]. Fourteen of our X-ray sources do not have an optical counterpart.

B.3.3 Members of M67 and Source Classification

There are several published proper motion membership studies for M67. Sanders (1977); Girard et al. (1989); Zhao et al. (1993) used photographic plates and are limited to stars with V$\lesssim$16. Yadav et al. (2008) calculated the proper motion membership probabilities for $\sim$2400 stars towards M67 having V$\lesssim$22.5. Recently, Vereshchagin et al. (2014) presented a revised list of M67 members among Yadav et al. sources using the convergent point method. We cross-matched our X-ray sources with Yadav et al. catalog and found 38 matches. For these sources, we obtained the membership information from Vereshchagin et al., thus finding 19 members and 19 non-members. Among the sources lacking a Yadav et al. counterpart, we searched for membership information in Girard et al. to get two additional members. Note that for sources present in both, Yadav et al. and Girard et al., we give precedence to the former. Lastly, for sources listed as non-members in Vereshchagin et al. (2014) that have $>80\%$ probability in both, Yadav et al. and Girard et al. catalogs, we used the binarity and photometric information of the optical counterparts to argue membership, wherever applicable.

We classified the remaining 35 sources as AGN, quasar, galaxy, or foreground/background stars based on multiwavelength spectral energy distributions using photometry from the SDSS, WISE, 2MASS and NOMAD catalogs. The membership information for sources having an optical counterpart is given in column (13) of Table B.2.

Since the membership of X-ray sources found by Belloni et al. (1998) and van den Berg et al. (2004) was based primarily on the work by Girard et al. (1989), we considered cross-matching their X-ray catalogs with Yadav et al. (2008), and looking at the membership of the corresponding source as given by Vereshchagin et al. (2014). Among the X-ray sources from Belloni et al. stated as non-members or sources without membership probability, we accept four (RX47=NX17=CX7; RX17=NX22=CX15; RX42=CX17; RX35=NX73) as members, and among their proposed members, we reject four (RX43=NX11=CX20; RX44=NX63=CX68 is a galaxy; RX49=NX12=CX21 is a type-2 AGN; RX19). Note that CX20 (quasar) and CX68 were already

[1] http://vizier.u-strasbg.fr/

[2] http://www.sdss.org/dr4/algorithms/sdssUBVRITransform.html

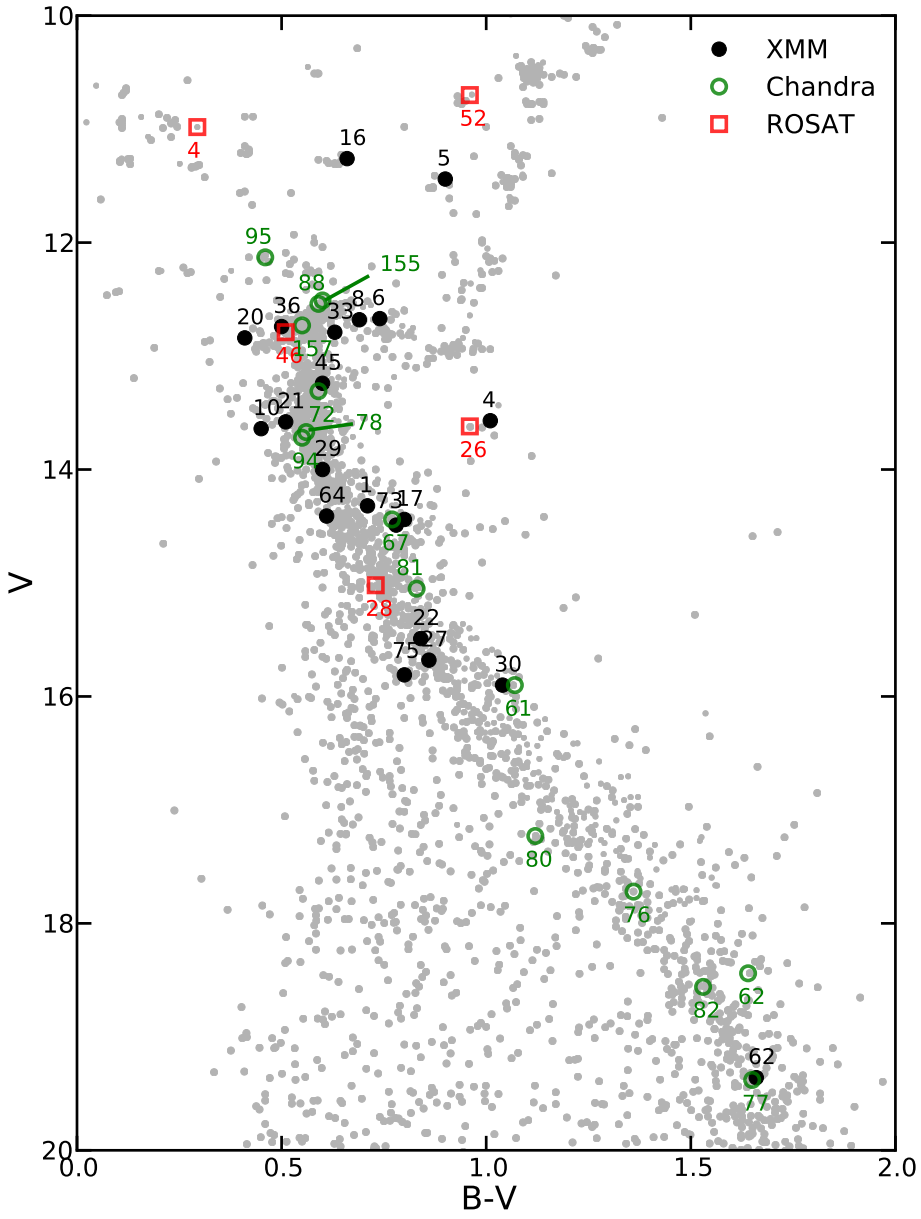

Figure B.3: $V/B-V$ color-magnitude diagram of X-ray members in M67 known till date, and listed in Table B.3. Members from this work, from Belloni et al. (1998) and those from van den Berg et al. (2004) are plotted as black filled filled circles, red squares and green open circles respectively. Numbers specified in these respective colors are the IDs of sources in the respective catalogs (NX, RX and CX). Sources from WEBDA, from Yadav et al. (2008) with membership probability greater than 80%, and all EIS sources are plotted in grey. Note that the $B-V$ colors for main sequence stars of spectral types A0, F0, G0, K0, M0, and M8 are 0.0, 0.3, 0.6, 0.8, 1.4, and 2.0 respectively (Johnson 1966).

Table B.3: Summary of X-ray members of M67. The *top panel* shown members among the sources that were detected in XMM-Newton observations (this work) and classified as members in Vereshchagin et al. (2014), The *middle panel* shows members detected in Chandra van den Berg et al. (2004), while the *lower panel* lists members from ROSAT Belloni et al. (1998). The source IDs from this work, from Belloni et al. and van den Berg et al. are given in columns 1–3, the optical counterpart and its spectral type are listed in columns 4–5, X-ray luminosity in column 6, the orbital period and ellipticity in columns 7–8, and source classification is in column 9. See §B.3.3 for details.

(1) NX	(2) RX	(3) CX	(4) opt	(5) SpT	(6) $L_X/10^{30}$ (erg s^{-1})	(7) P_{orb} (d)	(8) e	(9) comments
Members from This Work								
1	11	5	E1740	G0V	$6.68^{1.05}_{-1.02}$	1.36	0	RS CVn
4	8	1	HU Cnc	G8IV	$5.58^{1.30}_{-1.05}$	18.40	0.21	SGB,RS CVn
5	10	6	Y1289	G4III	$3.93^{1.33}_{-2.09}$	42.83	0	III+WD,YS
6	13	9	HW Cnc	G4V	$6.67^{1.50}_{-1.39}$	10.06	0	RS CVn
8	7	10	HT Cnc	F9V	$6.67^{1.78}_{-1.73}$	1.36	0.10	RS CVn
10	40	16	AH Cnc	F7V	1.78 ± 0.14	0.36		Ecl W UMa
16	37	24	Y1476	G3III-IV	1.51 ± 0.14	1495	0.32	SB,YS
17	47	7	LN Cnc		2.74 ± 0.41	0.54		Ecl W UMa
20	45	19	EV Cnc	F3	1.10 ± 0.14	0.44		W UMa
21		23	HS Cnc	F9V	1.65 ± 0.27	0.36		W UMa
22	17	15	E1175	G9V	1.10 ± 0.14	1.17	0	RS CVn
27	42	17	E2759	G6V	0.96 ± 0.14			RS CVn?
29	38	48	HX Cnc	G1V	1.65 ± 0.41	2.66	0	RS CVn
30		58	HR Cnc		1.51 ± 0.27	3.58		RS CVn
33	50	49	E1784	G1V	0.55 ± 0.14	31.78	0.66	SB
36	53	36	E1581	F9V	1.37 ± 0.69	4.36	0.0	RS CVn,triple
45	46		Y1212	G0V	0.41 ± 0.14			
62	54		E1498		0.41 ± 0.14			
64	41	104	E1723	F9V	0.27 ± 0.14	var		RS CVn?
73	35		E1475	G8V	3.06 ± 0.97			CV?
75			E4630	$\sim$K5V	0.65 ± 0.32			
Members from Belloni et al. (1998)								
37	4	3	ES Cnc	F5IV	1.78 ± 0.69	1.07		Algol
	26		AG Cnc		6.1	2.82	0	RS CVn
	28		HY Cnc	G6V	2.1	2.65		RS CVn
	46	111	E1589	F7IV	0.08	7.16	0	RS CVn
24	52	47	Y892	G8III-IV	1.10 ± 0.14	698	0.11	RGB,YS
Members from van den Berg et al. (2004)								
53		61	ET Cnc	$\sim$G4V	0.69 ± 0.14	0.27		WU
		62	E683		0.40			
		67	E1781	G4V	0.36			binary
		72	E1677	G0V	0.16	5.7		RS CVn
		73	E2650	$\sim$M3V	0.46			
		76	E1720	$\sim$K7V	0.21			binary
		77	E394		0.23			binary
		78	E1730	F9V	0.30	5.95	0	RS CVn
		80	E2650	$\sim$M3V	0.20			
		81	E429	G5V	0.12	6.7		RS CVn
		82	E1208		0.16			
		88	E1729		0.09	7.65	0	RS CVn
		94	E1777	F8V	0.16			binary
		95	E1590	F6V	0.12	4913	0.34	BS
		155	E2983	F7V	0.04	11.02	0.26	SB,RS CVn
		157	HV Cnc	$\sim$F0V+M1V	0.02	10.34	0	Ecl Algol,triple

Notes: (a) The countrates and hence the luminosity values from Belloni et al. (1998) and van den Berg et al. (2004) do not have associated uncertainties. (b) Some of the known binaries but do not have an orbital / period solution.

classified as non-members by van den Berg et al. (2004). One source having unknown membership probability (RX54=NX62) in Belloni et al., has been classified as a member based on new proper motion information. Similarly, RX16=NX42=CX57 and RX23 are found to be non-members of M67.

Among the Chandra X-ray sources (van den Berg et al. 2004) classified as probable non-members, we accept three (CX7=NX17=RX47 listed as a W UMa-type binary in SIMBAD; CX15=NX22=RX17 is a known binary with circularized 1.2-day orbit; and the unclassified source CX17=NX27=RX42) as proper motion.members. Twelve sources close to the M67 main sequence were accepted as probable members by van den Berg et al.. Among these, we accept eight sources as true members of M67. These are: (1) CX58=NX30 is listed as RS CVn in SIMBAD, and a known binary with a 3.6-day period, (2) CX61=NX53 with 75% proper motion membership probability in Yadav et al. (2008), and listed as a non-member in Vereshchagin et al. (2014), is a W UMa-type binary with period 0.27 days, has a photometric parallax distance of $\sim$820 pc, and lies along the M67 main sequence, (3–5) CX62, CX77, and CX82 are members in Yadav et al. and Vereshchagin et al. with a high probability, (6–7) CX73, an M3V star, and CX76, a K7V star have estimated distances of $\sim$950 pc based on SDSS and WISE photometry. CX73 has a counterpart in Yadav et al., where it has a proper motion membership probability of 48%, but it is listed as a non-member in Vereshchagin et al. (2014). However, the hardness ratios of this source in the Chandra source catalog (Evans et al. 2010) are consistent with that of an active star. CX76 has no counterpart in Yadav et al., (8) CX80 is a member of M67 in Yadav et al. and Vereshchagin et al.. Compared to the typical uncertainty in the Chandra X-ray source positions, the optical counterparts of CX73 and CX80 are quite far away ($\sim 4''$). This could be attributed to the large off-axis distance of the location where these sources were detected on the ACIS CCD. We reject the membership of the remaining four sources (CX117, CX129, CX141, and CX153) due to their very small membership probabilities in Yadav et al., and their classification as non-members in Vereshchagin et al..

A compilation of the spectral and orbital parameters and X-ray luminosities for all the 42 members of M67 detected as X-ray sources till date is given in Table B.3. Here, we list the optical counterparts, the spectral types (from SIMBAD, VizieR, van den Berg et al. 2000, or estimated from archival multiwavelength photometry), X-ray luminosity from our work or van den Berg et al. (2004) or Belloni et al. (1998) (in that order of preference), the orbital periods and ellipticities (from van den Berg et al. (2000, 2004) or VizieR), and the source types (from van den Berg et al. (2004) or SIMBAD). Note that the luminosities for sources detected in the XMM-Newton observations are quoted for the 0.2–7 keV energy band, and those from van den Berg et al. are for the 0.3–7 keV energy band, while luminosities of Belloni et al. sources were calculated using the ROSAT PSPC countrate converted to flux in the 0.2–7 energy keV band assuming an APEC 1.5 keV plasma model. The orbital periods and eccentricities have been reproduced from van den Berg et al. (2000, 2004). For all known X-ray members of M67, we plot the $V/B-V$ color-magnitude diagram in Figure B.3.

B.3.4 Chance Identification

We estimated the probability of identifying an XMM–Newton source with an optical counterpart by chance using a procedure similar to the one adopted by van den Berg et al. (2004). This chance identification probability is a function of the positional uncertainty of the X-ray sources (Δ) and the surface density of optical sources in the M67 field. We calculated the mean positional uncertainty of the XMM–Newton sources, $\Delta = 1.6''$, and the number of EIS sources inside the fov, N$\simeq$3035. We used a circle with radius equal to the quadratic sum of Δ and the error in the optical positions, $1''$, to calculate the search area around an X-ray source. Therefore, the probability that a randomly placed error circle includes an EIS-source is $N\pi(\Delta^2+1''^2)/A = 1.1\times10^{-2}$. Here, the area of the fov (red curve in Figure B.1) is denoted as A approximated by a circle with radius $16'$. Thus, for the 75 X-ray sources that we have considered here (Table B.2), the probability of 0, 1 or 2 chance identifications with EIS-sources is 42%, 37% and, 16% respectively. Similarly, we calculated the probability for the chance identification of our X-ray sources with M67 proper motion members to be 87%, 12%, and 1% respectively. We therefore conclude that one or two XMM–Newton sources have been falsely identified with optical counterparts while our M67 X-ray members are all likely to be genuine. Another simple and orthogonal way of finding the chance identification probability is to note that among the 50 sources in van den Berg et al. (2004) having X-ray fluxes greater than the flux threshold of the XMM observations ($\sim6\times10^{-15}$ erg cm^{-2} s^{-1}, corresponding to a Chandra countrate of 1 count per ks), about 40 have an optical counterpart. We can then ask the question: *given the probability of finding an optical source counterpart for an X-ray source as 0.8, what is the probability of finding counterparts to 62 XMM sources out of 75?* Considering binomial distribution for the fraction of optical counterparts among X-ray sources, we get the answer as 10%. The most-likely value is 60 counterparts with a probability of 11.5%.

We also estimated the probability for chance identification of XMM–Newton sources with ROSAT and Chandra sources. There are 47 ROSAT sources in the XMM–Newton fov, having their average 90% error radius as $12.25''$, so the chance identification of 0, 1, and 2 counterparts is 56%, 33%, and 9% respectively. For Chandra sources we calculated the average error in RA and Dec separately, combined them with the corresponding average 1σ positional error for XMM–Newton sources, and then used twice the resultant errors in RA and Dec as the sides of the error box. Thus, considering the 154 Chandra sources in XMM–Newton fov we obtain the probability for 0, 1, and 2 chance identification as 97%, 3%, and 0% respectively. Accordingly, the probability of identifying XMM X-ray members with ROSAT and Chandra sources by chance is $<$1%.

B.3.5 Background sources

We used the soft AGN number counts from Gilli et al. (2007) to estimate the expected background sources in the XMM-Newton observations. Approximating the flux limit of the XMM observations by 5×10^{-15} erg cm^{-2} s^{-1}, we find from Figure 9 of Gilli et al. (2007) that there are $\sim$230 AGN per deg^2 in the 0.5–2 keV band. Then, among the 75 unique sources in the XMM fov (approximately a $16''$radius circle), we expect

$\sim$50 extragalactic sources (AGN). Among the 75 unique sources in our X-ray source list given in Table B.2, 24 are probable M67 members (Table B.3), two are foreground stars. Four other non-members have V band magnitudes less than 17, and are probably foreground stars. The remaining 45 sources have V$>$20 or have no optical counterpart down to $\sim$22nd magnitude. These are all very likely to be AGN. In fact, we have confirmed that 18 of these are either galaxies (AGN status unknown) or AGN (see column 14 of Table B.2.

B.4 SPECTRAL AND TIMING ANALYSIS

B.4.1 Spectral Fitting and Luminosities

We extracted PN background and source spectra for the eight sources (NX1–8) in our source list (Table B.2) having total counts greater than 100. The spectrum for one of the sources (NX6) had to be extracted from the MOS1 detector since it is located in the PN CCD gap. To find the appropriate regions for the extraction of background and source spectra, we used DS9. Extraction of the source spectrum was usually done within a circle having 30$''$radius and centered on the X-ray source. Background spectra were extracted within annuli with inner radii between 35$''$–45$''$and widths between 60$''$–75$''$centered on the X-ray sources, the values chosen so as to avoid contamination from sources in the vicinity. For those X-ray sources where the annulus would spill over to the neighboring CCD, the region of choice for background spectral extraction was a circle close to and having a similar RAWY as for the source extraction region, and with radius between 40$''$–50$''$. Once the extraction regions were defined, we used the *SAS* task `especget` to perform the extraction of source and background spectra for NX1–8. For each extracted spectrum, we grouped the spectral (PHA) channels using the `specgroup` task such that each grouped PHA channel had 16 counts, sufficient for the assumption of Gaussian distribution of uncertainties. This task also performs the subtraction of background spectrum from the source spectrum.

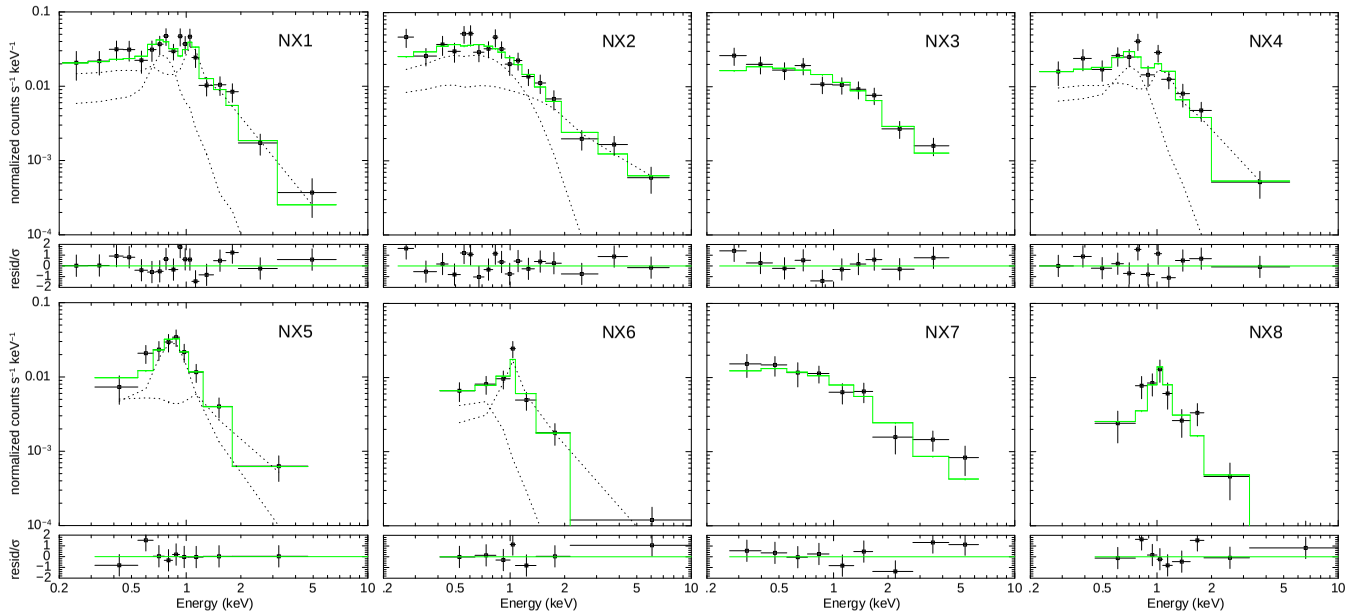

Figure B.4: Spectral fitting for sources having PN countrate greater than 100 (NX1–8). For each source, the top panel shows the binned background-subtracted normalized countrate (black points with error bars), the best-fit single-/multi-component spectrum (green), and the individual spectral components (dashed black curves), while the bottom panel shows the residual-to-noise ratio. For best-fit parameters, see Table B.4

Table B.4: The best-fit parameters and goodness-of-fit for the spectral fitting performed on sources NX1–8. The hydrogen column was held fixed and was calculated as described in §B.4.1. The columns are: (1) source ID; (2) single-multi-component model used for fitting along with photoelectric absorption; (3), (4) temperatures of the two APEC components used to fit spectra of member stars of M67, (5) ratio of the emission measures of the two APEC components; (6), (7) power-law index and blackbody temperature used for fitting non-members; (8) hydrogen column supplied to the photoelectric absorption model; (10) energy conversion factor (ECF=Rate/Flux; see §B.4.1); and (11) the reduced χ^2 of the fit and the degrees of freedom (dof; equal to the number of channel groups minus one). The corresponding fits are shown in Figure B.4. Note that NX6 fitting was done on MOS1.

(1) NX	(2) model	(3) kT_1 (keV)	(4) kT_2 (keV)	(5) EM1/EM2	(6) Γ	(7) kT (keV)	(8) N_H (10^{20} cm^{-2})	(9) F/10^{-14} (erg cm^{-2} s^{-1})	(10) ECF/10^{11} (cts cm^2 erg^{-1})	(11) χ^2_ν(dof)
1	2T	$0.39^{+0.66}_{-0.10}$	$1.95^{+0.90}_{-0.48}$	0.17 ± 0.10			2.2	$7.73^{+1.22}_{-1.18}$	6.6	0.82(14)
2	P+B				$1.36^{+0.62}_{-0.77}$	$0.19^{+0.04}_{-0.04}$	3.3	$10.83^{+1.70}_{-2.85}$	4.9	0.81(14)
3	P				$1.66^{+0.26}_{-0.25}$		3.2	$19.95^{+4.89}_{-3.67}$	4.7	0.69(8)
4	2T	$0.32^{+0.20}_{-0.08}$	$2.05^{+1.50}_{-0.51}$	0.24 ± 0.14			2.2	$6.45^{+1.50}_{-1.22}$	5.7	0.95(8)
5	2T	$0.76^{+0.16}_{-0.18}$	$3.30^{+0}_{-1.86}$	0.46 ± 0.29			2.2	$4.55^{+1.54}_{-2.42}$	6.2	0.63(5)
6	2T	$0.24^{+0.24}_{-0.12}$	$1.38^{+0.42}_{-0.15}$	0.43 ± 0.30			2.2	$7.71^{+1.73}_{-1.61}$	1.8	1.08(3)
7	P				$1.71^{+0.38}_{-0.35}$		3.3	$6.39^{+2.02}_{-1.41}$	4.1	0.91(7)
8	T		$1.51^{+0.55}_{-0.34}$				2.2	$7.71^{+2.06}_{-2.00}$	6.9	0.94(7)

The spectral fitting was done using the *XSPEC* package. We ignored spectral groups containing channels with energies less than 0.2 keV and those greater than 12 keV. Fitting for the M67 X-ray members was done using a photo-electric absorbed (`phabs`) emission spectrum of collisionally-ionized plasma (`apec` with one or two characteristic plasma temperatures and default element abundances) where N_H was fixed at 2.2×10^{20} cm^{-2} (converted from E_{B-V}=0.04 using R_V=3.1). For others, a photo-electrically absorbed power law with or without a blackbody component, as expected for AGN, was used for spectral fitting. In this case, the hydrogen column density was estimated using the `nh` task. For NX1–8, the fitted model, the best-fit parameters, their 90% uncertainties given by *XSPEC*, and the fixed hydrogen column used are shown in columns 2–8 in Table B.4, and the resulting reduced χ^2 and degrees of freedom (dof) are in column 11. Figure B.4 shows the spectra for the eight sources considered for fitting, of which five are members of M67.

Using the best-fit models, we calculated the fluxes of NX1–8 in the 0.2–7 keV band with the `flux` task in *XSPEC*. The resulting fluxes along with their 90% uncertainties are given in column 9 of Table B.4. The energy conversion factors (ECF=Rate/Flux) are tabulated in column 10. For members of M67 among sources in Table B.4, we find that the mean ECF is $6.3\pm0.4\times10^{11}$ counts cm^2 erg^{-1} (uncertainty in the countrate not folded in). We used this factor to calculate the X-ray fluxes in the 0.2–7 keV band for all the M67 members detected in the XMM observations. Similarly we determined the ECFs for the 0.3–7 keV and 0.1–2.4 keV bands. The former band is used by van den Berg et al. (2004) for Chandra observations of M67 while the latter is relevant for ROSAT. For coronal sources, we used the ECFs to calculate the multiplicative factors for converting from the Chandra and ROSAT bands to the 0.2–7 keV band as 1.0 ± 0.1 and 0.8 ± 0.1 respectively. X-ray luminosities were calculated assuming a mean distance of 850 pc to M67. The X-ray luminosities for all M67 members in the 0.2–7 keV band detected by XMM are given in Table B.3. For Obs ID 0212080601, we fitted the spectra for four bright members of M67 (NX4–6,NX8) using the parameters listed in Table B.4

as initial values, and calculated the ECFs. The mean ECF was found to be 6.2×10^{11} counts cm^2 erg^{-1}. We used this ECF to convert the countrates of NX73–75 to their corresponding fluxes.

B.4.2 Hardness Ratios

Spectral information for weak X-ray sources can be obtained by comparing the countrates in coarse spectral bins after applying the correction for exposure, vignetting, and background. Taking advantage of the wide bandpass of XMM-Newton, we defined two hardness ratios, $HR1$ and $HR2$, as given in equation B.1.

$$HR1 = \frac{(M_X - S_X)}{(M_X + S_X)}\,, \qquad HR2 = \frac{(H_X - M_X)}{(H_X + M_X)} \tag{B.1}$$

where S_X, M_X and H_X denote the exposure-corrected counts in the soft band (0.2 – 0.5 keV), the medium band (0.5 – 2.0 keV) and the hard band (2.0 – 7.0 keV), respectively. For each X-ray source detected, HR1 and HR2 are calculated within the best-fit source position, using the best-fit countrates in all the bands by the source-finding algorithm `emldetect`. They are tabulated in column 7 of Table B.2 for the PN detector (unless noted as MOS1). Sources with very soft spectra will have HR1$<$0 and those with hard spectra will have HR2$>$0. In Figure B.5 we plot HR2 against HR1 for all of our 75 unique sources. All members of M67 lie in the region HR1$\gtrsim$0.5, HR2$\lesssim$0.5. AGN and other non-members also tend to lie in this region, but their scatter is much larger. Hardness ratios expected from power-law (P), blackbody (BB) and collisionally-ionized plasma (APEC) are also shown. These were calculated using WebPIMMS using Galactic hydrogen column density of 2.2×10^{20} cm^{-2}. Note that the uncertainties of the source hardness ratios depend on the countrate and for our XMM sources they have a large scatter. Only the weighted mean uncertainties are shown as guidance in Figure B.5 for each class of object.

B.4.3 X-ray Variability

Using the source and background regions defined for the extraction of spectra for NX1–8 (see §B.4.1), we extracted light curves from the filtered PN (MOS1 for NX6) event list in the 0.2–10 keV band with tasks `evselect` and `epiclccorr`. The time bin size was set to 300 s (NX1) or 450 s (NX2–8) to get adequate signal-to-noise ratio in each bin. For PN we selected only those events with *PATTERN* keyword less than or equal to 4. The light curves for NX1–8 are shown in Figure B.6. The background-subtracted light curves are in blue and the background-only light curves are in grey.

We used the χ^2 test to check for the departure from white noise in the light curves, and selected sources having χ^2 probability $<$25% as significant variables. Sources NX1 to NX5 are thus found to be variable, while the variability in NX6–8 is not significant. Members of M67 showing significant variability are NX1, NX4 and NX5, which also exhibit short-term autocorrelation. For the RS CVn binary, NX1, the autocorrelation function shows significant correlated structure for lag time k$\leqslant$2 implying variability timescale of $\sim$10 min.

We also compared the X-ray luminosities of M67 members detected in the XMM-Newton observation ID

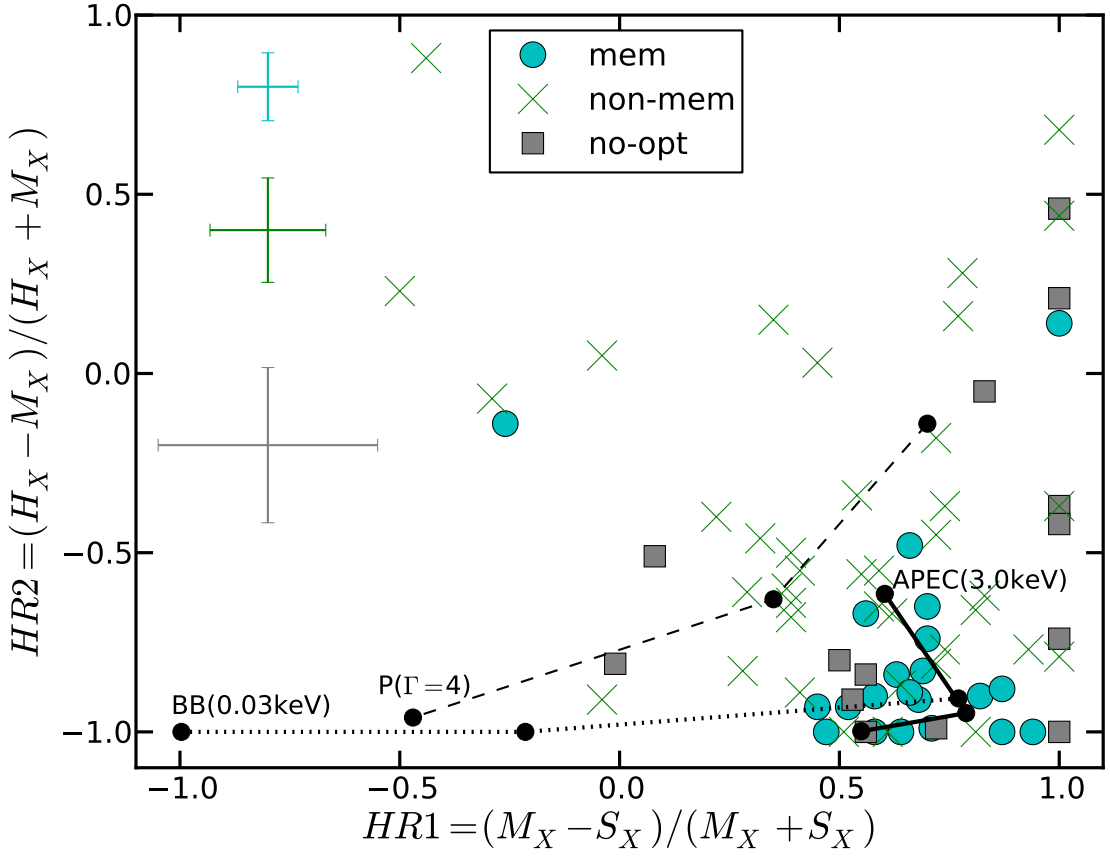

Figure B.5: Hardness ratios (see §B.4.2) of the 75 unique sources detected in the XMM observations. Sources identified as M67 members, non-members, and sources with no optical counterparts (also suggested as non-members in §B.3.3) are shown as cyan circles, green crosses, and grey squares respectively. The weighted mean error bars are shown to the left hand side of the plot, representative of sources in each of the three classes. Note that these error bars are just for guiding the eye, and the actual uncertainties (see Table B.2) depend on countrate. Note that the members NX 36 and NX 75 have large uncertainties in their hardness ratios ($\sim$0.6), and appear to be outliers with respect to the clustering of M67 members in the lower right hand corner of the plot. The expected hardness ratios for three kinds of spectra, power-law (P(Γ)), blackbody (BB), and collisionally-ionized plasma (APEC), are shown as black circles joined by black lines (dashed, dotted and solid lines respectively). Each black dot marks a unique value of temperature (in case of BB or APEC) or a power law index. the hardness ratios have been calculated for Γ=1, 2, and 4 in the case of power law; T=0.03, 0.1, and 0.3 keV for BB; and T=0.3, 1, and 3 keV for APEC. For each type of spectrum, one point has been labeled. These were calculated using WebPIMMS using Galactic hydrogen column density of 2.2×10^{20} cm^{-2}.

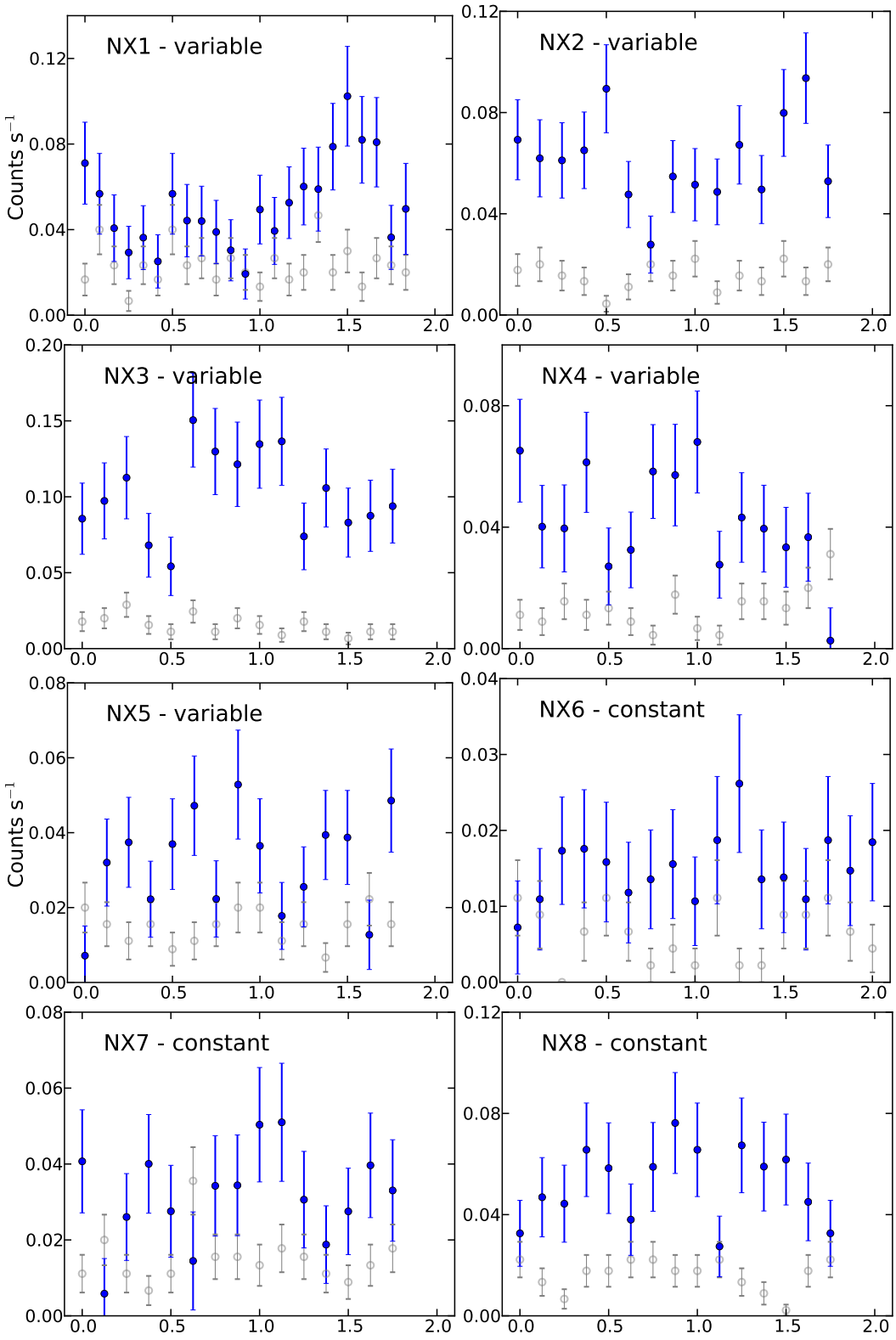

Figure B.6: The light curves for sources having 100 or more counts in PN (MOS1 for NX6). The background-subtracted light curves are in blue and the background-only light curves are in grey. Count-rate (counts per second) is on y-axis and time in hours is along the x-axis. The time bin size is set to 300 s for NX1 and 450 s for the rest in order to get >30 counts in each bin. Whether a source is variable or not according to the χ^2 test is denoted on the upper left side. See §B.4.3 for details.

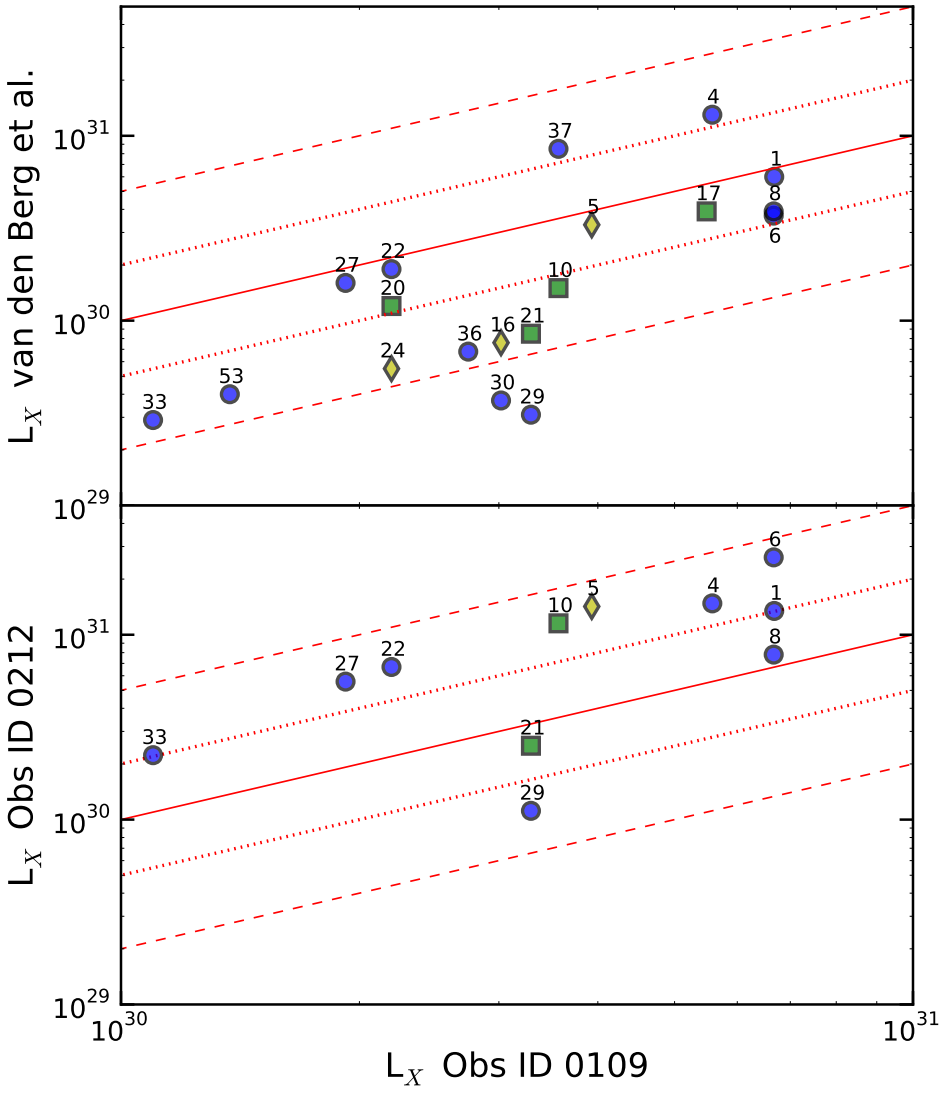

Figure B.7: Variability of X-ray members of M67 on 5-month (top) and 4-year (bottom) timescale shown using plots of the X-ray luminosities of sources in Obs ID 0109461001 versus X-ray luminosities in van den Berg et al. (2004) (top) and those in Obs ID 0212080601 (bottom) respectively. The solid red line marks equal luminosities in either quantity plotted, and the red dotted (dashed) lines denote variability of a factor of 2 (5). See §B.4.3 for details. Note that the implied X-ray luminosities in the 0.2–7.0 energy band are used.

0109461001 with those in the Chandra observation from van den Berg et al. (2004) separated by five months, and between ID 0109461001 and ID 0212080601 to find the variability over two observations spaced by $\sim$4 years. The comparison plots are shown in Figure B.7.

The RS CVn-type systems, NX1, NX6, NX22, and XN27, have relatively stable X-ray emission between ID 0109461001 and van den Berg et al., but are variable by more than a factor of two between ID 0109461001 and ID 0212080601, while NX8 appears stable between all three observations. NX4, NX16, NX33, NX36, NX37, and NX53 are variable by more than a factor of two between any of the two observations. NX29 and NX30 are variable by more than a factor of five over the observations spaced by five months. The W UMa-type system, NX21, varied by a factor of four between ID 0109461001 and Chandra observations. NX10 is variable by more than a factor of two over the observations separated by months as well as years. Figure B.7 suggests that 50% of the RS CVn-type and W UMa-type systems are variable on months timescale while a significantly larger fraction are variable on years timescale.

B.5 NOTES ON INDIVIDUAL CLASSES OF X-RAY SOURCES IN M67

Here we discuss about the X-ray members of M67 (Table B.3) with respect to the class of the X-ray source. We have reproduced the orbital parameters for X-ray members from van den Berg et al. (2004), who have in turn compiled them from Mathieu (1990), Latham et al. (1992), van den Berg et al. (2000), and from unpublished work by D. Latham, R. Mathieu et al.

B.5.1 RS CVn / similar binaries

In an initially-wide binary of main-sequence stars, tidal interaction takes place when one of the stars evolves into a subgiant, following which, co-rotation and circularization of the orbit takes place (e.g. Verbunt 1999). When the resulting rapid rotation of the companion star leads to enhanced chromospheric activity and X-ray emission, the binary is known as an RS CVn-type system. In such binaries, both stars are usually of late-type and magnetically active. However, for a close initial binary, tidal interaction can take place even while the stars are on the main sequence, which may lead to active chromosphere(s) and X-rays. We call such systems as being similar to RS CVn systems, but where both the stars in the binary are on the main sequence.

All the RS CVn candidates or similar tidally locked systems that we find in the XMM observations have been detected previously in X-rays. We detect three RS CVn binaries (NX6,NX8,NX36) that lie along the subgiant branch. These have orbital periods $P_{\rm orb} \lesssim 10$ d and ellipticities $e \lesssim 0.1$. Seven X-ray sources (NX1,22,29;RX26,46;CX78,88) have similar orbital parameters, and they have been proposed as RS CVn systems by van den Berg et al. (2004) and Belloni et al. (1998) based on the presence of Ca H & K emission lines, X-ray spectrum, orbital period and circularization. However, these systems lie along the M67 main

sequence in the color-magnitude diagram shown in Figure B.3, and are likely not true RS CVn systems, but rather similar to these systems where both members of the binary system are main-sequence stars spun up through tidal interaction resulting in enhanced chromospheric activity. Three other sources (NX27,64;RX28) are candidate RS CVns or their main-sequence analogs, but their complete orbital solution is not available. We note that sources with $P_{\rm orb} \lesssim 10$ d are expected to have near-circularized orbits (e.g. Latham 2007).

B.5.1.1 Luminosity functions of RS CVn-type systems

Luminosity functions allow us to the study of the formation, evolution, and distribution of source populations. One of the most widely-occurring X-ray emitters in old clusters are RS CVn-type systems, which typically have X-ray luminosities 10^3–10^4 times larger than that of the Sun. In Figure B.8 we plot the X-ray luminosity functions (XLFs) of RS CVn-type systems in M67 in comparison with other intermediate-to-old open star clusters. The figure shows coronally-emitting X-ray members in M67 (4 Gyr; Table B.3), NGC 6633, IC 4756 (0.7 Gyr; Briggs et al. 2000), NGC 6791 (8 Gyr; van den Berg et al. 2013), and NGC 188 (7 Gyr; Belloni et al. 1998; Gondoin 2005). The XLF of field RS CVn binaries from Singh et al. (1996) is shown for guidance. The clusters, in general have different median values for the X-ray luminosity. In fact, the XLFs reveal an increased number of higher luminosity stars in the older clusters. This is suggestive of the intuitive notion that, as the clusters age, more active binary systems and active stars are produced (see also Verbunt 1999; van den Berg 2013). The XLFs of M67 and the Singh et al. sample have a much shallower slope than those of the other clusters, possibly indicating two distinct distributions of RS CVn-type systems in open clusters.

B.5.2 Algol Systems

When the subgiant star in an RS CVn system evolves into a giant, mass transfer starts. Such a binary is known as an Algol-type system. We have at least one previously known Algol system (NX37=RX4=CX3) in our XMM data. This object has an orbital period of 1.1 d. Another candidate Algol is CX157, which is an eclipsing system. However, CX157 contains an F0-type and an early M-type main sequence star (Gökay et al. 2013), so the presence of a gaint star is unlikely

B.5.3 Contact Binaries

In some cases, a close eccentric binary can lose a large fraction of its initial angular momentum before achieving co-rotation. The two stars may come into contact while continuing to rotate very rapidly. These stars are called W UMa-type binaries. The X-rays of contact binaries are believed to result from coronal activity around the rapidly rotating stars in the binary (e.g. Verbunt 1999).

We have detected five contact binaries (NX10,17,20,21,53) previously known in literature, all of which are W UMa-type. All these W UMa systems have $P_{\rm orb} \lesssim 0.5$ d; NX10 and NX17 are eclipsing binaries. Although

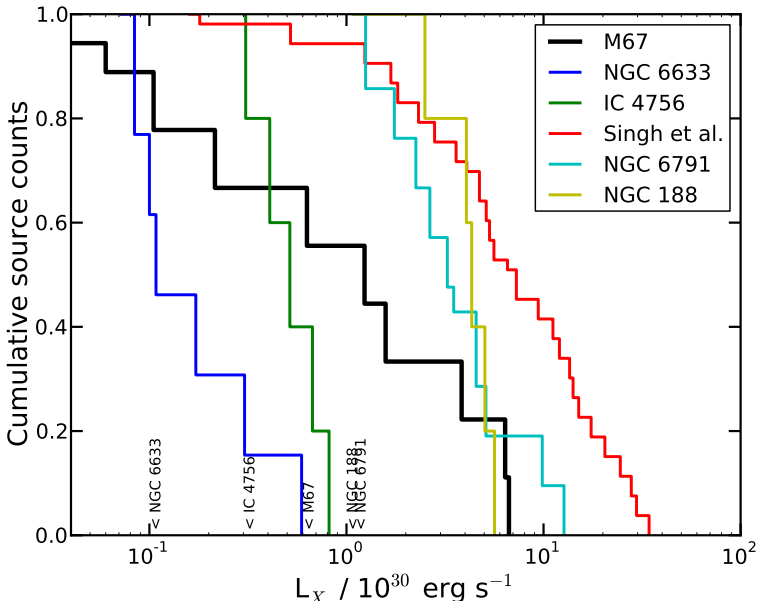

Figure B.8: The X-ray luminosity functions for RS CVn-type sources in different star clusters. The sensitivity threshold for different star clusters below which the source counts are incomplete are shown at the bottom. See §B.5.1.1 for details.

the other four systems were recognized members of M67, NX61 had been assigned unknown membership probability in van den Berg et al. (2004). Here, we confirm NX61 to be a member. Out of the five contact binary systems, three lie close to the M67 main-sequence turnoff, while two lie along the main sequence (Figure B.3).

B.5.4 Cataclysmic Variables

Cataclysmic variables (CVs) are short-period (majority have orbital periods of a few hours) binaries comprising of an accreting white dwarf primary, and a secondary donor star which is typically low-mass main sequence. The white dwarf distorts the secondary, leading to Roche-lobe overflow, and may form an accretion disk around the white dwarf depending on the magnetic field of the white dwarf. X-rays from CVs result primarily due to the mass transfer (e.g. Kuulkers et al. 2006), and the resulting accretion disk or accretion column and the heating of the white dwarf surface, thus giving a soft blackbody and a hard shock-heated plasma component in the X-ray spectrum.

Belloni et al. (1998) argued that RX35=NX73 is a cataclysmic variable since its position in the color-magnitude diagram can arise when a main-sequence star is accompanied by a hot white dwarf, and the hardness of the X-ray spectrum suggests an accreting white dwarf. None of the orbital parameters are known for this system. The Belloni et al. position on the $V/B-V$ plot was towards the left of the main sequence, based on the $B-V$ color of 0.38 from Sanders (1977). However, from EIS we have the $B-V$ color as

0.79, which is consistent with Yadav et al. (2008) and Montgomery et al. (1993). It is possible that the Sanders (1977) photometry is erroneous, and that this source is not a CV. Our hardness ratios for NX73, $HR1 = 0.66 \pm 0.20$, HR2=–0.48 ± 0.30, do not show soft and hard components, arguing against the CV hypothesis.

We also detect the well-known AM Her-type CV in the M67 field, EU Cnc (NX42=RX16=CX57). It is not related with M67, but we discuss about EU Cnc briefly here. Although ROSAT detected this CV only below 0.4 keV, van den Berg et al. (2004) find a relatively high hardness ratio. In our XMM detection, the hardness ratios are $HR1 = -0.50 \pm 0.33$, $HR2 = 0.23 \pm 0.46$, consistent with the high hardness ratio. As stated above, the hard and soft X-rays are believed to come from shocks in the accretion stream and the heated surface of the white dwarf respectively (e.g. Kuulkers et al. 2006). X-ray emission comprising of soft as well as hard components is typical of polars. Using a thermal brehmsstrahlung spectrum (0.1 keV), we can convert the observed countrate of NX42 into an X-ray luminosity of 2.1×10^{29} erg s^{-1}. This is a factor of two lower than the value reported by van den Berg et al..

B.5.5 Blue and Yellow Stragglers, Peculiar Stars

Blue stragglers are bluer and more luminous than stars that are evolving off the main-sequence (turnoff). Several mechanisms have been suggested for the formation of blue stragglers, including stellar collisions and mass transfer in binaries (Stryker 1993). X-rays from these systems are likely due to magnetic / chromospheric activity (e.g. van den Berg et al. 2001) resulting from spin up in a binary.

Three blue stragglers have been known to be X-ray emitters (CX3=RX4,CX94,CX95). We do not detect any of these even though they are within the XMM fov. CX3 is in a 1.1 d orbit for the inner binary of a possible triple system (Goranskij et al. 1992; van den Berg et al. 2001). van den Berg et al. (2000) find the spectral type to be F5IV, and van den berg 2001 suggest that the X-ray emission could be due to magnetic activity in the rapidly rotating subgiant. CX94 was noted as a blue straggler in Sandquist & Shetrone (2003), but with the EIS $B-V$ color, we find that it is well within the main sequence, but close to turnoff. van den Berg et al. (2004) noted that CX94 shows no radial-velocity variations over six observations spanning 3923 days. CX95 is a blue straggler with a 4913 d orbit and eccentricity of 0.3. The primary has spectral type F6V and a projected rotation speed, v $sin(i) \simeq 20$ km s^{-1} (Latham & Milone 1996; Liu et al. 2008). van den Berg et al. postulate that CX95 could have an undetected close binary, hence explaining the X-ray emission. Both, CX94 and CX95 are below our XMM detection thresholds.

We have detected three yellow stragglers (NX5,NX16,NX24) previously identified by Belloni et al. (1998). NX5=RX10=CX6 is known to be a binary with a G4 giant and a cool white dwarf. The system has Ca II H,K emission lines Pasquini & Belloni (1998). The binary is in a 43 d circularized orbit. The orbital circularization suggests that strong tidal forces exist between the two components of the system, but the fact that the white dwarf is cool precludes mass transfer. NX16 and NX24 have measured orbital periods of 1495 d and 698 d, and eccentricities 0.32 and 0.11 respectively. This precludes, strong tidal interaction,

and the X-ray emission from these stars is not well understood.

NX4=RX8=CX1 lies about one mag below the subgiant and giant branches in the $V/B-V$ diagram (Figure B.3). The X-ray spectrum and variability suggest that the emission is coronal.

B.5.6 New Member NX75 and Other Members

We have detected a new member of M67, NX75, associated with the V=15 mag optical counterpart, E4630. Unfortunately, orbital parameters and well-constrained hardness ratios are not available for NX75. However, we are able to estimate the spectral type of this source as K4V and distance of 860 pc based on archival multiwavelength photometry. It is possible that this source is an RS CVn-type system. Optical spectroscopy will be useful for understanding chromospheric activity in this star (through the Ca H & K emission lines), and radial velocity monitoring is necessary for deriving the orbital parameters.

There are several other M67 X-ray members that do not have any orbital information or any assigned class. NX45=RX46, CX67, CX73, and CX94 lie along the F/G/K main sequence and are known binaries with undetermined orbital solutions. NX 45 has a spectral type G0V and is close to the main-sequence turnoff in Figure B.3. NX62=RX54, CX62, CX73, CX77, CX80, CX82 lie along the M dwarf part of the main sequence of M67. These members are possibly spun-up binaries with active chromospheres where both members are main sequence stars.

B.6 SUMMARY

We have processed archival data from two XMM-Newton observations of the old open cluster, M67. We have used the updated cluster member list from Yadav et al. (2008) and Vereshchagin et al. (2014) to find 21 X-ray cluster members. Twenty of these have been detected in previous observations of M67 with Chandra (van den Berg et al. 2004) and ROSAT (Belloni et al. 1993, 1998), and one is a newly-detected member. We have also tested the X-ray source lists from Chandra and ROSAT for membership to compile an updated list of 42 X-ray members of M67 (Table B.3). Sixteen X-ray members are likely to be RS CVn or related binaries with circularized or near-circularized orbits having periods $P_{orb} \lesssim 10$ d. We also detected five contact binaries with $P_{orb} \lesssim 0.5$ d. X-ray emission from three yellow stragglers and two blue stragglers detected in the XMM-Newton observations is not well understood. Another peculiar source, HU Cnc, lies below the intersection of the subgiant and red giant branches in the HR diagram (Figure B.3), and may be a coronal emitter. Fourteen X-ray members do not have any definitive classification; some of these are known binaries with undetermined orbital solutions. Spectroscopic followup and radial velocity monitoring will be useful for elucidating the nature of these sources. A multiwavelength study of the X-ray members of M67 and other clusters will give insight into the coronal and chromospheric emission processes at different frequencies and also binary evolution processes. We already have an existing program to study the ultraviolet emission from M67 members and compare it with their X-ray emission (Subramaniam et al., in prep). Finally, we have

studied the X-ray luminosity function of RS CVn-type systems from M67 in comparison with that of other intermediate-to-old open clusters (Figure B.8). We see an increased number of higher luminosity stars in the older clusters which may suggest that more active binary systems and active stars are produced with aging of clusters. Sensitive X-ray observations of intermediate-to-old star clusters are encouraged in order to find fainter sources and thus extend the RS CVn luminosity functions to the faint end and also derive the luminosity function for other classes of X-ray sources.

ACKNOWLEDGMENTS

KM would like to thank Himali Bhatt and Dom Walton for useful discussions and guidance on X-ray data processing. This research has made extensive use of Vizier, SIMBAD, and SDSS.

Bibliography

Baldi A., Molendi S., Comastri A., et al. 2002, ApJ, 564, 190

Belloni T., Verbunt F., Schmitt J. H. M. M. 1993,A&A, 269, 175

Belloni T., Verbunt F., Mathieu R.D. 1998, A&A, 339, 431

Briggs, K. R., Pye, J. P., Jeffries, R. D. & Totten E. J. 2000, MNRAS, 319, 826

Cruddace R., Hasinger G., Schmitt J. 1988, in F. Murtagh, A. Heck (eds.), Astronomy from large databases, p. 177

Charles P. & Seward F. 1995, Exploring the X-ray Universe (Cambridge University Press), p.

Evans, I. N., Primini, F. A., Glotfelty, K. J. et al 2010 ApJS, 189, 37

Fan X., Burstein D., Chen J. S., Zhu J. et al. 1996, AJ, 112, 628

Feigelson, E. .D. & Babu, J. B. 2012 Modern Statistical Methods for Astronomy, Cambridge University Press

Friel E. D. 1995, ARA&A, 33, 381

Gilli, R., Comastri, A. & Hasinger, G. 2007, A&A, 463, 79

Girard, T. M., Grundy, W. M., Lopez, C. E., et al. 1989, AJ, 98, 227

Gondoin, P. 2005, A&A, 438, 291

Gökay, G., Gürol, B. & Derman, E., 2013, AJ, 146, 123

Goranskij, V. P., Kusakin, A. V., Mironov, A. V., et al. 1992, A&AT, 2, 201

Gudel M. 2004, A&A, 12, 71

Jansen F., Lumb D., Altieri B., Clavel J., Ehle M., Erd C., Gabriel C., Guainazzi M. et al. 2001, A&A, 365, 1

Jester, S., Schneider, D., Richards, G. et al. 2005, arXiv:astro-ph/0506022

Johnson, H. 1966, ARA&A, 4, 193

Kuulkers, E., Norton, A., Schwope, A., et al. 2006, in Compact stellar X-ray sources, 39, 421

Latham, D. W., Mathieu, R. D., Milone, A. A. E. et al. 1992, Proceedings of the IAU Symposium 1991, 151, 471

Latham, D. W. & Milone, A. A. E. 1996, ASPC, 90, 385

Latham, D., Highlights of Astronomy, 14, 444

Liu, G. Q., Deng L. & Chavez M. 2008, MNRAS, 390, 665

Mathieu, R. D., Latham, D. W., Griffin, R. F. et al. 1990, AJ, 100, 1859

Momany Y., Vandame B., Zaggia S., Mignani, R. P. et al. 2001, A&A, 379, 436

Montgomery K. A., Marschall L. A., Janes K. A. 1993, AJ, 106, 181

Pallavicini, R. 1989, A&ARv, 1, 177

Pasquini, L. & Belloni, T., 1998, A&A, 336, 902

Randich S. 1997, in Cool stars in clusters and associations: magnetic activity and age indicators, ed. G. Micela, R. Pallavicini, S. Sciortino Vol. 68, 971

Sanders W. L. 1977, A&AS, 27, 89

Sandquist, E. L. & Shetrone, M. D. 2003, AJ, 125, 2173

Sarajedini, A., von Hippel, T., Kozhurina-Platais, V., et al. 1999, AJ, 118, 2894

Singh, K. P., Drake, S. A. & White, N. E. 1996, ApJ, 111, 2415

Strüder L., Briel U., Dennerl K., Hartmann R., Kendziorra E., Meidinger N., Pfeffermann E., Reppin C., 2001, A&A, 365, 18

Stryker, L. L. 1993, PASP, 105, 1081

Turner M. J. L., Abbey A., Arnaud M., Balasini M., Barbera M., Belsole E., Bennie P. J., Bernard J. P. et al., 2001, A&A, 365, 27

van den Berg M., Verbunt, F., & Mathieu, R. D., et al. 2000, ASP Conference Series, 198, 503

van den Berg M., Orosz, J., Verbunt, F. & Stassun, K. 2001, A&A, 375, 375

van den Berg M., Tagliaferri G., Belloni T., Verbunt F. 2004, A&A, 418, 509

van den Berg M., Verbunt, F., Tagliaferri, G., et al. 2013, ApJ, 770, 98

van den Berg M. 2013, ASP Conference Series, Vol. 470. San Francisco: Astronomical Society of the Pacific

Verbunt F., 1999, Highlights in X-ray astronomy, ed. Bernd Aschenbach & Michael J. Freyberg, Garching

Vereshchagin S. V., Chupina N. V., Sariya D. P., et al. 2014, arXiv:1403.2532

Watson M. G., Schröder A. C., Fyfe D., et al. 2009, A&A, 493, 339

Yadav R.K.S., Bedin L.R., Piotto G., Anderson J., Cassisi S., Villanova S., Platais I., Pasquini L., Momany Y., Sagar R. 2008, A&A, 484, 609

Zamorani G., Mignoli M., Hasinger G. et al. 1999, A&A, 346, 731

Zhao J. L., Tian K. P., Pan R.S., He Y. P., Shi H. M. 1993, A&AS, 100, 243